1. Report No. FHWA/TX-15/0-6722-1	2. Government Accession No.	3. Recipient's Catalog No.
4. Title and Subtitle SPREAD PRESTRESSED CONCRETE SLAB BEAM BRIDGES		5. Report Date Published: April 2015
		6. Performing Organization Code
7. Author(s) Mary Beth D. Hueste, John B. Mander, Tevfik Terzioglu, Dongqi Jiang, and Joel Petersen-Gauthier		8. Performing Organization Report No. Report 0-6722-1
9. Performing Organization Name and Address Texas A&M Transportation Institute College Station, Texas 77843-3135		10. Work Unit No. (TRAIS)
		11. Contract or Grant No. Project 0-6722
12. Sponsoring Agency Name and Address Texas Department of Transportation Research and Technology Implementation Office 125 E. 11th Street Austin, Texas 78701-2483		13. Type of Report and Period Covered Technical Report: September 2011–August 2014
		14. Sponsoring Agency Code
15. Supplementary Notes Project performed in cooperation with the Texas Department of Transportation and the Federal Highway Administration. Project Title: Precast Prestressed Concrete Spread Slab Beam Bridges URL: http://tti.tamu.edu/documents/0-6722-1.pdf		

16. Abstract

TxDOT uses prestressed slab beam bridges for short-span bridges ranging from approximately 30–50 ft in length. These bridges have precast, pretensioned slab beams placed immediately adjacent to one another with a cast-in-place slab made composite with the beams. While these bridges are used extensively, they are more expensive than traditional prestressed I-beam structures on a per-square-foot basis. The objective of this project was to investigate the use of slab beams that are spread apart with precast panel stay-in-place forms between beams and a cast-in-place concrete deck, and to develop appropriate design guidelines for this alternate spread slab beam bridge system.

The project objectives were met through a series of tasks. The research team reviewed the relevant literature and the current state of the practice. Preliminary designs were developed to assess the potential of a spread slab beam bridge system. A full-scale spread slab beam bridge was constructed at the Texas A&M University Riverside Campus and tested to assess constructability, in-service performance, and behavior. Field testing was conducted for the Riverside Bridge and a US 69 on-system bridge to evaluate load distribution behavior and to provide data to guide analytical modeling of this bridge system. Additional analytical models were developed to investigate an array of possible bridge geometries and load sharing behavior. Based on these models, recommendations were developed for load distribution factor relationships for the design of spread slab beam bridges.

17. Key Words Precast Prestressed Concrete, Bridge Girders, Spread Slab Beams, Load Distribution Factors		8. Distribution Statement No restrictions. This document is available to the public through NTIS: National Technical Information Service Alexandria, Virginia 22312 http://www.ntis.gov	
19. Security Classif. (of this report) Unclassified	20. Security Classif. (of this page) Unclassified	21. No. of Pages 406	22. Price

Form DOT F 1700.7 (8-72) Reproduction of completed page authorized

SPREAD PRESTRESSED CONCRETE SLAB BEAM BRIDGES

by

Mary Beth D. Hueste, Ph.D., P.E.
Research Engineer
Texas A&M Transportation Institute

John B. Mander, Ph.D.
Research Engineer
Texas A&M Transportation Institute

Tevfik Terzioglu
Graduate Research Assistant
Texas A&M Transportation Institute

Dongqi Jiang
Graduate Research Assistant
Texas A&M Transportation Institute

and

Joel Petersen-Gauthier
Graduate Research Assistant
Texas A&M Transportation Institute

DISCLAIMER

This research was performed in cooperation with the Texas Department of Transportation (TxDOT) and the Federal Highway Administration (FHWA). The contents of this report reflect the views of the authors, who are responsible for the facts and the accuracy of the data presented herein. The contents do not necessarily reflect the official view or policies of the FHWA or TxDOT. This report does not constitute a standard, specification, or regulation. This report is not intended for construction, bidding, or permit purposes. The researcher in charge of the project was Mary Beth D. Hueste, Ph.D., P.E. (TX 89660).

ACKNOWLEDGMENTS

TABLE OF CONTENTS

LIST OF FIGURES

LIST OF TABLES

xviii

1   INTRODUCTION

1.1   BACKGROUND

Precast prestressed concrete girders have been used effectively in Texas and other states for over 60 years. The majority of these prestressed concrete bridges are simply supported spans where the cast-in-place (CIP) deck slab is made composite with precast pretensioned girders. Currently, the use of precast prestressed concrete girders provides economical bridges for short to medium spans.

Slab-on-girder bridges with medium spans ranging from 50 to 150 ft are typically constructed by seating the precast prestressed girders on bearing pads on the piers or abutments and then casting a concrete deck on top of the girders. Although different types of decks have been constructed over the years, decks in Texas are typically currently constructed to be 8 in. thick and consist of 4 in. thick stay-in-place precast prestressed concrete panels (PCPs) that are placed to span between girders with an additional 4 in. thick CIP two-way reinforced concrete topping slab.

For shorter span lengths, up to 50 ft in length, a variety of alternatives exist to the standard I-girder design. The Texas Department of Transportation (TxDOT) often uses prestressed concrete slab beam bridges as a common alternative, as shown in Figure 1.1(a). The conventional approach consists of placing the slab beams side by side and casting a 5 in. CIP reinforced concrete deck on top of the slab beams. This shallow bridge superstructure system is attractive in locations where there is a low clearance below the bridge. However, conventional slab beam bridges are more expensive compared to standard I-girder bridges that are constructed using PCPs as stay-in-place formwork between girders.

To address this issue, TxDOT has shown interest in exploring new bridge systems that may provide more economical solutions for short-span bridges. One such idea that has been developed by TxDOT is to modify the current short-span bridge design that uses immediately adjacent prestressed concrete slab beams, as shown in Figure 1.1(a). The proposed solution is to spread out the slab beams and to use a conventional topped panelized deck, as shown in Figure 1.2. It is anticipated that spread slab beam bridges will result in a possible reduction in the overall bridge cost while providing another design alternative for short-span bridges. Figure 1.2(b) shows a typical cross-section of a spread slab beam bridge superstructure.

For spread slab beam construction, the moments imposed by eccentrically located truck loads will differ in the individual slab beams across the overall bridge deck cross-section. Appropriate girder load distribution factor (LDF) formulas for this case are not available in the *American Association of State Highway and Transportation Officials (AASHTO) LRFD Bridge Design Specifications* (AASHTO 2012) and need to be investigated. While this study aimed to improve the overall economy of the proposed spread slab beam deck configuration, the principal research focus was directed toward developing recommendations for this bridge type, with a particular emphasis on establishing appropriate LDFs for this class of spread slab beam bridges.

1.2   SIGNIFICANCE

Bridges built using prestressed concrete girders topped with PCPs as stay-in-place formwork and a CIP reinforced concrete deck provide an economical approach for bridge construction. Designers and contractors are still investigating the possibilities of building prestressed concrete bridges with greater economy. There are several ways of reducing the overall cost of a bridge. This research focused on reducing the number of girder lines for slab beam bridges.

TxDOT already utilizes slab beam bridges for short-span bridges up to 50 ft in length. While conventional slab beam bridges are used extensively, experience shows they are more expensive than traditional slab-on-I-girder structures on a per-square-foot basis. Spread slab beam bridges use the same idea as I-girder bridges by spreading the slab beams to reduce the overall cost of that type of bridge. This research investigated the potential of the spread slab beam bridge systems, evaluated the constructability and in-service performance, and developed design recommendations with a focus on appropriate relationships for load distribution factors.

1.3   OBJECTIVES AND SCOPE

The objective of this project was to explore the use of slab beams that are used in a spread configuration for short-span bridges and to provide appropriate design recommendations. Finally, field investigations were undertaken to experimentally observe load distribution factors under static and dynamic truck loading. Two bridges were used for this purpose, the first with widely spaced slab beams constructed at the Texas A&M University (TAMU) Riverside Campus as part of this research, and a second bridge (US 69 overpass over Day Street in Denison, Texas)

with closely spaced slab beams. The purpose of these field studies was to evaluate the in-service performance and to measure the shear and moment LDFs during controlled load tests. The development of LDFs for slab beam bridges is achieved using appropriate models that are calibrated with field measurements and exploring the design space to determine appropriate load sharing relationships for this class of bridges.
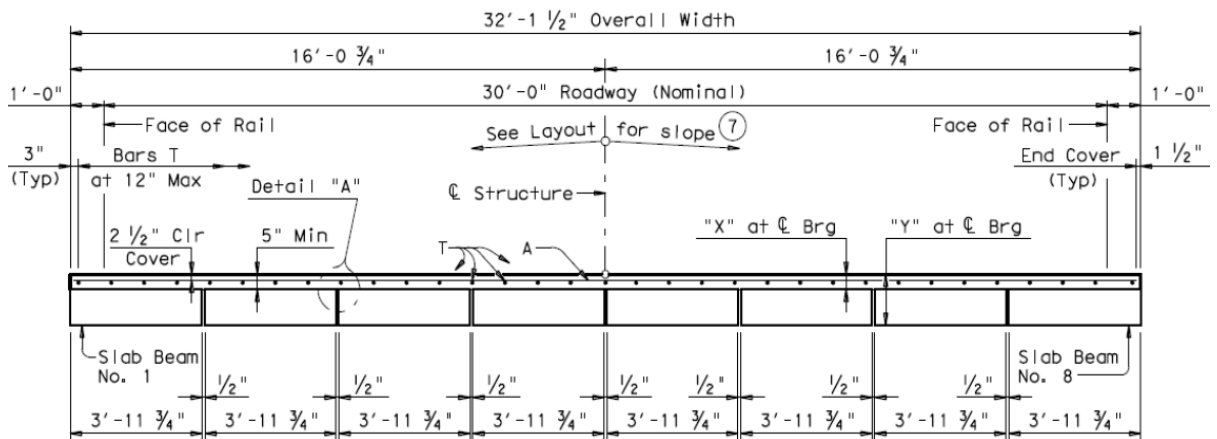
(a) Conventional Prestressed Concrete Slab Beam Bridge Design
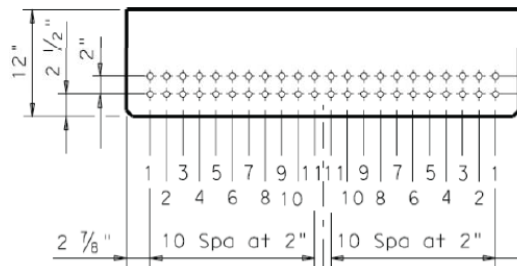
(b) 4SB12 Slab Beam Prestressing Locations
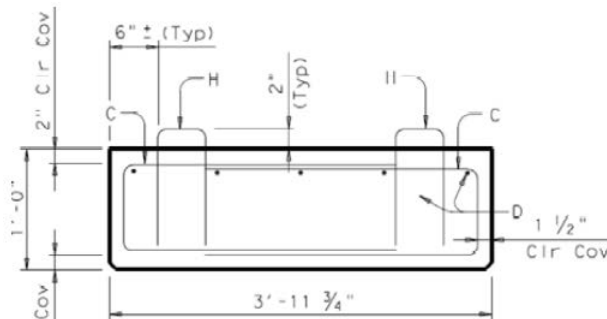
(c) 4SB12 Slab Beam Mild Steel Reinforcing

Figure 1.1. Typical Details of Prestressed Concrete Slab Beams and Bridge Deck (TxDOT 2013b).

PRESTRESSED CONCRETE SPREAD SLAB BEAMS

Bars P over exterior beams are still required when no overhang is used. In this case, only one Bar D, 2" from slab edge, is required.
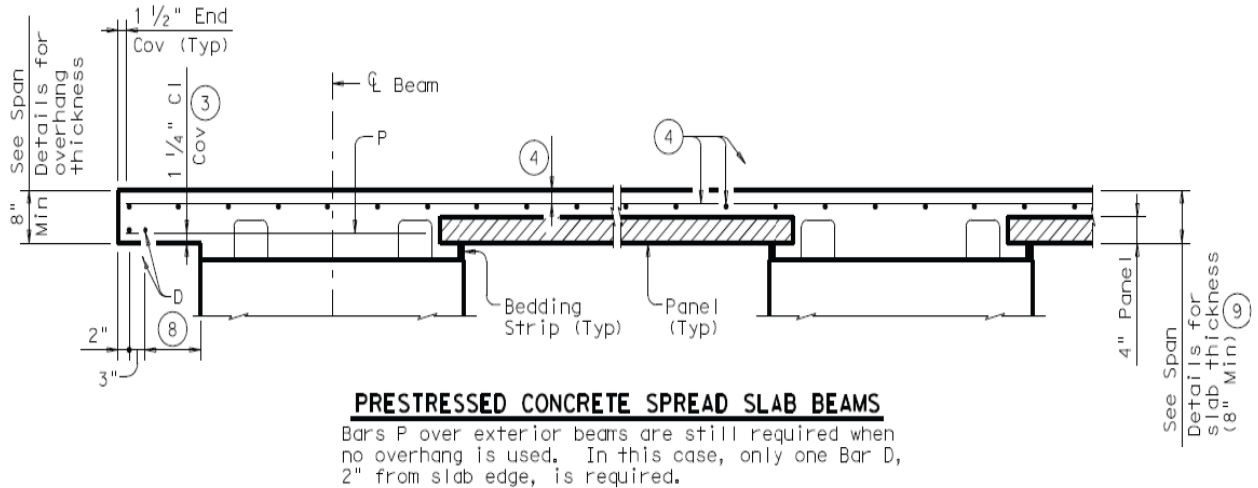
(a) Bridge Deck with PCPs
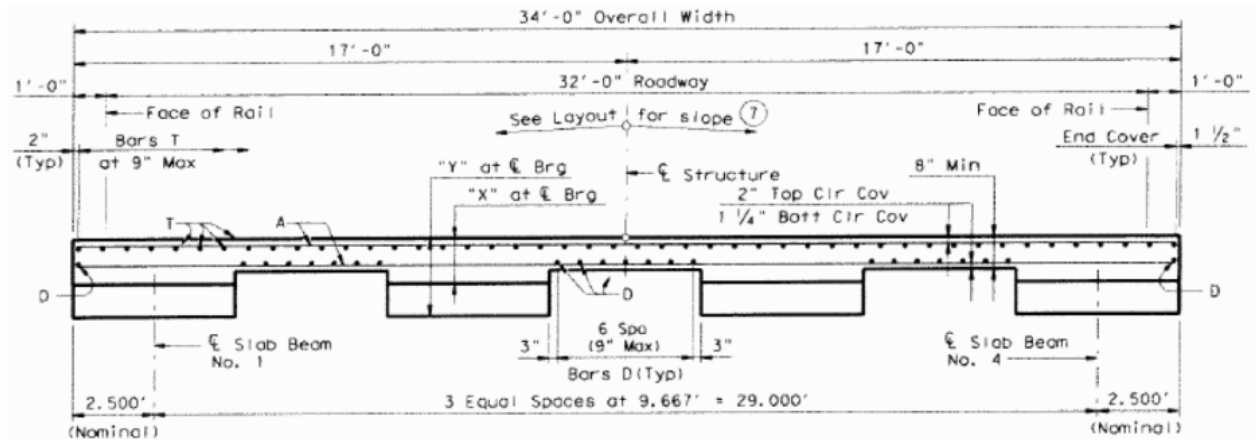
(b) Transverse Section with Fully Cast-in-Place Deck

Figure 1.2. Recent TxDOT Bridge Design Details for Spread Slab Beam Bridges (TxDOT 2013b).

1.4   RESEARCH PLAN

The major objective of this research was to explore the possibility of using slab beams in a spread configuration in order to provide an alternative bridge type for TxDOT for short-span bridges that are potentially more economical than conventional slab beam bridges. The research included experimental assessment of spread slab beam systems by testing a full-scale field bridge and monitoring an existing in-service bridge. The bridge data were used to confirm the modeling approach for this bridge configuration. Appropriate live load distribution factors for spread slab beams were developed based on analytical models representing the design space for this bridge

4

type. The proposed LDFs were compared with the AASHTO LRFD Specifications (2012) spread box beam LDF formulas to investigate their applicability to spread slab beam bridges.

The following work plan was carried out in order to achieve the objectives of the project. The work plan consisted of eight tasks, and the details of each task are described herein.

1.4.1 Synthesize Literature and State of the Practice

The research team compiled a comprehensive literature review related to development of live load distribution factors and available methods of analysis. The comprehensive review includes papers published in journals and conferences, along with agency reports. Very limited information is available in the literature specifically for spread slab beam bridges; however, researchers found some information for spread box beam bridges. Key findings of the literature review were documented. These findings were used in this study to guide the development of the experimental program along with determination of appropriate live load distribution factors.

1.4.2 Preliminary Designs

Preliminary designs were carried out using the AASHTO LRFD Specifications (2012) and the design guidelines provided in *TxDOT Bridge Design Manual* (TxDOT 2013a) to ensure that the findings could be compared with typical slab beam bridge geometries and standard designs. This comparison provided initial assessment of the potential benefits of a spread slab beam configuration. Material properties, standard slab beam types, and common Texas bridge widths were selected based on input from TxDOT.

Viable spread slab beam bridge geometries were chosen according to practical beam spacing and bridge width criteria. A total of 44 spread slab beams were designed using the maximum permissible concrete design strength. One of the preliminary designs with a large eccentricity due to a wide beam spacing and a relatively longer span length was chosen for the full-scale bridge construction and field testing. This report documents the detailed design of that bridge (34 ft wide, 46 ft 7 in. long, using four 5SB15 slab beams).

1.4.3 Full-Scale Bridge Field Test

A full-scale spread slab beam bridge was constructed and field tested at the Texas A&M University Riverside Campus. The final bridge geometry was determined based on the preliminary designs and input from the TxDOT Project Monitoring Committee (PMC). The

spread slab beam bridge has a 46 ft 7 in. (center to center of bearing pads) span, 34 ft width, 9 ft 8 in. center-to-center beam spacing, and four 5SB15 slab beams.

The slab beam girders were produced by Bexar Concrete Works in San Antonio, Texas. Numerous samples were taken from the concrete mixes used to construct the precast girders to test various mechanical properties of the girder concrete. The girders were transported to Riverside Campus and erected on the bridge supports that were constructed in advance such that the top of the bridge would be even with the existing runway. Then PCPs were placed between slab beam girders as stay-in-place formwork. After placing the precast components, a reinforced concrete CIP deck was placed on top of the slab beams. The concrete mixture for the deck concrete was also sampled in order to measure and document the fresh and hardened properties.

The full-scale Riverside Bridge was fully instrumented to evaluate the bridge response under service loads. Load cells that were placed at the abutment seats at both ends of slab beams were used to monitor the load sharing between girders. Measured reactions were used for validating the analytical model and determining experimental live load distribution factors for shear. Deflection measurements along the length of each beam at frequent intervals were obtained using string potentiometers. Moments at the midspan of each beam were then inferred using the deflection profiles of the slab beams. In addition, accelerometers were installed to measure the modal characteristics of the bridge. Measured deflection profiles and frequency response were used for verification of the bridge models developed using the finite element method (FEM)

Secondary instrumentation was also installed for verification of instrumentation methods that could be deployed for field testing. Strain gages were installed at the midspan to infer moment LDFs through variation of strains between girders. Calculated moment LDFs were then compared with those calculated from deflection profiles measured using string potentiometers. Linear variable displacement transducers (LVDTs) were used at the supports to measure bearing pad deformation to infer variation of the reactions between girders. The calculated shear distribution factors were compared with those based on the direct load cell measurements. The different instrumentation systems were assessed for accuracy and deployability for use in field measurements of the in-service US 69 Bridge.

The static and dynamic loading of the bridge was achieved using a Texas A&M Transportation Institute (TTI) dump truck and TTI water tanker with known axle weights.

Vehicles were placed statically at critical moment and shear locations for investigating the LDFs and evaluating the bridge response. The same vehicles were also driven along the predefined lanes at speeds from 30 to 40 mph. The measured response was used to evaluate the appropriateness of different analytical models and to validate the chosen finite element modeling technique.

1.4.4 Field Monitoring of an In-Service TxDOT Bridge

A recently constructed spread slab beam bridge on US 69 North in the city of Denison, Texas (Grayson County), was temporarily instrumented and monitored to evaluate the response under vehicular live load. This test provided another opportunity for testing the in-service performance of spread slab beam bridges. The US 69 northbound bridge is 48 ft 7 in. long, 38 ft wide, and uses six 5SB15 slab beams with a 16 in. clear spacing between slab beams, which is significantly less than the 56 in. clear spacing for the Riverside Bridge. This difference is useful for bounding the potential variation of beam spacing, which is one of the important parameters impacting the load distribution factors.

The experimental program at the US 69 Bridge provides insight for a bridge system with more closely spaced slab beams. The instrumentation included strain gages, LVDTs, string potentiometers, and accelerometers. All six beams of the northbound bridge were instrumented. The bearing pad deflections obtained using LVDTs at the bearing pad level were used to infer shear distribution factors between girders. Strain gages were installed at approximately midspan on the bottom surface of the slab beams and on the top surface of the deck to determine flexural distribution factors. String potentiometers were also installed to measure the deflection profiles of the girders. The frequency response of the bridge was also obtained using the accelerometer data.

The research team evaluated the load sharing between slab beams under static and dynamic loading using a TxDOT dump truck with known individual axle weights. Static loading was applied at critical moment and shear locations to create the most adverse conditions. Experimental live load shear and moment distribution factors were calculated from the measured response. The experimental measurements were also used to validate the analytical modeling approach.

1.4.5 Analysis of Field Testing and Field Monitoring Results

All instrumentation readings from the Riverside Bridge and US 69 Bridge tests were digitally recorded using a PC-based data acquisition system. The measured experimental results were processed and reviewed to better understand the in-service response of the spread slab beam system. The measured data were processed to obtain moment and shear distribution factors. The load sharing between slab beam girders for flexural and shear responses was obtained. In addition, deflection profiles in the longitudinal directions of each girder and the frequency response of the bridge were also obtained. The measured response was then used to validate the finite element analytical models.

1.4.6 Live Load Distribution Factors

Designing a bridge girder requires computing the moment and shear demands for an individual girder. Calculating the response of an individual bridge girder to a vehicular live load is a complex task due to coupled transverse and longitudinal effects. This complexity stems from the variation of girder spacing, span length, vehicle positions, etc. Designers and bridge design specifications simplify the problem by uncoupling the transverse and longitudinal effects using live load distribution factors. The AASHTO LRFD Specifications (2012) lists LDFs for several standard bridge types and their applicable ranges. Because slab beam girders are TxDOT girder types, AASHTO LRFD Specifications (2012) does not have approximate LDFs for spread slab beam bridges. However, spread box beam LDF formulas are provided by AASHTO LRFD Specifications (2012). As part of this research, the AASHTO LRFD Specifications (2012) spread box beam formulas were reviewed for their applicability to spread slab beam bridges. Total bridge spans between 31–52 ft (back wall to back wall) and girder spacings from 6.5–11 ft (center to center) were investigated for evaluating the LDFs. Load distribution factors were obtained for 31 spread slab beam bridges having different geometries using FEM techniques that were validated with experimental results. The research team provides recommendations for LDFs that may be used for design of spread slab beam bridges.

1.4.7 Report Preparation

A compete research report and a project summary report have been written to document the findings of this research. The above listed tasks and related findings are reported herein. This report includes (a) a comprehensive synthesis of literature and the current state of the practice,

(b) preliminary designs for spread slab beam bridges, (c) construction and results of the full-scale bridge field test, (d) results of field monitoring of an in-service TxDOT bridge, (e) analysis of experimental and field monitoring results, (f) results of analytical studies to evaluate the AASHTO LRFD Specifications (2012) live load distribution factors, and (g) recommended design guidelines and a detailed example.

1.5   OUTLINE

Following this introductory chapter, Chapter 2 provides a comprehensive literature review related to slab beam bridges, current analysis methods, and live load distribution factors. Relevant journal papers and reports are summarized within the chapter. Chapter 3 describes all preliminary designs that were investigated to evaluate spread slab beam bridges in terms of ranges of applicability of critical parameters, including beam spacing, span length, and girder depth. Also, the field bridge geometry was selected using these preliminary designs. Chapter 4 and Chapter 5 document the experimental program for the Riverside Bridge and the US 69 Bridge, respectively. Analyses of the experimental results are also provided in these chapters. Chapter 6 outlines the current analytical methods for modeling bridges and evaluates the results for the Riverside Bridge and US 69 Bridge models by comparing them to experimental results. Chapter 7 discusses the methods for deriving the current LDFs found in the AASHTO LRFD Specifications (2012) and derivation of new LDFs for spread slab beam bridges following a similar methodology. Chapter 8 presents a summary, conclusions, design recommendations, and recommendations for future research. Appendix A presents a detailed design example for a typical interior prestressed slab beam in a spread slab beam bridge based on the AASHTO LRFD Specifications (2012) and the *TxDOT Bridge Design Manual* (TxDOT 2013a). The designed bridge geometry is the same as the Riverside Bridge. Appendix B summarizes the Riverside Bridge construction process. Appendix C provides tabular summaries of the load distribution factor results used for derivation of the proposed load distribution factor formulas. Appendix D presents additional details and findings from the verification of the instrumentation used to measure bridge response in the field. A complete set of drawings for the Riverside Bridge, along with as built information, is provided in the Supplement to this report.

2   LITERATURE REVIEW

2.1   BACKGROUND

Several early studies have focused on developing more economical precast concrete bridge types for short-span bridges. TxDOT sponsored a research study conducted by Panak (1982). This study indicated that prestressed I-beams with cast-in-place slabs and pan girder slabs were the most economical and common bridge types in Texas in the 1960s and 1970s. In 1969 Texas was the first state to use side-by-side precast box beam bridges. In those days, the cost of box beam bridges was significantly higher than the other two bridge types. Panak proposed five alternative precast superstructure types including precast concrete box beams, Precast/Prestressed Concrete Institute (PCI) box beams, precast concrete double tee beams, precast concrete voided slabs, and precast concrete solid slabs. Unfortunately, none of these alternatives provided more economical solutions in the 1980s due to lack of economical manufacturing and construction techniques and lack of competition within the precast industry.

The Louisiana Department of Transportation (DOT) sponsored a research investigation focused on reducing the cost of short-span bridges with spans up to 50 ft (McKee and Turner 1975). The study investigated superstructure options that can be erected rapidly while using the erected portions as working platforms. The designs were limited to a 100 ton crane capacity. Several popular precast girder types including voided slabs, channels, and box sections were designed. However, designers indicated that these new designs did not appear to provide more economical solutions. It was concluded that substantial progress in both manufacturing and construction procedures, along with increased competition in the industry, was needed to reduce costs.

Substantial progress has been made in both the construction and precast manufacturing industry during the last 30 years. Also, there have been some changes to the design criteria that impact the design of prestressed concrete bridge structures. Currently, slab beam bridges are used extensively due to their ease of fabrication and transport, along with constructability. However, they are more expensive than traditional prestressed I-beam and I-girder bridges because the slab beams are placed immediately adjacent to one another. As such, the proposed spread prestressed slab beam bridge system presents a timely opportunity to revisit this important class of bridge structures with the goal of increasing the economy of short-span bridges.

One key issue for developing a new bridge superstructure system is identifying appropriate live load distribution factors (LDFs). Although there are other viable methods of analysis for calculating moment and shear demands, such as the grillage and the finite element method (FEM), bridge design engineers prefer using approximate LDFs that are provided in the *AASHTO LRFD Bridge Design Specifications* (AASHTO 2012) for several bridge superstructure types. There are no approximate formulas provided for spread slab beams; thus, as part of this study, researchers sought to determine whether the spread box beam formulas might also be applicable to spread slab beams.

The main topics covered by this literature review include the history of the *S*/*D* LDFs used from the 1930s until 1996 in the *AASHTO Standard Specifications for Highway Bridges* (AASHTO 1996; Newmark 1938). The development, use, and assessment of modern bridge LDFs (AASHTO 1994a; AASHTO 2012) are also summarized herein. Analytical models are also discussed, including the FEM and grillage methods of analysis that were used in conjuncture with LDFs to accurately determine and confirm load distribution.

2.2   LIVE LOAD DISTRIBUTION FACTORS

2.2.1   Historical Development of *S*/*D* LDFs (1931–1996)

Newmark (1938) developed the first empirical load distribution factor formulas. After that time, Newmark's LDFs were used without any major changes by AASHO (later to become AASHTO) in all AAHTO Standard Specifications until the 16th edition (AASHTO 1996). These original LDFs, often termed the "*S*-over" equations, were used to estimate the design moments and shears applied to individual beams within a bridge. The LDFs were found by the calculation of *S*/*D*, where *S* is the spacing between girders and *D* is a specified value that depends on the type of bridge. For example, a bridge constructed with a concrete deck on spread girders and having two or more lanes of traffic has a *D* value of 5.5. The *D* constant was originally taken as being the distance between wheels of the HS20 design truck, which is 6 ft, but was altered for increased accuracy.

Figure 2.1 lists the *D* values for several pertinent bridge types, where *S* is in feet (AASHTO 1996). When load distribution is considered in this way, it is easy to understand and utilizes the most important parameter, the girder spacing, within a simple formula. Although simple to use, the *S*/*D* equation ignores the effect of several important parameters such as relative

deck stiffness, span length, and skew. Therefore, it gives accurate results for a few selected bridge geometries but is considered conservative for long spans, unconservative for short spans, and simply inaccurate for a wide range of bridge geometries and spans. Due to these facts and research on a substantial amount of information on different bridge types, it was decided that revision for the AASHTO Standard Specifications (AASHO 1931) was needed.

Kind of Floor	Bridge Designed for One Traffic Lane	Bridge Designed for Two or more Traffic Lanes
Concrete:		
On steel I-Beam stringers[f] and prestressed concrete girders	S/7.0 If S exceeds 10' use footnote f.	S/5.5 If S exceeds 14' use footnote f.
On concrete T-Beams	S/6.5 If S exceeds 6' use footnote f.	S/6.0 If S exceeds 10' use footnote f.
On timber stringers	S/6.0 If S exceeds 6' use footnote f.	S/5.0 If S exceeds 10' use footnote f.
Concrete box girders[h]	S/8.0 If S exceeds 12' use footnote f.	S/7.0 If S exceeds 16' use footnote f.
On steel box girders	See Article 10.39.2.	
On prestressed concrete spread box Beams	See Article 3.28.	

[f]In this case the load on each stringer shall be the reaction of the wheel loads, assuming the flooring between the stringers to act as a simple beam.

3.28 DISTRIBUTION OF LOADS FOR BENDING MOMENT IN SPREAD BOX GIRDERS*

3.28.1 Interior Beams

The live load bending moment for each interior beam in a spread box beam superstructure shall be determined by applying to the beam the fraction (D.F.) of the wheel load (both front and rear) determined by the following equation:

$$D.F. = \frac{2N_L}{N_B} + k\frac{S}{L} \qquad (3\text{-}33)$$

where,

N_L = number of design traffic lanes (Article 3.6);
N_B = number of beams ($4 \leq N_B \leq 10$);
S = beam spacing in feet ($6.57 \leq S \leq 11.00$);
L = span length in feet;
k = $0.07 W - N_L (0.10N_L - 0.26) - 0.20N_B - 0.12$; (3-34)
W = numeric value of the roadway width between curbs expressed in feet ($32 \leq W \leq 66$).

3.28.2 Exterior Beams

The live load bending moment in the exterior beams shall be determined by applying to the beams the reaction of the wheel loads obtained by assuming the flooring to act as a simple span (of length S) between beams, but shall not be less than $2N_L/N_B$.

Figure 2.1. *S/D* Distribution Factors from *AASHTO Standard Specifications for Highway Bridges* (US Customary Units; (AASHTO 1996)).

2.2.2 Background and Development of Current AASHTO LRFD LDFs (1994–Present)

2.2.2.1 Overview

Zokaie et al. (1991) conducted a study as part of the National Cooperative Highway Research Program (NCHRP) 12-26 project *Distribution of Wheel Loads on Highway Bridges* to assess and fill the need for a more accurate and broader range of LDFs. This study presents updated and more comprehensive formulas for calculating the LDFs. While these equations are also approximate, they give consistently conservative results for the specified range of bridge geometries. All LDF equations were based on FEM analysis and statistical evaluation of typical families of bridge types. In 1994, more accurate LDF equations based on the work done during

the NCHRP 12-26 project were introduced as part of the *AASHTO Guide Specifications for Distribution of Loads for Highway Bridges* (AASHTO 1994b) and the AASHTO LRFD Specifications (1994a). AASHTO Guide Specifications (1994b) formulas are similar to those from AASHTO LRFD Specifications (1994a), except that they only apply to non-LRFD applications and are to be used only when reverting to AASHTO Standard Specifications (1996). Table 2.1 shows some select bridge types relevant to this project, and Table 2.2 shows the formulas for LDFs for these bridge types. These values have not been changed in AASHTO since 1994 (AASHTO 2012).

The NCHRP 12-26 research project (Zokaie et al. 1991) focused on the response of bridges to AASHTO HS truck loads. Available methods for wheel load distribution were evaluated for beam and slab, box girder, slab, multi-box beam, and spread box beam bridges. In order to allow more structures to be designed with simplified methods, a complete and consistent set of formulas for LDFs was developed. In order to cover most of the common bridge types nationwide, several hundred of the most common bridge types were selected from the National Bridge Inventory File (NBIF). This bridge database was studied to identify the common values of various parameters such as beam spacing, span length, slab thickness, overhang, and skew angle, among others. A hypothetical bridge that possessed the average properties and parameters from the database was defined and was referred to as the "average bridge."

Table 2.1. Common Bridge Deck Superstructures (AASHTO 2012).
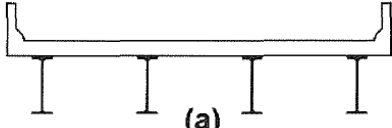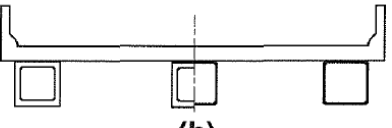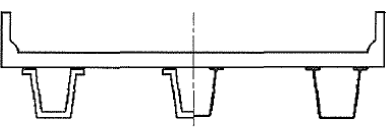
Supporting Components	Type Of Deck	Typical Cross-Section
Steel Beam	Cast-in-place concrete slab, precast concrete slab, steel grid, glued/spiked panels, stressed wood	(a)
Closed Steel or Precast Concrete Boxes	Cast-in-place concrete slab	(b)
Open Steel or Precast Concrete Boxes	Cast-in-place concrete slab, precast concrete deck slab	(c)

Table 2.2. Interior Beam Moment LDFs from AASHTO LRFD Specifications (AASHTO 2012).

Type of Superstructure	Applicable Cross-Section from Table 4.6.2.2.1-1	Distribution Factors	Range of Applicability
Wood Deck on Wood or Steel Beams	a, l	See Table 4.6.2.2.2a-1	
Concrete Deck on Wood Beams	l	One Design Lane Loaded: $S/12.0$ Two or More Design Lanes Loaded: $S/10.0$	$S \leq 6.0$
Concrete Deck, Filled Grid, Partially Filled Grid, or Unfilled Grid Deck Composite with Reinforced Concrete Slab on Steel or Concrete Beams; Concrete T-Beams, T- and Double T-Sections	a, e, k and also i, j if sufficiently connected to act as a unit	One Design Lane Loaded: $$0.06 + \left(\frac{S}{14}\right)^{0.4}\left(\frac{S}{L}\right)^{0.3}\left(\frac{K_g}{12.0 L t_s^3}\right)^{0.1}$$ Two or More Design Lanes Loaded: $$0.075 + \left(\frac{S}{9.5}\right)^{0.6}\left(\frac{S}{L}\right)^{0.2}\left(\frac{K_g}{12.0\, L t_s^3}\right)^{0.1}$$	$3.5 \leq S \leq 16.0$ $4.5 \leq t_s \leq 12.0$ $20 \leq L \leq 240$ $N_b \geq 4$ $10{,}000 \leq K_g \leq 7{,}000{,}000$
		use lesser of the values obtained from the equation above with $N_b = 3$ or the lever rule	$N_b = 3$
Cast-in-Place Concrete Multicell Box	d	One Design Lane Loaded: $$\left(1.75 + \frac{S}{3.6}\right)\left(\frac{1}{L}\right)^{0.35}\left(\frac{1}{N_c}\right)^{0.45}$$ Two or More Design Lanes Loaded: $$\left(\frac{13}{N_c}\right)^{0.3}\left(\frac{S}{5.8}\right)\left(\frac{1}{L}\right)^{0.25}$$	$7.0 \leq S \leq 13.0$ $60 \leq L \leq 240$ $N_c \geq 3$ If $N_c > 8$ use $N_c = 8$
Concrete Deck on Concrete Spread Box Beams	b, c	One Design Lane Loaded: $$\left(\frac{S}{3.0}\right)^{0.35}\left(\frac{Sd}{12.0 L^2}\right)^{0.25}$$ Two or More Design Lanes Loaded: $$\left(\frac{S}{6.3}\right)^{0.6}\left(\frac{Sd}{12.0 L^2}\right)^{0.125}$$	$6.0 \leq S \leq 18.0$ $20 \leq L \leq 140$ $18 \leq d \leq 65$ $N_b \geq 3$
		Use Lever Rule	$S > 18.0$
Concrete Beams used in Multibeam Decks	f	One Design Lane Loaded: $$k\left(\frac{b}{33.3L}\right)^{0.5}\left(\frac{I}{J}\right)^{0.25}$$ where: $k = 2.5(N_b)^{-0.2} \geq 1.5$	$35 \leq b \leq 60$ $20 \leq L \leq 120$ $5 \leq N_b \leq 20$
	g if sufficiently connected to act as a unit	Two or More Design Lanes Loaded: $$k\left(\frac{b}{305}\right)^{0.6}\left(\frac{b}{12.0L}\right)^{0.2}\left(\frac{I}{J}\right)^{0.06}$$	

Average bridges for each of the above-mentioned bridge types were established. To obtain the effect of different parameters on wheel load distribution, each parameter was varied one at a time for the average bridge under consideration. From this technique, LDFs for both shear and moment were obtained for each parameter.

The LDF formulas were then established with errors minimized by applying a three-level analysis. Level 1 was defined as the simplified method, which uses load distribution factors for calculating moments and shears. Level 2 included graphical and simplified grillage methods. Level 3 was defined as a detailed FEM analysis.

To derive the simplified formulas, assumptions were made and some parameters were discarded when they were not particularly relevant. Therefore, it was essential to verify the accuracy of the simplified formulas against real bridge behavior to ensure no important bridge characteristics were omitted. The bridge database and average bridges were used for this verification. Five average bridges were evaluated by Level 3 analysis and the LDFs verified. The distribution factors found from the most accurate method were compared with those found from the simplified method, and ratios between the two values were calculated and examined to assess the accuracy of the simplified formulas. The methods or formulas that had the smallest standard deviation and an average closest to unity were adopted as the most applicable formulas.

As part of the work to support the development of the LDFs, Nowak (1993) developed new load models for dead, live, and dynamic loads on highway bridges. He built these models based on the available statistical data on dead loads, truck loads, and dynamic loads. Considering the lifetime of a bridge is around 75 years, extreme loads that would have the probability of occurring once in 75 years were determined. During the modeling process, LDFs and multiple-presence (more than one truck on the bridge) were considered as important parameters and conditions. Multiple-presence loading was modeled in both one-lane and in side-by-side situations, with different correlations between truck weights. Because live and dynamic loading are random variables in nature, their variations were described by cumulative distribution functions, mean values, bias factors, and correlation coefficients.

The dynamic model in Nowak's project was developed as a function of three main properties: road surface roughness, bridge dynamics (frequency of vibration), and vehicle dynamics (suspension system). Nowak (1993) stated that the dynamic deflection was found to be independent of truck weight, thus inferring that with increased truck weight, the dynamic load

decreases as compared to the live load. The results from this study also indicated that the dynamic load factor (DLF) values were quite equally based on all three of the main properties listed above. The actual contribution of these parameters will change slightly from bridge to bridge, making this very challenging to predict accurately, so it was recommended that the DLF be specified as a percentage of the live load.

The analytical model was also analyzed for the distribution of live load to girders by two-lane loading. The resulting LDFs were then compared with the AASHTO Standard Specifications (1931) values and those recommended by Zokaie et al. (1991). Figure 2.2 shows the calculated and AASHTO moment distribution factors. As can be seen, for long spans and large girder spacing values, the AASHTO Standard Specifications (1931) LDFs become over conservative, often resulting in almost 50 percent higher factors than the analytical results. The results of the analytical models were also compared with the recommendations of Zokaie et al. (1991) and showed good agreement with the suggested simplified method.

Nowak (1993) concluded that for one-lane bridges, the positive moment from lane live load is governed not by multiple presence but by a single truck on bridge spans of up to 40 m. Similarly, the shear and negative moment are also controlled by a single truck on spans up to 35 m and 15 m, respectively. However, two-lane bridge LDFs depend on both span length and girder spacing. Nowak stated that this analysis showed that the AASHTO Standard Specifications (1931) equations are overly conservative for most cases, especially for larger girder spacing.
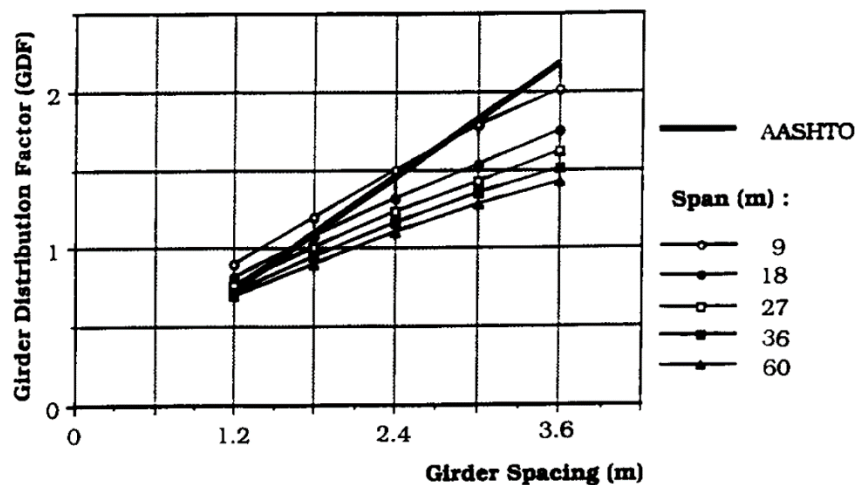
Figure 2.2. Girder Distribution Factors: Calculated and Specified by AASHTO Standard Specifications (Nowak 1993).

17

2.2.2.2 Identifying Key Parameters

Researchers studied the bridge database to identify the range of applicability and variation of each parameter. A sensitivity study was conducted to identify the importance of each parameter for the live load distribution factors. Key parameters that affect the LDFs were determined for different bridge types based on the sensitivity studies. Several bridge finite element models having the same properties except the parameter being investigated were loaded with HS20 trucks, and load distribution factors were obtained for moments and shears. Then the variations of LDFs were investigated to evaluate the importance of each parameter. This procedure was used for each parameter being considered for the approximate LDF equations.

The bridge database was also investigated to identify the relationship between different parameters. Several bridge parameters were plotted versus one another to identify any possible relationship between different parameters. The correlation between key parameters, such as girder spacing versus slab thickness and span length versus moment of inertia, was investigated. This study showed that mostly these parameters are not correlated to each other. Figure 2.3 shows the relationship of slab thickness and girder spacing as an example.
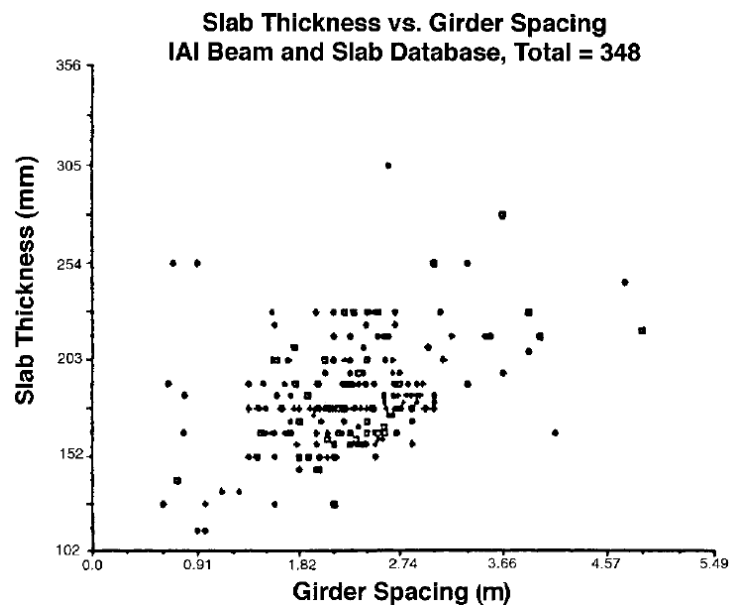
Figure 2.3. Relationship of Slab Thickness and Girder Spacing in Beam and Slab Bridges.

2.2.2.3   Loading of Bridge Deck

Live load distribution factors were calculated by loading the bridge with trucks placed at the longitudinal position that produces the maximum moment or shear reaction. Then vehicles were moved transversely across the bridge width. The maximum moment or shear reaction for each position was obtained using accurate computational methods (FEM or grillage). The maximum of these results was chosen as the critical moment or shear demand. This procedure was repeated for different numbers of trucks that fit on the bridge transversely. The maximum moment and shear reactions were multiplied by the multiple-presence factor. The LDF equations in AASHTO LRFD Specifications implicitly include multiple-presence factors. Therefore, the multiple-presence factors must only be used when the lever rule is used. Also, the vehicle loading was achieved using truck loads only. AASHTO uniform lane loading was not included for the derivation of the AASHTO LRFD Specifications LDF equations (Zokaie et al. 1991).

The controlling moment force or shear reaction was selected for one-lane-loaded and multiple-lane-loaded cases. Then a ratio was computed to compare this controlling moment or shear to the moment or shear that was found by analyzing a simply supported isolated beam having the same span length. This ratio represented the live load distribution factor for that particular case. Because different critical positions were analyzed and the maximum was chosen, the LDF formulas provided an envelope of all possible load configurations.

2.2.3   Assessment of Current LDFs in AASHTO LRFD Specifications

Chen and Aswad (1996) investigated refined analysis procedures to determine LDFs for simply supported bridges under flexure. AASHTO LRFD Specifications (1994a) live load distribution factor formulas for flexure were reviewed for prestressed concrete I-girders and spread box beam bridges. The shortcomings of the simplified formulas in the LRFD code were also listed. First, the average bridge span for I-girder bridges was considered to be about 50 ft in the study of Zokaie et al. (1991). However, this span is rather short when compared to many modern and future bridge designs. Secondly, the multilane reduction factor was often ignored for bridges with three lanes. This should not be the case because many times when all three lanes are loaded, the situation will be controlling for design and multilane factors will then make a significant contribution in moment and shear reductions. Furthermore, the study by Zokaie et al. (1991) conservatively did not take into account the effects of midspan diaphragms.

This study developed refined analysis techniques that allowed the presence of midspan diaphragms and slab orthotropy for beam-slab bridges. Additionally, a parametric study was conducted on a wide array of span-to-depth ratios for spread box and I-girder bridges. This revealed that for reasonably large span-to-depth ratios, the refined methods of analysis (FEM or grillage analysis) gave midspan moments that were about 20 percent smaller than those returned by the simplified formulas in the AASHTO LRFD Specifications (1994a). Similarly, in spread box beams, the FEM results gave values that were about 10 percent lower than the equations. Examining the results, the most significant case occurred at the exterior girders when midspan diaphragms were used; the refined analysis indicated 30 percent smaller load distribution values than the LRFD formulas. Therefore, the author recommended that either FEM or grillage analysis be used for long-span bridges, as these methods permit a significant reduction in the release strength or, alternatively, lengthening of the span capability.

Zokaie (2000) discussed further details of the new simplified LDFs developed during NCHRP 12-26 (Zokaie et al. 1991) and presented the background on the development of the formulas, comparing their accuracy with the previous S/D method. Although the NCHRP 12-26 project considered five different types of bridges, Zokaie only concentrated on slab-on-girder bridges in his study in order to further detail the methods used to develop the LDF formulas. The computer program GENDEK5A (Powell and Buckle 1970) was used for modeling these slab-on-girder type bridges. The average slab-and-beam bridge was then modeled using this chosen computer program. To identify which parameters have considerable influence on the load distribution, a sensitivity study was performed.

HS20 truck loads were used to load the FEM of the bridge deck to determine the live load distribution factors for shears and moments. This analysis was then repeated many times, each time for a different parameter, keeping all other parameters as their mean values while changing the one being investigated from its minimum to maximum value. To assess how important each parameter was to the overall load distribution, the results for each parameter were plotted together on the same graph for visual inspection. From this examination, the author decided that the girder spacing, span length, and girder and slab stiffness were the most significant parameters related to load distribution.

Results obtained from Zokaie's proposed formulas were compared with more accurate FEM analysis results. The *g*-ratio was calculated by taking the ratio of the distribution

factor obtained from the formula to the one obtained from FEM analysis. These ratios were used to tune the simplified formulas. The intention was to obtain a standard deviation less than the earlier *S/D* AASHTO Standard Specifications (1996) formulas. Also, the average value of the *g*-ratios must be larger than unity in order to create some conservatism but not be overly conservative. By visually inspecting the plots and examining the trends, the formulas were given their final form.

Figure 2.4 shows the histogram of the *g*-ratios for the historic *S/D* equations and the proposed approach. As the figure illustrates, the standard deviation and accuracy of the proposed approach are significantly improved compared to the historic *S/D* equations.

| (a) AASHTO *S/D* | (b) Proposed Formulas |
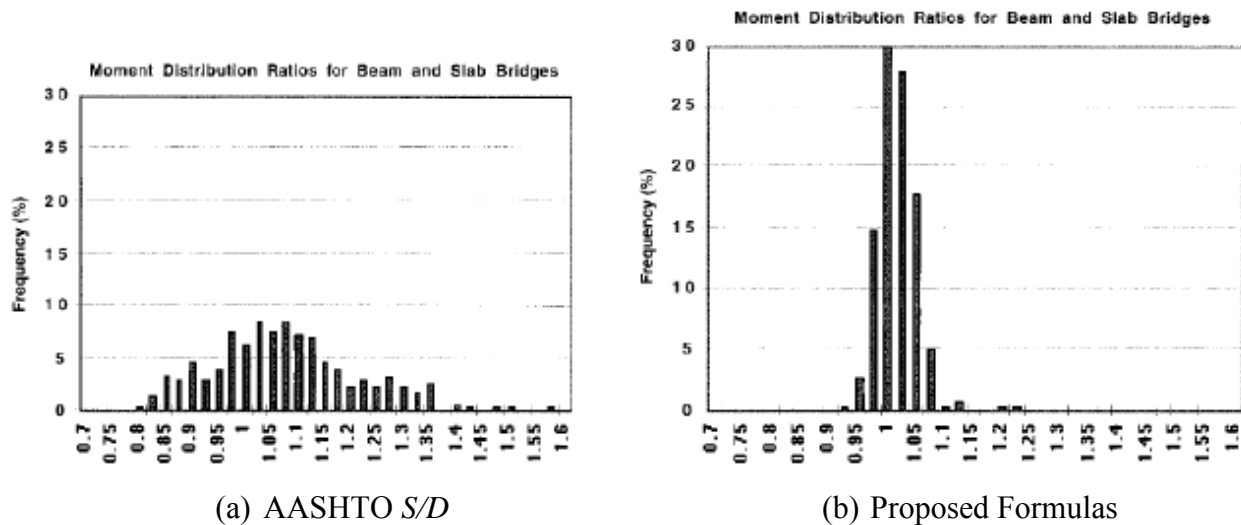
Figure 2.4. Comparison of Simple Formulas with More Accurate Analysis (Zokaie 2000).

2.2.4   Research Studies Evaluating AASHTO LRFD Specifications LDFs

2.2.4.1   Nonstandard Trucks

Goodrich and Puckett (2000) explored the effects of nonstandard axle gages on the wheel live load distribution. They also developed a simplified method for calculating the LDFs caused by trucks with axle gage widths differing from the specified 6 ft in the AASHTO LRFD Specifications (1994a). This simplified method was based on a rigorous finite strip method analysis and was compared with the results from the program BRASS-Dist (WYDOT 1996) for several combinations of axle configurations and bridge geometries. The simplified method presented by Goodrich and Puckett (2000) generally gives conservative results that show a strong relationship to the results found from the rigorous analysis. Tanbsh and Tabatabai (2001) also

investigated the effects of oversized trucks on the live load distribution in bridges. The LDFS in AASHTO LRFD Specifications (1994a) are based on specific truck geometries and loads. There are, however, some cases where trucks with larger gage widths, axle spacing, or loads are used. In these cases, engineering analysis is needed before a permit may be acquired. To make this process easier, Tanbsh and Tabatabai (2001) proposed modification factors for the specification-based LDFs to account for these overload situations and thus make it possible to design for these events. Through a parametric study involving FEM analysis, the authors found that the LDFs for oversized loads were less than those found using the AASHTO LRFD Specifications (1994a) LDF equations. The main overload parameter investigated (a larger truck gage width) was also shown to have a greater influence on the shear distribution than the flexural distribution between girders.

2.2.4.2 *Experimental Studies*

Barr et al. (2001) conducted a study to further verify the LDFs by experimentation. The project was based on the experimental results of a continuous high-performance prestressed concrete girder bridge designed by the Washington Department of Transportation (WSDOT). The measured response of this bridge during static live load testing was used to confirm FEM analysis. Then 24 variations of this model were studied in order to evaluate flexural LDFs. These FEM models were also analyzed to evaluate the effects of lifts, intermediate diaphragms, continuity, skew angle, end diaphragm, and load type on the LDFs. The FEM models also provided LDFs for bridges with fairly standard geometries within 6 percent of the AASHTO LRFD Specifications (1998) LDF values. However, the bridge in question for this study had a more irregular geometry, and therefore AASHTO LRFD Specifications values were conservative by 28 percent. Barr et al. found that lifts, skew angle, end diaphragms, and load type significantly influenced the LDF, while continuity and intermediate diaphragms had little effect on the load distribution.

Eom and Nowak (2001) conducted a study to evaluate the LDFs of truck loads on girder bridges. Previous studies showed that the LDFs specified in the earlier AASHTO Standard Specifications (1996) were not accurate for longer span bridges and for wide girder spacings. Therefore, this research was intended to validate LDFs for steel girder bridges with spans of 32.8–147.6 ft. Experimental field tests on 17 steel girder bridges were conducted by the

22

Michigan DOT to help understand their load distributions. The bridges were instrumented by strain gages and loaded with heavy trucks (up to 761 kN or 171 kips). Trucks were placed on the bridges and from the recorded strains LDFs were calculated for one-lane-loaded and two-lane-loaded cases. An analytical study was also conducted using FEM models with three different boundary conditions (simple supports, hinged supports, and partially fixed supports). The final LDFs obtained through experimental tests and FEM models were then compared with the AASHTO Standard Specifications (1996) and the AASHTO LRFD Specifications (1998).

For all bridges tested, the experimentally obtained LDFs from the field tests were less than the code formula values. The ratios of these two LDF values were then compiled for all bridges analyzed, and their patterns were studied. The results indicate that for short-span bridges, the AASHTO Standard Specifications (1996) and the AASHTO LRFD Specifications (1998) specify that LDFs that are not unconservative. This difference may mean that the real bridge conditions were different from those assumed in the code. Eom and Nowak (2001) also stated that the results of the study showed that particularly for longer-span bridges, the AASHTO LRFD Specifications (1998) provides more consistent LDFs than the AASHTO *Standard Specifications for Highway Bridges* (1996).

Different boundary conditions were used in the FEM models to determine which one returned the most accurate results. (Eom and Nowak 2001) noted that the LDFs were found to be more uniform for ideal simply supported bridges. The strain values for simply supported cases as compared to those with some fixity were shown to be much higher, which made the measured strain in the tests lower than predicted by the simply supported analysis. In essence, the field testing led to the belief that there was some support fixity, but the FEM results conflicted with this finding and showed the most accurate results for the simply supported case. The authors stated that for bridges with ideal simple supports, the more realistic LDFs for one-lane-loaded cases come from the AASHTO LRFD Specifications (1998). However, for the use of these code formulas it is important to consider some partial fixity of the supports to avoid overly conservative results.

2.2.4.3   *Edge Stiffening Effects*

Eamon and Nowak (2002) investigated how edge stiffening secondary elements affect LDFs in bridges. The specific secondary elements that were investigated in this study included barriers, sidewalks, and diaphragms. Only two-lane highway bridges with composite steel and prestressed

concrete girders were considered, and the FEM was used to develop the models of these bridges. During the elastic range of deformations, these types of edge stiffening secondary elements were shown to reduce the interior girder distribution factors by 10 to 40 percent, while for the inelastic range, the reductions tended to be one-half as large, being only 5 to 20 percent. Barriers and sidewalks carried some of the load that would have been otherwise distributed to interior girders, while it was observed that diaphragms have the effect of evening girder deflections and therefore load distribution by essentially pulling down the exterior girders and raising interior girders.

2.2.4.4   *Development of New LDF Expressions*

Sotelino et al. (2004) conducted a study to develop a simplified equation based on the AASHTO LRFD Specifications (1998) load distribution formula that can be used easily in design and does not require an iterative procedure. Although the equations presented by Zokaie et al. (1991) are more accurate and consistently conservative than the previous S/D equations, they still have their limitations and drawbacks. Due to the fact that Zokaie et al.'s equations include a longitudinal stiffness parameter, the LDF formulas are more difficult to use during design than analysis because the stiffness parameters may not yet be known. In addition to this main goal, the project also focused on other potential flaws in Zokaie et al.'s equations. Additional objectives included investigating the effects of several bridge features that were not included in the AASHTO LRFD Specifications (1998) LDF equations, such as cross-bracing diaphragms, parapets, and deck cracking.

The project successfully developed a new simplified load distribution equation for design. After analyzing 43 steel girder bridges and 17 prestressed concrete girder bridges with a FEM model and with the AASHTO LRFD Specifications (1998) LDF equations and the new simplified equation, the researchers compared the results. Sotelino et al. (2004) determined that the proposed equation always returned more conservative values than the FEM analyses and was also typically more conservative than the AASHTO LRFD Specifications equations, thus giving an appropriate simplified formula for LDFs. The study also found that the use of secondary elements such as cross-bracing diaphragms and parapets could reduce the LDF found by the AASHTO LRFD Specifications (1998) equations by up to 40 percent. However, longitudinal cracking was shown to increase the AASHTO LRFD Specifications (1998) LDFs by up to 17 percent, while transverse cracks did not seem to affect the load distribution. The range of application of Sotelino et al.'s simplified formula is shown in Table 2.3.

Table 2.4 shows the actual proposed wheel load distribution equation for concrete slab on steel girder bridges, compared to the current AASHTO LRFD Specifications (1998) LDFs as well as the previous S/D method.

Table 2.3. Range of Application for Simplified LDF Formula (adapted from Sotelino et al. 2004).

Parameters	Girder Spacing: S, ft (mm)	Span Length: L, ft (mm)	Slab Thickness: t_s, in. (mm)	Skew Angle (θ, degree)	Stiffness Parameter, K_g, in^4
Applicable Range	4–10 (1220–3050)	44–122 (13400-37200)	8 (200)	0–45	0–189,940e$^{L/59}$

Table 2.4. Simplified LDF Equations for Concrete Slab on Steel Girder Bridges (US Customary Units; Sotelino et al. 2004).

Specification	Basic LDF Formula	Skew correction factor
AASHTO Standard	$\dfrac{S}{5.5}$	N/A
AASHTO LRFD	$0.15 + \left(\dfrac{S}{3}\right)^{0.6}\left(\dfrac{S}{L}\right)^{0.2}\left(\dfrac{K_g}{12Lt_s^3}\right)^{0.1}$	for $\theta \geq 30°$ $1 - 0.25\left(\dfrac{K_g}{12Lt_s^3}\right)^{0.25}\left(\dfrac{S}{L}\right)^{0.5}(\tan\theta)^{1.5}$
Simplified	$0.15 + 0.73 \cdot \dfrac{S^{0.8}}{L^{0.3}} \cdot e^{\left(\frac{L}{590}\right)}$	for $\theta \geq 30°$ $1 - 0.59 \cdot \dfrac{S^{0.5}}{L^{0.75}} \cdot (\tan\theta)^{1.5} \cdot e^{\left(\frac{L}{236}\right)}$

*Units of S, L, K_g, and t_s are ft, ft, in^4, and in., respectively.

Kocsis (2004) evaluated the AASHTO Guide Specifications (1994b) and AASHTO Standard Specifications (1996) in terms of line load and live load distribution factor requirements for I-girders. He also introduced a user-friendly software program, SECAN that more accurately predicts live load distribution factors and line load distributions. Previous studies have shown that the AASHTO Standard Specifications (1996) line load distribution (line load distributed equally among all girders) was not accurate. Kocsis concluded that for line load

distributions more accurate results could be obtained by using the SECAN software. The analysis program SECAN was developed by comparing the results of established analytical methods and field experimental testing. Kocsis also stated that the live load distribution factors for AASHTO Guide Specifications (1994b) trucks provide more accurate results than those given by AASHTO Standard Specifications (1996). These LDFs from the AASHTO Guide Specifications (1994b) are shown to be similar in accuracy to those found from SECAN, and are considerably easier to use.

Puckett et al. (2005) conducted a broad study to develop new formulas for calculating LDFs. This project, similar to that of Zokaie et al. (1991), focused on a wide array of bridge types as well as several different analysis methods. The goal of the project was to improve upon the current NCHRP 12-26 based equations in the AASHTO LRFD Specifications (2004). An automated process that compared the live load distribution factors from several simplified analysis methods to those calculated by grillage analysis were compared to determine an appropriate analysis method for the project. The lever rule was investigated further as a simple analysis method and converted into equation form. The lever rule equation was then calibrated and combined with an adjusted uniform distribution method to give the final load distribution method. According to Puckett et al. (2005), this new method provides more accurate LDFs than those within AASHTO LRFD Specifications (2004) and without many of the restricted ranges of application.

Harris et al. (2010) studied a new type of steel bridge termed the sandwich plate system (SPS), focusing on the load distribution, and evaluated how well the AASHTO LRFD Specifications (2007) LDF equations worked for this new bridge system. The system possessed a different deck stiffness compared to a typical reinforced concrete deck. The results from the AASHTO LRFD Specifications (2007) LDF equations developed by Zokaie et al. (1991) during the NCHRP 12-26 project were thus affected due to the deck stiffness parameter in the equations. After investigating the difference and its effects, Harris et al. (2010) found that although deck stiffness differences may cause a 20 percent difference in the LDFs, the AASHTO LRFD Specifications (2007) equations for concrete decks may be used to estimate LDFs for SPS bridges.

Harris (2010) also conducted a study assessing flexural load distribution methodologies used for analysis of stringer bridges. Potential discrepancies within several methods of load

distribution factor analysis for slab-girder bridges that were investigated included relationships of member load effects, impact of boundary conditions, and effects of secondary members. The project's objective was to define which methods are most appropriate and when it is best to use them. Harris (2010) concluded that most current methodologies have similar trends as long as the internal member load effects and boundary conditions are modeled correctly and considered appropriately.

2.3 METHODS OF ANALYSIS TO DETERMINE LDFS

2.3.1 Overview

Live load distribution factors can be assessed analytically using simple grillage or finite element models (Hueste et al. 2006). Guidelines for developing grillage models are available in several journal articles (Hambly 1975; Zokaie et al. 1991) as well as multiple books and manuals (Barker and Puckett (2007); Hambly (1976); Ryall et al. (2000); Surana and Agrawal (1998)). Instructions and recommendations for properly developing FEM models can also be found in a multitude of scholarly articles and books (Barker and Puckett (2007); Puckett et al. (2005); Ryall et al. (2000); Zokaie et al. (1991)). A three-dimensional FEM analysis is a more computationally intensive approach that can also be calibrated with comparisons to actual measured bridge response data, but for LDF calculations, grillage analysis is a simpler method that may still provide adequately accurate results in many cases.

2.3.2 Grillage Method of Analysis

Hambly (1976) discussed several different types of structural bridge decks, their components, and the analysis types that can be used to better understand them. As part of the slab deck section of his book, the details of the grillage method of analysis are explained. At the time of writing, he stated that grillage analysis was one of the most popular computer-aided analysis methods for bridge decks. Accuracy was considered adequate, with the grillage method being relatively easy to understand and implement.

The grillage method was developed in the early days of matrix structural analysis by Lightfoot and Sawko (1959). Since that time, the grillage method has become increasingly accurate and easy to use with the advancement of computational capability. The strategy behind the method is to simply divide a bridge deck into several equivalent longitudinal and transverse

beams resembling a grillage. Figure 2.5 shows examples of grillage idealizations of bridge decks.

For analysis purposes, the grillage members are assigned the same bending and torsional stiffness parameters as the section of the bridge that they represent. Generally, for slab-on-girder bridges, in the longitudinal direction, the grillage members coincide with the centerlines of the girders, thereby keeping those elements concentrated where they have the largest influence in the physical bridge system. Cross beams are used at appropriate spaces to represent the deck slab. Placing grillage members at locations known to have high force and stress magnitudes, such as supports and prestressing strands, is also good practice. If the analysis is set up appropriately, the grillage model should deflect in the same fashion as the bridge deck; the portion of moment, shear, and torsion in each grillage element should be similar to those in the section of the bridge they represent.

Despite the fact that the grillage method attempts to take the real bridge's properties and shape into account, it simplifies the bridge, and some aspects of the physical bridge are lost in the model. Although force equilibrium equivalence between the grillage model and bridge deck are easy to capture accurately, the main drawback is the lack of displacement compatibility between cross beams. However, it can be shown that if the grillage mesh is sufficiently refined, meaning that as the grillage members are spaced more closely, results approach real bridge behavior. Hambly (1976) stated that the grillage spacing in both directions should be similar in order to accurately model load distribution in between members. Once an appropriate grillage mesh is developed and set up with the correct parameters in a computer program, the grillage model may be loaded. Point loads are used in grillage analysis and are usually placed at the intersection of the longitudinal and transverse member nodes. Any type of static load may be applied to the bridge with equivalent point loads at the nodal locations.
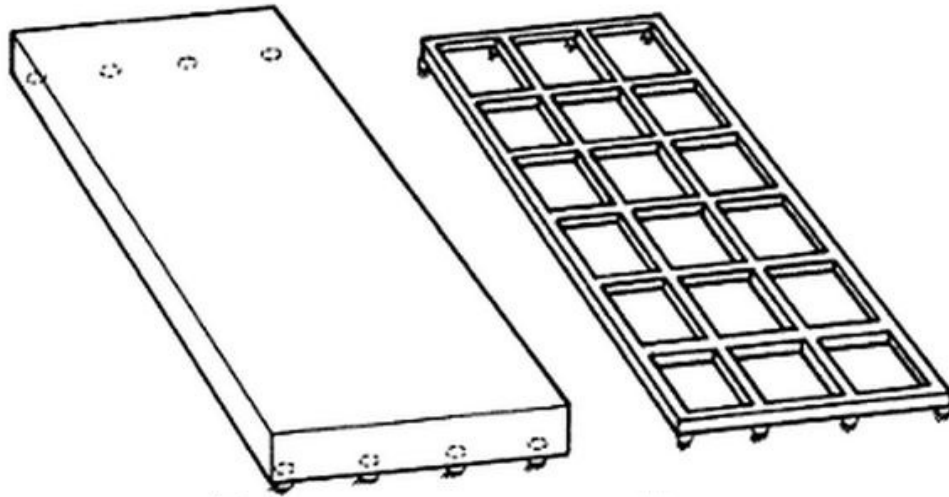
(a) Hambly (1991)
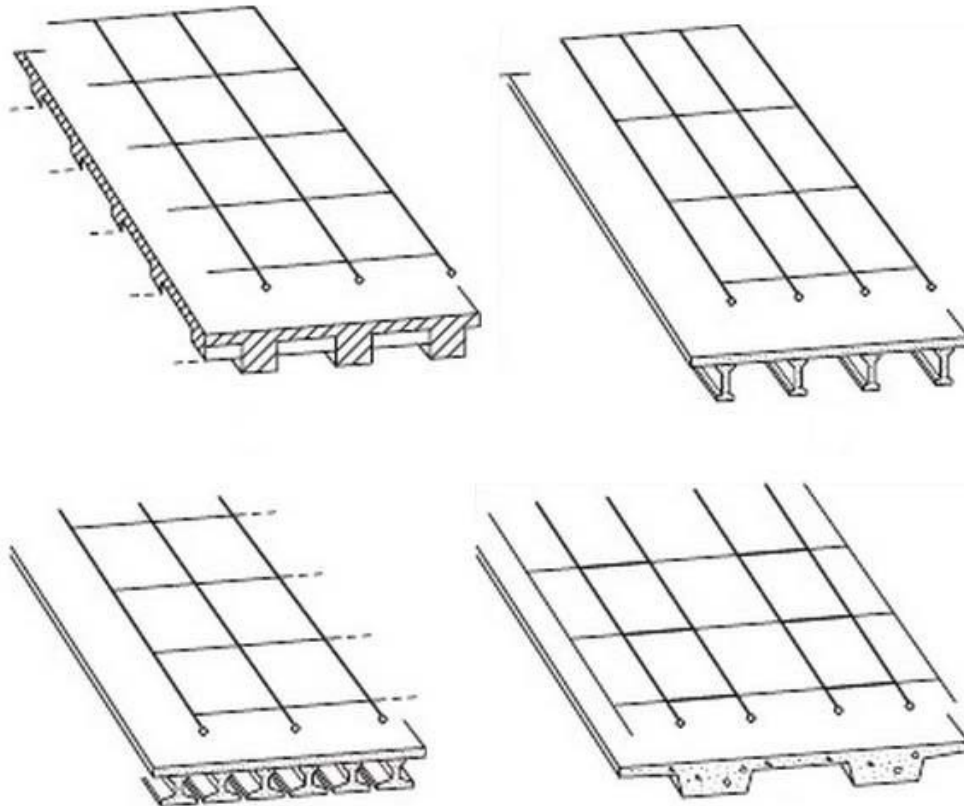
(b) Parke and Hewson (2008)

Figure 2.5. Examples of Grillage Idealizations of Bridge Decks.

Surana and Agrawal (1998) discussed a wide array of aspects involved in the grillage method of analysis and the bridge types that are good candidates for this method. Comparisons with several other analysis techniques including the finite element method were also explored. The grillage method and the finite element method can both be used accurately for numerous types of bridges; the finite element method can be somewhat more complex, and thus time consuming and costly to implement and run. However, the grillage method can be applied to complicated bridge designs with edge stiffening beams, large skew angles, and unusual support conditions.

2.3.3 Finite Element Method of Analysis

FEM has its roots in analyzing aerospace structures and was first developed by Clough and his coworkers at the University of California Berkeley in the late 1950s (Turner et al. 1956). The power of FEM quickly became self-evident, and other groups formed around the world to exploit its capabilities, including Argyris in Germany (Argyris and Kelsey 1960) and Zienkiewicz in the United Kingdom (Zienkiewich 1971).

Barker and Puckett (2007) discussed the fundamentals and application of FEM. They stated that this method has the ability to combine many mathematical representations within one large model that will merge all boundary conditions and solve all sets of equations to more fully and accurately simulate the complex behavior of an entire structure. The FEM is based on a direct stiffness method of analysis, such that a system of displacement equations is solved to satisfy equilibrium and compatibility. However, unlike the grillage method, the FEM aims to make as few assumptions and simplifications as possible to obtain a more rigorous computational model of a physical bridge system. Although the FEM has the potential for a high level of accuracy, its high level of sophistication means that additional care must be taken during modeling development to ensure all aspects are accurately captured.

FEM models can be analyzed in two dimensions (2D) or three dimensions (3D), with the latter clearly having a higher level of refinement and additional degrees of freedom. Bridge girders may be modeled as grillage or plane grid elements with many input properties including bending and torsional moments of inertia, while deck parameters such as flexural rigidity and level of connection with the girders are also highly important. How different elements in

the bridge (deck, girders, secondary elements, etc.) are meshed and modeled together is also imperative to model correctly.

2.3.4 Application and Verification of Grillage and FEM Analysis for LDF Confirmation

Zokaie et al. (1991) recommended more accurate load distribution factor equations from the early "S-over" equations based on grillage and FEM analysis for a wide array of bridges. The AASHTO LRFD Specifications (1994a) then adopted these formulas to more accurately calculate the load distribution in bridges. Zokaie (2000) reviewed his work from the 1991 NCHRP Project 12-26 to further ensure that these formulas accurately calculate the load distribution factors. To do this, it was necessary to compare their output with proven analytical methods, such as grillage analysis and FEM model.

In order to prove the accuracy of FEM and grillage analyses, several methods were used to determine and compare the LDFs for several field bridges. These bridges were instrumented and experimentally loaded with trucks at different locations across the bridge width to determine their load distributions. Once adequate FEM and grillage models were established, they were calibrated based on test results and confirmed to be working correctly within their computer programs. Similar FEM and grillage models were made for several "average bridges" as discussed in Section 2.2.2. LDFs found for these bridges from the grillage and finite element methods were then compared to the distribution factors given by the new AASHTO LRFD Specifications (1998) equations. In addition to this comparison, the parameters that were found to have the most impact on the load distribution were investigated to ensure they were accounted for in the equations. It was concluded that the formulas were generally accurate, often giving load distributions within 5 percent of the FEM results. The grillage analysis results were also often close to those found from the FEM analysis. For cases when the formulas could not be applied, Zokaie (2000) recommended that a grillage model be made to determine the LDFs.

Schwarz and Laman (2001) used the grillage method to model three test bridges and predict the live load distribution factors in each. These values were then compared to experimental data from each bridge under static and dynamic truck loading, as well as the calculated load distribution and dynamic impact from the AASHTO Standard Specifications (1996) and AASHTO LRFD Specifications (1998) equations. The grillage models tested a few different grillage characteristics to see what aspects were most effective in attaining the true

nature of a bridge. For instance, their Bridges 2 and 3 were each modeled with and without a midspan diaphragm (which was present in both test bridges). Meanwhile, the small skew of Bridge 2 resulted in the diaphragm being set perpendicular to the longitudinal direction, while the large skew in Bridge 3 caused the diaphragm to be modeled perpendicular to the girders (skewed from the longitudinal direction). It was found that the AASHTO LRFD Specifications (1998) and AASHTO Standard Specifications (1996) equations for girder distribution factors gave higher values than the distribution factors measured from the experiment. However, the grillage model closely predicted the transverse load distribution observed by the experimental loading of the bridges. It was also shown that for shorter spans, ignoring the diaphragms in the grillage modeling provided more accurate results.

Hueste et al. (2006) investigated the TxDOT bridge design changes that would occur by changing from the AASHTO Standard Specifications (1996) to the AASHTO LRFD Specifications (2004). As part of a parametric study, the grillage analysis technique was used to assess the accuracy of the live load distribution factors found by AASHTO LRFD Specifications (2004) equations for spread box beams applied to Texas U54 girder simply supported bridges. To determine whether AASHTO LRFD Specifications (2004) equations accurately predict the load distribution for spans slightly larger than the 140 ft limit, grillage models were developed for two bridge geometries using Texas U54 girders (spans of 140 ft and 150 ft with 8.5 ft girder spacing and 60 degree skew). Detailed development and calibration information about each model, completed using the program SAP2000, is included in their report. From the AASHTO LRFD Specifications (2004) equations and the grillage analysis, the critical locations for placing the HL-93 design truck were found. LDF results for one and two or more lanes loaded by the grillage method were compared with those from the equations in AASHTO LRFD Specifications (2004). It was found that the LDFs for moment in interior and exterior girders and for shear in interior girders were applicable for the spans considered. The AASHTO LRFD Specifications (2004) LDF for shear in exterior girders was found to be very conservative. Finally, researchers recommended that the grillage results be confirmed by an even higher method of analysis such as FEM.

3 PRELIMINARY DESIGNS FOR SPREAD SLAB BEAM BRIDGES

3.1 GENERAL

The research team conducted a detailed parametric study to investigate the potential benefits of using spread slab beam bridges. The main focus of the parametric study was to develop preliminary designs for alternative design parameters and geometries. The design parameters were chosen based on the common Texas Department of Transportation (TxDOT) slab beam types, bridge widths, and girder spacings. The specified material properties chosen are consistent with TxDOT practice. The preliminary designs were carried out following the *American Association of Highway and Transportation Officials* (*AASHTO) Load and Resistance Factor Design* (*LRFD) Bridge Design Specifications* (AASHTO 2012) and *TxDOT Bridge Design Manual* (TxDOT 2013a). TxDOT standard practices were followed to ensure that the results could be compared to typical TxDOT slab beam bridges.

The example provided in Appendix A describes a detailed design methodology for spread slab beam bridges. The procedure includes service load design based on allowable stresses in flexure, and ultimate flexural strength and shear strength design. The allowable deflection limit and the stress limits at release were also investigated. The details and findings of the parametric study are documented in this chapter.

3.2 DESIGN PARAMETERS

3.2.1 Geometric Properties of Bridge Alternatives

3.2.1.1 Slab Beam Types

The main geometric bridge design parameters were based on the four different slab beam types and typical TxDOT bridge widths. The four standard slab beam types are differentiated by the width and depth of the beam section, which has a 12 in. or 15 in. depth with a 4 ft or 5 ft width. These standard beam types are named by their width and depth dimensions. For example, the slab beam section with a 4 ft width and 12 in. depth is called 4SB12. The four alternatives are 4SB12, 4SB15, 5SB12, and 5SB15. Figure 3.1 shows the section geometry and strand details of the standard slab beam sections. The 4 ft wide slab beams can hold a maximum of 44 strands,

and the 5 ft wide slab beams can hold a maximum of 56 strands. The bottom concrete cover must be 2.5 in., and the spacing between two rows of strand layers is 2 in. center to center.

(a) 4 ft Wide Slab Beam   (b) 5 ft Wide Slab Beam
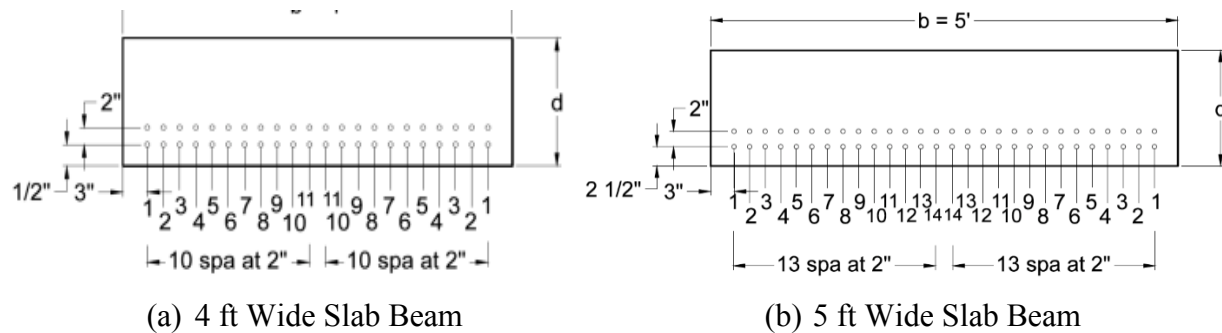
Figure 3.1. Section Geometry and Strand Details of Slab Beam Girders.

3.2.1.2 Bridge Widths and Number of Slab Beams

The total bridge widths were based on standard TxDOT bridge practice and the suggestions from the TxDOT Project Monitoring Committee (PMC). A total of six different bridge widths were investigated including 26 ft, 30 ft, 34 ft, 40 ft, and 46 ft wide bridges.

Another initial design parameter is the number of slab beams. Based on the use of stay-in-place precast concrete panels between the slab beams, the clear spacing between beams should not exceed 6 ft. There is no practical limit for the minimum spacing of the slab beams; they have already been used side by side for conventional slab beam bridges. However, for implementing a spread configuration, and in order to investigate all possible cases, the feasible minimum clear spacing between slab beams was chosen to be 2 ft. Based on the total bridge widths and clear spacing requirements, four options are available: three, four, five, or six slab beam girders can be utilized within the bridge width to satisfy the practical limitations discussed above.

3.2.1.3 Final Bridge Geometries

Given that there are four possible girder quantities, four different slab beam types, and six different bridge widths, a total of 96 different bridge configurations are possible. The minimum and maximum spacing constraints reduce the number of possibilities to 44 bridges that have clear beam spacings between 2 ft to 6 ft. These 44 bridge geometries are summarized in Table 3.1.

3.2.1.4   Deck Geometry

The cast-in-place (CIP) deck uses unshored construction with 4 in. thick stay-in-place (SIP) precast concrete panels (PCPs). A minimum of 4 in. of CIP concrete on top of the PCPs is required by the *TxDOT Bridge Design Manual* (TxDOT 2013a). The PCPs are placed on bedding strips that are attached along the top longitudinal edges of the slab beams. The details of the PCP section are shown in Figure 1.2. The average bedding strip thickness is assumed to be 2 in. However, the contribution of the haunch to the stiffness of the composite section is neglected because the haunch thickness can vary and may decrease down to 0.5 in. due to the initial camber of the slab beams. The weight of a 2 in. haunch was included in the design loads to be conservative. Therefore, for the calculation of the composite section properties, the total deck thickness was taken as 8 in.

Table 3.1. Alternative Geometries for Parametric Study.

No.	Bridge Width (ft)	Number of Beams	Type of Beam	Clear Beam Spacing (ft)	No.	Bridge Width (ft)	Number of Beams	Type of Beam	Clear Beam Spacing (ft)
1		3	5SB12	5.50	23		5	5SB12	3.75
2		3	5SB15	5.50	24		5	5SB15	3.75
3	26	4	5SB12	2.00	25		5	4SB12	5.00
4		4	5SB15	2.00	26	40	5	4SB15	5.00
5		4	4SB12	3.33	27		6	5SB12	2.00
6		4	4SB15	3.33	28		6	5SB15	2.00
7		4	5SB12	3.33	29		6	4SB12	3.20
8		4	5SB15	3.33	30		6	4SB15	3.20
9	30	4	4SB12	4.67	31		5	5SB12	4.25
10		4	4SB15	4.67	32		5	5SB15	4.25
11		5	4SB12	2.50	33		5	4SB12	5.50
12		5	4SB15	2.50	34	42	5	4SB15	5.50
13		4	5SB12	4.67	35		6	5SB12	2.40
14		4	5SB15	4.67	36		6	5SB15	2.40
15		4	4SB12	6.00	37		6	4SB12	3.60
16		4	4SB15	6.00	38		6	4SB15	3.60
17	34	5	5SB12	2.25	39		5	5SB12	5.25
18		5	5SB15	2.25	40		5	5SB15	5.25
19		5	4SB12	3.50	41		6	5SB12	3.20
20		5	4SB15	3.50	42	46	6	5SB15	3.20
21		6	4SB12	2.00	43		6	4SB12	4.40
22		6	4SB15	2.00	44		6	4SB15	4.40

3.2.2   Material Properties and Superimposed Dead Loads

3.2.2.1   Concrete Compressive Strength

The concrete compressive strengths at release and at service (28 days) are key parameters for the design of a prestressed component using allowable stress criteria. To maximize the span lengths, spread slab beam bridge design requires that every available strand position be used. The high prestressing force causes tensile stress exceedance at the ends of the slab beam for almost all configurations. Therefore, the maximum allowable initial concrete compressive strength value was used in the parametric study. The *TxDOT Bridge Design Manual* (TxDOT 2013a) suggests

that the maximum initial concrete compressive strength at transfer be limited to 6 ksi with a maximum 28-day concrete compressive strength of 8.5 ksi.

As noted above, the CIP deck uses unshored construction with 4 in. thick PCPs as stay-in-place forms. The concrete compressive strength at service f_c' of the PCPs is specified to be 5 ksi, and the CIP deck concrete f_c' is specified to be 4 ksi. For the parametric study, the deck compressive strength was conservatively assumed to be 4 ksi throughout, with the PCPs assumed to be part of CIP deck.

3.2.2.2 *Prestressing Strands*

Two prestressing strand diameters are available. The *TxDOT Bridge Design Manual* (TxDOT 2013a) recommends using 0.5 in. diameter strands but allows for 0.6 in. diameter strands when necessary. The spread slab beam bridge design requires high prestressing forces, but the concrete tensile stress limits at service and at release nearly always control the spread slab beam designs. When all strand locations are used, 0.5 in. diameter strands provide the required prestressing force to stay within the allowable concrete stress limit. Therefore, 0.5 in. diameter seven-wire low-relaxation strands were used with a specified ultimate tensile strength f_{pu} of 270 ksi.

3.2.2.3 *Superimposed Dead Loads*

The superimposed dead loads include the guardrail and wearing surface. The weight of the guardrail was considered for the superimposed dead load calculations, but the stiffness contribution was neglected. A T551 rail was assumed since it is one of the heaviest guardrail types. The wearing surface was taken to be 2 in. of asphalt having a 0.14 k/ft^3 unit weight.

3.2.3 **Summary of Parameters and Design Assumptions**

The design parameters used in the parametric study are summarized in Table 3.2. The designs were carried out with the same procedure used for the detailed example provided in Appendix A. Like the detailed example, a refined method of analysis was used for the estimation of prestress losses. The AASHTO LRFD Specifications (2012) do not provide approximate LDFs for spread slab beam bridges. Therefore, for these preliminary designs, the AASHTO LRFD Specifications (2012) spread box beam LDF formulas were used. For service load analysis, the AASHTO HL-93 live load model was adopted. The allowable compressive stress limit at release is given as 0.6

f'_{ci} in the AASHTO LRFD Specifications (2012). However, the *TxDOT Bridge Design Manual* (TxDOT 2013a) permits an allowable compressive stress at release of $0.65 f'_{ci}$. Therefore, the increased compressive stress limit was adopted for the preliminary designs. The other stress limits used are as defined in the AASHTO LRFD Specifications (2012) and summarized in Appendix A.

All geometric combinations listed in Table 3.1 were investigated to determine the maximum span length versus number of strands provided. Although TxDOT indicated a preference for 5 ft slab beams, the 4 ft sections were included for completeness. The design procedures outlined in Appendix A were followed for the parametric study. However, for the parametric study, each slab beam was not designed based on a given span length; rather, it was designed based on a given number of strands. Initially, all strand locations were considered to be filled (44 strands for 4 ft wide slab beams and 56 strands for 5 ft wide slab beams) and then two strands were subtracted at each step until the section reached the cracking limit. The maximum achievable span lengths for eight different limit states were calculated at each step. These limit states are as follows:

- Allowable tension stress limit at release.
- Allowable compression stress limit at release.
- Allowable tension stress at time of deck placement.
- Allowable compression stress at time of deck placement.
- Allowable tension stress at service.
- Allowable compression stress at service.
- Ultimate flexural strength.
- Deflection limit at service.

Table 3.2. Alternative Geometries and Design Parameters.

Parameter	Description/Value
Number of Beams	3, 4, 5, or 6
Bridge Width, w (ft)	26, 30, 34, 40, 42, 46
Slab Beam Type	4SB12, 4SB15, 5SB12, 5SB15
Clear Beam Spacing	Varies from 2 ft to 6 ft
Deck Thickness, t_s	8 in.
Haunch Thickness, t_h	Assumed constant 2 in. for weight calculation. Not included for stiffness calculation.
Precast Concrete Strength at Release, f'_{ci}	6 ksi
Precast Concrete Strength at Service, f'_c	8.5 ksi
Deck Concrete Strength, f'_{cd}	4.0 ksi
Prestressing Strand Diameter, d_p	0.5 in.
Rail	T551 (0.326 k/ft, distributed to 3 beams from the edge)
Wearing Surface	2 in. thick asphalt assumed
Unit Weight of Concrete, w_c	0.15 kcf
Unit Weight of Asphalt Overlay, w_s	0.14 kcf
Prestressing Strands	0.5 in. diameter 7-wire low-relaxation strands
Ultimate Strength of Prestressing Stands, f_{pu}	270 ksi
Modulus of Elasticity of Strands, E_p	28,500 ksi

Deflection limit criteria were applied based on the (2012) Articles 2.5.2.6.2 and 3.6.1.3.2, which indicate that the maximum live load deflection limit may be considered as L/800 for general vehicle loading, where L is the span in inches.

The dead load due to self-weight of the slab beam and deck slab is carried by the non-composite slab beam section. The superimposed dead loads (guardrails and wearing surface) and live load are considered to act on the composite section. The results and findings of the parametric study for all viable geometries are presented in the following section. Section 3.4 presents an assessment of the transverse shear and interface shear limit states.

3.3 RESULTS OF THE PARAMETRIC STUDY

The achievable span length for a given number of strands was plotted for all eight limit states. All 44 viable geometric configurations listed in Table 3.1 are presented below. Figure 3.2 shows an example chart, where the five curves shown with symbols indicate an upper bound span length solution for the limit state considered. These limit states include the allowable tension and compression stress limits for flexure at service and at the time of deck casting, the ultimate flexural strength limit, and the maximum live load deflection limit. The allowable stress limits at release are upper bounds that limit the number of strands that can be used. The release limit corresponds to the upper bound for the allowable compression or tension limit (whichever governs) at release when no strands are debonded. The debonded release limit corresponds to the upper bound for the allowable compression or tension limit (whichever governs) when some strands are debonded up to 6 ft for 15 in. deep slab beams or up to 9 ft (or 0.2L for beams shorter than 45 ft) for 12 in. deep slab beams. For all the analyzed cases, the service tension stress limit and tension stress limit at release (with debonding) control the solution domain. The solution domain between these two curves is shown with yellow shading. The maximum achievable span length is indicated with a red check mark.
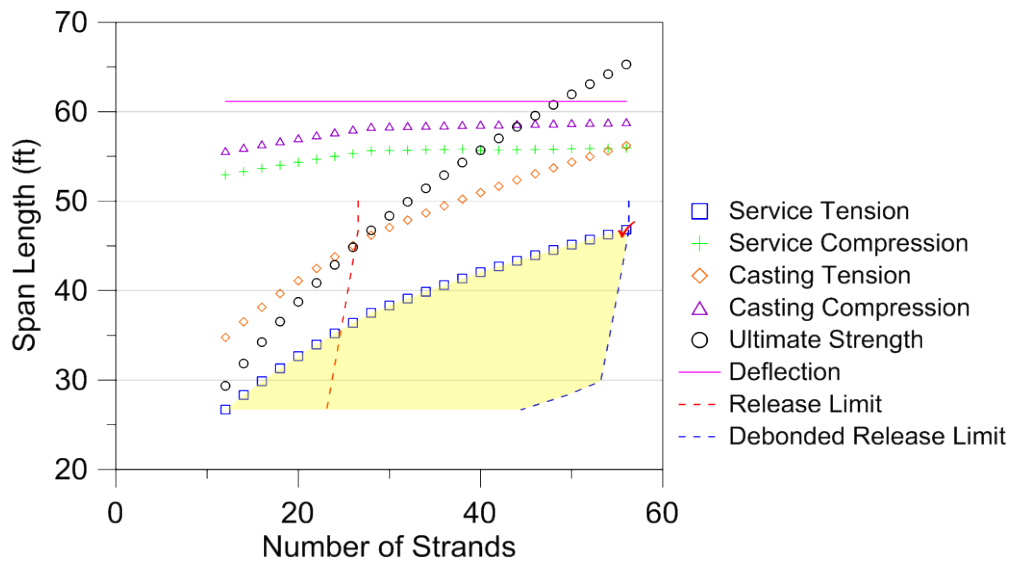
Figure 3.2. Solution Domain for 34 ft Wide Bridge with Four 5SB15 Beams.

The maximum span lengths for all 44 cases considered are listed in Table 3.3. The results are presented for six different bridge widths. The theoretical span length is shown as the maximum span length. The practical span length is the center to center of the bearing pad span length considering that the practical span length is 17 in. shorter than the total bridge span. The total bridge span has been kept to an integer number of feet and is defined as the back-wall-to-back-wall span length in TxDOT practice.

3.3.1 Achievable Span Lengths for 26 ft Wide Slab Beam Bridges

The 26 ft bridge width is the smallest within the bridge alternatives investigated. This is a common slab beam bridge width for a two-lane roadway. Therefore, it is important to note the limits and boundaries of this bridge width using a spread slab beam system. The solution domain charts for 26 ft wide spread slab beam bridge systems are shown in Figure 3.3. The maximum achievable total span is 52 ft when four 5SB15 slab beams are used. This results in a small clear spacing between slab beams of only 2 ft with the four 5 ft wide slab beams. This span length is the maximum achievable span out of all 44 viable bridge geometries considered in this preliminary study. It is possible to achieve a 47 ft span length using just three 5SB15 slab beams, which results in a 5 ft 6 in. clear spacing between slab beams. Although the beam spacing is relatively large, it is within the allowable limits of the stay-in-place PCPs.

3.3.2 Achievable Span Lengths for 30 ft Wide Slab Beam Bridges

There are six alternative geometries that can be achieved within the spacing limitations for a 30 ft total bridge width. All six design cases are shown graphically in Figure 3.4. The maximum achievable total span is 50 ft, which is 2 ft less compared to the 26 ft wide bridge. Again the maximum span length is achieved when four 5SB15 slab beams are used, resulting in a 3 ft 4 in. clear spacing between slab beams.

The investigation of the six alternatives showed no direct correlation between the achievable span length and the beam spacing. When five 4SB15 slab beams are used, the clear beam spacing is smaller (2 ft–6 in.) and the maximum achievable span is 49 ft, which is one foot less than the 4-5SB15 case. This shows that the slab beam width has a more prominent effect on the maximum span length as compared to the number of beams. The same observation is valid for all bridge widths.

41

Table 3.3. Maximum Span Lengths for Spread Slab Beam Bridges.

No.	Bridge Width (ft)	Number of Beams	Type of Beam	Clear Beam Spacing (ft)	Maximum Span (ft)	Practical Span (ft)	Total Bridge Span (ft)
1		3	5SB12	5.50	38.57	38.58	40
2		3	5SB15	5.50	45.99	45.58	47
3	26	4	5SB12	2.00	43.99	43.58	45
4		4	5SB15	2.00	50.78	50.58	52
5		4	4SB12	3.33	40.06	39.58	41
6		4	4SB15	3.33	46.53	45.58	47
7		4	5SB12	3.33	42.07	41.58	43
8		4	5SB15	3.33	48.68	48.58	50
9	30	4	4SB12	4.67	36.96	36.58	38
10		4	4SB15	4.67	44.46	43.58	45
11		5	4SB12	2.50	41.27	40.58	42
12		5	4SB15	2.50	47.77	47.58	49
13		4	5SB12	4.67	39.82	39.58	41
14		4	5SB15	4.67	46.82	46.58	48
15		4	4SB12	6.00	34.72	34.58	36
16		4	4SB15	6.00	42.66	42.58	44
17	34	5	5SB12	2.25	43.43	42.58	44
18		5	5SB15	2.25	50.14	49.58	51
19		5	4SB12	3.50	39.61	39.58	41
20		5	4SB15	3.50	46.04	45.58	47
21		6	4SB12	2.00	42.04	41.58	43
22		6	4SB15	2.00	48.50	47.58	49
23		5	5SB12	3.75	41.27	40.58	42
24		5	5SB15	3.75	47.85	47.58	49
25		5	4SB12	5.00	35.76	35.58	37
26	40	5	4SB15	5.00	43.78	43.58	45
27		6	5SB12	2.00	43.64	43.58	45
28		6	5SB15	2.00	50.34	49.58	51
29		6	4SB12	3.20	39.92	39.58	41
30		6	4SB15	3.20	46.33	45.58	47
31		5	5SB12	4.25	40.60	40.58	42
32		5	5SB15	4.25	47.15	46.58	48
33		5	4SB12	5.50	35.62	35.58	37
34	42	5	4SB15	5.50	43.10	42.58	44
35		6	5SB12	2.40	43.03	42.58	44
36		6	5SB15	2.40	49.68	49.58	51
37		6	4SB12	3.60	38.72	38.58	40
38		6	4SB15	3.60	45.67	45.58	47
39		5	5SB12	5.25	38.92	38.58	40
40		5	5SB15	5.25	45.85	45.58	47
41	46	6	5SB12	3.20	41.89	41.58	43
42		6	5SB15	3.20	48.43	47.58	49
43		6	4SB12	4.40	37.00	36.58	38
44		6	4SB15	4.40	44.43	43.58	45
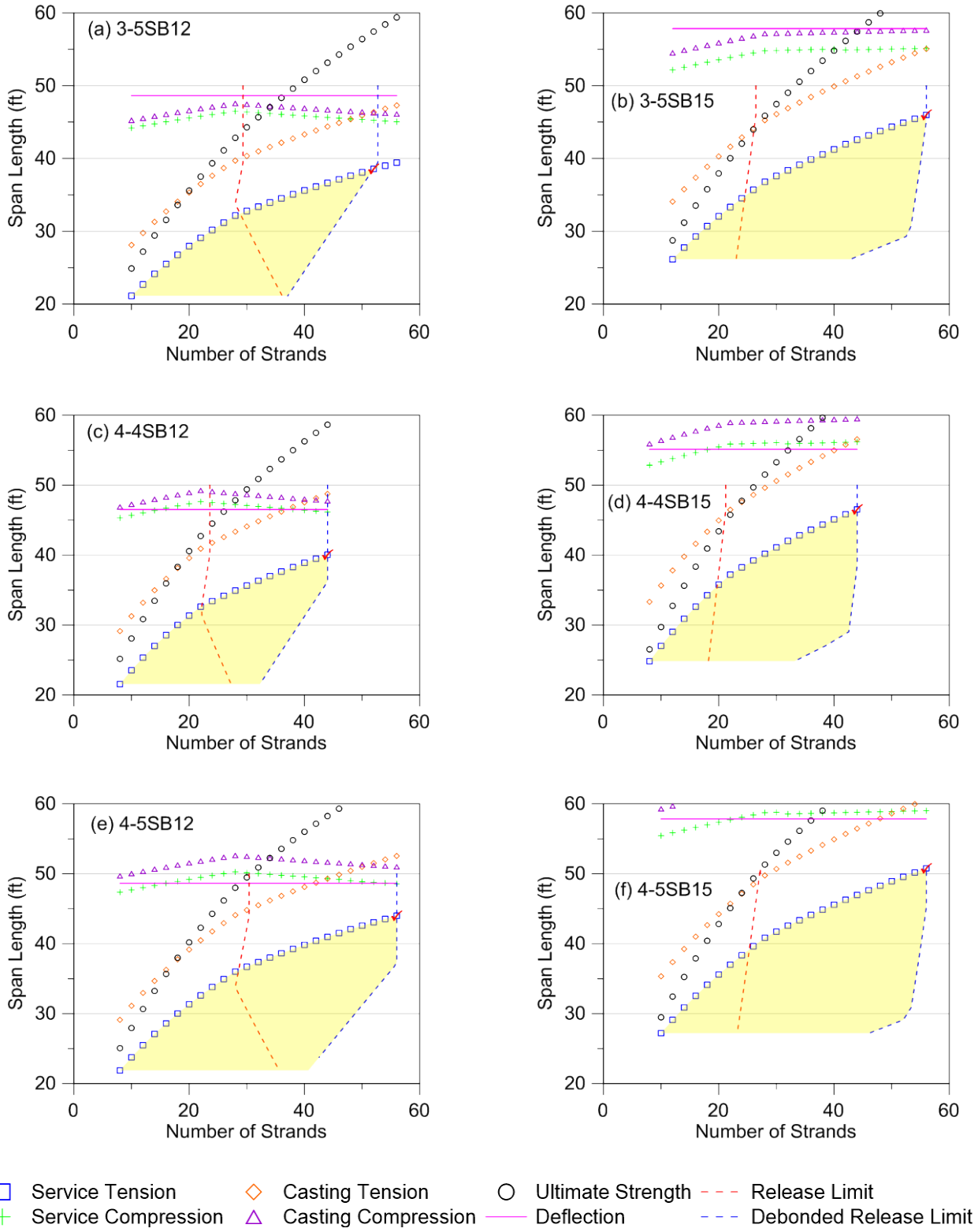
Figure 3.3. Span Length Solution Domain for 26 ft Wide Spread Slab Beam Bridges.
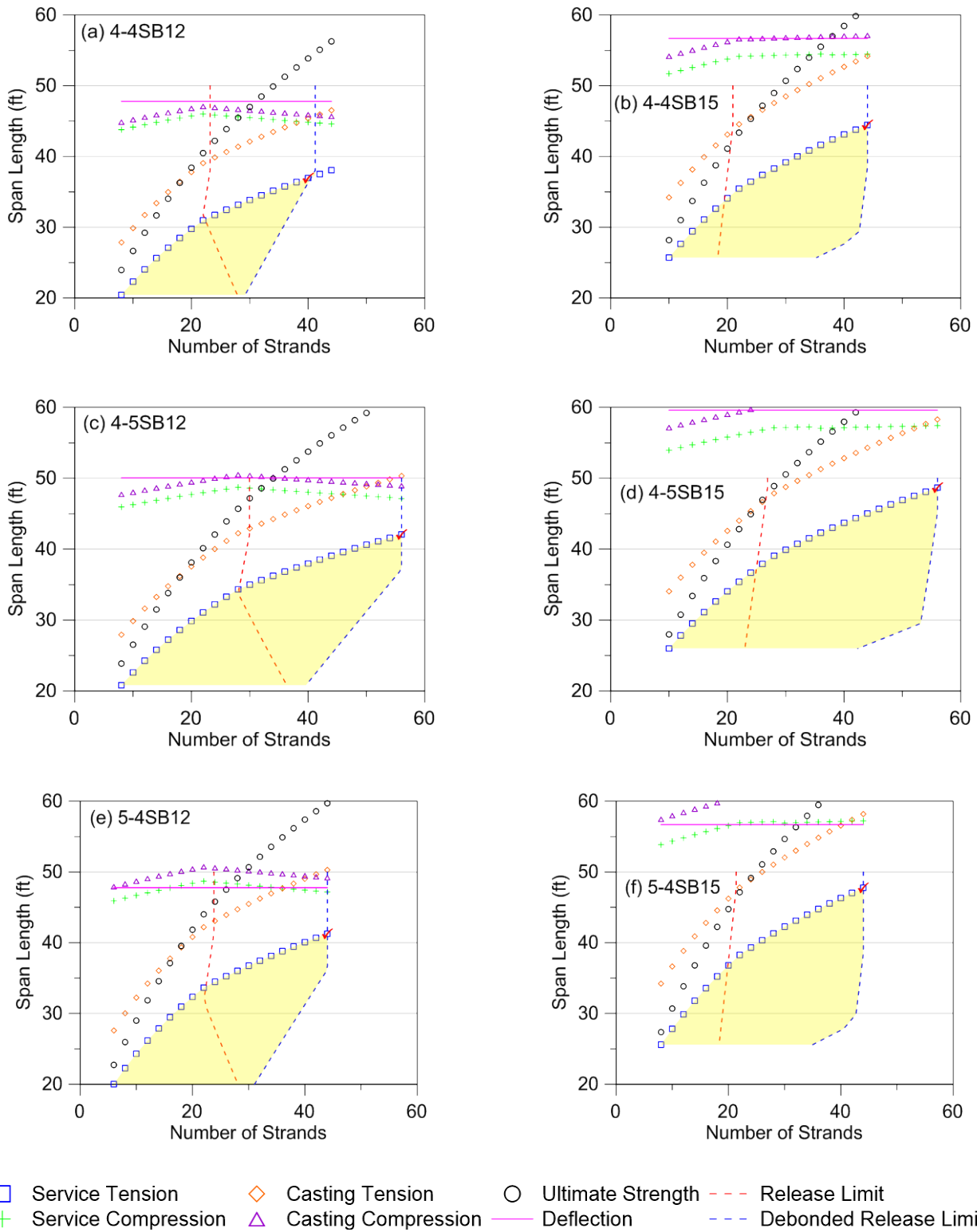
Figure 3.4. Span Length Solution Domain for 30 ft Wide Spread Slab Beam Bridges.

3.3.3 Achievable Span Lengths for 34 ft Wide Slab Beam Bridges

Another common slab beam bridge width is 34 ft, which has 10 different possible spread slab beam bridge geometries. Figure 3.5 presents span length solution domains for all 10 cases. The maximum achievable span is 51 ft when five 5SB15 slab beams are used.

The smallest maximum achievable span length out of all 44 bridge alternatives is for a 34 ft wide bridge with only four 4SB12 slab beams. The clear beam spacing is 6 ft and the maximum achievable span is 37 ft. The 12 in. slab beam depth results in relatively smaller span lengths as expected due to its smaller moment of inertia coupled with the limited strand positions in the 4 ft width.
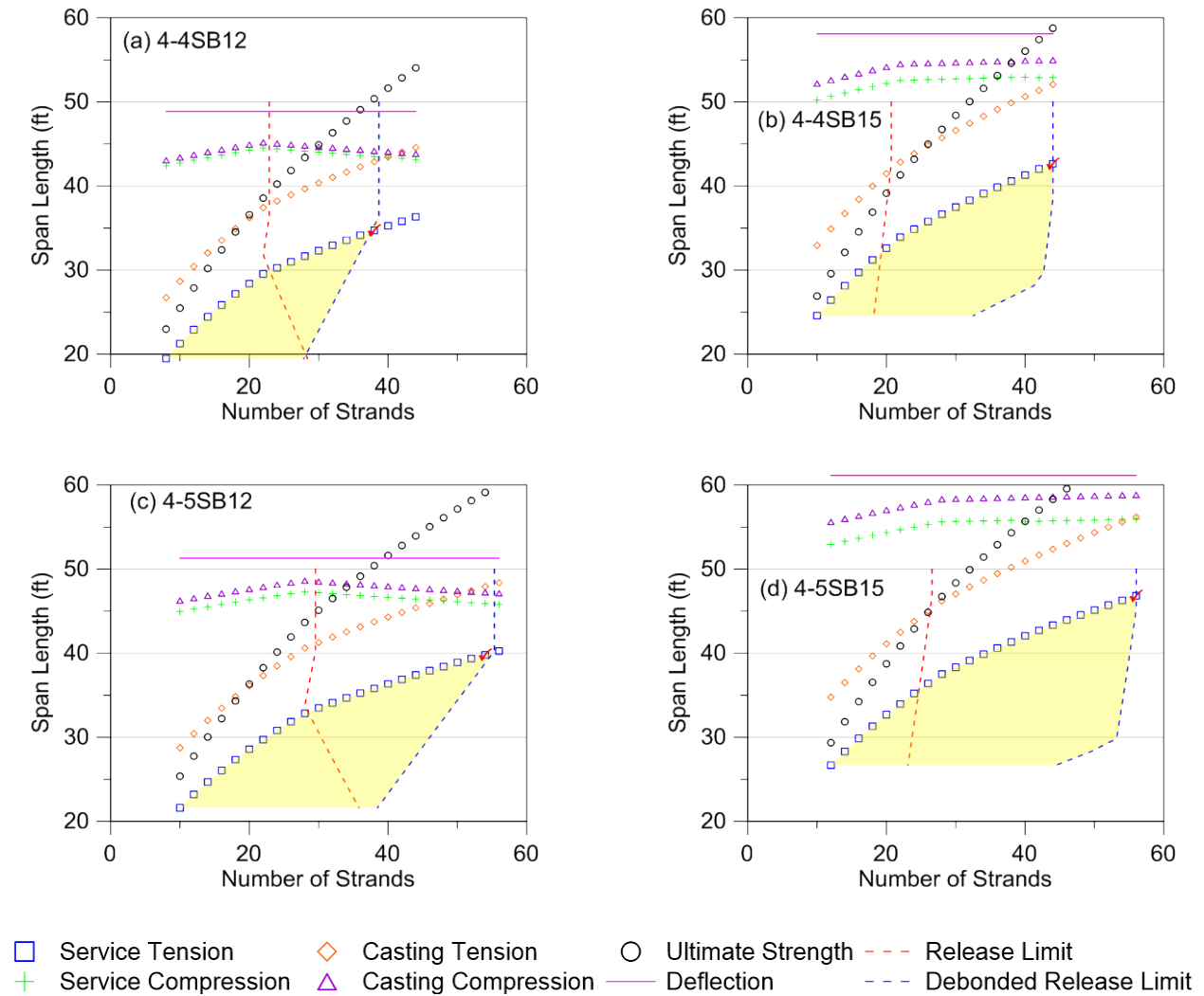
Figure 3.5. Span Length Solution Domain for 34 ft Wide Spread Slab Beam Bridges.
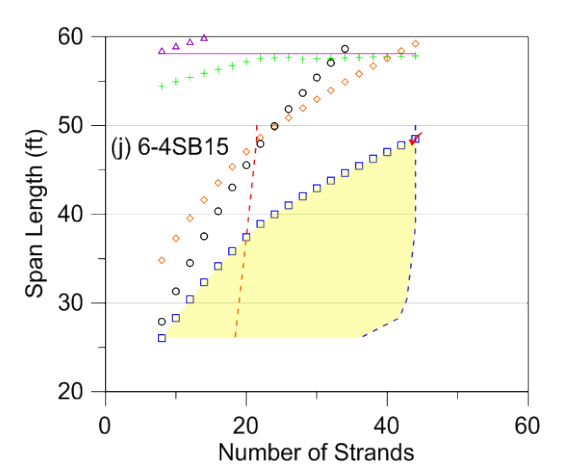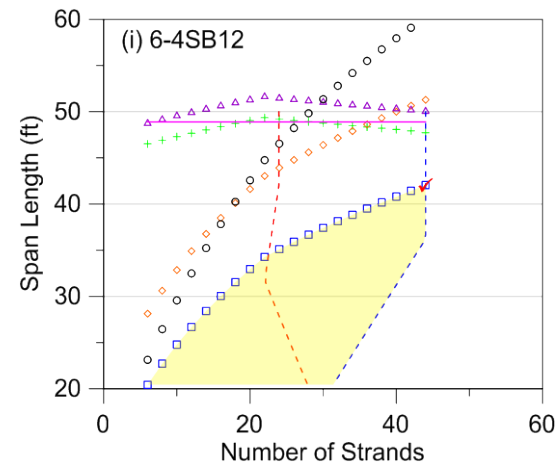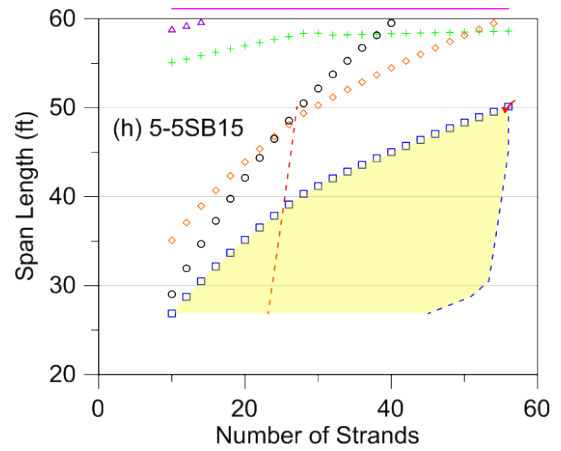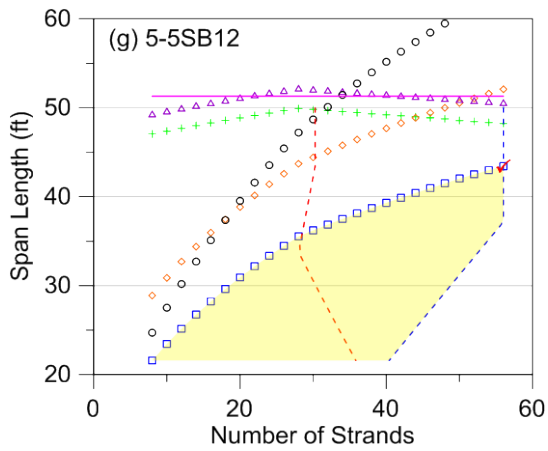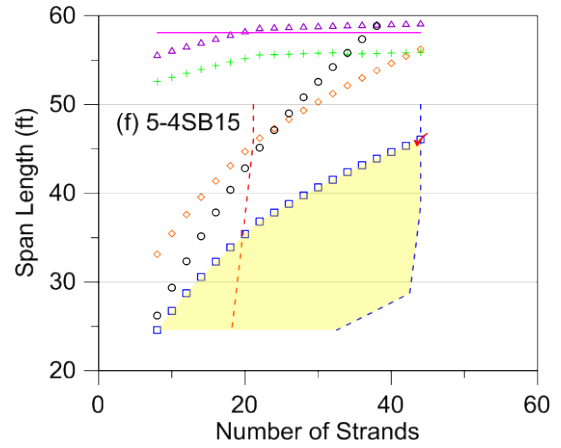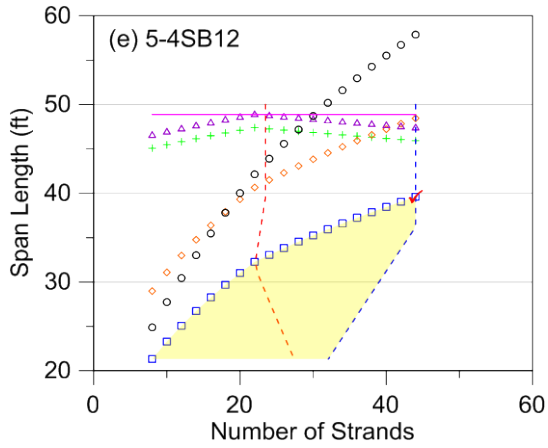
Figure 3.5. Span Length Solution Domain for 34 ft Wide Spread Slab Beam Bridges (Continued).

46

3.3.4 Achievable Span Lengths for 40 ft Wide Slab Beam Bridges

Although wider bridge widths are not very common for slab beam bridge types, several wider bridge widths for three lanes (40 ft, 42 ft, and 46 ft) were included in the parametric study based on the PMC's suggestions. The solution domains for a 40 ft bridge width are shown in Figure 3.6. Due to the increased bridge width, the number of girders cannot be less than five in order to satisfy practical slab beam spacing criteria. A total of eight different practical spread slab beam geometries can be achieved for 40 ft wide bridges.

A 40 ft bridge width is the smallest common TxDOT bridge width for a three-lane bridge. The preliminary designs that were included in the parametric study showed that the spread slab beam configuration could be utilized for three-lane bridges up to 51 ft span length. This maximum achievable span was obtained for six 5SB15 slab beams, which results in the smallest beam clear spacing of 2 ft.
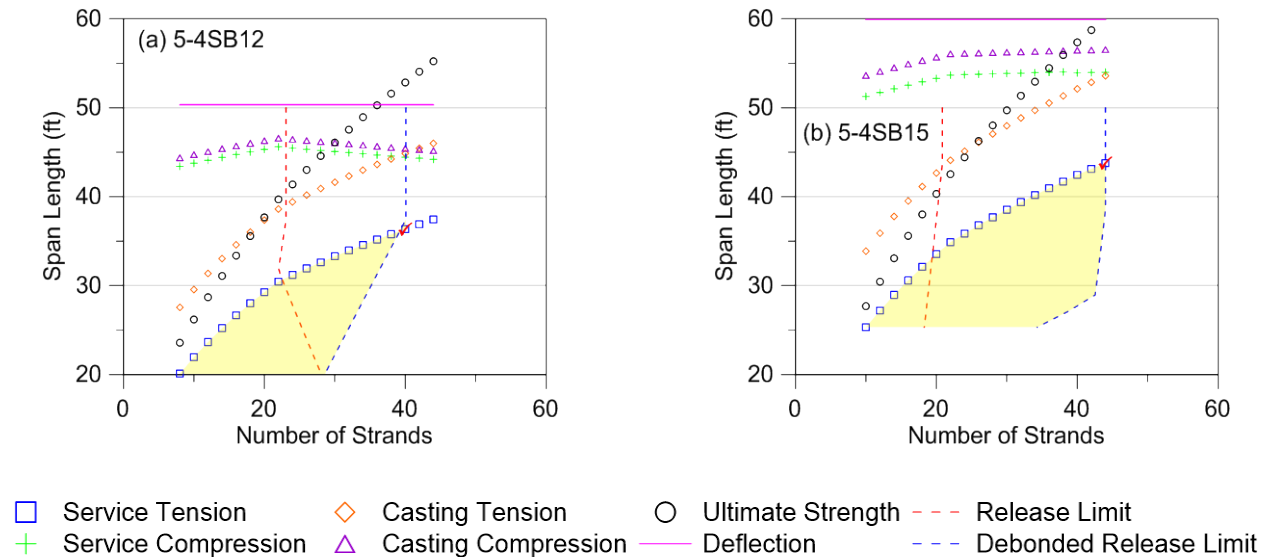
Figure 3.6. Span Length Solution Domain for 40 ft Wide Spread Slab Beam Bridges.
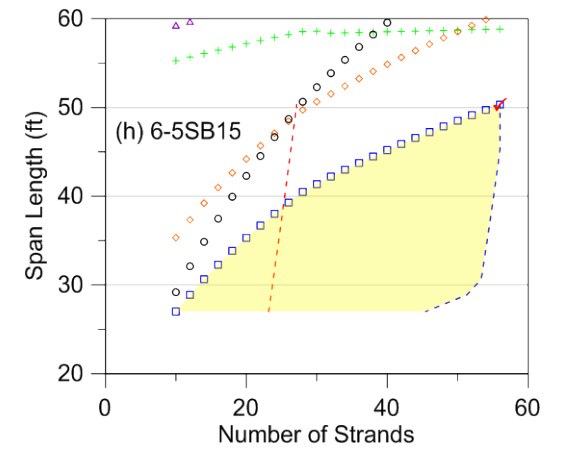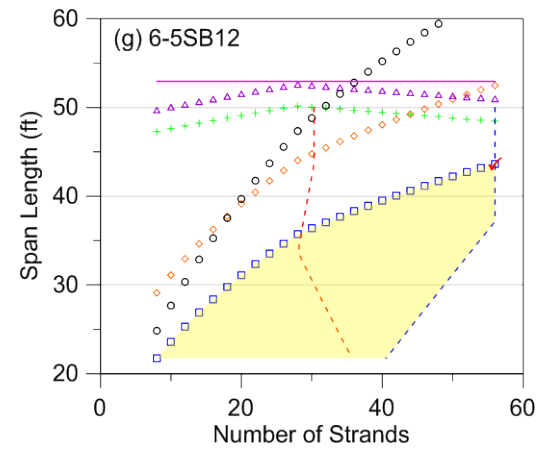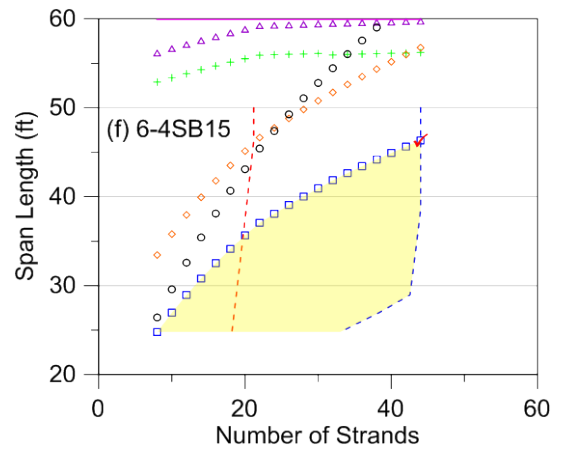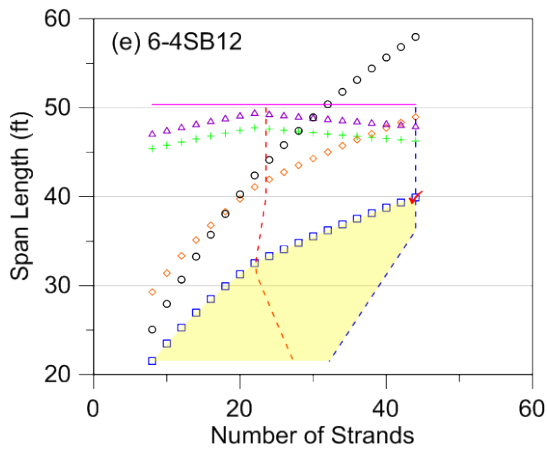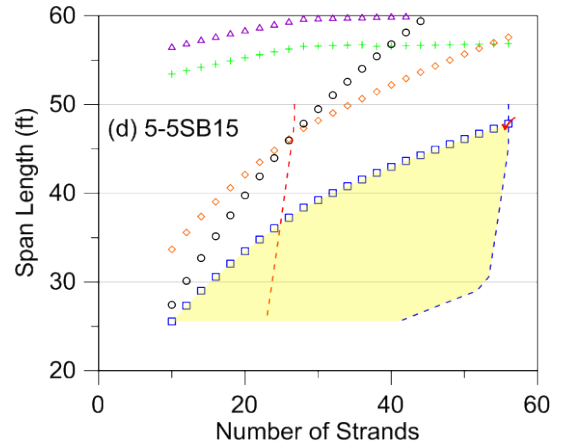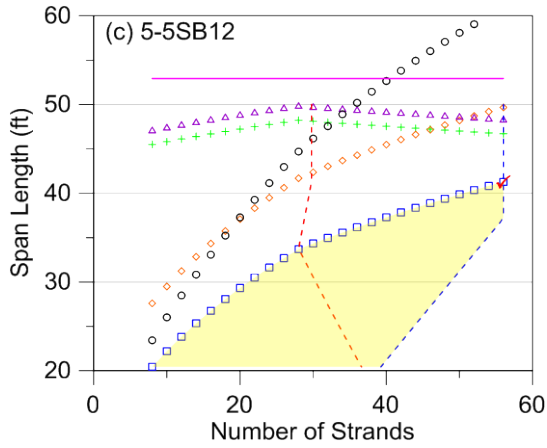
Figure 3.6. Span Length Solution Domain for 40 ft Wide Spread Slab Beam Bridges (Continued).

3.3.5 Achievable Span Lengths for 42 ft Wide Slab Beam Bridges

Another common bridge width is 42 ft. Although this width is very close to the 40 ft bridge width and will give similar results, the research team included it in the parametric study for completeness. The results for 42 ft wide spread slab beam bridges are shown in Figure 3.7.

Similar to 40 ft wide bridges, there are eight possible geometries that satisfy the spacing requirements. Either five or six slab beams can be used to maintain the practical spacing limits. The maximum achievable span length is 51 ft and corresponds to the use of six 5SB15 slab beams.

One of the smallest maximum span lengths is observed within the 42 ft bridge width group. Only a 38 ft span length is achievable when five 4SB12 slab beams are used. This also creates one of the highest eccentricities, with a 5 ft 6 in. clear spacing between slab beams.

3.3.6 Achievable Span Lengths for 46 ft Wide Slab Beam Bridges

The widest common TxDOT bridge width is 46 ft. There are six possible spread slab beam bridge geometries for a 46 ft wide bridge. All six cases were investigated and the results are shown in Figure 3.8. The maximum achievable span length is 49 ft, which corresponds to the use of six 5SB15 slab beams with a 3.2 ft clear spacing between slab beams.
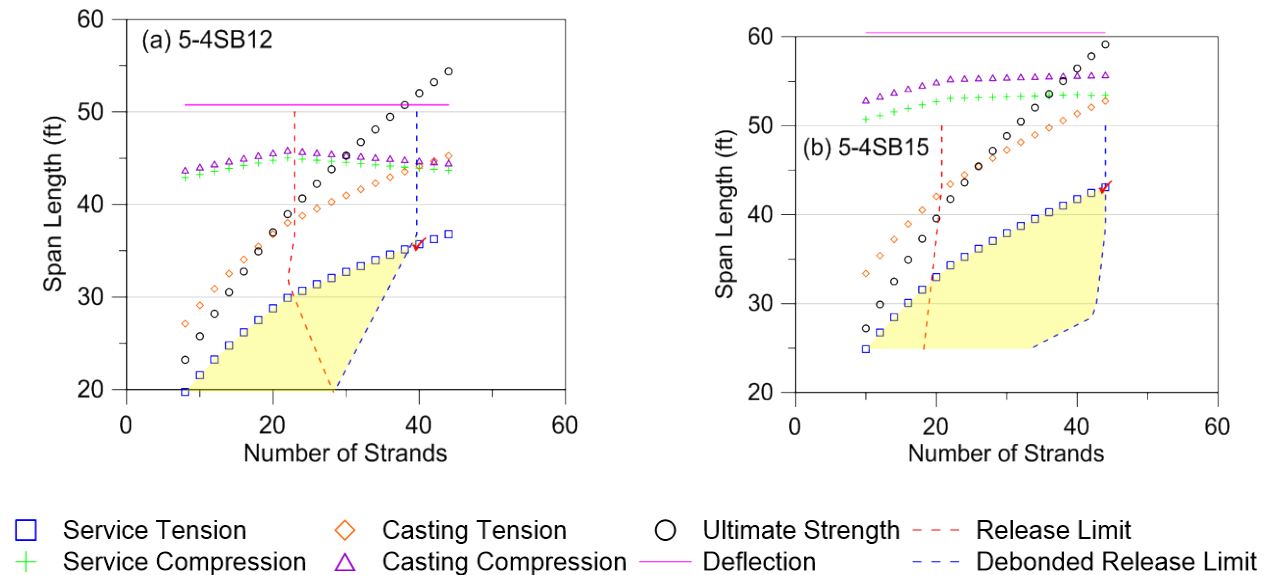
Figure 3.7. Span Length Solution Domain for 42 ft Wide Spread Slab Beam Bridges.
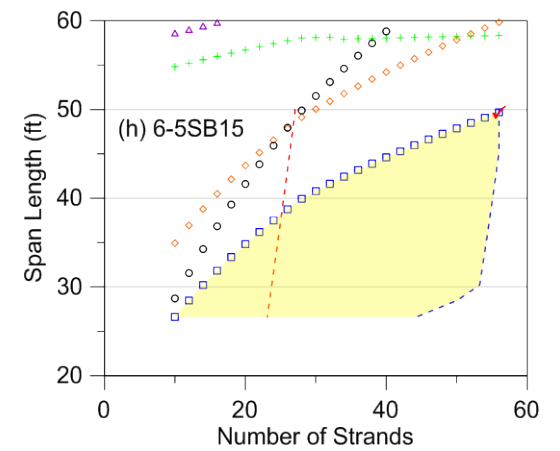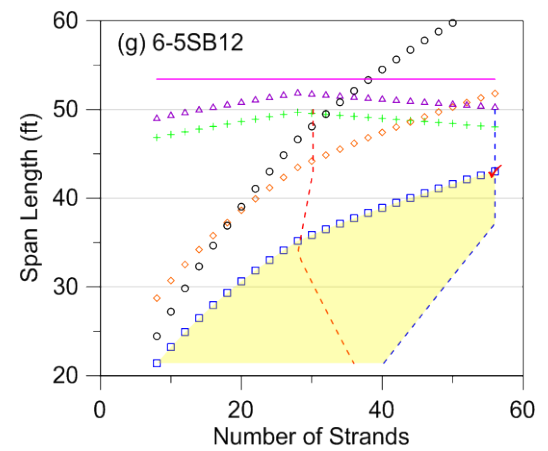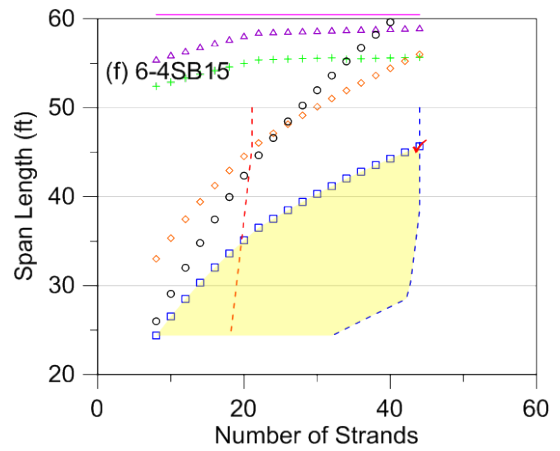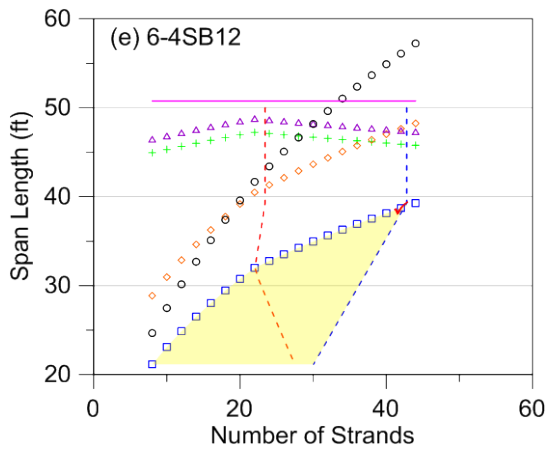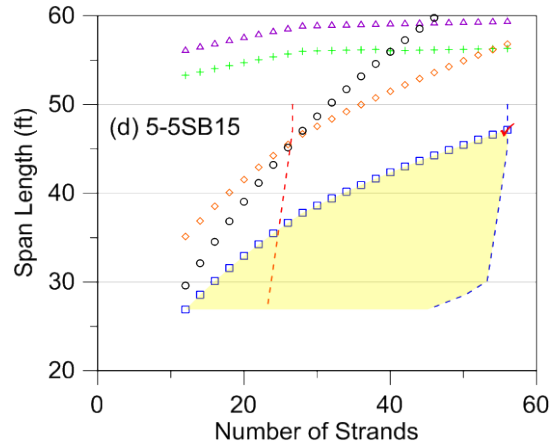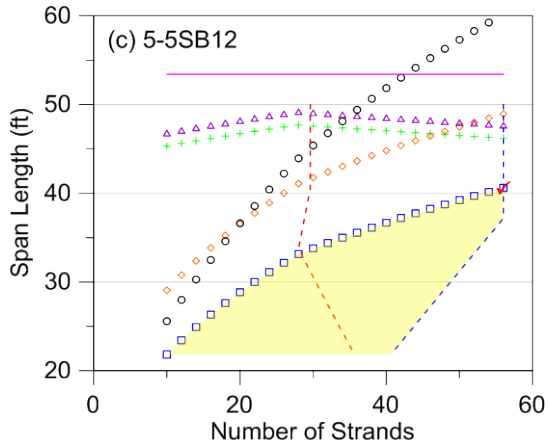
Figure 3.7. Span Length Solution Domain for 42 ft Wide Spread Slab Beam Bridges (Continued).

50
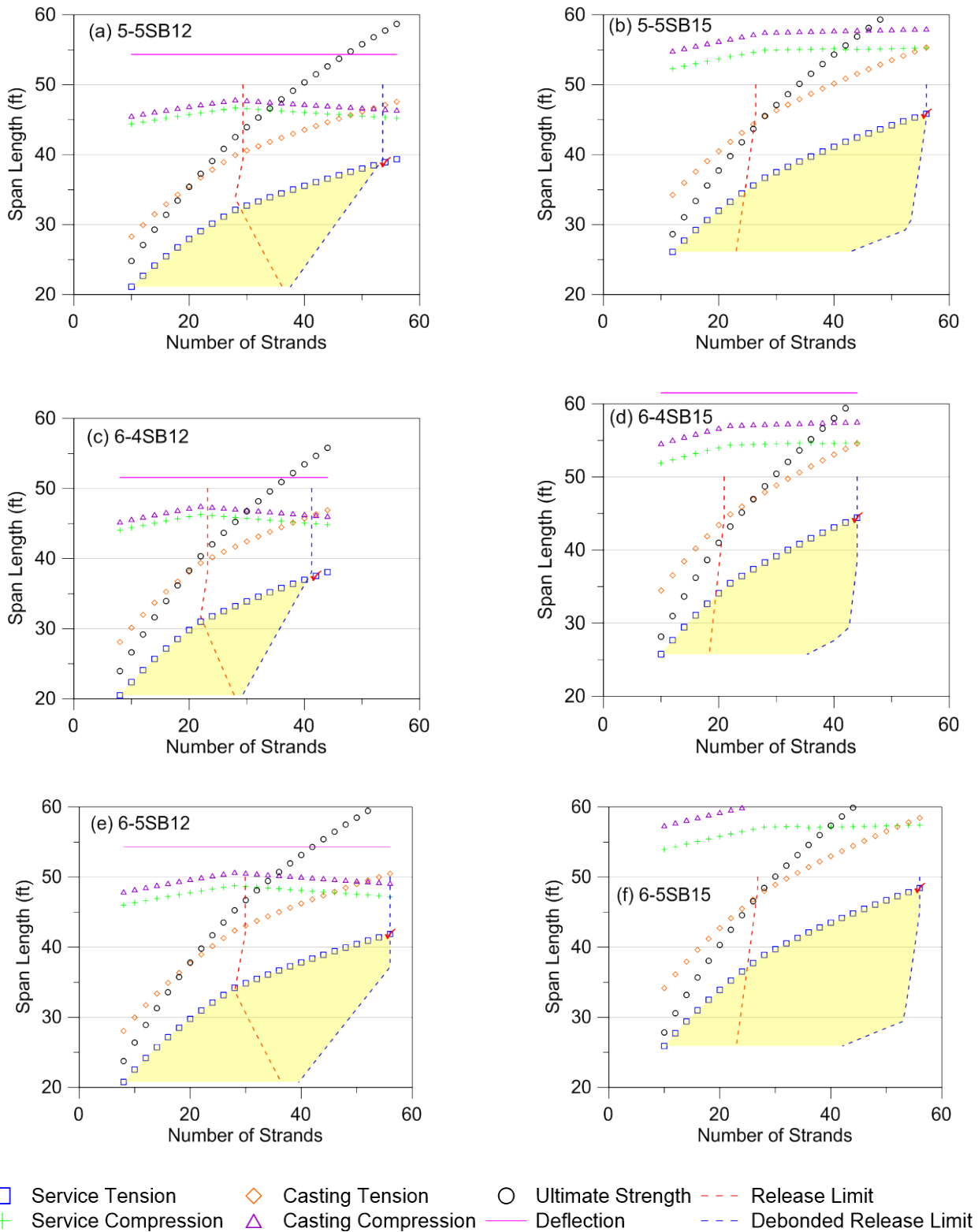
Figure 3.8. Span Length Solution Domain for 46 ft Wide Spread Slab Beam Bridges.

51

3.4   SHEAR LIMIT STATES

The parametric study described in the first part of this chapter considered the flexural limit states to determine span length limits for various bridge geometries. As an additional check, the shear limit states were checked based on the requirements of the AASHTO LRFD Specifications (2012). The transverse shear capacity of the standard slab beam types were evaluated under service loads in accordance with the AASHTO LRFD Specifications (2012) Article 5.8.3.4. The interface shear resistance was also checked using the requirements provided in the AASHTO LRFD Specifications (2012) Article 5.8.4. Appendix A provides detailed procedures for transverse and interface shear limit state checks for the Riverside Bridge. Shear checks of four critical bridge superstructure geometries utilizing the 4SB12, 4SB15, 5SB12, and 5SB15 standard slab beam types are summarized in this section. Details of transverse and interface shear reinforcement are shown in Figure 3.9 and Figure 3.10. Table 3.4 lists the critical bridge geometries and Table 3.5 summarizes the critical shear section positions.

3.4.1   Transverse Shear Design Check of Critical Bridges

A total of four bridges having the largest beam spacing for the parametric study were chosen and analyzed under service loads. Design shear forces and corresponding moments are listed in Table 3.6. The shear capacity of these slab beam sections was checked at three critical locations where different transverse shear reinforcement spacing was provided (C-bars in Figure 3.9). The locations of these critical sections are as follows:

- Section A: Face of support (maximum shear demand for 4 in. C-bar spacing).
- Section B: Shear critical section (maximum shear demand for 6 in. C-bar spacing).
- Section C: End of reinforced zone containing 6 in. C-bar spacing (maximum shear demand for 9 in. or 12 in. C-bar spacing, depending on slab beam width).

AASHTO LRFD Specifications AASHTO (2012) Article 5.8.2.4 requires that the following equation must be satisfied at each section.

$$V_r = \phi V_n \geq V_u \tag{3.1}$$

Where:

V_r	=	Design shear resistance, kips.
V_n	=	Nominal shear resistance, kips.
V_u	=	Factored shear force, kips.
ϕ	=	Strength reduction factor for shear = 0.9 for normal weight concrete.

Table 3.4. Selected Bridge Geometries.

No.	Beam Type	Bridge Width (ft)	Center-to-Center Span (ft)	No. Strands per Beam
1	5SB12	26	38.58	52
2	5SB15	26	45.58	56
3	4SB12	34	34.58	38
4	4SB15	34	42.58	44

Table 3.5. Positions of Sections for Shear Checks.

No.	Beam Type	Section A (in.)	Section B (in.)	Section C (in.)
1	5SB12	13	20	42
2	5SB15	13	24	42
3	4SB12	13	20	38
4	4SB15	13	24	38

Note: Distances are from end of beam.

Table 3.6. Design Forces for Selected Bridges.

No.	V_u (kips)			M_u (kip-ft)		
	Section A	Section B	Section C	Section A	Section B	Section C
1	183	180	105	171	262	438
2	208	204	128	192	356	569
3	163	161	88	153	236	357
4	190	186	113	176	325	479
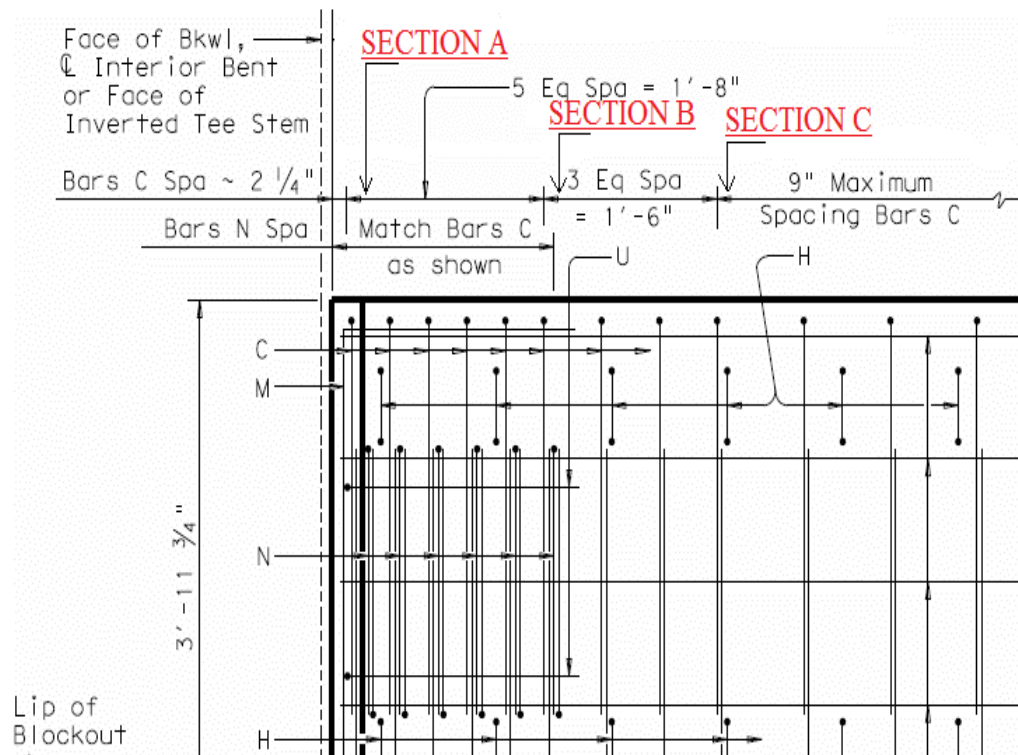
Figure 3.9. Sections Checked for Shear (TxDOT 2013b).

The shear resistance at three critical sections for all four bridges was calculated using the sectional design model provided in the AASHTO LRFD Specifications (2012). The nominal shear resistance at a given section is the sum of the concrete contribution to shear strength, the transverse reinforcement shear strength, and the component of the prestressing force in the direction of the applied shear.

$$V_n = V_c + V_s + V_p \tag{3.2}$$

Where:

V_c	=	Nominal shear resistance provided by tensile stresses in the concrete, kips.
V_s	=	Shear resistance provided by shear reinforcement, kips.
V_p	=	Component of the effective prestressing force in the direction of the applied shear, kips ($V_p = 0$ because all strands are straight).
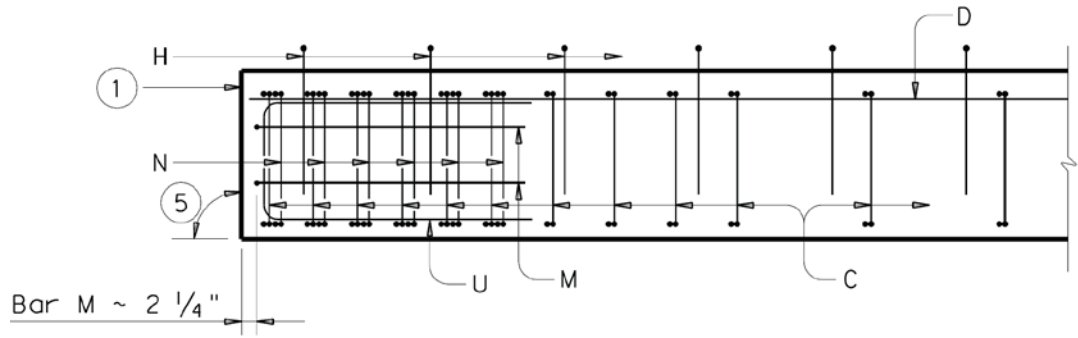
(a) Elevation View
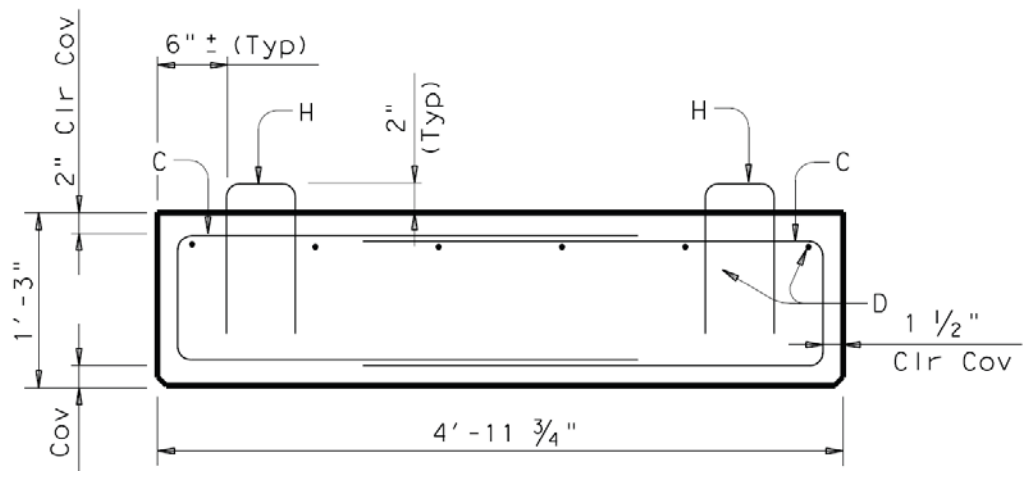
(b) Section View
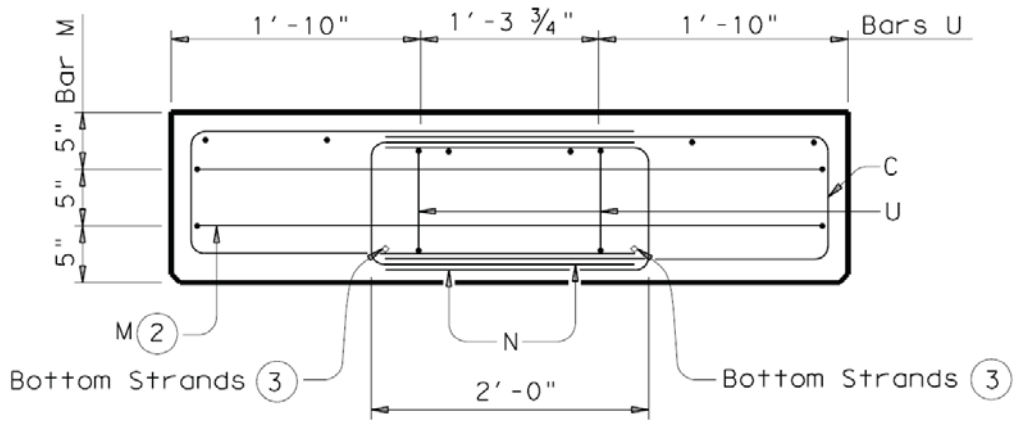
(c) End Zone Reinforcing

Figure 3.10. Shear Reinforcement Detail for 5SB15 Slab Beams (TxDOT 2013b).

The shear resistance provided by the concrete is calculated using the following expression from the AASHTO LRFD Specifications (2012).

$$V_c = 0.0316\beta\sqrt{f_c'}b_v d_v \tag{3.3}$$

Where:

f_c' = Design concrete compressive strength at 28 days (f_c' = 8.5 ksi).

b_v = Effective web width, in.

d_v = Effective shear depth, in.

d_e = Effective depth for bending, in.

d_v = Larger of $0.9d_e$ or $0.72h$, in.

The shear resistance provided by the shear reinforcement is calculated using the following expression from the AASHTO LRFD Specifications (2012).

$$V_s = A_v f_y \frac{d_v}{s}\cot\theta \tag{3.4}$$

Where:

β = Factor indicating the ability of diagonally cracked concrete to transmit tension between cracks.

A_v = Area of transverse reinforcing steel (in^2) within a distance s (in.).

f_y = Yield strength of transverse steel reinforcement, ksi (f_y = 60 ksi).

θ = Angle of inclination of diagonal compressive struts, degrees.

To determine the nominal shear resistance provided by the concrete and shear reinforcement (V_c, V_s) the β and θ parameters must be calculated. For prestressed members, β and θ are computed using Equations (3.5) and (3.6).

$$\beta = \frac{4.8}{(1+750\varepsilon_s)}\frac{51}{(39+s_{xe})} \tag{3.5}$$

$$\theta = 29 + 3500\varepsilon_s \tag{3.6}$$

Where:

ε_s = Longitudinal strain in the web (assumed positive for tension) found using Equation (3.6).

s_{xe} = Crack spacing parameter.

$$\varepsilon_s = \frac{|M_u / d_v| + 0.5N_u + |V_u - V_p| - A_{ps}f_{po}}{E_s A_s + E_p A_{ps}} \tag{3.7}$$

AASHTO LRFD Specifications (2012) Article 5.8.3.4 states that the parameter f_{po} is appropriate for both pretensioned and post-tensioned members when taken as follows.

$$f_{po} = 0.7 f_{pu} = 189 \text{ ksi} \tag{3.8}$$

The net longitudinal strain (ε_s) values for all four beams are negative even if half the strands are debonded. In this case, the AASHTO LRFD Specifications (2012) state that ε_s may be taken as zero or the denominator of Equation (3.7) is changed to $(E_s A_s + E_p A_{ps} + E_c A_{ct})$. The value for ε_s was conservatively taken as zero for the transverse shear strength check.

Shear capacities for all four slab beams at the three critical sections are summarized in Table 3.7. Half of the reduced nominal shear strength contribution of the concrete $(0.5\phi V_c)$ is slightly lower than the ultimate factored shear V_u within the end zone region. Therefore, transverse shear reinforcement is required. The values for V_s based on the standard transverse reinforcing steel provided for each slab beam type were calculated. It was found that the values for the reduced nominal shear capacity (ϕV_n) for all selected critical bridge superstructures are higher than the corresponding values of V_u. Therefore, the transverse steel currently provided in the TxDOT standard slab beam details is adequate based on the design calculations.

Table 3.7. Nominal Shear Capacity of Selected Bridges.

No.	Beam Type	Section	A_v (in²)	s (in.)	b_v (in.)	d_v (in.)	β	θ (deg.)	V_c (kips)	V_s (kips)	V_n (kips)
1	5SB12	A	0.8	4.0	60	16.65	3.96	29	364	360	725
		B	0.4	5.5	60	16.65	3.96	29	364	131	495
		C	0.4	9.0	60	16.65	3.96	29	364	80.1	444
2	5SB15	A	0.8	4.0	60	19.35	3.73	29	399	419	818
		B	0.4	5.5	60	19.35	3.73	29	399	152	552
		C	0.4	12	60	19.35	3.73	29	399	69.8	469
3	4SB12	A	0.8	4.0	48	16.65	3.96	29	291	360	652
		B	0.4	6.0	48	16.65	3.96	29	291	120	412
		C	0.4	9.0	48	16.65	3.96	29	291	80.1	371
4	4SB15	A	0.8	4.0	48	19.35	3.73	29	319	419	738
		B	0.4	6.0	48	19.35	3.73	29	319	140	459
		C	0.4	12	48	19.35	3.73	29	319	69.8	389

3.4.2 Interface Shear Design Check for Standard Slab Beam Types

3.4.2.1 General

An example of a detailed interface shear design check is shown in Appendix A for the Riverside Bridge. Interface shear designs for the selected critical bridge geometries were conducted using the same procedure. Researchers took cohesion (c) and friction (μ) factors from the AASHTO LRFD Specifications (2012). These parameters were selected for a CIP concrete slab on a clean girder surface not intentionally roughened ($c = 0.075$ and $\mu = 0.6$) based on observed surface conditions for precast slab beams during fabrication.

AASHTO LRFD Specifications (2012) Article 5.8.4 indicates that the reduced nominal interface shear resistance V_{ri} should be greater than the factored interface shear force due to the total load at service.

$$V_{ri} = \phi\, V_{ni} \tag{3.9}$$

In addition, the design should satisfy:

$$V_{ri} \geq V_{ui} \tag{3.10}$$

Where:

V_{ni} = Nominal interface shear resistance, kip/ft.

ϕ = Strength reduction factor for shear = 0.9 for normal weight concrete.

V_{ui} = Factored interface shear force due to the total load, kip/ft.

According to AASHTO LRFD Specifications (2012) Article 5.8.4, the minimum reinforcement area crossing the interface area shall satisfy:

$$A_{vf} \geq \frac{0.05 A_{cv}}{f_y} \tag{3.11}$$

Where:

A_{vf} = Area of shear friction reinforcement, in^2.

A_{cv} = Area of concrete section resisting shear transfer, in^2.

f_y = Specified minimum yield strength of reinforcing bars, ksi.

Equation (3.11) suggests that 5 ft wide slab beams shall have minimum 0.56 in^2/ft interface shear reinforcement and 4 ft slab beams shall have minimum 0.44 in^2/ft interface shear reinforcement. The TxDOT standard slab beam details satisfy this requirement by having a 0.8 in^2/ft reinforcing bar area crossing the interface plane.

Kovach and Naito (2008) suggested that the ACI 318-08 (ACI Committee 318 2008) and AASHTO LRFD Specifications (2007) requirements for the interface shear design are highly conservative and a greater reliance can be placed on the cohesion of the concrete interface. ACI 318-08 allows a maximum of 80 psi horizontal shear stress for an unreinforced interface if the contact surface is clean, free of laitance, and intentionally roughened to 0.25 in. The AASHTO LRFD Specifications (2007) allow a maximum of 240 psi horizontal shear stress for similar conditions if the minimum reinforcement requirement is disregarded. Kovach and Naito (2008) reported that previous research has shown that the same amount of roughened interface can achieve an average of 450 psi horizontal shear stress capacity (Evans and Chung 1969; Hanson 1960; Nosseir and Murtha 1971). Kovach and Naito (2008) concluded that the shear strength values obtained from the experiments are about six to 10 times greater than the values presented by ACI 318-08 for unreinforced composite sections. In addition, composite beams with a broom finish can achieve a horizontal shear capacity of 435 psi.

TxDOT Bridge Division Standard Drawings (TxDOT 2013b) do not specify an intentionally roughened surface for precast slab beams. The interface shear design was conducted using two alternative methods permitted in the AASHTO LRFD Specifications (2012), including a sectional method and global force equilibrium. Each method is discussed below.

3.4.2.2 Sectional Method

The sectional method uses simplified elastic beam behavior, where for a unit length (1 ft) segment, the factored shear force may be calculated as:

$$V_{ui} = \frac{12V_u}{d_v} \tag{3.12}$$

Where:

V_{ui} = Factored interface shear force per length, kip/ft.

V_u = Factored shear force at section, kips.

AASHTO LRFD Specifications (2012) Article 5.8.4 states that the nominal shear resistance (V_{ni}) of the interface shear plane at the shear critical section shall be taken as:

$$V_{ni} = cA_{cv} + \mu\left(A_{vf}f_y + P_c\right) \tag{3.13}$$

Where:

A_{cv} = $b_v L_v$ = Area of concrete engaged in interface shear transfer, in.^{2}.

b_v = Width of the interface, in.

L_v = Length of the interface, in.

A_{vf} = Area of interface shear reinforcement, in.^{2}.

P_c = Permanent net compressive force acting normal to the shear plane, kips (assumed to be zero).

c = Cohesion factor = 0.075 ksi for not intentionally roughened surface.

μ = Friction factor = 0.6 for not intentionally roughened surface.

f_y = Yield stress of reinforcement, ksi.

The interface shear resistance for each selected bridge was determined for the TxDOT standard slab beam interface shear reinforcement. The computed values are listed in Table 3.8. As the table shows, the reduced total nominal interface shear resistance (ϕV_{ni}) is not sufficient for these critical spread slab beam bridges at the locations of maximum shear demand when the beam surface is not intentionally roughened, which was the case for the standard slab beams used for the Riverside Bridge. Therefore, the standard interface shear reinforcement must be increased for spread slab beam bridges with relatively large spacings and spans. Or the beam surface can be roughened to 0.25 in. in order to have a higher cohesion factor and shear friction coefficient. Nominal interface shear resistances for an intentionally roughened surface and the same amount of interface shear reinforcement are also provided in Table 3.8. Note that the bridges selected for investigation have the largest shear forces in the parametric study for each slab beam type.

Table 3.8. Interface Shear Check for Selected Bridges Using Sectional Method.

Interface Shear Parameters at Critical Section					Intentionally Roughened to 0.25 in.			Not Intentionally Roughened		
No.	Beam Type	A_{cv} (in^2)	A_{vf} (in^2)	V_{ui} (kip/ft)	c (ksi)	μ	ϕV_{ni} (kip/ft)	c (ksi)	μ	ϕV_{ni} (kip/ft)
1	5SB12	672	0.8	162	0.28	1.0	213	0.075	0.6	71.3
2	5SB15	672	0.8	151	0.28	1.0	213	0.075	0.6	71.3
3	4SB12	528	0.8	145	0.28	1.0	177	0.075	0.6	61.6
4	4SB15	528	0.8	138	0.28	1.0	177	0.075	0.6	61.6

For all four selected critical bridge geometries, the typical slab beam interface shear reinforcement does not satisfy the design requirements provided in AASHTO LRFD Specifications (2012) Article 5.8.4 when the beam surface is not intentionally roughened, as observed for the Riverside Bridge slab beams. However, if the surface is roughened to a 0.25 in. amplitude, the standard interface shear reinforcement area is adequate. The required amount of interface shear reinforcement was then investigated for these selected bridges using the global force equilibrium approach.

3.4.2.3 *Global Force Equilibrium*

AASHTO LRFD Specifications (2012) Commentary C5.8.4.1 notes that a global force equilibrium method may be used to determine the distribution of interface shear reinforcement.

The beam horizontal shear over a segment is calculated from the change in compression forces between two points, as shown in Figure 3.11.
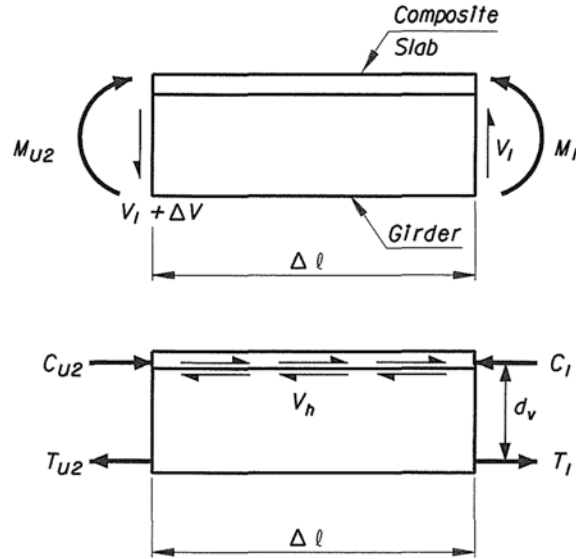
Figure 3.11. Horizontal Shear Demand—Global Force Equilibrium (AASHTO 2012).

In Figure 3.11, the following equations and parameters are employed.

$$C_1 = M_1 / d_v \tag{3.14}$$

$$V_h = C_1 - C_2 \tag{3.15}$$

$$v_h = \frac{C_1 - C_2}{l \cdot b_v} \tag{3.16}$$

Where:

C_1 = Compression force above the shear plane associated with M_1, kips.

C_{U2} = Compression force above the shear plane associated with M_{U2}, kips.

M_1 = Factored moment at Section 1.

M_{U2} = Factored moment at Section 2.

d_v = Distance between the centroid of the tension steel and the mid-thickness of the slab, in.

b_v = Width of the interface, in.

l = Length of the considered interface plane, in.

V_h = Horizontal shear force demand within the horizontal shear plane considered, kips.

v_h = Horizontal shear stress demand within the horizontal shear plane considered, ksi.

Horizontal shear demands were calculated between the support and quarter point of the span length and between the quarter point and midspan locations, along with the corresponding interface shear reinforcement requirements.

Table 3.9. Interface Shear Design Using Global Force Equilibrium.

Parameter					Support to Quarter Span			Quarter Span to Midspan		
No.	Beam Type	c (ksi)	μ	A_{cv} (in^2)	A_{vf} (in^2/ft)	ϕV_{ni} (kips)	V_h (kips)	A_{vf} (in^2/ft)	ϕV_{ni} (kips)	V_h (kips)
1	5SB12	0.075	0.6	6480	1.8	1000	992	0.56	455	258
2	5SB15	0.075	0.6	7660	1.6	1110	1110	0.56	535	310
3	4SB12	0.075	0.6	4570	1.7	784	777	0.44	322	206
4	4SB15	0.075	0.6	5620	1.7	965	941	0.44	393	253

For the selected critical bridge geometries, the standard interface shear reinforcement between the support and quarter span length must be doubled, while the minimum interface shear reinforcement may be used for the region between the quarter span and midspan for these standard slab beam types.

3.4.2.4 Development Length of Interface Shear Reinforcement

The interface shear resistance of the composite section is calculated based on the full yield strength of the reinforcement. Therefore, the interface shear reinforcement (denoted as H-bars in TxDOT Standard Drawings (2013b)) should have sufficient development length into the slab beam and into the CIP deck concrete.

The required development length for the H-bars was calculated using AASHTO LRFD Specifications (2012) Article 5.11.2.4. The basic development length for a hooked bar l_{hb} with yield strength not exceeding 60 ksi can be calculated as:

$$l_{hb} = \frac{38 d_b}{\sqrt{f_c'}} \tag{3.17}$$

The parameter d_b is the diameter of the interface shear reinforcement (0.5 in. for the #4 H-bars in the TxDOT Standard Drawings (2013b)). A modification factor of 0.7 can be applied because the cover normal to the plane of hook is not less than 2.5 in.

$$l_{hb} = 0.7 \times \frac{38 \times 0.5}{\sqrt{4}} = 6.65 \text{ in.} \tag{3.18}$$

Note that near midspan, the total CIP concrete thickness may be as low as 8.5 in., which includes a minimum 8 in. thick deck plus a 0.5 in. thick bedding strip. To maintain 2.5 in. clear cover, the hook height should be limited to 6 in. within the midspan region. To avoid using different extensions of the H-bars above the slab beams, a 6 in. dimension is suggested for all H-bars. The required development length can be further reduced to 6 in. using the excess reinforcement factor as long as the ratio of steel area required to steel area provided is 0.90 or less. For the critical bridge geometries considered, this would require the use of slightly more interface steel area than noted in Table 3.9 for the region between the support and quarter span.

3.5   SUMMARY

The research team conducted a parametric study to investigate preliminary designs for spread slab beam bridges. The effects of different parameters such as beam depth, beam width, number of beams, and beam spacing on the resulting maximum span length are summarized in Table 3.3.

3.5.1   Parametric Study Observations

The following observations were made based on the results of the parametric study.

1. For all bridge widths considered (26 ft, 30 ft, 34 ft, 40 ft, and 46 ft) it is possible to span approximately 50 ft.

2. For 26 ft and 30 ft wide bridges, maximum span lengths of 50 ft 7 in. and 48 ft 7 in., respectively, are achieved when four 5SB15 slab beams are used.

3. For 34 ft wide bridges, the use of five 5SB15 slab beams results in a 49 ft 7 in. span length.

4. In order to achieve the maximum possible span length for 40 ft, 42 ft, or 46 ft wide bridges, six 5SB15 slab beams must be used.

5. The slab beam depth is the most prominent parameter for achieving longer span lengths.

6. Beam depth and beam width have a more prominent effect on the maximum span length as compared to the number of beams.

7. In general, smaller beam spacing results in a greater span length.

8. For the same number of slab beams, 4SB15 beams allow greater span lengths compared to 5SB12 beams despite a larger beam spacing. This shows that the beam depth effect is more pronounced than the beam spacing and beam width effects.

3.5.2 Shear Reinforcement

Shear checks of four critical bridge superstructure geometries utilizing the 4SB12, 4SB15, 5SB12, and 5SB15 standard slab beam types were conducted, and the following observations were made.

1. The current transverse and interface shear reinforcement provided in the standard TxDOT slab beam sections should be maintained as a minimum for spread slab beam designs.

2. The standard transverse shear reinforcement currently provided by TxDOT for standard slab beam types satisfies the required transverse shear strength criteria for the critical spread slab beam bridge geometries investigated in the parametric study.

3. Because the shear per beam increases in a spread configuration, the shear requirements should be carefully reviewed during design to ensure that the standard transverse and interface shear reinforcement is adequate. In particular, the interface shear reinforcement (H-bars) may need to be increased in the end regions for more shear critical cases when the beam surface is not intentionally roughened to a 0.25 in. amplitude.

4. Based on observed typical precast fabrication practices, standard slab beams do not have an intentionally roughened surface. The manufacturing process currently includes the use of self-consolidating concrete, and curing is achieved by soaking the beams in water and leaving the surface untouched. Therefore, the slab beam surface ends up being relatively smooth.

5. The design checks indicate that interface shear reinforcement (H-bars) area per foot length can potentially be reduced for the midspan regions. However, the interface shear reinforcement area per foot length may need to be increased for the end regions of standard slab beams, particularly for the more shear critical cases with longer spans and wider beam spacings.

6. Until further research is conducted to evaluate the interface shear strength of slab beam bridges, the research team recommends maintaining the use of the interface shear reinforcement based on current practice and performance of conventional slab beam bridges. Interface shear reinforcement requirements should be checked as part of spread slab beam bridge designs.

7. The H-bars provided for interface shear should be properly developed into both the precast slab beams and the CIP deck. Therefore, the standard H-bar detail should be

modified to extend 6 in. into the CIP deck to provide the required development length. Note that sufficient steel area should be provided to justify this dimension, which is slightly smaller than the calculated hook length. This reduction is justified based on maintaining the ratio of area of steel required to area of steel provided at or below 0.90.

4   EXPERIMENTAL STUDY OF RIVERSIDE BRIDGE

4.1   GENERAL

One of the main objectives of this research project was to identify moment and shear load distribution factors (LDFs) for spread slab beam bridges. The experimental part of the research project consisted of building a full-scale spread slab beam bridge and testing it under service loads in order to assess the constructability and serviceability of the bridge, and to study live load distribution factors. For that purpose, a simply supported bridge was designed and built at the edge of a runway located at the Texas A&M University Riverside Campus. Figure 4.1 shows the bridge site location and plan view.

4.2   GENERAL DESCRIPTION OF RIVERSIDE BRIDGE

As depicted in Figure 4.2, the bridge has a 46 ft 7 in. span length (from center to center of the bearing pads) and an overall width of 34 ft. The bridge superstructure has four slab beam girders spaced at 4 ft 8 in. clear spacing with prestressed concrete panels (PCPs) between the slab beams as stay-in-place (SIP) forms. The slab beam girders are standard TxDOT 5SB15 slab beams. The 4 in. thick PCPs are 8 ft long and have an overall width of 5 ft 4 in. The CIP deck thickness varies slightly along the length to accommodate the camber of the prestressed slab beams. The minimum deck overall topping plus PCP thickness at the center of the bridge is 8 in. Figure 4.2 and Figure 4.3 show detailed drawings of the bridge superstructure and substructure components, which were designed based on the *AASHTO LRFD Bridge Design Specifications* (AASHTO 2012) and *TxDOT Bridge Design Manual* (TxDOT 2013a).

All the substructure components are reinforced concrete and were designed based on ultimate strength design requirements. Reinforced concrete spread footings were used to support the abutments. A reinforced concrete slab on grade was poured in order to create a working surface. The thickness of the slab on grade increased to 12 in. under the spread footing locations.

The standard TxDOT practice for bridge substructures is to use drilled shafts or piles to support the abutments or piers. However, to reduce costs, the Riverside Bridge substructure was designed and built using spread footings instead of drilled shafts. Appendix B provides detailed documentation of the Riverside Bridge construction process, and Supplement 1 to this report provides a complete set of structural plans.

(a) Location of Bridge Site (Google Maps 2005)
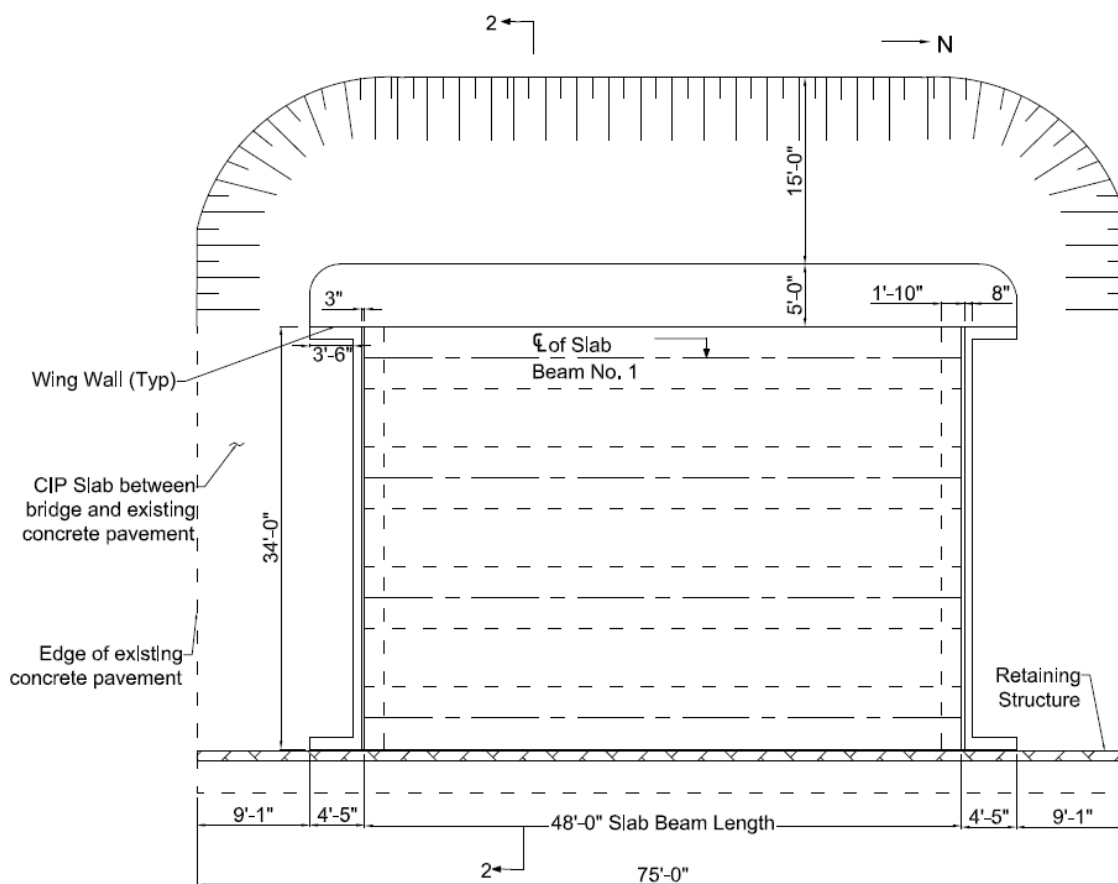
(b) Plan View

Figure 4.1. Bridge Location and Plan View.
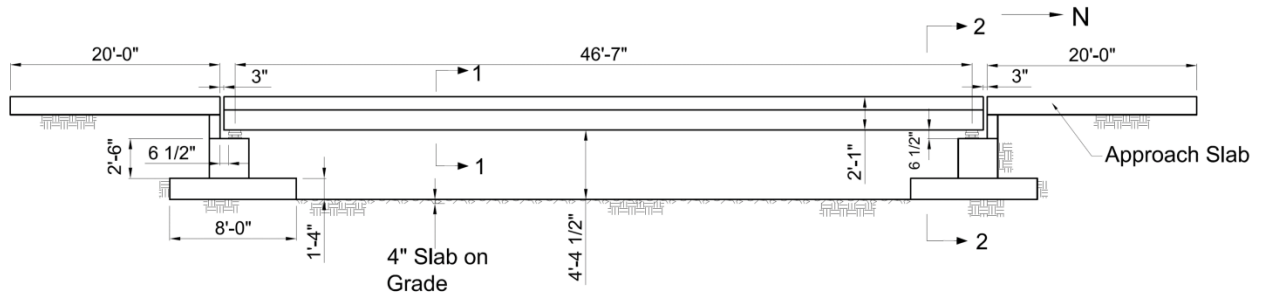
(a) Side Elevation View
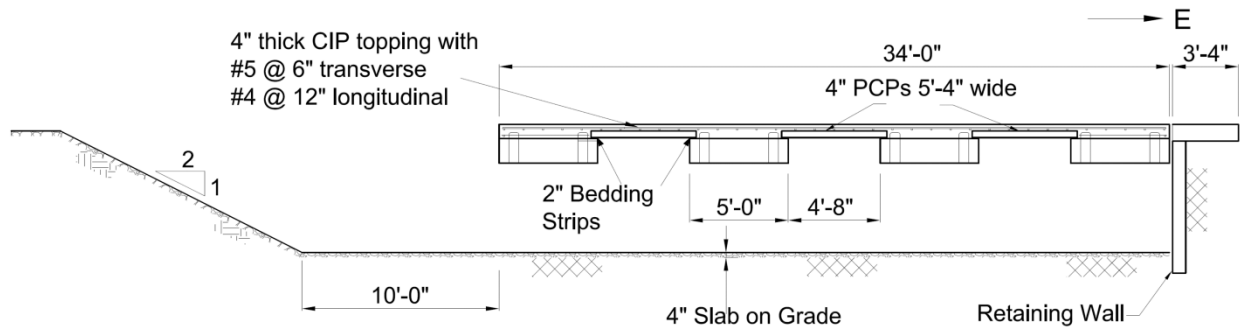
(b) Section 1-1: Cross-Section of Spread Slab Beam Deck
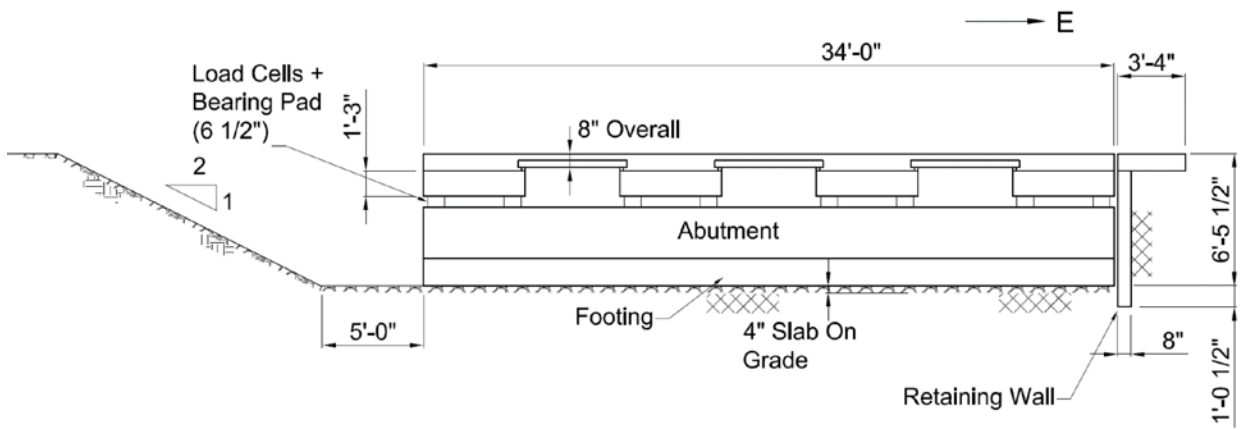
(c) Section 2-2: Cross-Section at Abutment

Figure 4.2. The Riverside Bridge Superstructure.
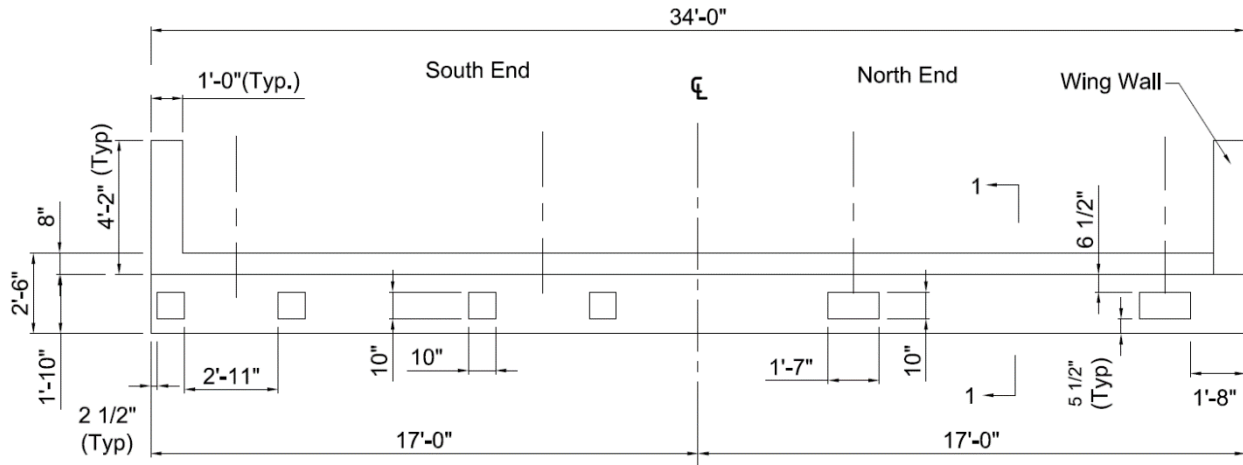
(a) Plan View at Abutment
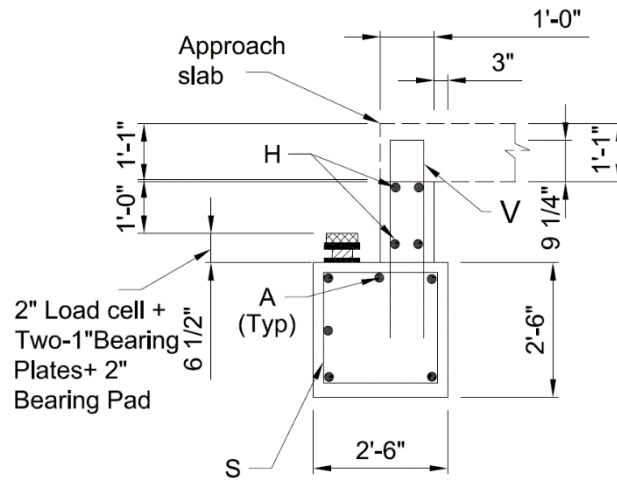
(b) Cross-Section 1-1 at Abutment
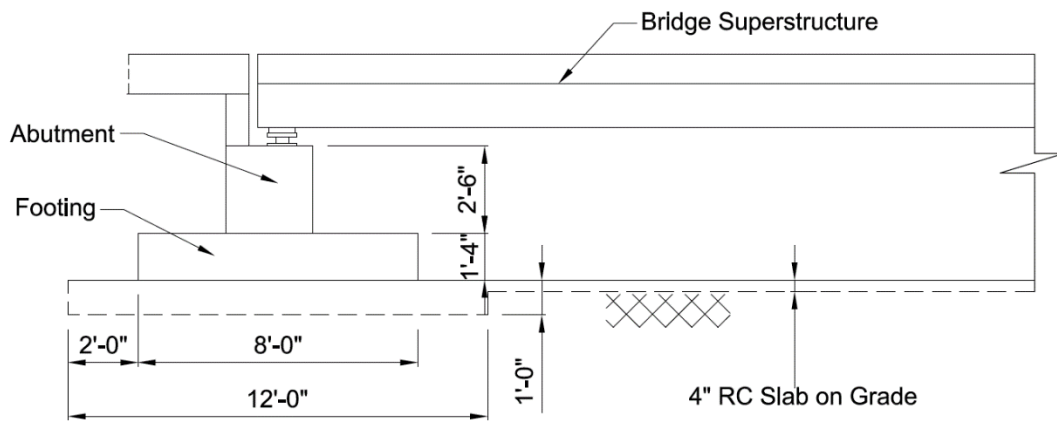
(c) Side Elevation of Abutment

Figure 4.3. The Riverside Bridge Substructure.

4.2.1   Load Cell Assembly and Bridge Superstructure

Figure 4.4 presents several photographs that show the load cell assembly and placement at each abutment. One of the difficulties when investigating live load distribution factors is the identification of shear reactions for individual girders. For the test bridge, load cell assemblies were placed beneath each girder before the erection of the slab beams. The load cell assembly consists of a 1 in. thick bottom steel plate and a 1.5 in. thick top plate sandwiching a 100-kip rated load cell (Figure 4.4(b]). There are two different load cell assemblies as a result of a two-bearing-pad and a one-bearing-pad configuration, as shown in Figure 4.4(a) and (b). Figure 4.4(a) shows the south end of the bridge where there are two bearing pads (9x9 in.) at the slab beam ends, one at each corner, with 10x10 in. steel plates. Figure 4.4(b) shows the north end of the bridge where there is one bearing pad (9x18 in.) at the centerline of each slab beam; the steel plates are 10x20 in. The bottom plates were placed and attached to their exact locations using a high early strength grout. Load cells were placed inside small circular indentations machined on the steel plates. Then the top steel plates were also machined and placed on the button of the load cells. Small Styrofoam pieces were temporarily placed between the steel plates at the corners to enhance stability during the erection of the slab beams.

After the erection of the slab beams, bedding strips were cut to the required depth. The bedding strip depth was calculated according to the camber of the slab beams. Bedding strip depth can be a minimum of 0.5 in. and a maximum of 4 in. according to the *TxDOT Bridge Design Manual* (TxDOT 2013a). Based on these calculations, the bedding strip depth was decided to be 0.5 in. at the midspan and 3.5 in. at the end of the slab beams, changing linearly in between. The width of the bedding strips was 2 in., as specified by *TxDOT Bridge Design Manual* (TxDOT 2013a). Figure 4.5 shows a view of precast beams and panels during erection. A total of 18 PCPs were placed along the span between slab beams (six for each clear space). According to the *TxDOT Bridge Design Manual* (TxDOT 2013a), the length of the PCP projecting past the bedding strip should be at least 1.5 in. For the Riverside Bridge, this length was designed to be 2 in. During the erection of the PCPs, the construction crew ensured a minimum projection of at least 1.5 in. was provided along each edge for all panels.

(a) South End Load Cell Assembly and Layout

(b) North End Load Cell Layout

(c) Bridge Span Ready to Receive Slab Beams

Figure 4.4. Load Cell Assembly and Layout.

(a) Slab Beam Placement

(b) Bedding Strip Application

(c) Placement of Precast Concrete Panels

Figure 4.5. Placement of Precast Slab Beams and Panels.

4.3   INSTRUMENTATION OF BRIDGE

Figure 4.6 shows the detailed naming and position of each sensor that was used during preliminary testing. The instrumentation of the Riverside Bridge was designed based on the objectives of the research program. A total of 16 load cells were placed at both ends of each slab beam during the construction process. The load cells are used to determine the load sharing between slab beams under vehicle loading and the corresponding shear distribution factors.

Moment live load distribution factors under vehicular loading must also be determined. The moments for each girder can be calculated from the deflection profiles of the slab beams. In order to obtain the moments, at least three deflection values along the length must be known, but more points are advantageous for numerical differentiation using recorded deflection values. Based on the available channels on the data acquisition system it was decided that a total of 10 string potentiometers per girder would be used.

A total of four tests were conducted to investigate load sharing between girders for the spread slab beam bridge at Riverside. The first three tests included preliminary testing to explore the appropriate instrumentation layout and methods to determine shear and moment LDFs.

The preliminary instrumentation layout suggested using the string potentiometers at seven stations. For three of those seven stations, string potentiometers were provided at both edges of the slab beams to capture torsional deformations of the slab beam girders.

In order to be able to capture natural frequency and mode shapes of the girders during dynamic testing, a total of eight accelerometers were attached on the bottom of the slab beams. Five accelerometers were attached along one of the interior beams, and the remaining three accelerometers were attached at the midspan locations of each of the other slab beams.

The data acquisition system used for testing is capable of supporting 64 channels with one main box. There were 16 load cells (eight at each end of the bridge), 40 string potentiometers, and eight accelerometers attached to the bridge, for a total of 64 channels of data. In order to have one fixed instrumentation setup, an initial configuration for the location of each device was determined.
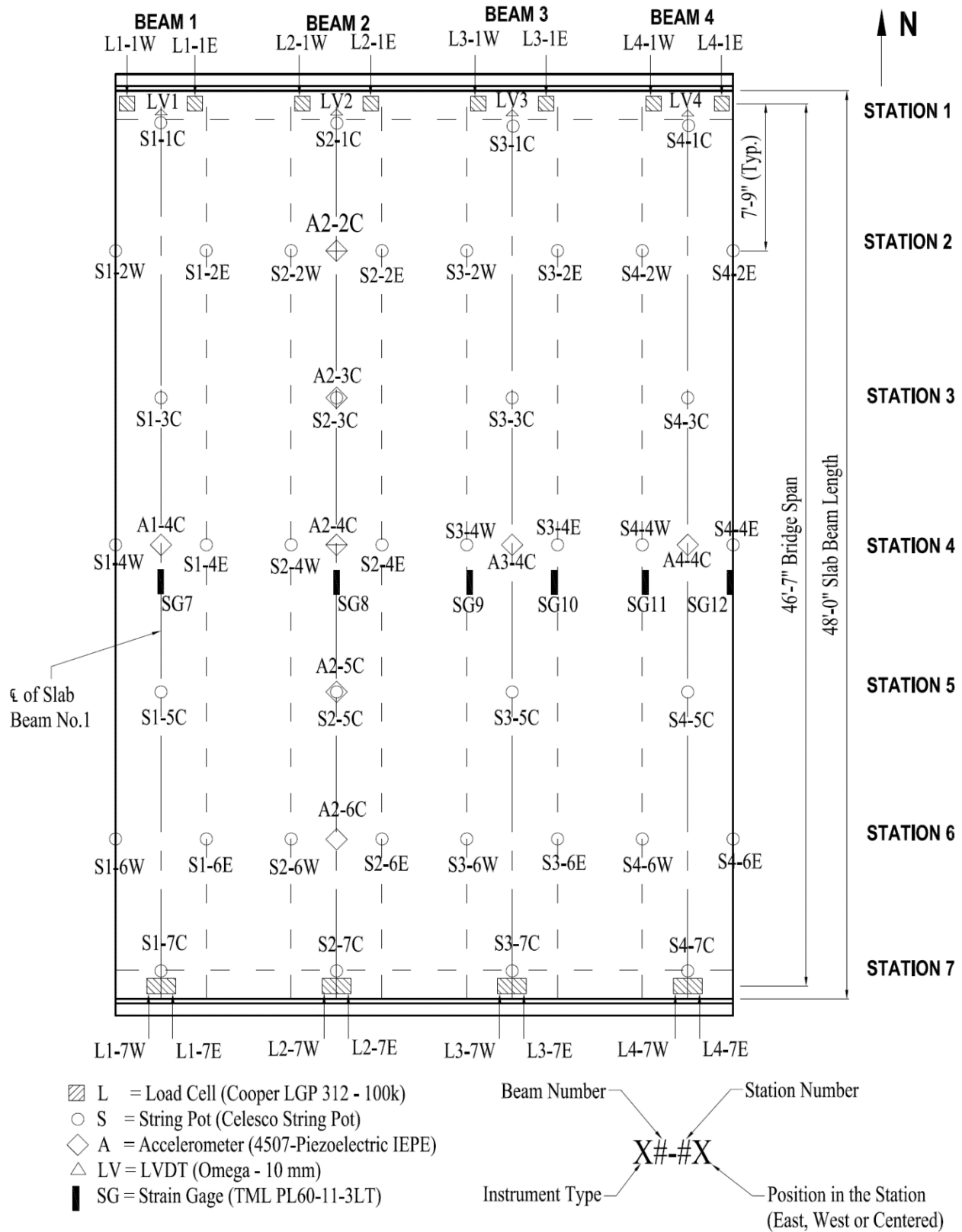
Figure 4.6. Initial Instrumentation Layout and Labeling.

The instrumentation layout shown in Figure 4.6 includes the labeling of all sensors, based on this layout. The locations of the sensors were labeled according to the station numbers and the beam number. The location of the sensors, except the string potentiometers, remained the same throughout the experimental program. The sensors shown were attached at the bottom surface of the slab beams. The only sensors on the top surface (deck surface) were six strain gages (SG1– SG6) that were attached at the same position in the plan as the bottom strain gages.

4.4   TESTING OF INDIVIDUAL SLAB BEAMS

Figure 4.7 shows a photograph of a typical layout for the accelerometers on a slab beam. Accelerometers were attached along one of the slab beams to identify frequency characteristics of an individual non-composite slab beam. Accelerometers were attached at the top surface of the slab beam at 6 ft 8 in. spacing starting at the center of the bearing pad. Before casting the deck concrete, the data acquisition system was connected to the load cells to obtain the individual weights of the slab beam girders and test the performance of the load cells. Data were processed, and individual beam reactions at the north and south ends of each beam were obtained.

Figure 4.7. Accelerometer Positions for Individual Beam Test.

Individual slab beam support reactions are also listed in Table 4.1. An approximate weight calculation based on the unit weight of concrete shows that the weight of the 48 ft long 5SB15 slab beam is 44 kips. The load cell readings showed the average weight of the four slab beams as 44.7 kips, which is reasonably close when the reinforcing bars, non-uniformity of the beams, and sensitivity of load cells are considered. The signal from the load cells during the 30-second time interval is very quiet and stable. Figure 4.8 shows the results from preliminary testing of the individual slab beam.

Figure 4.9(a) shows the amplitude-frequency plot for the tested slab beam based on the accelerometer close to midspan. The accelerometer data were processed in the frequency domain, and the first two natural frequencies of the slab beam were obtained. Because there were eight accelerometers on the beam, the mode shapes for these two modes were also captured.

Figure 4.9(b) shows the amplitude spectrum along the length, which is an indicator of the mode shapes. The natural frequency of the beam is 3.9 Hz and the natural frequency of the second mode is 28.9 Hz. A relatively low natural vibration period is a result of high stiffness due to a high amount of prestressing and high modulus of elasticity. The mode shapes can be clearly identified from the amplitude spectrum. The first mode corresponds to the flexural bending mode, and the second mode is the second bending mode of the beam.

Table 4.1. Individual Slab Beam Weights.

	North Reaction (kips)	South Reaction (kips)	Beam Weight (kips)
Beam 1	22.3	22.0	44.3
Beam 2	22.1	22.7	44.8
Beam 3	22.4	22.2	44.6
Beam 4	22.2	22.9	45.1
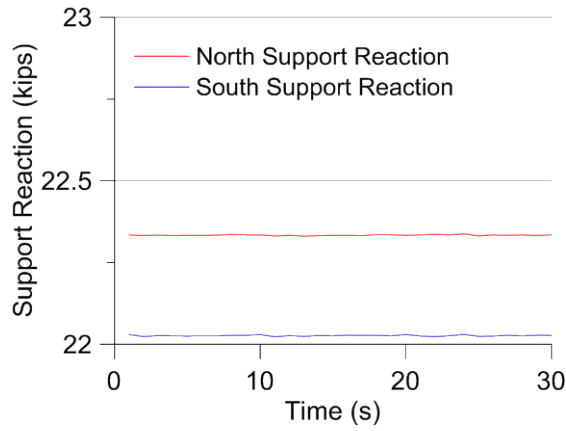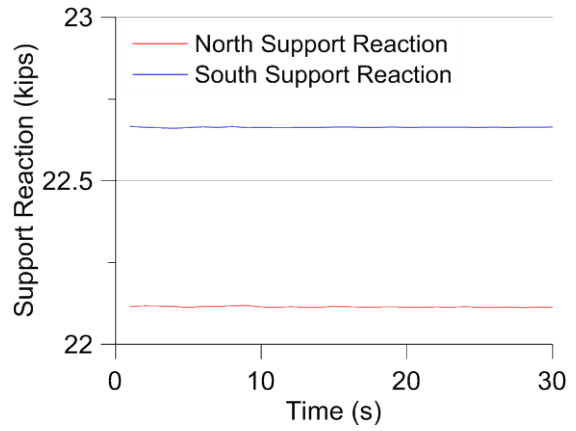
(a) Slab Beam 1   (b) Slab Beam 2
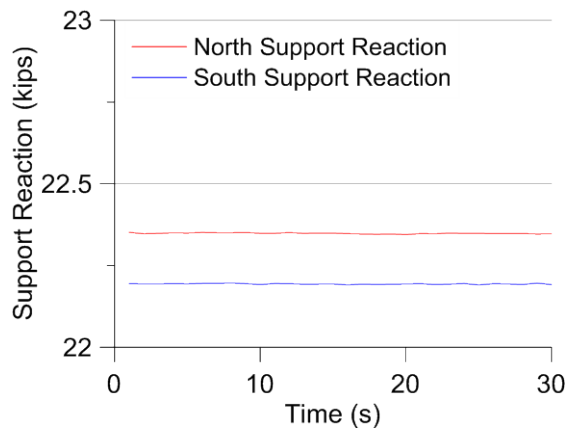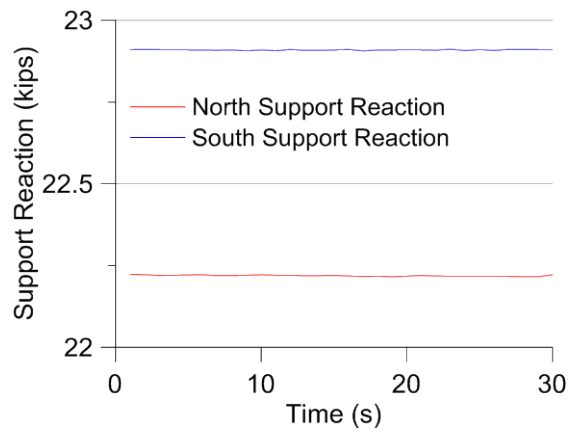
(c) Slab Beam 3   (d) Slab Beam 4

Figure 4.8. Slab Beam Support Reactions before Deck Pour.
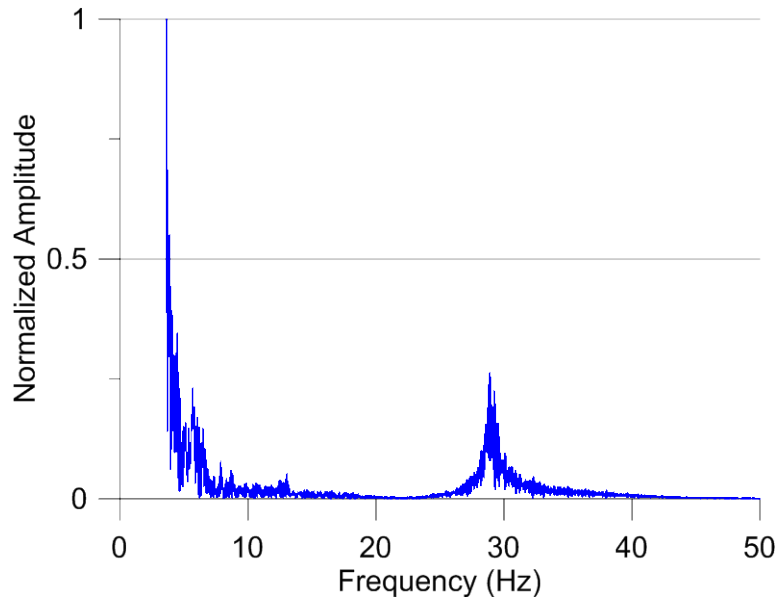
(a) Modal Frequencies for Slab Beam 4
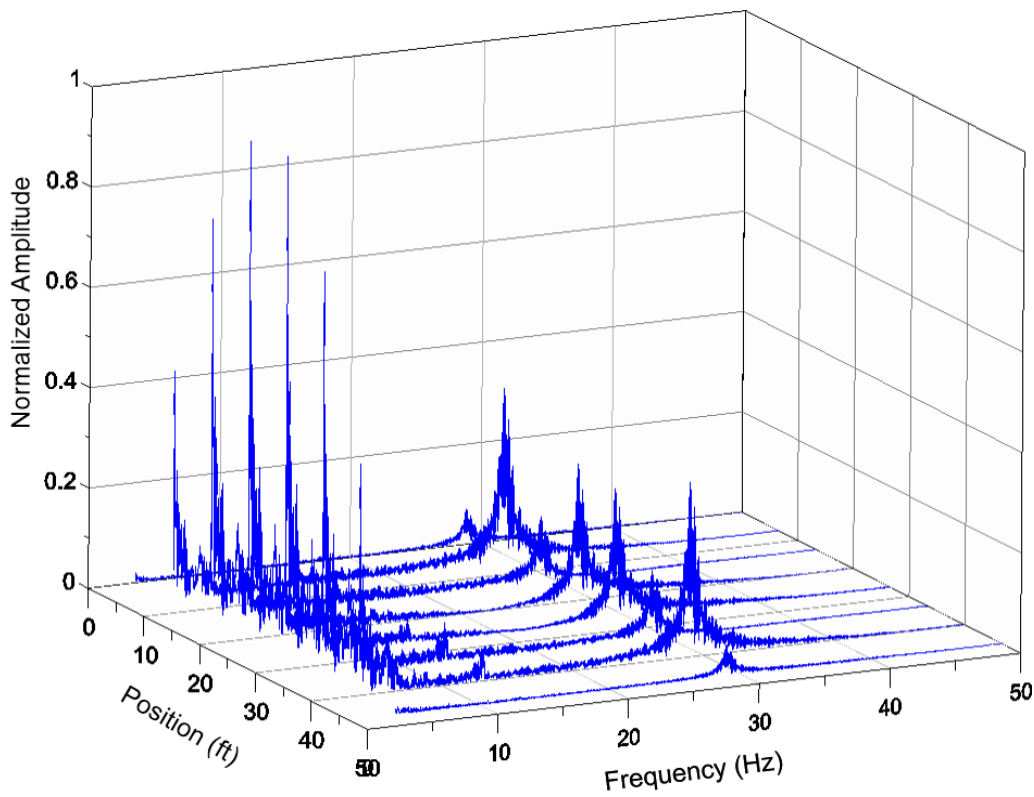
(b) Amplitude Spectrum along the Length of Slab Beam 4

Figure 4.9. Dynamic Characteristics of a Slab Beam.

4.5 TESTING OF RIVERSIDE BRIDGE

4.5.1 Test Vehicles

Figure 4.10 shows the photographs of both test trucks used during the Riverside Bridge testing. Two different TTI vehicles were used for static and dynamic testing of the Riverside Bridge. The TTI dump truck was loaded with a steel frame to increase its weight to approximately 32 kips with a 15 ft 2.5 in. spacing between the front axle and centerline of the two rear axles. The TTI water tanker was filled and weighed approximately 88 kips total; however, only two axles weighing about 75 kips could be positioned on the bridge span. For each test case, all three axles of the TTI dump truck were on the bridge. However, only the rear axle of the TTI water tanker, which weighed about 38 kips, was used for the moment critical and north support shear cases. The rear axle and middle axle of the water tanker (weighing approximately 75 kips) was on the bridge for the south support shear critical case.

4.5.2 Preliminary Testing

Three trial tests were conducted prior to the final comprehensive testing of the Riverside Bridge. The trial testing allowed determination of the appropriate instrumentation types and configurations for use in final testing to obtain the experimental shear and moment live load distribution factors. Table 4.2 provides a summary of the tests performed on the Riverside Bridge.

4.5.2.1 Load Cells and Data Acquisition System (Trial 1)

The first preliminary static test (Trial 1) was conducted in November 14, 2013, in order to test the load cells and data acquisition system. Only the load cells were in place during preliminary testing. The rear axles of a TTI trailer were used as a static load placed to maximize the beam shear. All 16 load cells performed well, and the shear distribution factors could be identified. However, the use of this particular trailer was abandoned because the total weight of the rear axles was around 20 kips, which is relatively small compared to design tandem loading, and increasing the load was not possible. A TTI water tanker and a TTI dump truck were used for the remaining tests.

(a) TTI Dump Truck

(b) TTI Water Tanker

Figure 4.10. Test Vehicles Used for Riverside Bridge Tests.

Table 4.2. Riverside Bridge Tests.

Description	Test Date	TTI Vehicles	Deployed Instruments	String Potentiometer Layout for Moment
Trial 1	Nov. 14, 2013	Trailer	Load Cells	Distributed along span with 7' 9" spacing
Trial 2	Feb. 21, 2014	Dump Truck Water Tanker	Load Cells, String Potentiometers, LVDTs, Strain Gages	Distributed along span with 7' 9" spacing
Trial 3	April 2, 2014	Dump Truck Water Tanker	Load Cells, String Potentiometers, LVDTs, Strain Gages, Accelerometers	Clustered at midspan with 1' 3" spacing
Final Test	May 7, 2014	Dump Truck Water Tanker	Load Cells, String Potentiometers, LVDTs, Strain Gages, Accelerometers	Clustered at midspan with 3' 11" spacing

4.5.2.2   Support Reactions, Midspan Moments, and Distribution Factors (Trial 2)

A second preliminary static test (Trial 2) was conducted on February 21, 2014. Load cells were in place to measure support reactions and determine corresponding shear distribution factors. Linear variable displacement transducers (LVDTs) were also installed at each beam end in order to infer shear distribution factors by measuring bearing pad deformations. The reliability of the LVDTs was evaluated by comparing the corresponding shear LDFs to the ones obtained by direct measurement of reactions by load cells. All 40 string potentiometers were installed at equal spacing along the entire span, as shown in Figure 4.6, to infer moment LDFs by measuring the deflection profile for each slab beam. Strain gages were also installed at midspan of each beam as a secondary way of inferring moment LDFs by measuring the midspan curvature. Dynamic load testing was not planned at the time of Trial 2; therefore, the accelerometers were not installed.

4.5.2.3 Support Reactions, Midspan Moments, and Distribution Factors (Trial 3)

Figure 4.11 shows the instrument layout of the preliminary static test (Trial 3) that was conducted on April 2, 2014, with modified string potentiometer spacing. The string potentiometers were clustered at the center of the slab beams with 15 in. spacing. The accelerometers were also attached for the dynamic test. The rest of the instrumentation was kept the same as the previous test.
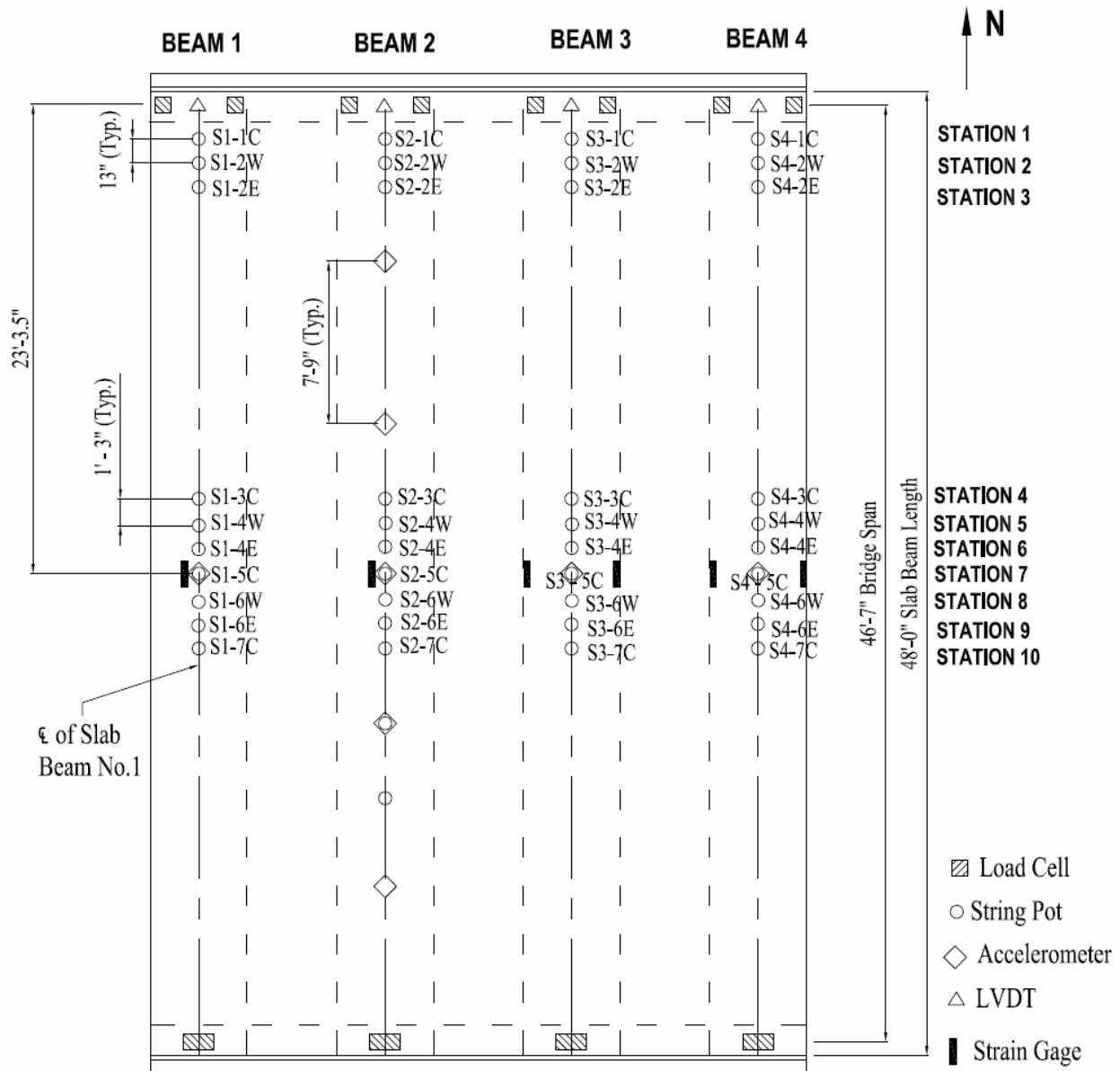
Figure 4.11. Instrumentation Layout for Trial 3.

The analysis of the data indicated that the string potentiometer spacing was too close to determine meaningful moment LDFs. The sensitivity of the string potentiometers was not sufficient to differentiate the displacement differences at very close intervals. The string potentiometers used for the test are capable of detecting up to 0.005 in. deflection. Smaller deflection measurements than that are not reliable. The April test showed that the deflection change between stations that were 15 in. apart was smaller than 0.003 in. Based on the investigation of deflection profiles from the preliminary tests and analytical predictions it was determined that a spacing of 4 ft between successive stations, as compared to 8 ft spacing, was preferable for determining the midspan moment while still giving displacement differences that could be reliably measured by the string potentiometers.

4.5.2.4 *Static and Dynamic Load Tests*

Figure 4.12 shows the detailed layout of the instruments for the May tests, and the results are reported in Section 4.6. The final comprehensive static and dynamic tests of the Riverside Bridge were conducted on May 7, 2014. The instrumentation layout was kept the same as Trial 3, except the spacing of the string potentiometers was modified.

4.5.2.5 *Longitudinal Vehicle Positions*

Individual axle weights of the test vehicles were determined using portable scales. Axle spacing was measured and the location of the resultant force was determined. The maximum bending moment in a beam occurs when the resultant of the three axles and the second axle are located at an equal distance from the midspan location. This is called the critical moment position in the longitudinal direction.

The maximum shear in a beam member occurs when the load is located a member depth away from the support (St. Venant's shear principle; [Ugural and Fenster 2012]). According to St. Venant's principle, for the Riverside Bridge, the centroid of the rear axle should be located 25 in. from the centerline of the bearing pads. This loading case creates maximum shear stresses at one member depth away. Two different shear critical longitudinal positions, one at the south support and one at the north support, were defined.

The longitudinal positions of the dump truck and water tanker are shown in Figure 4.13 and Figure 4.14, respectively. A total of three longitudinal positions were defined for each vehicle: south support, center (near midspan), and north support. All axles of the dump truck were on the bridge for each of the three longitudinal positions. For the north support case, the dump truck was turned around in order to achieve the highest shear force and create similar loading to the south support case. In the case of the water tanker, only the rear axles (similar to a design tandem loading) were placed on the bridge for the center and north support cases. For the south support position of the water tanker, the middle set of axles was also on the bridge, which created the highest total load. Therefore, the south and north support positions of the water tanker did not induce the same shear force.
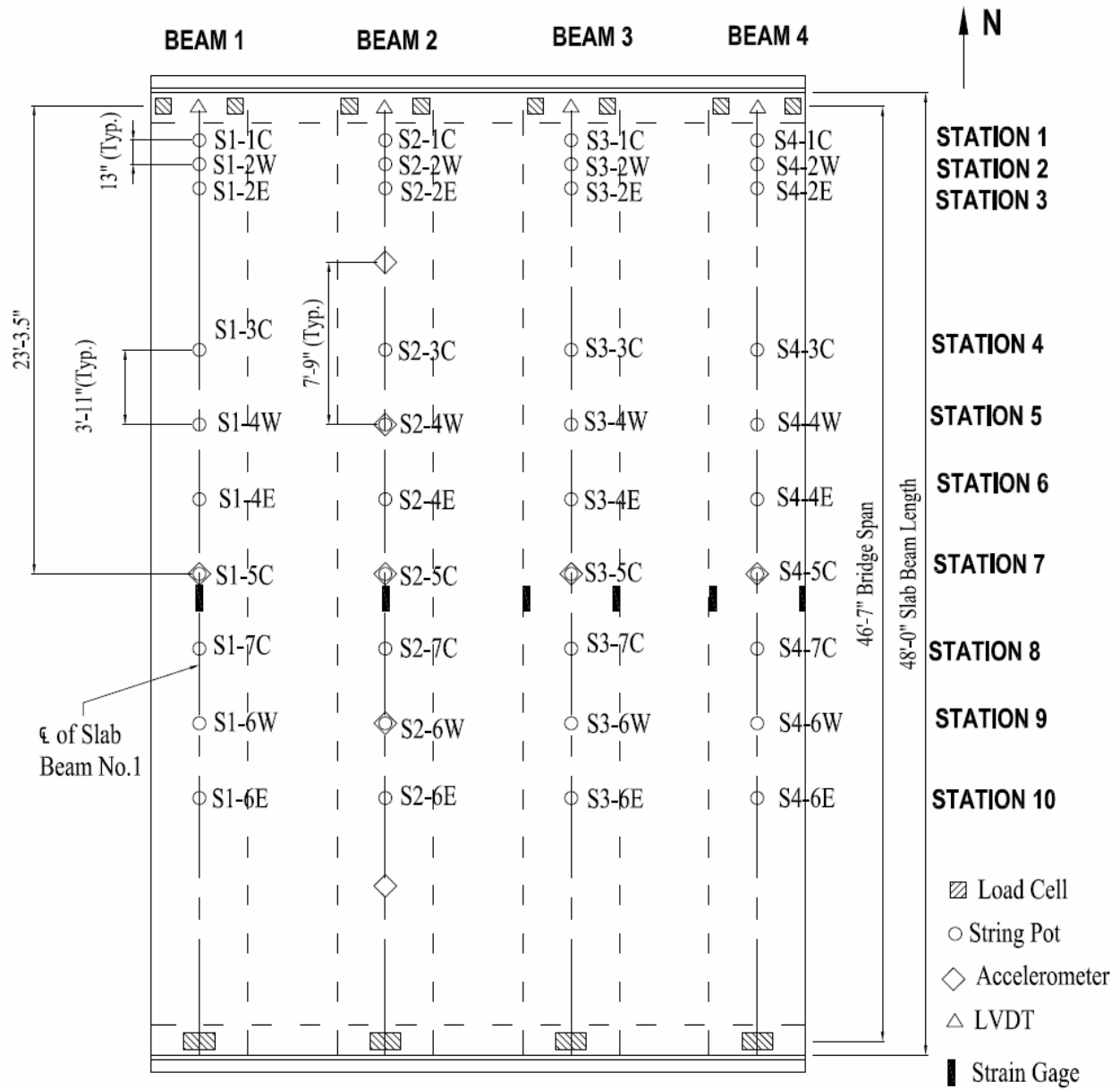
Figure 4.12. Instrumentation Layout for May Tests.
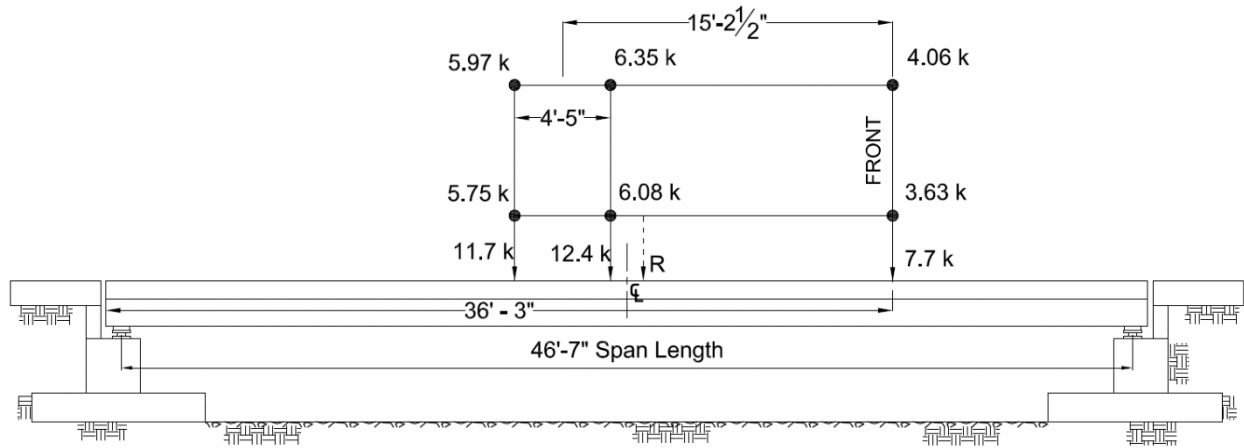
(a) Moment Critical Position near Midspan
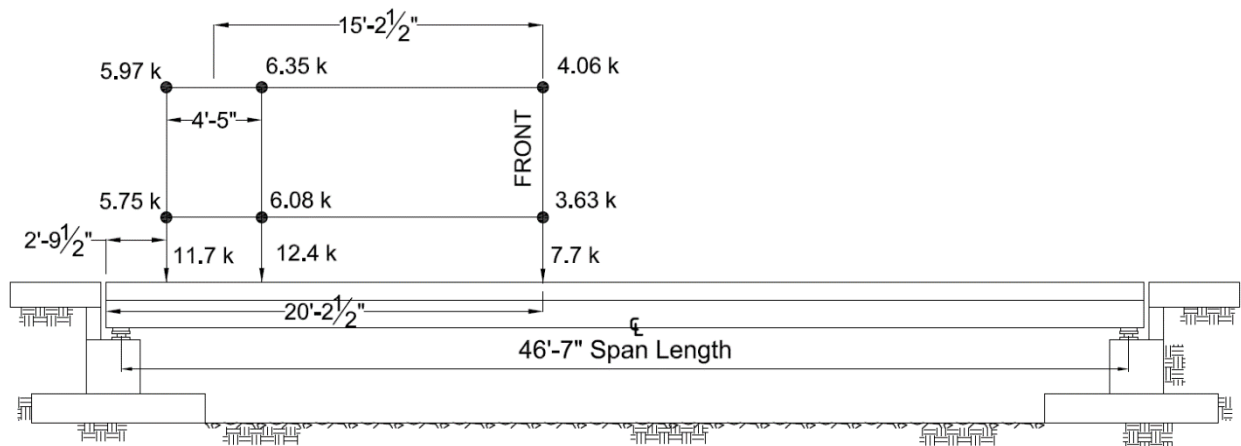
(b) South Support Shear Critical Position
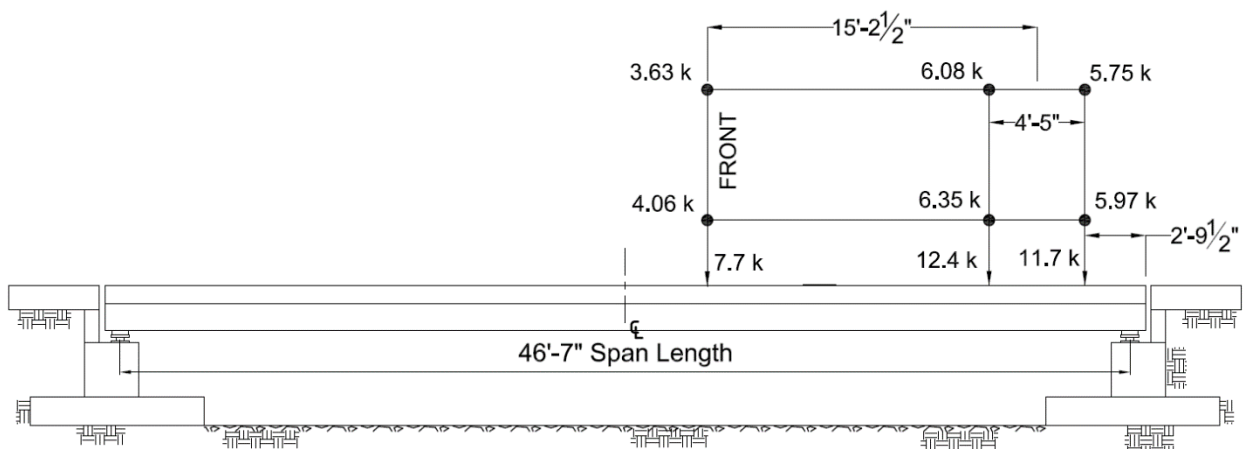
(c) North Support Shear Critical Position

Figure 4.13. Longitudinal Positions of Dump Truck.
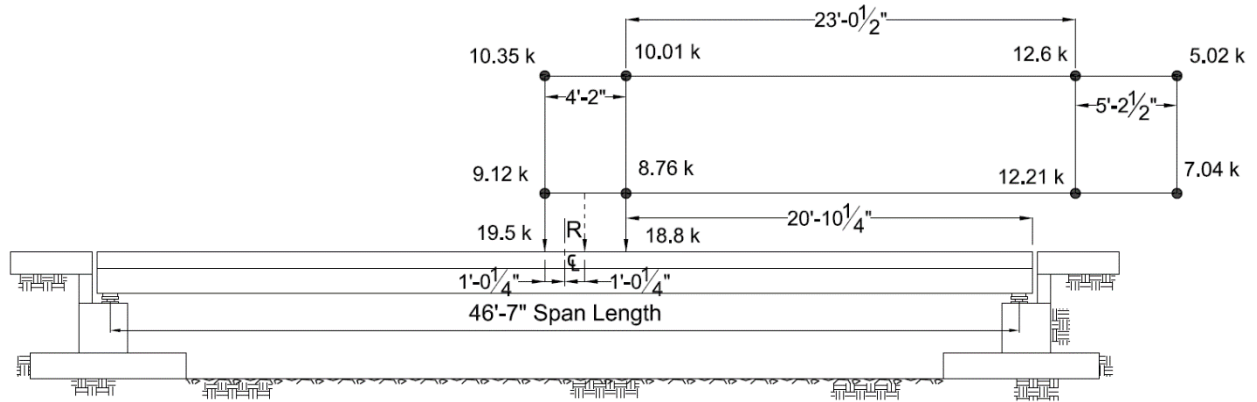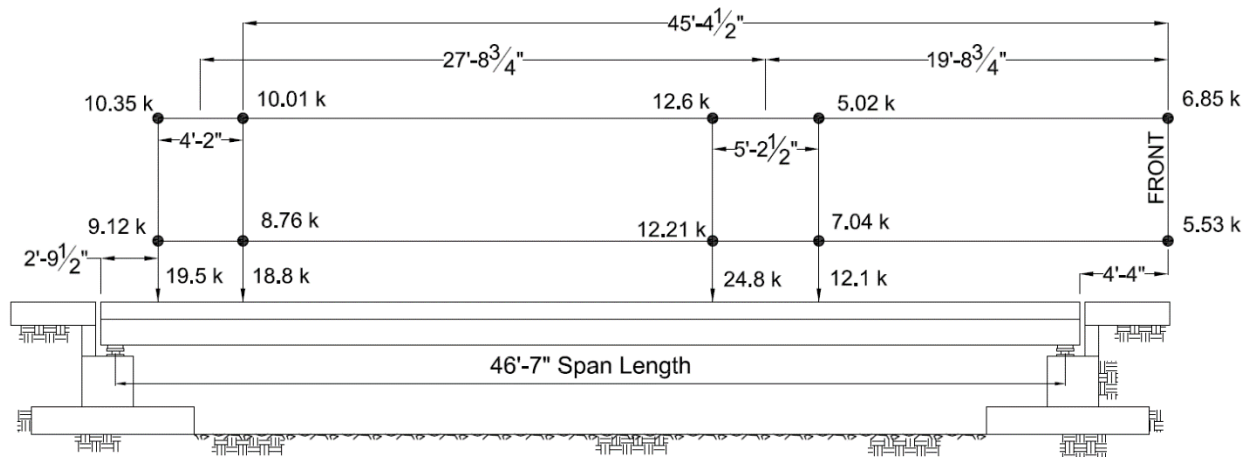
87

(a) Moment Critical Position near Midspan

(b) South Support Shear Critical Position
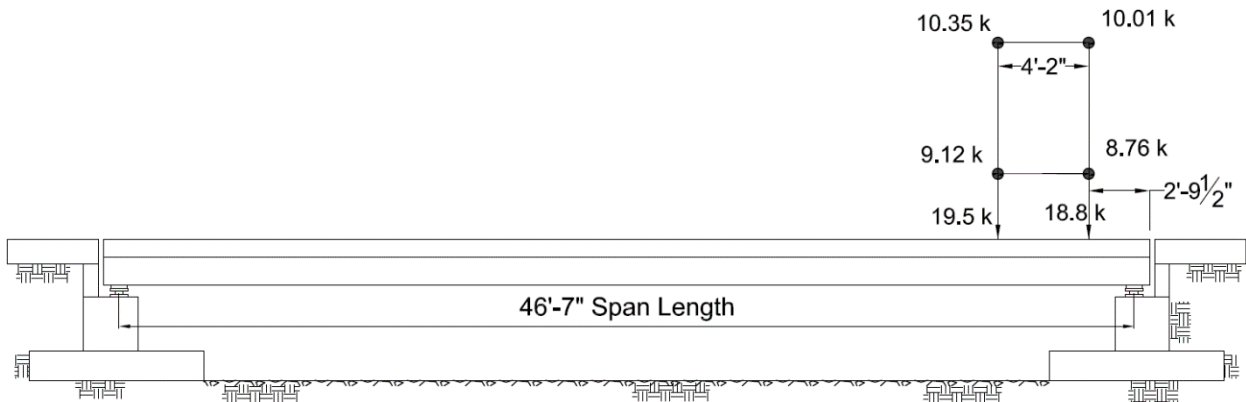
(c) North Support Shear Critical Position

Figure 4.14. Longitudinal Positions for Water Tanker.

4.5.2.6 Transverse Alignments

The transverse alignments are shown in Figure 4.15. For dynamic tests, the vehicles were driven along the same four alignments. The Riverside Bridge is a two-lane bridge, and the critical moment and shear force occur when both lanes are loaded. According to the AASHTO LRFD Specifications (2012) Article 3.6.1.3.1, the minimum vehicle distance from the edge of a design lane is 2 ft. Therefore, the minimum lateral distance between two trucks traveling in adjacent lanes is 4 ft. The edge of a lane can be at the edge of the bridge, such as when two bridges are built side by side. When the tire thickness is taken into account, the center of the exterior tire can be 1 ft away from the edge. In light of the above-mentioned criteria, a total of four transverse alignments were defined.
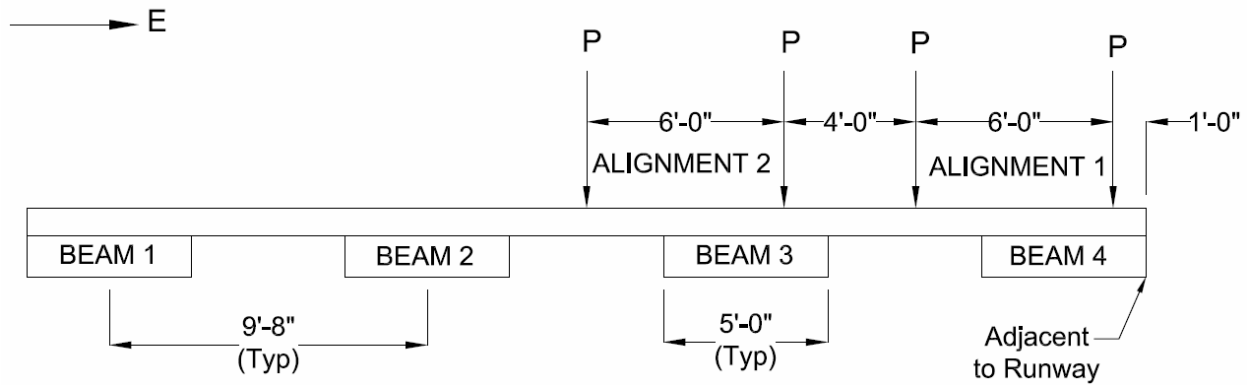
(a) Exterior Girder Critical Case
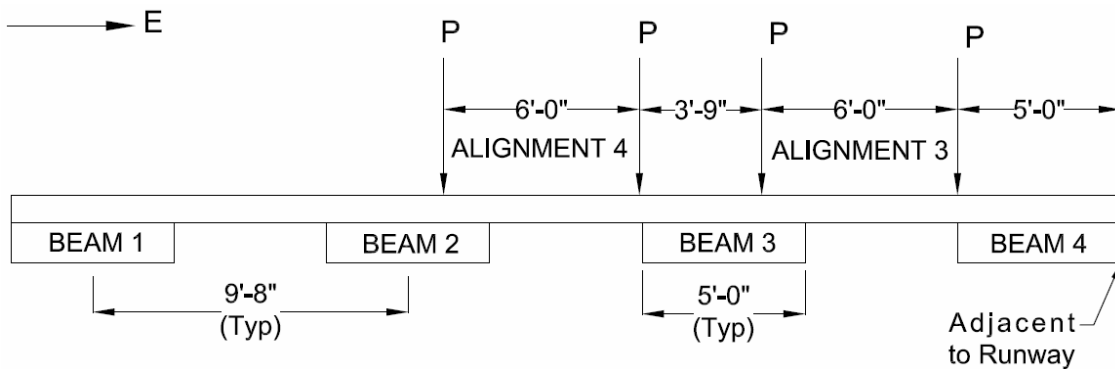
(b) Interior Girder Critical Case

Figure 4.15. Transverse Alignments for Static and Dynamic Tests.

Live load distribution factors are different for exterior and interior girders. The transverse alignments were selected based on the load configuration that gives the critical moment or shear reaction for exterior and interior slab beams. The case where Alignment 1 and Alignment 2 are loaded gives the highest moment LDFs for both the exterior and interior slab beams. The same load case gives shear critical loading for the exterior beam. The case where Alignment 3 and Alignment 4 are loaded gives the highest shear LDF for an interior slab beam. These alignments were set during the preliminary tests and confirmed with the FE model of the bridge.

4.5.2.7 *Instrumentation*

The Riverside Bridge was instrumented using string potentiometers, LVDTs, load cells, accelerometers, and strain gages during the tests conducted on May 7, 2014. The detailed instrumentation layout is shown in Figure 4.12 above. Instrumentation readings and physical observations were carefully documented during field testing of the Riverside Bridge. These experimental results were processed and reviewed to better understand the in-service response of the spread slab beam bridge system. The load sharing observed in the field tests provided input to the development of load distribution factors for this bridge system.

The experimental results presented in the next section are from the tests conducted on May 7, 2014. Ten string potentiometers were attached to each beam. Seven potentiometers were clustered at the center of each beam with 3 ft 11 in. spacing to obtain sufficient measurements of the deflection profile in the midspan region. An additional three string potentiometers were attached at each beam end with a 13 in. spacing to investigate the possibility of determining the shear force distribution from deflection data. Theoretically, only four data points are necessary for determining the shear reaction. Including the deflection data obtained from the LVDT at the bearing pad level gave a total of four deflection measurements per beam near the north support. The rest of the sensors were attached at their fixed locations, as defined in Figure 4.6 above. The deflection profiles were obtained when the dump truck was at the longitudinal center of the bridge (moment critical position).

4.6 ANALYSIS OF TEST RESULTS

4.6.1 Load Distribution Factor Calculation Method

The load distribution factor, g, is defined as the ratio of maximum load effect created on the bridge girder due to HL-93 loading to the maximum load effect created on an isolated beam element due to same loading.

A similar approach as that in the AASHTO LRFD Specifications (2012) was followed for live load distribution factor calculation. For calculating the load distribution factors, a one-dimensional isolated beam having the same span length as the bridge is analyzed under uniform lane load and HS20 truck or tandem load. The maximum beam force (moment and shear), $F_{1D\text{-}Girder}$, and the longitudinal position of the vehicle for maximum moment and shear are recorded. The bridge is loaded by the same vehicle at the same longitudinal position for different transverse positions. The maximum force, $F_{2D\text{-}Girder}$, that occurs for interior girders and exterior girders are measured and recorded. Then the load distribution factor g is determined as:

$$g = \frac{F_{2D-Girder}}{F_{1D-Girder}} \tag{4.1}$$

The forces are moments or shears depending on the analysis. The force that is obtained from the single isolated beam analysis is always obtained by loading it with one vehicle only. However, the actual experimental bridge or the FEM model of the bridge should be analyzed for the one-lane-loaded and two-or-more-lanes-loaded cases. This means $F_{1D\text{-}Girder}$ is always a moment or shear of an exterior or interior girder calculated using one vehicle and a uniform lane load, whereas $F_{2D\text{-}Girder}$ includes multiple vehicles and multiple lanes.

The number of design lanes is computed according to AASHTO LRFD Specifications (2012) Article 3.6.1.1.1. The number of design lanes is equal to the integer part of the ratio of the clear roadway width in feet divided by 12 ft, which resulted in two lanes for the Riverside Bridge.

Although the maximum load distribution factor occurs due to the two-lane-loaded case, the one-lane-loaded case was also investigated.

$$g_{M-INT} = \frac{M_{INT,2D}}{M_{1D}} \tag{4.2}$$

$$g_{V-INT} = \frac{V_{INT,2D}}{V_{1D}} \tag{4.3}$$

Where:

$g_{M\text{-}INT}$ = Moment distribution factor of interior girders for one-lane-loaded case if $M_{INT,2D}$ is due to one-lane loading.

Moment distribution factor of interior girders for two-lane-loaded case if $M_{INT,2D}$ is due to two-lane loading.

$M_{INT,2D}$ = Maximum moment for all interior girders, kip-ft.

M_{1D} = Moment due to one-lane loading, kip-ft.

$g_{V\text{-}INT}$ = Shear distribution factor of interior girders for one-lane-loaded case if $V_{INT,2D}$ is due to one-lane loading.

Shear distribution factor of interior girders for two-lane-loaded case if $V_{INT,2D}$ is due to two-lane loading.

$V_{INT,2D}$ = Maximum shear for all interior girders, kips.

V_{1D} = Shear due to one-lane loading, kips.

The exterior girder load distribution factors are calculated similar to interior girders.

$$g_{M-EXT} = \frac{M_{EXT,2D}}{M_{1D}}$$ (4.4)

$$g_{V-EXT} = \frac{V_{EXT,2D}}{V_{1D}}$$ (4.5)

Where:

$g_{M\text{-}EXT}$ = Moment distribution factor of exterior girders for one-lane-loaded case if $M_{INT,2D}$ is due to one-lane loading.

Moment distribution factor of exterior girders for two-lane-loaded case if $M_{INT,2D}$ is due to two-lane loading.

$M_{EXT,2D}$ = Maximum moment for all exterior girders, kip-ft.

$g_{V\text{-}EXT}$ = Shear distribution factor of exterior girders for one-lane-loaded case if $V_{INT,2D}$ is due to one-lane loading.

Shear distribution factor of exterior girders for two-lane-loaded case if $V_{INT,2D}$ is due to two-lane loading.

$V_{EXT,2D}$ = Maximum shear for all exterior girders, kips.

For both the interior and exterior distribution factors, the longitudinal position of the vehicle is calculated based on the single isolated beam loading with one vehicle only. This

position is used as the critical position for moment for both the one-dimensional and 2D analyses.

4.6.2 Experimental Results for Dump Truck Loading

4.6.2.1 Deflection Profiles Due to Dump Truck Static Loading

The static loading was achieved using a dump truck at four different alignments and three different longitudinal positions along each alignment, as described in Figure 4.13 and Figure 4.15. Figure 4.16 shows an example static loading case with the dump truck at one of the positions. The total gross weight of the dump truck was approximately 31 kips with the measured wheel loads provided in Figure 4.13. The deflection profiles obtained from all string potentiometers are shown in Figure 4.17.

Figure 4.16. Static Loading with Dump Truck.

The maximum deflection (0.12 in.) was observed at Beam 4 when the vehicle was located at the center of Alignment 1. The deflection profiles changed as the vehicle moved transversely, as expected. Maximum deflections were observed for Beam 4 when the vehicle was at Alignment 1 and Alignment 3. Beam 3 had the highest deflection when the vehicle was at Alignment 2. Beam 2 had the highest deflection when the vehicle was moved to Alignment 4.
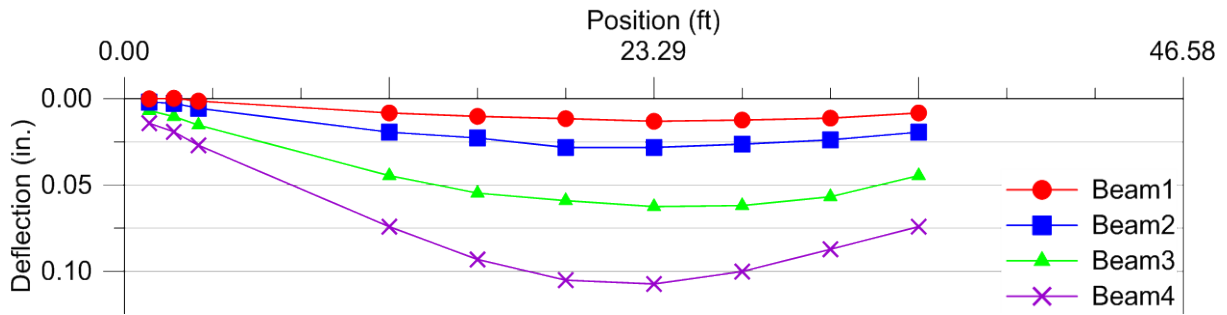
(a) Beam Deflections for Alignment 1
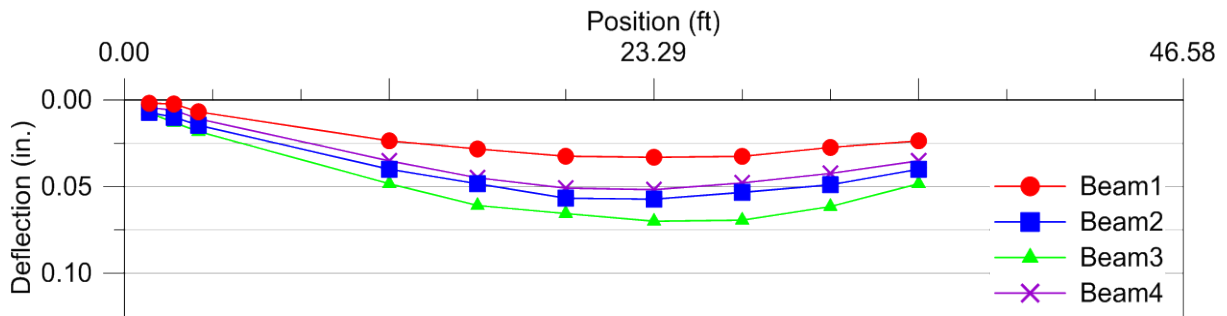
(b) Beam Deflections for Alignment 2
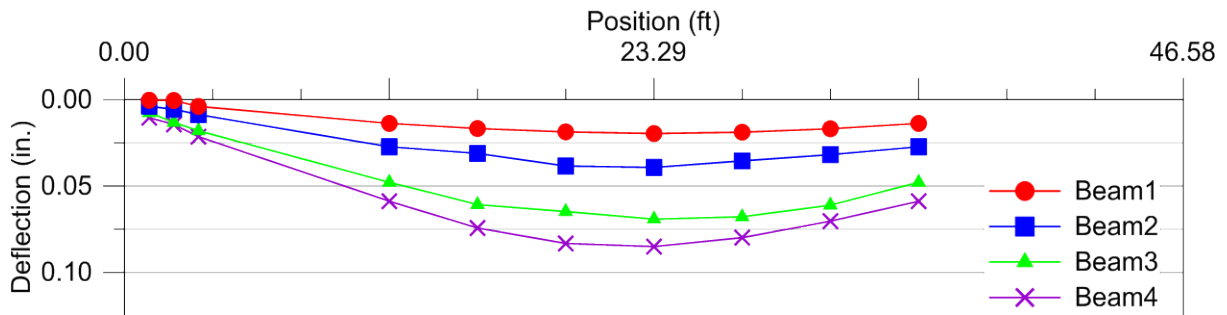
(c) Beam Deflections for Alignment 3
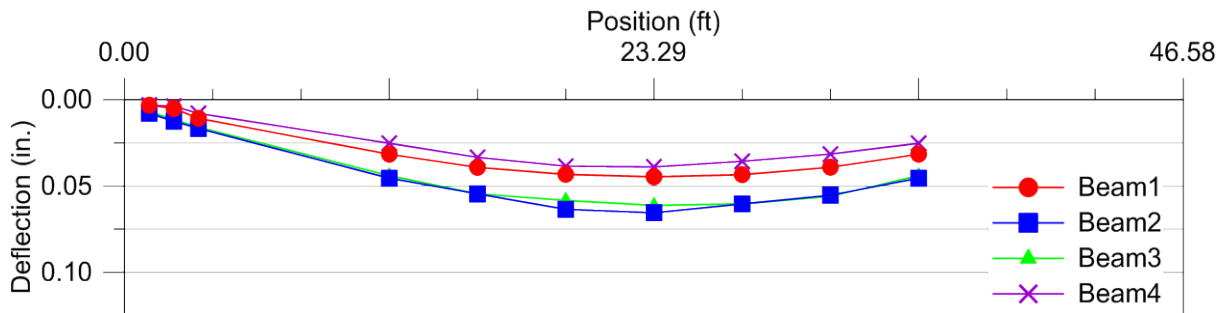
(d) Beam Deflections for Alignment 4

Figure 4.17. Deflection Profiles for Dump Truck Load.

4.6.2.2   Moment Results for Dump Truck Static Loading

4.6.2.2.1 Measured Data

One of the main objectives of this research was to identify moment LDFs. The moments at the midspan were obtained using the deflection profile from seven string potentiometers that were clustered at the center of the beams. A third-order polynomial having the form shown in Equation (4.6) was fit through the deflection curve. The curvature of the fitted curve was calculated by twice differentiating the fitted third-order polynomial using Equation (4.6). The moment at midspan was then calculated using the curvature at midspan and multiplying it by EI. The moment at midspan was calculated for each one of the four beams for the moment critical position of the vehicles.

$$y = ax^3 + bx^2 + cx + d \tag{4.6}$$

$$y'' = 6ax + 2b \tag{4.7}$$

$$M(x) = EI\,y'' \tag{4.8}$$

Moments at midspan were also calculated using strain values obtained from strain gages. Only the strain gages attached at the bottom surface of the slab beams were used together with the theoretical center of gravity. Strain gages at the top deck surface were attached to determine the experimental center of gravity of the composite sections for interior and exterior beams. However, the top strain gages did not provide the intended data. They captured strains were not only due to longitudinal stresses but also due to the longitudinal components of surface stresses in multiple directions because of local stresses applied by the wheel loads. Therefore, the moments were calculated using the theoretical center of gravity and bottom strain gages. The theoretical centroid could be calculated accurately because the modulus of elasticity (E_c) of the beams and deck concrete was determined for different ages of the concrete. Mechanical properties of the superstructure concrete, closest to the day of bridge testing, are summarized in Table 4.3. For experimental moment calculations, the modulus of elasticity of the concrete was assumed to be 10 percent higher at the day of testing than the material test results. Complete data for tested mechanical properties of the concrete are provided in Appendix B.

Table 4.3. Mechanical Properties of Riverside Bridge Concrete.

Superstructure Component	Age of Concrete (days)	Compressive Strength (ksi)	Modulus of Elasticity (ksi)
Slab Beams	56	11.25	5349
Precast Concrete Panels	28	9.93	5489
CIP Deck	28	6.45	6467

4.6.2.2.2 Experimental Moment Distribution Factors

The moment reactions and moment distribution factors calculated using two different methods (string potentiometers and strain gages) were plotted and are compared in Figure 4.18. The maximum moment values and experimental moment LDFs for the interior and exterior girders based on string potentiometer measurements are listed in Table 4.4. Researchers calculated experimental moment distribution factors from the moments obtained using the two alternative methods. The critical moment distribution factors are obtained when both lanes are loaded for a two-lane bridge. Therefore, the results of two different alignments were superimposed to obtain two-lane-loaded results. Alignment 1+2 and Alignment 3+4 were already defined as alignment couples that allow two trucks traveling as close as possible to each other.

The results indicate that the moments obtained using bottom strain gage data are slightly higher than those calculated using string potentiometer data. However, the moment LDF values are similar with the two different measurement methods providing consistent results. The moments calculated using string potentiometer data are used as the experimental values for further comparison in the following chapters. The maximum moment LDFs recorded due to the dump truck loading are 0.65 for an interior beam and 0.72 for an exterior beam when Alignment 1+2 is loaded.

Midspan moments were calculated based on strain gage measurements, and experimental moment LDFs were obtained using the relative moment sharing between slab beams. The measured midspan moment values are listed in Table 4.5, and the corresponding moment LDFs are provided in Table 4.6.
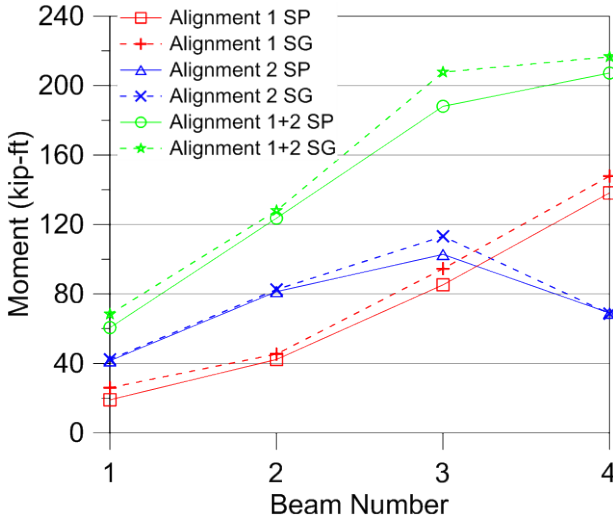
(a) Moments for Alignment 1+2
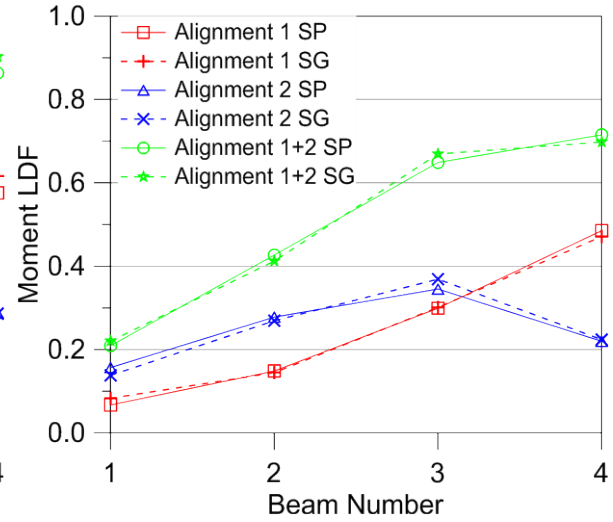
(b) Moment LDFs for Alignment 1+2
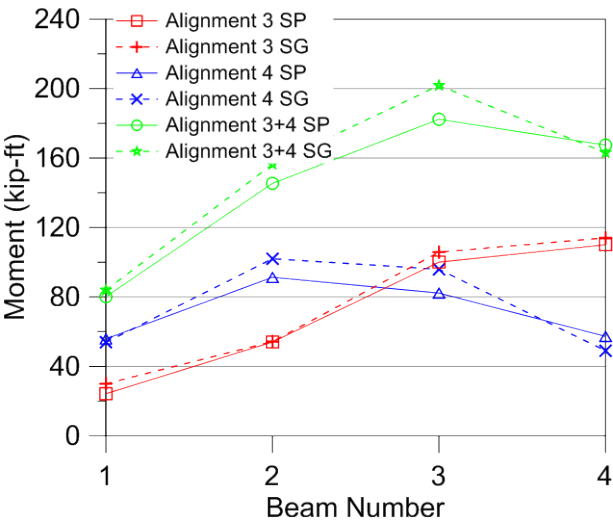
(c) Moments for Alignment 3+4
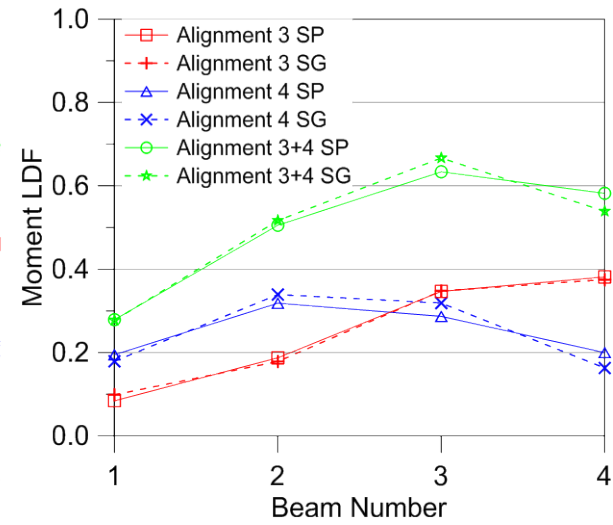
(d) Moment LDFs for Alignment 3+4

Note: SP = String Potentiometer, SG = Strain Gage

Figure 4.18. Midspan Moments and Moment LDFs for Dump Truck Loading.

Table 4.4. Maximum Moment Results for Dump Truck Loading.

No. Lanes Loaded	Slab Beam ID	Max. Moment (kip-ft)	Exp. Moment LDF	Transverse Load Position
One Lane	Beam 3 (Interior)	103	0.35	Alignment 2
	Beam 4 (Exterior)	138	0.49	Alignment 1
Two Lanes	Beam 3 (Interior)	188	0.65	Alignment 1+2
	Beam 4 (Exterior)	207	0.72	Alignment 1+2

Table 4.5. Moment Values Based on Strain Gage Data for Dump Truck Loading (kip-ft).

Load Case	Beam 1	Beam 2	Beam 3	Beam 4
Alignment 1	26	45	95	148
Alignment 2	42	83	113	69
Alignment 3	30	54	106	114
Alignment 4	54	102	96	49

Table 4.6. Moment Distribution Factors Based on Strain Gage Data for Dump Truck Loading.

Load Case	Beam 1	Beam 2	Beam 3	Beam 4
Alignment 1	0.08	0.14	0.30	0.47
Alignment 2	0.14	0.27	0.37	0.22
Alignment 3	0.10	0.18	0.35	0.37
Alignment 4	0.18	0.34	0.32	0.16

4.6.2.3   North Support Shear Results for Dump Truck Loading

4.6.2.3.1 Static Results

North support reactions and experimental shear load distribution factors for all alignments are shown in Figure 4.19. Maximum reactions and experimental shear LDFs for interior and exterior girders are presented in Table 4.7. The support reactions at both the north and south ends of each beam were recorded using load cells. To create the maximum reactions, the rear axle of the dump truck was located close to the supports. For the north support critical case, the vehicle was facing toward the north, and for the south support critical case, the vehicle was facing toward the south. The maximum exterior beam shear LDF = 0.78 was recorded when Alignment 1+2 was loaded. The maximum interior beam shear LDF = 1.02 was obtained when Alignment 3+4 was loaded.

98

4.6.2.3.2 Dynamic Results

Figure 4.19 shows amplified north support reactions due to dynamic impact. Reaction data recorded during the dynamic tests were analyzed and compared to the static data. For the dynamic tests, the dump truck was driven at a speed of 40 mph along the same four transverse alignments used for the static tests. The total north support reaction was calculated for each time step. Individual north support beam reactions were recorded at the time step when the total north support reaction attained its maximum value.

For all the dynamic tests, vehicles were driven from south to north. The dynamic amplification at the north support was prominent when the dump truck was driven along Alignment 2. The amplification was about 37 percent for Beam 3. This is larger than the standard 33 percent increase for impact specified by the AASHTO LRFD Specifications (2012). One of the reasons for this high value may be the asphalt patch that was in line with Alignment 2 at the south end of the bridge. The maximum dynamic impact for Beam 4 was about 17 percent when the dump truck was driven along Alignment 3. Beam 2 had 19 percent dynamic amplification for the Alignment 4 dynamic load test.

Table 4.7. Maximum North Support Shear Results for Dump Truck Loading.

No. Lanes Loaded	Slab Beam ID	Max. Reaction (kips)	Exp. Shear LDF	Transverse Load Position
One Lane	Beam 3 (Interior)	16.1	0.63	Alignment 2
	Beam 4 (Exterior)	18.3	0.72	Alignment 1
Two Lanes	Beam 3 (Interior)	26.0	1.02	Alignment 3+4
	Beam 4 (Exterior)	19.8	0.78	Alignment 1+2

(a) Reactions for Alignment 1+2

(b) Shear LDFs for Alignment 1+2

(c) Reactions for Alignment 3+4

(d) Shear LDFs for Alignment 3+4
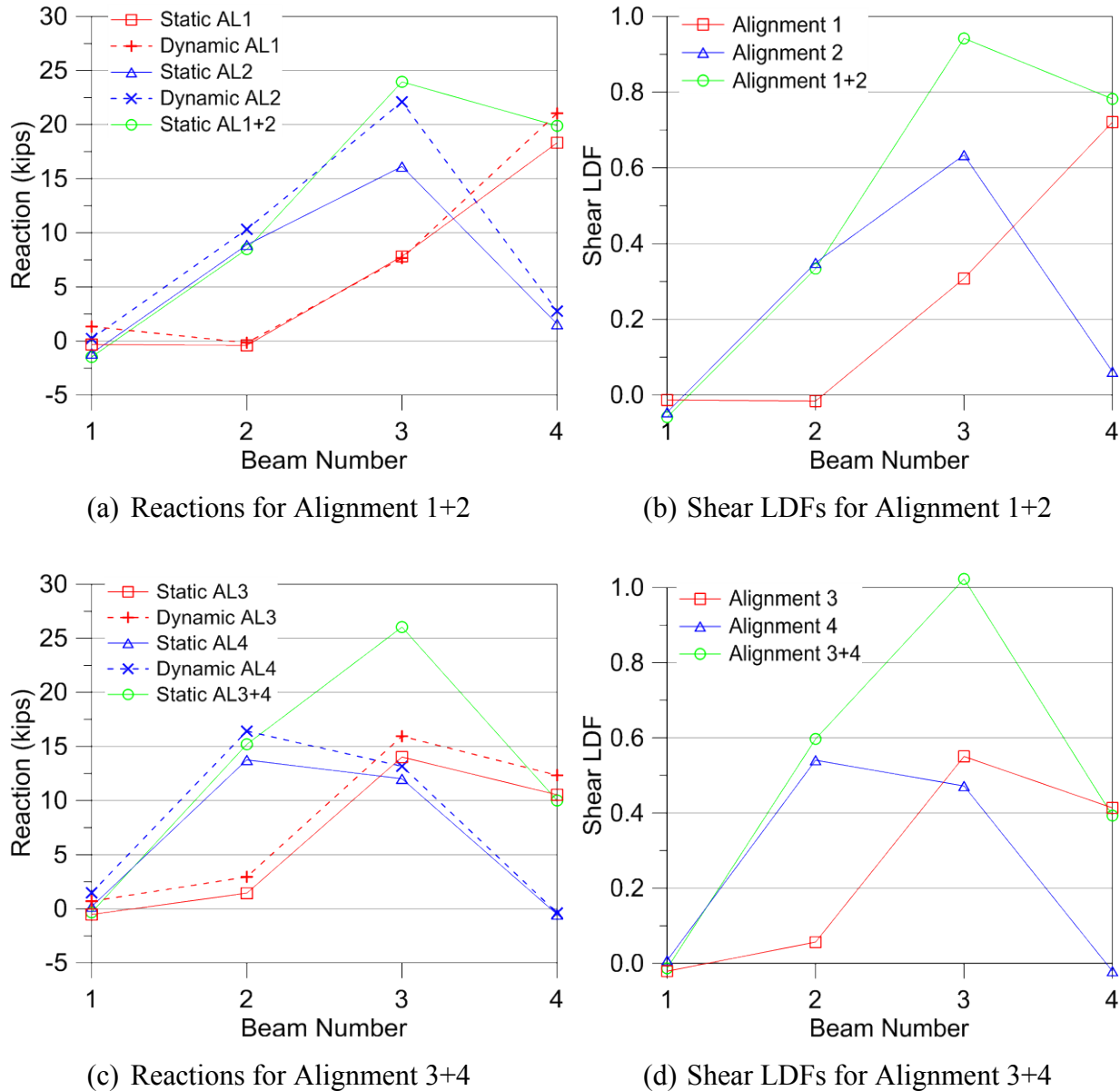
Figure 4.19. North Reactions and Experimental Shear LDFs for Dump Truck Loading.

4.6.2.4   South Support Shear Results for Dump Truck Loading

4.6.2.4.1   Static Results

Maximum reaction values and shear LDFs for interior and exterior girders are summarized in Table 4.8. Figure 4.20 shows shear forces and experimental shear LDFs for both static and dynamic loading. A similar analysis approach was followed to calculate shear LDFs for the south support reactions. The maximum shear LDF for an exterior beam was 0.80 and was obtained when Alignment 1+2 was loaded. A maximum shear LDF of 0.92 was measured for an interior

girder for Alignment 3+4. The experimental shear LDF for the interior girder was lower compared to the north support loading case. This difference may be due to differential tire reactions between wheel lines. The driver side of the vehicle is slightly heavier than the passenger side.

Table 4.8. Maximum South Support Shear Results for Dump Truck Loading.

No. Lanes Loaded	Slab Beam ID	Max. Reaction (kips)	Exp. Shear LDF	Transverse Load Position
One Lane	Beam 3 (Interior)	14.9	0.58	Alignment 2
	Beam 4 (Exterior)	18.1	0.72	Alignment 1
Two Lanes	Beam 3 (Interior)	23.6	0.92	Alignment 3+4
	Beam 4 (Exterior)	20.4	0.80	Alignment 1+2
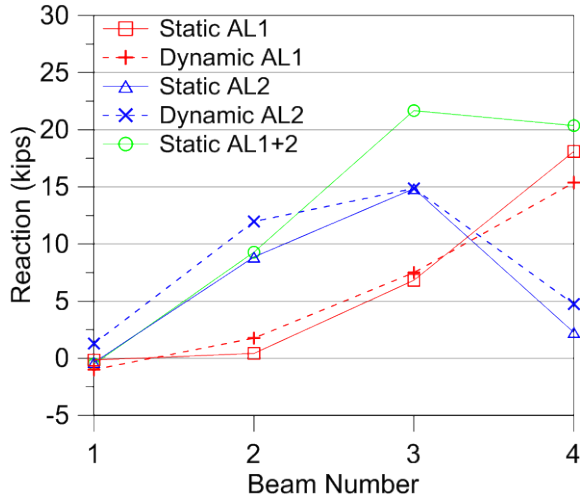
(a) Reactions for Alignment 1+2
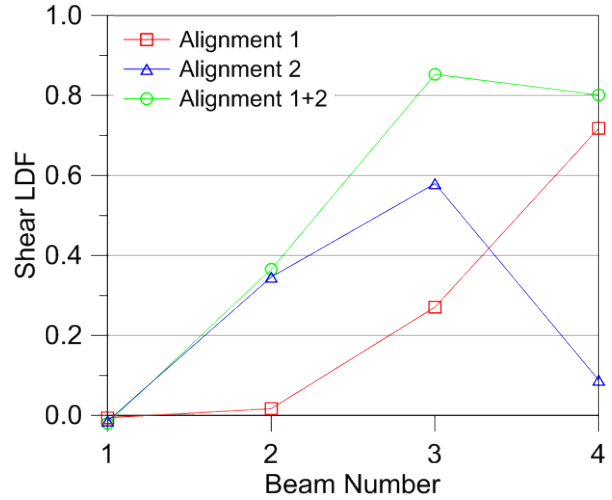
(b) Shear LDFs for Alignment 1+2
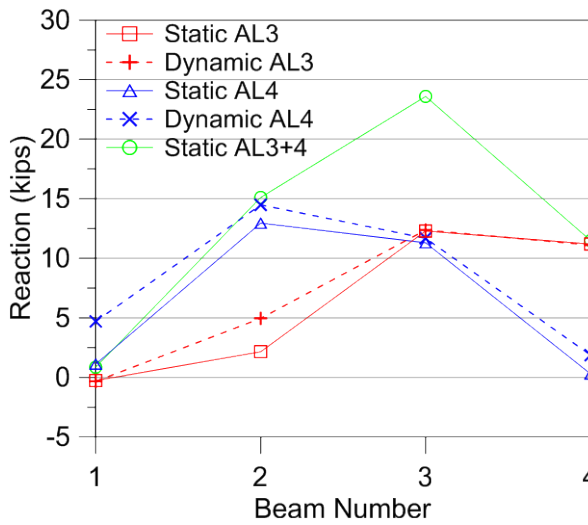
(c) Reactions for Alignment 3+4
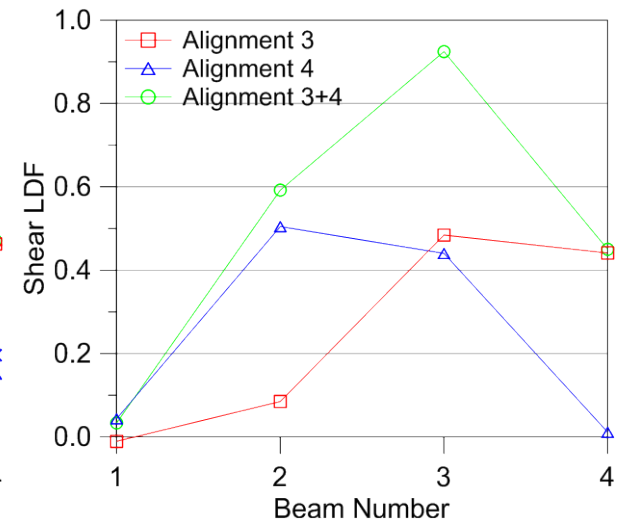
(d) Shear LDFs for Alignment 3+4

Figure 4.20. South Support Reactions and Shear LDFs for Dump Truck Loading.

4.6.2.4.2 Dynamic Results

The observed maximum dynamic amplification at the south support was 35 percent. This value was obtained for Beam 2 when the vehicle was driven along Alignment 2. An interesting observation was that there was no dynamic amplification for Beams 3 and 4 when the vehicle was driven along Alignment 1 or 3. The south end reaction for Beam 1 even decreased for the Alignment 1 dynamic load test.

Dynamic amplifications observed for the north support are more prominent than the south support dynamic amplifications. Ratios of the dynamic reaction to static reaction for each alignment, corresponding to the beams that had the maximum reaction, are listed in Table 4.9.

The difference between north support and south support impact factors may be due to the relationship between the dump truck's vibration frequency and structure's natural frequency. The vehicle was traveling from south to north and evidently entered the bridge with an impact when it crossed the south end, and that effect was reduced as it crossed the north end. The time and position of these jumps are related to the vehicle's vibration frequency as well as the location of the bump before the bridge.

Table 4.9. Dynamic Amplifications for Dump Truck Tests.

Alignment	Dynamic/Static Reaction		Beam with Maximum Reaction
	North Support	South Support	
Alignment 1	1.15	0.85	Beam 4
Alignment 2	1.37	1.00	Beam 3
Alignment 3	1.14	1.01	Beam 3
Alignment 4	1.19	1.12	Beam 2

4.6.3 Experimental Results for Water Tanker Loading

4.6.3.1 Deflection Profiles Due to Water Tanker Static Loading

Because of the axle spacing of the water tanker, only two axles could be placed on the bridge at the same time. The water tanker's rear axles were used to represent the close axle spacing defined for the design tandem loading in the AASHTO LRFD Specifications (2012) (two 25-kip axles that are 4 ft apart), with a total load for the rear axles of 38.3 kips. For deflection studies and moment analysis, the rear axles were placed at the moment critical position (longitudinal center) of the bridge, as shown in Figure 4.14 above.

Figure 4.21 shows deflection profiles of each slab beam for the four different transverse alignments. A maximum deflection of 0.16 in. was observed for Beam 4 when the rear axles of the water tanker were located at Alignment 1 and the center position.

4.6.3.2 Moment Results for Water Tanker Static Loading

The moments and experimental moment distribution factors were calculated as described in the previous section. The rear axles were placed at the longitudinal moment critical position, which was calculated based on a simply supported single beam analysis.

Moment results for the water tanker loading for each alignment and for two-lane-loaded cases are shown in Figure 4.22. The maximum moments and experimental moment LDFs for interior and exterior girders are listed in Table 4.10.

Midspan moment values for water tanker loading for four alignments are provided in Table 4.11, and the corresponding moment LDF values are listed in Table 4.12. The maximum experimental moment LDF for an interior beam is 0.65 and was observed for Beam 3 for Alignment 1+2. Similarly, the maximum exterior beam moment LDF is 0.71 and was obtained due to loading on Alignment 1+2. The moment values that are calculated from bottom strain gage values and theoretical centroids are slightly higher than the values calculated through curve fitting of the deflection data. On the other hand, the computed moment LDFs are very close for the two different measurement techniques. The moment values determined from the string potentiometer measurements were used for further comparison to numerical models. The moment values are higher compared to the dump truck loading due to the heavier load of the water tanker. However, the moment LDFs are very close to those calculated for the dump truck loading.
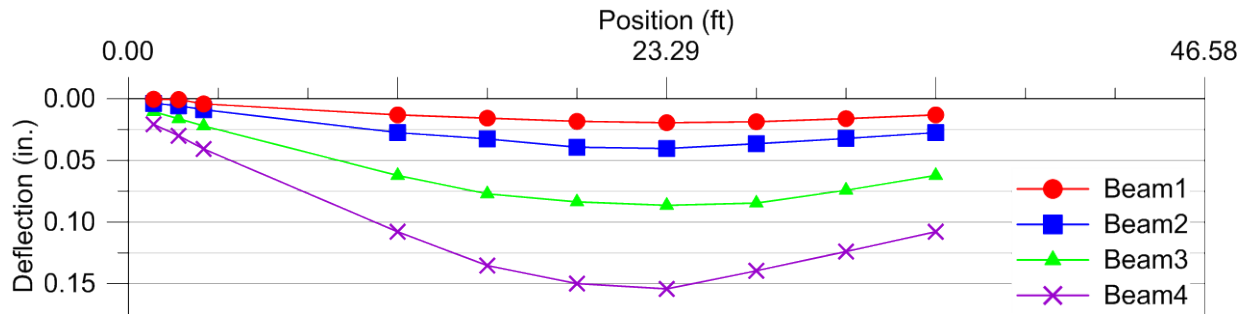
(a) Beam Deflections for Alignment 1
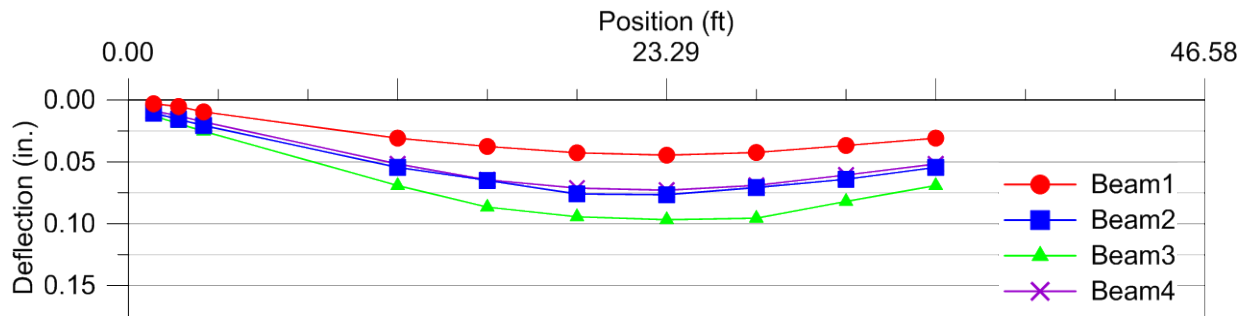
(b) Beam Deflections for Alignment 2
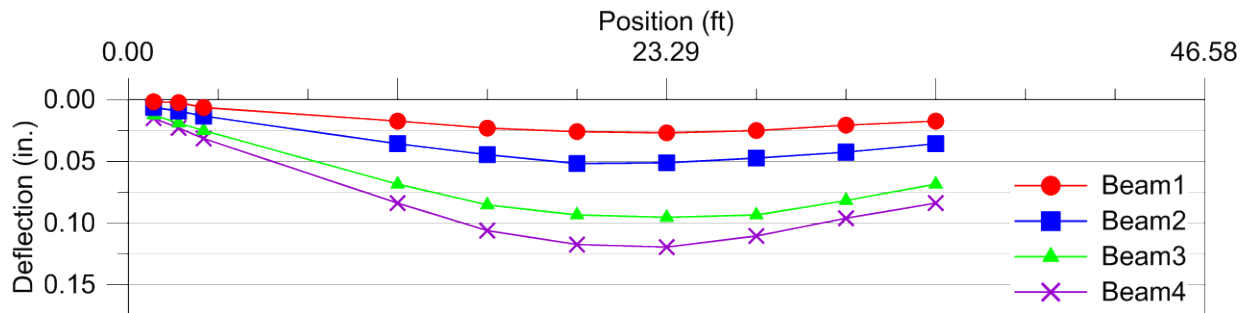
(c) Beam Deflections for Alignment 3
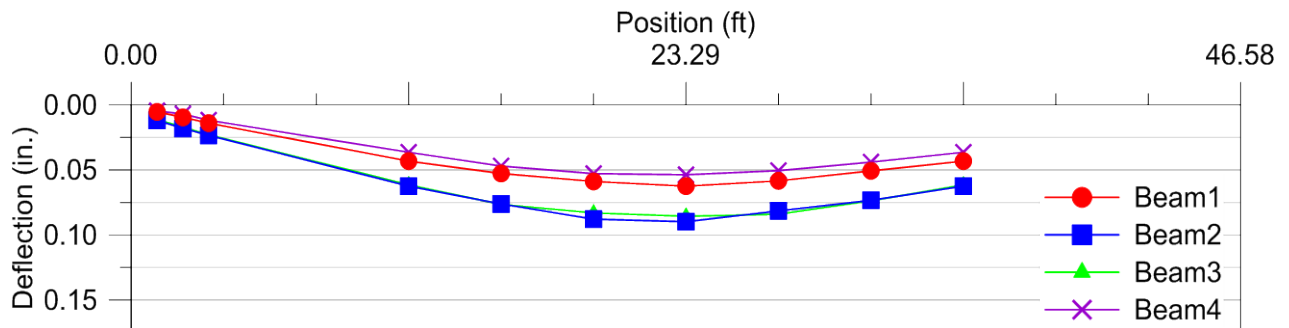
(d) Beam Deflections for Alignment 4

Figure 4.21. Deflection Profiles for Water Tanker Load.
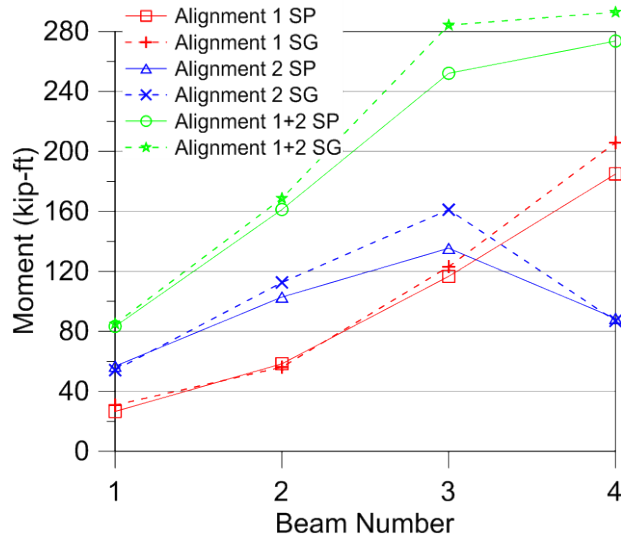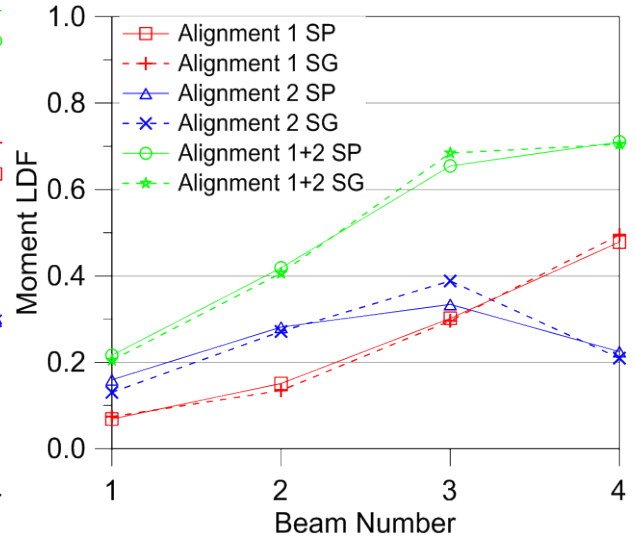
105

(a) Moments for Alignment 1+2

(b) Moment LDFs for Alignment 1+2
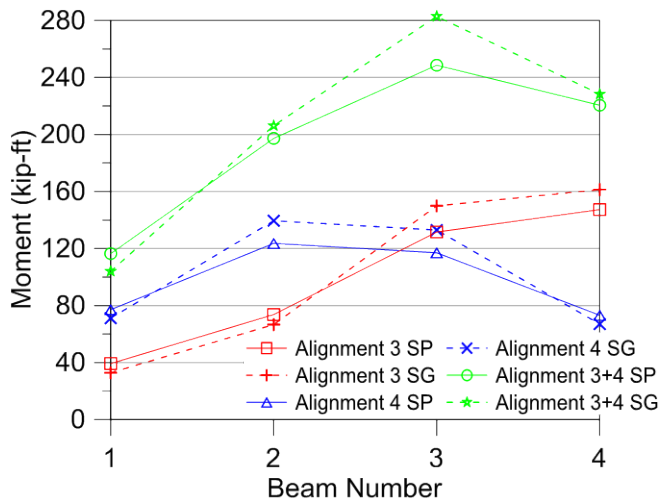
(c) Moments for Alignment 3+4
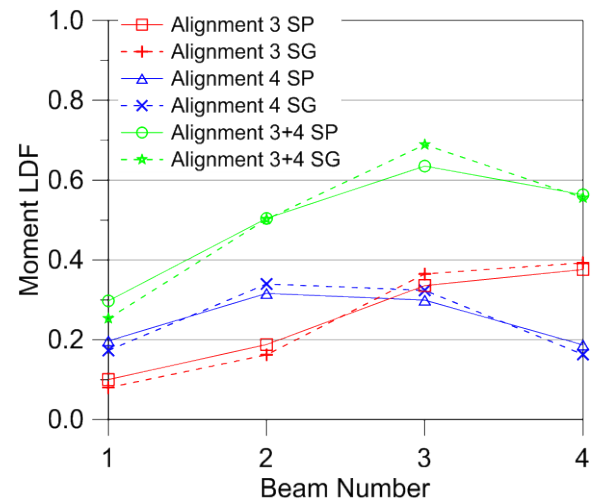
(d) Moment LDFs for Alignment 3+4

Figure 4.22. Midspan Moments and Moment LDFs for Water Tanker Loading.

Table 4.10. Maximum Moment Results for Water Tanker Tests.

No. Lanes Loaded	Slab Beam ID	Max. Moment (kip-ft)	Exp. Moment LDF	Transverse Load Position
One Lane	Beam 3 (Interior)	135	0.33	Alignment 2
	Beam 4 (Exterior)	185	0.48	Alignment 1
Two Lanes	Beam 3 (Interior)	252	0.65	Alignment 1+2
	Beam 4 (Exterior)	274	0.71	Alignment 1+2

Table 4.11. Moment Values Based on Strain Gage Data (kip-ft).

Load Case	Beam 1	Beam 2	Beam 3	Beam 4
Alignment 1	31	56	123	206
Alignment 2	54	113	161	87
Alignment 3	33	67	150	161
Alignment 4	71	140	133	67

Table 4.12. Moment Distribution Factors Based on Strain Gage Data.

Load Case	Beam 1	Beam 2	Beam 3	Beam 4
Alignment 1	0.07	0.13	0.30	0.49
Alignment 2	0.13	0.27	0.39	0.21
Alignment 3	0.08	0.16	0.36	0.39
Alignment 4	0.17	0.34	0.32	0.16

4.6.3.3   North Support Shear Results for Water Tanker Static Loading

The north support shear loading was achieved by placing the rear axles of the TTI water tanker on the bridge near the north support. The inner rear axle was placed 25 in. from the centerline of the bearing pads. More details showing the longitudinal positioning of the water tanker are provided in Figure 4.14 above. The maximum north support reactions and experimental shear distribution factors are summarized in Table 4.13. The north support shear results are shown in Figure 4.23.

Because of the long axle spacing, it was not possible to place all nine axles of the water tanker on the bridge. The vehicle was traveling from south to north for all three longitudinal

positions in order to make the testing procedure more convenient and create one more alternative loading. Therefore, unlike the dump truck tests, the north support and south support loadings were not the same. For the south support, the critical case occurred when both the rear axles and the middle axles were on the bridge. For the moment critical and north support critical cases, only the rear axles were on the bridge.

There are no comparable dynamic results for the north support reactions due to the length of the vehicle and the static north support shear critical position of the water tanker. The dynamic maximum north support reaction was due to of the application of both the rear axles and the middle axles, whereas the static north support critical loading was achieved by placing only the rear axles close to the north support. Therefore, there are no dynamic results to directly compare to the static north support reactions.

The maximum shear LDF for the interior girders was 1.07 and was recorded when Alignment 3+4 was loaded. The maximum shear LDF of 0.82 was obtained for an exterior girder when Alignment 1+2 was loaded. The LDF values when the north support was loaded by the water tanker are about 5–10 percent higher compared to the dump truck tests. The weight of the dump truck was approximately 31 kips and was applied by three axles, where the front axle was 15 ft 2.5 in. away from the rear axles; in contrast, the water tanker's rear axles weighed approximately 38 kips, and the load was applied by the two rear axles, which were 4 ft 2 in. apart. The difference between the north support LDFs for the dump truck and water tanker may be due to the longitudinal positions of the axles. The water tanker axles were closely spaced and concentrated close to the north support.

Table 4.13. Maximum North Support Shear Results for Water Tanker Tests.

No. of Lanes Loaded	Slab Beam No.	Maximum Reaction (kips)	LDF	Load Position
One Lane	Beam 3 (Interior)	24.7	0.70	Alignment 2
	Beam 4 (Exterior)	27.0	0.78	Alignment 1
Two Lanes	Beam 3 (Interior)	37.4	1.07	Alignment 3+4
	Beam 4 (Exterior)	28.7	0.82	Alignment 1+2
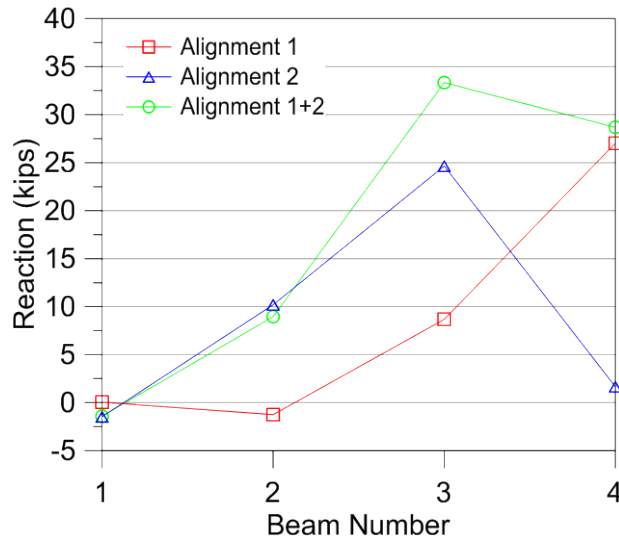
(a) Reactions for Alignment 1+2
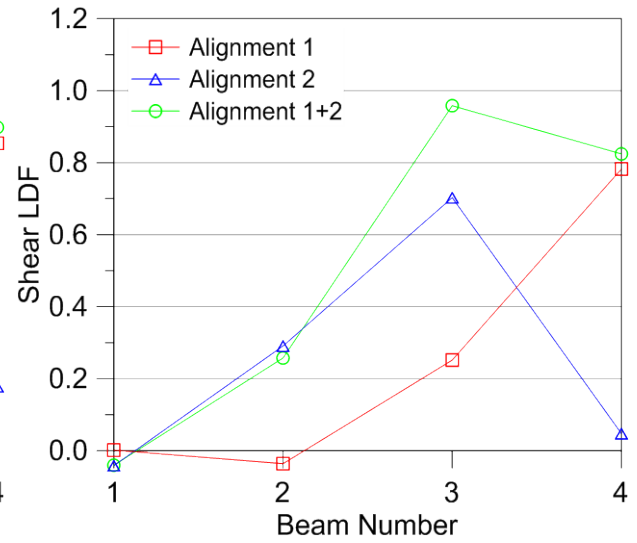
(b) Shear LDFs for Alignment 1+2
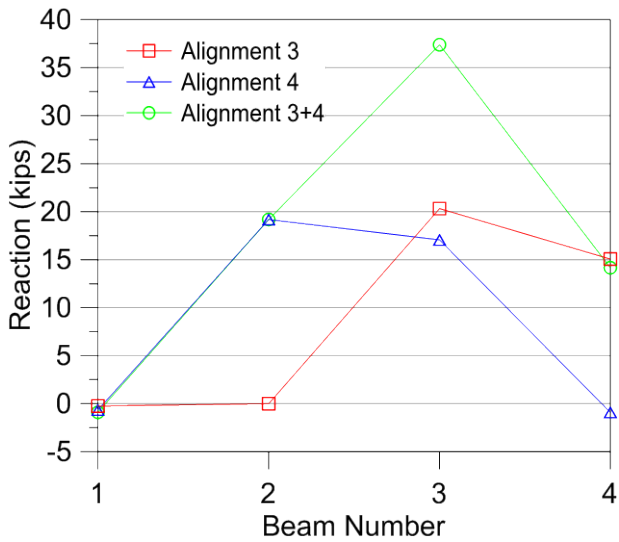
(c) Reactions for Alignment 3+4
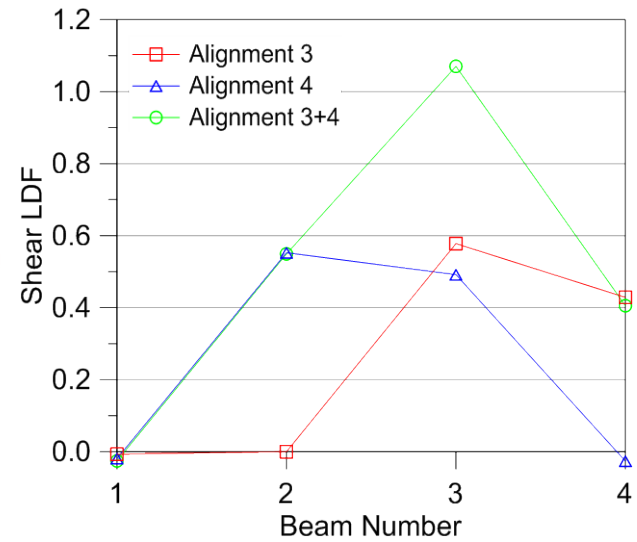
(d) Shear LDFs for Alignment 3+4

Figure 4.23. North Support Reactions and Shear LDFs for Water Tanker Loading.

4.6.3.4   South Support Shear Results for Water Tanker Loading

Table 4.14 lists the maximum south support reactions and experimental shear LDFs. Figure 4.24 shows the south support shear results for static and dynamic loading for the water tanker loading. The south support critical loading case was achieved when the rear axles were placed close to the south support and the middle axles were past the midspan of the bridge. This loading case resulted in the maximum bridge live load with the vehicles used for testing. The total weight on the bridge was 75.2 kips and was applied by four axles that were better distributed along the length compared to the north support critical loading.

The maximum experimental shear LDF of 0.92 was obtained for an interior beam when Alignment 3+4 was loaded. The exterior girders attained a maximum shear LDF of 0.80 for the Alignment 1+2 case. The south support shear LDF values for the water tanker are very close to the dump truck results, unlike in the north support case. As noted above, the total load of the water tanker was better distributed along the length for the south support shear critical loading, and the resulting reactions at the south support were lower as compared to the north support test. This finding indicates that the concentrated loads placed close to the support to maximize the reaction create a more adverse case that results in higher shear LDFs.

Table 4.14. Maximum South Support Reactions for Water Tanker.

No. Lanes Loaded	Slab Beam ID	Max. Reaction (kips)	Exp. Shear LDF	Tranverse Load Position
One Lane	Beam 3 (Interior)	25.7	0.58	Alignment 2
	Beam 4 (Exterior)	31.9	0.74	Alignment 1
Two Lanes	Beam 3 (Interior)	40.6	0.92	Alignment 3+4
	Beam 4 (Exterior)	36.5	0.84	Alignment 1+2
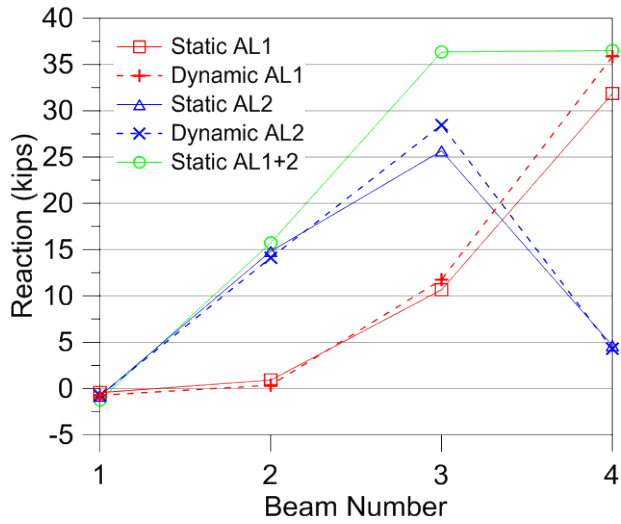
(a) Reactions for Alignment 1+2
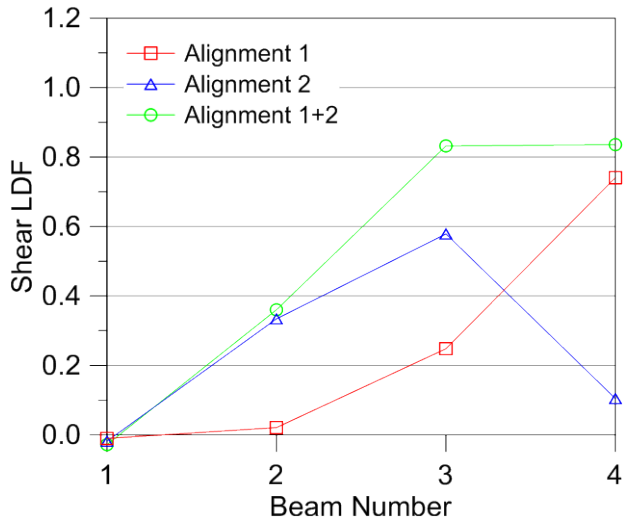
(b) Shear LDFs for Alignment 1+2
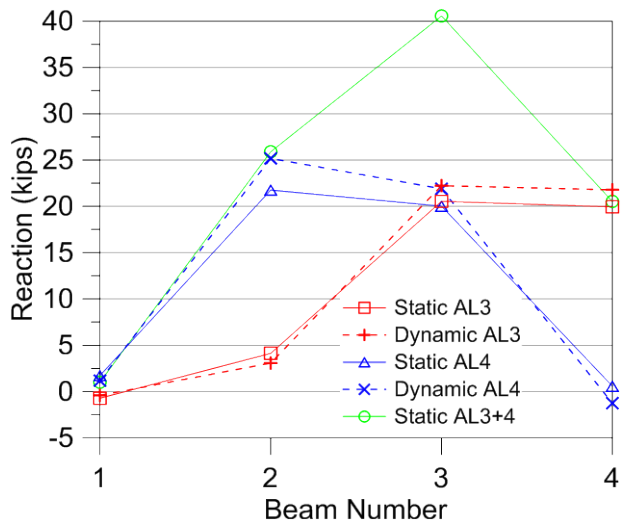
(c) Reactions for Alignment 3+4
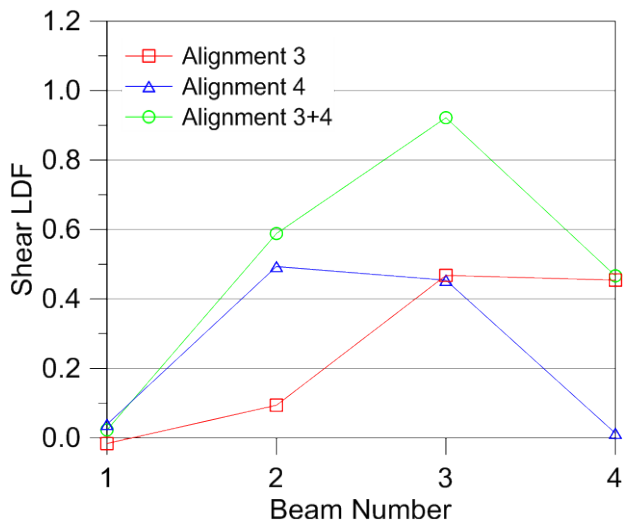
(d) Shear LDFs for Alignment 3+4

Figure 4.24. South Support Reactions and Shear LDFs for Water Tanker Loading.

4.6.4 Dynamic Characteristics of Riverside Bridge

The research team identified the dynamic properties of the bridge by evaluating the acceleration data in the frequency domain. A total of eight accelerometers were attached to the bridge. Five accelerometers were attached to the bottom of Beam 2 and distributed in the longitudinal direction. The other three were attached at the midspan of the remaining three slab beams to capture transverse mode shapes. Figure 4.12 shows the exact layouts of the accelerometers.

Modal analysis of the bridge was conducted by running the dump truck along two different alignments and also by applying an impulse at selected points with a sledge hammer. The impulse loading test was conducted to identify possible vehicle structure interaction. The impulse test was conducted by hitting a sledge hammer on the deck surface at the longitudinal midspan and at three different transverse locations: east edge, west edge, and center. Obtained modal frequencies from impulse testing and vehicle tests are summarized in Table 4.15.

Mode shapes were identified during the dump truck testing along Alignment 1. The normalized amplitudes of each mode plotted along Beam 2 (longitudinal direction) and in the transverse direction are shown in Figure 4.25.

Table 4.15. First Three Modal Frequencies.

Description	Vehicle Speed (mph)	1st Mode (Hz)	2nd Mode (Hz)	3rd Mode (Hz)
Impulse	N.A.	5.22	8.22	13.8
Alignment 1	40	5.37	7.97	13.5
Alignment 2	40	5.37	7.94	13.3
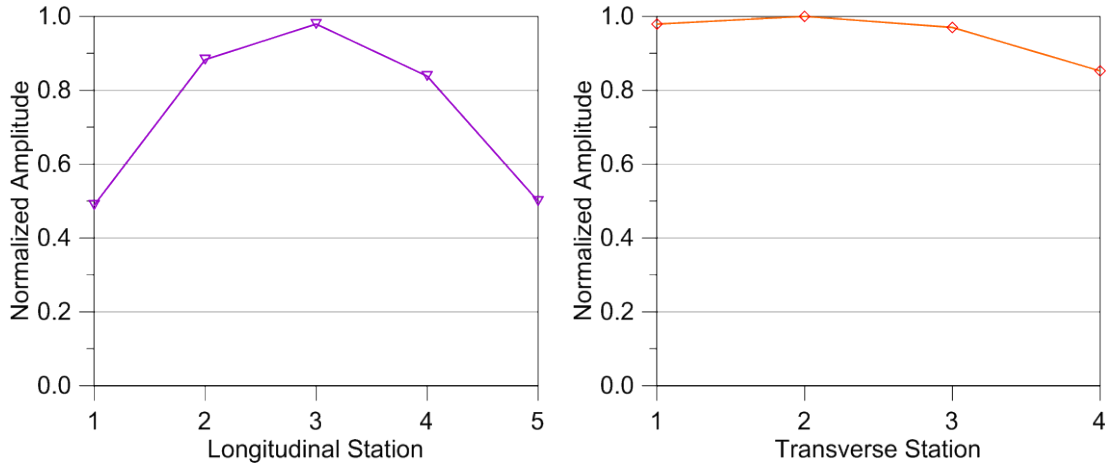
(a) 1st Mode Shape
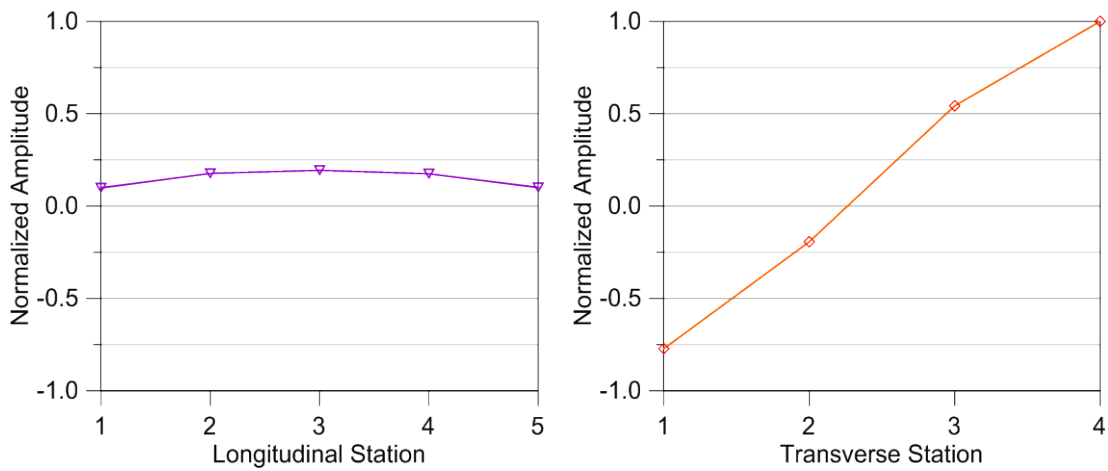
(b) 2nd Mode Shape
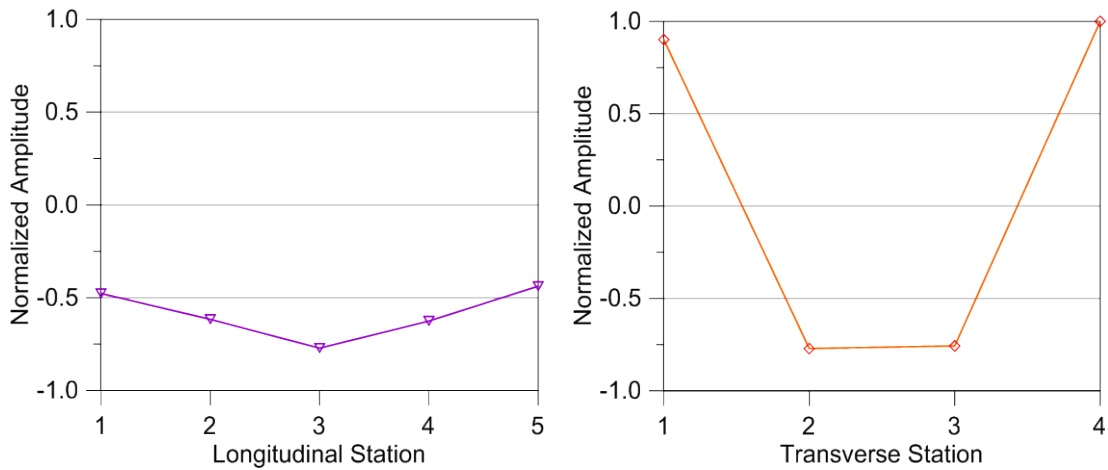
(c) 3rd Mode Shape

Figure 4.25. Identified Mode Shapes in Longitudinal and Transverse Directions.

4.7   SUMMARY AND FINDINGS

4.7.1   Constructability and Related Observations

This research investigated the possibility of using slab beams in a spread configuration for short-span bridges. A full-scale bridge utilizing widely spaced (4 ft 8 in. clear) slab beams was constructed at the Texas A&M University Riverside Campus, and then the research team tested the bridge under static and dynamic service loads. Based on the observations during construction and experimental investigation of the Riverside Bridge, the following conclusions were drawn with respect to constructability and related observations.

1. Spread slab beam bridge systems that utilize PCPs with a CIP concrete deck, similar to I-girder bridges, provide a viable construction method for short-span bridges approximately 30–50 ft long.

2. Spread prestressed slab beam bridge construction was successfully implemented for the Riverside test bridge.

3. Camber of the spread slab beams tends to increase due to higher prestressing forces. Thus, the bedding strip installation can require increased depths (up to 4 in. total) at the beam ends. Camber should be evaluated as part of spread slab beam bridge designs to ensure the value is acceptable with regard to construction and serviceability considerations.

4. Care should be taken during deck curing to avoid any unexpected cracking. For the Riverside Bridge, a single longitudinal crack was observed on the deck surface along the entire length of the bridge at the transverse centerline (centered on a PCP). The crack occurred within the first week after deck placement. The width did not increase after the crack appeared. It appears that the crack developed because of stresses due to combined shrinkage and differential temperature effects. The crack may potentially be due to hot weather and inadequate curing. However, the deck was sprayed with water daily and covered with a curing blanket and plastic sheet during the first four days. It appears that this type of crack is not related to the spread slab beam implementation.

4.7.2   Field Testing

Field testing was conducted for the Riverside Bridge to investigate the effect of beam spacing on the structural behavior of the composite bridge system. Experimental results were processed and reviewed, and are summarized below.

1. The desired performance was achieved for in-service loading. During field testing, the beam live load deflections were within the design limits. No major cracking or reduction in the overall stiffness of the bridge superstructure was observed during static and dynamic testing (up to 40 mph). The Riverside Bridge remained in the linear range of behavior when the water tanker loading of about 75 kips (slightly above HS20 loading) was applied.

2. Experimental LDFs were evaluated using alignments that provided the most adverse loading cases. The following observations were made for the Riverside Bridge, which was tested with a dump truck and a water tanker.

    a. Experimental shear LDFs for both interior and exterior girders were about 5 percent higher when the Riverside Bridge was loaded with the rear axle of the water tanker compared to the dump truck loading. This may be due to more concentrated loading achieved with the water tanker.

    b. Experimental moment LDFs were similar for both the dump truck and the water tanker loadings for the Riverside Bridge.

3. Bridge responses under dynamic loads were larger compared to static values. With the increase of vehicle speed, bridge responses became larger. In spite of the changes in moment magnitude under dynamic loading, the moment LDFs were quite similar to their static counterparts.

4. The observed bridge responses under dynamic loads were larger when compared to the static counterparts; the dynamic bridge response became larger with increasing vehicle speed. Evidently, for short-span bridges, the dynamic impact may exceed the AASHTO LRFD Specifications (2012) design value of 33 percent. However, the observed impact depended upon the position of the approach bump as well as the dynamic characteristics of the vehicle and the bridge.

5   EXPERIMENTAL STUDY OF US 69 BRIDGE

5.1   INTRODUCTION OF US 69 BRIDGE

A spread slab beam bridge was recently constructed on US 69 in Grayson County, Texas, in the city of Denison. The research team temporarily instrumented and monitored the bridge to gain additional information on the in-service performance and load distribution of a second spread slab bream bridge. This bridge, shown in Figures 5.1 and 5.2, was designed by the TxDOT Bridge Division in 2010. The entire bridge consists of a total of 18 spans, of which the first three simply supported spans are designed and constructed utilizing spread slab beam sections. The third span has the longest slab beams of 50 ft, while the other two spans have 30 ft long slab beams. The bridge was constructed as two symmetric structures, with one structure for the northbound lanes and one structure for the southbound lanes, with a 1 in. joint between the bridge structures. Therefore, only the northbound structure, with six 50 ft long simply supported slab beams that pass over Day Street, was instrumented and monitored during the field test. The construction of the northbound structure was completed at the end of 2012. Figure 5.1(a) shows the location of the US 69 Bridge site, and photographs of the bridge elevation are shown in Figures 5.1(b) and 5.1(c). The elevation view and side view of the first three spans with a spread slab beam section are shown in Figure 5.2(a), and a typical transverse cross-section of the first three spans is shown in Figure 5.2(b).

The span length between the centerlines of bearing pads of the simply supported bridge is 48 ft 7 in. The total width of the two adjacent bridges making up the northbound and southbound lanes is 76 ft, including a 1 ft overhang and 6 ft sidewalks on the west and east sides. The northbound structure is 37 ft 11.5 in. wide and has six 5SB15 slab beams with an approximate 16 in. clear spacing, which is much less than the 56 in. clear spacing of the full-scale Riverside Bridge built at the TAMU Riverside Campus. According to the structural drawings, the thickness of the reinforced concrete deck on the top of the slab beams is 12 in. at the bearing locations, and a corrugated steel plate was utilized to support the 8 in. thick CIP deck between slab beams. Figure 5.2(c) shows detailed information for the northbound structure's transverse cross-section. Note that the location of the median changes along the test span due to the presence of a turn lane. The median layout is shown in Figure 5.3. The structural drawings indicate that the specified minimum 28-day concrete compressive strength for the precast, pretensioned 5SB15 slab beams and the CIP deck is 5.4 ksi and 4 ksi, respectively.

(a) Location of US 69 Bridge over Day Street (Google Maps 2005)

(b) Side View of Three Spread Slab Beam Spans (30 ft, 30 ft, and 50 ft Spans)

(c) Elevation View of 50 ft Northbound Bridge Span over Day Street

Figure 5.1. Location and Photos of US 69 Bridge in Denison, TX.
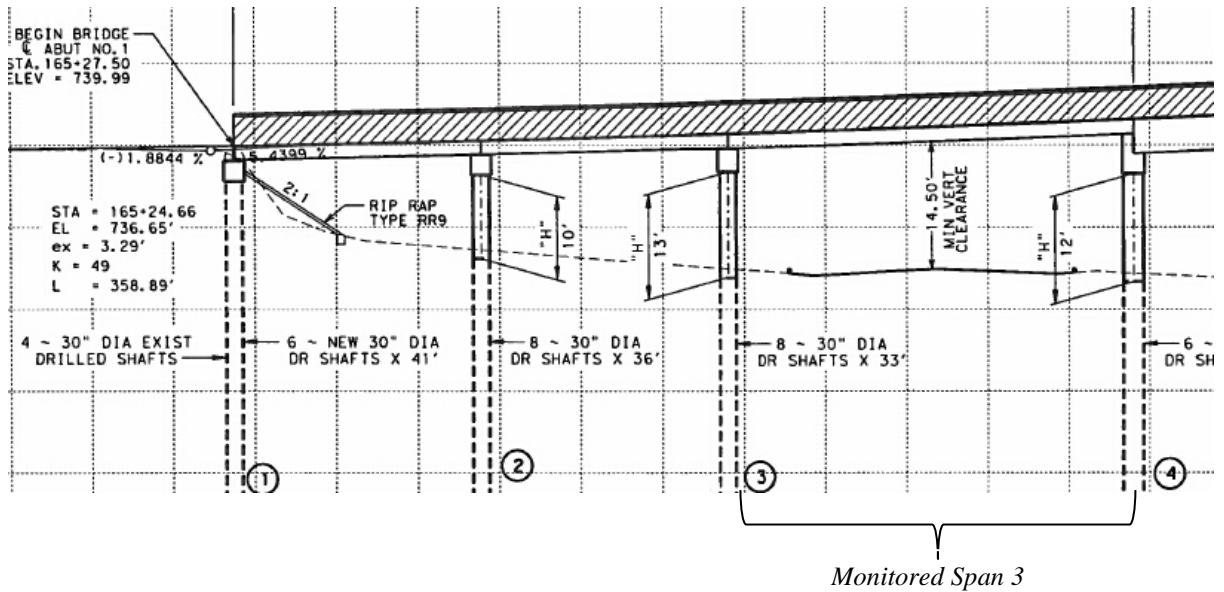
(a) Elevation View of First Three Spread Slab Beam Spans
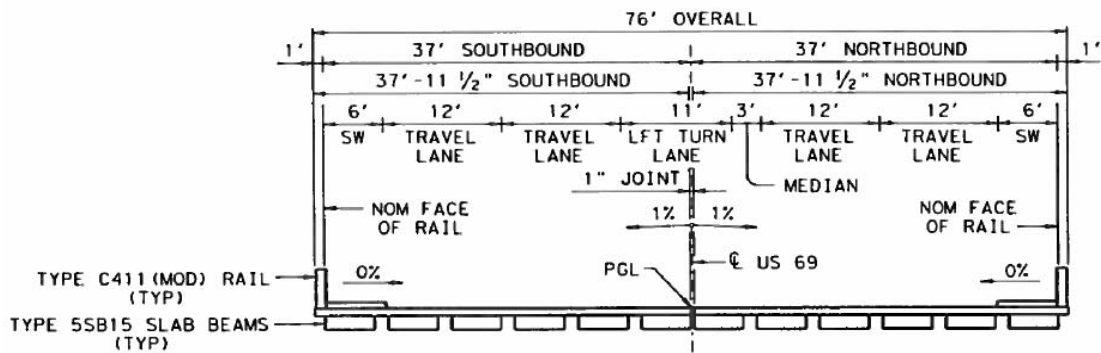
(b) Transverse Section of First Three Spread Slab Beam Spans
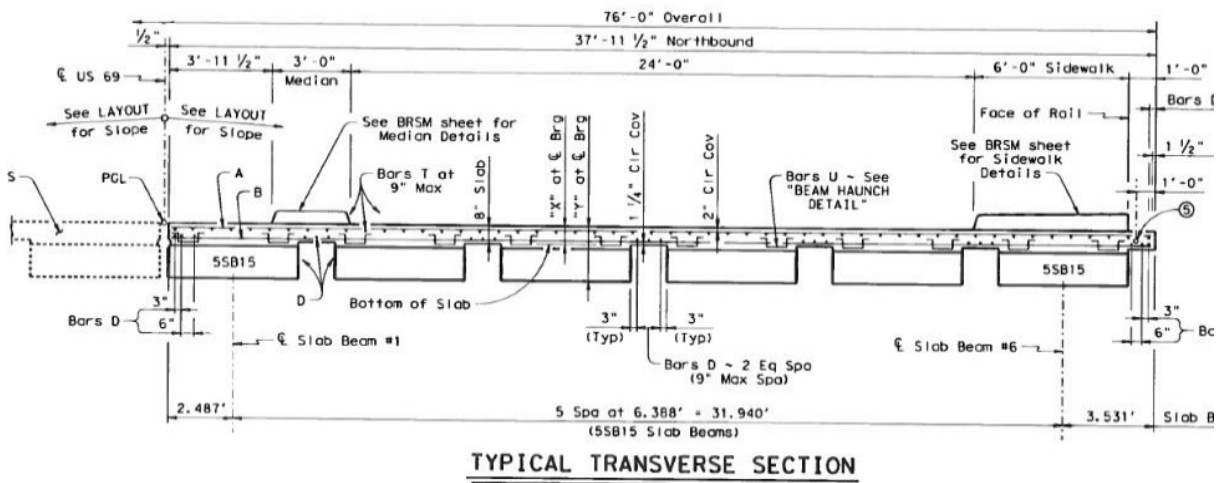
(c) Transverse Section of Northbound Bridge

Figure 5.2. Design Drawings for US 69 Bridge (TxDOT 2010).
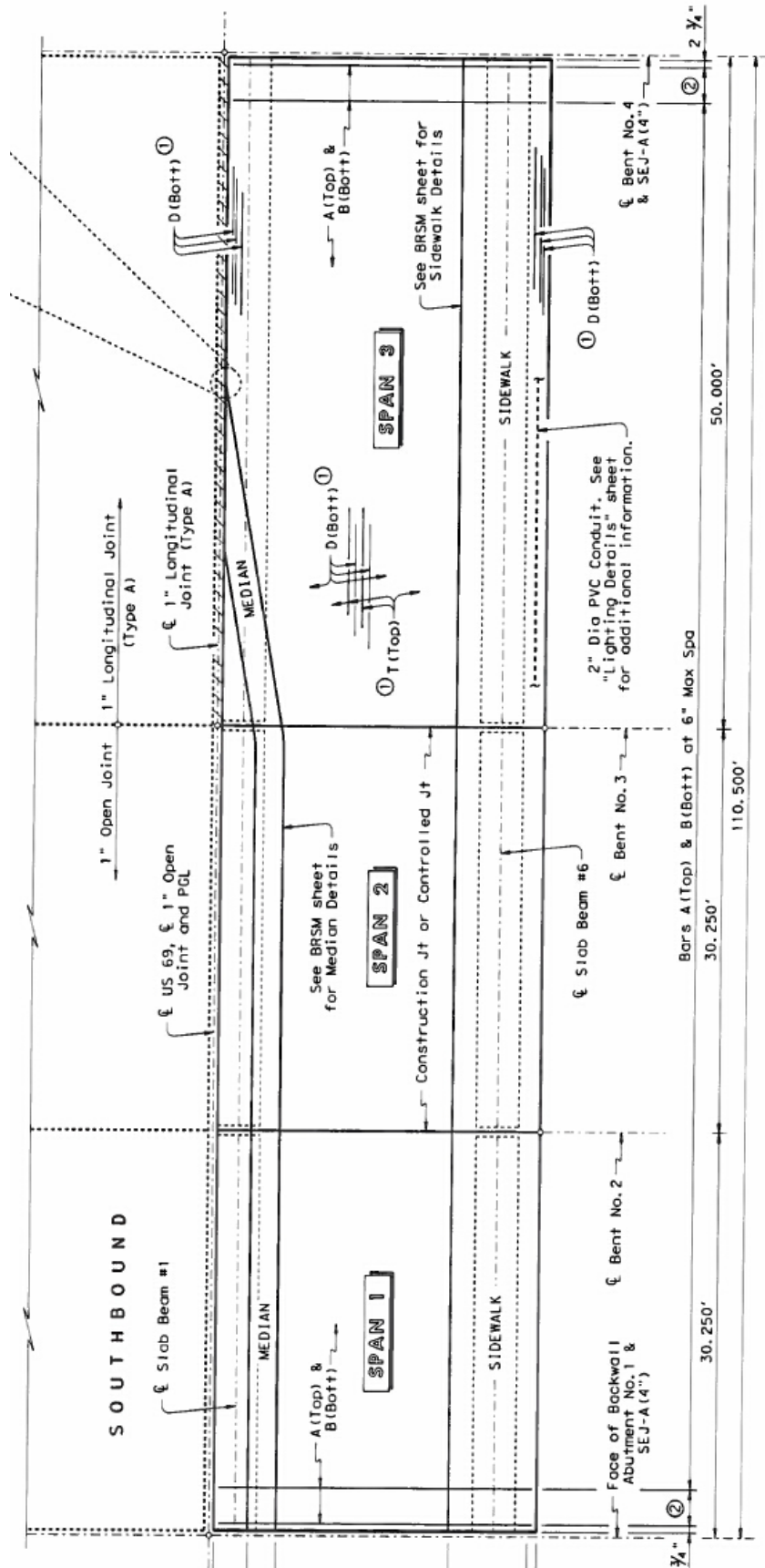
Figure 5.3. Median Layout on Deck Surface of Northbound Bridge (TxDOT 2010).

The northbound bridge was instrumented with various types of sensors to determine the load distribution behavior and structural dynamic properties as the truck load was applied both statically and dynamically on the test bridge. The information gained from field testing on the US 69 Bridge provides an opportunity to obtain important insight on the performance of a spread slab beam bridge system with more closely spaced beams.

5.2   INSTRUMENTATION PLAN

The instrumentation plan for field monitoring the US 69 northbound bridge in Grayson County was designed based on the objectives of the research project and site-specific conditions. Three types of sensors were used, as shown in Figure 5.4. Strain gages, linear variable differential transformers (LVDTs), and string potentiometers were installed on the test span to measure the structural response under vehicular loading and ultimately determine load sharing among slab beams. Also, accelerometers were utilized during the dynamic testing to capture bridge system parameters.

5.2.1   Instrument List and Data Acquisition System

The instruments used during field testing the US 69 Bridge consisted of 12 strain gages, six LVDTs, 36 string potentiometers, and eight accelerometers. A total of 62 data acquisition channels were utilized to collect data from the sensors. A Measurement and Computing (MC) Strain Book/616 data acquisition (DAQ) unit was used as the main box and was connected to a laptop personal computer. The Strain Book/616 DAQ unit has an eight-channel data acquisition capacity and can transfer up to 1 million samples per second. Four WBK16/SSH extension modules with eight DSUB9 input channels per module were utilized for additional strain gages, LVDTs, and string potentiometers. Also, another WBK18 extension module with eight Bayonet Neill-Concelman (BNC) input channels was used for the integral electronic piezoelectric (IEPE) accelerometers. Figure 5.4(a) shows the main box and extension modules of the data acquisition system.

5.2.1.1   Strain Gages

In order to infer moments resisted by individual slab beams under vehicular loading, 12 strain gages were installed at midspan of the bridge on both the deck and beam soffit surfaces. Four strain gages were installed on the surface of the sidewalk and guardrail section in order to evaluate the composite action of the deck, sidewalk, and guardrail sections. Given that the

maximum aggregate size of the self-consolidating concrete (SCC) used for the slab beams is approximately 0.75 in., the PL-60-11-3LT strain gages provided by the Tokyo Sokki Kenkyujo Co., Ltd. (TML) were selected so that the gage length of 2.25 in. was three times larger than the aggregate size. PL-60-11-3LT gages are a wire type strain gage with a polyester resin backing. They are mainly used for measurements on concrete, mortar, or rock with a gage factor of 2.13. Also, these gages have 9.8 ft long pre-attached vinyl lead wires, which saves time and labor for lead wire connections such as terminal installation and lead wire soldering. Figure 5.4(b) shows the strain gage used in the field bridge test.

5.2.1.2 LVDTs

In order to determine the shear LDFs under vehicular loading, six LVDT transducers were installed close to the north support end to capture the deformation of each bearing pad. Omega GP911-5-S LVDTs, which have spring-loaded analog gaging probes with a ±0.20 in. (±5 mm) range, were utilized during the US 69 Bridge test. These LVDTs need an alternating current (AC) excitation voltage, but the data acquisition system could only supply 10 volts of direct current (DC) voltage. Therefore, the research team developed a voltage converter system. Figure 5.4(c) and Figure 5.4(d) show the Omega GP911-5-S LVDTs and the transducer amplifier.

5.2.1.3 String Potentiometers

A total of 36 Celesco string potentiometers were installed along the six slab beams at six different stations to obtain the bridge deflection field. Based on the estimated deflection values, 24 Celesco SP1-4 string potentiometers with a 4 in. stroke and 12 SM1-2 string potentiometers with a 2 in. stroke were utilized during the field test. Specifically, 12 SM1-2 string potentiometers with higher resolution were arranged at two stations located near the north end of the bridge. Figure 5.4(e) shows the string potentiometers used during the field test.

5.2.1.4 Piezoelectric Accelerometers

To obtain the bridge system parameters (natural frequency and mode shapes) during the dynamic test, eight piezoelectric accelerometers (Model 4507 manufactured by Brüel & Kjaer Sound & Vibration Measurement) were attached at the midspan location of each slab beam and distributed along the north half span of the fourth slab beam (Figure 5.5). The resonance frequency of the accelerometers is 18 kHz, which is far from the bridge natural frequency. High sensitivity, low mass, and small physical dimensions make this type of accelerometer suitable for modal analysis. Figure 5.4(f) shows the piezoelectric accelerometers used during the dynamic test.

StrainBook/616   WBK16/SSH   WBK18

(a) Main Box and Extension Modules (Measurement Computing 2014)
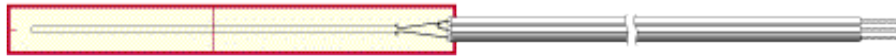
(b) TML PL-60-11-3LT Strain Gage (Tokyo Sokki Kenkyujo Co. 2014)

(c) Omega LVDT (Omega 2014)

(d) Transducer Amplifier

(e) String Potentiometer (Celesco Measurement 2014)

(f) Accelerometers (Brüel & Kjaer 2014)

Figure 5.4. Data Acquisition System and Instrumentation.

5.2.2   Instrumentation Plan for US 69 Bridge

Following lessons learned from the comprehensive instrumentation used in testing the Riverside Bridge, as described in Appendix D, researchers adopted a simplified instrumentation plan for the US 69 Bridge tests.

To determine the moment LDFs under vehicular loading, 12 strain gages were installed at the midspan of the six bridge girders, on both the top and bottom surface. The moment of each slab beam can be calculated from the measured strain values, and the moment sharing ratio can be obtained by comparing the strain distribution for each beam. In addition, four strain gages were installed on the sidewalk and guardrail to investigate the composite action between the deck, sidewalk, and guardrail sections.

After conducting a series of static and dynamic tests on the bearing pads in the laboratory, researchers found that the bearing pads exhibit linear elastic behavior in the vehicular load range. Experimental shear LDFs were obtained by comparing the deformation of the bearing pads at the north support. Six LVDTs were attached to the surface of the bent cap close to the bearing pads under each slab beam to measure their deformations. In addition, 36 string potentiometers were installed at six stations distributed between the north support and midspan to obtain the bridge deflection field for half the span.

In order to capture bridge system parameters (natural frequencies and mode shapes) during dynamic testing, a total of eight accelerometers were attached on the bottom surface of the slab beams. Six accelerometers were located at the midspan location of each slab beam, and the remaining two accelerometers were attached to Beam 4 between the midspan and north support (see Figure 5.6).

The selected data acquisition system is capable of supporting 64 channels, and 62 channels were utilized during the field test. All instruments were arranged in the north half span of the bridge. The top, bottom, and section views of all instruments on the test bridge are shown in Figures 5.6 and Figure 5.7 Detailed information describing the data acquisition equipment, channel numbers, sensor labels, and sensor types is given in Table 5.1. The sensors were labeled based on type and location. Labeling notes for all sensors are shown in Figure 5.7.
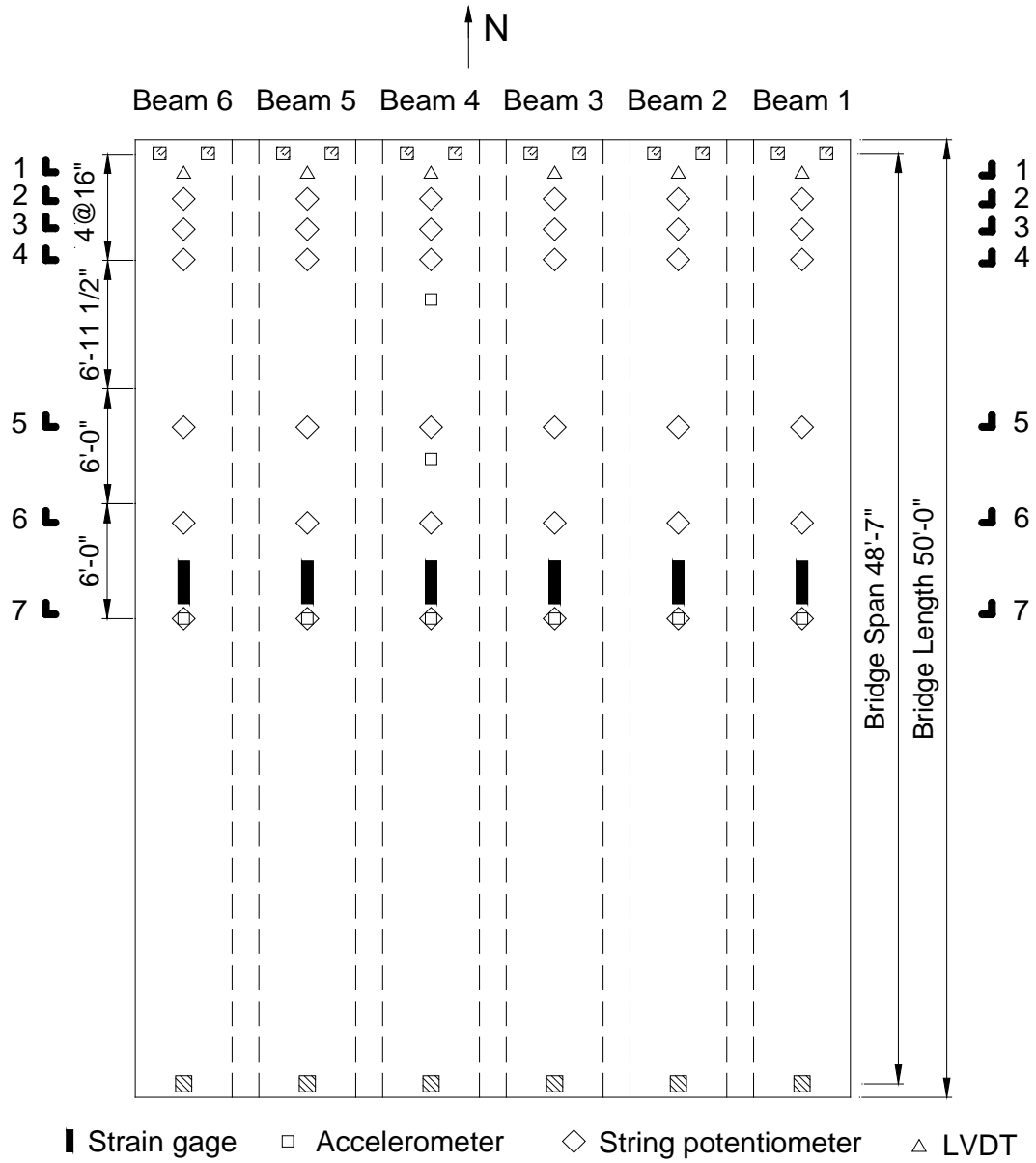
Figure 5.5. Bottom View of Instrumentation on US 69 Bridge.
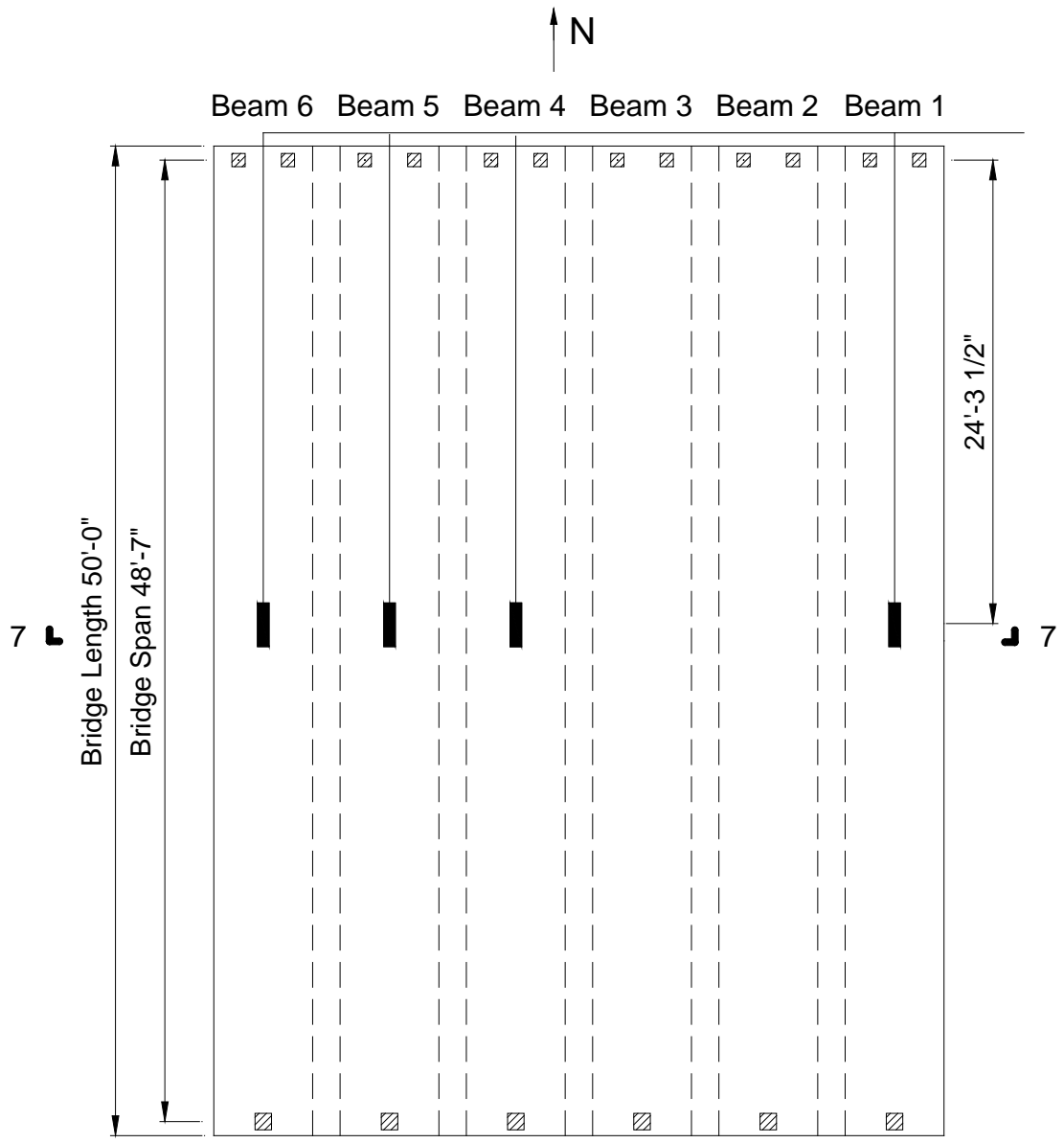
Figure 5.6. Top View of Instrumentation on US 69 Bridge.

Station 1-1

| Beam 6 | Beam 5 | Beam 4 | Beam 3 | Beam 2 | Beam 1 |

Station 2-2, 3-3, 4-4, 5-5, 6-6

| Beam 6 | Beam 5 | Beam 4 | Beam 3 | Beam 2 | Beam 1 |

Station 7-7

| Beam 6 | Beam 5 | Beam 4 | Beam 3 | Beam 2 | Beam 1 |
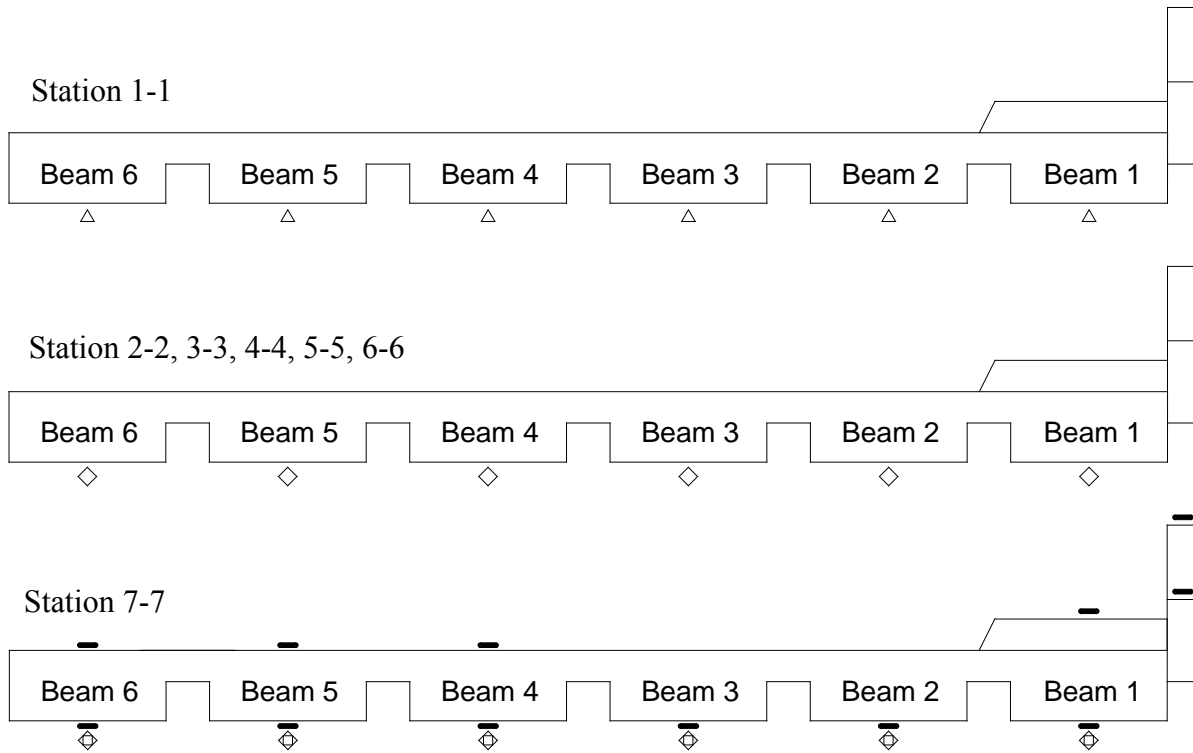
(a) Section Views of Instrumentation

Sensor Type

Top/Bottom
East/West

$$X\#\text{-}\#X$$

Beam No.

Station No.
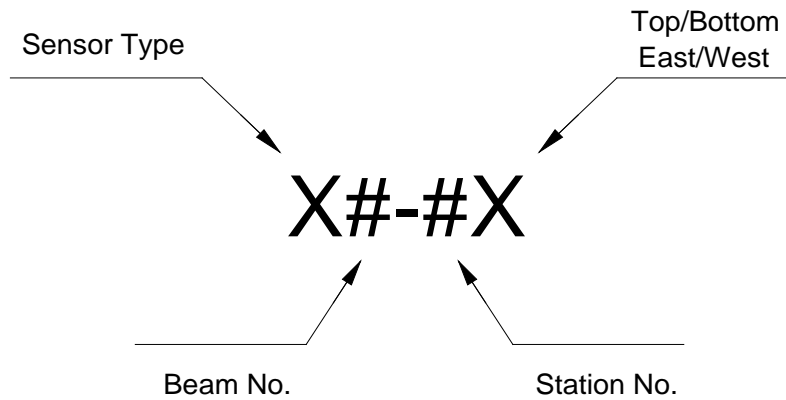
(b) Instrumentation Labeling Notes

Figure 5.7. Section View and Labeling Notes of Instrumentation on US 69 Bridge.

127

Table 5.1. Instrumentation Information for US 69 Bridge.

DAQ	Channel ID	Label	Type	DAQ	Channel ID	Label	Type
Strain Book	CH1	SG1-4T	PL60-11-3LT	WBK16-4	CH33	SP3-4B	Celesco SP1-4
	CH2	SG2-4T	PL60-11-3LT		CH34	SP4-4B	Celesco SP1-4
	CH3	SG3-4T	PL60-11-3LT		CH35	SP5-4B	Celesco SP1-4
	CH4	SG4-4T	PL60-11-3LT		CH36	SP6-4B	Celesco SP1-4
	CH5	SG5-4T	PL60-11-3LT		CH37	SP1-5B	Celesco SP1-4
	CH6	SG6-4T	PL60-11-3LT		CH38	SP2-5B	Celesco SP1-4
	CH7	SG1-4B	PL60-11-3LT		CH39	SP3-5B	Celesco SP1-4
	CH8	SG2-4B	PL60-11-3LT		CH40	SP4-5B	Celesco SP1-4
WBK16-1	CH9	SG3-4B	PL60-11-3LT	WBK16-5	CH41	SP5-5B	Celesco SP1-4
	CH10	SG4-4B	PL60-11-3LT		CH42	SP6-5B	Celesco SP1-4
	CH11	SG5-4B	PL60-11-3LT		CH43	SP1-6B	Celesco SP1-4
	CH12	SG6-4B	PL60-11-3LT		CH44	SP2-6B	Celesco SP1-4
	CH13	L1-1B	Omega		CH45	SP3-6B	Celesco SP1-4
	CH14	L2-1B	Omega		CH46	SP4-6B	Celesco SP1-4
	CH15	L3-1B	Omega		CH47	SP5-6B	Celesco SP1-4
	CH16	L4-1B	Omega		CH48	SP6-6B	Celesco SP1-4
WBK16-2	CH17	L5-1B	Omega	WBK16-6	CH49	SP1-7B	Celesco SP1-4
	CH18	L6-1B	Omega		CH50	SP2-7B	Celesco SP1-4
	CH19	SP1-2B	Celesco SM1-2		CH51	SP3-7B	Celesco SP1-4
	CH20	SP2-2B	Celesco SM1-2		CH52	SP4-7B	Celesco SP1-4
	CH21	SP3-2B	Celesco SM1-2		CH53	SP5-7B	Celesco SP1-4
	CH22	SP4-2B	Celesco SM1-2		CH54	SP6-7B	Celesco SP1-4
	CH23	SP5-2B	Celesco SM1-2		CH55	–	–
	CH24	SP6-2B	Celesco SM1-2		CH56	–	–
WBK16-3	CH25	SP1-3B	Celesco SM1-2	WBK18	CH57	A1-4B	4507 IEPE
	CH26	SP2-3B	Celesco SM1-2		CH58	A2-4B	4507 IEPE
	CH27	SP3-3B	Celesco SM1-2		CH59	A3-4B	4507 IEPE
	CH28	SP4-3B	Celesco SM1-2		CH60	A4-4B	4507 IEPE
	CH29	SP5-3B	Celesco SM1-2		CH61	A5-4B	4507 IEPE
	CH30	SP6-3B	Celesco SM1-2		CH62	A6-4B	4507 IEPE
	CH31	SP1-4B	Celesco SP1-4		CH63	A3-2B	4507 IEPE
	CH32	SP2-4B	Celesco SP1-4		CH64	A3-3B	4507 IEPE

5.3 EXPERIMENTAL PROGRAM

A comprehensive static and dynamic test program was carried out in order to evaluate the in-service performance and investigate the load sharing behavior of the slab beam system for the US 69 Bridge over Day Street in the city of Denison, Grayson County, Texas. The experimental program consisted of three parts: static load tests, controlled dynamic load tests, and ambient traffic load tests. Given that it is an in-service highway bridge, traffic control of the northbound US 69 Bridge and Day Street below was provided by the TxDOT Sherman Area Office during the instrument installation and bridge testing process. The actual testing took place on May 22, 2014.

5.3.1 Test Vehicles

The TxDOT Sherman Area Office provided a 10 cubic yard (cyd) dump truck for vehicle loading during the bridge test. The dump truck was loaded with an asphalt base material, and individual axle weights were measured at the Denison weigh station on the southbound frontage road of US 75 on the morning of the test day. The axle and wheel spacing and the measured axle loads of the dump truck are shown in Figure 5.8.

For the purpose of investigating moment and shear load distribution factors of exterior and interior slab beams, a series of static load tests including two longitudinal positions and five transverse alignments was conducted. In the longitudinal direction, the maximum bending moment occurs when the axle load closest to the resultant load and the resultant load are placed at equal distance from the midspan of the bridge. This is called the moment critical position in the longitudinal direction and is shown in Figure 5.9(a) for the TxDOT dump truck. The maximum shear force occurs when the load is located a member depth away from the support (St. Venant's shear principle; (Ugural and Fenster 2012). Therefore, the maximum shear force occurred when the last axle load was placed at a distance equal to the beam depth (25 in.) to the centerline of the bearing pad during this bridge test. This is called the shear critical position in the longitudinal direction and is shown in Figure 5.9(b) for the TxDOT dump truck.

In the transverse direction, the critical moment and shear forces occur when two vehicles are loaded simultaneously. Given that only one dump truck was available during the field test, the vehicle was parked at different transverse alignments and the superposition method was utilized during the data analysis to calculate two-lane-loaded reactions. The minimum distance

between two vehicles is 4 ft in accordance with AASHTO LRFD Specifications (2012). Preliminary finite element models of the bridge based on load configuration and several critical vehicle positions were developed before field testing. Analysis showed the most critical position for the exterior slab beam was when the two trucks were parked as close as possible to the bridge's west edge. For an interior slab beam, the maximum LDF occurred when the two trucks were loaded 7 ft away from the bridge's west edge. Another transverse alignment where the vehicle was parked just at the edge of the sidewalk was taken into consideration in order to investigate the composite action between the deck, sidewalk, and guardrail. All transverse alignments for the static load tests are shown in Figure 5.10.

Researchers found that the vehicle could not reach the exact longitudinal moment critical position when it was parked along Alignment 1 due to the existence of the median (Figure 5.3); thus, the moment critical load case for Alignment 1 was conducted when the last tire of the dump truck touched the median. The vehicle location in the moment critical load case for Alignment 1 is shown in Figure 5.11.
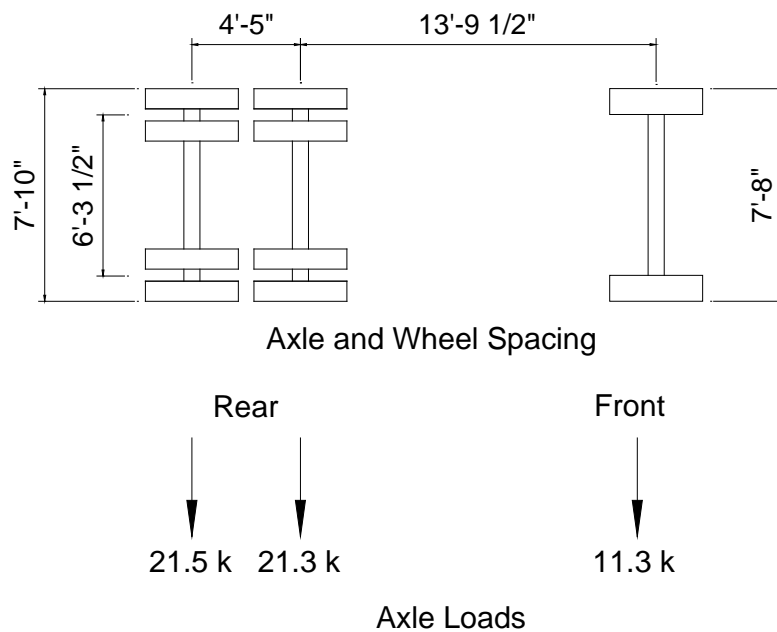
Figure 5.8. Test Vehicle Axle and Wheel Spacing and Axle Loads.
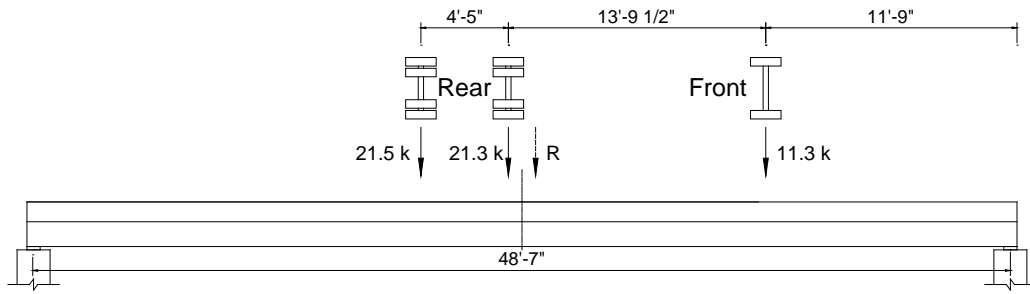
(a) Moment Critical Position
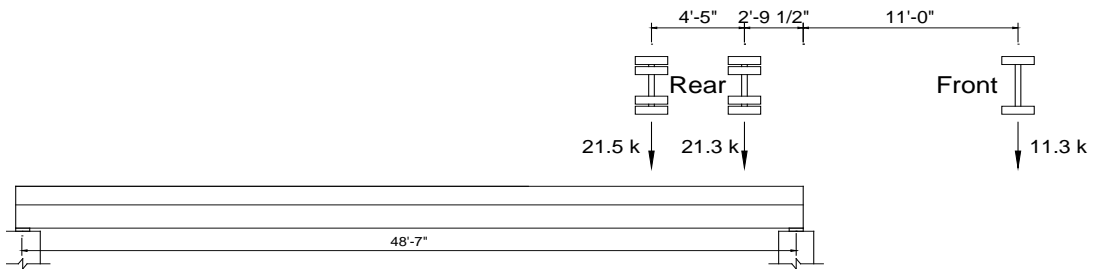
(b) Shear Critical Position

Figure 5.9. Longitudinal Positions for Static Load Tests.
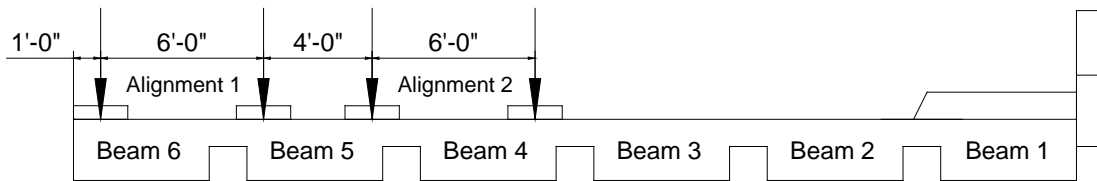
(a) Transverse Critical Alignments for Exterior Slab Beam
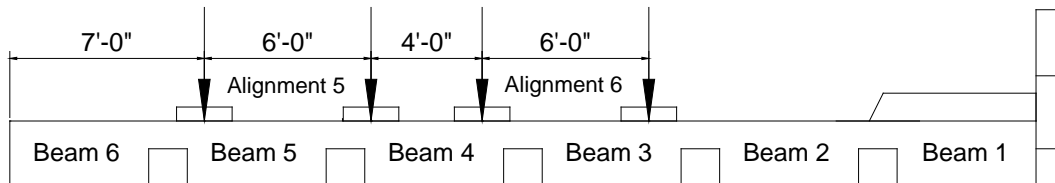
(b) Transverse Critical Alignments for Interior Slab Beam
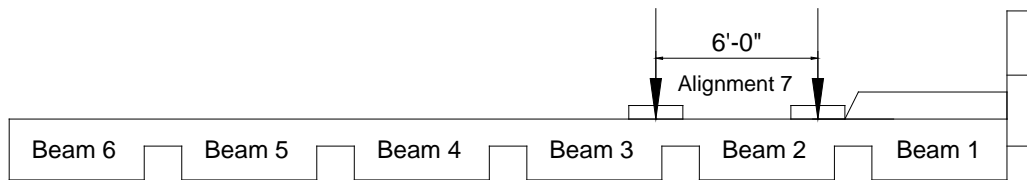
(c) Transverse Alignment for Composite Action Investigation

Figure 5.10. Transverse Alignments for Static Load Tests.

131

The details of the static load test protocol are listed in Table 5.2. All instruments are kept on the bridge to measure the bridge response under static vehicular loading. During the data acquisition and instrument signal check process, researchers found that strain gages on both the top and bottom surfaces of Beam 5 performed well with a low noise level. One more load case was added before static testing began for the purpose of determining the neutral axis location of the slab beam section. This information is essential in the moment calculation process. In this additional load case, the vehicle was driven at a very low speed along the transverse alignment at the location of Beam 5, where the closest distance between the strain gage and the last tire of the dump truck was 2 ft for the purpose of avoiding local stress effects. The vehicle location in this additional load case is shown in Figure 5.12.

Table 5.2. Static Load Test Protocol.

Test Number	Vehicle Position	Purpose
–	Initial Alignment 7	Composite Action
1	Center Alignment 7	
2	North Alignment 7	
–	Initial Alignment 6	Interior Beam Critical
3	Center Alignment 6	
4	North Alignment 6	
–	Initial Alignment 5	Interior Beam Critical
5	Center Alignment 5	
6	North Alignment 5	
–	Initial Alignment 2	Exterior Beam Critical
7	Center Alignment 2	
8	North Alignment 2	
–	Initial Alignment 1	Exterior Beam Critical
9	Center Alignment 1	
10	North Alignment 1	
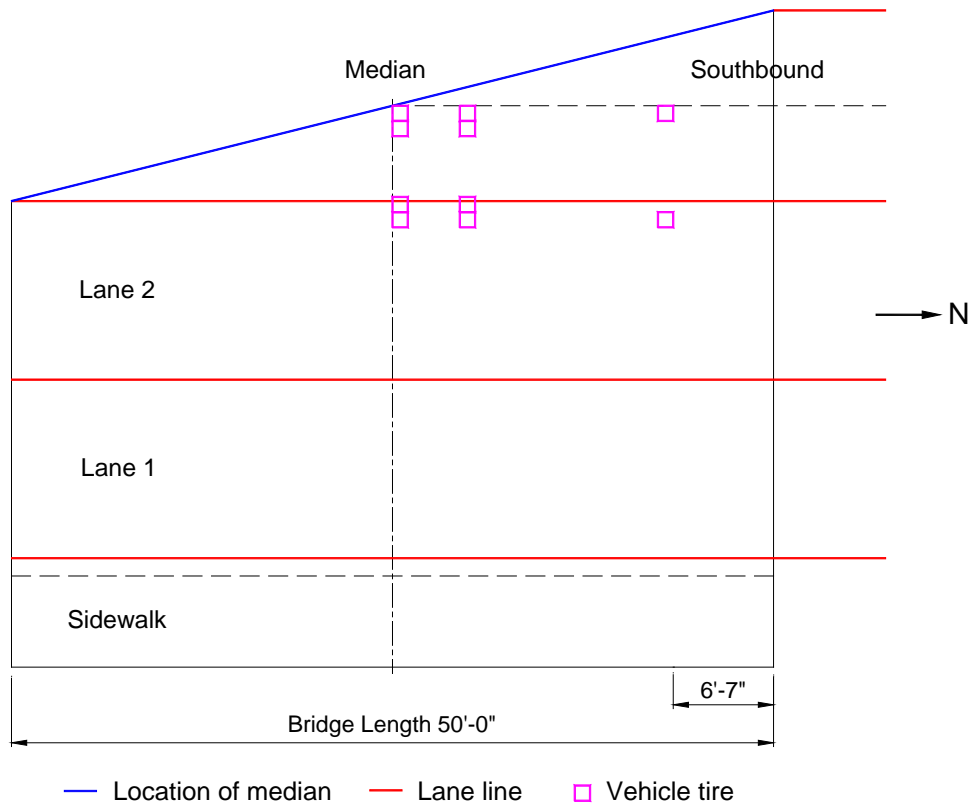
Figure 5.11. Vehicle Position for Moment Critical Case (Alignment 1).

Lane 2

Lane 1

Sidewalk

6'-7"

Bridge Length 50'-0"

— Location of median   — Lane line   □ Vehicle tire

Median   Southbound

N
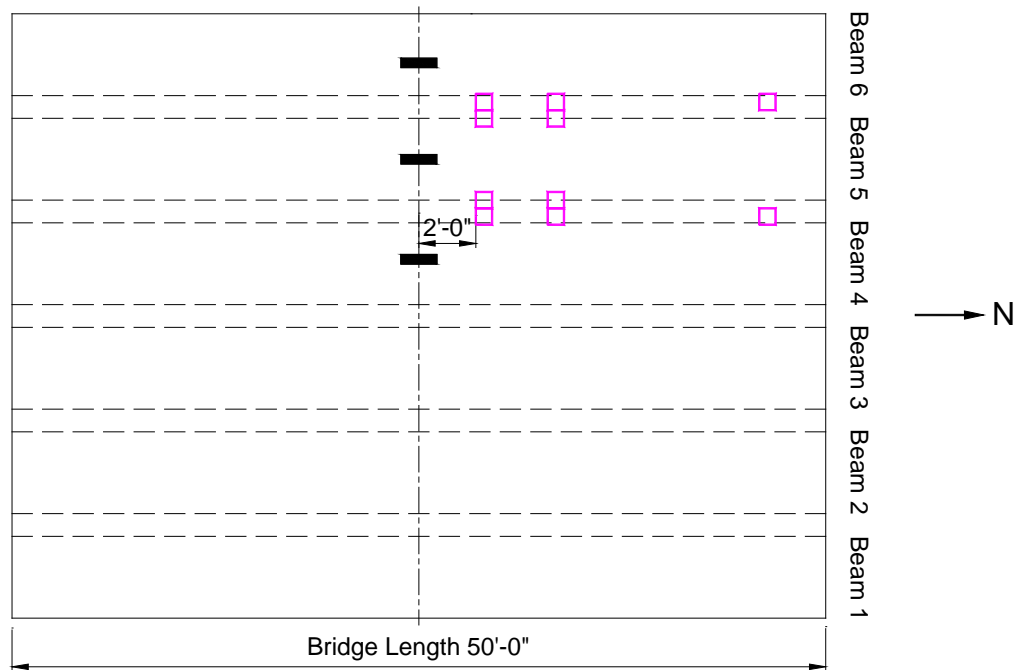
Figure 5.12. Vehicle Location for Additional Load Case.

2'-0"

Bridge Length 50'-0"

Beam 6   Beam 5   Beam 4   Beam 3   Beam 2   Beam 1

N

133

5.3.2 Controlled Dynamic Load Tests

Controlled dynamic load tests were conducted to determine the dynamic factor when the vehicle was passing over the bridge at different speeds and to obtain the bridge's dynamic properties (natural frequencies and mode shapes). The TxDOT dump truck was driven along each of the two lanes at specific speeds during the controlled dynamic load tests. Before conducting the dynamic tests, the strain gage cables on the deck surface were removed and the remaining instruments were kept on the bridge to record the structural response. With the purpose of comparing the bridge static and dynamic responses, reference static load cases with the vehicle parked at the moment and shear critical positions along the two different lanes were also conducted. All vehicle locations were marked with colored tape to guide the driver to the exact position. A radar gun was utilized to measure the vehicle speed when it passed over the bridge. The detailed controlled dynamic load test protocol is listed in Table 5.3. The moment and shear critical positions aligned with the two different lanes for the reference static load cases are shown in Figure 5.13.

Table 5.30Controlled Dynamic Load Test Protocol.

Test Number	Observed Speed (mph)	Lane
1	0	1 (Center)
2	0	1 (North End)
3	0	2 (Center)
4	0	2 (North End)
5	17	1
6	20	2
7	40	1
8	35	2

5.3.3 Ambient Traffic Load Test

The ambient traffic load test was conducted when the bridge was opened to normal traffic. Instrumentation on the underside of the bridge (accelerometers, strain gages, and LVDTs) was used to record the bridge response when various types of vehicles passed over the bridge, including a school bus, tow truck, water tanker, etc. Ambient traffic load testing was continued for approximately one hour.
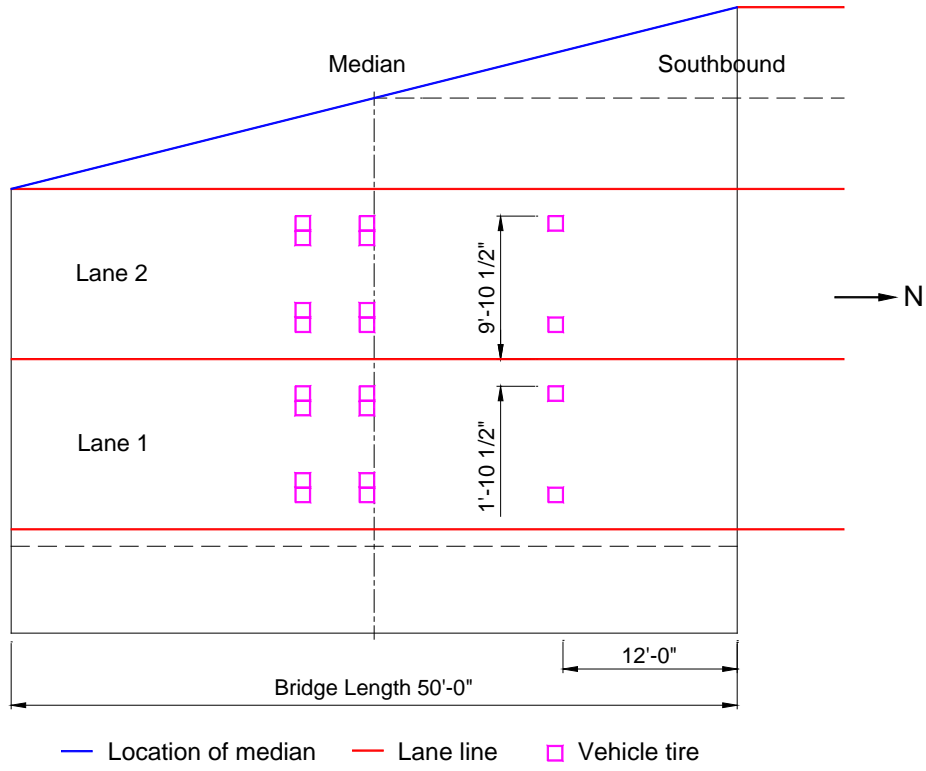
(a) Static Moment Critical Positions along Lanes 1 and 2
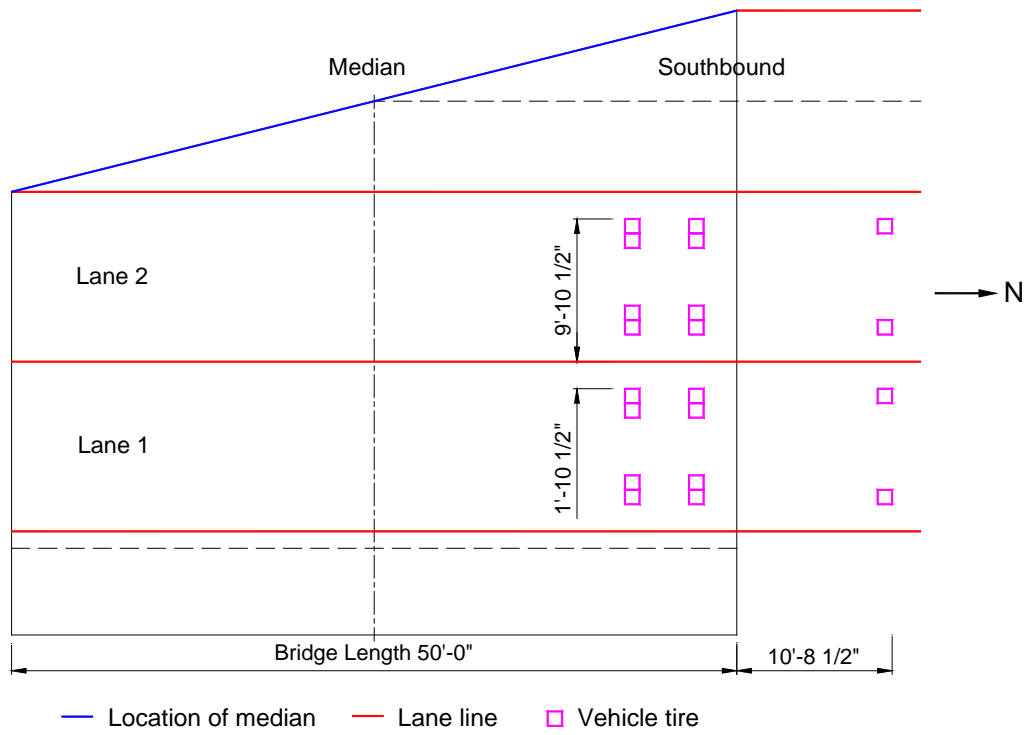
(b) Static Shear Critical Position along Lane 1 and 2

Figure 5.13. Static Moment and Shear Critical Positions along Lanes 1 and 2.

5.3.4 Test Operations

The comprehensive US 69 Bridge test program lasted three days, from May 20 (Tuesday) to May 22, 2014 (Thursday), including instrumentation installation, vehicle preparation, bridge testing, and instrumentation removal. Day Street was closed on May 20, 2014, by the TxDOT Sherman Area Office, and the research team began to install strain gages, LVDTs, and string potentiometers on the underside of the bridge.

The posted clearance height of the US 69 Bridge is 14 ft 9 in., as shown in Figure 5.1(c). Thus, two scaffolding platforms were set up to prepare a working platform at 9 ft 6 in. above the Day Street roadway for research team members to access the underside of the bridge deck and install the instrumentation. Figure 5.14 shows the instrumentation setup and epoxy application process. Figure 5.15(a) shows the instrumentation installation process beneath the bridge deck. After completing the instrumentation installation on the underside of the bridge, ambient traffic load tests were conducted to record data from normal traffic during the afternoon of May 21.

US 69 northbound over Day Street was closed on the morning of May 22, 2014 by the TxDOT Sherman Area Office. Figure 5.15(b) shows the traffic control in place. The TxDOT dump truck was loaded and weighed at the Denison weigh station the same morning. The research team began to attach the strain gages on the top surface of the bridge and mark the vehicle locations with colored tape after traffic closure. Figure 5.14(c) shows top surface preparation and strain gage installation on the guardrail. Due to the intensity of the sun during the late morning and afternoon, the strain gages on the top surface were covered with white paper tents to minimize adverse temperature effects. Figure 5.16(a) shows the transverse alignments and longitudinal positions of the truck indicated with colored tape.

After completing all preparation work, a series of static and dynamic load tests were carried out, and data from all types of sensors were recorded. Figure 5.16(b) shows a photograph of a static load test with the TxDOT 10 cyd dump truck parked along Alignment 5.

The northbound US 69 Bridge was reopened after all the load cases were finished. The research team removed all instrumentation below the bridge, and then Day Street reopened.

(a) Epoxy Application and String Potentiometer Setup Installation

(b) LVDT and String Potentiometer Setup Installation

(c) Top Surface Preparation

(d) Strain Gage on the Guardrail

Figure 5.14. Epoxy Application and Instrumentation Installation.

(a) Instrumentation Installation Underneath the Bridge

(b) Traffic Control on US 69 (Looking South from Bridge)

Figure 5.15. Instrumentation Installation and Traffic Control.

(a) Vehicle Locations Indicated with Colored Tape

(b) Static Load Test with TxDOT Dump Truck

Figure 5.16. Static Load Test of US 69 Bridge.

5.4   TEST RESULTS

A total of 10 moment and shear critical load cases were conducted with the TxDOT dump truck during the static load test to investigate the moment and shear LDFs of the exterior and interior slab beams. As for the controlled dynamic tests, the vehicle was driven along the two different lanes with various speeds. Dynamic factors and structural dynamic properties (natural frequencies and mode shapes) were determined from the controlled dynamic tests. For the ambient traffic load test, the observed structural response under normal traffic was recorded, from which the dynamic properties were then established. This section describes the analysis of data recorded from all types of sensors and explains the test results.

5.4.1   Moment Distribution Factors

5.4.1.1   Methodology

Load distribution factor, g, is defined as the ratio of a general reaction force (moment or shear) created in a bridge girder due to vehicular loading and the corresponding force created in an isolated beam element due to the same loading, which can be expressed as Equation (5.1). F_i represents the reaction force of beam i, and $F_{1D\text{-}Girder}$ represents the moment or shear force on a single beam with the same loading.

$$g_i = \frac{F_i}{F_{1D-Girder}}$$

(5.1)

For analysis of the experimental results, the load distribution factor can also be calculated by Equation (5.2) and is suitable for moment and shear distribution factors.

$$g_i = \frac{F_i}{\sum F_i}$$

(5.2)

The theoretical uniform lane load (0.64 kip/ft) should be used when determining the LDFs in accordance with AASHTO LRFD Specifications (2012) Article 4.6.2.2. However, this was not possible during physical testing; thus, only a truck load was used during the static tests.

By installing the strain gages on the top and bottom surfaces of the bridge girders, it is possible to measure the strain values and obtain the moment distribution factors under vehicular loading. The normal stress at the bottom surface caused by moment may be calculated according to Equation (5.3). By substituting the stress-strain relationship in Equation (5.4), it is possible to express the moment on each beam, M_i, in terms of strain, ε_{bi}; moment of inertia, I_i; neutral

axis location, c_{bi}; and Young's modulus, E (Equations (5.5) and (5.6)). Finally, the moment distribution factor for each slab beam can be obtained according to Equation (5.8).

$$\sigma_{bi} = \frac{M_i}{I_i} c_{bi} \tag{5.3}$$

$$\sigma_{bi} = E\varepsilon_{bi} \tag{5.4}$$

$$E\varepsilon_{bi} = \frac{M_i}{I_i} c_{bi} \tag{5.5}$$

$$\varepsilon_{bi} = \frac{M_i}{EI_i} c_{bi} \tag{5.6}$$

$$M_i = \frac{\varepsilon_{bi} I_i}{c_{bi}} E \tag{5.7}$$

$$g_{Mi} = \frac{M_i}{\sum M_i} = \frac{E \varepsilon_{bi} I_i / c_{bi}}{\sum E \varepsilon_{bi} I_i / c_{bi}} = \frac{\varepsilon_{bi} I_i / c_{bi}}{\sum \varepsilon_{bi} I_i / c_{bi}} \tag{5.8}$$

Where:

σ_{bi}	=	Concrete stress on the bottom surface of slab beam i, ksi.
M_i	=	Moment on slab beam i under vehicular loading, kip-in.
I_i	=	Moment of inertia for slab beam i, in⁴.
c_{bi}	=	Distance between neutral axis and bottom face of beam section, in.
E	=	Young's modulus of concrete, ksi.
ε_{bi}	=	Concrete strain on bottom surface of slab beam i.
g_{Mi}	=	Moment distribution factor of slab beam i.

5.4.1.2 Section Properties

An additional load case was conducted before the comprehensive static load test began in order to determine the neutral axis location of Beam 5. Figure 5.17(a) shows time-history data recorded by top and bottom strain gages when the vehicle was driven along Beam 5. Figure 5.17(a) clearly illustrates that the strain gage values changed when the vehicle moved onto and away from the bridge. By using top and bottom strain values, the neutral axis location of Beam 5 at any moment could be determined. Figure 5.17(b) shows the centroid location during the time period (23-33 seconds) when the absolute strain gage values were larger than 20 με. Researchers

observed that the neutral axis location remained constant with little fluctuation during the specific time period. The average of the measured distance between the neutral axis and the bottom face of the beam section was 11.6 in. This value was used for further analysis of the test results.
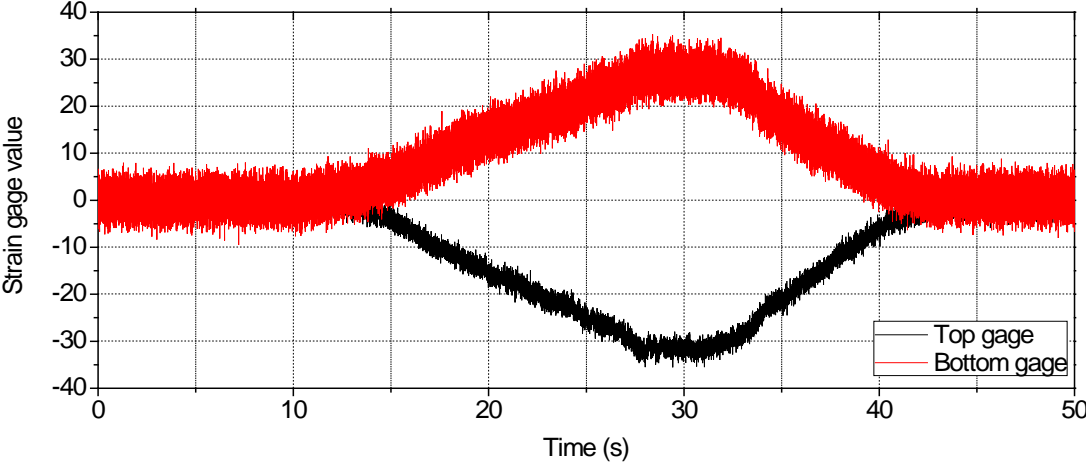
(a) Time-History Data from Top and Bottom Gages
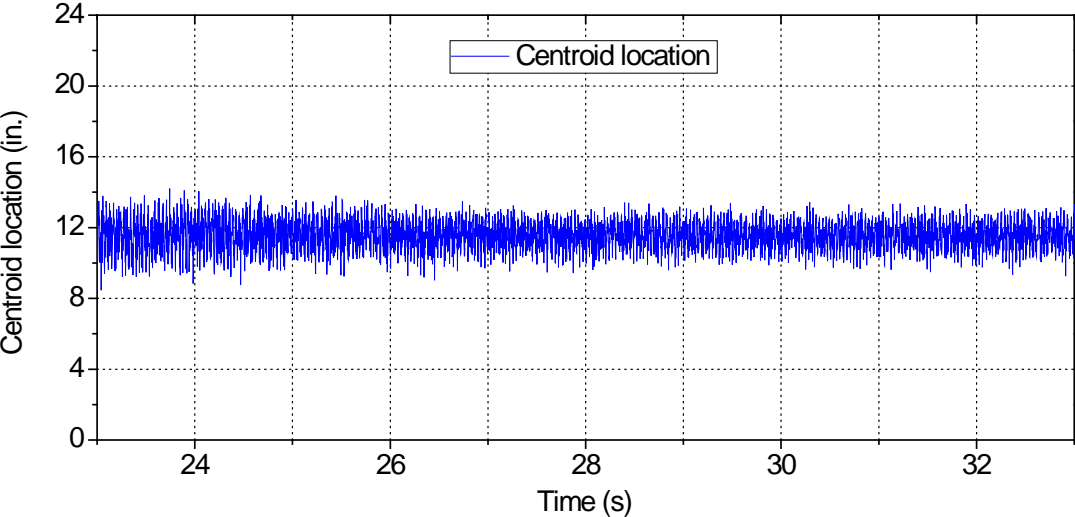
(b) Centroid Location of Beam 5 during Selected Time Period

Figure 5.17. Beam 5 Strain Gage Readings and Centroid Location Investigation.

With the neutral axis location identified, the transformed deck width could be determined by equating first moments of the tensile and compressive areas of the composite section. Then the moment of inertia of the transformed Beam 5 section could be calculated. Figure 5.18(a) shows the experimental transformed section and neutral axis location for Beam 5. The dashed lines in the figure show the location of the neutral axis. The centroid distance and moment of inertia of this section are 11.6 in. and 68,400 in^4; these two values were adopted in further calculations. Given that the clear spacing between different slab beams is only 16 in., researchers considered that beam sections without the sidewalk and guardrail have the same section properties as Beam 5.

(a) Experimental Transformed Section and Neutral Axis

Interior Beam   Exterior Beam

(b) Theoretical Transformed Section and Neutral Axis
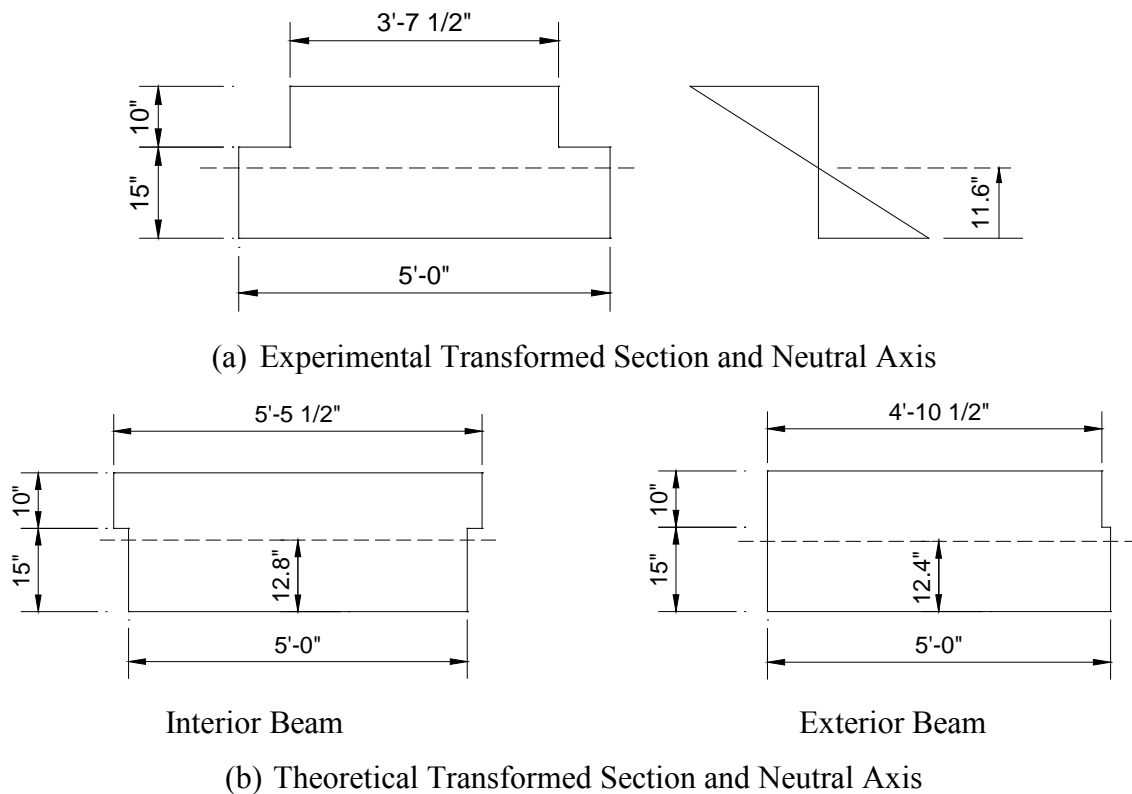
Figure 5.18. Transformed Section for Beams without the Sidewalk and Guardrail.

Given that the prestressed slab beams were fabricated at a precast plant and the deck concrete was cast in one pour, the Young's modulus was considered to be the same for all beam sections. Concrete cylinder samples were made during the slab beam casting process, and compressive tests were carried out on those samples by the precaster. The available compressive strengths of slab beams at different ages are listed in Table 5.4. The actual concrete strength of

the slab beams in service (average of 11.37 ksi) is much higher than the specified design value of 5.4 ksi.

Table 5.4. Compressive Strengths of Slab Beams.

Age	Cylinder #1 (ksi)	Cylinder #2 (ksi)	Average (ksi)
Release	6.42	6.26	6.34
24 hours	6.42	6.28	6.35
3 days	8.23	8.10	8.17
7 days	9.34	9.18	9.26
14 days	10.33	10.47	10.40
28 days	11.40	11.33	11.37

In the absence of measured data, the modulus of elasticity, E_c, for concrete with unit densities between 0.090 and 0.155 kcf and compressive strength up to 15.0 ksi may be calculated by Equation (5.9), as recommended by AASHTO LRFD Specifications (2012).

$$E_c = 33,000 K_1 w_c^{1.5} \sqrt{f_c'} \qquad (5.9)$$

Where:

E_c = Elastic modulus of elasticity of concrete, ksi.

K_1 = Correction factor for source of aggregate, typically taken as 1.0.

w_c = Unit density of concrete, kcf.

f_c' = Compressive strength of concrete, ksi.

As for the deck concrete, no cylinder data were available. Therefore, the modulus of elasticity value of deck concrete was inferred from that of the slab beam concrete based on Equation (5.10) and the specified design strengths.

$$n = \frac{E_{deck}}{E_{beam}} = \sqrt{\frac{f_{c,deck}'}{f_{c,beam}'}} = \sqrt{\frac{4}{5.4}} = 0.86 \qquad (5.10)$$

Where:

E_{deck} = Modulus of elasticity of deck concrete, ksi.

E_{beam} = Modulus of elasticity of slab beam concrete, ksi.

$f_{c,deck}'$ = Specified design strength of deck concrete, ksi.

$f_{c,beam}'$ = Specified design strength of slab beam concrete, ksi.

The calculated modulus of elasticity at 28 days is 6140 ksi. As time proceeds, both the concrete strength and modulus increase; the long-term concrete strength is typically 20 percent stronger than the 28-day strength. Therefore, for calculation purposes, the modulus of elasticity was assumed to be 20 percent higher than the calculated 28-day value. Thus, E_c was taken as 7368 ksi.

The theoretical transformed section may be obtained by scaling the effective flange width by the modulus ratio n, which was used to determine the theoretical transformed section properties, such as neutral axis location and moment of inertia. The slab beam's elastic modulus was then used to describe the entire transformed section. Figure 5.18(b) shows the theoretical transformed section for an interior beam and exterior beam. The dashed line in the figures denotes the neutral axis location. Equation (5.8) shows that the ratio I_i/c_{bi} plays a very important role in the load distribution factor calculation because E is considered to be the same across the bridge section. A summary of experimental and theoretical section properties for beams without the sidewalk and guardrail is given in Table 5.5.

Table 5.5. Experimental and Theoretical Section Properties.

Item	Experimental	Theoretical		Ratio (Exp./Theory)	
		Interior	Exterior	Interior	Exterior
Neutral Axis, c_b (in.)	11.6	12.8	12.4	0.90	0.93
Moment of Inertia, I_i (in^4)	68,400	81,400	77,100	0.84	0.89
Critical Parameter, I_i/c_{ib}	5900	6400	6200	0.93	0.95

Table 5.5 illustrates that the experimental neutral axis location was close to the theoretical value, indicating that the test results are reasonable. Also, the ratios for I_i/c_{bi} obtained from experimental and theoretical derivations are similar to each other. The experimental section properties were used for further calculations when interpreting the experimental measurements.

A summary of experimental and theoretical section properties for Beam 1 at the east edge is given in Table 5.6. As for the Beam 1 section, which includes the sidewalk and guardrail along the east edge, another specific load case was conducted with the dump truck driven at a very slow speed along Alignment 7 (see Figure 5.10). This load case was used to investigate the composite action between the deck, sidewalk, and guardrail. Similarly, the experimental section

145

properties including neutral axis location and moment of inertia were determined from the strain gage readings in this load case. Figure 5.19(a) shows the time-history data recorded by top and bottom strain gages when the vehicle was driven along Alignment 7. Top Gage 1 represents the strain gage attached on the surface of the sidewalk. Top Gages 2 and 3 are the strain gages installed on the guardrail. Figure 5.19(a) illustrates that the strain gage values changed when the vehicle moved on and off the bridge. By using top and bottom strain values, the neutral axis location of the composite sections at any moment could be determined. Figure 5.19(b) shows the centroid location during the time period (20–25 seconds) when the absolute strain gage values are larger than 10με. Centroid locations 1–3 were determined using top strain gages 1–3 and the bottom strain gage. The neutral axis locations remained unchanged with low fluctuation during the specific time period.

The measured strain profile for the Beam 1 section with the sidewalk and guardrail is shown in Figure 5.20, where the strain gage values do not appear to exhibit plane section behavior. According to the design drawings for the bridge, some reinforcing bars are provided at the surface between the sidewalk and guardrail to provide interface shear resistance. Researchers inferred that the deck, sidewalk, and guardrail are fully composite with each other, and composite action was considered in further calculations and finite element modeling. The transformed section properties were determined in a similar way for the Beam 5 section. The centroid distance and moment of inertia of this section are 19.0 in. and 405,600 in^4, and these two values were used in further calculations.

Table 5.6. Experimental and Theoretical Section Properties for Beam 1.

Item	Experimental	Theoretical	Ratio (Exp./Theory)
Neutral Axis, c_b (in.)	19.7	19.0	1.04
Moment of Inertia, I_i (in^4)	431,100	405,600	1.06
Critical Parameter, I_i/c_{ib}	21,900	21,300	1.03
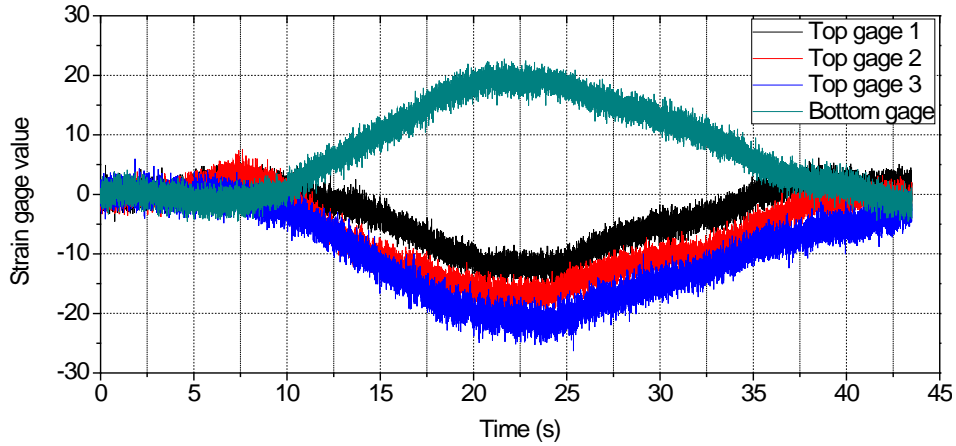
(a) Time-History Data from Strain Gages
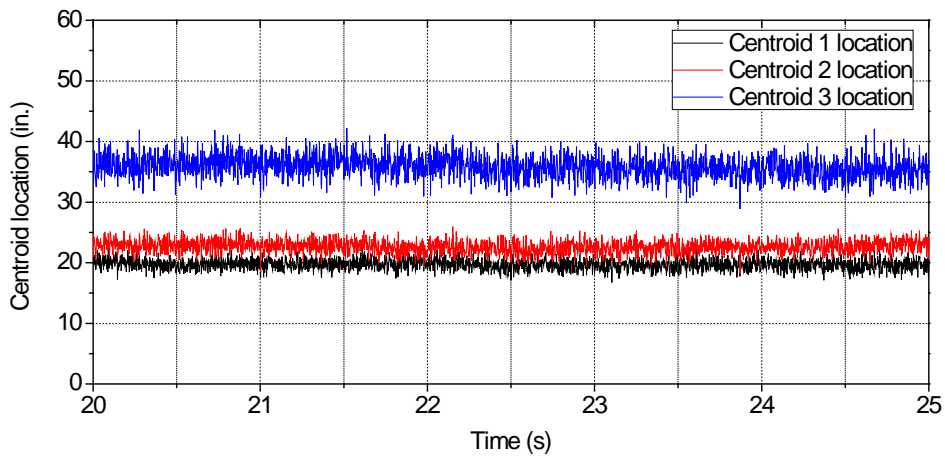
(b) Centroid Locations during Specific Time Period

Figure 5.19. Beam 1 Strain Gage Readings and Centroid Location Investigation.
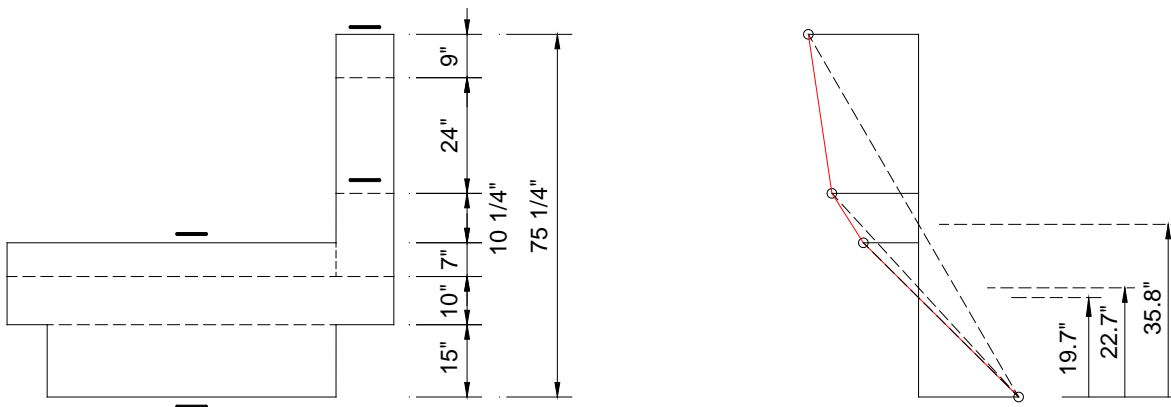
Figure 5.20. Measured Neutral Axis of Beam 1 Section with Sidewalk and Guardrail.

147

5.4.1.3 *Observed Distribution of Beam Moments*

During the testing process, the strain gages on the bottom surface were not directly exposed to sunlight and were in a more ideal environment as compared to the top gages. In addition, strain gages were provided on the bottom surface of all six beams. Thus, only the strain values from the bottom gages were utilized to calculate moment values and moment distribution factors based on Equations (5.7) and (5.8). Table 5.7 and Table 5.8 list the moment values and moment distribution factors calculated based on bottom strain gage measurements. Figure 5.21 and Figure 5.22 show the moment values and moment distribution factor curves across the bridge section for different load cases. As the figure shows, the observed distribution of moments among the beams changed when the truck was positioned at different locations on the bridge. The existence of the sidewalk and guardrail stiffened Beam 1, which attracted a greater load share to that beam section, leading to a higher observed moment.

Table 5.7. Moment Values Based on Strain Gage Data (kip-ft).

Load Case	East Edge					West Edge
	Beam 1	Beam 2	Beam 3	Beam 4	Beam 5	Beam 6
Alignment 1	71	28	39	64	101	121
Alignment 2	61	33	54	78	75	60
Alignment 5	105	31	57	89	112	108
Alignment 6	164	59	83	80	66	54
Alignment 7	276	82	77	55	41	34

Table 5.8. Moment Distribution Factors Based on Strain Gage Data.

Load Case	East Edge					West Edge
	Beam 1	Beam 2	Beam 3	Beam 4	Beam 5	Beam 6
Alignment 1	0.167	0.066	0.093	0.151	0.239	0.284
Alignment 2	0.169	0.090	0.150	0.217	0.209	0.165
Alignment 5	0.209	0.062	0.114	0.178	0.223	0.215
Alignment 6	0.325	0.117	0.164	0.158	0.131	0.106
Alignment 7	0.488	0.145	0.136	0.098	0.072	0.061
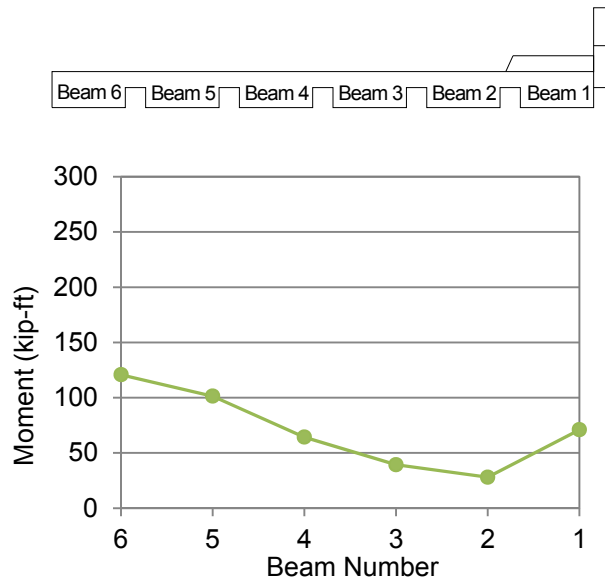
(a) Alignment 1
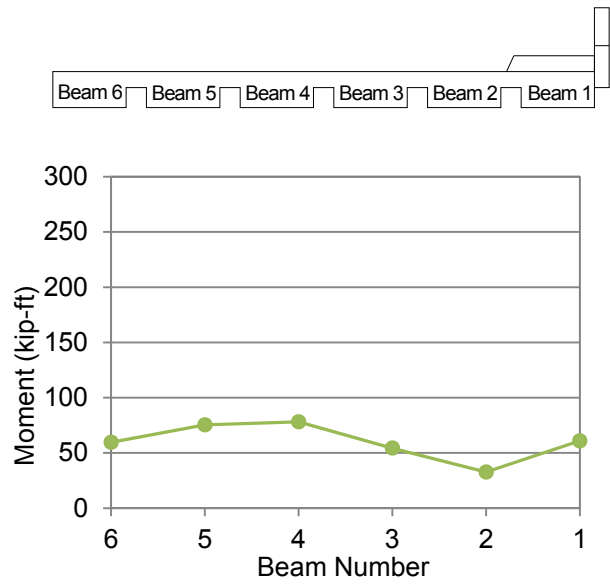
(b) Alignment 2
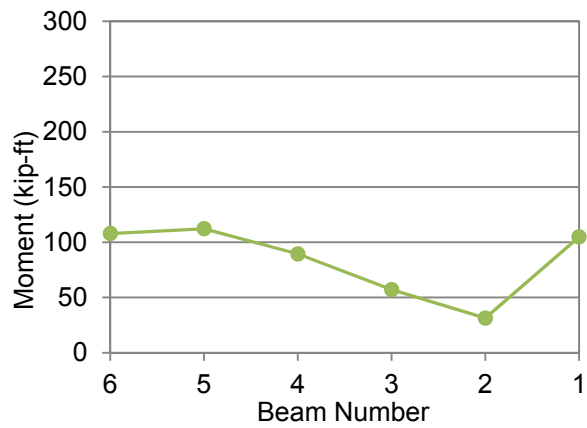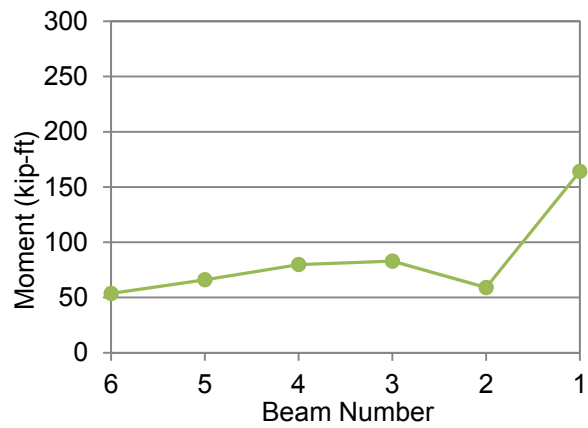
(c) Alignment 5
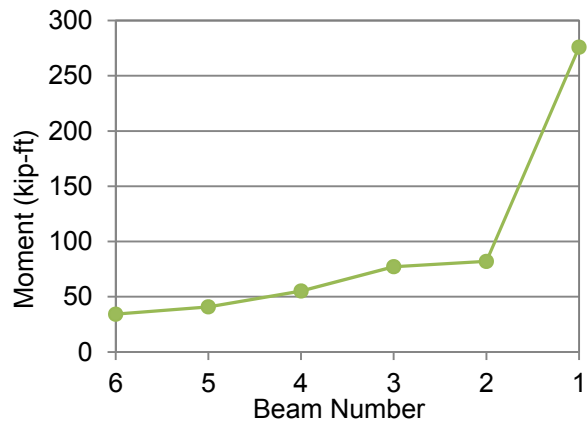
(d) Alignment 6

(e) Alignment 7

Figure 5.21. Measured Midspan Moments for US 69 Bridge.
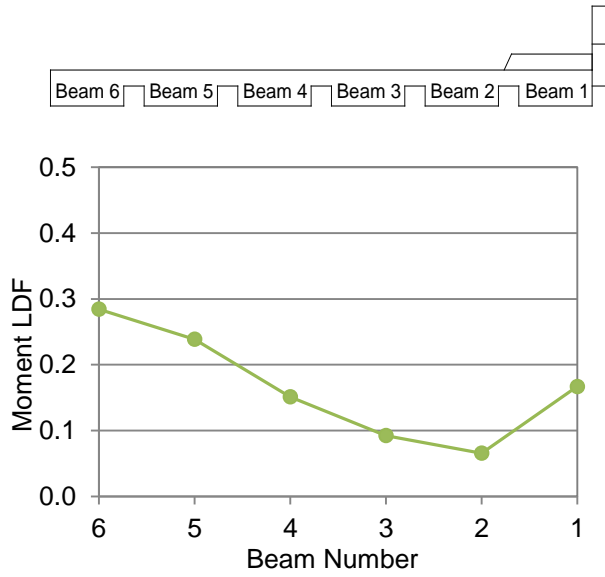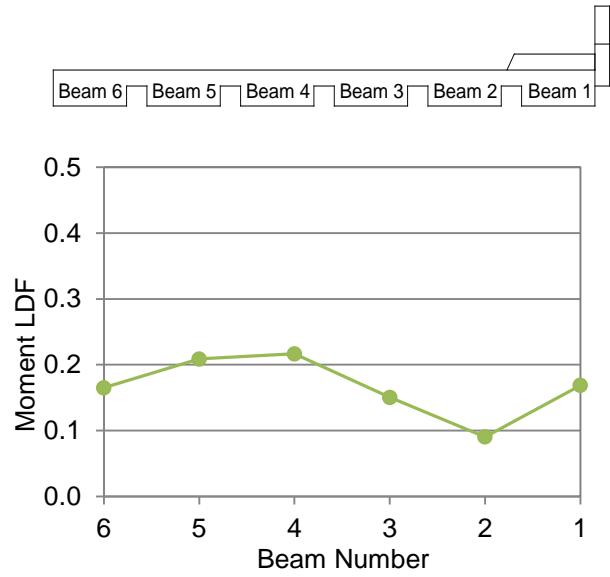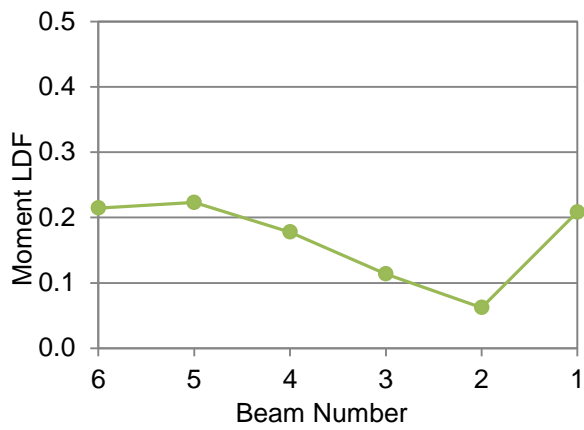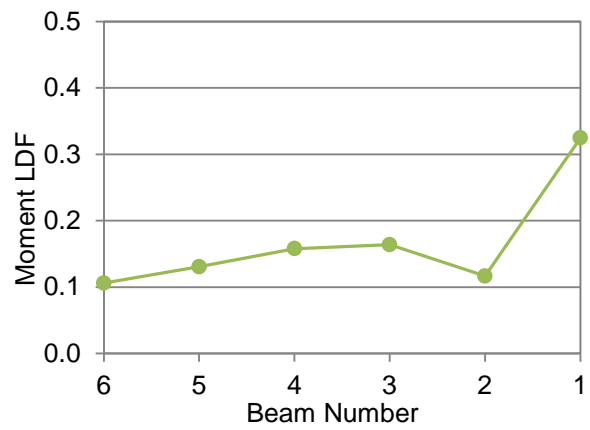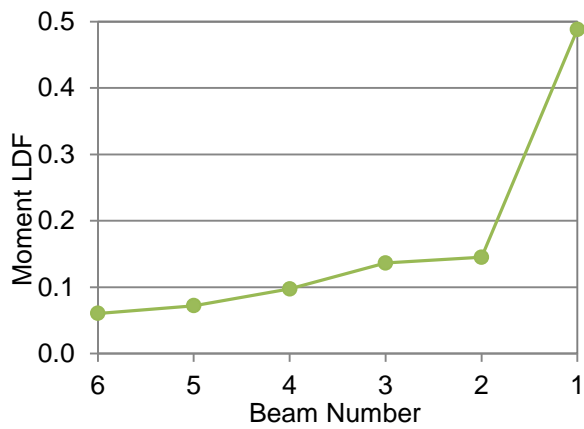
Figure 5.22. Experimental Moment LDFs for US 69 Bridge.

150

5.4.2 Experimental Shear Distribution Factors

By installing six LVDTs close to the bearing pads at the north end of each slab beam of the US 69 northbound bridge, researchers were able to obtain shear LDFs by measuring and comparing the bearing pad deformation under vehicular loading because the bearing pad stayed in the linear elastic range of behavior during testing, as indicated by the laboratory tests discussed in Section 5.2.2. Equations (5.11) and (5.12) are used to determine shear LDFs based on LVDT data.

$$V_i = R_i = K\delta_i \tag{5.11}$$

$$g_{Vi} = \frac{V_i}{\sum V_i} = \frac{K\delta_i}{\sum K\delta_i} = \frac{\delta_i}{\sum \delta_i} \tag{5.12}$$

Where:

V_i = Shear force of slab beam i, kips.

R_i = Reaction force at bearing pad location of slab beam i under vehicular loading, kips.

δ_i = Bearing pad deformation for slab beam i, in.

K = Stiffness of bearing pad, kip/in.

g_{Vi} = Shear load distribution factor of slab beam i.

Shear LDFs for each slab beam corresponding to different load cases are calculated based on bearing pad deformations according to Equation (5.12). The stiffness, K, is calculated by dividing the total shear force, the same as the equivalent single beam shear force, by the total deformation for the different shear critical load cases.

Tables 5.9 and 5.10 list the experimental shear force values and corresponding LDFs for each load case. Figures 5.23 and 5.24 show the experimental shear LDF curves across the bridge section for the different load cases. The measured shear distribution behavior changed when different load cases were applied to the bridge.

Table 5.9. Shear Force Values Based on Bearing Pad Deformation (kips).

| Load Case | East Edge | | | | | West Edge |
	Beam 1	Beam 2	Beam 3	Beam 4	Beam 5	Beam 6
Alignment 1	-0.28	0.02	0.23	3.50	12.08	24.22
Alignment 2	0.01	2.87	7.60	13.55	10.50	3.52
Alignment 5	-0.50	0.99	3.45	11.05	13.99	9.24
Alignment 6	2.08	7.76	13.19	10.90	5.05	1.26
Alignment 7	6.86	12.81	10.67	4.18	1.26	-0.01

Table 5.10. Experimental Shear LDFs Based on Bearing Pad Deformation.

| Load Case | East Edge | | | | | West Edge |
	Beam 1	Beam 2	Beam 3	Beam 4	Beam 5	Beam 6
Alignment 1	-0.007	0.001	0.006	0.088	0.304	0.609
Alignment 2	0.000	0.075	0.200	0.356	0.276	0.093
Alignment 5	-0.013	0.026	0.090	0.289	0.366	0.242
Alignment 6	0.052	0.193	0.328	0.271	0.125	0.031
Alignment 7	0.192	0.358	0.298	0.117	0.035	0.000
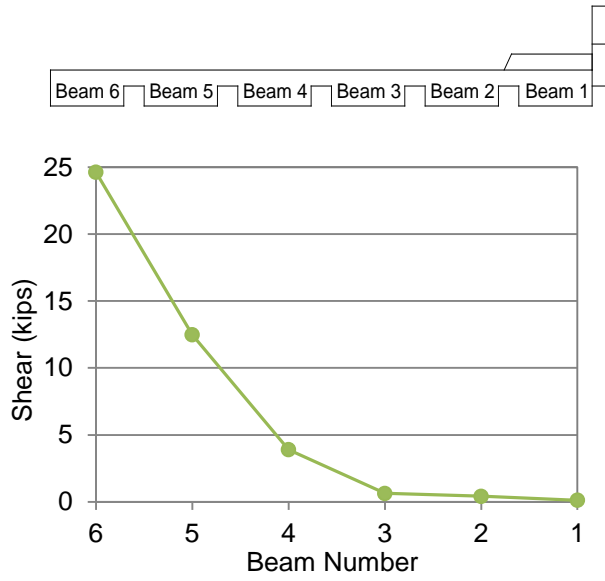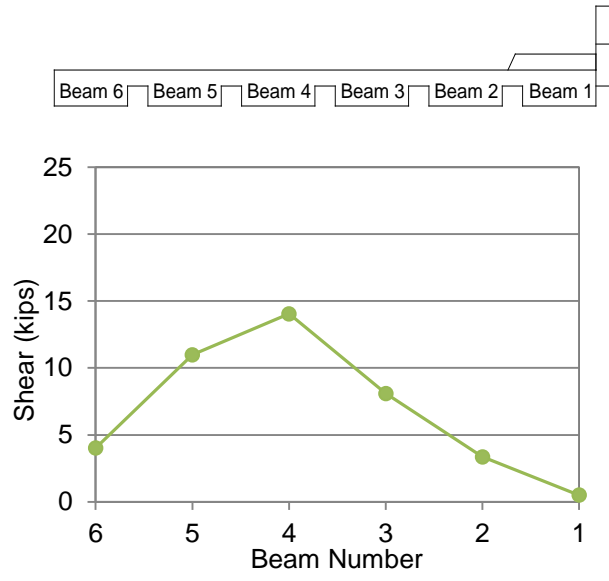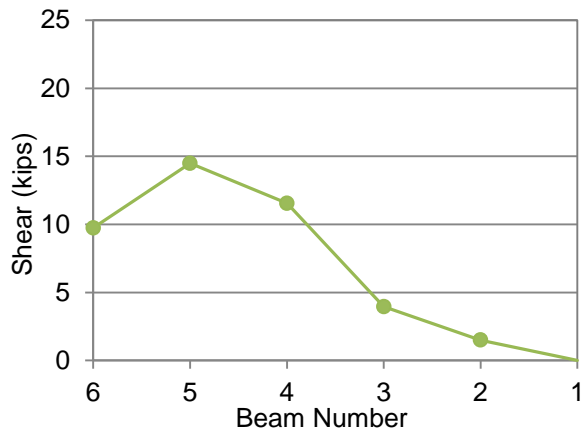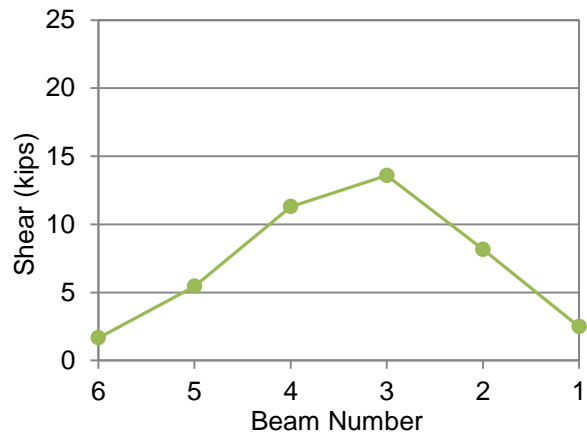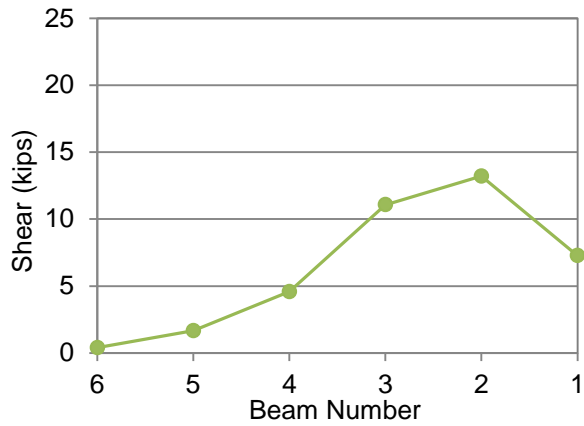
Figure 5.23. Measured Shear Values for US 69 Bridge.

153
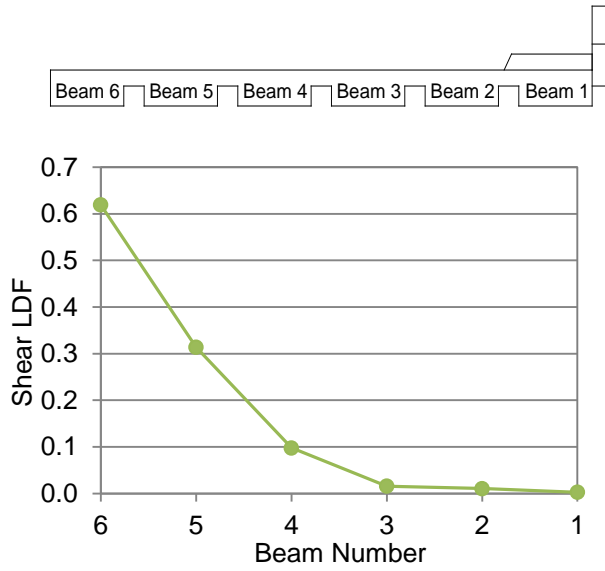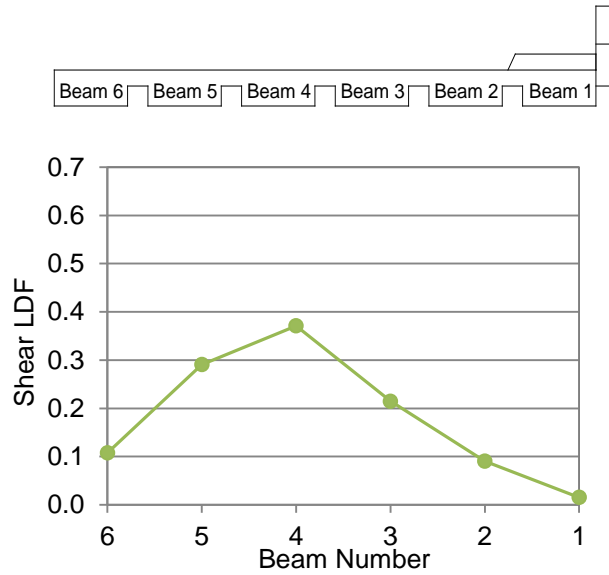
(a) Alignment 1
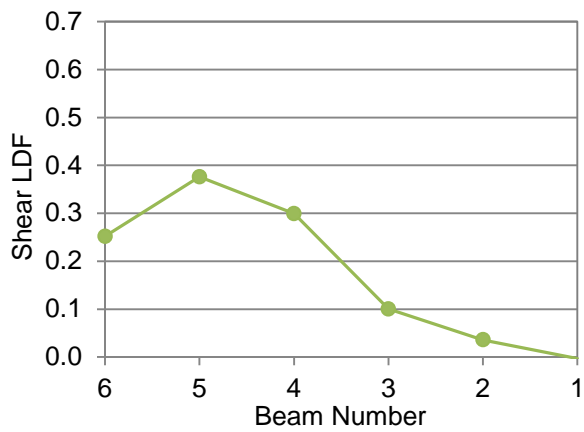
(b) Alignment 2
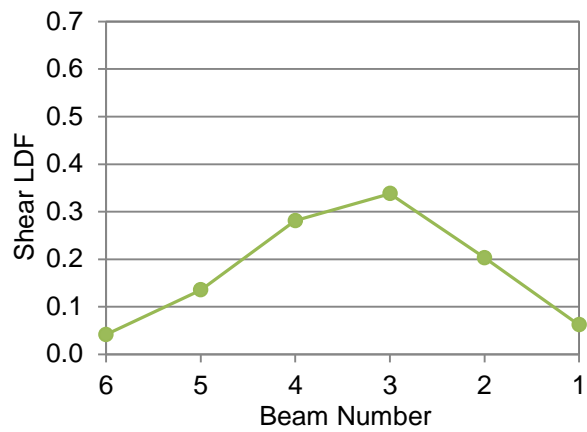
(c) Alignment 5
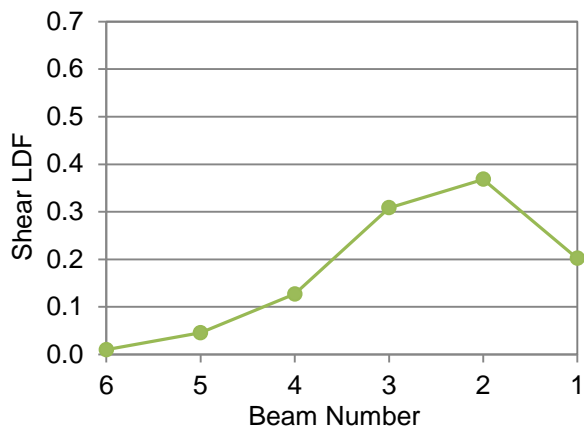
(d) Alignment 6

(e) Alignment 7

Figure 5.24. Experimental Shear LDFs for US 69 Bridge.

154

5.4.3 Deflection Values

By installing 36 string potentiometers at six stations distributed between the north support and midspan, researchers were able to obtain the bridge deflection field along the half span under static vehicular loading. Figure 5.25 shows the deflection curves for all moment critical load cases. The slab beam nearest the vehicle experienced larger deflections, as expected.

5.4.4 Dynamic Factors

In the controlled dynamic load tests, the structural response was recorded by all types of sensors when the vehicle passed over the bridge for the considered load cases, including two different lanes at various speeds. Also, the relevant static moment and shear critical load cases were conducted during the test process. By comparing the structural response including strain values, bearing pad deformations, and bridge deflections for both the static and dynamic load cases, it was possible to evaluate the dynamic effects.

Figure 5.26(a) shows a comparison of bearing pad deformations under static and dynamic loads. Compression values were considered to be positive. The figure shows that bearing pad deformation values under dynamic loads are larger than the values under static loads. Also, with an increase in vehicle speed, the dynamic bearing pad deformation values became larger. A comparison of experimental shear load distribution factors under static and dynamic loads is shown in Figure 5.26(b). The shear distribution curves did not change significantly when the vehicle was passing over the bridge.

Figure 5.27(a) shows a comparison of strain values on the bottom surface at midspan under static and dynamic loads, and illustrates that strain values under dynamic loads are larger than the values under static loads in most cases. Also, with the increase of vehicle speed, strain values became larger. A comparison of experimental moment LDFs under static and dynamic loads is shown in Figure 5.27(b). The moment distribution curves did not change significantly when the vehicle was passing over the bridge. Figure 5.27(c) shows the comparison of beam deflections at midspan locations under static and dynamic loads. It is illustrated in the figure that (a) the profile of the deflection curve remained unchanged when the vehicle passed over the bridge; (b) the deflection values under dynamic loads are larger than the deflection values under static loads; (c) at the location of maximum deflection, the dynamic factors reached approximately 1.3; and (d) the deflection values under moving vehicle loads became larger when the vehicle speed increased.
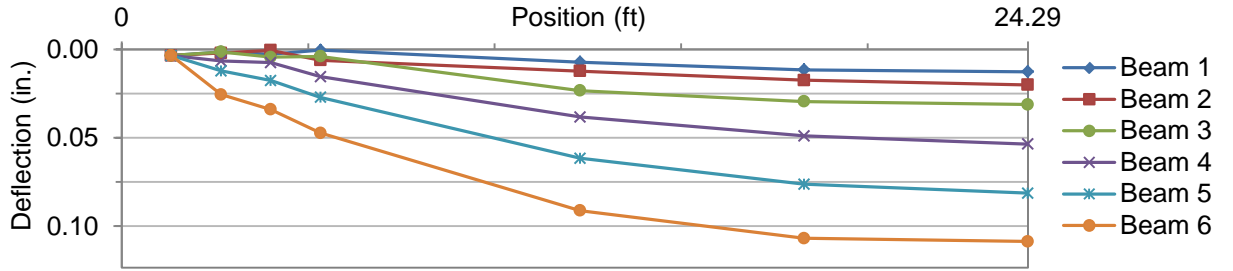
(a) Alignment 1
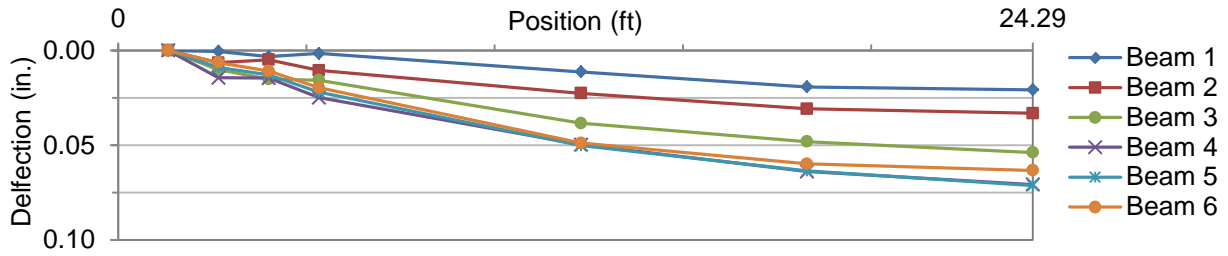
(b) Alignment 2
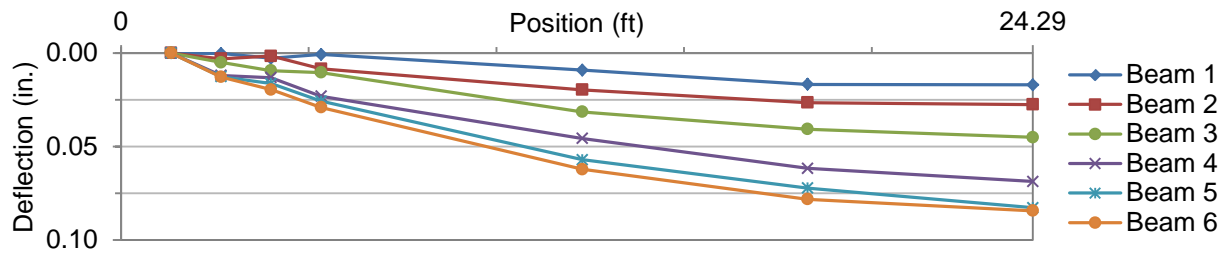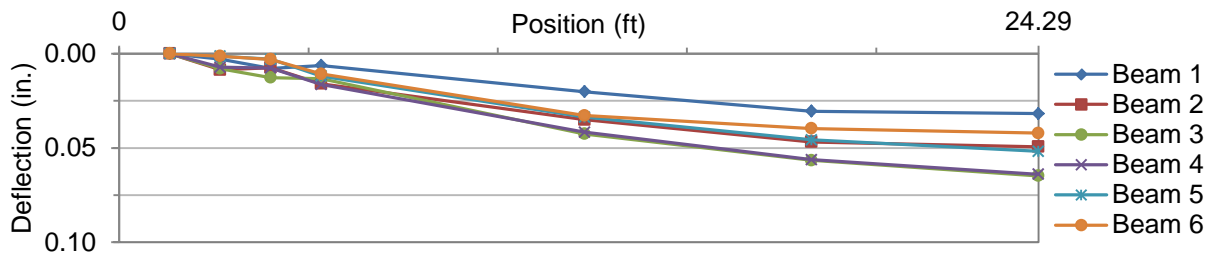
(c) Alignment 5
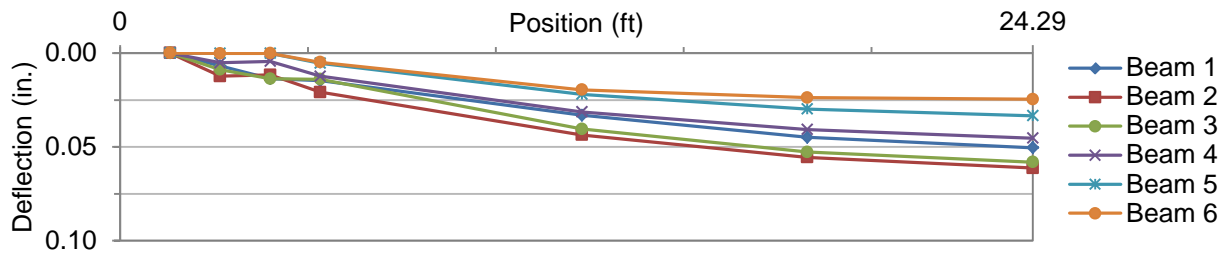
(d) Alignment 6

(e) Alignment 7

Figure 5.25. Deflection Curves for All Moment Critical Load Cases.
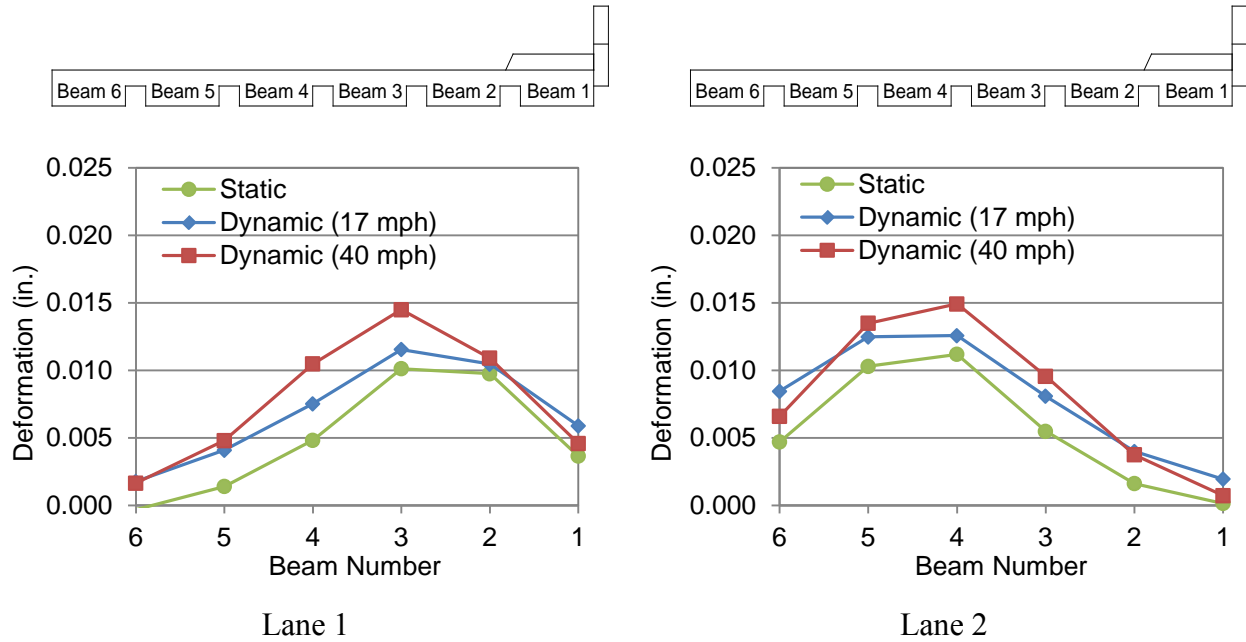
(a) Bearing Pad Deformations
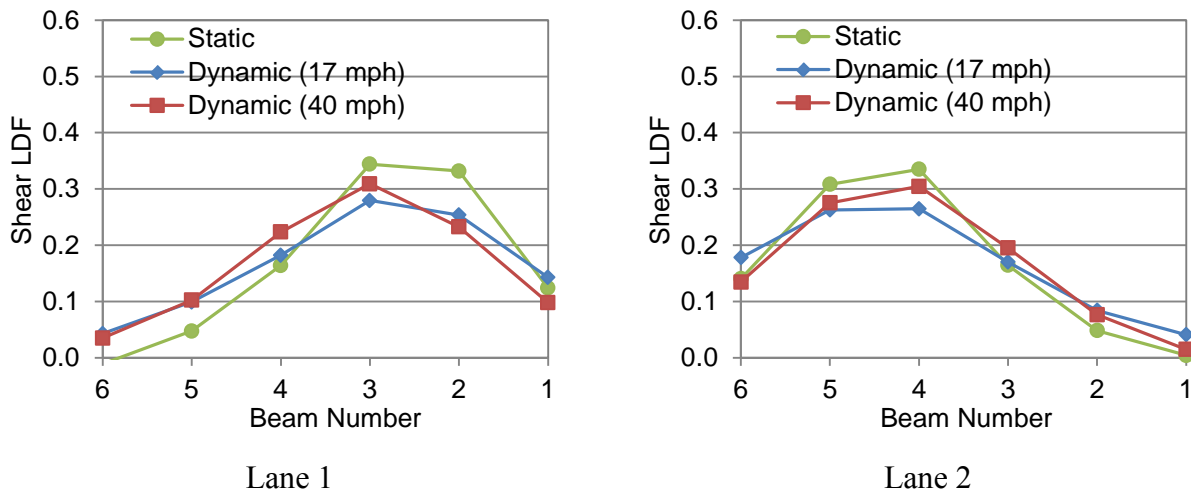
(b) Experimental Shear LDFs

Figure 5.26. Bearing Pad Deformations and Experimental Shear LDFs under Static and Dynamic Loading.
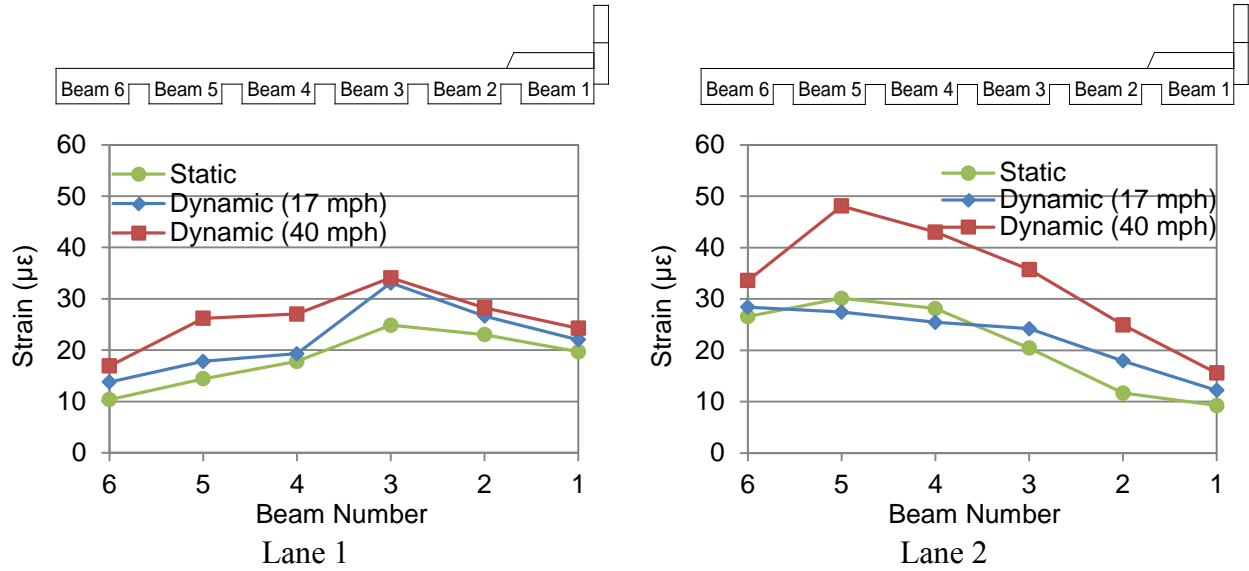
(a) Strain Gage Values
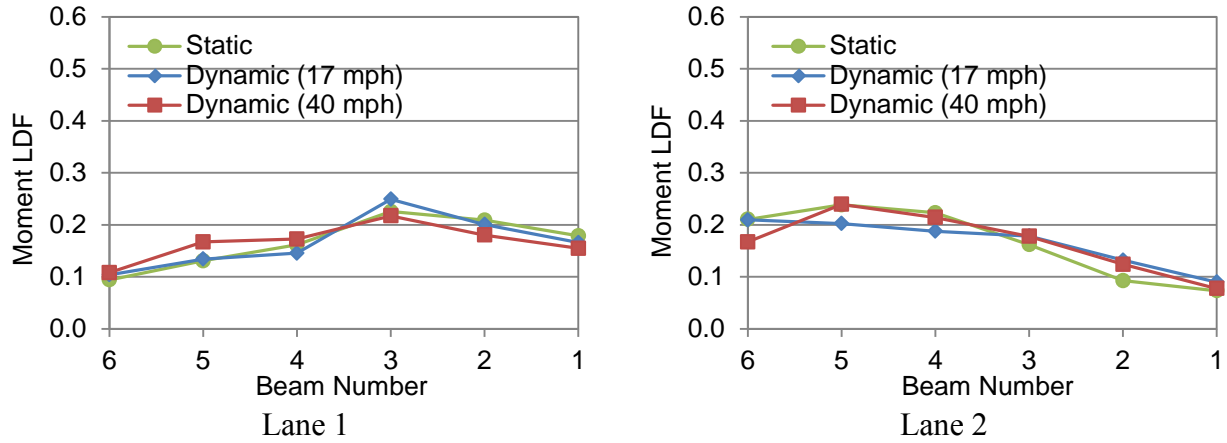
(b) Experimental Moment LDFs
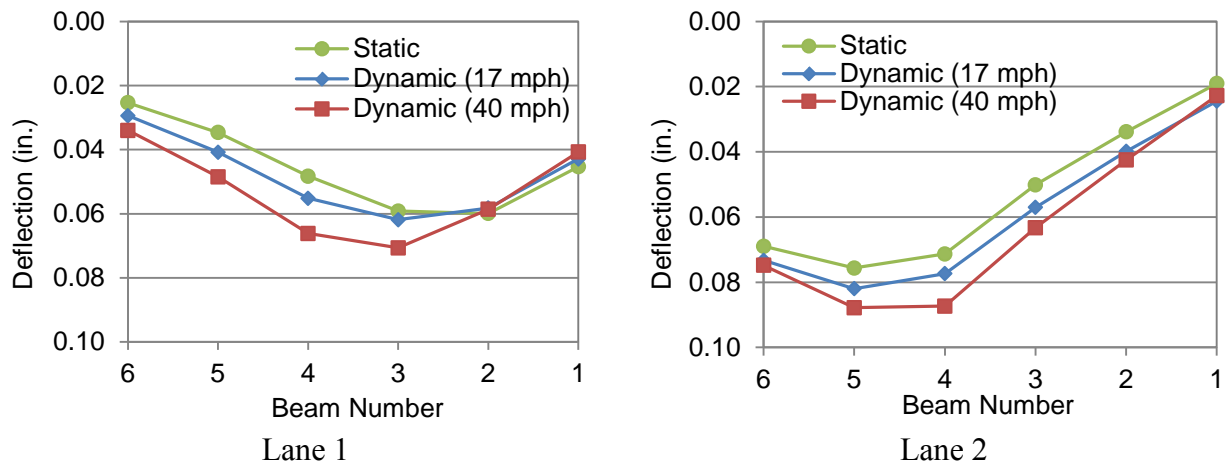
(c) Deflections at Midspan

Figure 5.27. Strain and Experimental Moment LDFs under Static and Dynamic Loading.

158

5.4.5 Dynamic Properties

A total of eight accelerometers were attached on the bottom face of the bridge to record acceleration data during the controlled dynamic load tests and ambient traffic load tests. Six accelerometers were located at the midspan of each slab beam, and the other two were attached within the half span of Beam 4. By processing acceleration data in the frequency domain, the first three natural frequencies and corresponding mode shapes of the US 69 Bridge could be identified. Symmetry was utilized to determine the mode shape in the longitudinal direction because the accelerometers were only arranged in the north half span of the bridge. The first three natural frequency values (f_1, f_2, and f_3) determined from the dynamic load tests are listed in Table 5.11.

Table 5.11 shows that the natural frequency values are very close to each other when the vehicle was passing through different lanes at various speeds. The first three mode shapes in the longitudinal and transverse directions are shown in Figure 5.28.

Table 5.11. First Three Natural Frequencies in Controlled Dynamic Load Test.

Lane	Speed (mph)	f_1 (Hz)	f_2 (Hz)	f_3 (Hz)
1	17	6.35	9.28	14.7
2	25	5.86	9.28	15.1
3	40	6.10	9.28	14.8
4	35	6.10	9.16	14.9
Average	–	6.10	9.25	14.9
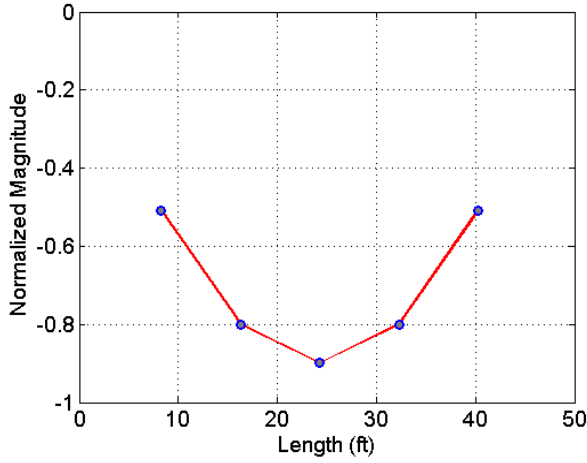
(a) 1st Mode Shape (Longitudinal)
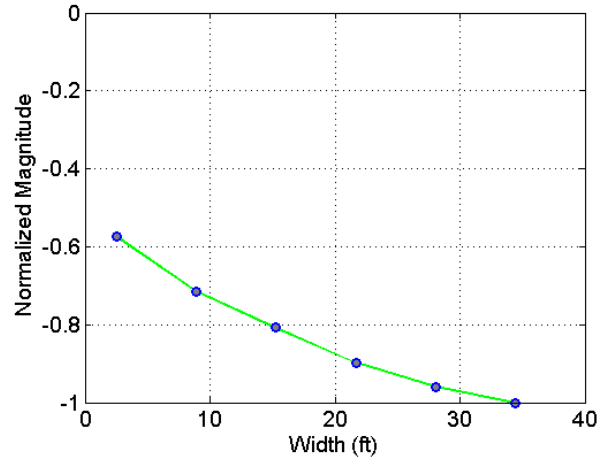
(b) 1st Mode Shape (Transverse)
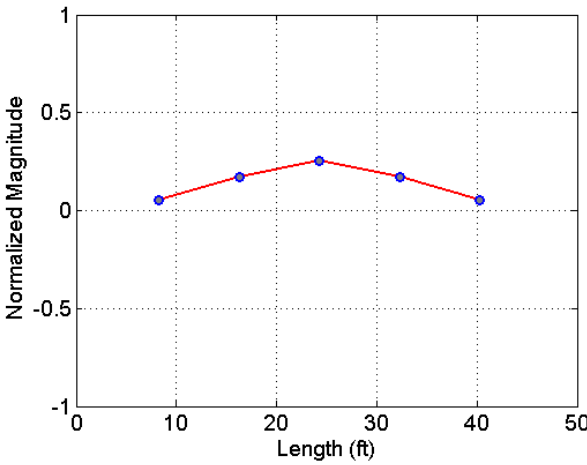
(c) 2nd Mode Shape (Longitudinal)
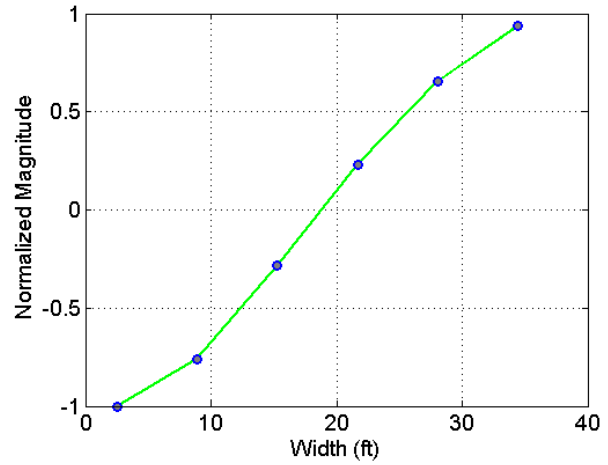
(d) 2nd Mode Shape (Transverse)
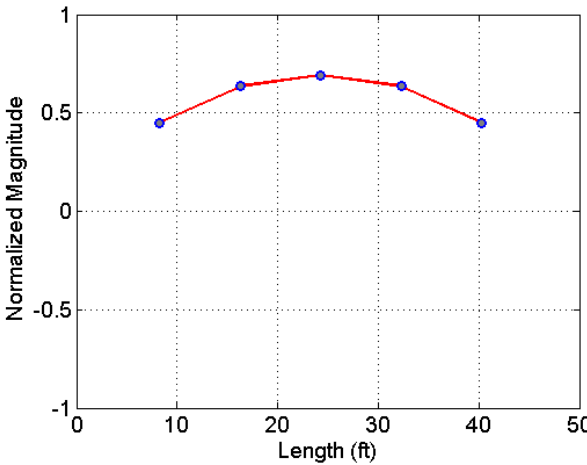
(e) 3rd Mode Shape (Longitudinal)
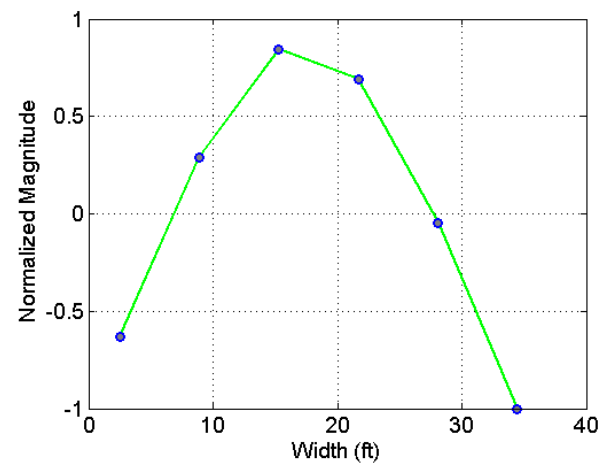
(f) 3rd Mode Shape (Transverse)

Figure 5.28. First Three Mode Shapes in Longitudinal and Transverse Direction.

5.4.6 Ambient Test Results

The first three natural frequency values obtained from ambient traffic load testing are listed in Table 5.12. When the bridge was open to normal traffic, instrumentation below the bridge, including strain gages, LVDTs, and accelerometers, was used to record the structural response. Figure 5.29(a) shows the bearing pad deformations and bottom strain values when various types of vehicles passed over the bridge. Compression values of the bearing pad were considered to be positive.

Figure 5.29(b) shows that the bridge response including bearing pad deformations and bottom strain gage values changed with different vehicle types and weights. In addition, when different vehicles passed through the same lane, the structural response curves across the bridge section are similar. Table 5.12 indicates that the natural frequency values are very close to each other when different types of vehicles passed over the bridge. Also, through analysis of the accelerometer data, researchers found that the mode shapes are similar to those obtained in the controlled dynamic load test (they are not repeated here).

Table 5.12. First Three Natural Frequencies from Ambient Traffic Load Test.

Vehicle	Lane	f_1 (Hz)	f_2 (Hz)	f_3 (Hz)
School Bus	1	6.04	9.46	14.9
Fire Truck	1	6.26	9.25	14.9
Water Tanker	2	6.01	9.31	14.9
Tow Truck	1	6.04	9.12	14.7
18 Wheeler	1	6.13	9.12	14.5
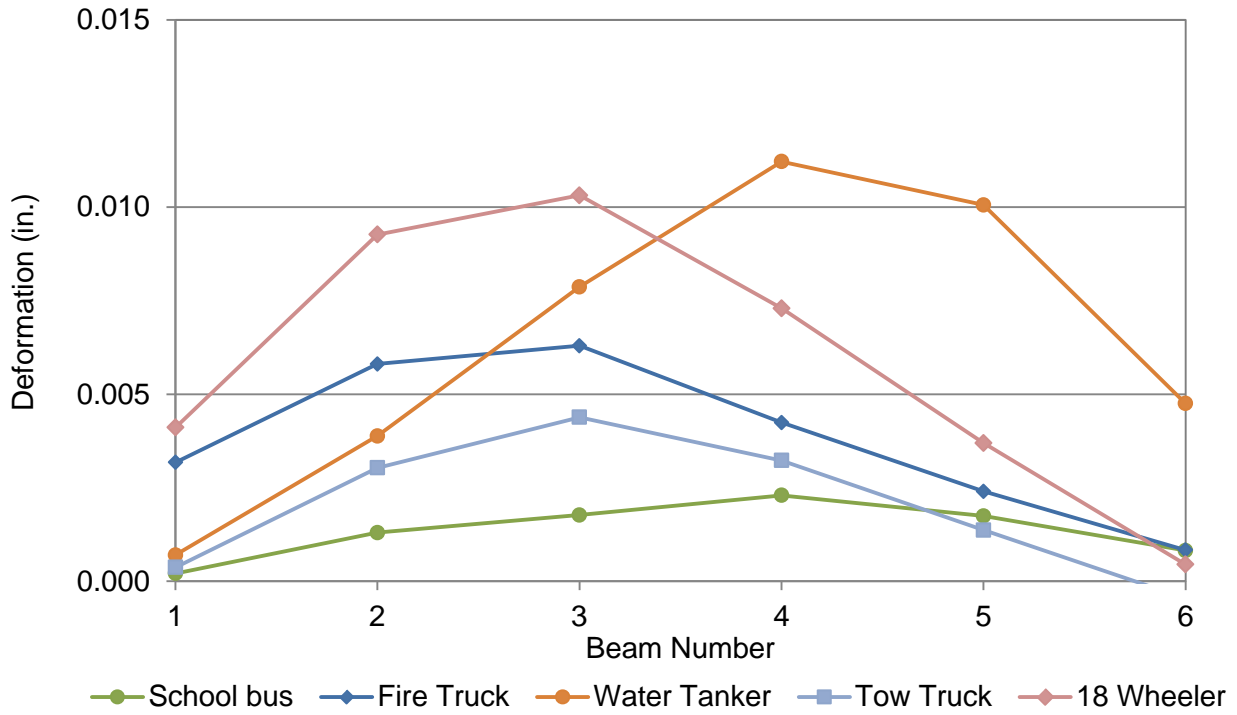
(a) Bearing Pad Deformations
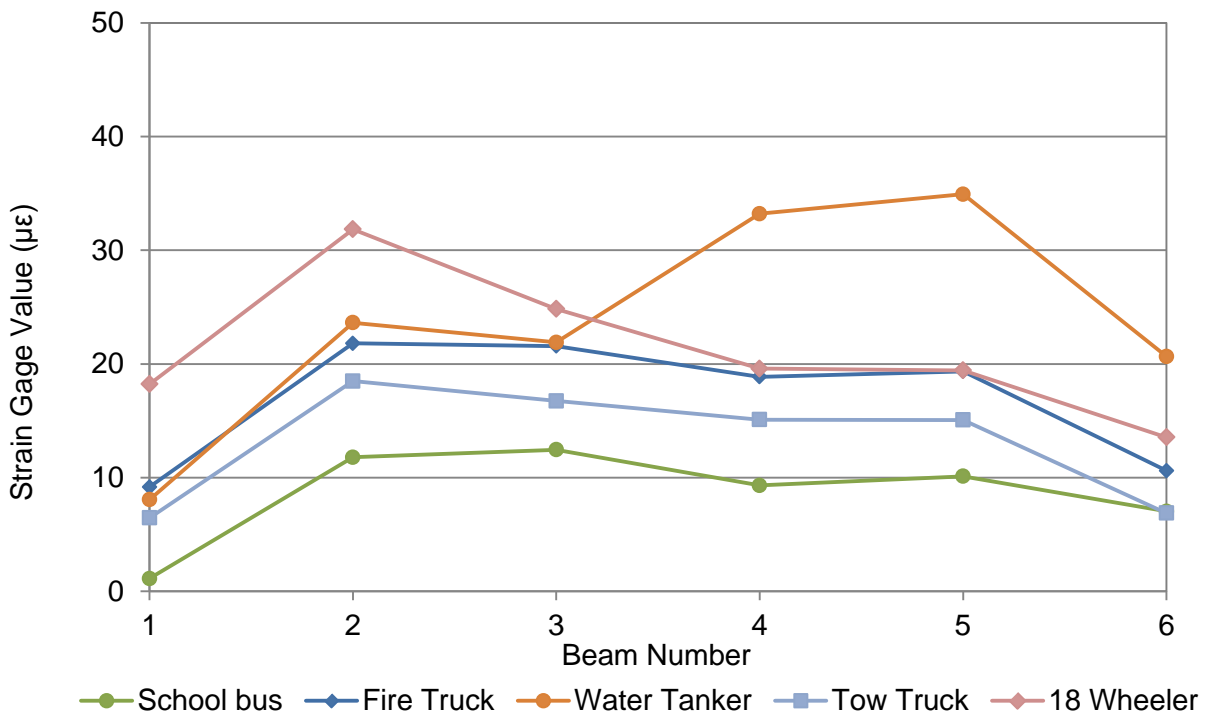
(b) Strain Values on Bottom Surface

Figure 5.29. Bearing Pad Deformations and Strain Values during Ambient Traffic Test.

5.5   SUMMARY AND FINDINGS

Comprehensive static and dynamic testing was conducted on the northbound US 69 Bridge over Day Street in the city of Denison, Grayson County, Texas, to investigate the in-service performance and load sharing behavior of the spread slab beam bridge system. Several types of sensors (strain gages, LVDTs, string potentiometers, and accelerometers) were installed on the bridge to measure the structural response under static and dynamic vehicular loading. Testing consisted of three parts: static load tests, controlled dynamic load tests, and ambient traffic load tests.

After analyzing the data collected from all tests, the research team made the following conclusions based on the results.

1. The strain gage readings indicated that the deck, sidewalk, and guardrail did not exhibit plane section behavior.

2. The load distribution curve changed when the vehicle was parked in different transverse alignments, and the value for one specific beam is higher if the alignment location is close to the beam.

3. Observed bridge responses under dynamic loads were larger when compared to their static counterparts; the dynamic bridge response became larger with the increase of vehicle speed. Evidently, for short-span bridges, the dynamic impact may exceed the AASHTO LRFD Specifications (2012) design value of 33 percent.

4. In spite of the changes in moment magnitude under dynamic loading, the moment LDFs were quite similar to their static counterparts.

6 MODELING OF TESTED SPREAD SLAB BEAM BRIDGES

6.1 SCOPE

In order to computationally model the moment and shear design actions and hence derive load distribution factors (LDFs) for spread slab beam bridge systems, several modeling strategies are explored. The different computational techniques discussed in this chapter include the historic grillage analysis and the more computationally rigorous finite element method (FEM). First, comparative accuracy with physical test results is examined for a similar class of bridge tested by Douglas and Vanhorn (1966), referred to herein as the Drehersville Bridge. For this bridge and the two bridges tested as part of the present research (Riverside Bridge and US 69 Bridge), researchers found that while each considered method is arguably valid, improved accuracy is achieved when a higher level of computational rigor is used. Therefore, a finely meshed FEM solution was adopted for further use in parametric studies used to obtain LDFs for moment and shear forces from which empirical LDF formulas were derived (see Chapter 7).

6.2 COMPUTATIONAL TECHNIQUES

In this research, two computational modeling techniques were utilized in the bridge modeling process. The most basic type of modeling that was historically used is the grillage method of analysis. SAP2000 Version 16 (Computers and Structures 2013) was used to build and apply the grillage modeling approach. The second technique is the more contemporary FEM. Two different commercial software packages were used to simulate the tested bridges: Abaqus® Version 6.13 (Dassault Systemes 2013) and CSiBridge® Version 15 (Computers and Structures 2013).

6.2.1 The Grillage Model

The grillage method is a simplified method of analysis in which the girders and the deck of the bridge superstructure are assumed to be a mesh of beam elements in two orthogonal directions. This is the most basic computational modeling approach for long and wide structures that are loaded out of plane. By modeling the bridge superstructure as an equivalent grillage of rigidly connected beams at discrete nodes, the number of degrees of freedom within a single bridge span is quite small, and the load transfer mechanism of the span is somewhat simplified. This

simplified method of analysis lowers computational complexity and decreases the time needed for modeling and computation. The grillage models developed as part of this study were guided by the earlier recommendations of Hambly (1976) and Zokaie et al. (1991). Further adjustments of the grillage topology were often necessary based on convergence studies.

6.2.2 FEM Modeling

In contrast to the historical method for establishing load distribution factors using a grillage analysis, the FEM is a more exacting approach where fewer approximations and simplifications are necessary. Two contemporary commercial FEM software packages were used, and the results are compared in this chapter. Abaqus is a general purpose FEM code used for solving a broad range of advanced problems in civil and mechanical engineering. CSiBridge, which is from a software suite similar to SAP2000 (Computers and Structures 2013), is more specific for bridge engineering. This research does not promote either code; rather, researchers sought to apply two independent programs seeking analysis accuracy and comparable confirmation of the results. Solid brick elements were used throughout with the appropriate elastic material properties.

6.3 VERIFICATION OF COMPUTATIONAL TECHNIQUES

Prior to developing LDF solutions for the two bridges investigated in this research, the research team considered it prudent to do several methodological verification analyses on known test data. Grillage and FEM models were built for the Drehersville Bridge, a spread box beam structure located in Pennsylvania crossing the Little Schuylkill River. The Drehersville Bridge was instrumented and experimentally tested in 1966 as part of a Lehigh University research project to study the lateral distribution of static loads (Douglas and Vanhorn 1966); therefore, test data are available to validate the results of the numerical models developed in this study as described herein.

6.3.1 Background

Figure 6.1 presents the Drehersville Bridge. The superstructure consists of three simply supported spans with no skew angle. The northwest span was instrumented and tested. This span has a length of 61.5 ft and a roadway width of 30 ft. Figure 6.1 also shows (a) the transverse, and (b) the longitudinal location of the applied truck loads, while Figure 6.2 shows the two loaded test trucks used for the applied loads.

(a) Transverse Section

(b) Elevation View

Figure 6.1. Drehersville Bridge (Douglas and Vanhorn 1966).

The structural components for the Drehersville Bridge include five prestressed concrete box beam girders in a spread configuration, a reinforced concrete deck, sidewalks and parapets on both sides, and diaphragms at midspan and both ends. The box girders have an overall depth of 2 ft 9 in. and an overall width of 4 ft with a web thickness of 5 in. The bridge deck is specified as 7.5 in. thick, and the diaphragms are 10 in. thick and as deep as the beams.

The elastic modulus for the box beam concrete was obtained as E_c = 6806 ksi (Douglas and Vanhorn 1966). The deck strength was assumed to be f'_c = 5 ksi, and the calculated elastic modulus was E_c = 5752 ksi. These values were adopted for the grillage and the FEM analyses for this bridge.
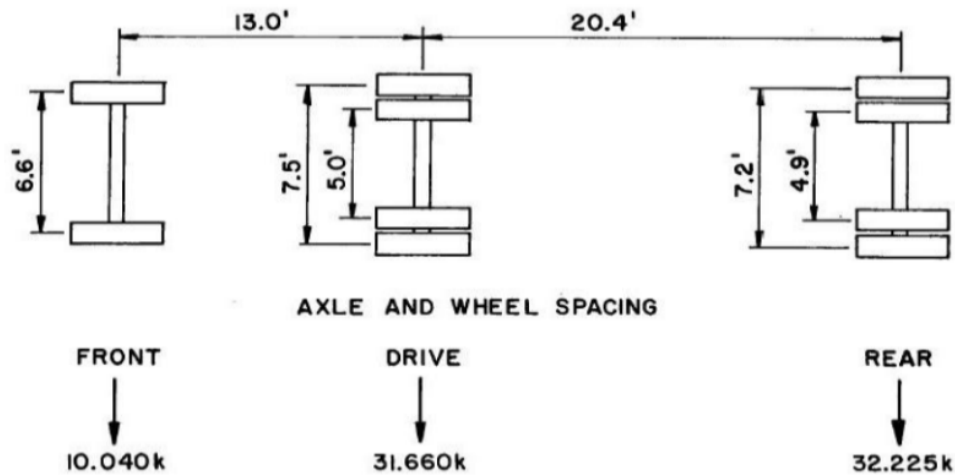
(a) Test Vehicle T1

Figure 6.2. Axle Loads of Test Trucks (Douglas and Vanhorn 1966).

For each load case, an analysis was conducted placing the test truck(s) with their central axles at the location of Section M in Figure 6.1(b) to create the maximum moment and to replicate the loading during the field test. The transverse location of the axle loads was determined in a test-lane format, as shown in Figure 6.1(a), where there were seven possible transverse stations.

6.3.2 Computational Modeling and Results

The grillage model was set up with frame elements using the commercial software SAP2000. There were five longitudinal grillage members representing the prestressed box beams and 11 grillage members in the transverse direction. Two finite element models were also developed

utilizing solid brick elements using two commercial software codes: Abaqus and CSiBridge. Figure 6.3 depicts the grillage and FEM models for the Drehersville Bridge.

Results of only two load cases are discussed herein for the sake of brevity. The Lane 4 load case is a central load; thus, computational moment results are symmetric about the longitudinal centerline of the bridge. The Lanes 1 and 4 load case provides the maximum external girder moment. Figure 6.4 depicts the final comparison between the different modeled moment results and experimental results as a graphical representation.

The moment and moment LDF values for the Drehersville Bridge obtained from the field test (Douglas and Vanhorn 1966) and computational analysis (both grillage and FEM approaches) are listed in Tables 6.1, 6.2, 6.5, and 6.6. The errors of the computational to the experimental moment and moment LDF values are listed in Tables 6.3, 6.4, 6.7, and 6.8. Within these tables, the beam identifiers corresponding to critical moment and critical LDF values for exterior and interior beams are highlighted with bold font.

Tables 6.1 and 6.3 show that both grillage and FEM solutions gave reasonably accurate results when the vehicle was loaded on Lane 1. The FEM solution, especially the Abaqus model, gave more accurate LDFs for both the exterior and interior box beams when compared to the test results. However, for the case when both Lanes 1 and 4 were loaded, it is evident from Tables 6.2 and 6.4 that the grillage model more accurately captured the girder moments and LDFs than the FEM solutions. Especially for exterior Girder A, the LDFs determined from FEM are around 30 percent lower than the test results, which is an unconservative outcome. Similar observations are evident in Figure 6.4.
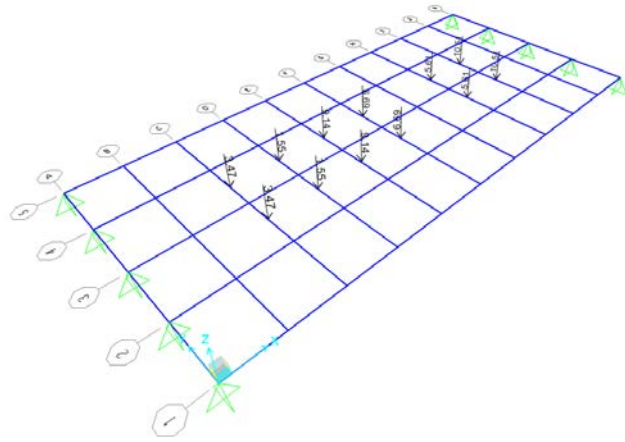
(a) Grillage Model
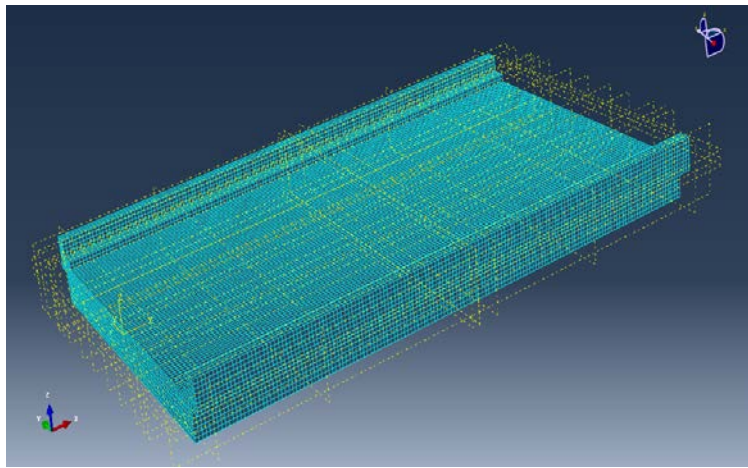
(b) FEM Model (Abaqus)
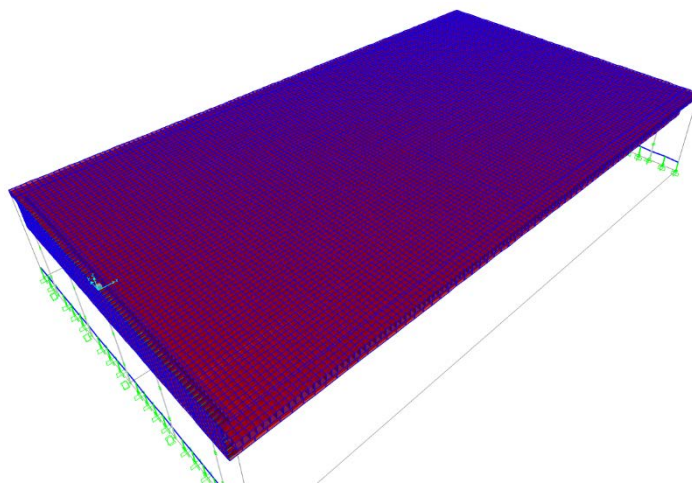
(c) FEM Model (CSiBridge)

Figure 6.3. Grillage and Finite Element Models for Drehersville Bridge.

170
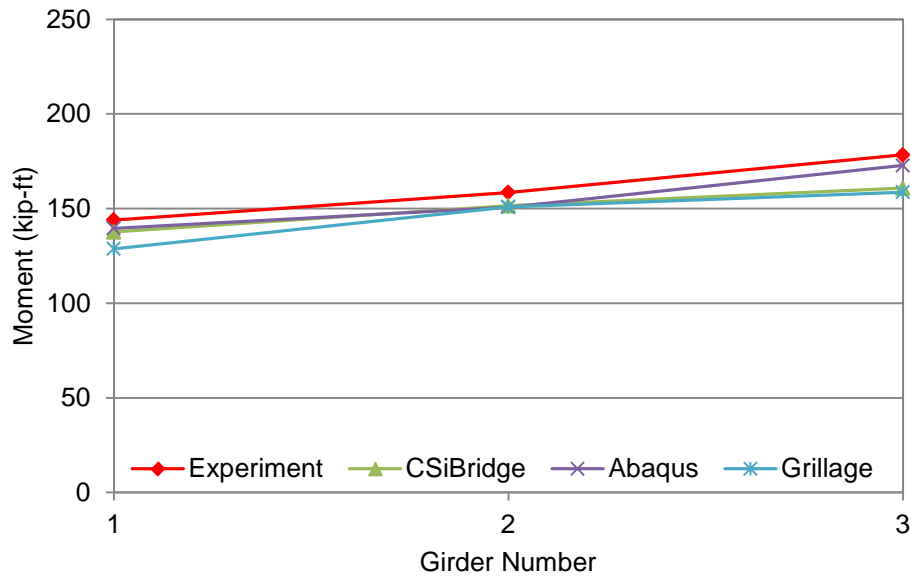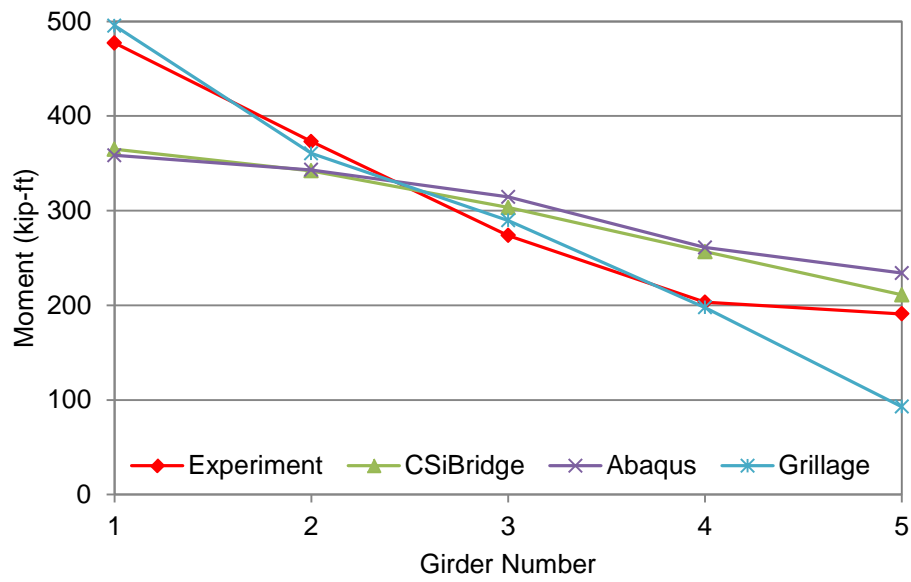
(a) Lane 4 Loaded

(b) Lanes 1 and 4 Loaded

Figure 6.4. Drehersville Bridge Moment Comparison.

171

Table 6.1. Maximum Moments for Drehersville Bridge Loaded in Lane 4.

Girder Location	Moment (kip-ft)			
	Experiment	**Grillage**	**Abaqus**	**CSiBridge**
A	144.0	128.8	139.6	137.6
B	158.5	150.9	150.8	151.5
C	178.3	158.7	172.8	160.8

Table 6.2. Maximum Moments for Drehersville Bridge Loaded in Lanes 1 and 4.

Girder Location	Moment (kip-ft)			
	Experiment	**Grillage**	**Abaqus**	**CSiBridge**
A	477.1	495.4	358.4	364.8
B	373.0	360.6	343.1	342.1
C	273.8	289.7	314.6	303.3
D	203.2	197.7	261.0	256.7
E	190.9	92.9	234.0	211.0

Table 6.3. Drehersville Bridge Lane 4 Moment Errors.

Girder Location	Error in Moment Relative to Experiment		
	Grillage/Exp. (%)	**Abaqus/Exp. (%)**	**CSiBridge/Exp. (%)**
A	−1	−3	−4
B	−5	−5	−4
C	−11	−3	−10

Table 6.4. Drehersville Bridge Lanes 1 and 4 Moment Errors.

Girder Location	Error in Moment Relative to Experiment		
	Grillage/Exp. (%)	**Abaqus/Exp. (%)**	**CSiBridge/Exp. (%)**
A	+4	−25	−24
B	−3	−8	−8
C	+6	+15	+11
D	−3	+28	+26
E	−51	+23	+11

Table 6.5. Maximum Moment LDFs for Drehersville Bridge Loaded in Lane 4.

Girder Location	Moment LDF			
	Experiment	**Grillage**	**Abaqus**	**CSiBridge**
A	0.184	0.179	0.185	0.186
B	0.202	0.210	0.200	0.205
C	0.228	0.221	0.229	0.218

Table 6.6. Maximum Moment LDFs for Drehersville Bridge Loaded in Lanes 1 and 4.

Girder Location	Moment (k-ft)			
	Experiment	**Grillage**	**Abaqus**	**CSiBridge**
A	0.314	0.345	0.237	0.247
B	0.246	0.251	0.227	0.231
C	0.180	0.202	0.208	0.205
D	0.134	0.138	0.173	0.174
E	0.126	0.065	0.155	0.143

Table 6.7. Drehersville Bridge Lane 4 Moment LDF Errors.

Girder Location	Error in Moment LDF Relative to Experiment		
	Grillage/Exp. (%)	**Abaqus/Exp. (%)**	**CSiBridge/Exp. (%)**
A	−2	+1	+1
B	+4	−1	+1
C	−3	+1	−4

Table 6.8. Drehersville Bridge Lanes 1 and 4 Moment LDF Errors.

Girder Location	Error in Moment LDF Relative to Experiment		
	Grillage/Exp. (%)	**Abaqus/Exp. (%)**	**CSiBridge/Exp. (%)**
A	+10	−25	−21
B	+2	−8	−6
C	+12	+15	+14
D	+3	+29	+30
E	−49	+23	+14

6.4 MODELING OF THE TWO TESTED BRIDGES

6.4.1 Grillage Model

6.4.1.1 Grillage Model Geometry

For the slab beam bridge decks employed in this research, one longitudinal member was used to represent each slab beam, regardless of the spacing of the beams. Then, transverse beams were placed to distribute the applied bridge deck loads. Hambly (1976); Zokaie et al. (1991) recommended that the spacing between transverse grillage members should not be larger than 10 percent of the overall span length. In order to apply the vehicle load directly in shear critical load cases, an additional transverse beam member was placed at the last rear tire location, 25 in. away from the span end. Given that it was necessary to apply wheel loads external to the centerline of the exterior slab beam, near-rigid transverse grillage member extensions were added to apply wheel loads at the same locations with the physical structure.

Figure 6.5 represents the grillage topology for modeling the Riverside Bridge and US 69 Bridge. All longitudinal and transverse grillage members were meshed every 4 in. and at every intersection point. This fine mesh permitted a higher accuracy in the model and more points where all forces were calculated, rather than just the intersection points of grillage members.

6.4.1.2 Grillage Member Properties

Longitudinal grillage members were modeled as a composite T-beam including the slab beam and deck. The section designer function in SAP2000 was used to correctly reflect section properties in the model. Given that only one material property could be applied to each member in the software, transformed sections were used for the longitudinal member modeling process. Transverse grillage members were modeled as rectangular sections representing the 10 in. thick deck. The tributary width of the interior transverse members section was taken as the center-to-center spacing of the transverse grillage members, while for the end two transverse beam sections, 50 percent of the spacing was used as the section width.

Two section properties, moment of inertia I and torsional constant J, are needed for each grillage member in the analysis process. Values of these parameters are sensitive to the outcome of the results; therefore, an accurate assessment is essential. Because the section designer function in SAP2000 was utilized to model longitudinal and transverse grillage members, the software calculated the section properties automatically based on the geometric dimensions.
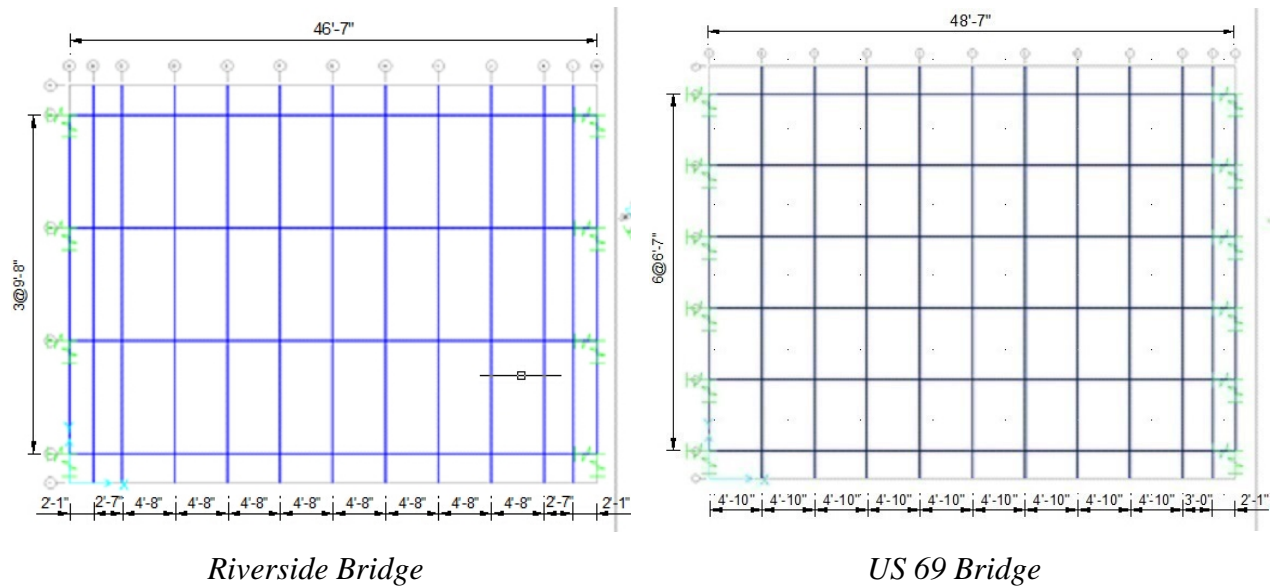
Riverside Bridge   *US 69 Bridge*

(a) Plan View of Two Tested Bridge Models
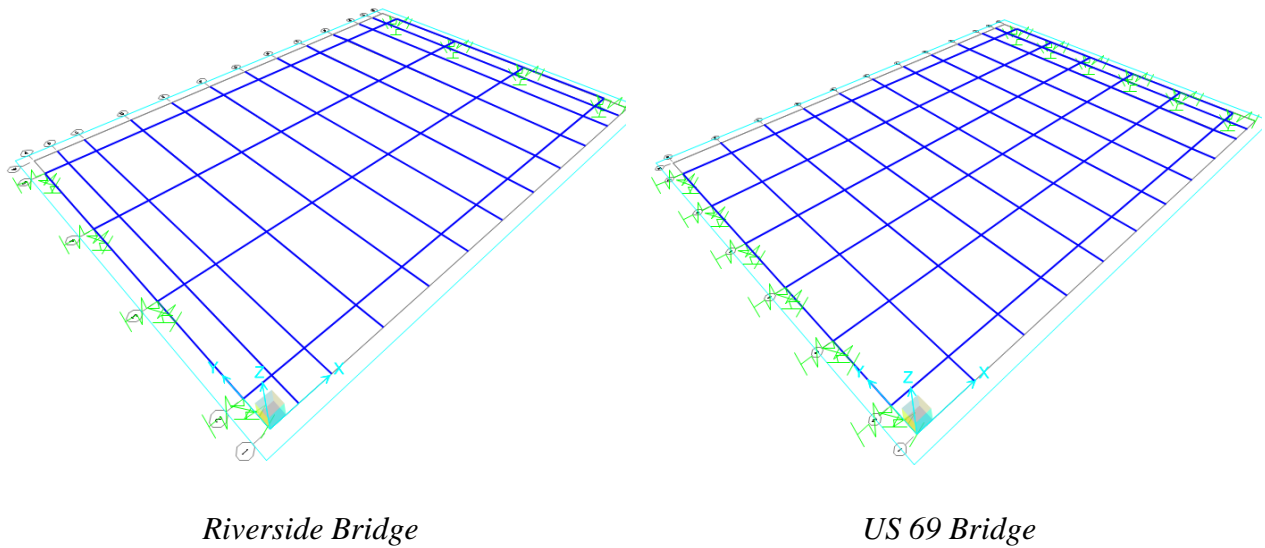
Riverside Bridge   *US 69 Bridge*

(b) 3D View of Two Tested Bridge Models

Figure 6.5. Longitudinal and Transverse Grillage Members Arrangements.

The torsional constant, *J*, is an important and sensitive parameter that requires an appropriately accurate calculation. In this research, the torsional constant was calculated by the section designer function of SAP2000. These results were then checked against the recommendations given in the commentary of the AASHTO LRFD Specifications (2012), Clause C.4.6.2.2.1. Good agreement between the two values was obtained.

For the US 69 Bridge, the sidewalk and guardrail are considered composite with the deck, forming a stiffer edge section along the east side of the bridge. This edge section was also modeled using the section designer function to obtain an effective moment of inertia, I, and torsional constant, J. A property modifier function was used to adjust the torsional constant values to avoid double counting the stiffness effects.

Figure 6.6 presents the effective modeled shapes of longitudinal grillage members for the Riverside Bridge and US 69 Bridge. Tables 6.9 through 6.12 list the sectional properties of longitudinal and transverse grillage members for the two bridges. The transverse grillage member placed 25 in. away from the end support to apply the critical load is called Interior 1 in Tables 6.11 and 6.12.

(a) Riverside Exterior Beams

(b) Riverside Interior Beams

(c) US 69 West Edge Beam   (d) US 69 Interior Beams   (e) US 69 East Edge Beam
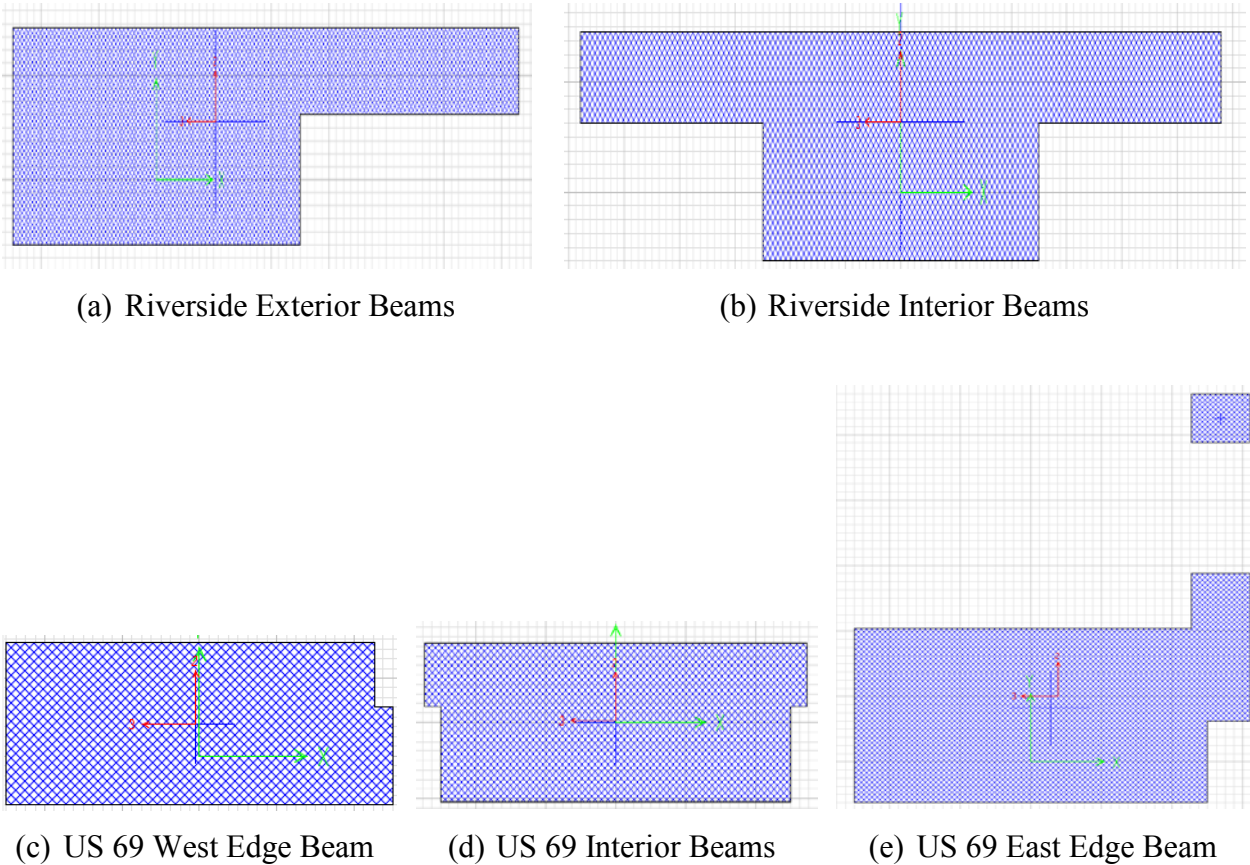
Figure 6.6. Longitudinal Grillage Member Section in Two Tested Bridge Models.

176

Table 6.9. Longitudinal Grillage Member Parameters (Riverside Bridge).

Parameter	Interior Beams	Exterior Beams
Deck Width, b_d (in.)	139	106
Deck Depth, d_d (in.)	10.0	10.0
Beam Width, b_b (in.)	60.0	60.0
Beam Depth, d_b (in.)	15.0	15.0
Modulus of Elasticity, E (ksi)	5880	5880
Moment of Inertia, I (in^4)	114,000	102,000
Torsional Constant, J (in^4)	265,000	245,000

Table 6.10. Longitudinal Grillage Member Parameters (US 69 Bridge).

Parameter	West Beam	Interior Beams	East Beam
Deck Width, b_d (in.)	57.1	63.9	67.2
Deck Depth, d_d (in.)	10.0	10.0	10.0
Beam Width, b_b (in.)	60.0	60.0	60.0
Beam Depth, d_b (in.)	15.0	15.0	15.0
Modulus of Elasticity, E (ksi)	6810	6810	6810
Moment of Inertia, I (in^4)	76,200	81,500	458,000
Torsional Constant, J (in^4)	225,000	237,000	472,000

Table 6.11. Transverse Grillage Member Parameters (Riverside Bridge).

Parameters	Exterior	Interior	Interior 1
Deck Width, b_d (in.)	21.1	55.9	5.90
Deck Depth, d_d (in.)	10.0	10.0	10.0
Modulus of Elasticity, E (ksi)	7050	7050	7050
Moment of Inertia, I (in^4)	1800	4700	492
Torsional Constant, J (in^4)	4900	16,500	433

Table 6.12. Transverse Grillage Member Parameters (US 69 Bridge).

Parameters	Exterior	Interior	Interior 1
Deck Width, b_d (in.)	20.9	58.3	8.30
Deck Depth, d_d (in.)	10.0	10.0	10.0
Modulus of Elasticity, E (ksi)	6810	6810	6810
Moment of Inertia, I (in^4)	1700	4900	692
Torsional Constant, J (in^4)	4900	17,300	949

6.4.1.3 Support Restraints

For seating the slab beams on the test bridges, two types of bearing pads were placed on the abutments or piers. As mentioned in Chapter 5, a series of tests were conducted on the bearing pads in the laboratory. The pads performed in an essentially linear fashion over the applied vehicular loading range, and the resulting inferred stiffness values were used in the analysis discussed here. In SAP2000, the bearing pads were modeled as vertical and horizontal springs in three dimensions to simulate the field conditions of the test bridges. Rotational restraints were released. A vertical spring stiffness of 1270 kip/in. was used based on laboratory testing of bearing pads with the same properties as those used for the Riverside Bridge. A horizontal spring stiffness value of 4.8 kip/in. was used based on research by Kim et al. (1996).

6.4.1.4 Loading Arrangement

The locations of the applied loads for the grillage models were taken to be the same as the positions of truck wheels in the various tests. Those vehicle test positions were described in Chapters 4 and 5. However, the actual applied test loads were often not concentric with the grillage nodes or members. Therefore, actual loads were proportionally distributed to the nearest surrounding nodes or grillage members to give the equivalent net effect. Figure 6.7 to Figure 6.8 show load configurations for both the Riverside and US 69 Bridges.
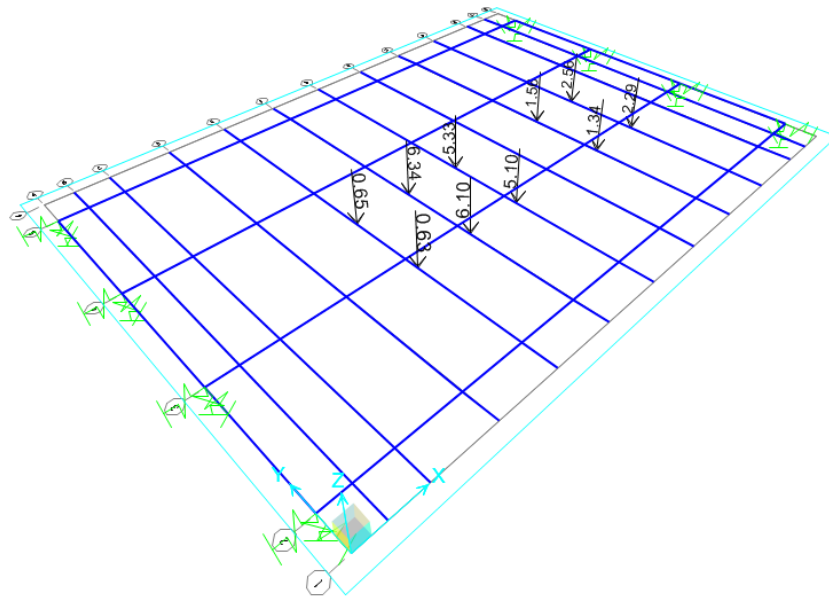
(a) Loading Configuration for Typical Moment Critical Load Case
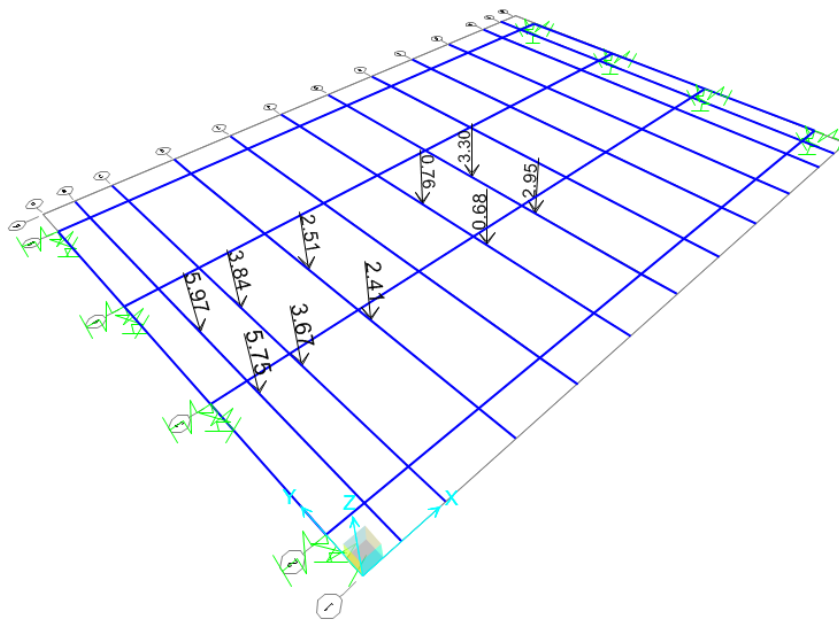
(b) Loading Configuration for Typical Shear Critical Load Case

Figure 6.7. Grillage Models for Riverside Bridge.
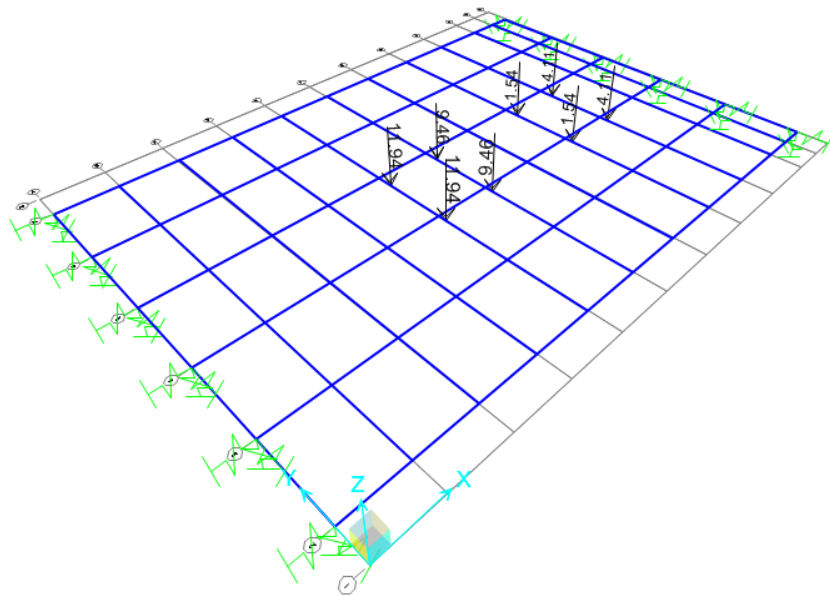
179

(a) Loading Configuration for Typical Moment Critical Load Case
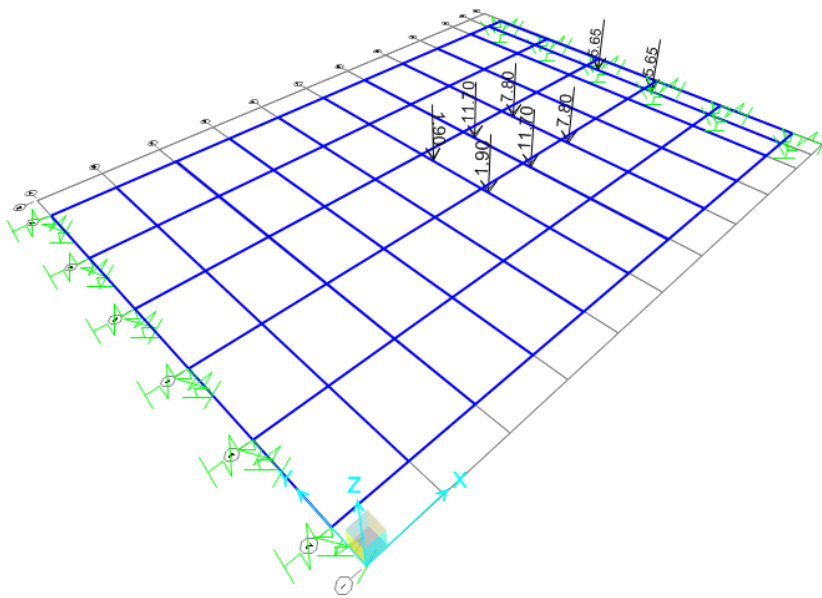
(b) Loading Configuration for Typical Shear Critical Load Case

Figure 6.8. Grillage Models for US 69 Bridge.

6.4.2 Finite Element Model

6.4.2.1 Bridge Model Description

The geometric information for the two test bridges was introduced in detail in previous chapters. Three-dimensional FEM solutions were developed based on the design drawings and actual on-site conditions for both bridges using commercial software Abaqus (Version 6.13) and CSiBridge (Version 15). For the Riverside Bridge, the precast concrete panels (PCPs) were conservatively considered as part of the entire 10 in. thick reinforced CIP concrete deck in the model. For the US 69 Bridge, the sidewalk and guardrail were modeled and considered to be fully composite with the reinforced concrete deck. Table 6.13 lists major geometric information for the two bridges. Concrete properties for the Riverside Bridge were determined from specimen test results (see Appendix B). For the US 69 Bridge, the same calculated modulus of elasticity (MOE) value used in the experimental results analysis (Section 5.4.1) was applied to the computational modeling herein. The MOE, Poisson's ratio, and unit weight for deck and slab beam concrete used in the two bridge models are listed in Table 6.14. Figure 6.9 and Figure 6.10, respectively, show the Abaqus and CSiBridge finite element models for the two tested bridges.

Table 6.13. Major Geometric Information of Riverside and US 69 Bridge.

Type	Bridge	Span Length	Bridge Width	Slab Beam	Deck Thickness	Girder Clear Spa.
Simply Supported Prestressed Spread Slab Beam Bridge	Riverside	46′-7"	34′-0"	5SB15	10"	4'-8"
	US 69	48′-7"	37′-11.5"	5SB15	10"	1'-4"

Table 6.14. Material Properties for Two Bridge Models.

Bridge	Modulus of Elasticity (ksi)		Poisson's Ratio	Unit Weight (pcf)
	Deck	Slab Beam		
Riverside	7054	5883	0.2	150
US 69	5861	6811	0.2	150
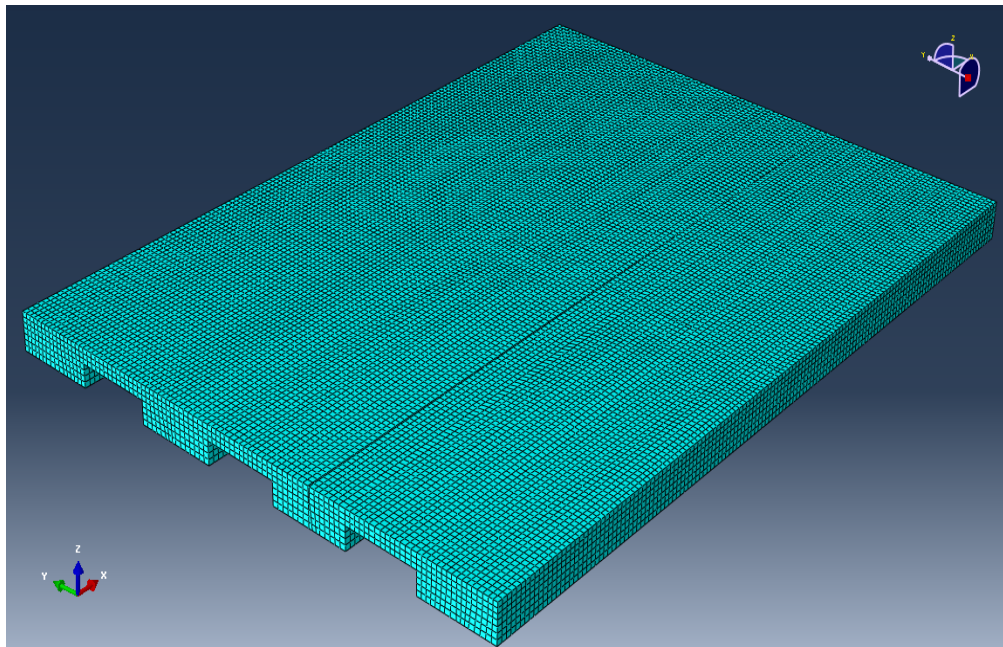
(a) Abaqus Model
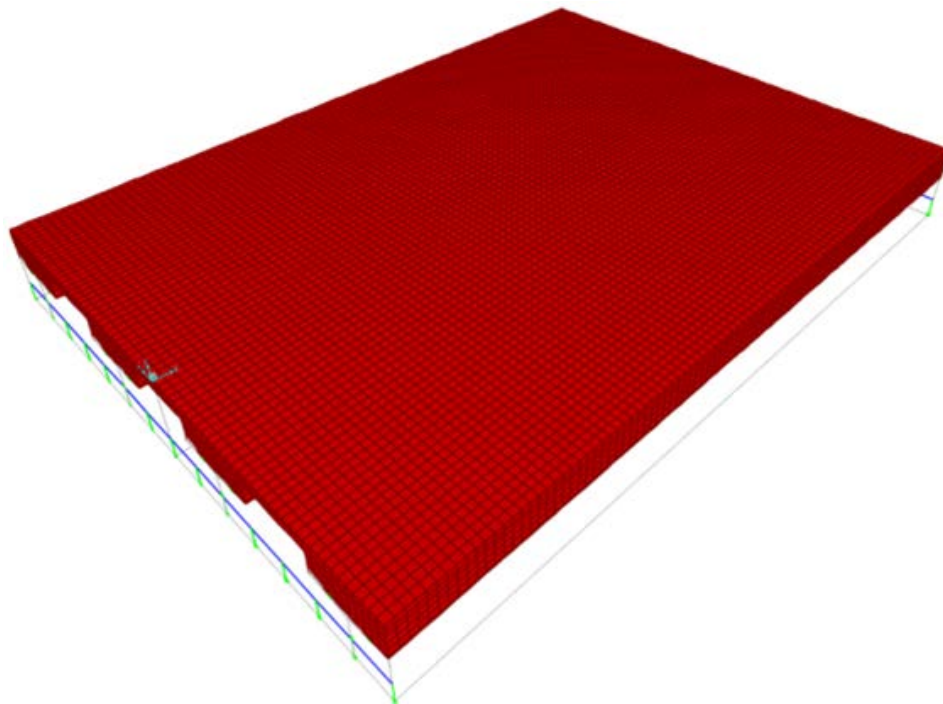
(b) CSiBridge Model

Figure 6.9. Finite Element Models of Riverside Bridge.
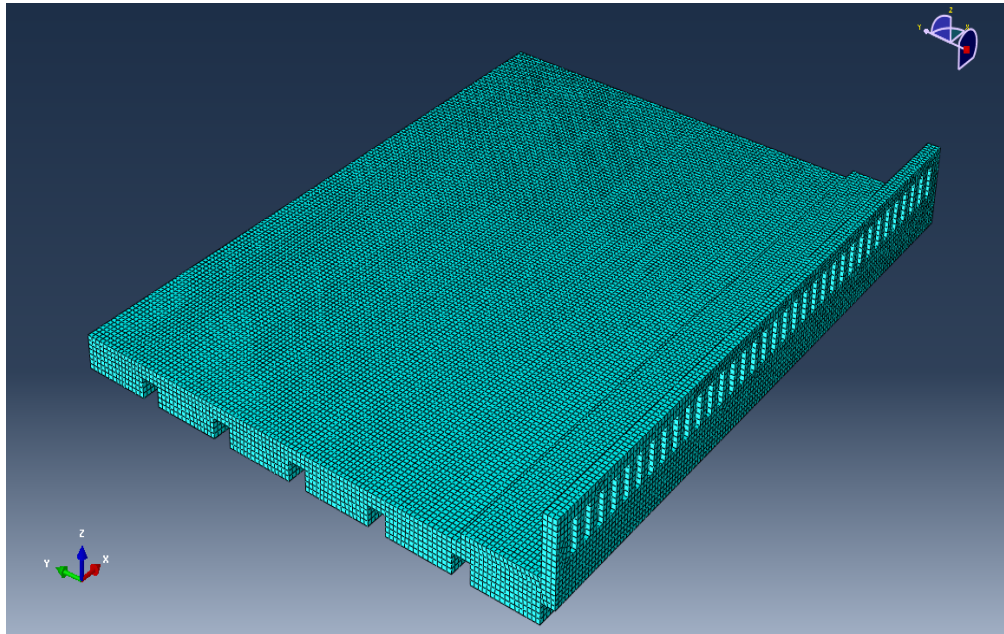
(a) Abaqus Model
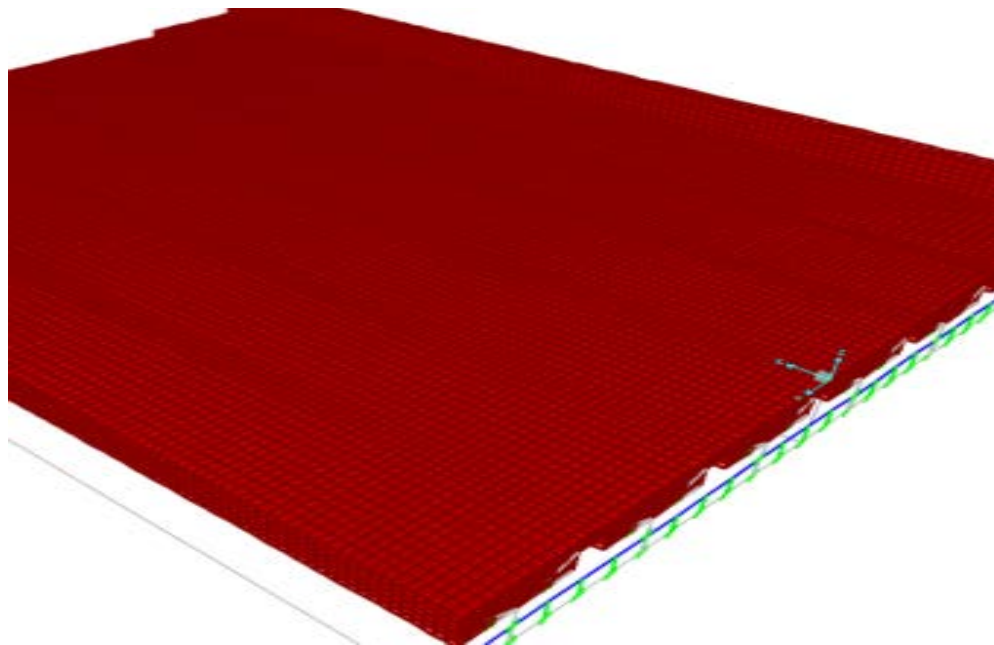
(b) CSiBridge Model

Figure 6.10. Finite Element Models of US 69 Bridge.

6.4.2.2 Mesh Sensitivity

As mentioned previously, three-dimensional solid elements were adopted in modeling the prestressed spread slab beam bridges. In the Abaqus commercial software, the C3D8R element is a general purpose linear eight-node brick element with three degrees of freedom at each node. This element type was used to model all structural components of the test bridges. The effects of the secondary members (sidewalk and guardrail) were also taken into consideration in the analysis procedure. A 20-node quadratic brick element with reduced integration, C3D20R, was adopted in one specific load case, and the numerical results with different types of brick elements were compared. The mesh of each model was generated with evenly spaced nodes. Several models with different mesh sizes (4 in., 6 in., and 12 in.) were investigated as a mesh sensitivity study.

Tables 6.15 and 6.16 list the shear forces and moments calculated from the Abaqus solutions with different element types and mesh sizes. For this study, one truck was parked along Alignment 1 of the Riverside Bridge. Figure 6.11 shows the shear and moment values and corresponding LDF value distribution across the bridge section. As the figure illustrates, the numerical results converged as the mesh size became smaller, and the quadratic brick element gave similar results. Also, the differences between test results and FEM solutions became smaller when the absolute values were converted to load distribution factors. Results show satisfactory outcomes could be achieved with the 12 in. meshes. However, researchers deemed it prudent to use the finer 6 in. mesh in Abaqus FEM models, as the extra computational effort was not onerous.

Table 6.15. FEM Shear Force Results with Different Element Types and Mesh Sizes (Abaqus).

Element Type	Mesh Size	Shear Force (kips)			
		Beam 1	Beam 2	Beam 3	Beam 4
C3D8R	12 in.	−0.5	0.7	7.2	19.0
	6 in.	−0.5	0.7	7.4	18.7
	4 in.	−0.6	0.8	7.3	18.8
C3D20R	4 in.	−0.7	0.6	7.2	19.2
Test Results		−0.2	0.5	6.8	17.0

Table 6.16. FEM Moment Results with Different Element Types and Mesh Sizes (Abaqus).

Element Type	Mesh Size	Moment (kip-ft)			
		Beam 1	Beam 2	Beam 3	Beam 4
C3D8R	12 in.	22.1	42.5	90.3	131.1
	6 in.	25.4	47.9	91.3	122.8
	4 in.	26.2	48.4	90.7	121.9
C3D20R	4 in.	26.8	48.8	90.4	121.2
Test Results		20.5	43.1	84.2	144.0

(a) Moment

(b) Moment LDF

(c) Shear Force

(d) Shear LDF
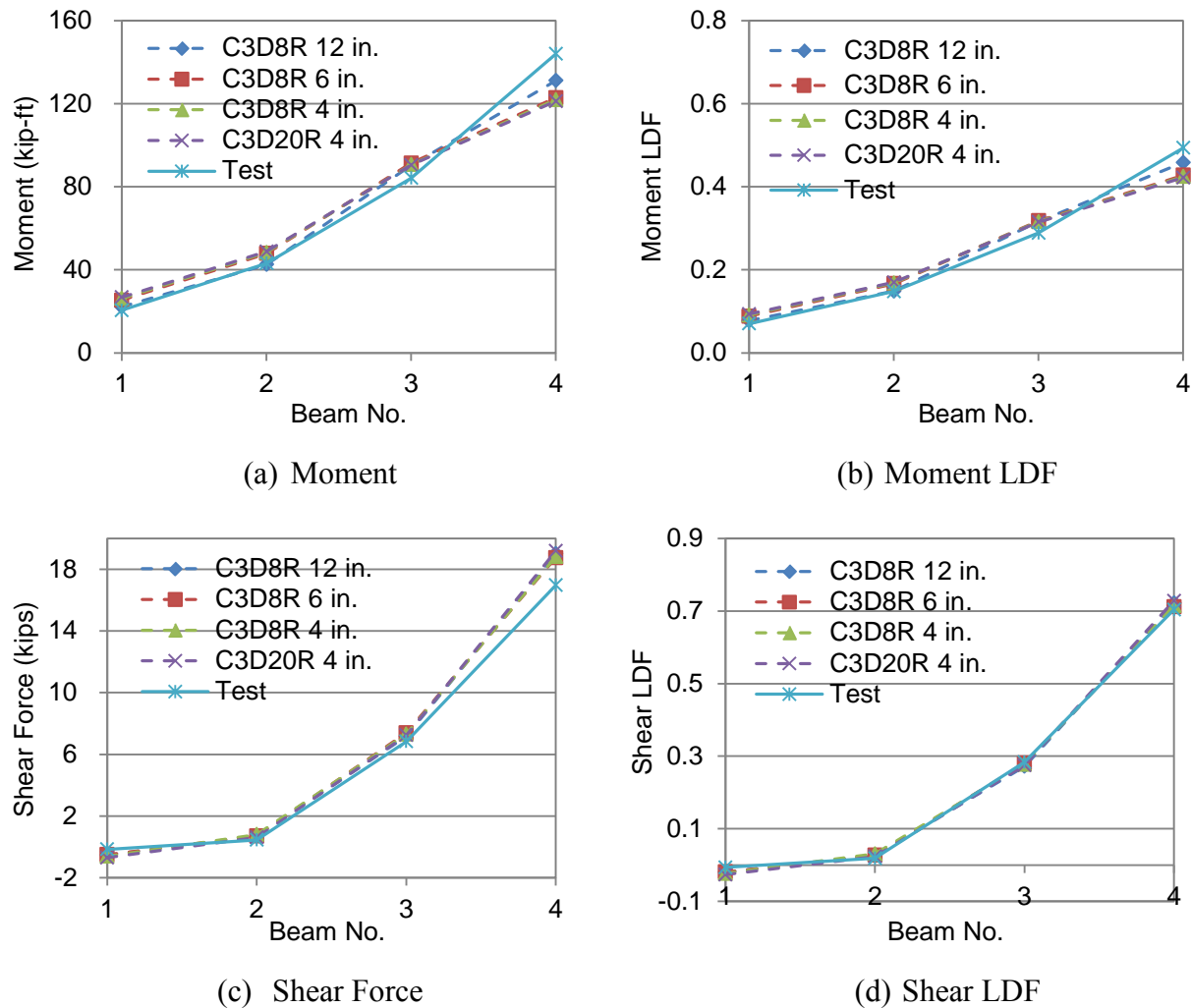
Figure 6.11. Shear Force and Moment Distribution Curves (Abaqus).

For the CSiBridge software, the eight-node isotropic solid element having three degrees of freedom at each node was available to model the different components of the test bridges. Several models of the Riverside Bridge with different mesh sizes (6 in., 12 in., 18 in., and 24 in.)

185

were investigated using this FEM analysis tool. The dump truck load was also placed along Alignment 1 in these models.

Tables 6.17 and 6.18 list the shear forces and moments calculated from the CSiBridge software with different mesh sizes. Figure 6.12 shows the shear and moment values and corresponding LDF value distributions across the bridge section. It is clear that the shear force and moment values did not change significantly when the mesh size changed from 24 in. to 6 in. By taking the computational effort into account, a 12 in. mesh size to model a series of bridges with different span lengths, beam spacings, and beam depths (see Chapter 7).

Table 6.17. FEM Shear Force Results with Different Mesh Sizes (CSiBridge).

Mesh Size	Shear Force (kips)			
	Beam 1	Beam 2	Beam 3	Beam 4
24 in.	0.0	0.3	6.6	19.5
18 in.	−0.1	0.2	6.6	19.6
12 in.	−0.1	0.1	6.6	19.8
6 in.	−0.3	0.0	6.6	20.1
Test Results	−0.2	0.5	6.8	17.0

Table 6.18. FEM Moment Results with Different Mesh Sizes (CSiBridge).

Mesh Size	Moment (kip-ft)			
	Beam 1	Beam 2	Beam 3	Beam 4
24 in.	22.7	43.9	88.2	122.7
18 in.	22.3	43.6	88.4	123.3
12 in.	21.6	43.1	88.6	124.5
6 in.	20.9	42.6	88.9	125.6
Test Results	20.5	43.1	84.2	144.0
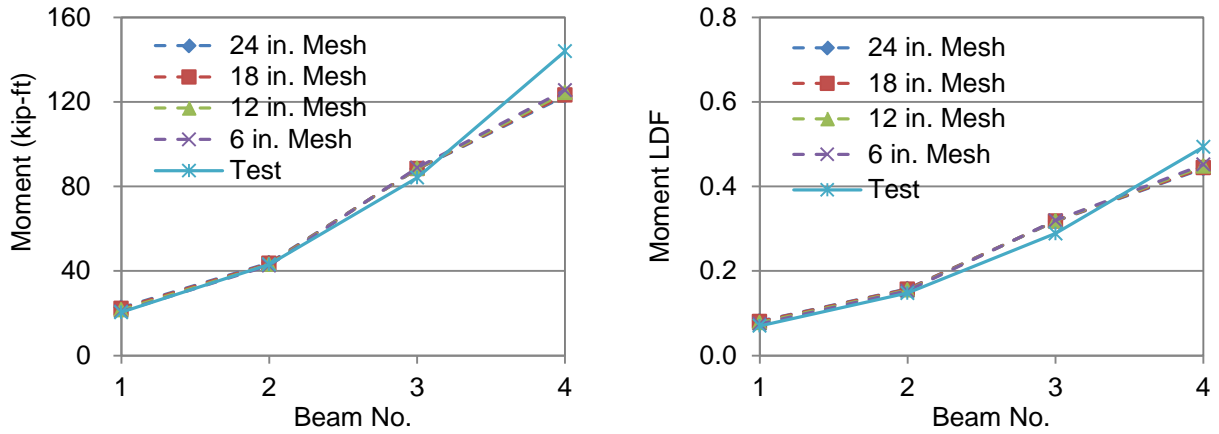
(a) Moment LDF
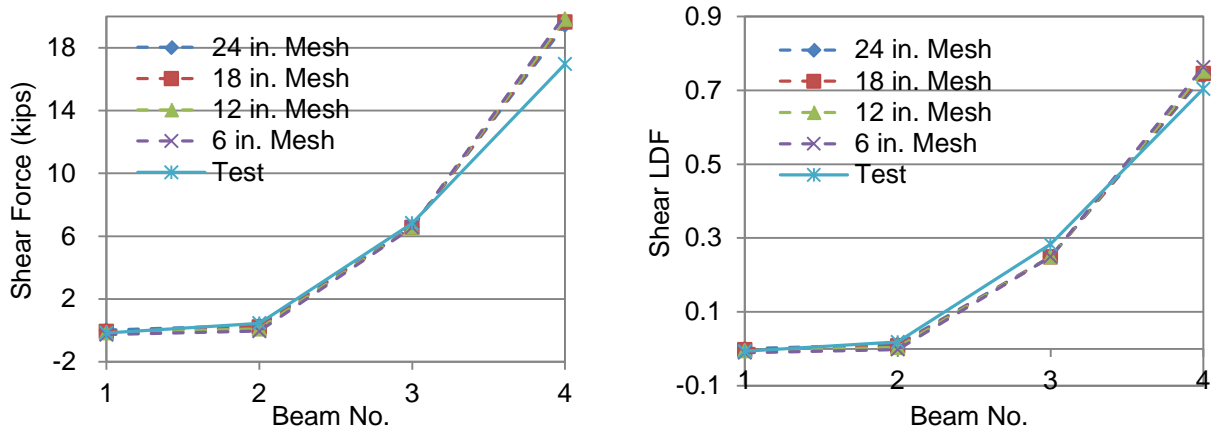
(b) Shear LDF

Figure 6.12. Shear Force and Moment Distribution Curves (CSiBridge).

6.4.2.3 Loading Arrangement and Boundary Conditions

Wheel loads were applied on the deck surface based on the actual vehicle positions during the test. Small areas similar to the tire contact surface were defined in the FEM models to place the vehicle loads uniformly. As mentioned previously, bearing pads at both ends were simulated as three-dimensional springs, and the vertical and horizontal spring stiffness values are 1270 and 4.8 kip/in, respectively.

6.5   ANALYTICAL RESULTS FOR THE RIVERSIDE BRIDGE

6.5.1   Static and Dynamic Properties

The deflection values at selected stations were measured by string potentiometers during testing. Figure 6.13 shows the deflection field calculated by the Abaqus FEM software for the moment critical load case when the vehicle was parked along Alignment 1 (see Figure 4.15). Maximum beam deflections under vehicle loading are listed in Table 6.19. The comparison of the experimental and numerical deflection values for selected beams in the same load case are shown in Figure 6.14.

Table 6.19 shows that in spite of the small displacements, the FEM model was able to capture the maximum beam deflections under vehicle loading during the test reasonably well. The differences between measured deflections and predicted values are very small and within 0.012 in. for most load cases. Figure 6.14 shows that the FEM solution provides reasonable agreement with the measured deflection field. It should be noted that it is challenging to more accurately measure deflections smaller than 1/32 in. (0.031 in.).

Perhaps more important and more challenging than capturing the deflection field, is to accurately model the dynamic properties of the bridge. Natural frequencies and mode shapes were obtained from accelerometer readings following the dynamic tests. In this research, frequency and mode shape analysis was also conducted using the Abaqus software. Table 6.20 lists the natural frequencies calculated by the Abaqus software and the comparison between experimental and numerical values. The bottom row of Table 6.20 also presents the ratio of the FEM to test results. It is clear that the finite element model captured the first three natural frequencies quite well, with the predicted frequencies being within 8 percent of the observed frequencies. Finally, and for the sake of completeness, Figure 6.15 shows the first three mode shapes determined from the Abaqus FEM analysis.
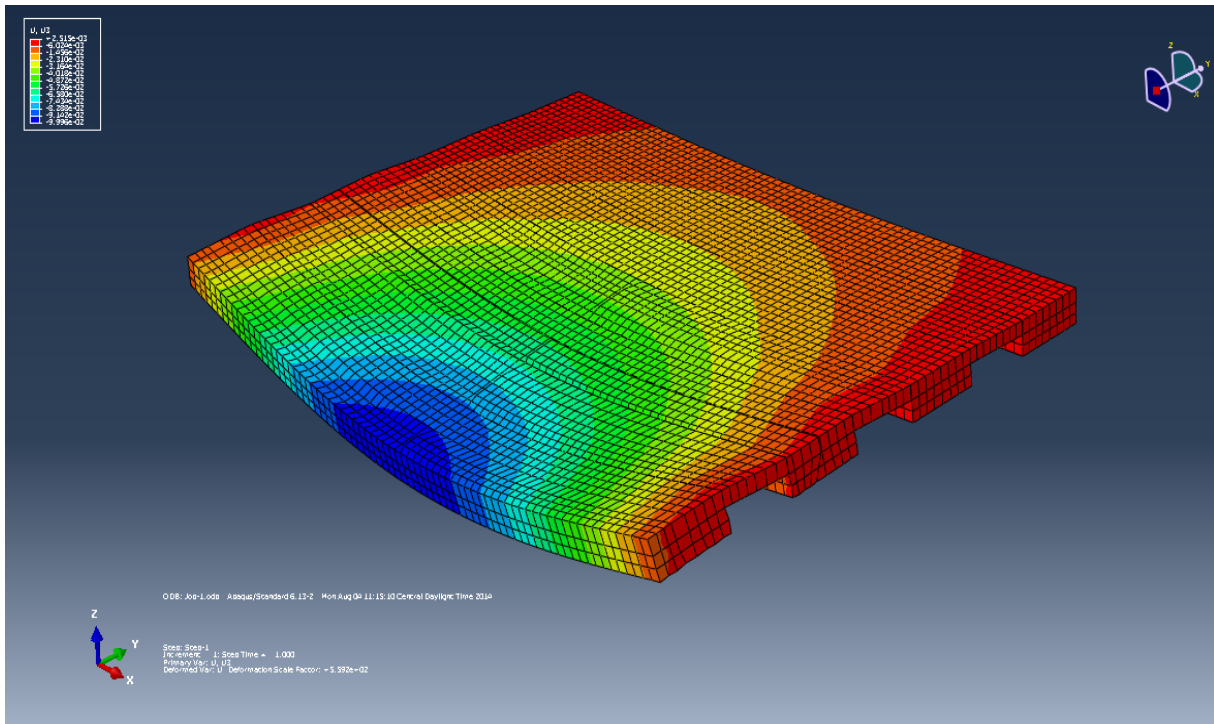
Figure 6.13. Deflection Field Calculated by Abaqus Software (Alignment 1).
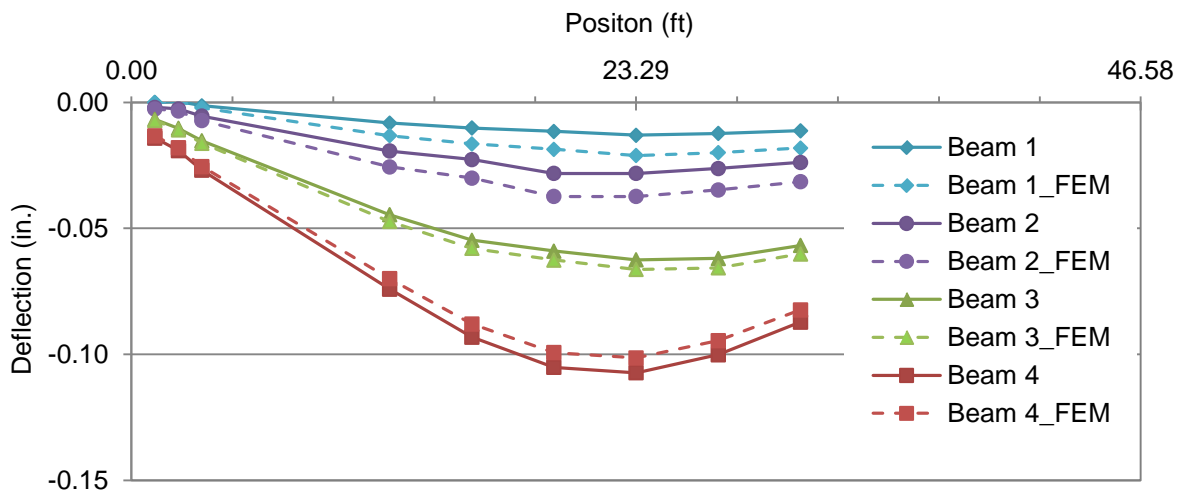
Figure 6.14. Comparison of Experimental and Numerical Deflection Values.

Table 6.19. Maximum Live Load Beam Deflections (Riverside Bridge).

Deflection	Beam 1	Beam 2	Beam 3	Beam 4
Test (in.)	0.013	0.028	0.063	0.107
FEM (in.)	0.021	0.037	0.066	0.101
Difference (in.)	0.008	0.009	0.003	-0.006

Table 6.20. Comparison of Experimental and Numerical Natural Frequencies.

Mode	1st (Hz)	2nd (Hz)	3rd (Hz)
Test	5.22	8.22	13.8
FEM	5.66	8.01	13.3
Ratio = FEM/Test	1.08	0.97	0.96

6.5.2 Results for Moment and Shear Predictions and the LDFs

Computational LDFs for all slab beams in different static load cases were determined from the moments and shear forces calculated by the grillage and the two FEM models. Figures 6.16 and 6.17, respectively, show the comparison of experimental and computational moment and LDF curves across the bridge section. Shear values and corresponding LDFs are depicted in Figures 6.18 and 6.19.

Figure 6.16 and Figure 6.18 show that the computational moment values obtained from the grillage and FEM models are similar to observed test results for both moment and shear critical cases. As for the load distribution behavior, it is evidently shown from Figure 6.17 and Figure 6.19 that both the grillage and the two FEM solutions provide LDF curves close to the observed test results for the moment and shear critical load cases.
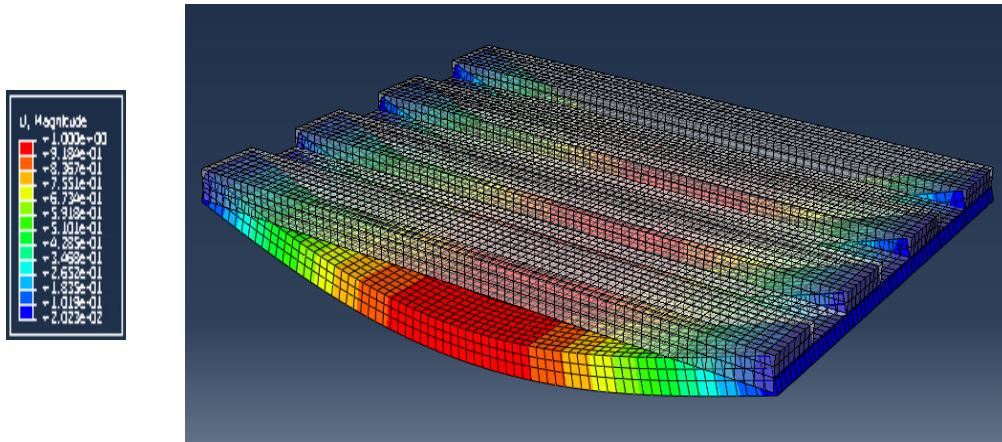
(a) 1st Mode Shape (f = 5.66 Hz, Longitudinal Bending)
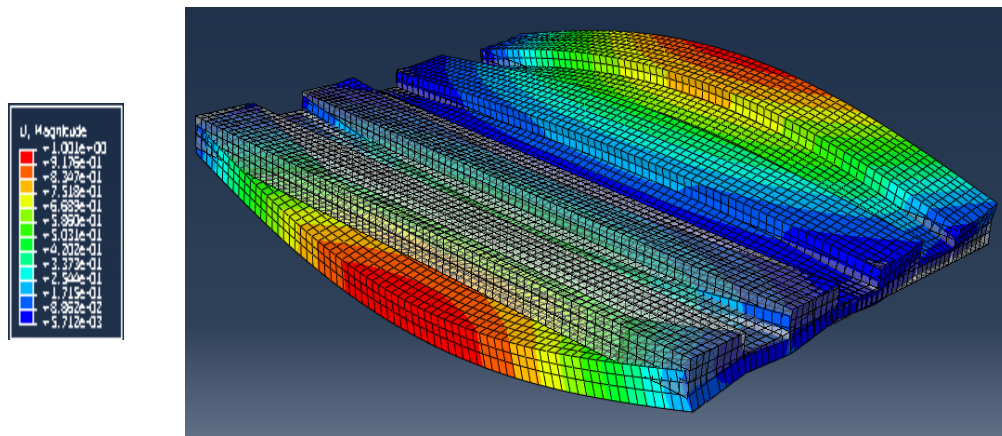
(b) 2nd Mode Shape (f = 8.01 Hz, Torsion)
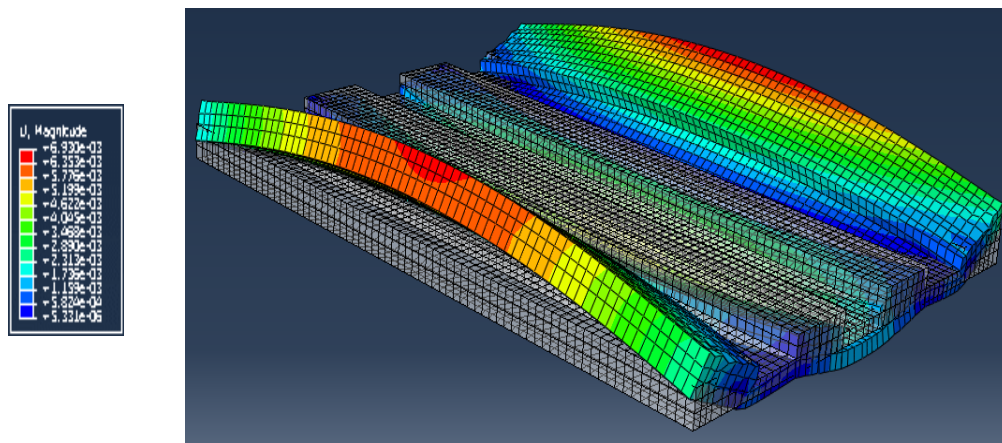
(c) 3rd Mode Shape (f = 13.3 Hz, Transverse Bending)

Figure 6.15. First Three Mode Shapes from Finite Element Analysis.
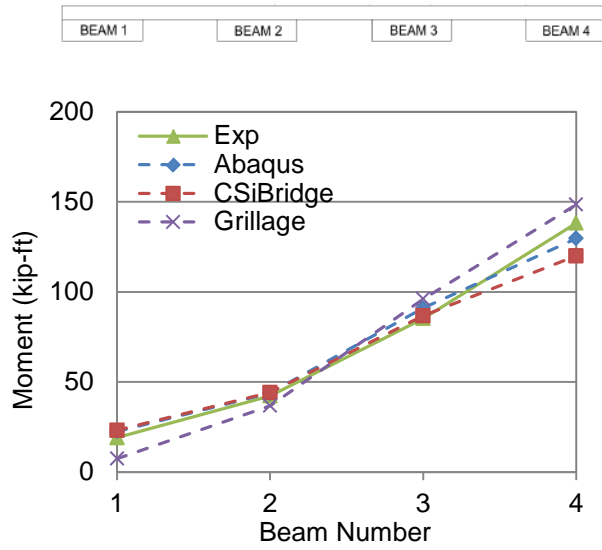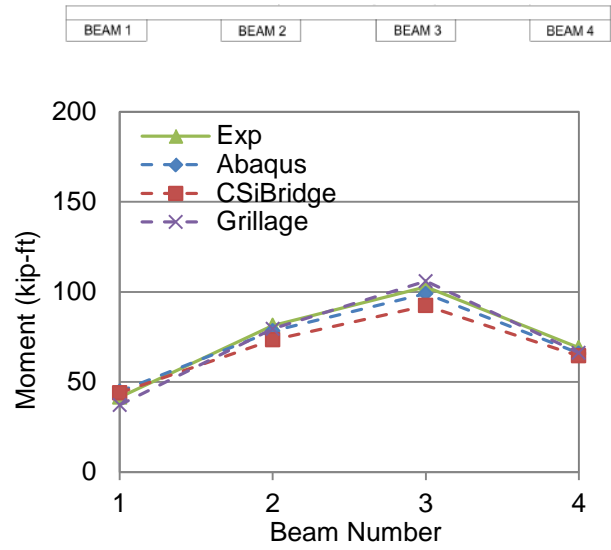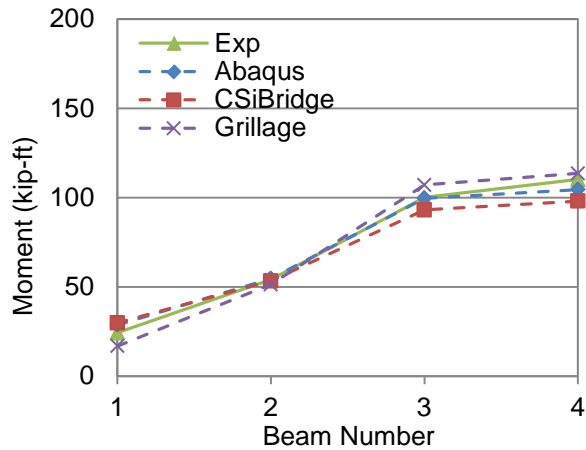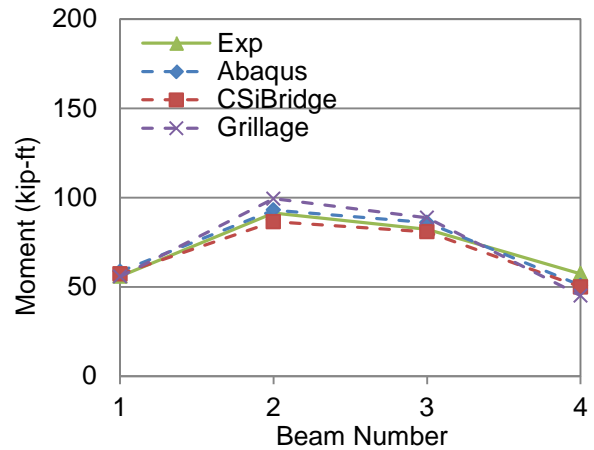
Figure 6.16. Comparison of Moment Values for Riverside Bridge.
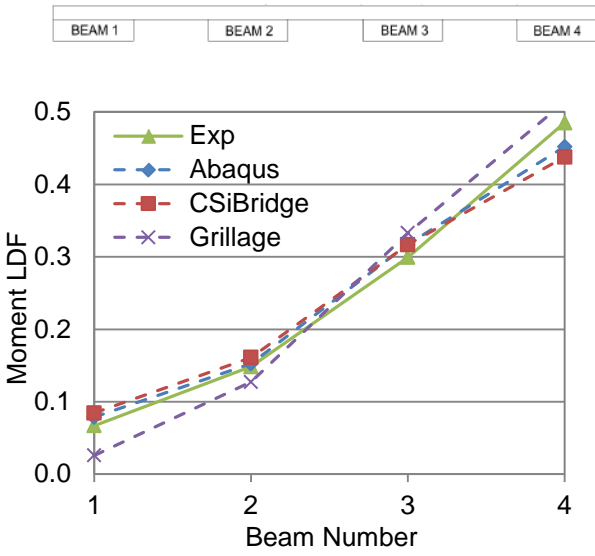
(a) Alignment 1
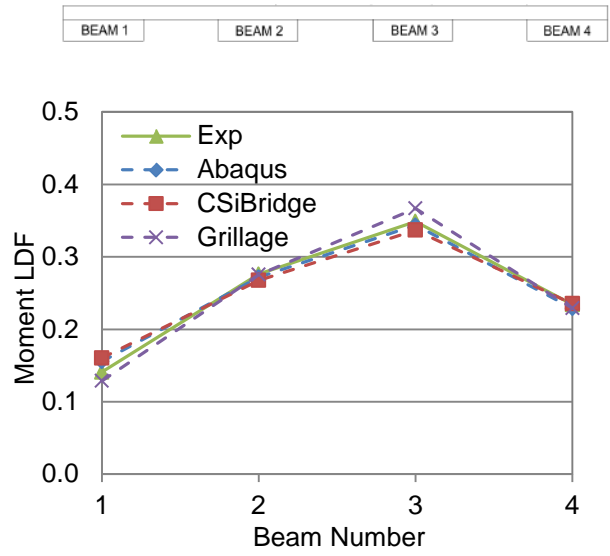
(b) Alignment 2
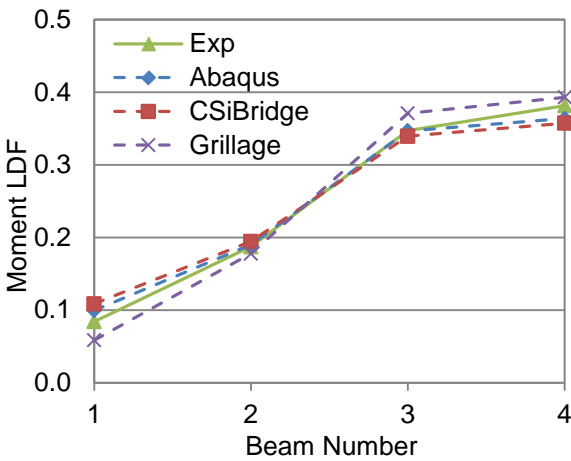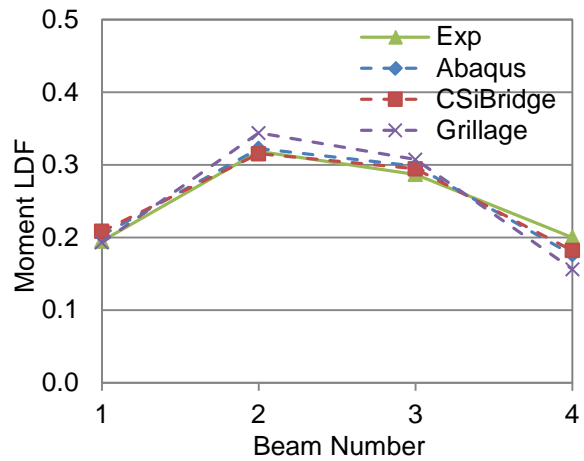
(c) Alignment 3

(d) Alignment 4

Figure 6.17. Comparison of Moment LDFs for Riverside Bridge.

193
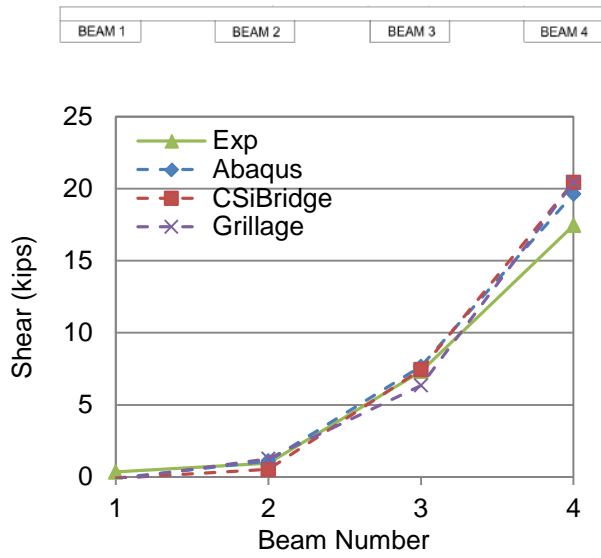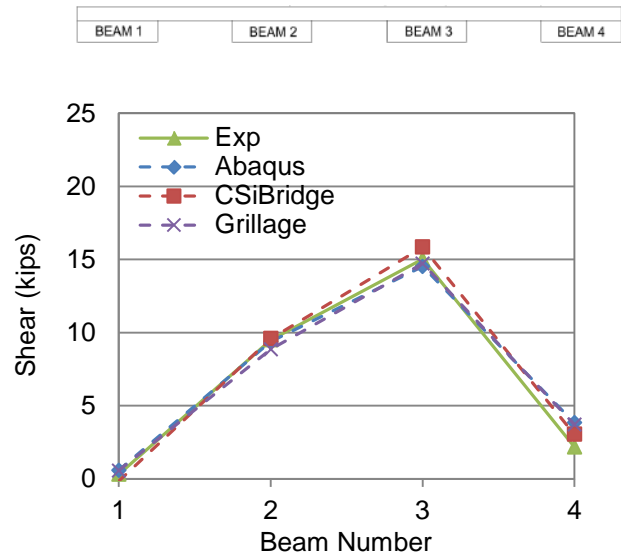
(a) Alignment 1
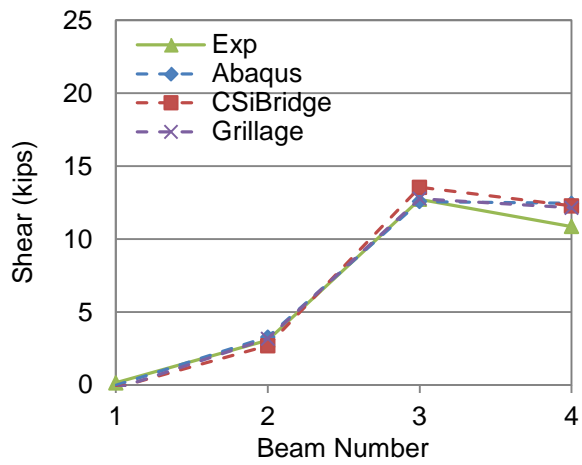
(b) Alignment 2
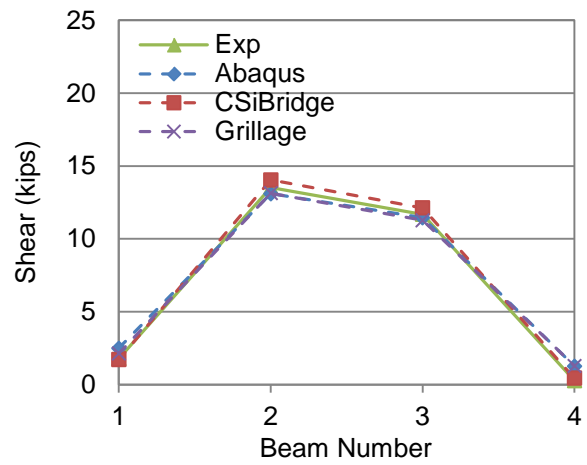
(c) Alignment 3

(d) Alignment 4

Figure 6.18. Comparison of Shear Forces for Riverside Bridge.

194
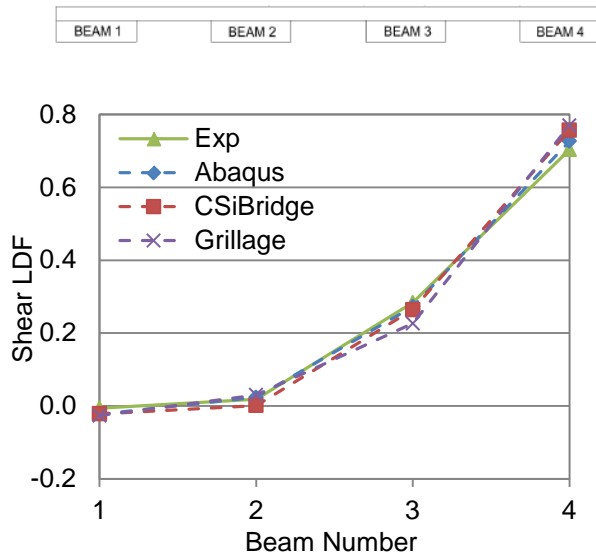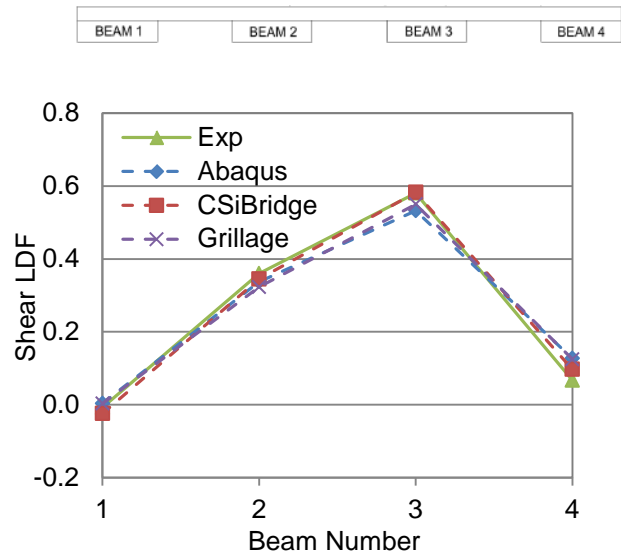
(a) Alignment 1
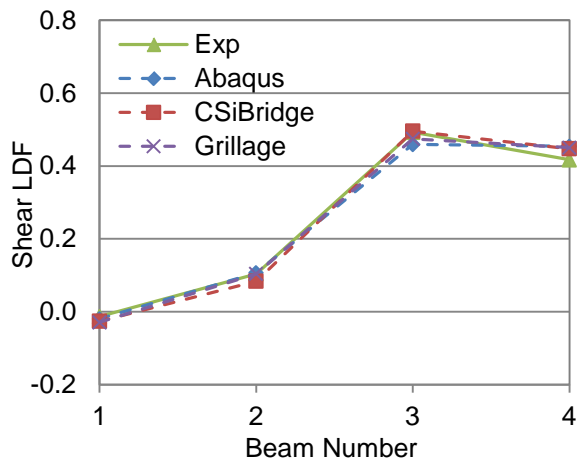
(b) Alignment 2
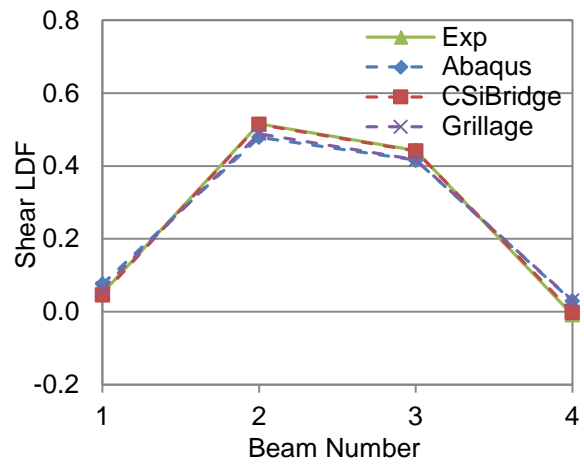
(c) Alignment 3

(d) Alignment 4

Figure 6.19. Comparison of Shear LDFs for Riverside Bridge.

Table 6.21 provides critical maximum moment and shear values for both exterior and interior slab beams. Table 6.22 lists the critical maximum LDF values and shows that both grillage and FEM LDFs are similar to the test results with differences generally less than 10 percent. By comparing the difference values listed in Table 6.21 and Table 6.22, it is shown that while the errors of the absolute force values may be significant in some cases, the LDF errors are smaller.

Table 6.21. Summary of Key Moment and Shear Values.

Load Case	Beam	Item	Test	Abaqus	CSiBridge	Grillage
Moment Critical	Exterior	Moment	138	130	120	149
		Difference	–	−6%	−13%	+8%
	Interior	Moment	100	100	93.1	107
		Difference	–	0%	−7%	+7%
Shear Critical	Exterior	Shear	17.0	19.1	19.9	19.9
		Difference	–	+13%	+18%	+17%
	Interior	Shear	14.5	14.0	15.4	14.2
		Difference	–	−3%	+6%	−2%

Table 6.22. Summary of Key LDF Results.

Load Case	Beam	Item	Test	Abaqus	CSiBridge	Grillage
Moment Critical	Exterior	LDF	0.49	0.45	0.44	0.51
		Difference	–	−8%	−10%	+4%
	Interior	LDF	0.35	0.35	0.34	0.37
		Difference	–	0%	−3%	+6%
Shear Critical	Exterior	LDF	0.70	0.73	0.76	0.77
		Difference	–	+4%	+8%	+9%
	Interior	LDF	0.58	0.55	0.58	0.55
		Difference	–	−5%	0%	−5%

6.6 ANALYTICAL RESULTS FOR THE US 69 BRIDGE

6.6.1 Static and Dynamic Properties

In the static load test of the US 69 Bridge, the deflection field within a half span was measured by string potentiometers installed on a grid pattern. By conducting the FEM analysis using the commercial software Abaqus, the research team was able to predict the deflection of the test bridge under vehicle loading. The experimental and computational maximum deflection values of each beam under vehicle loading are listed in Table 6.23. Figure 6.20 shows the deflection field calculated by the Abaqus software load case when the vehicle was parked along Alignment 1 (see Figure 5.10). The comparison of the experimental and numerical deflection values for selected beams in the same load case are shown in Figure 6.21.

From Table 6.23, it is clear that the FEM solution accurately captured the maximum live load deflections for all slab beams when the dump truck was parked along Alignment 1. In most cases, the predicted deflections were remarkably close and within 0.01 in. of the experimental values. Figure 6.21 shows that the deflection field was successfully determined by the FEM analysis.
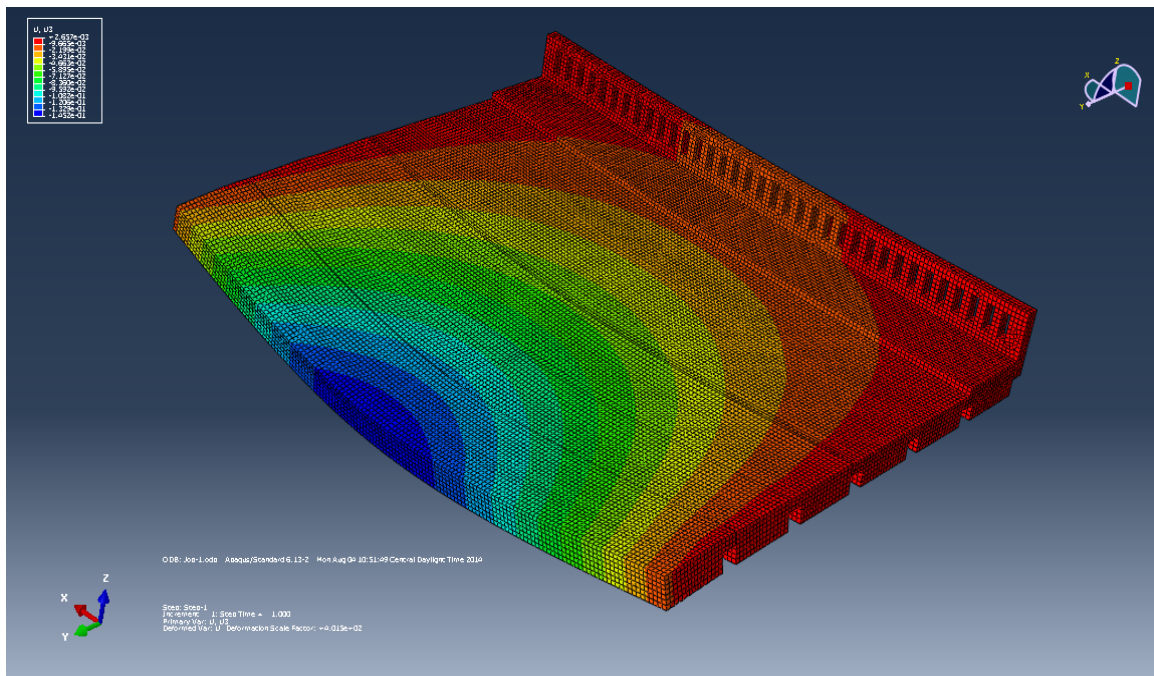
Figure 6.20. Deflection Field Calculated by Abaqus Software.

Table 6.23. Maximum Live Load Beam Deflections (US 69 Bridge)

Deflection	Beam 1	Beam 2	Beam 3	Beam 4	Beam 5	Beam 6
Test (in.)	0.009	0.017	0.028	0.050	0.078	0.105
FEM (in.)	0.011	0.021	0.036	0.058	0.086	0.114
Difference	0.002	0.004	0.008	0.008	0.008	0.009
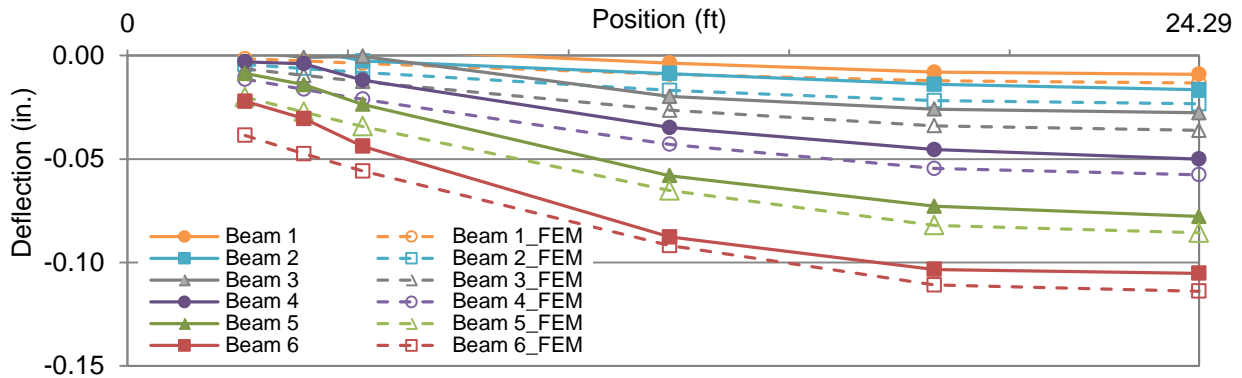
Figure 6.21. Comparison of Experimental and Numerical Deflection Values.

Dynamic properties (natural frequencies and mode shapes) were also obtained using accelerometer readings during the dynamic test of the US 69 Bridge. By conducting a frequency analysis, researchers determined the natural frequencies and mode shapes. Table 6.24 lists the natural frequencies calculated by Abaqus software and the comparison with experimentally observed results for the first three mode shapes. From Figure 6.22 and Table 6.24, it is evident that the natural frequencies obtained from the FEM analysis and test results are in good agreement, the differences being 4 percent or less. Also, the computational mode shapes are similar with the experimental observations shown in Figure 5.28. The satisfactory agreement for the deflection field and dynamic properties between computational and experimentally observed results validate the finite element model for the US 69 Bridge. The computational methods were therefore considered validated for further LDF analysis.

Table 6.24. Comparison of Experimental and Numerical Natural Frequencies.

Mode	1st (Hz)	2nd (Hz)	3rd (Hz)
Test	6.10	9.25	14.9
FEM	6.16	9.09	14.3
Ratio = FEM/Test	1.01	0.98	0.96
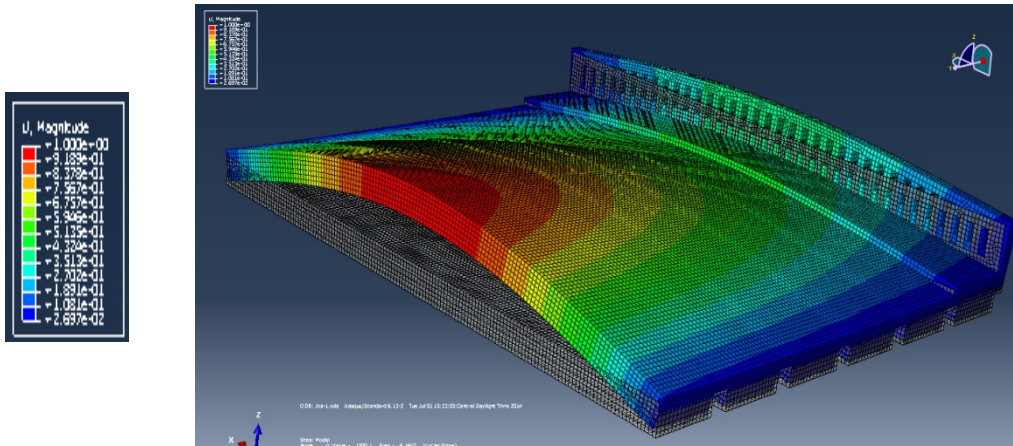
(a) 1st Mode Shape (*f* = 6.16 Hz, Longitudinal Bending)
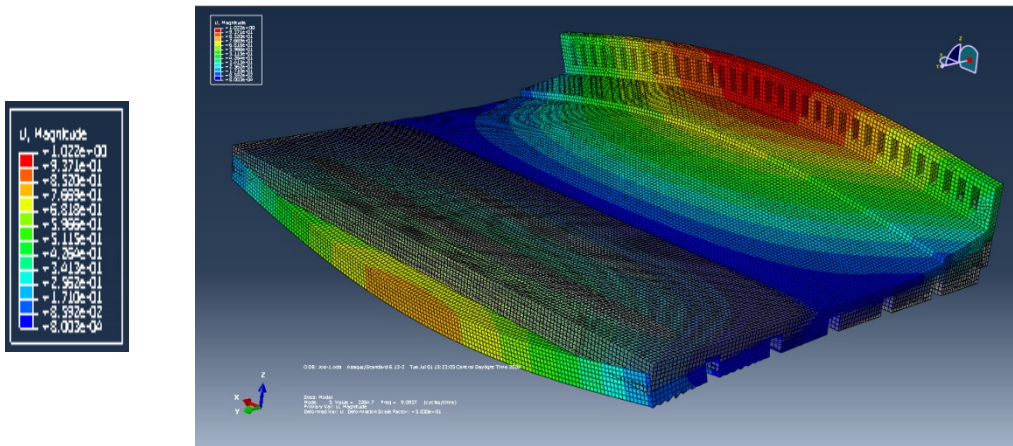
(b) 2nd Mode Shape (*f* = 9.09 Hz, Torsion)
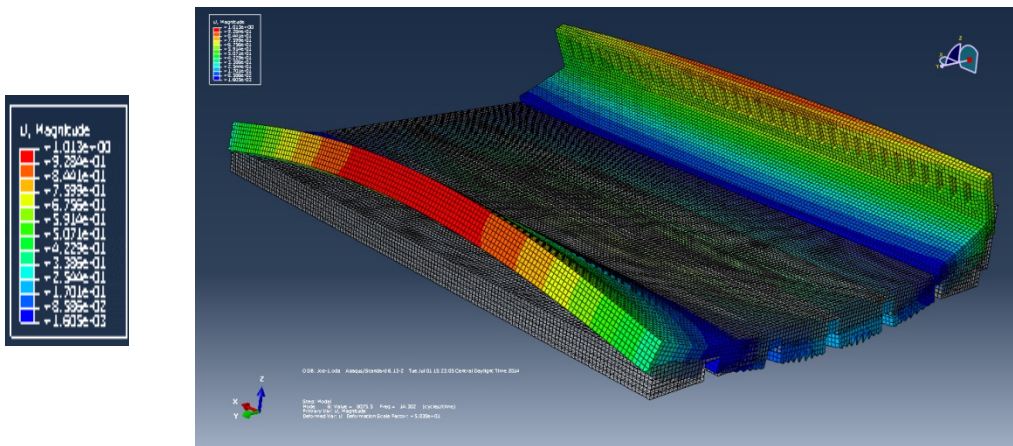
(c) 3rd Mode Shape (*f* = 14.3 Hz, Transverse Bending)

Figure 6.22. First Three Mode Shapes from Finite Element Analysis.

6.6.2 Results for Moment and Shear Predictions and the LDFs

Shear force and moment values were extracted from the FEM solutions, and then LDFs for all slab beams in different load cases were determined. The moment and shear values determined from field testing and computational analysis are shown in Figures 6.23 and 6.25. Figures 6.24 and 6.26, respectively, show the comparison for flexure and shear experimental and computational load distribution factor curves.

Figures 6.24 and 6.26 show that FEM results show promise when compared with observed field test results, and the LDF values obtained from two different FEM codes (Abaqus and CSiBridge) are close. While some differences exist between the grillage model and observed test values, especially in the moment critical load case when the dump truck was parked along Alignment 6, the LDFs from the grillage model are unconservative for the exterior beams.

Table 6.25 provides critical maximum moment and shear values for both exterior and interior slab beams. Critical maximum moment and shear LDF values are listed in Table 6.26. It is evident from Table 6.26 that the FEM LDF results are similar to the test results in most load cases. However, for the east exterior slab beam that has the sidewalk and guardrail, the CSiBridge value is 40 percent higher than the test result. For the grillage model, the moment LDF for the east exterior beam is unconservative (−10 percent) compared with the experimental value. By comparing the difference values listed in Tables 6.25 and 6.26, it is shown that while the errors of the absolute values may be significant in some cases, the LDF errors are smaller.

Table 6.25. Summary of Key Moment and Shear Values.

Load Case	Beam Location	Item	Test	Abaqus	CSiBridge	Grillage
Moment Critical	Exterior (West Edge)	Moment (kip-ft)	120.8	141.8	145.8	179.7
		Difference	–	+17%	+21%	+49%
	Interior	Moment (kip-ft)	101.3	118.9	118.2	141.9
		Difference	–	+17%	+17%	+40%
	Exterior (East Edge)	Moment (kip-ft)	275.9	234.4	259.0	232.4
		Difference	–	−15%	−6%	−16%
Shear Critical	Exterior (West Edge)	Shear (kips)	24.2	25.1	23.8	24.9
		Difference	–	+4%	−2%	+3%
	Interior	Shear (kips)	14.0	16.0	14.2	14.2
		Difference	–	+15%	+2%	+1%
	Exterior (East Edge)	Shear (kips)	6.9	8.9	9.1	8.6
		Difference	–	+30%	+32%	+26%

Table 6.26. Summary of Key LDF Results.

Load Case	Beam Location	Item	Test	Abaqus	CSiBridge	Grillage
Moment Critical	Exterior (West Edge)	LDF	0.28	0.28	0.29	0.35
		Difference	–	0%	+4%	+25%
	Interior	LDF	0.24	0.24	0.24	0.28
		Difference	–	0%	0%	+17%
	Exterior (East Edge)	LDF	0.49	0.47	0.53	0.44
		Difference	–	−4%	+8%	−10%
Shear Critical	Exterior (West Edge)	LDF	0.61	0.64	0.61	0.66
		Difference	–	+5%	0%	+8%
	Interior	LDF	0.36	0.40	0.38	0.35
		Difference	–	+11%	+6%	−3%
	Exterior (East Edge)	LDF	0.20	0.23	0.28	0.23
		Difference	–	+15%	+40%	+15%
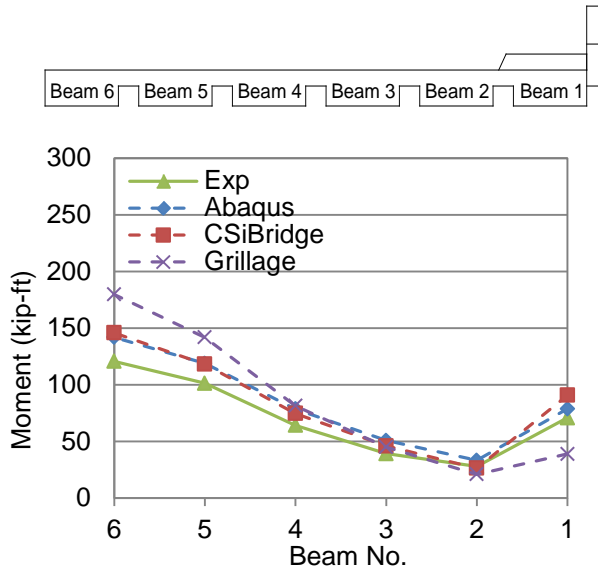
(a) Alignment 1
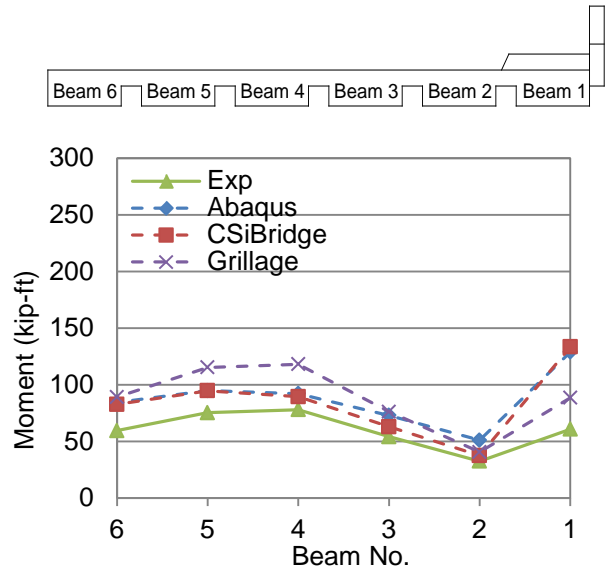
(b) Alignment 2
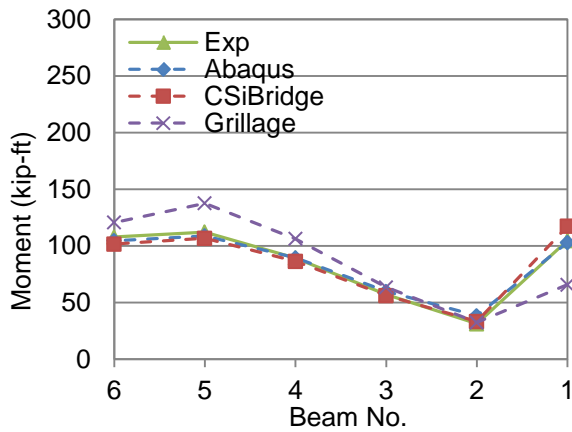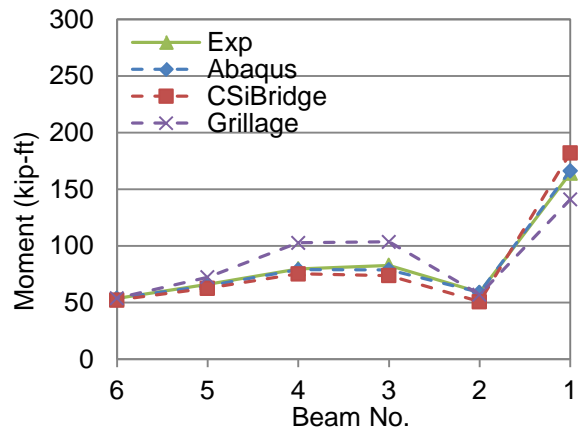
(c) Alignment 5
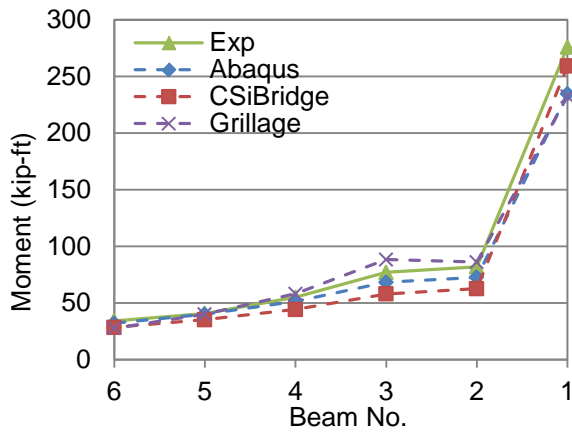
(d) Alignment 6

(e) Alignment 7

Figure 6.23. Comparison of Experimental and Numerical Moment Values.
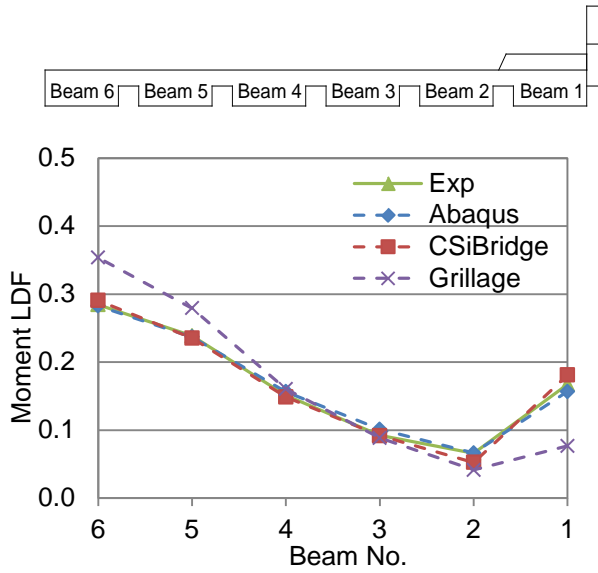
(a) Alignment 1
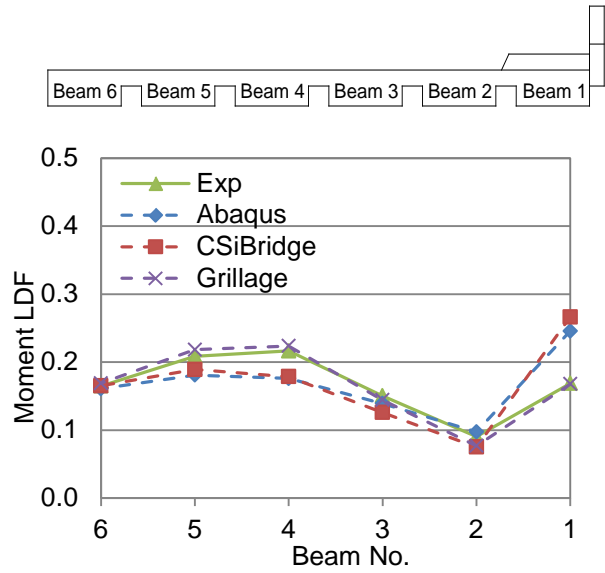
(b) Alignment 2
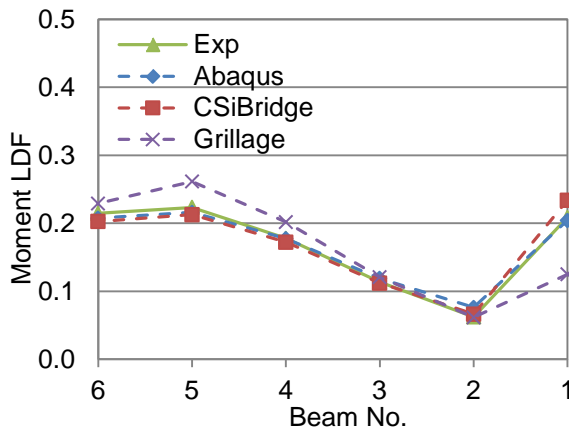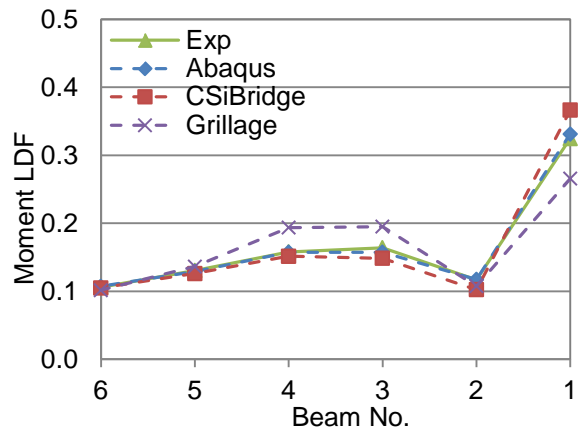
(c) Alignment 5
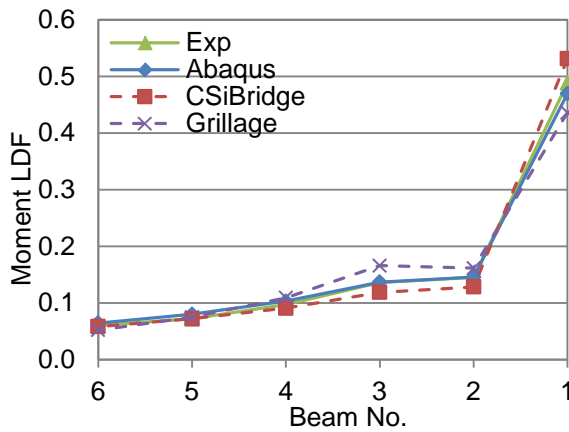
(d) Alignment 6

(e) Alignment 7

Figure 6.24. Comparison of Experimental and Numerical Moment Distribution Factors.
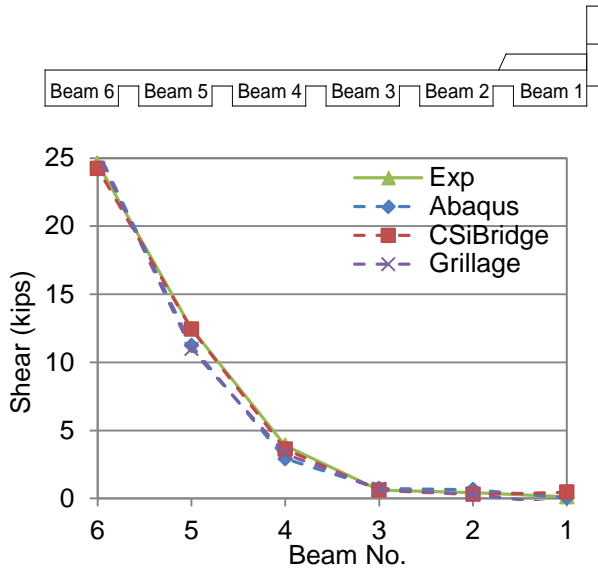
(a) Alignment 1
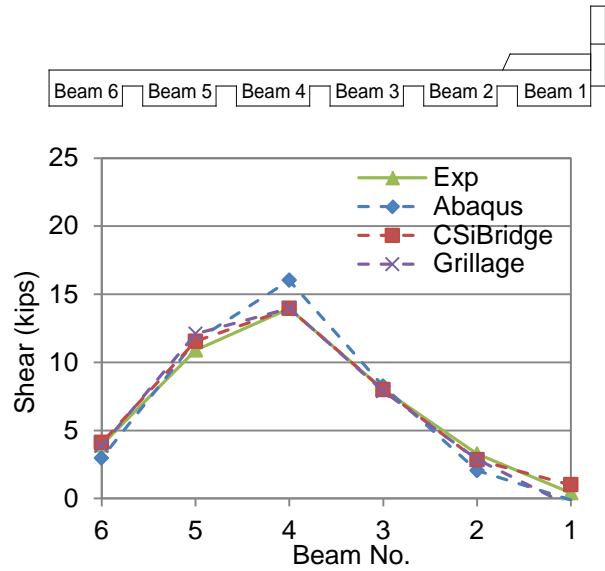
(b) Alignment 2
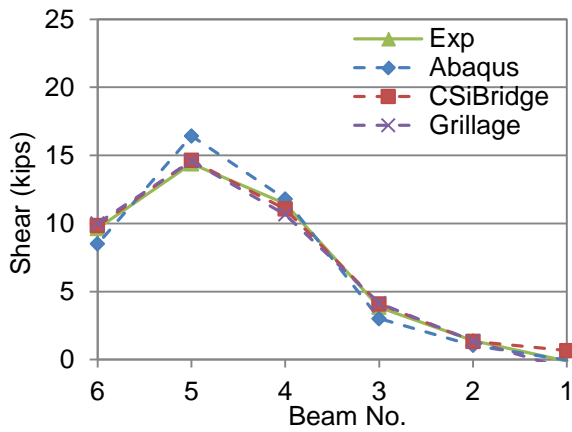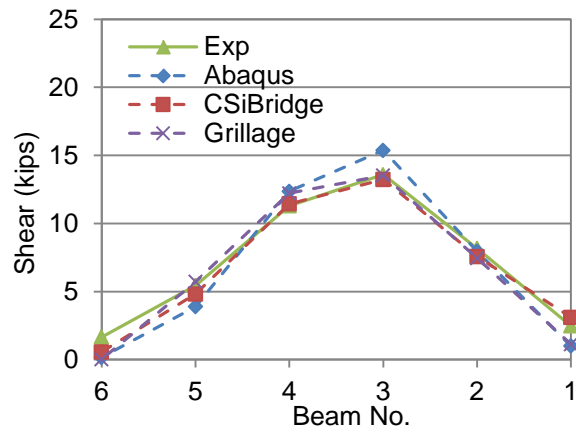
(c) Alignment 5
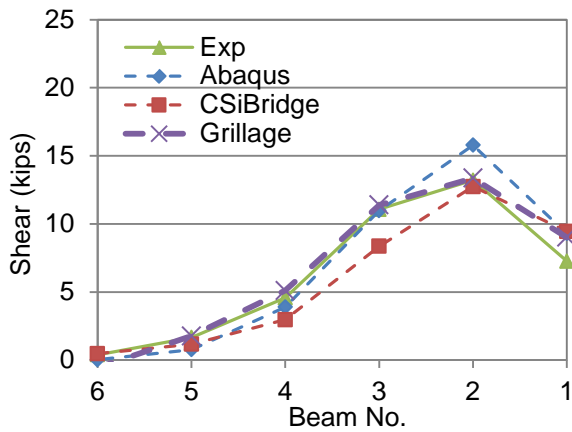
(d) Alignment 6

(e) Alignment 7

Figure 6.25. Comparison of Experimental and Numerical Shear Values.
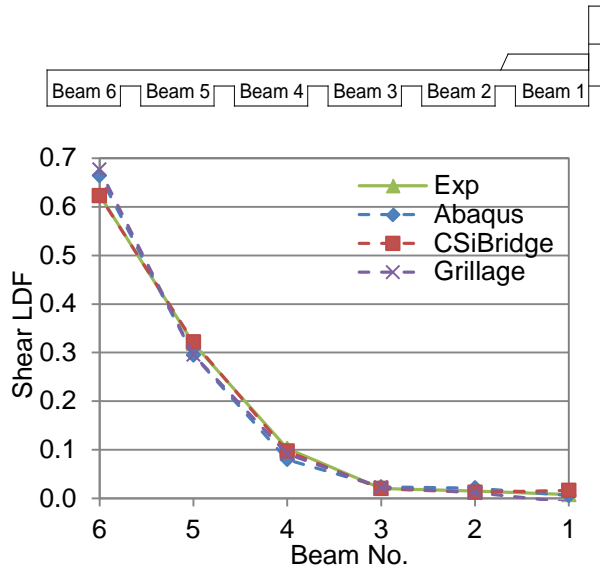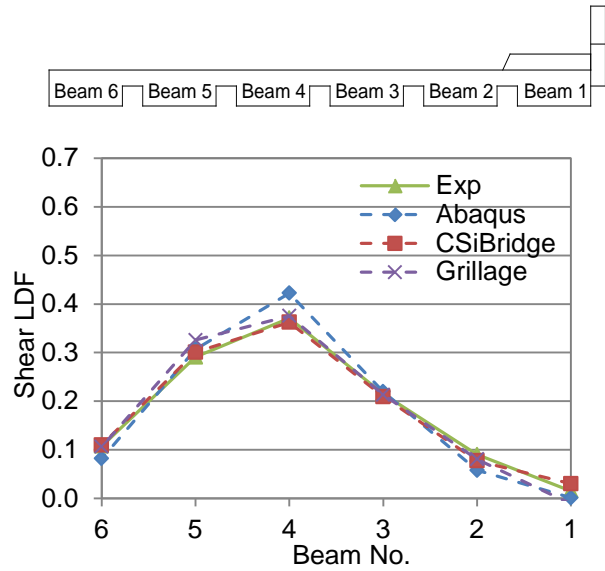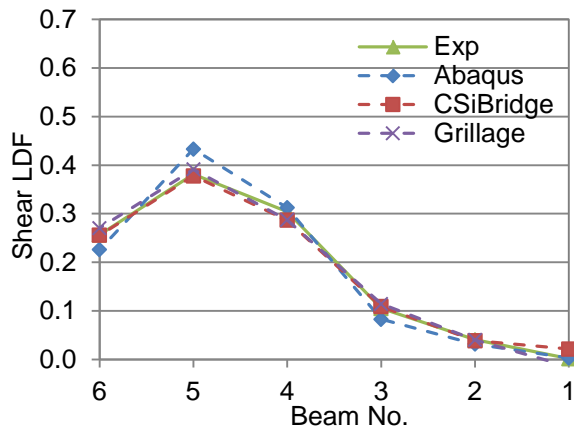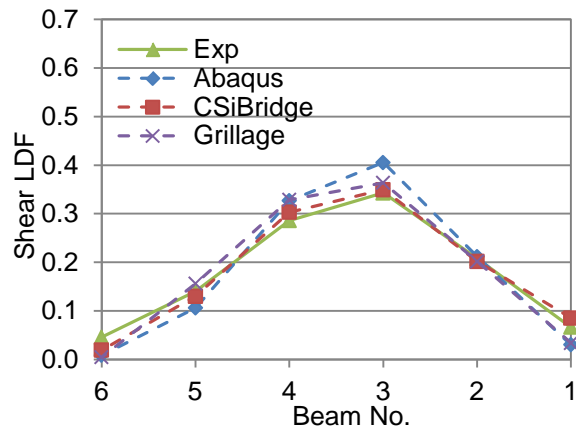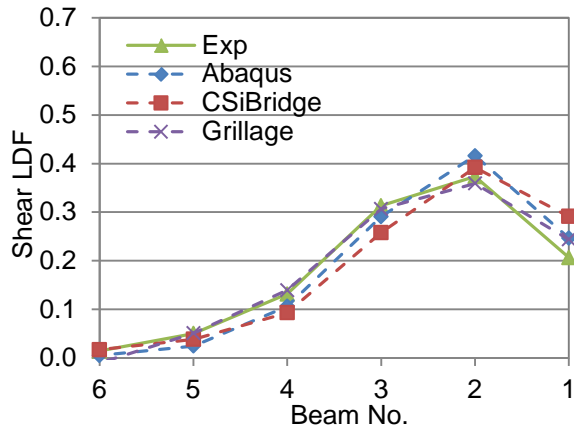
Figure 6.26. Comparison of Experimental and Numerical Shear Distribution Factors.

6.7   KEY FINDINGS FROM THE COMPUTATIONAL MODELING STUDIES

The computational models were developed for a spread box beam bridge (Drehersville Bridge) and the two tested spread slab beam bridges (Riverside and US 69 Bridges) applying different analysis methods (grillage and FEM) and utilizing different commercial software. By comparing the computational results with experimental values, the following conclusions may be drawn:

1. For the spread box beam bridge, the grillage model generally gives reasonable estimates of the measured girder moments and LDFs. It is reasonable to simplify this type of bridge as several major longitudinal grillage members due to the greater box beam depth.

2. For the two spread slab beam bridges tested as part of the present research, the FEM solutions provide moderately accurate deflections, but given the small magnitude of deflection, it is difficult to discriminate where the errors arise—whether they are predominantly from measurement error or modeling simplifications.

3. The computed natural frequencies when compared to observed test results for the two tested bridges are remarkably close. Therefore, the FEM models are considered valid for further LDF analysis.

4. The FEM LDFs for the two tested spread slab beam bridges are similar to the observed test values with some small differences. With careful development of the grillage model, this simplified analysis method also predicts the structural behavior well and may be utilized for design purposes.

5. The general conclusion from this dual experimental and computational study is the following: given the ease of developing and applying advanced computational FEM solutions, one should use the best available analysis tools. Regardless of the claimed accuracy, it remains prudent to validate results against realistic experimental evidence, if available.

7 LOAD DISTRIBUTION FACTORS FOR SPREAD SLAB BEAM BRIDGES

7.1 INTRODUCTION

The complexity of calculating the design moment and shear actions for an individual bridge girder member under imposed live plus impact loads necessitates simplified analysis methods. The design moment and shear demands for an individual beam or bridge girder depend on various parameters such as the position of the load, the girder spacing, the span length, and the relative deck-to-girder stiffness. In order to simplify the design process, a longstanding methodology has evolved whereby a multiple girder bridge deck can be reduced to permit the structure to be a one-girder line or beam element. Thus, load distribution factors are applied to convert a single lane load into the actions necessary to design one girder and its associated deck slab.

The objective of the study described in this chapter is the empirical derivation of live load distribution factors (LDFs) for the interior and exterior girders of spread slab beam bridges for span lengths within the range of 31 to 51 ft. The proposed load distribution factor expressions were derived by analyzing 31 bridge models using the finite element method (FEM), with each bridge model having different geometries. Proposed equations were obtained using a methodology similar to that adopted for developing the LDF equations found in the *AASHTO LRFD Bridge Design Specifications* (AASHTO 2012). The parameters for the equations were chosen based on similar formulas used for spread box beam bridges in the current AASHTO LRFD Specifications (2012). FEM analyses were used to determine the effect of the chosen parameters, which are span length, beam spacing and beam depth.

7.2 FORMULATION OF LOAD DISTRIBUTION FACTORS

Equations for LDFs were developed following the same methodology as Zokaie et al. (1991) and Zokaie (2000) for the AASHTO LRFD Specifications (2012). The effects of each parameter on LDFs were assumed to be independent. It was also assumed that the effect of each parameter could be modeled using a power function of the general form ax^b, where x is the parameter under consideration, and a and b are the coefficients that were determined by nonlinear least

squares regression. After defining the separate effect of each parameter with a power curve, the combined effect was modeled by multiplying those power terms with a combined coefficient as follows:

$$g = a\left(L^{b_1}\right)\left(S^{b_2}\right)\left(d^{b_3}\right)(...)$$ (7.1)

where the coefficient a was determined once all the parameters (b_1, b_2, b_3) were established. The powers were calculated by studying the effect of each parameter with respect to the LDF when only that parameter was changed while keeping the other parameters constant.

The same procedure was applied to all key parameters in the equation. Then the common coefficient of the final equation (a) was calculated using the expression provided below.

$$a_i = \frac{g_i}{\left(L_i\right)^{b_1}\left(S_i\right)^{b_2}\left(d_i\right)^{b_3}}$$ (7.2)

Naturally, slightly different values of a_i will result for each specific (i^{th}) bridge design. Therefore, an average or a design value was adopted to form a universally applicable solution for the design space.

7.2.1 Methods for Developing LDFs

The research team used the following approach for developing LDFs:

1. A number of bridges were designed and modeled using the FEM.

2. Trucks were placed in numerous locations to obtain the most adverse combination for midspan moment and beam shear for interior and exterior slab beams. Cases for one and multiple lanes loaded were considered. Thus, for each bridge a matrix of LDFs was calculated and tabulated by group types.

3. For each bridge within a specific grouping, all parameters (except one) were held constant (the variable), and a log-log graph of LDF versus the key variable was plotted. A nonlinear least square best fit was found for the form $y = ax^b$, where in particular the parameter b, the slope of the log-log plot, was obtained, plotted, and recorded.

4. Once all results for the power indices were found, the value of a_i for the ith bridge was determined such that:

208

$$a_i = \frac{g_i}{(L)^{b_1} (S)^{b_2} (d)^{b_3}}$$ (7.3)

5. Collectively, when all values of a_i were plotted they formed a lognormal distribution for which the median of all a_i values (that is the geometric mean, $\tilde{a}$ or 50th percentile) gives the overall "best fit" for all bridges, and the lognormal standard deviation β_D describes the dispersion in the load demand actions.

6. Formulas were grouped by type, such as moments, shears, one-lane cases, and multiple-lane cases.

7. A reexamination of the resulting empirical formulas from Step 6 was made and then rationally adjusted to provide revised versions that are more compatible with companion formulas in the AASHTO LRFD Specifications (2012). The coefficients were adjusted so that there is approximately a non-exceedance probability of 5 percent (lognormal minus 1.65 lognormal standard deviations), and the final empirical design LDF formulas are mostly conservative (i.e., 95 percent chance of being conservative).

7.3 METHODS FOR THE MOMENT AND SHEAR DESIGN ACTIONS FOR A MATRIX OF SLAB BEAM BRIDGES

Live load distribution factors were evaluated for selected bridge geometries, using the results computed with FEM analysis. The parametric study was conducted to define the boundaries of the problem. The findings of the parametric study are summarized in Chapter 3. Alternative bridge geometries for derivation of LDF formulas were defined utilizing the results of the parametric study. Moment and shear LDFs for each bridge superstructure alternative were obtained from the FEM results. These LDFs were then compared with the distribution factors obtained from the proposed equations and the AASHTO LRFD Specifications (2012) spread box beam formulas.

7.3.1 Alternative Bridge Superstructure Geometries Considered

It is important to note the applicable range for each parameter under consideration. These are:

- Bridge Span: 31 ft $\leq L \leq$ 51 ft
- Beam Spacing: 6.5 ft $\leq S \leq$ 11 ft
- Beam Depth: 12 in. $\leq d \leq$ 21 in.

Spread beam bridges are one of the new TxDOT bridge superstructure types. TxDOT specifies a standard deck slab thickness of 8 in. for these bridges. Because slab thickness was considered constant for all bridges, the relative slab-to-beam stiffness was not directly considered, and slab beam thickness was considered as a parameter instead. One of the assumptions for the preliminary designs was to initially use spread box beam formulas for the 31 prototype designs. Therefore, it was presumed that the equations will include the same parameters as the spread box beam formulas, which are span length, beam spacing, and beam depth. The parameter selection is consistent with the findings of Zokaie et al. (1991) documented in the NCHRP 12-26 report. According to the sensitivity study Zokaie et al. conducted, the most sensitive parameter for LDF calculation is the girder spacing, S. The second most sensitive parameter is span length, L. The longitudinal stiffness parameter affects the LDF slightly. Figure 7.1 shows a generalized bridge with the key parameters.

Table 7.1 presents the design attributes chosen for the overall general design space. The prototype bridges are grouped by their principal parameters (L, S, and d) for the first 25 bridges. Thereafter, Bridges 26 through 31 are a general assortment of structures not included as part of the parameter identification but rather for general use in validating the identified parameters.

(a) Elevation View   (b) Section View
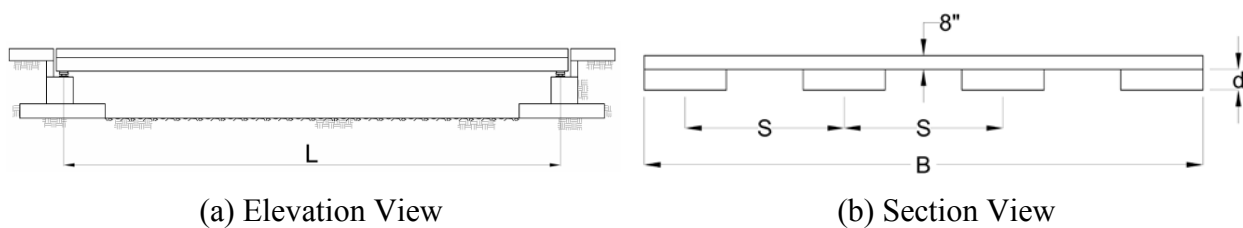
Figure 7.1. Key Geometric Parameters for Spread Slab Beam Bridges.

Table 7.1. Alternative Bridge Geometries for LDF Study.

No.	Number of Beams	Type of Beam	Bridge Width (ft)	Clear Beam Spacing (ft)	Beam Spacing (ft)	Span Length
L = Span Length Effect						
1	4	5SB15	34	4.67	9.67	45′-7″
2	4	5SB15	34	4.67	9.67	44′-7″
3	4	5SB15	34	4.67	9.67	41′-7″
4	4	5SB15	34	4.67	9.67	39′-7″
5	4	5SB15	34	4.67	9.67	37′-7″
6	4	5SB15	34	4.67	9.67	33′-7″
7	4	5SB15	34	4.67	9.67	29′-7″
S = Beam Spacing Effect						
8	4	5SB15	26	2.00	7.00	44′-7″
9	4	5SB15	28	2.67	7.67	44′-7″
10	4	5SB15	30	3.33	8.33	44′-7″
11	4	5SB15	32	4.00	9.00	44′-7″
12	4	5SB15	34	4.67	9.67	44′-7″
13	4	5SB15	36	5.33	10.33	44′-7″
14	4	5SB15	38	6.00	11.00	44′-7″
15	5	5SB15	40	3.75	8.75	44′-7″
16	5	5SB15	42	4.25	9.25	44′-7″
17	5	5SB15	44	4.75	9.75	44′-7″
18	5	5SB15	46	5.25	10.25	44′-7″
d = Beam Depth Effect						
19	4	5SB12.0	34	4.67	9.67	39′-7″
20	4	5SB13.5	34	4.67	9.67	39′-7″
21	4	5SB15.0	34	4.67	9.67	39′-7″
22	4	5SB16.5	34	4.67	9.67	39′-7″
23	4	5SB18.0	34	4.67	9.67	39′-7″
24	4	5SB19.5	34	4.67	9.67	39′-7″
25	4	5SB21.0	34	4.67	9.67	39′-7″
General—Verification and Evaluation (*L*, *S*, and *d*)						
26	4	4SB12	26	3.33	7.33	39′-7″
27	5	4SB12	30	2.50	6.50	40′-7″
28	4	4SB12	34	6.00	10.00	35′-7″
29	5	5SB15	34	2.25	7.25	49′-7″
30	5	4SB12	40	5.00	9.00	36′-7″
31	6	5SB15	40	2.00	7.00	49′-7″

All 31 bridges were modeled using a detailed FEM analysis. LDFs were calculated from the moment and shear forces obtained from these 31 models. The FEM analysis was performed using CSiBridge (2014) software. Each of the 31 single-span bridge superstructures was modeled using eight-node isotropic solid elements having three degrees of freedom at each node. A maximum of 12 in. mesh size was utilized throughout based on a mesh sensitivity study (see Chapter 6).

Table 7.2 lists the parameters adopted for the 31 prototype designs. Values of the design parameters were chosen in accordance with TxDOT standard design and construction practice.

Table 7.2. Bridge Parameters and Material Properties for LDF Study.

Parameter	Description/Value
Center-to-Center of Bearing Pad Span Length, L	29 ft 7 in. $\leq L \leq$ 49 ft 7 in.
Total Bridge Width, B	26 ft $\leq B \leq$ 46 ft
Center-to-Center Beam Spacing, S	6.5 ft $\leq S \leq$ 11 ft
Slab Beam Width	4 ft and 5 ft
Slab Beam Thickness	12 in. $\leq d \leq$ 21 in.
Deck Thickness, t_s	8 in.
Concrete Compressive Strength for Beams	$f_c' = 8.5$ ksi
Concrete Compressive Strength for Deck	$f_c' = 4$ ksi
Modulus of Elasticity of Slab Beam Concrete	$E_b = 4933$ ksi
Modulus of Elasticity of Deck Concrete	$E_d = 3834$ ksi
FEM Element Size	12 in.
Boundary Conditions	Only Vertical Degree of Freedom Fixed
Haunch Thickness, t_h	Neglected

7.3.2 Lane Loading Analysis

Figure 7.2 presents the various spatial alignments adopted for the bridge deck analysis. These alignments were arranged in such a fashion that the most adverse combination of moments and shears would be captured through rigorous analysis.

Many load cases were investigated using the AASHTO LRFD Specifications (2012) design truck loading and uniform lane loading. The CSiBridge software simulates vehicles moving along the bridge and gives the maximum moment or shear forces for each girder utilizing the influence line method. Thus, there was no need to define critical positions in the longitudinal direction.

The transverse positions were selected based on the allowable travel distances in the AASHTO LRFD Specifications (2012), field observations, and engineering judgment. Transverse positions of the lanes were defined by dividing the bridge into as many 12 ft wide lanes as possible. Vehicles and uniform lane loading were then allowed to move within their own lane for multiple-lane-loaded cases. For the one-lane-loaded case, the vehicle was permitted to pass between lanes. Therefore, a transverse loading position crossing the design lane could be defined for the single-lane-loaded case to achieve the most critical loading for an interior girder. In cases where vehicles moved within their own lanes, they were moved in the transverse direction in 2 ft increments.

Bridges that have a roadway width greater than or equal to 36 ft were considered to be three-lane bridges. A similar procedure was followed when determining the critical transverse positions for truck loading. Because only half of the bridge was analyzed due to symmetry, the third lane load was placed as closely as possible to the interior edge of the design lane. The AASHTO LRFD Specifications (2012) design lane load (0.64 kip/ft) was applied over a 6 ft width in the transverse direction for each loaded design lane.

Table 7.3 lists the computational results of the LDF values for Bridges 1 through 25. The most critical moment and shear LDFs were obtained for the multiple-lane-loaded interior beam case, and these cases are highlighted in Table 7.3.
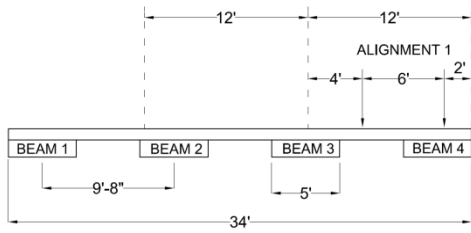
(a) One Lane Loaded—Exterior Beam
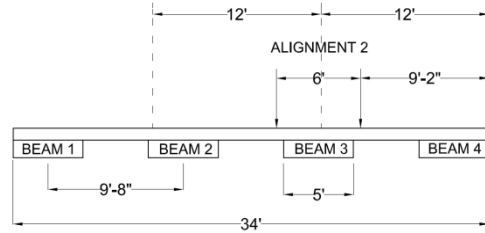
(b) One Lane Loaded—Interior Beam
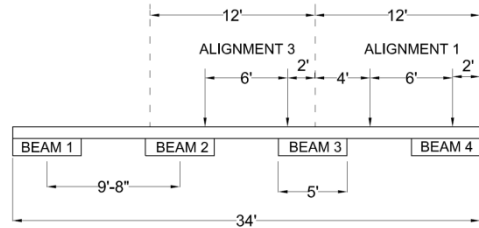
(c) Two Lanes Loaded—Exterior Beam
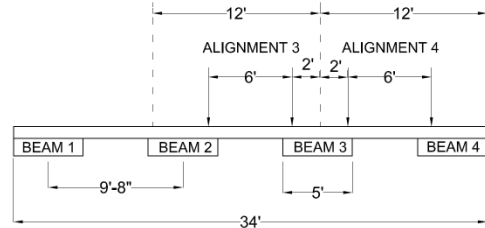
(d) Two Lanes Loaded—Interior Beam
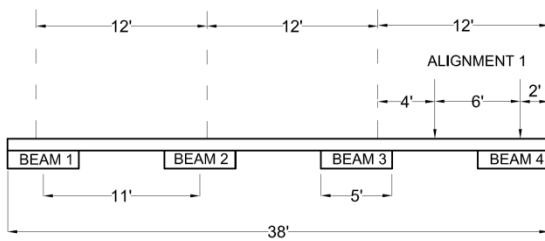
(e) One Lane Loaded—Exterior Beam
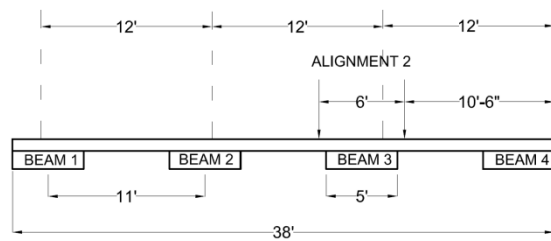
(f) One Lane Loaded—Interior Beam
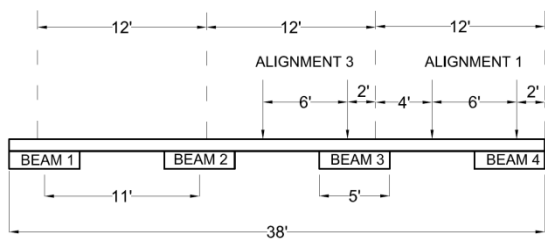
(g) Two Lanes Loaded—Exterior Beam
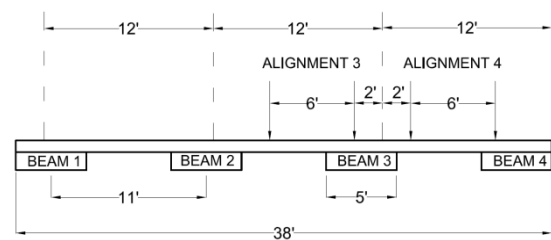
(h) Two Lanes Loaded—Interior Beam
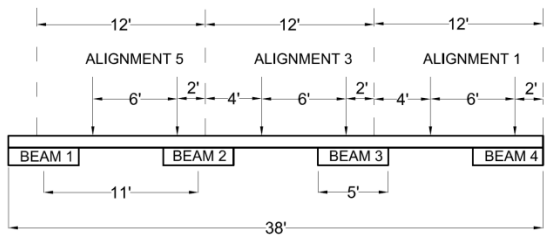
(i) Three Lanes Loaded—Exterior Beam
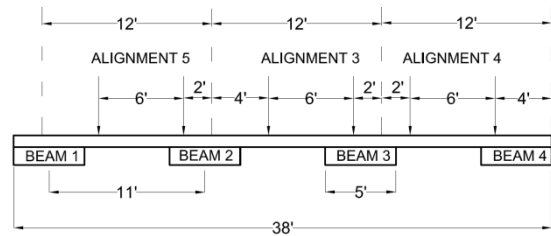
(j) Three Lanes Loaded—Interior Beam

Figure 7.2. Transverse Positions for Two-Lane and Three-Lane Bridges.

214

Table 7.3. LDFs for Evaluating the Key Parameters.

L = Span Length

No.	Width	No. of Beams	Beam Type	S (ft)	L	One Lane Loaded Interior Beam g_M	g_V	Exterior Beam g_M	g_V	Multiple Lanes Loaded Interior Beam g_M	g_V	Exterior Beam g_M	g_V
1	34'-0"	4	5SB15 d=15"	9'-8"	29'-7"	0.55	0.85	0.63	0.71	0.76	0.96	0.66	0.63
2					33'-7"	0.51	0.81	0.59	0.69	0.72	0.93	0.65	0.63
3					37'-7"	0.48	0.79	0.56	0.70	0.69	0.91	0.64	0.64
4					39'-7"	0.47	0.77	0.54	0.70	0.68	0.90	0.63	0.64
5					41'-7"	0.45	0.76	0.52	0.70	0.66	0.89	0.62	0.64
6					44'-7"	0.43	0.74	0.50	0.69	0.64	0.87	0.61	0.64
7					45'-7"	0.42	0.73	0.49	0.70	0.64	0.87	0.60	0.65

S = Beam Spacing

No.	L	No. of Beams	Beam Type	Bridge Width (ft)	S	g_M	g_V	g_M	g_V	g_M	g_V	g_M	g_V
8	44'-7"	4	5SB15 d=15	26	7'-0"	0.36	0.57	0.39	0.56	0.53	0.64	0.51	0.55
9				28	7'-8"	0.38	0.64	0.41	0.60	0.56	0.67	0.53	0.57
10				30	8'-4"	0.40	0.68	0.44	0.63	0.59	0.77	0.55	0.59
11				32	9'-0"	0.41	0.71	0.46	0.66	0.62	0.83	0.58	0.61
12				34	9'-8"	0.43	0.74	0.50	0.69	0.64	0.87	0.61	0.64
13				36	10'-4"	0.45	0.76	0.53	0.73	0.67	0.92	0.64	0.68
14				38	11'-0"	0.47	0.78	0.56	0.77	0.74	0.96	0.67	0.71
15		5		40	8'-9"	0.39	0.70	0.45	0.65	0.59	0.80	0.55	0.60
16				42	9'-3"	0.40	0.72	0.47	0.67	0.62	0.84	0.58	0.62
17				44	9'-9"	0.42	0.73	0.50	0.70	0.64	0.87	0.60	0.64
18				46	10'-3"	0.43	0.75	0.52	0.73	0.66	0.90	0.63	0.67

d = Beam Depth

No.	L	Bridge Width (ft)	Beam Spacing (ft)	No. Beams	Beam Type	d (in.)	g_M	g_V	g_M	g_V	g_M	g_V	g_M	g_V
19	39'-7"	34"-0"	9'-8"	4	5SB	12.0	0.45	0.74	0.52	0.69	0.66	0.87	0.62	0.64
20						13.5	0.46	0.75	0.53	0.69	0.67	0.88	0.63	0.64
21						15.0	0.47	0.77	0.54	0.70	0.68	0.90	0.63	0.64
22						16.5	0.48	0.79	0.55	0.70	0.69	0.91	0.63	0.63
23						18.0	0.49	0.80	0.57	0.71	0.70	0.93	0.64	0.63
24						19.5	0.50	0.81	0.58	0.71	0.71	0.94	0.64	0.63
25						21.0	0.51	0.82	0.59	0.71	0.72	0.95	0.65	0.63

7.4 EMPIRICAL MODELING OF THE LDF RESULTS

Table 7.4 presents the results of the powers (b_1, b_2, b_3) fitted in accordance with the least square analysis in log-log space. The results were also plotted in log-log graphs, provided in Figure 7.3 through Figure 7.5.

The effect of each chosen key parameter (span length, beam spacing, and beam depth), on live load distribution factors was investigated. Load distribution factors for all eight formulas, for each girder, and for each of the 31 bridge geometries were obtained from the FEM models and used for developing the empirical LDFs for design applications. The maximum moment and shear values for interior and exterior girders were obtained from the FEM analysis. These moment and shear forces for one-, two-, and three-lane-loaded cases were multiplied with the AASHTO LRFD Specifications (2012) multiple presence factors of 1.2, 1.0, and 0.85, respectively. Then the LDFs for all eight formulas were calculated by dividing the maximum moment (or shear value) with the moment (or shear value) of an isolated simply supported beam having the same span length.

Table 7.4. Powers of the Fitted Curves.

			Formula	Span, L		Spacing, S		Beam Depth, d	
				b_1	R^2	b_2	R^2	b_3	R^2
Moment LDF	Interior Beam	One Lane Loaded	1	-0.6125	0.996	0.5208	0.923	0.2166	0.992
		Multiple Lanes Loaded	2	-0.4002	0.994	0.6537	0.946	0.1393	0.993
	Exterior Beam	One Lane Loaded	3	-0.6108	0.985	0.7976	0.984	0.2011	0.997
		Multiple Lanes Loaded	4	-0.2211	0.974	0.5886	0.940	0.0744	0.999
Shear LDF	Interior Beam	One Lane Loaded	5	-0.3296	0.999	0.6626	0.954	0.1967	0.999
		Multiple Lanes Loaded	6	-0.2337	0.999	0.9337	0.977	0.1616	1.000
	Exterior Beam	One Lane Loaded	7	-0.0329	0.206	0.6862	0.993	0.0663	0.999
		Multiple Lanes Loaded	8	0.0662	0.890	0.5758	0.96	0.0324	0.995

7.4.1 Sensitivity of LDF to Span Length, L

Figure 7.3 presents the effect of span length, L, on LDFs. One of the most important parameters influencing the LDFs is the span length of the bridge. In order to evaluate the variation of the

LDF with changing span length, all other parameters were kept constant and the span length was changed between 29 ft 7 in. to 45 ft 7 in. The complete list of the seven bridge superstructures is provided in Table 7.1 and labeled with bridge numbers 1 to 7. The calculated LDF values for these seven bridge decks are listed in Table 7.3, where g_M is the moment LDF and g_V is the shear LDF. The LDF values listed in Table 7.3 were also plotted on a log-log graph to provide visual examination of the effect of the span length on the LDFs.

7.4.2   Sensitivity of LDF to Beam Spacing, S

Figure 7.4 depicts in log-log space the sensitivity of beam spacing, S, on LDFs. LDFs are most sensitive to the changes in beam spacing. A total of 11 superstructure geometries were modeled to evaluate the variation of LDFs with beam spacing. The investigation of the effect of beam spacing on LDFs revealed that the relationship between beam spacing and LDFs was more prominent for all the LDF cases except the one-lane-loaded moment in interior beams. A complete list of maximum LDF values is summarized in Table 7.3.

7.4.3   Sensitivity of LDF to Beam Depth, d

Figure 7.5 shows how variation in beam depth, d, affects the LDFs. Although there are only two different standard slab beam depths, 12 in. and 15 in., seven different beam depths were analyzed to develop more data points to fit a power curve and gain a better understanding of the effect of beam depth. A total of seven hypothetical beam depths between 12 in. to 21 in. were introduced, and seven bridge superstructures were modeled for investigating the influence of beam depth on LDFs. As discussed earlier, beam depth somewhat affects the LDF but is not as prominent as beam spacing and span length. An investigation of the graphs for the sensitivity of beam depth shows that the LDF values for shear in an exterior beam are not sensitive to the beam depth. The slopes of these curves are almost zero. All eight LDF values for each bridge analyzed are summarized in Table 7.3.
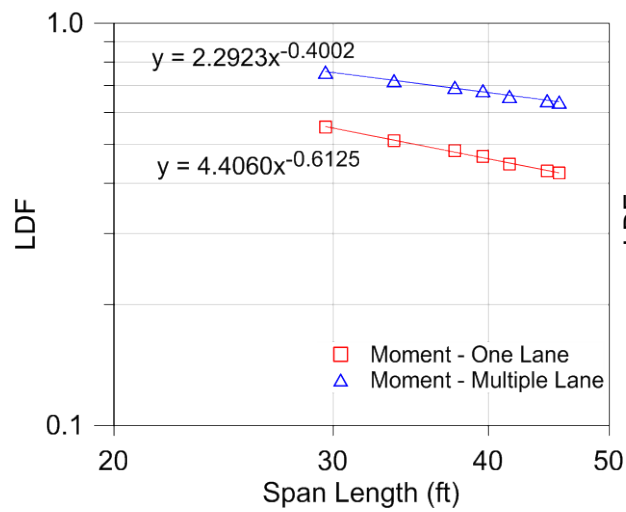
(a) Interior Beam Moment LDF
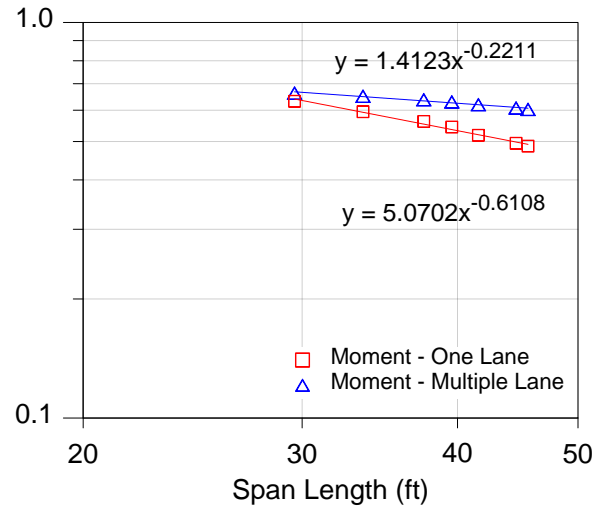
(b) Exterior Beam Moment LDF
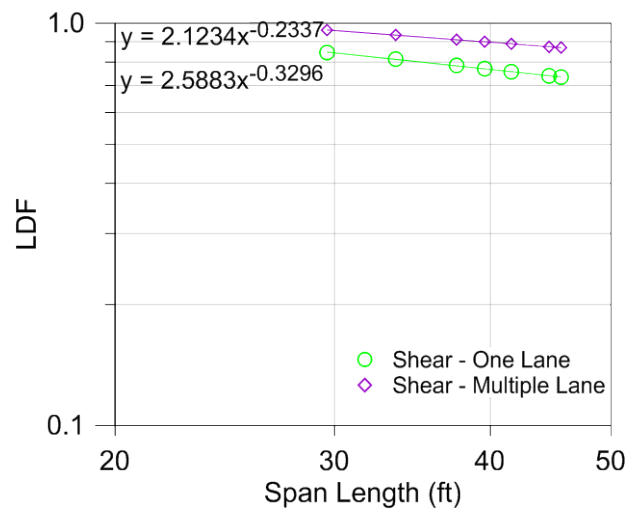
(c) Interior Beam Shear LDF
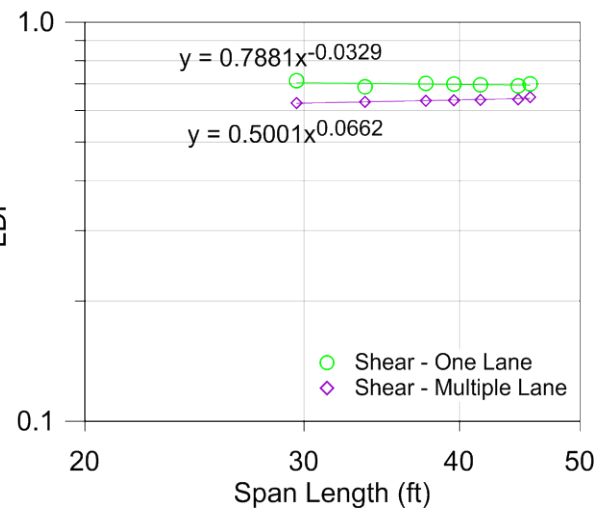
(d) Exterior Beam Shear LDF

Figure 7.3. Effect of Span Length on Load Distribution Factor.
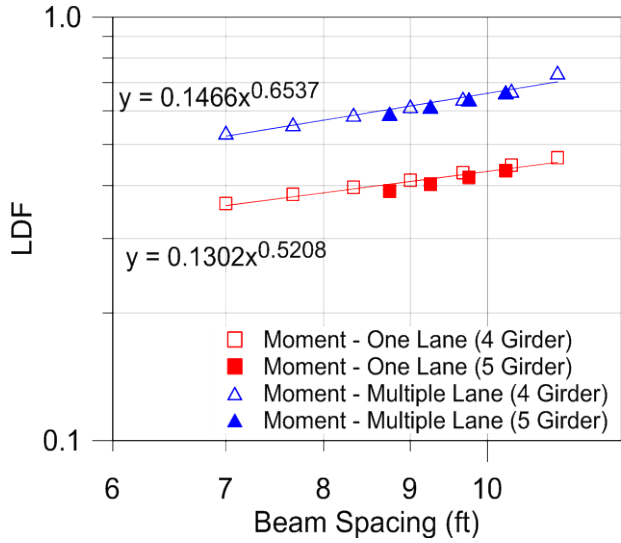
218

(a) Interior Beam Moment LDF

(b) Exterior Beam Moment LDF

(c) Interior Beam Shear LDF

(d) Exterior Beam Shear LDF

Figure 7.4. Effect of Beam Spacing on Load Distribution Factor.
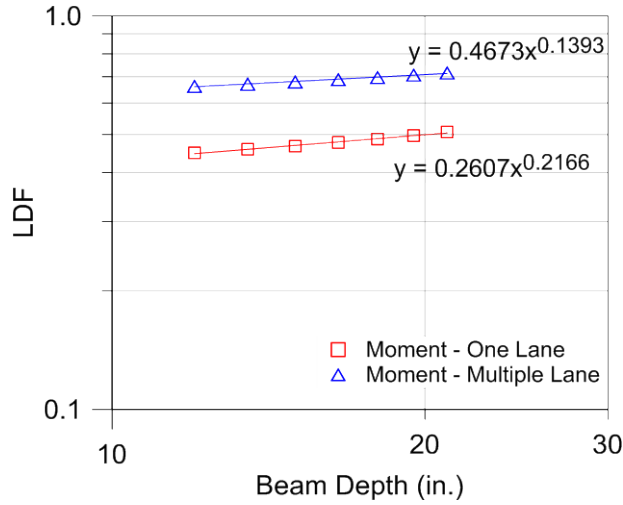
(a) Interior Beam Moment LDF (b) Exterior Beam Moment LDF
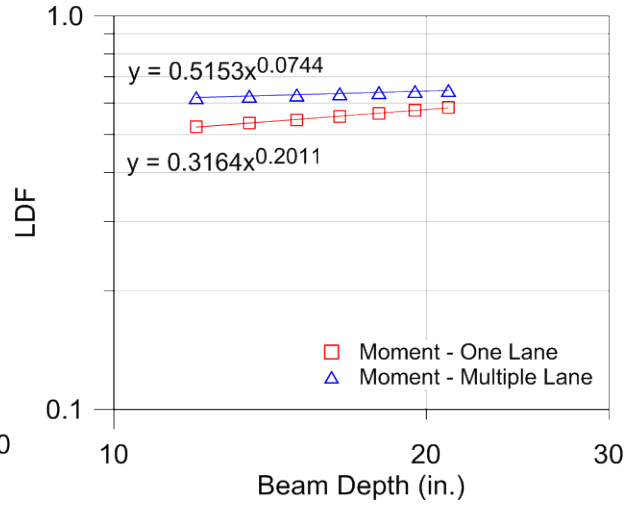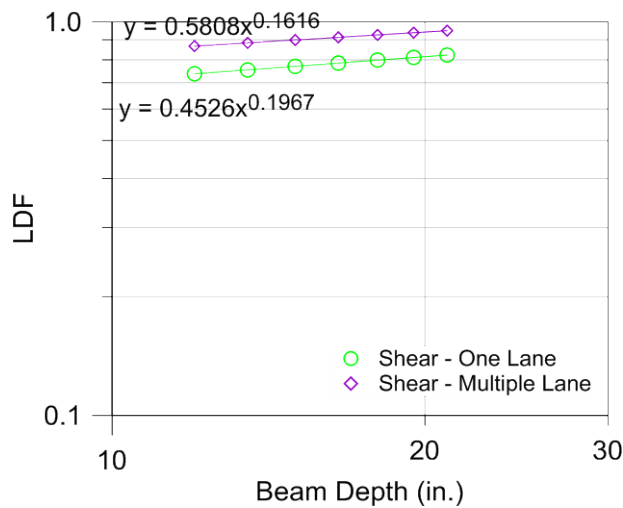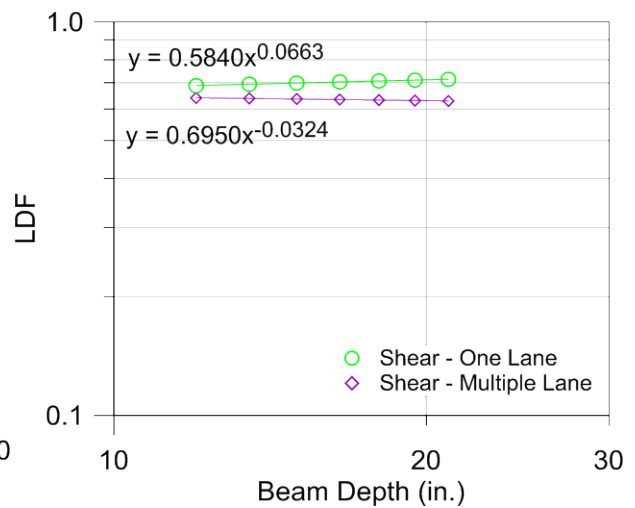
(c) Interior Beam Shear LDF (d) Exterior Beam Shear LDF

Figure 7.5. Effect of Beam Depth on Load Distribution Factor.

220

7.5   DERIVATION OF LDF FORMULAS

Table 7.5 lists all the coefficients calculated for the 31 bridges and eight LDF formulas. The columns corresponding to critical moment and shear LDFs are shaded. The previous section documents how the powers of the parameters were determined by fitting a power curve through for each one of the eight LDF cases. A total of 25 bridges were modeled using FEM in order to find the powers of the key parameters. Because some assumptions were made and some parameters were neglected (such as beam width), it was crucial to verify the accuracy of the assumptions and the proposed equations using other geometries and types of slab beams than the ones used for obtaining the power curves. For that purpose, six more bridge superstructures were defined; four of them utilize 4SB12 slab beams, and the other two have the longest span length achievable using a spread slab beam configuration. The geometries of these additional bridge superstructures are listed in Table 7.1. The LDFs obtained from an accurate FEM analysis for these six bridges were also included in the calculation of coefficients for new equations.

Live load distribution factors for each one of the 31 bridge superstructures for all eight LDF cases, including moment in interior and exterior beams and shear in interior and exterior beams, were obtained and are listed in Appendix C. These FEM values were also compared with those obtained from the AASHTO LRFD Specifications (2012) spread box beam formulas, theoretical LDFs, and new proposed LDF equation values. The equations for these LDF values are provided in Table 7.6.

The calculation of the *a* coefficient for one of the LDF cases is explained herein. For a given bridge superstructure, the coefficient *a* can be calculated using Equation (7.3). This calculation results in 31 different *a* coefficients that are close but slightly different from each other. The median (average of $\ln a_i$ values) of these coefficients was used as an initial estimate, while the lognormal standard deviation, β, was used as a measure of scatter of the results. Note that when $\beta < 0.2$, the lognormal standard deviation was approximately equal to the coefficient of variation for a normal distribution. Note also that the two distributions have a similar shape and either could be used, but the lognormal distribution is the most appropriate due to their linear nature when plotted on log-log paper. The final *a* coefficient for that specific LDF case was calculated to minimize the lognormal standard deviation, β. This procedure was repeated for all eight LDF cases for calculating the coefficients of the theoretical equations. The theoretical equations derived using these calculated coefficients and the powers of the parameters that were calculated during the sensitivity study are listed in Table 7.6.

Table 7.5. Coefficients of the Formulas for Each Bridge.

Domain	Case No.	L (ft)	S (ft)	d (in.)	a_i Values for Equations							
					1	2	3	4	5	6	7	8
Span Length	1	29.58	9.67	15.0	0.75	0.46	0.48	0.30	0.34	0.16	0.14	0.15
	2	33.58	9.67	15.0	0.75	0.46	0.48	0.30	0.34	0.16	0.14	0.15
	3	37.58	9.67	15.0	0.76	0.46	0.49	0.31	0.34	0.16	0.14	0.15
	4	39.58	9.67	15.0	0.76	0.46	0.49	0.31	0.34	0.16	0.14	0.15
	5	41.58	9.67	15.0	0.75	0.46	0.48	0.30	0.34	0.16	0.14	0.15
	6	44.58	9.67	15.0	0.75	0.46	0.48	0.30	0.34	0.16	0.14	0.15
	7	45.58	9.67	15.0	0.75	0.46	0.48	0.30	0.34	0.16	0.14	0.15
Beam Spacing	8	44.58	7.00	15.0	0.75	0.47	0.49	0.31	0.32	0.16	0.14	0.15
	9	44.58	7.67	15.0	0.75	0.46	0.48	0.30	0.34	0.16	0.14	0.15
	10	44.58	8.33	15.0	0.75	0.46	0.48	0.30	0.34	0.17	0.14	0.15
	11	44.58	9.00	15.0	0.75	0.46	0.47	0.30	0.34	0.17	0.14	0.15
	12	44.58	9.67	15.0	0.75	0.46	0.48	0.30	0.34	0.16	0.14	0.15
	13	44.58	10.33	15.0	0.75	0.46	0.48	0.31	0.33	0.16	0.14	0.15
	14	44.58	11.00	15.0	0.76	0.48	0.49	0.31	0.33	0.16	0.14	0.15
	15	44.58	8.75	15.0	0.71	0.45	0.47	0.29	0.34	0.17	0.14	0.15
	16	44.58	9.25	15.0	0.72	0.45	0.47	0.29	0.34	0.16	0.14	0.15
	17	44.58	9.75	15.0	0.73	0.45	0.48	0.30	0.33	0.16	0.14	0.15
	18	44.58	10.25	15.0	0.74	0.46	0.48	0.30	0.33	0.16	0.14	0.15
Beam Depth	19	39.58	9.67	12.0	0.76	0.46	0.49	0.31	0.34	0.16	0.14	0.15
	20	39.58	9.67	13.5	0.76	0.46	0.49	0.31	0.34	0.16	0.14	0.15
	21	39.58	9.67	15.0	0.76	0.46	0.49	0.31	0.34	0.16	0.14	0.15
	22	39.58	9.67	16.5	0.76	0.46	0.49	0.31	0.34	0.16	0.14	0.15
	23	39.58	9.67	18.0	0.76	0.46	0.49	0.31	0.34	0.16	0.14	0.15
	24	39.58	9.67	19.5	0.76	0.46	0.49	0.31	0.34	0.16	0.14	0.15
	25	39.58	9.67	21.0	0.77	0.46	0.49	0.31	0.34	0.16	0.14	0.15
Others	26	39.58	7.33	12.0	0.78	0.47	0.50	0.30	0.34	0.17	0.14	0.14
	27	40.58	6.50	12.0	0.71	0.43	0.48	0.28	0.32	0.15	0.14	0.14
	28	35.58	10.00	12.0	0.78	0.47	0.48	0.30	0.34	0.17	0.13	0.14
	29	49.58	7.25	15.0	0.71	0.43	0.47	0.28	0.33	0.15	0.14	0.15
	30	36.58	9.00	12.0	0.76	0.44	0.48	0.29	0.34	0.17	0.13	0.14
	31	49.58	7.00	15.0	0.67	0.43	0.46	0.28	0.31	0.14	0.14	0.14
Median (50th Percentile)					0.7469	0.4567	0.4814	0.3001	0.3354	0.1625	0.1385	0.1468
Lognormal standard deviation, β_D					0.0295	0.0271	0.0182	0.0279	0.0226	0.0342	0.0173	0.0222

Table 7.6. LDF Equations.

			Formula	AASHTO Spread Box Beam Formulas	Least Square Best Fit Relations	Proposed LDF Design Equations
Moment LDF	Interior Beam	One Lane Loaded	1	$\left(\dfrac{S}{3.0}\right)^{0.35}\left(\dfrac{Sd}{12.0L^2}\right)^{0.25}$	$0.747\,S^{0.521}\dfrac{d^{0.217}}{L^{0.613}}$	$\left(\dfrac{S}{2.3}\right)^{0.35}\left(\dfrac{Sd}{12.0L^2}\right)^{0.25}$
		Multiple Lanes Loaded	2	$\left(\dfrac{S}{6.3}\right)^{0.6}\left(\dfrac{Sd}{12.0L^2}\right)^{0.125}$	$0.457\,S^{0.654}\dfrac{d^{0.139}}{L^{0.4}}$	$\left(\dfrac{S}{6.3}\right)^{0.6}\left(\dfrac{Sd}{12.0L^2}\right)^{0.125}$
	Exterior Beam	One Lane Loaded	3	Lever Rule	$0.482\,S^{0.798}\dfrac{d^{0.201}}{L^{0.611}}$	$\left(\dfrac{S}{1.7}\right)^{0.5}\left(\dfrac{Sd}{12.0L^2}\right)^{0.3}$
		Multiple Lanes Loaded	4	$g_{ext}=e\cdot g_{int}$ $e=0.97+\dfrac{d_e}{28.5}$	$0.301\,S^{0.589}\dfrac{d^{0.074}}{L^{0.221}}$	$\left(\dfrac{S}{9}\right)^{0.5}\left(\dfrac{Sd}{12.0L^2}\right)^{0.1}$
Shear LDF	Interior Beam	One Lane Loaded	5	$\left(\dfrac{S}{10}\right)^{0.6}\left(\dfrac{d}{12.0L}\right)^{0.1}$	$0.336\,S^{0.663}\dfrac{d^{0.197}}{L^{0.330}}$	$\left(\dfrac{S}{3.7}\right)^{0.65}\left(\dfrac{d}{12.0L}\right)^{0.25}$
		Multiple Lanes Loaded	6	$\left(\dfrac{S}{7.4}\right)^{0.8}\left(\dfrac{d}{12.0L}\right)^{0.1}$	$0.163\,S^{0.934}\dfrac{d^{0.162}}{L^{0.234}}$	$\left(\dfrac{S}{5}\right)^{0.9}\left(\dfrac{d}{12.0L}\right)^{0.2}$
	Exterior Beam	One Lane Loaded	7	Lever Rule	$0.139\,S^{0.686}\dfrac{d^{0.066}}{L^{0.033}}$	$\left(\dfrac{S}{15.7}\right)^{0.7}$
		Multiple Lanes Loaded	8	$g_{ext}=e\cdot g_{int}$ $e=0.8+\dfrac{d_e}{10}$	$0.147\,S^{0.576}\dfrac{d^{-0.032}}{L^{-0.066}}$	$\left(\dfrac{S}{19}\right)^{0.6}$

For deriving the new proposed design oriented equations, researchers adopted a slightly different approach to ensure a slight measure of conservatism remained. One of the objectives while deriving the equations was to keep the format of the LDF formulas similar to the AASHTO LRFD Specifications (2012) spread box formulas as much as possible. The criterion was to keep the lognormal standard deviation β as small as possible; note the smallest β value exists when the theoretical powers are used. Thus, in order to derive formulas that are similar to those in the AASHTO LRFD Specifications (2012) for spread box beams, the powers of the parameters were kept the same or as similar as reasonable to ensure β remained close to the theoretical equation. For the other cases where using the same power gives higher β values, the powers were chosen based on the theoretical power values and the format of the AASHTO LRFD Specifications (2012) spread box beam formulas. The principal proposed coefficient a

was increased by accepting 5 percent exceedance criterion, which means that up to 5 percent of the cases analyzed were permitted to be unconservative (smaller) compared to the more accurate FEM-based LDF values. All eight proposed LDF formulas for moment and shear are listed in Table 7.6.

LDFs obtained from the FEM-based analysis were compared with those calculated from the AASHTO LRFD Specifications (2012) spread box beam equations, the best fit theoretical equations, and the proposed design equations. The comparison of these three LDF equations versus FEM results is shown in the graphs provided in Figure 7.6 through Figure 7.13.

7.5.1   LDF for Moment in Interior Beam

Figure 7.6 provides plots of the moment results for the 31 bridges that were modeled using FEM. In the figure, the FEM solutions are considered exact. Therefore, the LDFs obtained from theoretical equations, new proposed equations, and the AASHTO LRFD Specifications (2012) spread box beam formulas are compared to the FEM-based LDFs. Each data point on the graphs represents an LDF for a specific case. Figure 7.6 shows the comparison of moment LDFs in interior slab beams for the one-lane-loaded case. The cumulative probabilities of the ratios (Theory/FEM, Proposed/FEM, and AASHTO/FEM) are also plotted to better visualize the distribution of each data point and their probability of occurrence.

The solid red line in Figure 7.6(d) represents the lognormal model curve for the proposed equation. The model curve is a lognormal curve that has the same lognormal standard deviation and median as the ratios of the proposed equation. The curve crosses the LDF ratio 1.0 at 5 percent probability. This indicates that there is only a 5 percent chance that the ratio of the new proposed equation to the FEM LDF is below 1.0. For the one-lane-loaded moment in interior beams, 80 percent of the results from the AASHTO LRFD Specifications (2012) formula are unconservative when compared to the exact FEM LDFs.

Figure 7.7 shows the comparative graphs for the multiple-lane-loaded moment in interior beams. The AASHTO LRFD Specifications (2012) formulas are slightly higher than the FEM values. Therefore, the spread box beam formula for the multiple-lane-loaded moment in interior beams was kept the same. All the LDF values for moment in interior beams are listed in Table C.1 and Table C.2 in Appendix C.
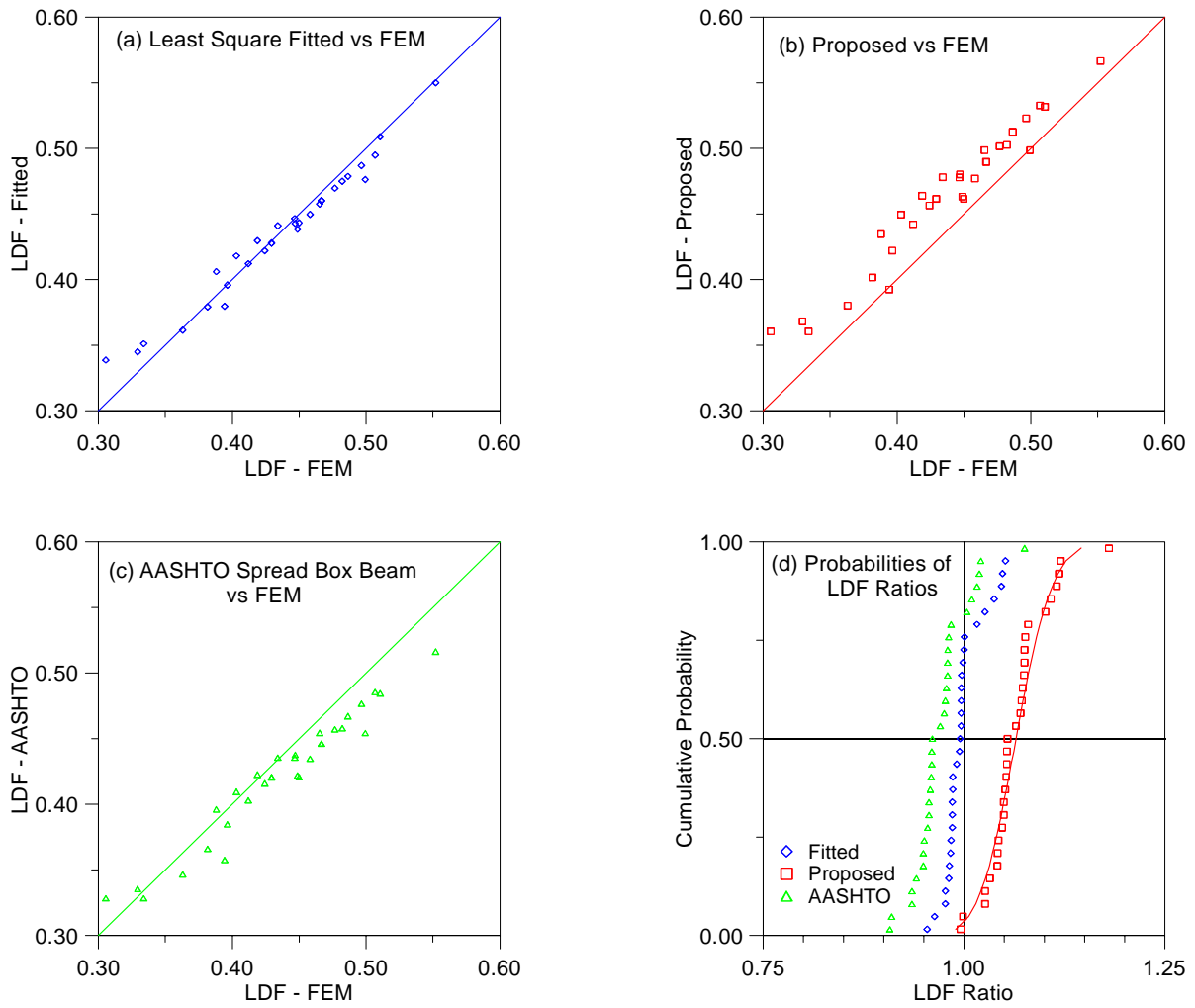
Figure 7.6. Comparison of LDFs for One-Lane-Loaded Moment in Interior Beams.
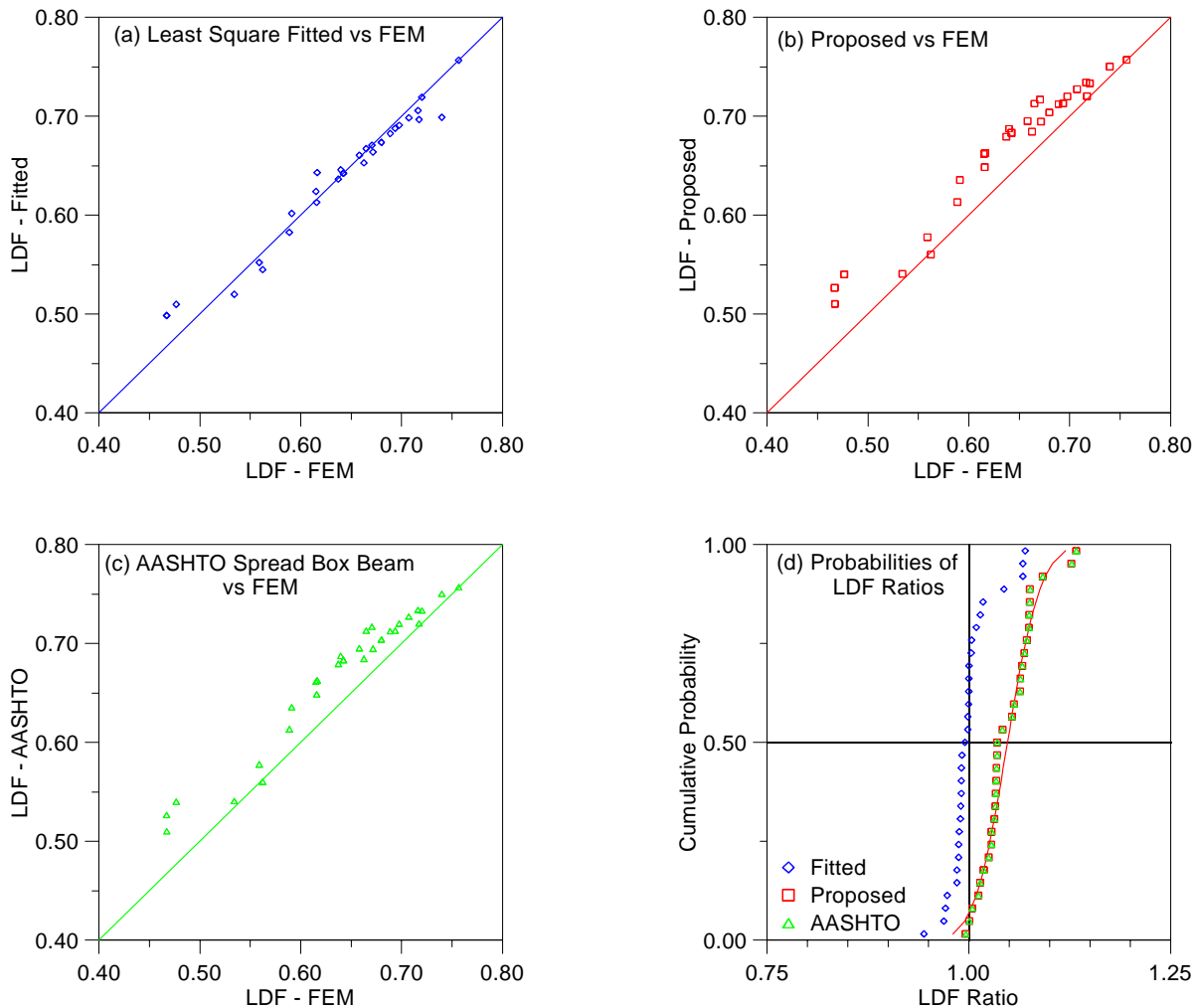
Figure 7.7. Comparison of LDFs for Multiple-Lane-Loaded Moment in Interior Beams.

7.5.2 LDF for Moment in Exterior Beam

FEM results for moment in exterior beams are well distributed along the diagonal line, which indicates a ratio of 1.0. The LDF values for all 31 bridges for moment in exterior beams are listed in Table C.3 and Table C.4 in Appendix C. These results are plotted for visual investigation in Figure 7.8 and Figure 7.9. Because the proposed equations were derived for a 5 percent exceedance limit, they give slightly conservative results for all points. This intentional result can be seen in the comparative plot and cumulative probability plot. Comparison of the AASHTO LRFD Specifications (2012) values with FEM LDFs revealed that the calculation of moment LDF for the one-lane-loaded case using the lever rule gives excessively conservative results. These AASHTO LRFD Specifications (2012) values are more than 50 percent

conservative. A new equation having a similar layout as the interior beam formulas is introduced instead of the lever rule.

The AASHTO LRFD Specifications (2012) spread box beam formula for moment in exterior beams for the multiple-lane-loaded case is obtained by adjusting the interior moment LDF with a certain multiplier. This multiplier is a function of the distance of an exterior beam from the interior face of the rail. For spread slab beam bridges, rails were not considered due to the above discussed reasons. Therefore, the parameter d_e was taken as the distance from the edge of the bridge. LDF values calculated from the AASHTO equation are 10–25 percent higher compared to FEM values. Therefore, a new equation having a similar format with other moment LDF equations was introduced. The new proposed equation gives slightly conservative results.
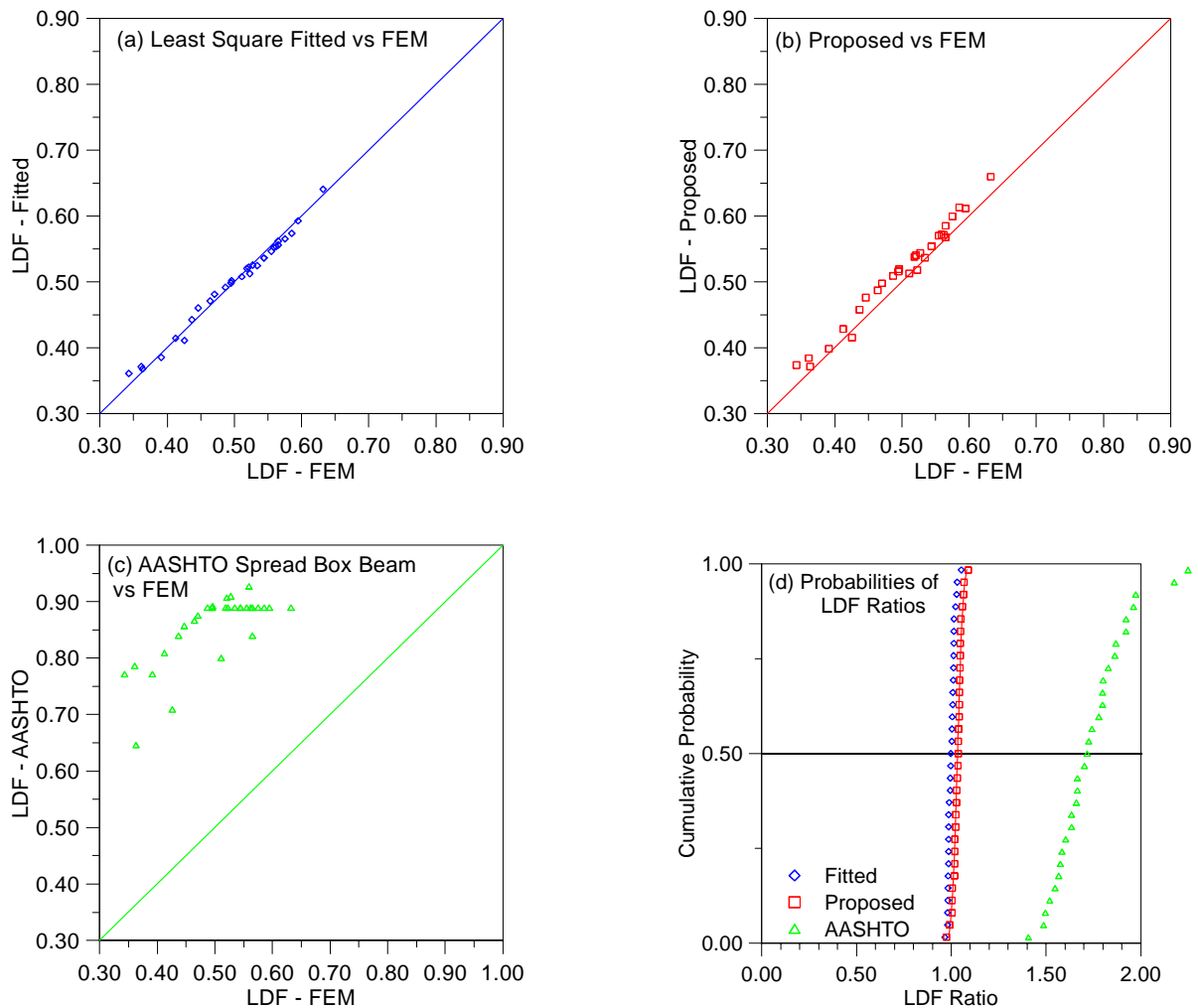
Figure 7.8. Comparison of LDFs for One-Lane-Loaded Moment in Exterior Beams.
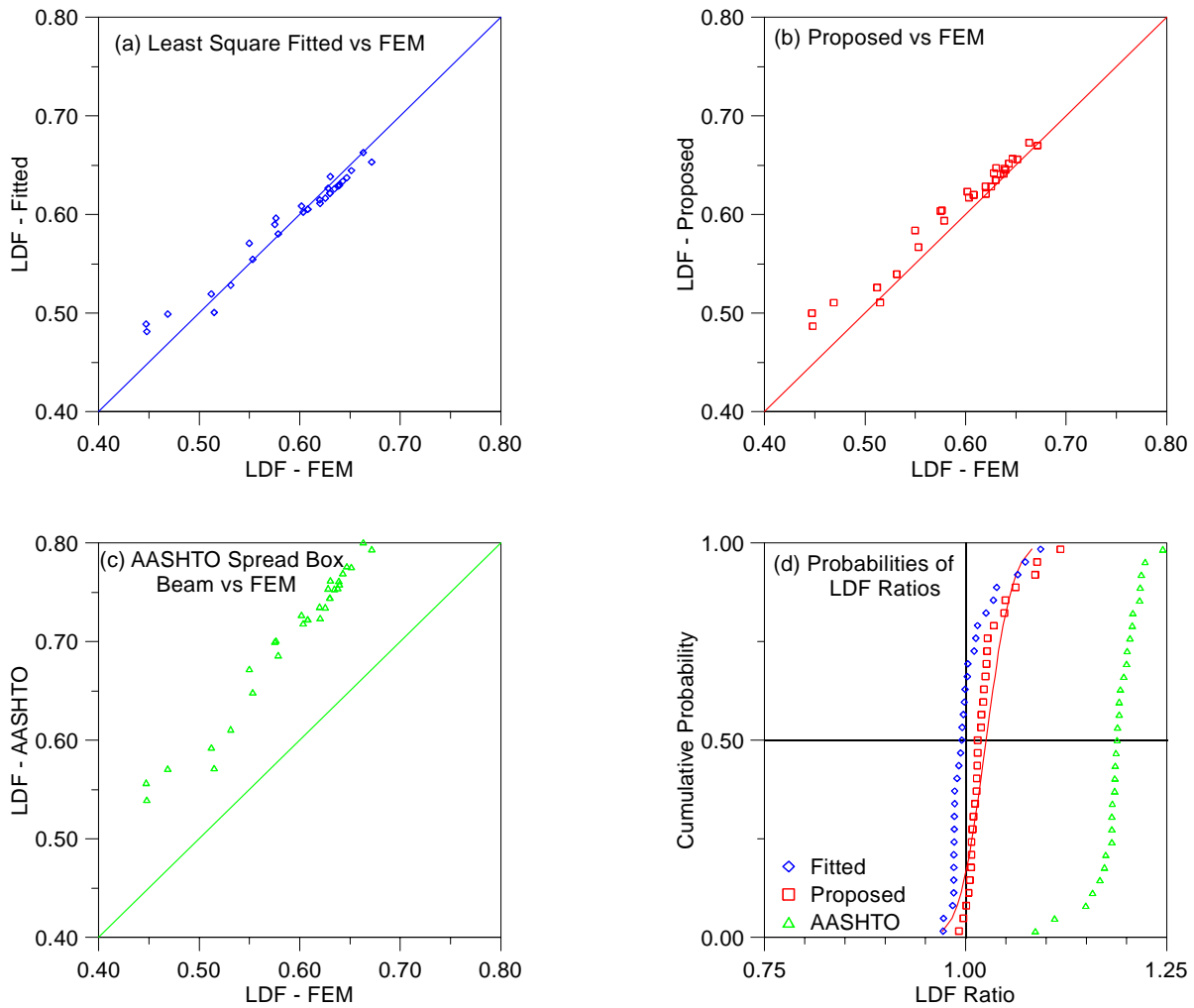
Figure 7.9. Comparison of LDFs for Multiple-Lane-Loaded Moment in Exterior Beams.

7.5.3 LDF for Shear in Interior Beam

Investigation of the LDFs for shear in interior beams revealed that the AASHTO LRFD Specifications (2012) values are unconservative for both one-lane-loaded and multiple-lane-loaded cases. This finding is consistent with the observations made during the experimental program. Therefore, new shear LDF equations are introduced that give higher LDF values. The parameters in the new shear LDF equations were arranged similar to the AASHTO LRFD Specifications (2012) spread box beam formulas. Figure 7.10 and Figure 7.11 show the comparative plots and probability plots for shear in interior beams. All the shear LDF values for shear in interior beams are listed in Table C.5 and Table C.6 in Appendix C.
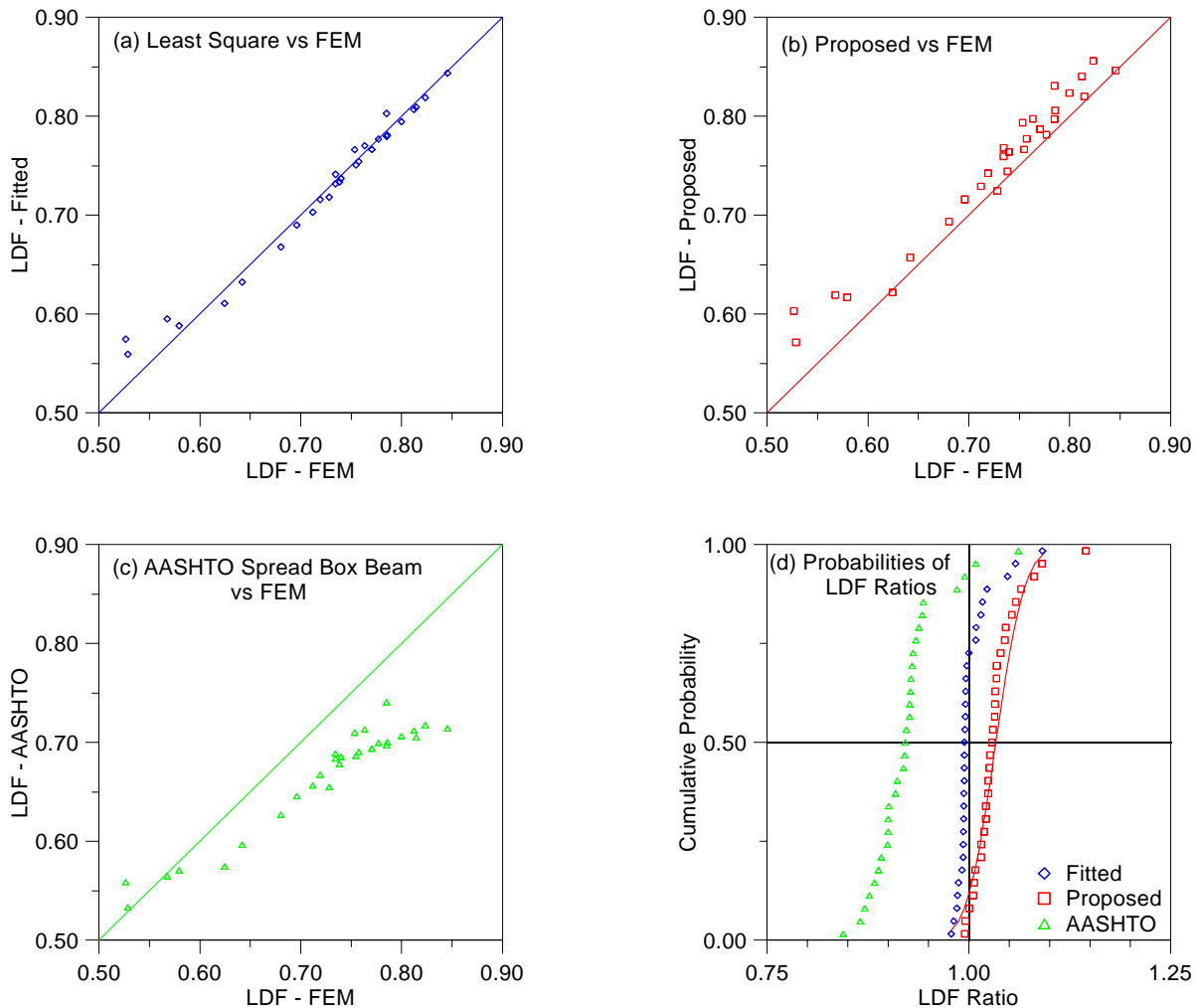
Figure 7.10. Comparison of LDFs for One-Lane-Loaded Shear in Interior Beams.

The AASHTO LRFD Specifications (2012) specify use of the lever rule for determining exterior girder shear for the one-lane-loaded case. Unlike the exterior girder moment LDFs, the lever rule gives unconservative shear LDF values for the considered spread slab beam bridges. The AASHTO LRFD Specifications (2012) spread box beam formulas give an average of 8 percent unconservative results for the one-lane-loaded shear LDFs in exterior slab beams. On the other hand, the AASHTO LRFD Specifications (2012) formulas are only about 3 percent unconservative for the multiple-lane-loaded shear LDFs in exterior beams. This small difference results in only about a 5 percent increase in the design shear force, which does not change the shear design for most bridges. Therefore, the use of the AASHTO LRFD Specifications (2012) spread box beam equations for shear LDFs based on the interior beam shear demand could provide a reasonable estimate of shear for spread slab beams.

229
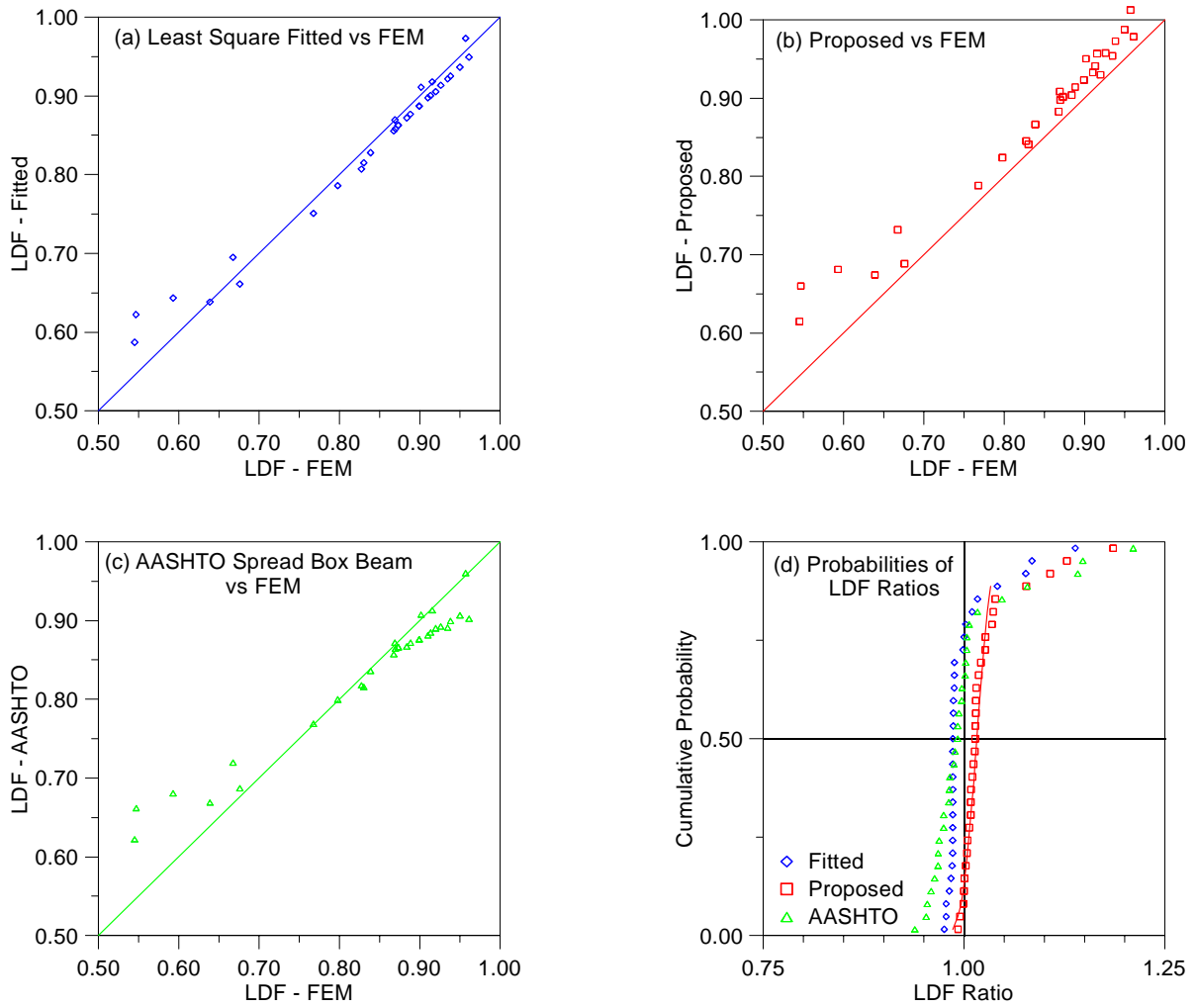
Figure 7.11. Comparison of LDFs for Multiple-Lane-Loaded Shear in Interior Beams.

230

7.5.4 LDF for Shear in Exterior Beams

Comparative plots showing all three LDF equations for shear in exterior beams versus the FEM results are shown in Figure 7.12 and Figure 7.13. Detailed LDF values are also listed in Table C.7 and Table C.8 in Appendix C. The AASHTO LRFD Specifications (2012) spread box beam formulas give an average 25 percent conservative LDFs for one-lane-loaded and more than 30 percent conservative LDFs for multiple-lane-loaded shear in exterior beams. As discussed earlier, the lever rule results in overly conservative LDFs for exterior girders. For the case of multiple-lane-loaded shear in exterior beams, the shear LDF is calculated by multiplying the interior beam shear LDF by a coefficient that is a function of the distance of the exterior beam from the edge of the bridge. This results in very conservative LDF values.
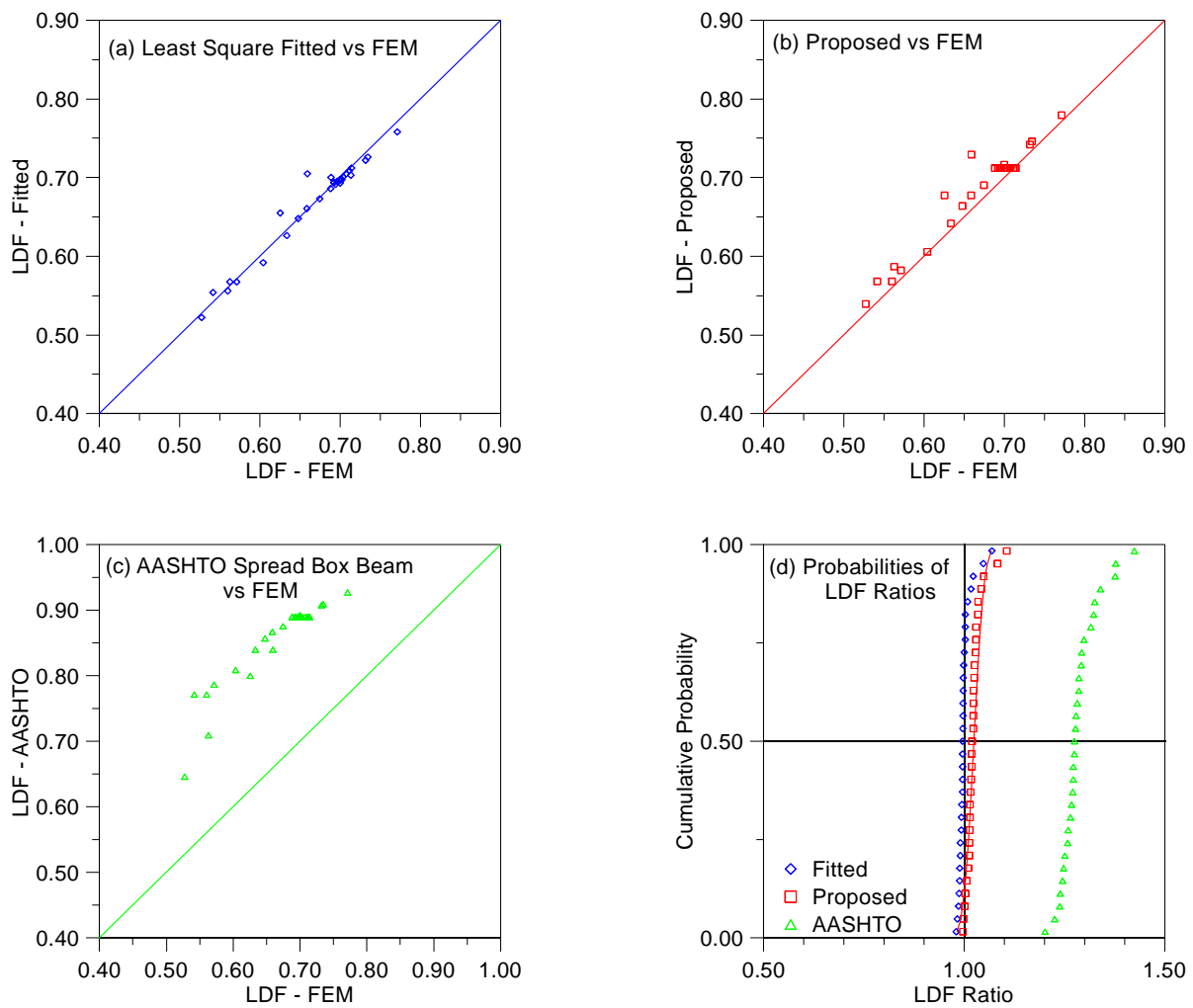
Figure 7.12. Comparison of LDFs for One-Lane-Loaded Shear in Exterior Beams.

Spread slab beam bridges are designed without a cantilever. In addition, rail thickness was not considered for the LDF study because of the possibility of having the interior edge of a bridge within a design lane for two adjacent bridges (similar to the US 69 Bridge). Therefore, the distance of the exterior beam from the edge of the bridge remains the same for all equal width beams. Because there are only two different standard slab beam widths, the variation of the shear LDF for exterior beams due to the exterior beam position is not critical. The new proposed shear LDFs in exterior beams consider the beam spacing as a more important parameter instead of the distance of the exterior beam from the edge. The obtained LDF values are slightly higher than the FEM results as intended.
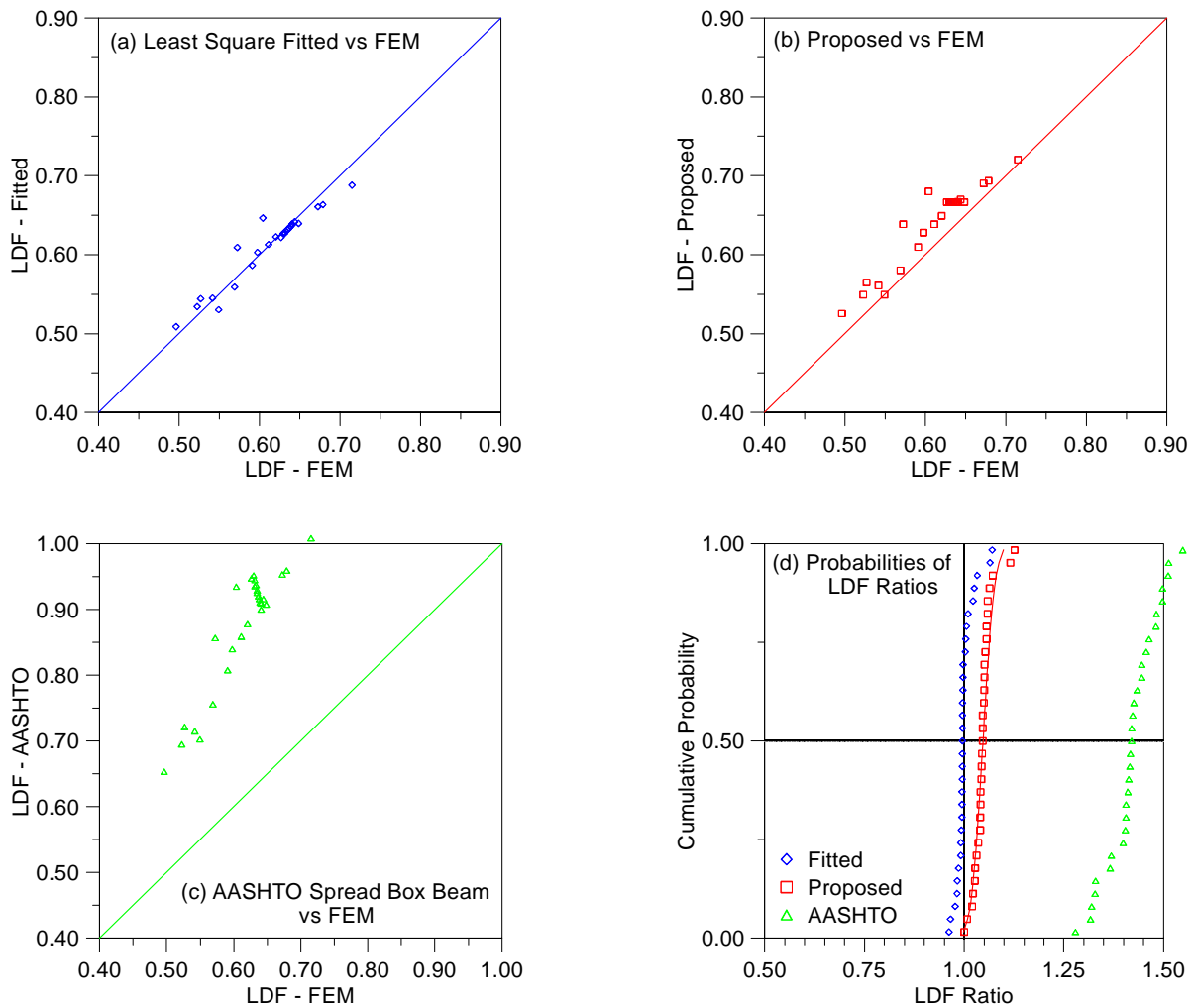
Figure 7.13. Comparison of LDFs for Multiple-Lane-Loaded Shear in Exterior Beams.

7.6   FINDINGS AND DESIGN RECOMMENDATIONS

LDFs were empirically derived for interior and exterior girders of spread slab beam bridges for span lengths within the range of 31 to 51 ft. Proposed equations were derived using a methodology similar to that adopted for developing the LDF equations found in the AASHTO LRFD Specifications (2012). A total of 31 bridge FEM models were developed and analyzed, with each bridge model having a different superstructure geometry selected from the domain investigated during the parametric study. Based on the comparative study conducted for three different sets of equations (AASHTO LRFD Specifications (2012) spread box beam formulas, theoretical best fit equations from FEM analysis, and new proposed LDF equations) the following conclusions were drawn.

1. The AASHTO LRFD Specifications (2012) LDF equations for spread box beams were reviewed for applicability to spread slab beams. The AASHTO LRFD Specifications (2012) LDFs range from being unconservative to very conservative.

    a. For interior beams, the AASHTO LRFD Specifications (2012) spread box beam formulas give slightly unconservative LDFs for the one-lane-loaded moment, whereas they are slightly conservative for the multiple-lane-loaded moment. Therefore, the new proposed equations match the AASHTO LRFD Specifications (2012) spread box beam formulas for the multiple-lane-loaded moment in interior beams.

    b. For exterior beams, the LDF values are always overestimated by the AASHTO LRFD Specifications (2012) spread box beam formulas.

    c. For one-lane-loaded shear and moment in exterior beams, the AASHTO LRFD Specifications (2012) suggest using the lever rule, which produces overly conservative LDFs (an average of 50 percent conservative for moment and 30 percent conservative for shear). Therefore, new LDF equations were proposed for exterior beams that are only slightly conservative compared to the FEM results.

    d. For multiple-lane-loaded moment and shear in exterior beams, the AASHTO LRFD Specifications (2012) suggest multiplying interior beam LDFs with a coefficient that is a function of the distance of the exterior beam from the interior edge of the rail. This parameter is not an effective parameter for the

233

spread slab beam bridges considered in this study. This approach produces up to 25 percent conservative results for moment and an average of 40 percent conservative results for shear in exterior beams. Thus, new LDF equations are suggested for multiple-lane-loaded moment and shear in exterior beams.

2. Unique LDF expressions were developed for spread slab beam bridges to provide an appropriate level of conservatism. The new proposed equations produce slightly conservative results for all LDF cases when compared with the LDFs calculated from FEM analysis. The proposed moment LDF for interior slab beams (multiple lanes loaded) is identical to the AASHTO LRFD Specifications (2012) spread box beam equation.

3. Examining the analytical results and recommended LDF formulas for spread slab beams reveal that some of the formulas govern the design most of the time.

    a. For all LDF equations, except for shear in exterior beams, multiple-lane-loaded formulas provide higher LDFs that control the design.

    b. For shear in interior beams, the multiple-lane-loaded shear LDF formula always gives higher results.

    c. For shear in exterior beams, the one-lane-loaded LDF formula gives higher results.

    d. For moment in both interior and exterior beams, multiple-lane-loaded formulas result in the highest LDF values.

4. Common TxDOT practice for precast prestressed concrete bridges is to design all the girders the same as an interior girder in order to take into account possible future widening of the bridge. Therefore, all girders are designed based on interior girder shear and moment demands, unless the exterior demands are greater.

5. The two governing equations for multiple-lane-loaded interior beams are:

$$\text{For moments:} \quad \left(\frac{S}{6.3}\right)^{0.6}\left(\frac{Sd}{12.0L^2}\right)^{0.125}$$

$$\text{For shear:} \quad \left(\frac{S}{5}\right)^{0.9}\left(\frac{d}{12.0L}\right)^{0.2}$$

Using the above results, the LDFs obtained from these two formulas were plotted against span length for different beam spacings for common 15 in. deep slab beams and are shown in

234

Figure 7.14. The solid lines show the LDF values within the applicable span length range, and the dashed lines show slightly beyond the applicable span range.

(a)   Moment LDF   (b)   Shear LDF
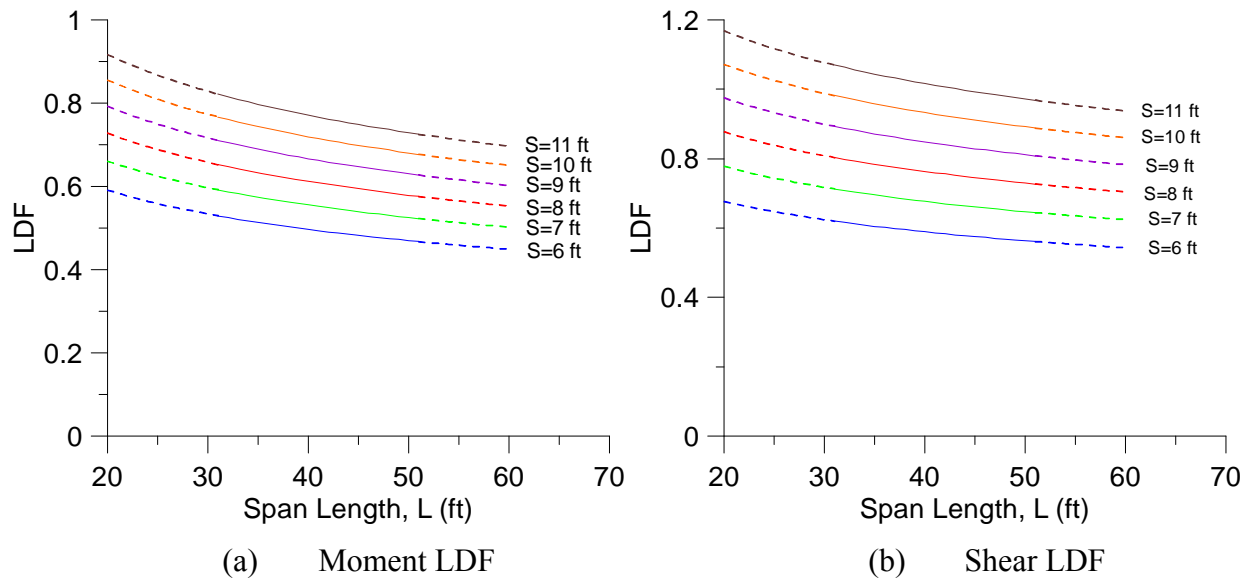
Figure 7.14. LDF Solution Domain for 15 in. Slab Beams Based on Proposed Multiple-Lane-Loaded Interior Beam Formulas.

8   SUMMARY, CONCLUSIONS, AND RECOMMENDATIONS

8.1   SUMMARY

TxDOT uses precast prestressed concrete slab beam bridges for short-span bridges ranging from approximately 30–50 ft in length. Historically, conventional slab beam bridges have slab beams placed immediately adjacent to one another with a cast-in-place (CIP) topping slab made composite with the beams. While these bridges are used extensively, they are more expensive than traditional prestressed I-beam structures on a per-square-foot basis. The objective of this project is to investigate the use of slab beams that are spread apart with 4 in. thick precast concrete panel (PCP) stay-in-place (SIP) forms between beams and a 4 in. thick CIP reinforced concrete topping deck. Design guidelines have been developed for this alternate spread slab beam bridge system.

The research team reviewed the relevant literature and current state of the practice. Preliminary designs were developed to assess the potential of a spread slab beam bridge system. A full-scale spread slab beam bridge was constructed at the Texas A&M University Riverside Campus and tested to assess constructability, in-service performance, and behavior. Field testing was conducted for the Riverside Bridge and a US 69 on-system bridge to evaluate load distribution behavior and to provide data to guide computational modeling for this class of bridge systems. Computational models using two broadly different approaches were developed to investigate an array of possible bridge geometries and load sharing behavior. Based on these models, the research team developed recommendations for shear and moment load distribution factor (LDF) relationships for the design of spread slab beam bridges.

8.2   CONCLUSIONS

8.2.1   Preliminary Design Study

A parametric study was conducted to investigate preliminary designs for spread slab beam bridges. The effects of different parameters such as beam depth, beam width, number of beams, and beam spacing on the resulting maximum span length were assessed. The following observations were made based on the results of the parametric study and evaluation of the shear reinforcement.

8.2.1.1 Parametric Study Observations

1. For all bridge widths considered (26 ft, 30 ft, 34 ft, 40 ft, and 46 ft), it is possible to span approximately 50 ft.

2. For 26 ft and 30 ft wide bridges, maximum span lengths of 50 ft 7 in. and 48 ft 7 in., respectively, are achieved when four 5SB15 slab beams are used.

3. For 34 ft wide bridges, the use of five 5SB15 slab beams results in a 49 ft 7 in. span length.

4. In order to achieve the maximum possible span length for 40 ft, 42 ft, or 46 ft wide bridges, six 5SB15 slab beams must be used.

5. The slab beam depth is the most prominent parameter for achieving longer span lengths.

6. Beam depth and beam width have a more prominent effect on the maximum span length as compared to the number of beams.

7. In general, smaller beam spacing results in a greater span length.

8. For the same number of slab beams, 4SB15 beams allow greater span lengths compared to 5SB12 beams despite a larger beam spacing. This shows that the beam depth effect is more pronounced than the beam spacing and beam width effects.

8.2.1.2 Shear Reinforcement

1. The current transverse and interface shear reinforcement provided in the standard TxDOT slab beam sections should be maintained as a minimum for spread slab beam designs.

2. The standard transverse shear reinforcement currently provided by TxDOT for standard slab beam types satisfies the required transverse shear strength criteria for the critical spread slab beam bridge geometries investigated in the parametric study.

3. Because the shear per beam increases in a spread configuration, the shear requirements should be carefully reviewed during design to ensure that the standard transverse and interface shear reinforcement is adequate. In particular, the interface shear reinforcement (H-bars) may need to be increased in the end regions for more shear critical cases when the beam surface is not intentionally roughened to a 0.25 in. amplitude.

4. Based on observed typical precast fabrication practices, standard slab beams do not have an intentionally roughened surface. The manufacturing process currently includes the use of self-consolidating concrete and curing, which is achieved by soaking the beams in water and leaving the surface untouched. Therefore, the slab beam surface ends up being relatively smooth.

5. The design checks indicate that interface shear reinforcement (H-bars) area per foot length can potentially be reduced for the midspan regions. However, the interface shear reinforcement area per foot length may need to be increased for the end regions of standard slab beams, particularly for the more shear critical cases with longer spans and wider beam spacings.

6. Until further research is conducted to evaluate the interface shear strength of slab beam bridges, the research team recommends maintaining the use of the interface shear reinforcement based on current practice and performance of conventional slab beam bridges. Interface shear reinforcement requirements should be checked as part of spread slab beam bridge designs.

7. The H-bars provided for interface shear should be properly developed into both the precast slab beams and the CIP deck. Therefore, the standard H-bar detail should be modified to extend 6 in. into the CIP deck to provide the required development length. Note that sufficient steel area should be provided to justify this dimension, which is slightly smaller than the calculated hook length. This reduction is justified based on maintaining the ratio of area of steel required to area of steel provided at or below 0.90.

8.2.2 Constructability and Related Observations

This research investigated the possibility of using slab beams in a spread configuration for short-span bridges. A full-scale bridge utilizing widely spaced (4 ft 8 in. clear) slab beams was constructed at the Texas A&M University Riverside Campus and was tested under static and dynamic service loads. Although there are no documented examples of spread slab beam bridges built prior to this project, an in-service bridge on US 69 in Denison, Texas, with closely spaced (1 ft 4 in. clear) slab beams was constructed by TxDOT during the project period. The US 69 Bridge was also tested by the research team to investigate structural response under

service loads. Based on the observations during construction and experimental investigation of the Riverside Bridge, along with field testing of the US 69 Bridge, the following conclusions were drawn with respect to constructability and related observations.

1. Spread slab beam bridge systems that utilize PCPs with a CIP concrete deck, similar to I-girder bridges, provide a viable construction method for short-span bridges, approximately 30–50 ft long.

2. Spread prestressed slab beam bridge construction was successfully implemented for the US 69 on-system bridge and the Riverside test bridge.

3. Camber of the spread slab beams tends to increase due to higher prestressing forces. Thus, the bedding strip installation can require increased depths (up to 4 in. total) at the beam ends. Camber should be evaluated as part of spread slab beam bridge designs to ensure the value is acceptable with regard to construction and serviceability considerations.

4. Care should be taken during deck curing to avoid any unexpected cracking. For the Riverside Bridge, a single longitudinal crack was observed on the deck surface along the entire length of the bridge at the transverse centerline (centered on a PCP). The crack occurred within the first week after deck placement. The width did not increase after the crack appeared. It appears that the crack developed because of stresses due to combined shrinkage and differential temperature effects. The crack may potentially be due to hot weather and inadequate curing. However, the deck was sprayed with water daily and covered with a curing blanket and plastic sheet during the first four days. It appears that this type of crack is not related to the spread slab beam implementation. Similar minor longitudinal cracks in the deck were also observed at the US 69 Bridge.

8.2.3 Field Testing

Field testing was conducted for the Riverside Bridge and the US 69 Bridge to investigate the effect of beam spacing on the structural behavior of the composite bridge system. Experimental results from both bridges were processed and reviewed, leading to the following conclusions.

1. For both bridges, the desired performance was achieved for in-service loading. During field testing the beam live load deflections were within the design limits. No

major cracking or reduction in the overall stiffness of the bridge superstructure was observed during static and dynamic testing (up to 40 mph). The Riverside Bridge remained in the linear range of behavior when the water tanker loading of about 75 kips (slightly above HS20 loading) was applied. The US 69 Bridge also remained in the linear range of behavior during static and dynamic testing.

2. Experimental LDFs were evaluated using alignments that provided the most adverse loading cases. The following observations were made for the Riverside Bridge, which was tested with a dump truck and a water tanker.

    a. Experimental shear LDFs for both interior and exterior girders were about 5 percent higher when the Riverside Bridge was loaded with the rear axle of the water tanker compared to the dump truck loading. This may be due to more concentrated loading achieved with the water tanker.

    b. Experimental moment LDFs were similar for both the dump truck and the water tanker loadings for the Riverside Bridge.

3. The strain gage readings during the US 69 Bridge test indicated that the deck, sidewalk, and guardrail did not exhibit plane section behavior. The existence of the sidewalk and guardrail at the bridge edge had a significant impact on the moment distribution across the bridge section.

4. Bridge responses under dynamic loads were larger compared to static values. With the increase of vehicle speed, bridge responses became larger. In spite of the changes in moment magnitude under dynamic loading, the moment LDFs were quite similar to their static counterparts.

5. The observed bridge responses under dynamic loads were larger when compared to the static counterparts; the dynamic bridge response became larger with increasing vehicle speed. Evidently, for short-span bridges, the dynamic impact may exceed the AASHTO LRFD Specifications (2012) design value of 33 percent. However, the observed impact depended upon the position of the approach bump as well as the dynamic characteristics of the vehicle and the bridge.

8.2.4   Computational Modeling

Computational models were developed for a spread box beam bridge (Drehersville Bridge) and the two tested spread slab beam bridges (Riverside and US 69 Bridges) by applying different analysis methods (grillage and FEM) and utilizing different commercial software. By comparing the computational results with experimental values, researchers drew the following conclusions.

1. For the spread box beam bridge, the grillage model generally gives reasonable estimates of the measured girder moments and LDFs. It is reasonable to simplify this type of bridge as several major longitudinal grillage members due to the greater box beam depth.

2. For the two spread slab beam bridges tested as part of the present research, the FEM solutions provided moderately accurate deflections, but given the small magnitude of deflection, it is difficult to discriminate where the errors arise—whether they are predominantly from measurement error or modeling simplifications.

3. The computed natural frequencies when compared to observed test results for the two tested bridges were remarkably close. Therefore, the FEM models are considered valid for further LDF analysis.

4. The FEM LDFs for the two tested spread slab beam bridges are similar to the observed test values with some small differences. With careful development of the grillage model, this simplified analysis method also predicts the structural behavior well and may be utilized for design purposes.

5. The general conclusion from this dual experimental and computational study is the following: Given the ease of developing and applying advanced computational FEM solutions, one should use the best available analysis tools. Regardless of the claimed accuracy, it remains prudent to validate results against realistic experimental evidence, if available.

8.2.5   Development of Load Distribution Formulas

LDFs were empirically derived for interior and exterior girders of spread slab beam bridges for span lengths within the range of 31 to 51 ft. Proposed equations were derived using a methodology similar to that adopted for developing the LDF equations found in the *AASHTO LRFD Bridge Design Specifications* (AASHTO 2012). A total of 31 bridge FEM models were

developed and analyzed, with each bridge model having a different superstructure geometry selected from the domain investigated during the parametric study. Based on the comparative study conducted for three different sets of equations (AASHTO LRFD Specifications (2012) spread box beam formulas, theoretical best fit equations from FEM, and new proposed LDF equations), researchers drew the following conclusions.

1. The AASHTO LRFD Specifications (2012) LDF equations for spread box beams were reviewed for applicability to spread slab beams. The AASHTO LRFD Specifications (2012) LDFs range from being unconservative to very conservative.

   a. For interior beams, the AASHTO LRFD Specifications (2012) spread box beam formulas give slightly unconservative LDFs for the one-lane-loaded moment, whereas they are slightly conservative for the multiple-lane-loaded moment. Therefore, the new proposed equations match the AASHTO LRFD Specifications (2012) spread box beam formulas for the multiple-lane-loaded moment in interior beams.

   b. For exterior beams, the LDF values are always overestimated by the AASHTO LRFD Specifications (2012) spread box beam formulas.

   e. For one-lane-loaded shear and moment in exterior beams, the AASHTO LRFD Specifications (2012) suggest using the lever rule, which produces overly conservative LDFs (an average of 50 percent conservative for moment and 30 percent conservative for shear). Therefore, new LDF equations were proposed for exterior beams that are only slightly conservative compared to the FEM results.

   c. For multiple-lane-loaded moment and shear in exterior beams, the AASHTO LRFD Specifications (2012) suggest multiplying interior beam LDFs with a coefficient that is a function of the distance of the exterior beam from the interior edge of the rail. This parameter is not an effective parameter for spread slab beam bridges. This approach produces up to 25 percent conservative results for moment and an average of 40 percent conservative results for shear in exterior beams. Thus, new LDF equations are suggested for multiple-lane-loaded moment and shear in exterior beams.

2. Unique LDF expressions were developed for spread slab beam bridges to provide an appropriate level of conservatism. The new proposed equations produce slightly conservative results for all LDF cases when compared with the LDFs calculated from FEM analysis. The proposed moment LDF for interior slab beams (multiple lanes loaded) is identical to the AASHTO LRFD Specifications (2012) spread box beam equation.

3. The analytical results and recommended LDF formulas for spread slab beams reveal that some of the formulas govern the design most of the time.

   a. For all LDF equations, except for shear in exterior beams, multiple-lane-loaded formulas provide higher LDFs that control the design.

   b. For shear in interior beams, the multiple-lane-loaded shear LDF formula always gives higher results.

   c. For shear in exterior beams, the one-lane-loaded LDF formula gives higher results.

   d. For moment in both interior and exterior beams, multiple-lane-loaded formulas result in the highest LDF values.

4. Common TxDOT practice for precast prestressed concrete bridges is to design all the girders the same as an interior girder in order to take into account possible future widening of the bridge. Therefore, all girders are designed based on interior girder shear and moment demands, unless the exterior demands are greater. The two governing equations for multiple-lane-loaded interior beams are:

   For moments: $\left(\dfrac{S}{6.3}\right)^{0.6}\left(\dfrac{Sd}{12.0L^2}\right)^{0.125}$

   For shear:　　$\left(\dfrac{S}{5}\right)^{0.9}\left(\dfrac{d}{12.0L}\right)^{0.2}$

8.3   DESIGN RECOMMENDATIONS

Recommendations for design include the following.

1. The new proposed LDF formulas for spread slab beam bridges are valid within the specified applicable range. For spread slab beam bridges outside of this range, more accurate analysis should be performed.

2. The AASHTO LRFD Specifications (2012) LDF equations for spread box beams can be used for designing spread slab beam bridges if all the slab beams are designed based on interior girder moment and shear demands.

3. Standard TxDOT slab beams are utilized to their design limits as the spacing between girders and span length increase. Therefore, it is good practice to use at least two girders per design lane to reduce the high demand on the slab beams. Generally, bridge geometries utilizing less than two girders per lane experience high shear demand, which may lead to interface shear problems and excessive camber that results in impractical haunch thicknesses. Interface shear and camber must be carefully checked if the designer chooses to use less than two beams per design lane.

8.4   RECOMMENDATIONS FOR FUTURE RESEARCH

Recommendations to extend the results of this research include the following.

1. In this research, LDF formulas were derived for spread slab beam bridges with zero skew and without overhang. Additional analytical and experimental studies that include varying overhang and skew parameters would allow an assessment of their influence on LDFs for spread slab beam bridges. Further development of LDFs that consider these parameters could be included.

2. In order to draw general conclusions about dynamic amplification, further testing that investigates different vehicle types, different speeds, and different approach bump sizes and conditions should be conducted.

3. Additional studies related to the interface shear strength between the slab beam and CIP deck would be useful for refining the corresponding interface shear details

REFERENCES

AASHO (1931). "Standard Specifications for Highway Bridges, 1st Edition." American Association of State Highway Officials, Washington,DC.

AASHTO (1994a). "AASHTO LRFD Bridge Design Specifications, 1st Edition." American Association of State Highway and Transportation Officials, Customary US Units, Washington, DC.

AASHTO (1994b). "Guide Specifications for Distribution of Loads for Highway Bridges." American Association of State Highway and Transportation Officials, Washington, DC.

AASHTO (1996). "Standard Specifications for Highway Bridges, 16th Edition." American Association of State Highway and Transportation Officials, Washington, DC.

AASHTO (1998). "AASHTO LRFD Bridge Design Specifications, 2nd Edition." American Association of State Highway and Transportation Officials, Washington, DC.

AASHTO (2004). "AASHTO LRFD Bridge Design Specifications, 3rd Edition." American Association of State Highway and Transportation Officials, Washington, DC.

AASHTO (2007). "AASHTO LRFD Bridge Design Specifications, 4th Edition."American Association of State Highway and Transportation Officials, Washington, DC.

AASHTO (2012). "AASHTO LRFD Bridge Design Specifications, 6th Edition." American Association of State Highway and Transportation Officials, Washington, DC.

ACI Committee 318 (2008). "Building Code Requirements for Structural Concrete (ACI 318-08) and Commentary (ACI 318R-08)."Farmington Hills, MI.

Argyris, J. H., and Kelsey, S. (1960). "Energy Theorems and Structural Analysis: A Generalised Disclosure with Applications on Energy Principles of Structural Analysis Including the Effects of Temperature and Nonlinear Stress-Strain Relations."Butterworths, London, UK.

ASTM (2009). "American Society for Testing and Materials (ASTM) " *C1611, Test Method for Slump Flow of Self-Consolidating Concrete,* West Conshohocken, Philadelphia.

ASTM (2010a). "American Society for Testing and Materials (ASTM)." *C39/C39M , Standard Test Method for Compressive Strength of Cylindrical Concrete Specimens,* West Conshohocken, Philadelphia.

ASTM (2010b). "American Society for Testing and Materials (ASTM)." *C78/C78M, Standard Test Method for Flexural Strength of Concrete (Using Simple Beam with Third-Point Loading),* West Conshohocken, Philadelphia.

ASTM (2010c). "American Society for Testing and Materials (ASTM)." *C470/C470M, Specification for Molds for Forming Concrete Test Cylinders Vertically,* West Conshohocken, Philadelphia.

ASTM (2011). "American Society for Testing and Materials (ASTM)." *C496/C496M, Standard Test Method for Splitting Tensile Strength of Cylindrical Concrete Specimens,* West Conshohocken, Philadelphia.

ASTM (2012a). "American Society for Testing and Materials." *C31/31M, Standard Practice for Making and Curing Concrete Test Specimens in the Field,* West Conshohocken, Philadelphia.

ASTM (2012b). "American Society for Testing and Materials (ASTM)." *C143, Standard Test Method for Slump of Hydraulic Cement Concrete,* West Conshohocken, Philadelphia.

ASTM (2013). "American Society for Testing and Materials." *C138, Standard Test Method for Density (Unit Weight), Yield, and Air Content (Gravimetric) of Concrete,* West Conshohocken, Philadelphia.

Barker, R. M., and Puckett, J. A. (2007). *Design of Highway Bridges: An LRFD Approach*, John Wiley & Sons, Inc., Hoboken, NJ.

Barr, P. J., Oberhard, M. O., and Stanton, J. F. (2001). "Live Load Distribution Factors in Prestressed Concrete Girder Bridges." *J Bridge Eng*, 6(5), 298.

Brüel & Kjaer (2014). "CCLD Accelerometer Type 4507." <http://www.bksv.com/products/transducers/vibration/accelerometers/accelerometers/4507-b-004>. (July 15, 2014).

Celesco Measurement (2014). "String Pots." <http://www.celesco.com/stringpots/>. (July 15, 2014).

Chen, Y., and Aswad, A. (1996). "Stretching Span Capability of Prestressed Concrete Bridges under AASHTO LRFD." *J Bridge Eng*, 1(3).

Computers and Structures, I. (2013). "CSI Knowledge Base." Computers and Structures, Inc., Berkeley, CA.

Computers and Structures, I. 2013. SAP2000, version 15. Computers and Structures, Inc., Berkeley, CA.

CSiBridge. 2014. CSiBridge, Integrated 3-D Bridge Analysis, Design and RatingComputers and Structures, Inc., California.

Dassault Systemes, S. A. 2013. Abaqus, version 6. Abaqus, Inc., Velizy-Villacoublay, France.

Douglas, W. J., and Vanhorn, D. A. (1966). "Lateral Distribution of Static Loads in a Prestressed Concrete Box-Beam Bridge - Drehersville Bridge." *Project 315*, Fritz Engineering Laboratory, Department of Civil Engineering, Lehigh University, Bethlehem, Pennsylvania.

Eamon, C. D., and Nowak, A. S. (2002). "Effects of edge-stiffening elements and diaphragms on bridge resistance and load distribution." *J Bridge Eng*, 7(5).

Eom, J., and Nowak, A. S. (2001). "Live Load Distribution for Steel Girder Bridges." *J Bridge Eng*, 6(6), 489.

Evans, R. H., and Chung, H. W. (1969). "Horizontal Shear Failure of Prestresses Composite T-Beams with Cast-in-Situ Lightweight Concrete Deck." *Concrete*, 124-126.

Gessner (2012). "Geotechnical Engineering Study, Bridge Abutments."

Goodrich, B. L., and Puckett, J. A. (2000). "Simplified Load Distribution for Vehicles with Nonstandard Axle Gauges." *Transportation Research Record: Journal of the Transportation Reasearch Board*(1696(1)), 158-170.

Google Maps (2005). <https://www.google.com/maps>. (July 15, 2014).

Hambly, E. C. (1975). "Grillage Analysis Applied to Cellular Bridge Decks." *The structural engineer*, 53(7), 267-276.

Hambly, E. C. (1976). *Bridge Deck Behaviour*, Halsted Press, New York, NY.

Hambly, E. C. (1991). *Bridge Deck Behaviour*, Taylor & Francis, New York, NY.

Hanson, N. W. (1960). "Precast-Prestressed Concrete Bridges; 2. Horizontal Shear Connections." *Journal of the Research and Development Laboratories, Portland Cement Association*, 2(2), 38-58.

Harris, D. K. (2010). "Assesment of Flexural Lateral Load Distribution Methodologies for Stringer Bridges." *Engineering Structures*, 32(11), 3443-3451.

Harris, D. K., Cousins, T., Sotelino, E. D., and Murray, T. M. (2010). "Flexural Lateral Load Distribution Characteristics of Sandwich Plate System Bridges: Parametric Investigation." *ASCE Journal of Bridge Engineering*, 15(6), 684-694.

Hueste, M. B. D., Adil, M. S., Adnan, M., and Keating, P. B. (2006). "Impact of LRFD Specifications on Design of Texas Bridges: Prestressed Concrete Bridge Girder Design Examples." Texas Transportation Institute and Texas Department of Transportation.

Kim, D. K., Mander, J., and Chen, S. (1996). "Temperature and Strain Rate Effects on the Seismic Performance of Elastomeric and Lead-Rubber Bearings." *ACI Special Publication*, 164.

Kocsis, P. (2004). "Evaluation of AASHTO Live Load and Line Load Distribution Factors for I-Girder Bridge Decks." *Practice Periodical on Structural Design and Construction*, 9(4), 211.

Kovach, J. D., and Naito, C. (2008). "Horizontal Shear Capacity of Composite Concrete Beams without Interface Ties." *ATLSS*, Lehigh University.

Lightfoot, E., and Sawko, F. (1959). "Structural Frame Analysis by Electronic Computer: Grid Frameworks by Generalised Slope Deflection." *Engineering*.

McKee, D. C., and Turner, H. T. (1975). "Design and Review of Precast Concrete Bridge Elements." FHWA and Luisiana Department of Highways, FHWA-LDH-LSU(75-1ST).

Measurement Computing (2014). "StrainBook/616." <http://www.mccdaq.com/products/strainbook616.htm>. (July 15, 2014).

Naaman, A. E. (2004). *Prestressed Concrete Analysis and Design : Fundamentals*, Techno Press, Ann Arbor, Mich.

Newmark, N. M. (1938). "A Distribution Procedure for Analysis of Slabs Continuous over Flexibale Beams."University of Illinois, Urbana , IL.

Nosseir, S. B., and Murtha, R. N. (1971). "Ultimate Horizontal Shear Strength of Prestresses Split Beams."Naval Civil Engineering Laboratory Technical Report NCEL TR.

Nowak, A. S. (1993). "Live Load Model for Highway Bridges." *Struct Saf*, 13(1-2), 53-66.

Omega (2014). "http://www.omega.com/pptst/GP911.html."

Panak, J. J. (1982). "Economical Precast Concrete Bridges." *FHWA-TX-83-08+226-1F Final Rpt.*, FHWA and Texas Department of Highway & Public Transportation, Austin, TX.

Parke, G., and Hewson, N. (2008). "ICE Manual of Bridge Engineering."

PGSuper (2013). "PGSuper Design Guide." Texas Department of Transportation.

Powell, G. H., and Buckle, I. (1970). "Computer Programs for Bridge Deck Analysis." College of Engineering, Office of Research Services, University of California.

Puckett, J. A., Mertz, D., Huo, X. S., C., J. M., Peavy, M. D., and Patrick, M. D. (2005). "Simplified Live Load Distribution Factor Equations for Bridge DEsign." *Journal of the Transportation Research Board*, 11(S), 67-78.

Ryall, M. J., Parke, G. A. R., and Harding, J. E. (2000). "ICE Manual of Bridge Engineering." E. Institution of Civil, ed., Thomas Telford, London.

Schwarz, M., and Laman, J. A. (2001). "Response of Prestressed Concrete I-Girder Bridges to Live Load." *J Bridge Eng*, 6(1), 1.

Sotelino, E., Liu, J., Chung, W., and Phuvoravan, K. (2004). "Simplified Load Distribution Factor for Use in LRFD Design." *Joint Transportation Research Program*, 191.

Surana, C. S., and Agrawal, R. (1998). *Grillage Analogy in Bridge Deck Analysis*.

Tanbsh, S., and Tabatabai, M. (2001). "Live Load Distribution in Girder Bridges Subject to Oversize Trucks." *ASCE Journal of Bridge Engineering*, 6((1)), 9-16.

Tokyo Sokki Kenkyujo Co., L. (2014). "http://www.tml.jp/e/product/strain_gauge/index.html."

Trejo, D., Hueste, M. B. D., and Kim, Y. G. (2008). "Characterization of Self-Consolidating Concrete for Design of Precast, Prestressed Bridge Girders ".

Turner, M. J., Clough, R. W., Martin, H. C., and Topp, L. J. (1956). "Stiffness and Deflection Analysis of Complex Structures." *Journal of the Aeronautical Sciences*, 23(9), 805-823.

TxDOT (2010). "Design Drawings of Highway US 69 ".

TxDOT (2012). "TxDOT Geotechnical Manual." Texas Department of Transportation.

TxDOT (2013a). "TxDOT Bridge Design Manual - LRFD." Texas Department of Transportation.

TxDOT (2013b). "TxDOT Bridge Division Standard Drawings." Texas Department of Transportation, http://www.txdot.gov/insdtdot/orgchart/cmd/cserve/standard/bridge-e.htm.

Ugural, A. C., and Fenster, S. K. (2012). *Advanced Mechanics of Materials and Aplied Elasticity*, Prentice Hall.

WYDOT (1996). "Bridge Rating and Analysis of Structural Systems (Brass) User`s Manual." Wyoming Department of Transportation, ed.

Zienkiewich, O. C. (1971). *The Finite Element Method in Engineering Science*, Mc-Graw-Hill, London.

Zokaie, T. (2000). "AASHTO-LRFD Live Load Distribution Specifications." *ASCE Journal of Bridge Engineering*, 5(2), 131-138.

Zokaie, T., Imbsen, R. A., and Osterkamp, T. A. (1991). "Distribution of Wheel Loads on Highway Bridges." *NHCRP Project Report 12-26*, Transportation Research Board, Washington, D.C.

Zokaie, T., Imbsen, R. A., and Osterkamp, T. A. (1991). "Distribution of Wheel Loads on Highway Bridges." *NCHRP Project Report 12-26*, Transportation Research Board, Washington, D.C.

APPENDIX A   DESIGN EXAMPLE FOR INTERIOR 5SB15 SPREAD SLAB BEAM

A.1   GENERAL

The following design illustrates a typical structural design procedure for an interior precast prestressed slab beam used in a spread configuration for a simply supported bridge. The design is based on the American Association of State Highway and Transportation Officials (AASHTO) Load and Resistance Factor Design (LRFD) Specifications (2012). Also the recommendations provided in the *Texas Department of Transportation (TxDOT) Bridge Design Manual—LRFD* (TxDOT 2013a) are considered in the design. The parameters used in this example are for the Riverside Bridge, which was constructed for this project and is discussed further in Chapter 4 of this report.Equation Chapter 1 Section 1

A.2   GEOMETRIC AND MATERIAL PROPERTIES OF THE BRIDGE

A.2.1   Bridge Geometry

Figure A.1 shows the bridge cross-section and Table A.1 summarizes the geometric parameters for the considered bridge. The spread slab beam bridge considered has a 46 ft 7 in. center-to-center of bearing pad span length, with a roadway width of 32 ft and total width of 34 ft. The bridge superstructure consists of four 5SB15 slab beams with 9 ft 8 in. center-to-center spacing. Precast prestressed concrete panels (PCP) that are 4 in. thick are used as stay-in-place forms between slab beams. The thickness of the cast-in-place (CIP) deck on top of the PCP is 4 in. Therefore, the total deck thickness is 8 in. between slab beams. However, due to camber, the deck thickness may be 0.5–4.0 in. thicker on top of the slab beams. This example follows TxDOT standard design procedure, which is to include a constant 2 in. haunch thickness in the girder weight but neglect the contribution of the haunch to the girder stiffness. Therefore, the total thickness of the bridge deck is taken as 8 in. constant everywhere. The CIP concrete bridge deck is designed to act compositely with the slab beam girders. The wearing surface is considered as 2 in. thick asphalt. Vehicular live loading is considered as the AASHTO LRFD Specifications (2012) HL-93 loading, consisting of a combination of HS20 design truck or design tandem, whichever is more critical, and a design lane load of 0.64 kips/ft. The precast prestressed beams are standard 5SB15 type slab beams. The width of the slab beams is $b = 5$ ft, and the depth of the slab beam is $d = 15$ in.
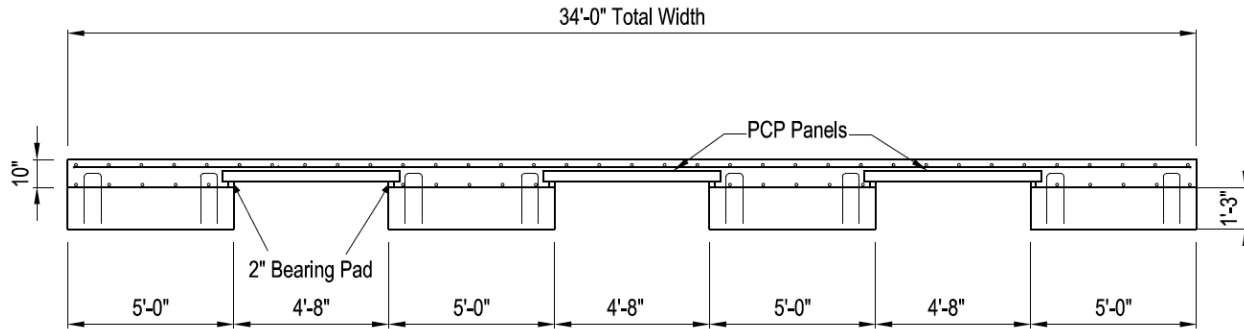
Figure A.1. Bridge Cross-Section.

Table A.1. Geometric Properties.

Parameter	Description/Value
Span Length (Center-to-Center of Bearing Pad), L	46 ft 7 in.
Total Bridge Width, w	34 ft
Slab Beam Type	5SB15 (5 ft width, 15 in. depth)
Center-to-Center Beam Spacing, S	9 ft 8 in.
Deck Thickness, t_s	8 in.
Haunch Thickness, t_h	Assumed constant 2 in. for weight calculation. Not included for stiffness calculation.
Rail	T551 (0.326 kips/ft, distributed to three beams from the edge)
Wearing Surface	2 in. thick asphalt assumed

The construction process of the superstructure consists of two phases. The first phase is the erection of the precast prestressed components, which includes precast prestressed slab beams and PCPs. The second phase is the casting of the CIP concrete deck on top of the PCPs. This type of construction process reduces the construction time and saves the contractor from constructing and shoring the formwork.

The number of design lanes is computed according to the AASHTO LRFD Specifications (2012) Article 3.6.1.1.1 as the number of design lanes is the integer part of the ratio of (w/12), where w is the clear roadway width between curbs or barriers. The value of w is 32 ft for this example, so the bridge that is being described herein is a two-lane bridge.

The bridge is constructed using the precast slab beams in a spread configuration. In order to maximize the load variation between slab beams, the spacing between the slab beams is maximized. Only four slab beams are used, resulting in a clear spacing of 4 ft 8 in. between slab beam girders.

In order to calculate section properties, the effective flange width needs to be calculated. The AASHTO LRFD Specifications (2012) define the effective flange width as being the tributary width, which is the center-to-center spacing of girders (9 ft 8 in. for the interior girders).

A.2.2 Material Properties

The material properties for the bridge are summarized in Table A.2. The specified 28-day compressive strength for the CIP deck is 4 ksi. Normal weight concrete is assumed throughout the construction with a 0.15 kcf unit weight. The wearing surface is considered as asphalt with a 2 in. thickness and 0.14 kcf unit weight.

Precast prestressed concrete slab beams are considered as self-consolidating concrete (SCC). Because the initial compressive stress limit is one of the controlling parameters for spread slab beam bridge design, the maximum permissible compressive strength at release is used. The *TxDOT Bridge Design Manual* (TxDOT 2013a) provides limits for the compressive strength of the concrete. The compressive strength of the concrete at release (f_{ci}') is specified to be between 4–6 ksi, and the compressive strength of the concrete at service (f_c') is specified to be between 5–8.5 ksi.

The standard prestressing for the slab beam girders is 0.5 in. diameter (nominal cross-sectional area of A_{ps} = 0.153 in^2), seven-wire, low-relaxation strands having an ultimate strength, f_{pu}, of 270 ksi. The yield strength for this type of strand is defined by manufacturers as $f_{py} = 0.9 f_{pu} = 243 \text{ ksi}$ and the modulus of elasticity is considered as $E_p = 28,500 \text{ ksi}$.

Mild steel reinforcement used for foundation elements, abutments, slab beams, and deck is specified to be American Society for Testing and Materials (ASTM) A615 Grade 60 steel with a modulus of elasticity of $E_s = 29,000 \text{ ksi}$.

A.2.3 Cross-Sectional Properties

The geometric dimensions and strand positions for a 5SB15 slab beam girder are provided in Figure A.2. The number and arrangement of prestressing strands follow the standard strand configuration that is set for TxDOT slab beam types. Based on geometric constraints and cover requirements, 56 strands (28 strands per row) can be placed in two rows with a 2 in. center-to-center spacing.

Table A.2. Specified Nominal Material Properties.

Parameter	Description/Value
28-Day Concrete Compressive Strength of Deck, f_{cd}'	4.0 ksi
Initial Concrete Compressive Strength of Precast Slab Beam, f_{ci}'	4.0–6.0 ksi
28-Day Concrete Compressive Strength of Precast Slab Beam, f_c'	5.0–8.5 ksi
Unit Weight of Concrete, w_c	0.15 kcf
Unit Weight of Asphalt Overlay, w_s	0.14 kcf
Prestressing Strands	7-wire low-relaxation strands
Ultimate Strength of Prestressing Stands, f_{pu}	270 ksi
Modulus of Elasticity of Strands, E_p	28,500 ksi

A.2.3.1 Precast Slab Beam

The section properties for the precast 5SB15 slab beam are found as follows. The moment of inertia about the centroid of the slab beam, I_b, is determined as:

$$I_b = \frac{1}{12}bd^3 = \frac{(60)(15)^3}{12} = 16,875 \text{ in}^4 \tag{A.1}$$

The section modulus of the slab beam referenced to extreme bottom fiber of the girder is:

$$S_b = \frac{I_b}{y_b} = \frac{16,875}{7.5} = 2250 \text{ in}^3 \tag{A.2}$$

The section modulus of the slab beam referenced to extreme top fiber of the girder is:

$$S_t = \frac{I_b}{y_t} = \frac{16,875}{7.5} = 2250 \text{ in}^3 \tag{A.3}$$

A.2.3.2 Composite Slab Beam and Deck Section

The tributary area for one girder is calculated based on the geometric properties of the bridge and number of girders used. The composite section has a 9 ft 8 in. flange width and an 8 in. slab thickness. The geometric dimensions of the composite section are shown in Figure A.2.
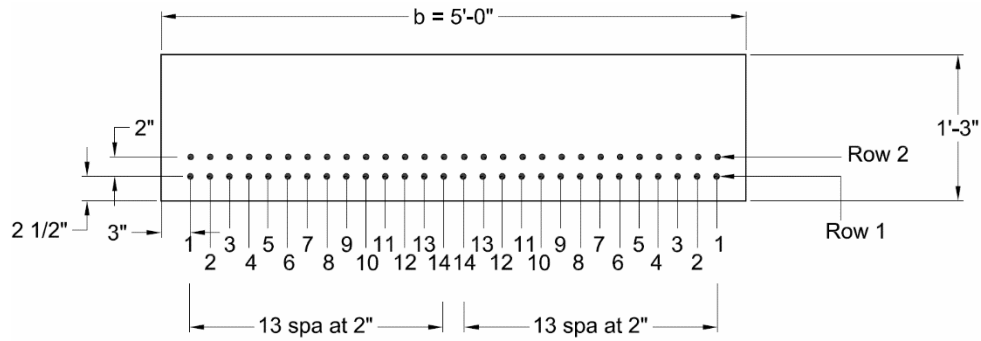
(a) Typical 5SB15 Slab Beam Section and Strand Configuration.
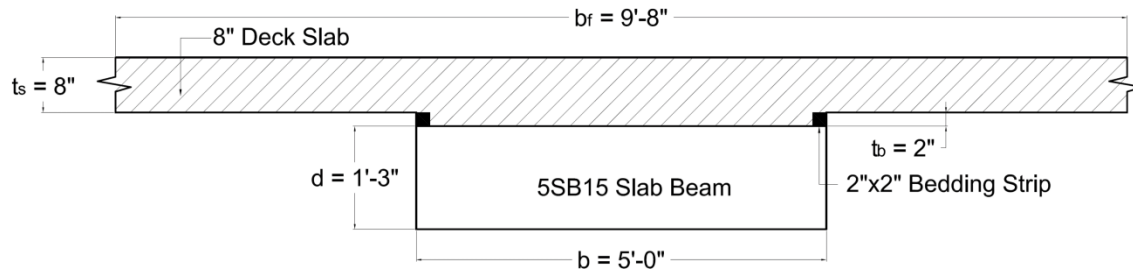
(b) Dimensions of Composite Cross-Section.

Figure A.2. Precast Slab Beam and Composite Beam Sections.

The values for the modulus of elasticity for the CIP deck and the precast concrete slab beam are different. Therefore, transformed section properties are calculated using the modular ratio between the CIP deck slab and precast prestressed slab beam girder. For the preliminary design example, a concrete compressive strength of $f_c' = 7$ ksi was used for slab beams.

The modular ratio is determined as:

$$\eta = \frac{E_{cd}}{E_c} = \sqrt{\frac{f_{cd}'}{f_c'}} = \sqrt{\frac{4}{7}} = 0.756 \tag{A.4}$$

Where:

E_{cd} = Modulus of elasticity of deck concrete, ksi.

E_c = Modulus of elasticity of slab beam concrete, ksi.

The transformed effective flange width is 87.688 in.

The haunch thickness is neglected, as suggested by the *TxDOT Bridge Design Manual* (TxDOT 2013a). The haunch thickness depends on the precast beam camber and may be smaller than 2 in. In some locations it may be as small as 0.5 in. Therefore, it is conservative to assume zero haunch thickness when determining cross-sectional properties. This assumption is used in the following calculation. On the other hand, an average 2 in. haunch thickness is included in the self-weight calculation to avoid being unconservative in the load calculations.

The transformed section properties are found as follows. The gross area of the transformed section is calculated using the expression below.

$$A_{gt} = b_e t_s + bd = 1601.5 \text{ in}^2 \tag{A.5}$$

The distance from the centroid of the composite section to the extreme top fiber of the slab (y_{tc}) is determined using the following expression.

$$y_{tc} = \frac{\left[(b_e t_s)\frac{t_s}{2} + (bd)\left(t_s + \frac{d}{2}\right)\right]}{A_{gt}} = \frac{\left[(87.688)(8)(4) + (60)(15)(15.5)\right]}{1,601.5} = 10.46 \text{ in.} \tag{A.6}$$

The distance from the centroid of the composite section to the extreme bottom fiber of the girder, y_{bc}, is determined as:

$$y_{bc} = H - y_{tc} = 23 - 10.46 = 12.54 \text{ in.} \tag{A.7}$$

Where:

H = Total depth of the composite section, in.

The moment of inertia about the centroid of the composite section is found using Equation (A.8).

$$I_c = \frac{1}{12}b_e t_s^3 + t_s b_e \left(y_{tc} - \frac{t_s}{2}\right)^2 + \frac{1}{12}bd^3 + bd\left(y_{bc} - \frac{d}{2}\right)^2 \tag{A.8}$$

$$I_c = \frac{1}{12}87.69(8)^3 + 87.69(8)(6.46)^2 + \frac{1}{12}(60)(15)^3 + (60)(15)(5.04)^2$$
$$= 72,753 \text{ in}^4$$

The composite section modulus referenced to the extreme bottom fiber of the girder, S_{bc}, is found using Equation (A.9).

$$S_{bc} = \frac{I_c}{y_{bc}} = \frac{72,753}{12.54} = 5803 \text{ in}^3 \tag{A.9}$$

The composite section modulus referenced to the extreme top fiber of the slab, S_{tc}, is found using Equation (A.10).

$$S_{tc} = \frac{I_c}{y_{tc}} = \frac{72,753}{10.46} = 6954 \text{ in}^3 \qquad (A.10)$$

The composite section modulus referenced to the top fiber of the precast girder, S_{tg}, is found using Equation (A.11).

$$S_{tg} = \frac{I_c}{y_{tg}} = \frac{72,753}{2.46} = 29,542 \text{ in}^3 \qquad (A.11)$$

Where y_{tg} is the distance of the top fiber of the precast beam to the centroid of the composite section and is calculated as:

$$y_{tg} = y_{tc} - t_s = 10.46 - 8 = 2.46 \text{ in.} \qquad (A.12)$$

A.3   STRESS LIMITS

All structural components must be designed to satisfy all appropriate service limit states. For prestressed or partially prestressed concrete structural components, these limit states are stress limit states. All concrete sections must be investigated at transfer and at service stress limits.

A.3.1   Allowable Stress Limits for Concrete

Allowable stress limits are specified in the AASHTO LRFD Specifications (2012). Slab beams are structural concrete members with bonded prestressing tendons. For the tensile stress limit check at service, the longitudinal members should be analyzed under load combination Service III, as specified in AASHTO LRFD Specifications (2012) Table 3.4.1-1.

A.3.1.1 Allowable Stress Limits at Transfer

The tensile stress limit at transfer, F_{ti}, is used as specified in the AASHTO LRFD Specifications (2012) Table 5.9.4.1.2-1. This limit allows the use of an increased tensile stress limit in areas with bonded reinforcement. The amount of bonded reinforcement is determined based on the tensile force at the critical section. The tensile stress limit in the sections with bonded reinforcement assuming an uncracked section, where reinforcement is proportioned using $0.5 f_y$, before losses is given as:

$$F_{ti} = 0.24\sqrt{f_{ci}^{'}} = (0.24)\sqrt{6} = 0.588 \text{ ksi} \tag{A.13}$$

AASHTO LRFD Specifications (2012) specifies a compressive stress limit before losses, F_{ci}, for pretensioned and post-tensioned concrete members in Article 5.9.4.1.1 as $0.6 f_{ci}^{'}$. However, *TxDOT Bridge Design Manual—LRFD* (TxDOT 2013a) specifies an increased compressive stress limit at transfer. The compressive stress limit at transfer before losses is given as:

$$F_{ci} = 0.65 f_{ci}^{'} = (0.65)(6) = 3.9 \text{ ksi} \tag{A.14}$$

A.3.1.2 Allowable Stress Limits at Service

The tensile stress limit for prestressed concrete at the service limit state after losses for fully stressed components, F_t, is given in AASHTO LRFD Specifications (2012) Table 5.9.4.2.2-1 as:

$$F_t = 0.19\sqrt{f_c^{'}} = 0.19\sqrt{7} = 0.503 \text{ ksi} \tag{A.15}$$

For the compressive stress limit state, service limit state load combination Service I, specified in AASHTO (2012) Table 3.4.1-1, is used. The compressive stress limit for prestressed concrete at the service limit state after losses, F_c, is given in AASHTO LRFD Specifications (2012) Table 5.9.4.2.1-1 as:

$$F_c = 0.45 f_c^{'} = (0.45)(7) = 3.15 \text{ ksi} \tag{A.16}$$

A.3.2   Stress Limits for Prestressing Strands

AASHTO LRFD Specifications (2012) Table 5.9.3-1 specifies tensile stress limits for tendons due to prestress or at the service limit state. For a low-relaxation strand, the stress limit prior to transfer, f_{pbt}, and at the service limit state after all losses, f_{pe}, is provided as:

Before transfer: $f_{pbt} \leq 0.75 f_{pu} = 202.5 \text{ ksi}$

At service: $f_{pe} \leq 0.8 f_{py} = 194.4 \text{ ksi}$

A.4   STRUCTURAL ANALYSIS RESULTS

Structural analysis of the superstructure is conducted using the AASHTO LRFD Specifications (2012) approximate analysis approach, which utilizes live load distribution factors for truck and uniform lane loading. Based on the approximate analysis approach, an interior slab beam

composite section is analyzed statically. The effective width of the concrete deck slab is taken as the tributary width perpendicular to the axis of the member, which is the center-to-center spacing between slab beams.

A.4.1 Shear Forces and Bending Moments for a Typical Interior Girder

Bending moments of an interior girder are calculated when the vehicle is at the critical bending moment location for combined loading. Combined loading includes the dead load of all structural components, superimposed dead loads, and the design live load.

A.4.1.1 Dead Load

Dead load is assumed to act on the non-composite slab beam section because it will be in place when the deck concrete is fresh. Although the haunch thickness is neglected when calculating the composite section modulus, the weight of the haunch concrete is included in the dead load calculation considering an average 2 in. thick haunch.

The dead load of all structural components and nonstructural attachments is determined as:

$$DC = \gamma_c (A_b + A_h + A_s) = 0.15 \times (5 \times 1.25 + 5 \times 0.167 + 9.667 \times 0.667) = 2.029 \text{ kips/ft} \text{ (A.17)}$$

Where:

γ_c = Density of the concrete, kips/ft^3.

A_b = Cross-sectional area of the slab beam, ft^2.

A_s = Cross-sectional area of the deck slab, ft^2.

A_h = Cross-sectional area of the haunch section, ft^2.

A.4.1.2 Superimposed Dead Load

Superimposed dead loads are assumed to act after the composite action between the slab beam girders and deck slab takes place. According to *TxDOT Bridge Design Manual* (TxDOT 2013a), the wearing surface load can be equally distributed among four girders, and the rail load can be distributed to no more than three girders from the edge of the deck.

The weight of the 2 in. asphalt wearing surface, W_{ws}, is calculated using the following expression.

$$W_{ws} = \frac{0.14 \times \left(\dfrac{2}{12} \times 34 \right)}{4} = 0.198 \text{ kips/ft}$$

The weight of T501 rails or barriers, W_r, on each interior girder is calculated as:

$$W_r = \frac{2 \times 0.326}{3} = 0.217 \text{ kips/ft}$$

The dead load of wearing surfaces and utilities (including the rails), DW, is calculated using Equation (A.18).

$$DW = W_{ws} + W_r = 0.415 \text{ kips/ft} \tag{A.18}$$

A.4.1.3 Live Load

AASHTO LRFD Specifications (2012) Article 3.6.1.2 specifies the design live load as HL-93, which consists of a combination of the design truck with dynamic allowance or the design tandem with dynamic allowance, whichever produces greater moments and shears, and design lane load without dynamic allowance.

A.4.1.3.1 Design Truck and Lane Loads

Figure A.3(a) shows the HS20 design truck and tire load positions. For a simply supported span, the design truck gives more critical moment when the distance between the second and rear axles is constantly equal and 14 ft.

Figure A.3(b) shows the load positions for a design tandem, which consists of a pair of 25-kip axles spaced 4.0 ft apart. For simply supported spans, the tandem loading governs for spans shorter than 40 ft.

The lane load consists of a load of 0.64 kips/ft uniformly distributed in the longitudinal direction (AASHTO LRFD Specifications (2012) Article 4.6.2.2). The bending moments due to vehicular live load can be distributed to individual girders using the simplified approximate distribution factor formulas specified by AASHTO LRFD Specifications (2012) if the following conditions are met.

- Width of the slab is constant.
- Number of girders is not less than four.
- Girders are parallel and of the same stiffness.

- Roadway part of the overhang is $d_e \leq 3.0$ ft.
- Curvature in plan is less than 4 degrees.
- Cross-section of the bridge girder is consistent with one of the cross-sections given in AASHTO LRFD Specifications (2012) Table 4.6.2.2.1-1.

8.0 KIP   32.0 KIP   32.0 KIP

14'-0"   14'-0" TO 30'-0"

6'-0"
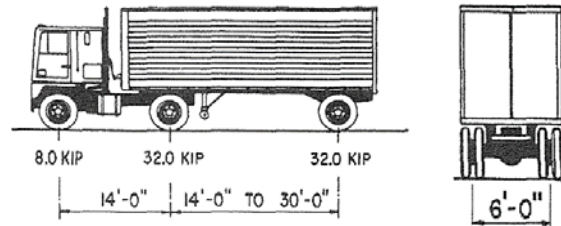
(a) HS20 Design Truck (AASHTO 2012)

25 kips   25 kips

Profile

Traffic Direction

12.5 k   12.5 k

Loading Lane   6'-0"   Top View

12.5 k   12.5 k

4'-0"
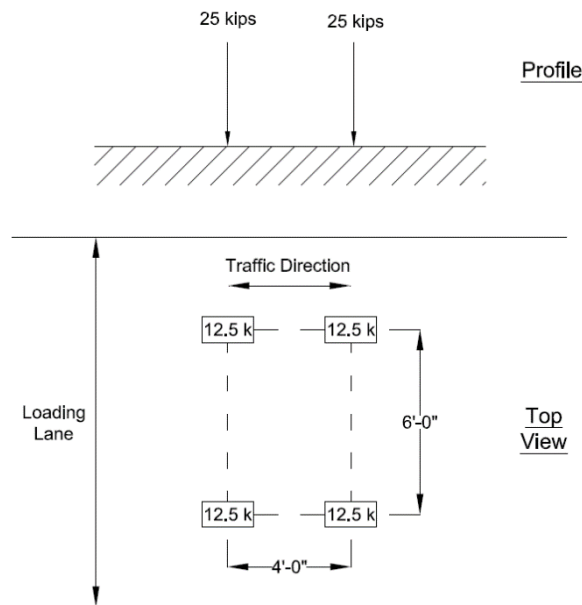
(b) Design Tandem

Figure A.3. AASHTO HL-93 Design Vehicles

A.4.1.3.2 Live Load Distribution Factors

Although there is no spread slab beam configuration defined in AASHTO LRFD Specifications (2012), spread box beam formulas are used per TxDOT`s suggestion as a preliminary design guide. Live load moment and shear distribution factors for interior girders are provided in AASHTO LRFD Specifications (2012) Tables 4.6.2.2.2b-1 and 4.6.2.2.3a-1.

264

Moment distribution factor for one design lane loaded case, g_{M1}, is calculated as:

$$g_{M1} = \left(\frac{S}{3.0}\right)^{0.35} \times \left(\frac{Sd}{12.0L^2}\right)^{0.25} = \left(\frac{9.67}{3.0}\right)^{0.35} \left(\frac{9.67 \times 15}{12 \times 46.58^2}\right)^{0.25} = 0.41 \qquad (A.19)$$

Moment distribution factor for two design lane loaded case, g_{M2}, is calculated as:

$$g_{M2} = \left(\frac{S}{6.3}\right)^{0.6} \times \left(\frac{Sd}{12.0L^2}\right)^{0.125} = \left(\frac{9.67}{6.3}\right)^{0.6} \times \left(\frac{9.67 \times 15}{12 \times 46.58^2}\right)^{0.125} = 0.68 \qquad (A.20)$$

Shear distribution factor for one design lane loaded case, g_{V1}, is calculated as:

$$g_{V1} = \left(\frac{S}{10}\right)^{0.6} \times \left(\frac{d}{12.0L}\right)^{0.1} = \left(\frac{9.67}{10}\right)^{0.6} \times \left(\frac{15}{12 \times 46.58}\right)^{0.1} = 0.68 \qquad (A.21)$$

Shear distribution factor for two design lane loaded case, g_{V2}, is calculated as:

$$g_{V2} = \left(\frac{S}{7.4}\right)^{0.8} \times \left(\frac{d}{12.0L}\right)^{0.1} = \left(\frac{9.67}{7.4}\right)^{0.8} \times \left(\frac{15}{12 \times 46.58}\right)^{0.1} = 0.86 \qquad (A.22)$$

Where:

g_M = $Max(g_{M1}, g_{M2}) = 0.676$ lanes/girder.

g_V = $Max(g_{V1}, g_{V2}) = 0.86$ lanes/girder.

g_M = Live load moment distribution factor.

g_v = Live load shear distribution factor.

S = Girder spacing, ft.

L = Girder span, ft.

d = Depth of the girder, in.

A.4.1.3.3 Dynamic Load Allowance

AASHTO LRFD Specifications (2012) Table 3.6.2.1-1 specifies the dynamic load effects as a percentage of the static live load effects and to be taken as 33 percent of the static load effects for all limit states except the fatigue limit state and 15 percent for the fatigue limit state.

A.4.2 Influence Line Analysis

Figure A.4 presents the load cases for the influence line analysis used herein. Bending moment and shear force due to truckload at any section at a distance x and for a truck position z are calculated as the truck passes over the span.

$$R_{TR} = 8 \times \left(1 - \frac{z}{L}\right) + 32 \times \left(1 - \frac{z+14}{L}\right) + 32 \times \left(1 - \frac{z+28}{L}\right) \tag{A.23}$$

$$V_{TR} = \begin{cases} g_V \times 1.33 \times R_{TR} & x \le z \\ g_V \times 1.33 \times (R_{TR} - 8) & z < x \le z + 14 \\ g_V \times 1.33 \times (R_{TR} - 40) & z + 14 < x \le z + 28 \\ g_V \times 1.33 \times (R_{TR} - 72) & x > z + 28 \end{cases} \tag{A.24}$$

$$M_{TR} = \begin{cases} g_M \times 1.33 \times R_{TR} x & x \le z \\ g_M \times 1.33 \times (R_{TR} x - 8(x-z)) & z < x \le z + 14 \\ g_M \times 1.33 \times (R_{TR} x - 8(x-z) - 32(x-z-14)) & z + 14 < x \le z + 28 \\ g_M \times 1.33 \times (R_{TR} x - 8(x-z) - 32(2x-2z-42)) & x > z + 28 \end{cases} \tag{A.25}$$

Where:

R_{TR} = Reaction force at the left end support, kips.

V_{TR} = Shear force as a function of truck position and location, kips.

M_{TR} = Bending moment as a function of truck position and location, kip-ft.

It is shown that the design tandem loading does not give the critical moment for a simply supported span that is longer than 40 ft. The maximum bending moment and shear forces are calculated using the influence line method. The shear force and bending moment at each section x (ft) are formulated based on the position of the tandem, z (ft), as it passes over the span.

$$R_{TN} = 25 \times \left(1 - \frac{z}{L}\right) + 25 \times \left(1 - \frac{z+4}{L}\right) \tag{A.26}$$
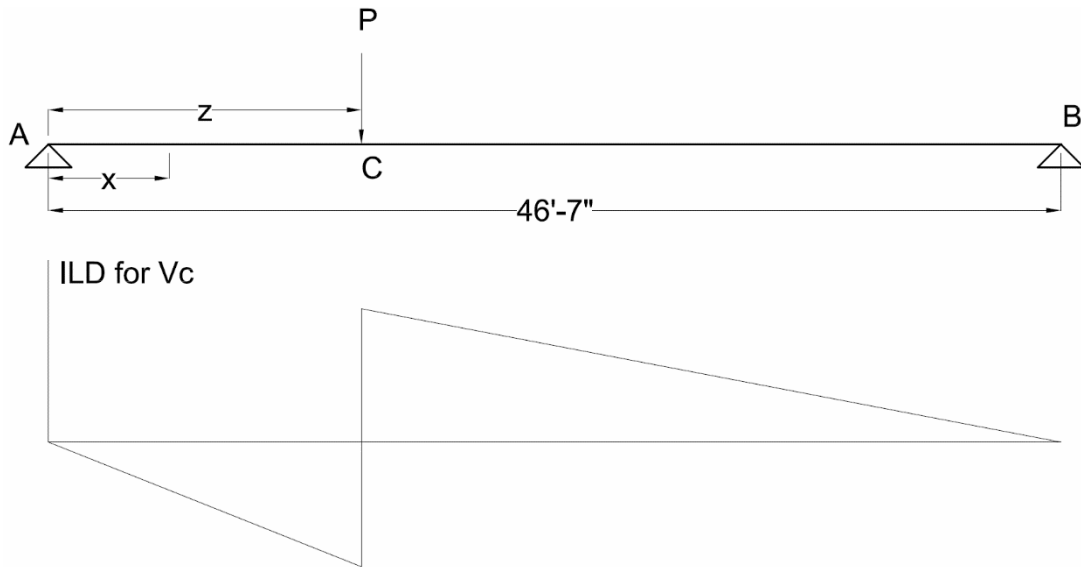
(a) Influence Line Diagram (ILD) for Shear for a Representative Point Load
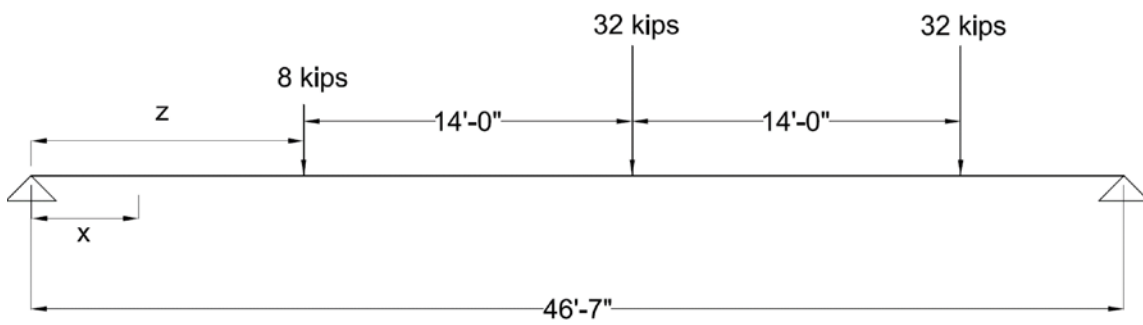
(b) HS20 Truck
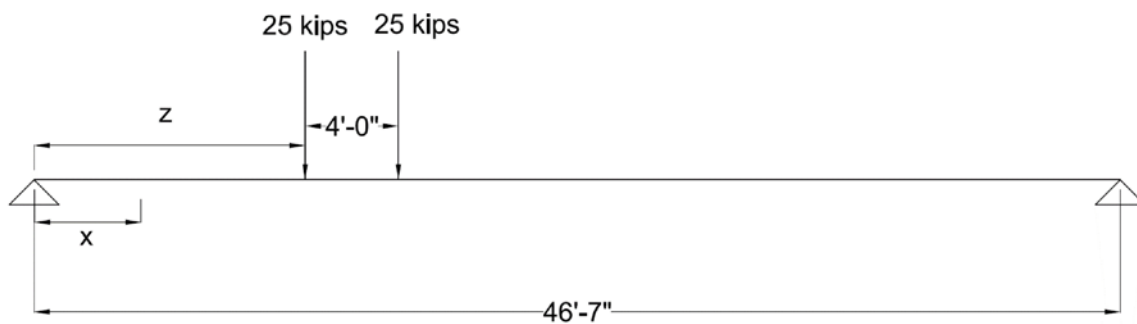
(c) Design Tandem

Figure A.4. Load Cases for Influence Line Analysis.

A.4.3 Maximum Moment and Shear

Design moment for an interior girder is calculated for two different vehicle positions in order to show the difference. The first calculation is done when the vehicle is located at a critical moment position for the HS20 truck only (HS20 critical). For a series of point loads over a simply supported span, the maximum moment occurs under the load closest to the resultant when the load and resultant are placed equidistant from midspan. For an HS20 truck that has second and rear axles 14 ft apart, the critical moment position is when the second axle is 2 ft 4 in. away from the midspan. The vehicle position and all the moment results for that vehicle position are shown in Figure A.5.

The second calculation is done when the vehicle is located at a critical moment position for the combined loading (combined loading critical). The maximum moment occurs at 2 ft 4 in. away from the midspan for the HS20 truck, whereas the maximum moment for the uniform lane load and dead loads occurs at the midspan. This means the maximum moment for combined loading occurs somewhere in between these two points. This point is calculated using more refined analysis by the influence line method. The results of this loading case are shown in Figure A.6. Although the maximum moment results are close, the second calculation gives a little higher maximum moment, and this is the one that should be used.

The shear forces and bending moments due to uniform dead loads and uniform superimposed dead loads, V_D and M_D, at any section at a distance x are calculated using the following expressions, where the uniform load is denoted as w.

$$M_D = \frac{wL}{2}x - \frac{wx^2}{2} \tag{A.27}$$

$$V_D = \frac{wL}{2} - wx \tag{A.28}$$

Superimposed dead loads are calculated separately since they will be acting on the composite section, whereas the self-weight of the beam and the deck slab will act on the girders only.

$$V_{TN} = \begin{cases} g_V \times 1.33 \times R_{TN} & x \le z \\ g_V \times 1.33 \times (R_{TN} - 25) & z < x \le z + 4 \\ g_V \times 1.33 \times (R_{TN} - 50) & x > z + 4 \end{cases} \tag{A.29}$$

$$
M_{TN} = \begin{cases}
g_M \times 1.33 \times R_{TN}x & x \leq z \\
g_M \times 1.33 \times (R_{TN}x - 25(x-z)) & z < x \leq z+4 \\
g_M \times 1.33 \times (R_{TN}x - 25(2x - 2z - 4)) & x > z+4
\end{cases} \tag{A.30}
$$

Where:

R_{TN} = Reaction force at the left end support, kips.

V_{TN} = Shear force as a function of tandem position and location, kips.

M_{TN} = Bending moment as a function of tandem position and location, kip-ft.

Shear forces and bending moments due to uniformly distributed lane load of 0.64 kips/ft are calculated using the following expressions.

$$
V_{LL} = \frac{wL}{2} - wx \tag{A.31}
$$

$$
M_{LL} = \frac{wL}{2}x - \frac{wx^2}{2} \tag{A.32}
$$

Where:

V_{LL} = Shear force due to uniformly distributed design lane load, kips.

M_{LL} = Moment due to uniformly distributed design lane load, kip-ft.

The bending moment results when the vehicle is at the HS20 critical position are shown in Figure A.5. Plot (b) shows unfactored moments for dead load of structural components (DC), dead load of wearing surface and utilities (DW), design truck live load (HS20), and uniform design lane live load (Lane). Plot (c) shows the total moments when all the live loads are multiplied by the moment distribution factor and dynamic allowance applied to the HS20 load.

The bending moment results when the HS20 truck is at the combined critical position are shown in Figure A.6. The bending moments are calculated using Equations (A.32) to (A.35), similar to the other case, but this time, all the loads are combined together to figure out the critical moment position of the vehicle. The combined moment results are shown in Figure A.6(b).

$$
R_{TR} = 8 \times \left(1 - \frac{z}{L}\right) + 32 \times \left(1 - \frac{z+14}{L}\right) + 32 \times \left(1 - \frac{z+28}{L}\right) \tag{A.33}
$$

$$V_{TR} = \begin{cases} g_V \times (1.33 \times R_{TR} + 0.64\dfrac{L}{2} - 0.64x) + W\dfrac{L}{2} - Wx & x \le z \\[2mm] g_V \times (1.33 \times (R_{TR} - 8) + 0.64\dfrac{L}{2} - 0.64x) + W\dfrac{L}{2} - Wx & z < x \le z + 14 \\[2mm] g_V \times (1.33 \times (R_{TR} - 40) + 0.64\dfrac{L}{2} - 0.64x) + W\dfrac{L}{2} - Wx & z + 14 < x \le z + 28 \\[2mm] g_V \times (1.33 \times (R_{TR} - 72) + 0.64\dfrac{L}{2} - 0.64x) + W\dfrac{L}{2} - Wx & z + 28 < x \end{cases}$$ (A.34)

$$M_{TR} = \begin{cases} g_M\left(1.33R_{TR}x + 0.64\dfrac{L}{2}x - 0.64\dfrac{x^2}{2}\right) + W\dfrac{L}{2}x - W\dfrac{x^2}{2} & x \le z \\[2mm] g_M\left(1.33\left(R_{TR}x - 8(x-z)\right) + 0.64\dfrac{L}{2}x - 0.64\dfrac{x^2}{2}\right) + W\dfrac{L}{2}x - W\dfrac{x^2}{2} & z < x \le z + 14 \\[2mm] g_M\left(1.33\left(R_{TR}x - 8(x-z) - 32(x-z-14)\right) + 0.64\dfrac{L}{2}x - 0.64\dfrac{x^2}{2}\right) + W\dfrac{L}{2}x - W\dfrac{x^2}{2} & z + 14 < x \le z + 28 \\[2mm] g_M\left(1.33\left(R_{TR}x - 8(x-z) - 32(2x - 2z - 42)\right) + 0.64\dfrac{L}{2}x - 0.64\dfrac{x^2}{2}\right) + W\dfrac{L}{2}x - W\dfrac{x^2}{2} & z + 28 < x \end{cases}$$

(A.35)

Where:

W = Sum of all dead loads (DC+DW), kips.

L = Span length, ft.

The maximum bending moment is obtained when the second axle of the design truck is 1 ft 1.5 in. away (combined loading critical position) from the midspan and the distance between the second axle and rear axle is 14 ft.

The bending moment values that are shown in the total bending moments plot (c) include the dynamic allowance and live load distribution factors, but they are not multiplied by any load factors. The design values should be multiplied by the load combination factors.
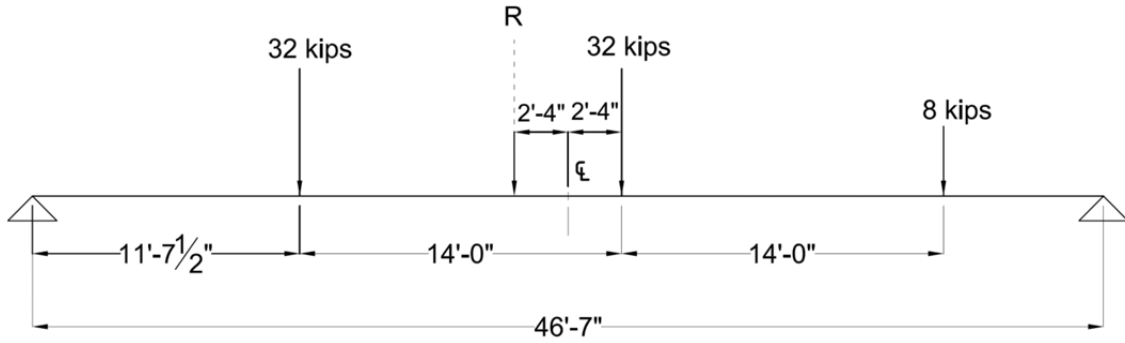
(a) HS20 Truck Position
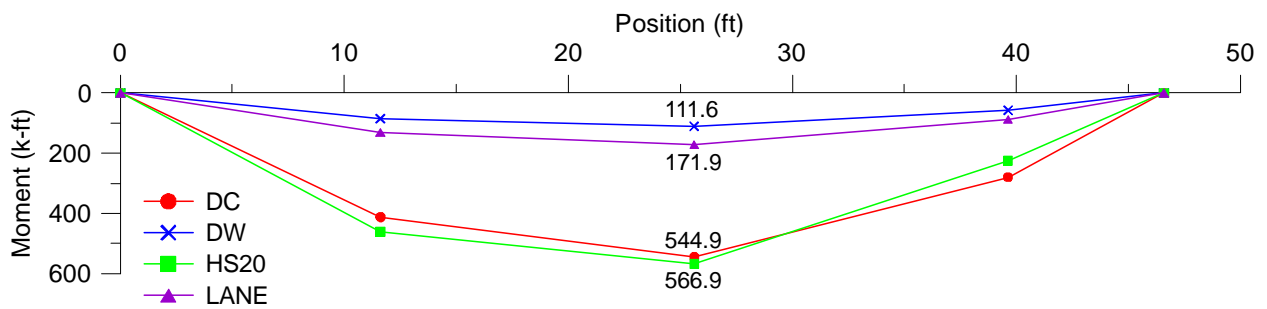
(b) Unfactored Bending Moments
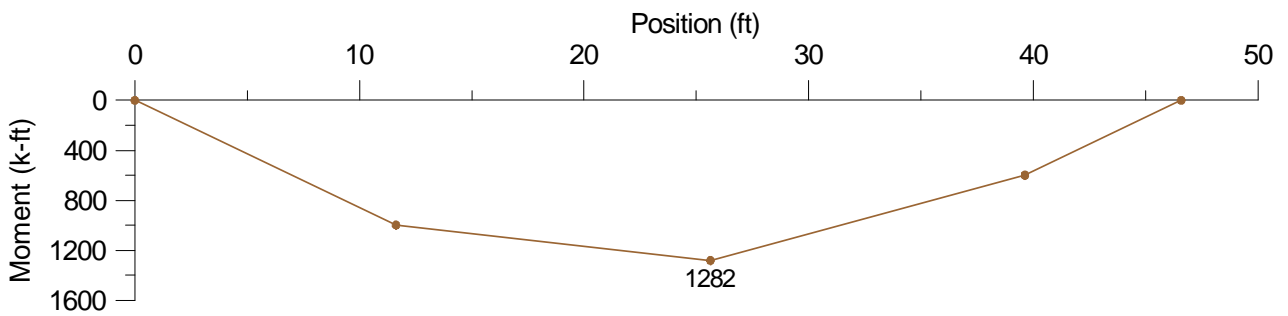
(c) Total Bending Moments

Figure A.5. Bending Moments When the Vehicle Is at Critical Position for HS20 Loading.
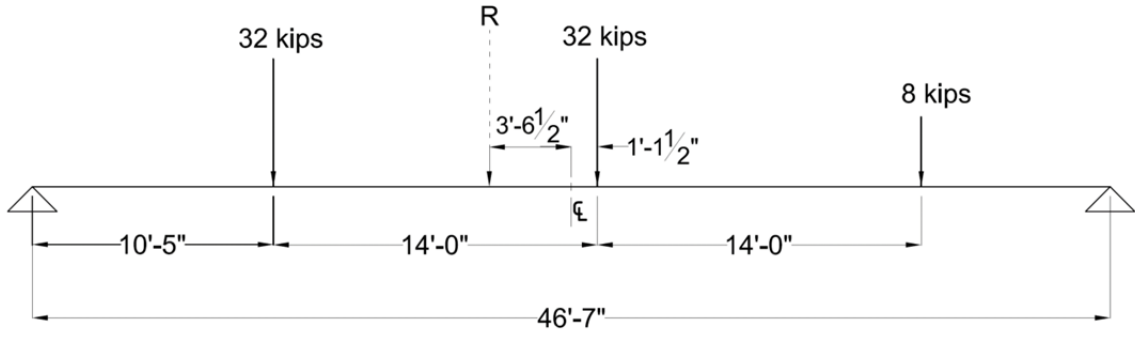
(a) HS20 Truck Position
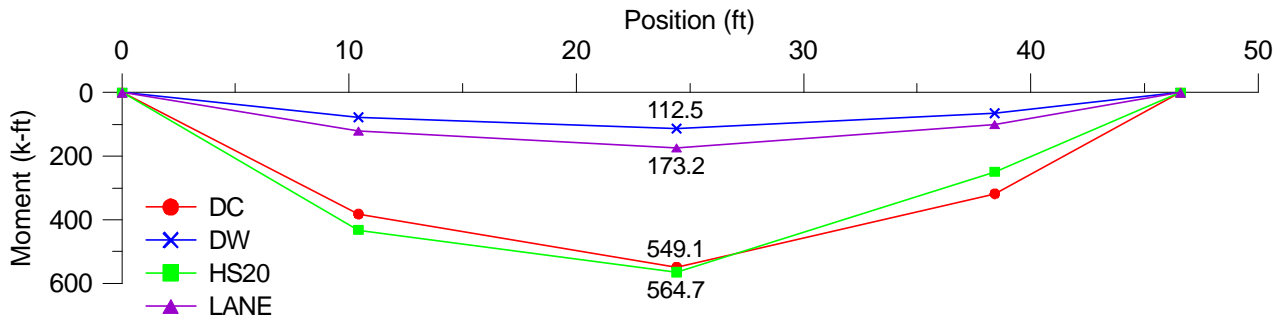
(b) Unfactored Bending Moments
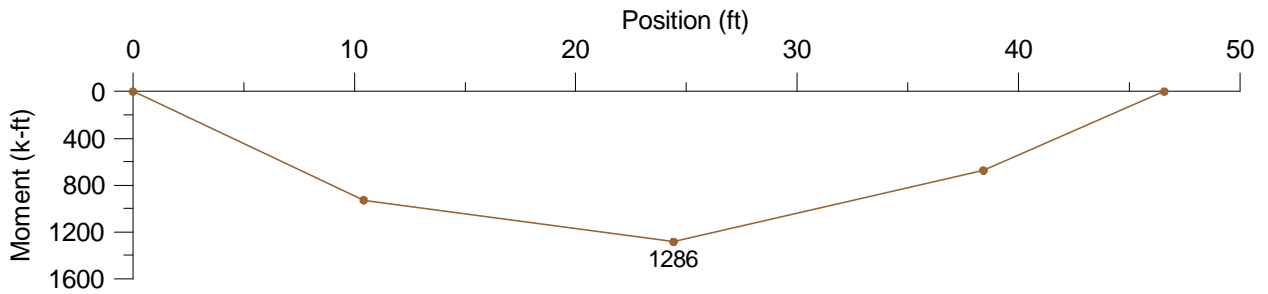
(c) Total Bending Moments

Figure A.6. Bending Moments When Vehicle is at Critical Position for Combined Loading.

A.4.4 Load Combinations

AASHTO LRFD Specifications (2012) Article 3.4.1 states that the total load effect can be calculated using certain service state load combinations. Service I and Service III load combinations are used for the design of a prestressed bridge superstructure as an uncracked section.

Service I load combination relates to the normal operational use of the bridge with a 55 mph wind and all loads taken at their nominal values. Service III load combination for longitudinal analysis relates to tension in prestressed concrete superstructures with the objective of crack control and to principal tension in the webs of segmental concrete girders.

AASHTO LRFD Specifications (2012) Table 3.4.1-1 specifies load combinations for various limit states. The load combinations that are critical for the designed bridge are as follows.

Service I—Check compressive stresses in prestressed concrete components:

$$Q = 1.00(DC + DW) + 1.00(LL + IM)$$

Service III—Check tensile stresses in prestressed concrete components:

$$Q = 1.00(DC + DW) + 0.80(LL + IM)$$

Strength I—Check ultimate strength [LRFD Table 3.4.1-1 & 2]:

$$\text{Maximum } Q = 1.25(DC) + 1.50(DW) + 1.75(LL + IM)$$

$$\text{Minimum } Q = 0.90(DC) + 0.65(DW) + 1.75(LL + IM)$$

Where:

DC =   Dead load of structural components and nonstructural attachments.

DW =   Dead load of wearing surface and utilities.

LL =   Vehicular live load.

IM =   Vehicular dynamic load allowance.

A.5   DESIGN FOR PRESTRESSING FORCE

A.5.1 Stresses at Midspan Due to Service Loads

Design of prestressed slab beams is based on the service limit stresses at the critical moment section of the bridge, assuming that the section is uncracked. The required prestressing force under service loads is calculated at the critical moment section. Other critical section stresses are

checked under the calculated prestressing force at transfer and at service after all prestressing losses.

A.5.1.1 Tensile Stress at Extreme Bottom Fiber of Interior Girder Due to Imposed Loads, f_b (Service III)

The maximum tensile stress at the bottom fiber of the slab beam girder is calculated using Equation (A.36). Live load moment at service (M_L) is calculated by multiplying the combined live load due to vehicle loading, which includes 33 percent dynamic impact, and AASHTO LRFD Specifications (2012) uniform distributed live load (0.64 kips/ft) with moment LDF.

$$f_b = \frac{M_b + M_s}{S_b} + \frac{M_{ws} + M_r + 0.8M_L}{S_{bc}} \tag{A.36}$$

$$M_L = g_M(1.33M_{TR} + M_{LL}) = 0.676 \times (1.33 \times 564.7 + 173.2) = 624.8 \text{ kip-ft}$$

$$f_b = \frac{549.1 \times 12}{2,250} + \frac{(112.5 + 0.8 \times 624.8) \times 12}{5802.88} = 4.2 \text{ ksi}$$

A.5.1.2 Compressive Stress at Top Fiber of Interior Girder Due to Imposed Loads, f_t (Service I)

Maximum compressive stress at the top fiber of the slab beam girder at service is calculated using Equation (A.37).

$$f_t = \frac{M_b + M_s}{S_t} + \frac{M_{ws} + M_r + M_L}{S_{tg}} \tag{A.37}$$

$$f_t = \frac{549.1 \times 12}{2250} + \frac{(112.5 + 624.8) \times 12}{29,542} = 3.23 \text{ ksi}$$

Where:

M_b = Bending moment due to self-weight of the slab beam at the moment critical section, kip-ft.

M_s = Bending moment due to CIP deck slab at the moment critical section, kip-ft.

M_{ws} = Bending moment due to wearing surface at the moment critical section, kip-ft.

M_r = Bending moment due to rail at the moment critical section, kip-ft.

M_L = Bending moment due to truck load plus the distributed lane load at the moment critical section, kip-ft.

The stress due to service loads and prestressing stresses should be within the allowable stress limits that are defined above.

A.5.1.3 Tensile Stress Limit

Tensile stress due to imposed loads at service shall satisfy the allowable tensile stress limit as defined in AASHTO LRFD Specifications (2012). Required prestressing force at service based on tensile stress limit can be calculated using Equation (A.38).

$$-\frac{F_{req}}{A_b}-\frac{F_{req}e}{S_b}+f_b < F_t \tag{A.38}$$

Where:

F_{req} = Total required pretension force after all losses to satisfy allowable stress limits, kips.

e = Eccentricity of prestressing force (4 in. when all 56 strand slots are used), in.

f_b = Bottom fiber tensile stress at service, ksi.

F_t = Tensile stress limit at service after all losses occur, ksi.

$$-\frac{F_{req}}{900}-\frac{F_{req}\times 4}{2250}+4.2 < 0.503 \text{ ksi}$$

$$\Rightarrow F_{req}=1280 \text{ kips}$$

A.5.1.4 Compressive Stress Limit

Required prestressing force at service based on compressive stress limit can be calculated using Equation (A.39).

$$-\frac{F_{req}}{A_b}+\frac{F_{req}e}{S_t}-f_t > F_c \tag{A.39}$$

Where:

F_c = Compressive stress limit at service after losses, ksi.

$$-\frac{F_{req}}{900}+\frac{F_{req}\times 4}{2250}-3.23 > -3.15 \text{ ksi}$$

$$\Rightarrow F_{req}=120 \text{ kips}$$

The total prestressing force should be at least 1280 kips in order to satisfy stress limits under service load conditions.

The number of strands can be calculated as:

$$F = N\left(A_{ps}\right)\left(f_{pe}\right)$$ (A.40)

Where:

N =   Number of prestressing strands.

f_{pe} =   Effective prestressing stress of one strand after all losses, ksi.

A_{ps} =   Nominal cross-sectional area of a prestressing strand (0.153 in^2 for 0.5 in. diameter strand), in^2.

In order to be able to calculate number of strands, prestress losses should be calculated.

A.5.2 Total Loss of Prestress

In pretensioned members, prestressing losses result from elastic shortening at the time of prestressing and long-term losses. Long-term losses for prestressed members include shrinkage, creep, and strand relaxation. Total prestress losses are calculated according to the empirical formulas provided in AASHTO LRFD Specifications (2012) Article 5.9.5. The formulas provided are for normal weight concrete only and valid for specified concrete strength up to 15 ksi.

$$\Delta f_{pT} = \Delta f_{pES} + \Delta f_{pLT}$$ (A.41)

Where:

Δf_{pT} =   Total prestress loss, ksi.

Δf_{pES} =   Sum of losses due to elastic shortening at the time of application of prestress, ksi.

Δf_{pLT} =   Losses due to long-term shrinkage and creep of concrete and relaxation of the steel, ksi.

A.5.2.1 Losses Due to Elastic Shortening

The loss due to elastic shortening in pretensioned members is calculated as:

$$\Delta f_{pES} = \frac{E_p}{E_{ct}} f_{cgp}$$ (A.42)

Where:

E_p = Modulus of elasticity of prestressing steel, ksi.

E_{ct} = Modulus of elasticity of concrete at transfer, ksi.

f_{cgp} = Concrete stress at the center of gravity of prestressing tendons due to prestressing force immediately after transfer and the self-weight of the member at the section of maximum moment, ksi.

F_i = Total prestressing force immediately after transfer.

$$f_{cgp} = \frac{F_i}{A} + \left(\frac{e}{d/2} \right) \left(\frac{F_i e}{S} - \frac{M_b}{S} \right) \tag{A.43}$$

For loss calculations, the number of strands used must be known. On the other hand, the required number of strands depends on the prestressing loss. This requires an iterative process. This calculation is carried out using an iterative calculation starting with 25 percent assumed total loss. The results show that all the prestressing strand locations must be used in order to achieve allowable stress limits under service loads.

$$F_i = N f_{pt} A_{ps} \tag{A.44}$$

$$f_{pi} = 0.75 \times 270 = 202.5 \text{ ksi}$$

Where:

f_{pi} = Prestressing stress immediately prior to transfer, ksi.

f_{pt} = Initial prestressing stress immediately after transfer, ksi.

$$f_{pt} = f_{pi} - \Delta f_{pES} \tag{A.45}$$

For calculating total prestressing force just after transfer, initial prestress after transfer, which depends on the elastic shortening loss, must be known. The initial prestress after transfer is assumed to be 90 percent of the prestress before transfer and analysis iterated until acceptable accuracy is achieved. The iterative calculation shows that the initial prestress after transfer is $f_{pt} = 186.9$ ksi.

$$F_i = 56 \times 186.88 \times 0.153 = 1601.2 \text{ kips}$$

$$f_{cgp} = \frac{1601.2}{900} + \left(\frac{4}{7.5} \right) \times \left(\frac{1601.2 \times 4}{2250} - \frac{254.3 \times 12}{2250} \right) = 2.574 \text{ ksi}$$

$$E_p = 28{,}500 \text{ ksi} \text{ and } E_c = 33{,}000 w_c^{1.5} \sqrt{f_{ci}'} \, (\text{ksi}) = 4696 \text{ ksi}$$

$$\Delta f_{pES} = \frac{28500}{4696}(2.574) = 15.62 \text{ ksi}$$

Initial prestress after elastic losses is calculated as, $f_{pt} = 202.5 - 15.62 = 186.9$ ksi, which is the same as the initial prestressing stress estimate.

A.5.2.2 Approximate Calculation of Time-Dependent Losses

Long term prestress losses are calculated using the approximate equation provided in AASHTO LRFD Specifications (AASHTO 2012) Article 5.9.5.3.

$$\Delta f_{pLT} = 10 \frac{\left(f_{pi} A_{ps} \right)}{A_g} \gamma_h \gamma_{st} + 12 \gamma_h \gamma_{st} + \Delta f_{pR} \qquad (A.46)$$

Where:

γ_h = Correction factor for relative humidity of the ambient air.

$$\gamma_h = 1.7 - 0.01H = 1.7 - 0.01(70) = 1 \qquad (A.47)$$

H = Average annual ambient relative humidity (%), which is obtained from AASHTO LRFD Specifications (2012) Figure 5.4.2.3.3-1.

γ_{st} = Correction factor for specified concrete strength at the time of prestress transfer to the concrete member.

$$\gamma_{st} = \frac{5}{1 + f_{ci}'} \qquad (A.48)$$

Δf_{pR} = Estimate of relaxation loss taken as 2.4 ksi for low-relaxation strands.

f_{pt} = Prestressing steel stress immediately prior to transfer, ksi.

$$\Delta f_{pLT} = 10 \times \frac{202.5 \times 56 \times 0.153}{900} \times 1 \times \frac{5}{7} + 12 \times 1 \times \frac{5}{7} + 2.4 = 24.74 \text{ ksi}$$

A.5.2.3 Refined Method for Estimating Time-Dependent Losses

Prestressing stress reduces over time due to elastic shortening and time-dependent effects. The total loss is calculated as cumulative of these losses. The prediction of prestress loss is important to accurately estimate the camber. AASHTO LRFD Specifications (2012) Article 5.9.5.4 provides a refined method for estimating the amount of prestress loss.

The prestressing loss in prestressing strands due to time-dependent effects, Δf_{pLT}, is determined as:

$$\Delta f_{pLT} = \left(\Delta f_{pSR} + \Delta f_{pCR} + \Delta f_{pR1}\right)_{id} + \left(\Delta f_{pSD} + \Delta f_{pCD} + \Delta f_{pR2} - \Delta f_{pSS}\right)_{df} \quad \text{(A.49)}$$

Where:

$\left(\Delta f_{pSR} + \Delta f_{pCR} + \Delta f_{pR1}\right)_{id}$ = Sum of time-dependent losses between transfer and deck placement, ksi.

$\left(\Delta f_{pSD} + \Delta f_{pCD} + \Delta f_{pR2} - \Delta f_{pSS}\right)_{df}$ = Sum of time-dependent prestress losses after deck placement, ksi.

Δf_{pSR} = Prestress loss due to shrinkage between transfer and deck placement, ksi.

Δf_{pCR} = Prestress loss due to creep between transfer and deck placement, ksi.

Δf_{pR1} = Prestress loss due to relaxation of strands between transfer and deck placement, ksi.

Δf_{pSD} = Prestress loss due to shrinkage between deck placement and final time, ksi.

Δf_{pCD} = Prestress loss due to creep between deck placement and final time, ksi.

Δf_{pR2} = Prestress loss due to relaxation of strands between deck placement and final time, ksi.

Δf_{pSS} = Prestressing gain due to shrinkage of deck in composite section, ksi.

Time of load application is considered to be 1 day, time of erecting the PCPs is assumed to be 30 days, and time of CIP deck construction is taken as 40 days after casting of slab beams. Final time is taken as 10 years (3650 days).

A.5.2.3.1 Prestress Losses Due to Shrinkage

The prestress loss due to shrinkage of girder concrete between time of transfer and deck placement is determined as:

$$\Delta f_{pSR} = \varepsilon_{bid} E_p K_{id} \quad \text{(A.50)}$$

Where:

ε_{bid} = Concrete shrinkage strain between transfer and deck placement, in./in.

K_{id} =   Transformed section coefficient that accounts for time-dependent interaction between concrete and bonded steel in the section being considered for time period between transfer and deck placement.

$$K_{id} = \frac{1}{1 + \left(\dfrac{E_p}{E_{ci}}\right)\left(\dfrac{A_{ps}}{A_g}\right)\left(1 + \dfrac{A_g e_{pg}^2}{I_g}\right)\left(1 + 0.7\psi_b\left(t_f, t_i\right)\right)} \tag{A.51}$$

ψ_b =   girder creep coefficient at final time due to loading introduced at transfer.

The calculation of prestress losses due to shear or creep depends on the shear strains and creep coefficients.

Shrinkage Strain:

Shrinkage is a volumetric change of concrete due to evaporation of excess water after hardening. Shrinkage causes tensile stresses, which may lead to cracking. There are several factors that increase the shrinkage amount, such as water-cement ratio, amount of moisture during curing, relative humidity, and member size. Shrinkage does not occur due to external stresses.

The shrinkage strain is calculated based on AASHTO LRFD Specifications (2012) Article 5.4.2.3 using the below formula.

$$\varepsilon_{sh} = k_s k_{hs} k_f k_{td} \left(0.48\right)\left(10^{-3}\right) \tag{A.52}$$

Where:

k_s =   Factor for effect of the volume-to-surface ratio of the component.

$$k_s = 1.45 - 0.13\left(\frac{V}{S}\right) \geq 1.0 \tag{A.53}$$

$V/S =$ Volume-to-surface ratio, in.

$$V = bdL \tag{A.54}$$

$$V = \left(\frac{60}{12}\right)\left(\frac{15}{12}\right)(48) = 300\,\text{ft}^3$$

$$S = 2\left[\left(\frac{60}{12}\right)(48) + \left(\frac{15}{12}\right)(48) + \left(\frac{60}{12}\right)\left(\frac{15}{12}\right)\right] = 612.5\,\text{ft}^2$$

$$k_s = 1.45 - 0.13\left(\frac{300}{612.5}\right) \times 12 = 0.686$$

k_{hs} =   Humidity factor for shrinkage.

$$k_{hs} = 2.0 - 0.014H \tag{A.55}$$

H =   Relative humidity, percent.

For College Station, the relative humidity is taken as 70 percent and $k_{hs} = 2.0 - 0.014(70) = 1.02$.

k_f =   Factor for the effect of concrete strength.

$$k_f = \frac{5}{1 + f_{ci}'} \tag{A.56}$$

$$k_f = \frac{5}{1+6} = 0.714$$

k_{td} =   Time development factor.

Time development factor between end of curing and deck placement is:

$$k_{td} = \frac{t}{61 - 4f_{ci}' + t} \tag{A.57}$$

$$k_{td} = \frac{35}{61 - 4(6) + 35} = 0.486$$

f_{ci}' =   Concrete compressive strength at release, ksi.

t =   Maturity of concrete (day), defined as age of concrete between time of loading for creep calculation, or time of curing for shrinkage calculations, and time being considered for analysis of creep or shrinkage effects, days.

Generally, prestressing factories apply the prestressing load after 24 hours, applying an accelerated curing. Based on the above introduced parameters and assumptions, shrinkage as a function of time is calculated.

Shrinkage strain at deck placement (40 days) is as follows.

$$\varepsilon_{sh} = (1.0)(1.02)(0.714)(0.486)(0.48)(10^{-3}) = 1.7(10^{-4})$$

Creep Coefficient:

When a girder is loaded, the girder deforms elastically. The girder continues deforming in time. The total deformation cannot be recoverable completely. This continued deformation is called creep. Creep deflection depends on many of the same factors that govern shrinkage. However, creep also depends on the age and magnitude of the load.

Both creep and shrinkage result from the removal of water from the calcium-silicate-hydrate (CSH) portion of the cement mix due to chemical reactions. This causes strain in the concrete, resulting in a volumetric change. The difference between these two is that creep is stress induced, while shrinkage is induced by ambient conditions. Because these phenomena are based on the same origin, they are interrelated. Since they occur simultaneously, it is impossible to test for them independently.

In order to estimate the amount of creep, the AASHTO LRFD Specifications (2012) method is employed. It uses a time-dependent function that is multiplied by factors that account for material and environmental effects. The creep coefficient is calculated using the below formula.

$$\psi_b(t, t_i) = 1.9 k_s k_{hc} k_f k_{td} t_i^{-0.118} \tag{A.58}$$

Where:

k_{hc} = Humidity factor for creep.

$$k_{hc} = 1.56 - 0.008 H = 1.0 \tag{A.59}$$

Creep coefficient between deck placement and transfer:

$$k_{td} = \frac{39}{61 - 4(6) + 39} = 0.513 \tag{A.60}$$

$$\psi_b(t_d, t_i) = (1.9)(1.0)(0.714)(0.513)(1)^{-0.118} = 0.696$$

Creep coefficient between final time and transfer:

$$\psi_b(t_f, t_i) = (1.9)(1.0)(1.0)(0.714)(0.99)(1)^{-0.118} = 1.344$$

Next, the creep coefficient and shrinkage strains at the time of deck placement are calculated.

$$K_{id} = \frac{1}{1 + \left(\dfrac{28500}{4696}\right)\left(\dfrac{8.568}{900}\right)\left(1 + \dfrac{(900)(4)^2}{16875}\right)(1 + 0.7(1.344))} = 0.828$$

$$\Delta f_{pSR} = (1.7 \times 10^{-4}) \times 28,500 \times 0.828 = 4.01 \text{ ksi}$$

The prestress loss due to shrinkage of girder concrete after deck placement until the final time can be calculated as follows:

$$\Delta f_{pSD} = \varepsilon_{bdf} E_p K_{df} \tag{A.61}$$

Where:

ε_{bdf} =   Concrete shrinkage strain between deck placement and final time $= 3.462 \times 10^{-4}$.

K_{df} =   Transformed section coefficient that accounts for time-dependent interaction between concrete and bonded steel in the section being considered for time period between deck placement and final time.

$$K_{df} = \frac{1}{1 + \left(\dfrac{E_p}{E_{ci}}\right)\left(\dfrac{A_{ps}}{A_c}\right)\left(1 + \dfrac{A_c e_{pc}^2}{I_c}\right)\left(1 + 0.7\psi_b\left(t_f, t_i\right)\right)} = 0.85 \tag{A.62}$$

A_c =   Area of the composite section using the deck-to-girder modular ratio, in^2.

$$A_c = b_{eff}t + bd = 87.688 \times 8 + 60 \times 15 = 1601.5 \ \text{in}^2 \tag{A.63}$$

e_{pc} =   Eccentricity of the strands with respect to center of gravity of the composite section, in.

$$e_{pc} = y_b - (d/2 - e) = 12.537 - 3.5 = 9.037 \ \text{in}. \tag{A.64}$$

I_c =   Moment of inertia of the composite section, in^4.

$$I_c = 72,753 \ \text{in}^4$$

$$\Delta f_{pSD} = (3.462 \times 10^{-4}) \times 28,500 \times 0.85 = 8.387 \ \text{ksi}$$

A.5.2.3.2 Prestress Losses Due to Creep

The AASHTO LRFD Specifications (2012) uses a time-dependent function that is multiplied by factors in order to represent material and environmental effects. This equation uses a similar approach as the shrinkage loss estimate; it is estimated in two phases. One is an estimate of loss between time of transfer and deck placement, and the other is between deck placement and final time. The prestress loss due to creep of girder concrete between transfer and deck placement is determined as:

$$\Delta f_{pCR} = \frac{E_p}{E_{ci}} f_{cgp} \psi_b\left(t_d, t_i\right) K_{id} \tag{A.65}$$

Where:

$\psi_b(t_d, t_i)$ =   Girder creep coefficient at the time of deck placement due to loading introduced at transfer.

$$\Delta f_{pCR} = \frac{28,500}{4696}(2.574)(0.6964)(0.828) = 9.0 \text{ ksi}$$

The prestress (loss is positive, gain is negative) due to creep of girder concrete between deck placement and final time is determined as:

$$\Delta f_{pCD} = \frac{E_p}{E_{ci}} f_{cgp} \left[\psi_b\left(t_f, t_i\right) - \psi_b\left(t_d, t_i\right) \right] K_{df} + \frac{E_p}{E_c} \Delta f_{cd} \psi_b\left(t_f, t_d\right) K_{df} \tag{A.66}$$

Where:

$$\psi_b(\text{t}_\text{f}, \text{t}_\text{d}) = (1.9)(1.0)(1.0)(0.714)(0.989)(40)^{-0.118} = 0.869$$

Δf_{cd} = Change in concrete stress at centroid of prestressing strands due to long-term losses between transfer and deck placement, combined with deck weight and superimposed loads, ksi.

$$\Delta f_{cd} = \left(\Delta f_p\right)_{id} \left(\frac{1}{A_g} + \frac{e_{pg}^2}{I_g} \right) + \frac{M_d e_{pg}}{I_g} \tag{A.67}$$

$\left(\Delta f_p\right)_{id}$ = Change in prestressing force between transfer and deck placement, kip.

$$\left(\Delta f_p\right)_{id} = NA_{ps}\left(\Delta f_{pSR} + \Delta f_{pCR} + \Delta f_{pR1}\right)_{id} \tag{A.68}$$

A_g = Gross area of slab beam section, in^2.

e_{pg} = Eccentricity of strands with respect to centroid of the girder, in.

M_d = Moment due to deck weight and superimposed loads, kip-ft.

I_g = Moment of inertia of slab beam section, in^4.

Prestress loss is due to creep of girder between deck placement and final time and is calculated from Equation (A.66) as:

$$\Delta f_{pCD} = 14.46 \text{ ksi}$$

A.5.2.3.3 Prestress Losses Due to Relaxation of Prestressing Strands

The prestress loss due to relaxation of prestressing strands between transfer and deck placement can be calculated as:

$$\Delta f_{pR1} = \frac{f_{pt}}{K_L}\left(\frac{f_{pt}}{f_{py}} - 0.55 \right) \tag{A.69}$$

Where:

f_{pt} = Stress in prestressing strands immediately after transfer, taken not less than 0.55f_{py}, ksi.

K_L = 30 for low-relaxation strands and 7 for other prestressing steel.

The relaxation loss may be assumed equal to 1.2 for low-relaxation strands. Research indicates that about one-half of the losses due to relaxation occur before deck placement; therefore, the losses after deck placement are equal to the prior losses.

$$\Delta f_{pR1} = \Delta f_{pR2} = 1.2 \text{ ksi}$$

A.5.2.3.4 Prestress Losses Due to Shrinkage of Deck Concrete

The prestress gain due to shrinkage of the deck composite section can be determined as:

$$\Delta f_{pSS} = \frac{E_p}{E_c} \Delta f_{cdf} K_{df} \left[1 + 0.7 \psi_b \left(t_f, t_d \right) \right] \tag{A.70}$$

Where:

Δf_{cdf} = Change in concrete stress at centroid of prestressing strands due to shrinkage of deck concrete, ksi.

ε_{ddf} = Shrinkage strain of deck concrete between placement and final time.

e_d = Eccentricity of deck with respect to the gross composite section, positive in typical construction where deck is above girder, in.

$$\Delta f_{cdf} = \frac{\varepsilon_{ddf} A_d E_{cd}}{\left[1 + 0.7 \psi_d \left(t_f, t_d \right) \right]} \left(\frac{1}{A_c} - \frac{e_{pc} e_d}{I_c} \right) \tag{A.71}$$

$$\Delta f_{pSS} = 1.05 \text{ ksi}$$

Using Equation (A.49):

$$\Delta f_{pLT} = (4.01 + 9.0 + 1.2) + (8.387 + 14.46 + 1.2 - 1.05) = 37.2 \text{ ksi}$$

From Equation (A.41):

$$\Delta f_{pT} = 15.62 + 37.21 = 52.83 \text{ ksi}$$

$$f_{pe} = f_{pi} - \Delta f_{pT} = 202.5 - 52.83 = 149.67 \text{ ksi} \tag{A.72}$$

From Equation (A.40):

$$N = \frac{F_{req}}{A_{ps} f_{pe}} = \frac{1280}{0.153 \times 149.67} = 55.9 \approx 56$$

A.5.3 Stress Checks at Critical Sections

A.5.3.1 Stress at Midspan Immediately after Deck Placement

A.5.3.1.1 Tensile Stress at the Bottom Fiber of the Girder

Maximum tensile stress at the extreme bottom fiber of composite girder was calculated using Equation (A.73).

$$f_b = \frac{M_b + M_s}{S_b} \tag{A.73}$$

$$f_b = \frac{(549.1)(12)}{2250} = 2.93 \text{ ksi}$$

Total tension force at the extreme bottom fiber of the slab beam due to prestressing force and self-weight of slab beam plus deck must be smaller than the tensile stress limit.

$$-\frac{F}{A_b} - \frac{Fe}{S_b} + f_b < F_t \tag{A.74}$$

$$F = NA_{ps} f_{ped}$$

Where:

f_{ped} = Effective prestressing stress at the time of deck placement, ksi.

Prestress losses at the time of deck placement only include elastic shortening losses and part of the long-term losses. Long-term prestress losses between transfer and deck placement are:

$$\Delta f_{pLT} = \left(\Delta f_{pSR} + \Delta f_{pCR} + \Delta f_{pR1} \right)_{id} = 4.01 + 9 + 1.2 = 14.21$$

$$f_{ped} = f_{pi} - \Delta f_{pES} - (\Delta f_{pLT})_{id} = 202.5 - 15.62 - 14.21 = 172.67 \text{ ksi}$$

$$F = 56 \times 0.153 \times 172.67 = 1479.4 \text{ kips}$$

From Equation (A.74):

$$-\frac{1479.4}{900} - \frac{(1479.4)(4.0)}{2250} + 2.93 < F_t$$

$$-1.34 < F_t \equiv 0.5027 \text{ ksi}$$

286

A.5.3.1.2 Compressive Stress at the Top Fiber of the Girder

The maximum compressive stress at the extreme top fiber of the composite section was calculated from Equation (A.75).

$$f_t = \frac{M_b + M_s}{S_t} \tag{A.75}$$

$$f_t = \frac{(-549.1)(12)}{2250} = -2.93 \text{ ksi}$$

The compressive stress created by the prestressing force, the weight of the slab beam, and CIP deck concrete should be smaller than the allowable compressive stress limit. The compressive stress is considered as negative.

$$-\frac{F}{A_b} + \frac{Fe}{S_t} - f_t > F_c \tag{A.76}$$

$$-\frac{1479.4}{900} + \frac{(1479.4)(4.0)}{2250} - 2.93 > F_c$$

$$-1.94 > F_c \equiv -3.15 \text{ ksi}$$

A.5.3.2 Stress at the Ends of the Slab Beam Girder

The initial prestress applied to the strands is $f_{pe} = 202.5 \text{ ksi}$, and the initial prestressing force per strand is $F_{pt} = f_{pt} A_{ps} = 202.5 \times 0.153 = 30.98 \text{ kips}$. The elastic shortening loss occurs immediately after transfer, which means the initial stress for checking the end stresses should take the elastic shortening losses into account.

$$f_{pi} = f_{pt} - \Delta f_{pES} \tag{A.77}$$

Where:

f_{pi} = Initial prestressing stress immediately after transfer, ksi.

The total prestressing force at each section immediately after transfer along the length is calculated using the f_{pi} value per Equation (A.77). The initial prestressing stress immediately after transfer is a function of initial prestressing force immediately after transfer (due to f_{cgp} parameter in Δf_{pES} calculation). Therefore, the initial prestressing force immediately after transfer, F_{pi}, is assumed to be 90 percent of F_{pt}, and the calculation is iterated until desired

accuracy is obtained for the F_{pi} value.

The other critical parameter is the transfer length for the prestressing force. Transfer length is the length over which prestressing force is transferred to the concrete by bonding in pretensioned members. This transfer does not occur immediately at the very end of the member. The full bonding between prestressing strands and the concrete develops within a specific distance from the end of the tendon. According to the *TxDOT Bridge Design Manual* (TxDOT 2013a), the prestress force may be assumed to vary linearly from zero at the end of the tendon to a full stress state at a distance of $60d_b = 60 \times 0.5 = 30$ in.

The elastic shortening calculation requires calculating the bending moment due to self-weight of the slab beam girder at the section of interest. Also, the stress state at the top and bottom surface of the prestressed slab beam is a function of the dead load moment and the prestressing force. The span length of an individual slab beam is considered to be the full length of the member based on the practices of the *PGSuper Design Guide* (PGSuper 2013) . The total length of the slab beam is $(46'-7") + (1'-5") = (48'-0")$.

The initial stress at 30 in. from the end of the beam at the extreme top fiber of the beam is calculated as:

$$f_{ti} = -\frac{F_{pi}}{A_b} + \frac{F_{pi}e}{S_t} - \frac{M_b}{S_t} \tag{A.78}$$

$$M_b = \frac{wL_b}{2}x - \frac{wx^2}{2} \tag{A.79}$$

Where:

L_b = 48 ft, the total length of the slab beam.

M_b = Dead load moment due to self-weight of the slab beam (53.3 kip-ft at 30 in. from the end of the beam), kip-ft.

F_{pi} = Total initial prestressing force immediately after transfer, kips.

$$F_{pi} = A_{ps}Nf_{pi} \tag{A.80}$$

Elastic shortening losses at the same section (30 in. away from the end) are calculated using the iterative process explained above and Equations (A.42) and (A.43).

$$(\Delta f_{pES})_{@30"} = 16.87 \text{ ksi}$$

$$f_{pi} = 202.5 - 18.75 = 183.75 \text{ ksi}$$

$$F_{pi} = 0.153 \times 56 \times 183.75 = 1574.4 \text{ kips}$$

$$f_{ti} = -\frac{1574.4}{900} + \frac{1574.4 \times 4}{2250} - \frac{53.3 \times 12}{2250} = 0.765 \text{ ksi}$$

The top stress immediately after transfer is higher than the increased tensile stress limit that is calculated as 0.588 ksi in Equation (A.13). This stress exceedance requires some of the tendons to be debonded. Whenever an increased tensile stress limit is used at a section with debonded strands, the AASHTO LRFD Specifications (2012) requires additional top mild steel for the tensile stresses that might develop.

A.5.4 Mild Reinforcement Calculation for Debonded End Regions

According to AASHTO LRFD Specifications (2012) Article 5.9.4.1.2, if an increased tensile limiting stress is used, the debonded ends must have mild steel located at the top of the beam to carry the extra tensile force. The following mild steel calculation procedure is laid out in AASHTO LRFD Specifications (2012).

The stresses at the top and bottom at the ends of the beam right after transfer can be found similarly to Section 3.8 of this report, as shown below.

$$f_{cit} = -\frac{F}{A_b} + \frac{Fe}{S_b} \tag{A.81}$$

$$f_{cit} = -\frac{1574.4}{900} + \frac{(1574.4)(4)}{2250} = 1.05 \text{ ksi}$$

$$f_{cib} = -\frac{F}{A_b} - \frac{Fe}{S_b} \tag{A.82}$$

$$f_{cib} = -\frac{1574.4}{900} - \frac{(1574.4)(4)}{2250} = -4.55 \text{ ksi}$$

Where:

f_{cit} =   Initial tensile stress at the top fiber of the beam at 30 in. from the end, ksi.

f_{cib} =   Initial compressive stress at the bottom of the beam at 30 in. from the end, ksi.

In order to calculate the average tensile force that is created in that section due to prestressing force, the depth of the neutral axis is calculated as:

$$x = \frac{hf_{cit}}{\left(f_{cit} - f_{cib}\right)} \tag{A.83}$$

$$x = \frac{15(1.05)}{(4.55 + 1.05)} = 2.8 \text{ in.}$$

The required reinforcement is calculated as:

$$T = \frac{f_{cit}}{2} bx \tag{A.84}$$

$$T = \frac{1.05}{2}(60)(2.8) = 88.2 \text{ kips}$$

$$f_s = 0.5f_y \le 30 \, ksi = 0.5(60) = 30 \text{ ksi} \tag{A.85}$$

$$A_s = \frac{T}{f_s} \tag{A.86}$$

$$A_s = \frac{88.2}{30} = 2.94 \text{ in}^2$$

Where:

T =   Tension force that is calculated using average tensile stress block, kips.

f_s =   Permitted tensile stress of the reinforcing steel, ksi.

A_s =   Area of required mild reinforcing steel, in^2.

Assuming #6 bars, the number of bars and spacing are calculated as:

$$N_s = \frac{A_s}{A_{\#6}} = \frac{2.94}{0.442} = 6.65 \rightarrow 7 \text{ bars}$$

A minimum of seven #6 bars must be used at the end regions and should be extended along the whole length.

A.5.5 Debonding Requirements and Debonding Length Calculation

According to the *TxDOT Bridge Design Manual* (TxDOT 2013a), debonded strands must conform to AASHTO LRFD Specifications (2012) Article 5.11.43, except as noted below:

- No more than 75 percent of the total number of strands shall be debonded.
- No more than 75 percent of the number of strands in that row shall be debonded.

- The maximum debonding length must be the lesser of one-half the span length minus the maximum development length, 0.2 times the beam length, or 15 ft.

- Not more than 75 percent of the debonded strands, or 10 strands, whichever is greater, shall have the debonding terminated at any section, where section is defined as an increment (e.g., 3 ft, 6 ft, 9 ft).

According to AASHTO LRFD Specifications (2012):

1. Maximum percentage of the debonded strands per row should not exceed 40 percent and maximum percentage of debonded strands per section should not exceed 25 percent of the total number of strands.

2. No more than 40 percent of the debonded strands or four strands, whichever is greater, shall have debonding terminated at the same section.

3. Debonded strands shall be symmetrically distributed about the centerline of the member. Exterior strands in each row shall be fully bonded. Debonded lengths of pairs of strands that are symmetrically positioned about the centerline of the member shall be equal.

The AASHTO LRFD Specifications (2012) recommends that the length of debonding should be such that all limit states are satisfied with consideration of the total developed resistance at any section being investigated. *TxDOT Bridge Design Manual* (TxDOT 2013a) recommends that the maximum debonding length can be chosen as the lesser of 15 ft, 0.2 times the span length, or half the span length minus the maximum development length, as specified in AASHTO LRFD Specifications (2012) Articles 5.11.4.2 and 5.11.4.2.3.

$$15 \text{ ft}$$

$$0.2L = 0.2(46.5833) = 9.317 \text{ ft}$$

$$0.5L - l_d$$

Where:

L = Span length, ft.

l_d = Development length, ft.

$$l_d \geq \kappa \left(f_{ps} - \frac{2}{3} f_{pe} \right) d_b \tag{A.87}$$

Where:

κ = 2.0 for pretensioned members where a portion of strands is not bonded and tension exists in the precompressed tensile zone.

f_{ps} = Average stress in the prestressing steel at the time for which the nominal resistance of the member is required, calculated with Equation (A.88), ksi.

f_{pe} = Effective stress in the prestressing steel after losses = 149.67 ksi.

d_b = Nominal strand diameter, 0.5 in.

$$f_{ps} = f_{pu}\left(1 - k\frac{c}{d_p}\right)$$ (A.88)

Where:

k = 0.28 for low-relaxation strands.

d_p = Depth of prestressing strands, $d_p = 15 - 3.5 = 11.5$ in.

$$c = \frac{A_{ps}f_{pu} + A_s f_s - A'_s f'_s}{0.85 f'_c \beta_1 b + kA_{ps}\left(\dfrac{f_{pu}}{d_p}\right)}$$ (A.89)

$$c = \frac{(0.153)(56)(270)}{0.85(7.0)(0.7)(60) + 0.28(8.568)\left(\dfrac{270}{11.5}\right)} = 7.55 \text{ in.}$$

Using the c value calculated in Equation (A.89) gives:

$$f_{ps} = 270\left(1 - 0.28\frac{7.55}{11.5}\right) = 220.4 \text{ ksi}$$

Therefore, the minimum development length must be:

$$l_d \geq 2\left(220.37 - \frac{2}{3}149.67\right)0.5 = 120.6 \text{ in } (10.05 \text{ ft})$$

$$0.5L - l_d = 0.5(46.583) - 10.05 = 13.24 \text{ ft}$$

According to the above calculations for debonding length, the maximum debonding length should not exceed 9 ft 4 in. Table A.3 shows the initial stress calculation for critical sections at the ends of the slab beam immediately after transfer. The stress values at the top and bottom of the girder are kept within the allowable stress limits by debonding some of the strands at 3 ft increments. The calculation is done using a similar approach that is shown above in Section A.5.3.2.

In order to get the prestressing stresses at each section immediately after transfer, the elastic shortening losses are calculated at each section. The calculated loss values and initial prestressing stresses at each section are listed in Table A.4. Table A.3 shows that the maximum tensile stress occurs at 2.5 ft (transfer length) at the extreme top fiber of the beam. This stress can be kept within the allowable tensile stress limit by debonding six strands at that section. Also, the maximum compressive stress occurs at 4 ft away from the end. The compressive stress is kept within the allowable compressive stress limit by debonding four strands at that location. Therefore, only six strands are debonded up to 3 ft from the ends and four strands are debonded between 3 ft – 6 ft from the ends.

A.5.6   Camber Estimate at Different Construction Stages

Prestressing is applied eccentrically in order to counteract the downward deflection due to gravity loads and service loads. The upward deflection of a flexural member due to eccentricity is called camber. The amount of camber depends on several factors, such as amount of prestressing force, span length, section properties, concrete modulus of elasticity, time, humidity, and concrete strength.

The amount of camber is a critical parameter in order to be able to adjust the haunch thickness throughout the span length at the time of PCP erection. However, prediction of deflections to a high degree of accuracy is not possible even in controlled conditions.

A.5.6.1   Camber Calculation at Different Stages

Total camber was calculated at different stages of construction until deck placement by solving Equation (A.90)

$$EIy'' = M$$

$$EIy' = Mx + c_1 \qquad\qquad (A.90)$$

$$EIy = \frac{Mx^2}{2} + c_1 x + c_2$$

The boundary conditions for the simply supported beam are:

$$y(0) = 0$$
$$y(L) = 0$$

293

With the above boundary conditions, the solution of Equation (A.90) becomes:

$$y(x) = \frac{1}{EI}\left(\frac{Mx^2}{2} - \frac{ML}{2}x\right)$$ (A.91)

The moment in Equation (A.90) is taken as the moment caused by the prestressing force only in order to calculate the upward deflection due to prestress. The net camber is calculated by subtracting the dead load deflections at different construction stages.

The upward deflection at the midspan is:

$$\delta_c(t) = y\left(\frac{L}{2}\right) = \frac{F(t)e}{E(t)I}\left(\frac{L^2}{8}\right)$$ (A.92)

Table A.3. Stress Check at Critical Sections Immediately after Transfer.

x (ft)	T_i (kips)	Bottom Row	Top Row	N	$N_{debonded}$	F_{pi} (kips)	e (in.)	M_g (kip-ft)	$f_{b\ release}$ (ksi)	$f_{t\ release}$ (ksi)
0.0	0.0	22	28	50	6	0.0	3.88	0.0	0.000	0.000
1.0	11.4	22	28	50	6	568.0	3.88	22.0	-1.493	0.231
2.0	22.8	22	28	50	6	1137.9	3.88	43.1	-2.997	0.468
2.5	28.5	22	28	50	6	1423.6	3.88	53.3	-3.752	0.588
3.0	28.5	22	28	50	6	1424.7	3.88	63.3	-3.702	0.536
4.0	28.4	24	28	52	4	1477.8	3.92	82.5	-3.779	0.495
5.0	28.5	24	28	52	4	1480.1	3.92	100.8	-3.688	0.399
6.0	28.5	24	28	52	4	1482.2	3.92	118.1	-3.601	0.307
7.0	28.3	28	28	56	0	1585.2	4.00	134.5	-3.862	0.339
8.0	28.3	28	28	56	0	1587.2	4.00	150.0	-3.785	0.258
9.0	28.4	28	28	56	0	1589.2	4.00	164.5	-3.713	0.182
10.0	28.4	28	28	56	0	1591.0	4.00	178.1	-3.646	0.111
23.3	28.6	28	28	56	0	1603.2	4.00	269.8	-3.193	-0.370

Table A.4. Elastic Shortening Loss Calculation at Critical Sections.

x (ft)	$(F_{pi})_{assumed}$ (kips)	f_{cgp}	Δf_{pES} (ksi)	f_{pi} (ksi)	F_{pi} (kips)
0.0	1417.3	2.84	17.23	185.27	1417.3
1.0	1419.9	2.78	16.89	185.61	1419.9
2.0	1422.4	2.73	16.57	185.93	1422.4
2.5	1423.6	2.70	16.41	186.09	1423.6
3.0	1424.7	2.68	16.26	186.24	1424.7
4.0	1477.8	2.76	16.75	185.75	1477.8
5.0	1480.1	2.71	16.47	186.03	1480.1
6.0	1482.2	2.67	16.20	186.30	1482.2
7.0	1585.2	2.88	17.49	185.01	1585.2
8.0	1587.2	2.84	17.25	185.25	1587.2
9.0	1589.2	2.80	17.02	185.48	1589.2
10.0	1591.0	2.77	16.81	185.69	1591.0
23.3	1603.2	2.53	15.38	187.12	1603.2

All the strands are assumed to be fully bonded. The effect of six strands being debonded over 3 ft is very small. The amount of upward deflection is a function of total prestressing force at that time and concrete modulus of elasticity at that time. The total prestressing force is calculated at each time step using the prestress loss formulas provided in Section A.5.2.3 as:

$$f_{pi} = f_{pt} - \Delta f_{pES} - \Delta f_{pR1}$$
$$f_p(t) = f_{pi} - \Delta f_{pSR}(t) - \Delta f_{pCR}(t) \qquad (A.93)$$
$$F(t) = A_{ps} \, f_p(t)$$

A.5.6.2 Concrete Compressive Strength as a Function of Time

Concrete strength varies over time; the variation is higher within the first month. Although 28-day concrete compressive strength is used as a reference parameter, it is important to know the change in concrete strength over time for an accurate estimate. Because the actual release and 28-day compressive strength of concrete is known, Equation (A.94) (Naaman 2004) can be used.

$$f_c'(t) = f_c'(28)\left(\frac{t}{b + ct}\right) \qquad (A.94)$$

Where:

$f_c'(t)$ = Concrete compressive strength, ksi.

$f_c'(28)$ = 28-day concrete compressive strength, ksi.

t = Age of concrete, days.

b =   Constant that changes the rate of increase.

c =   Constant that changes the ultimate value.

The required coefficients are provided in Table A.5. taken from Naaman (2004). It is important to note that actual 28-day compressive strength may differ from the design 28-day strength. The fabricator generally uses a higher-strength mix in order to achieve the required release strength within 24 hours. As a result, the ultimate 28-day strength is often higher than the strength used to estimate the camber. However, for the design calculation, the specified 28-day concrete compressive strength is used.

Table A.5. Concrete Compressive Strength Modeling Coefficients.

Curing Condition	Constant	Recommended (Naaman 2004)	Best Fit
Accelerated Cured	b	0.3	0.15
	c	0.98	1.06
Moist Cured	b	2.3	0.8
	c	0.99	0.99

Because the fabricator most likely will prefer accelerated curing, the accelerated cured constants are used for the estimation of time-dependent strength.

A.5.6.3 Modulus of Elasticity of Concrete

The modulus of elasticity is estimated based on the concrete compressive strength. Although there are different methods in the literature, only the AASHTO LRFD Specifications (2012) method is introduced and used herein for camber calculation. The following elastic modulus equation is defined as a time-dependent parameter based on time-dependent compressive strength.

$$E_c(t) = 33,000\gamma^{1.5}\sqrt{f_c'(t)} \tag{A.95}$$

Where:

γ =   Unit weight of concrete, kcf.

$f_c'(t)$ =   Concrete compressive strength, ksi.

Unit weight of the concrete is taken as 0.15 kcf because normal weight concrete is used.

A.5.6.4 Deflection Due to Self-Weight of the Slab Beam Girder

The deflection due to self-weight of the slab beam at midspan is also calculated as a function of time.

$$\delta_b(t) = \frac{5w_b L^4}{384 E_c(t) I_g} \tag{A.96}$$

A.5.6.5 Deflection Due to PCPs

The PCPs are assumed to be erected at 30 days after casting of the slab beams. The deflection is subtracted from the total camber at 30 days.

$$\delta_p = \frac{5w_p L^4}{384 E_c I_g} \tag{A.97}$$

$$\delta_p = \frac{5\left(\dfrac{0.267}{12}\right)(12 \times 48)^4}{384(5098)(16875)} = 0.37 \text{ in.}$$

A.5.6.6 Total Camber Considering Creep Effect

The total amount of camber at each time step is calculated using Equation (A.92). This equation only considers the time-dependent effects on total prestressing force and modulus of elasticity. The applied prestressing force causes creep over time, and creep is more prominent during the early ages of concrete. This creep effect is taken into account as an average creep at each time step and is calculated as:

$$\delta(t) = \delta_c(t) + \frac{\delta_c(1) + \delta_c(t)}{2} \psi(t, t_i) - \delta_b(t) \tag{A.98}$$

Where:

    δ_c = Camber at the time considering the time-dependent losses, in.

    δ = Total camber, upward deflection being positive, in.

    Figure A.7 shows the camber of a slab beam at each day until deck construction.
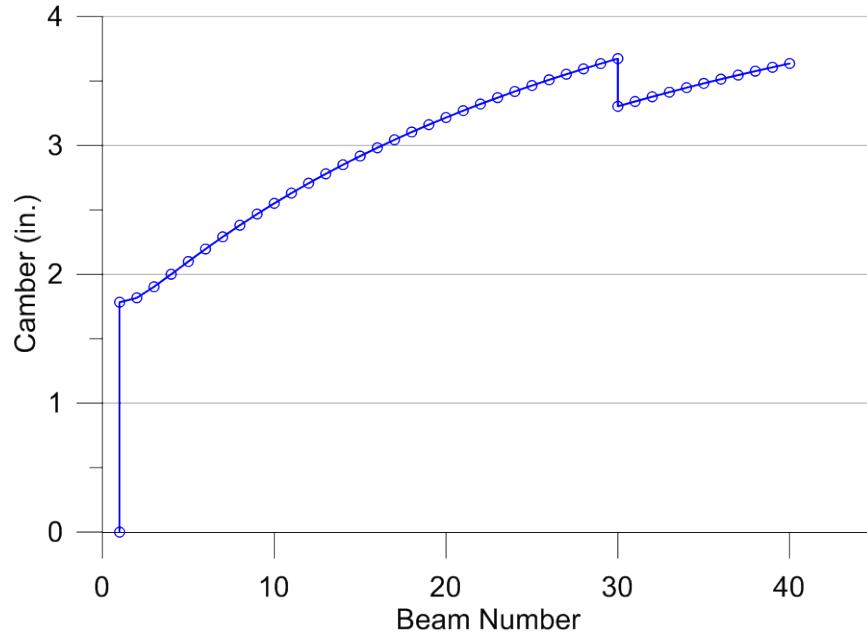
Figure A.7. Camber until CIP Deck Construction.

A.6   ULTIMATE STRENGTH CHECK

Prestressed concrete members are assumed to remain uncracked under service loads, and the allowable stress design philosophy is adopted from the AASHTO LRFD Specifications (2012). The specifications also require an ultimate strength check of prestressed members that are designed based on allowable stresses.

AASHTO LRFD Specifications 2012(2012) defines the Strength I limit state for ultimate conditions as:

$$Q = 1.25(DC) + 1.5(DW) + 1.75(LL + IM)$$ (A.99)

Where:

Q   =   Total factored load.

DC   =   Dead load of structural components and nonstructural attachments.

DW   =   Dead load of wearing surface and utilities.

LL   =   Vehicular live load.

Design requirements for flexural members is summarized in AASHTO LRFD Specifications (2012) Article 5.7.3. For rectangular sections under flexure about one axis, an approximate stress distribution is used. The formulation is summarized below. If f_{pe} is not less than 0.5 f_{pu}, the average stress in prestressing steel (f_{ps}) may be taken as:

$$f_{pe} = 149.7\,\text{ksi} > 0.5f_{pu} = 135\ \text{ksi}$$

$$f_{ps} = f_{pu}\left(1 - k\frac{c}{d_p}\right) \tag{A.100}$$

Where:

 f_{pe} = Effective prestressing stress at final time after all losses, ksi.

 f_{ps} = Average stress in prestressing steel, ksi.

 k = 0.28 for low-relaxation strands.

For rectangular section behavior:

$$c = \frac{A_{ps}f_{pu} + A_s f_s - A'_s f'_s}{0.85 f'_c \beta_1 b + kA_{ps}\left(\dfrac{f_{pu}}{d_p}\right)} \tag{A.101}$$

Where:

 f'_c = Specified compressive strength of concrete, 5 ksi.

 β_1 = Ratio of depth of the depth of the equivalent uniformly stressed compression block assumed in the strength limit state to the actual depth of the compression zone, 0.85 for 4 ksi compressive strength.

 d_p = Distance from extreme compression fiber to the centroid of the prestressing tendons, in.

 d_p = $15 + 8.5 - 3.5 = 20$ in.

The minimum bedding strip thickness is 0.5 in. Therefore, with the high expected camber, it is assumed that the deck slab thickness is 8.5 in. at midspan.

$$c = \frac{56(0.153)(270)}{0.85(4)(0.85)(116) + 0.28(56)(0.153)\dfrac{270}{20}} = 6.29\ \text{in.}$$

$$a = \beta_1 c = 0.85(6.29) = 5.35\ \text{in.} < t_s$$

The depth of the effective compressive stress block is smaller than the thickness of the deck slab. Therefore, the neutral axis does not go into the slab beam girder. The calculated c value is correct, with no need for iteration. Using the calculated c value in Equation (A.100) gives:

$$f_{ps} = (270)\left(1 - 0.28\frac{6.29}{20}\right) = 246.2\ \text{ksi}$$

The nominal flexural resistance of the slab beam can be calculated as:

$$M_n = A_{ps} f_{ps} \left(d_p - \frac{a}{2} \right)$$

(A.102)

$$M_n = (56)(0.153)(246.22)\left(20 - \frac{5.35}{2} \right) = 3046 \text{ k-ft}$$

The maximum moment under service loads is calculated using the Strength I load combination provided in Equation (A.99).

$$M_u = 1.25(549.1) + 1.5(112.5) + 1.75(625) = 1949 \text{ k-ft}$$

$$\phi M_n > M_u \Rightarrow 0.9(3046) = 2741 > 1949 \text{ k-ft}$$

The factored nominal ultimate strength capacity of the section is greater than the factored ultimate moment under service loads. The ultimate strength requirement is satisfied.

A.7   SHEAR DESIGN OF THE SLAB BEAM GIRDER

The shear resistance of the slab beam girder is checked using the guidelines provided by AASHTO LRFD Specifications (2012) Article 5.8.2. The shear resistance of the slab beam at the shear critical location is checked, and the required reinforcement is calculated. Due to the high cross-sectional area of the slab beam girders, the shear resistance of the concrete itself satisfies the required shear strength most of the time.

A.7.1 Transverse Shear Design

In line with the general approach for AASHTO LRFD Specifications (2012) Article 5.8.2.4, the following equation must be satisfied at each section.

$$V_r = \phi V_n \geq V_u$$

(A.103)

Where:

V_r =   Design shear resistance, kips.

V_n =   Nominal shear resistance, kips.

V_u =   Factored shear force, kips.

ϕ =   Strength reduction factor for shear = 0.9 for normal weight concrete.

The nominal shear resistance at a given section is the sum of the concrete contribution, transverse reinforcement, and transverse component of the prestressing force.

$$V_n = V_c + V_s + V_p$$

(A.104)

Where:

V_c =   Contribution of concrete to the shear strength, kips.

V_s =   Contribution of steel to the transverse shear resistance, kips.

V_p =   Component of prestressing force in the direction of applied shear, kips.

Nominal shear resistance, V_n , is constrained by the following upper limit:

$$V_n \leq 0.25 f_c' b_v d_v + V_p \qquad \text{(A.105)}$$

Where:

f_c' =   28-day design compressive strength of concrete, ksi.

b_v =   Effective web width = 60 in.

d_v =   Effective shear depth = $d_e - a/2$ in.

d_e =   Effective depth for bending = 19.5 in.

d_v =   The larger of $0.9d_e$ or $0.72h$.

$$d_v = \begin{cases} 19.5 - \dfrac{5.35}{2} = 16.83 \text{ in.} \\[2mm] 0.9(19.5) = 17.55 \text{ in.} \\[2mm] 0.72(23) = 16.56 \text{ in.} \end{cases}$$

The critical section near the support is located as the greater of d_v or $0.5d_v \cot(\theta)$ from the support face. As a preliminary estimate, use $\theta = 29°$ and $0.5(17.55)\cot(29) = 15.83$ in. Therefore, the critical section for shear should be taken as 17.55 in. from the face of the support, since d_v is greater than $0.5d_v \cot(\theta)$. Considering the 9 in. bearing pad length, the critical section is $17.55 + 4.5 = 22$ in. away from the center of the bearing pad.

The critical shear load occurs when the rear axle of the HS20 truck is located at 22 in. from the center of the bearing pad. The shear forces calculated for dead and live loads when the vehicle is at that location are presented in Figure A.8.

The ultimate factored design shear at 2 ft from the support is calculated using the Strength I load combination.

$$V_u = 1.25V_{DC} + 1.5V_{DW} + 1.75V_L \qquad \text{(A.106)}$$

$$V_L = g_v(1.33V_{TR} + V_{LL}) = 0.86 \times (1.33 \times 54.48 + 13.63) = 74 \text{ kips}$$

$$V_u = 1.25(43.2) + 1.5(8.85) + 1.75(74) = 196.8 \text{ kips}$$

The ultimate factored moment reaction under service loads at the critical shear section is also calculated. The moment value at the critical shear section is used to calculate the longitudinal strains in the web. The unfactored moment results at 2 ft from the support when the vehicle's rear axle is at 2 ft are shown in Figure A.8(c).

$$M_L = g_M (1.33 M_{TR} + M_{LL}) = 0.676 \times (1.33 \times 108.97 + 28.53) = 117.3 \text{ kip-ft}$$

$$M_u = 1.25(90.1) + 1.5(18.53) + 1.75(117.3) = 345.7 \text{ kip-ft}$$

The shear resistance provided by the component of the prestressing force in the direction of the applied shear can be calculated as:

$$V_p = F \sin \alpha \tag{A.107}$$

Where:

α =   The angle of the prestressing force with respect to the longitudinal axis of the beam.

$$V_p = F \sin 0 = 0$$

The shear resistance provided by the concrete can be calculated as:

$$V_c = 0.0316 \beta \sqrt{f_c'} b_v d_v \tag{A.108}$$

The shear resistance provided by the shear reinforcement can be calculated using the below formula.

$$V_s = A_v f_y \frac{d_v}{s} \cot \theta \tag{A.109}$$

Where:

β =   Factor indicating the ability of diagonally cracked concrete to transmit tension between cracks.

A_v =   Area of transverse reinforcing steel (in^2) within a distance s, in.

f_y =   Yield strength of the transverse steel reinforcement, ksi.

θ =   Angle of inclination of diagonal compressive struts.

In order to determine the nominal shear resistance (V_c, V_s), the β and θ parameters must be calculated. For prestressed members, β and θ are calculated using Equations (A.110) and (A.111):

$$\beta = \frac{4.8}{(1+750\varepsilon_s)}\frac{51}{(39+s_{xe})} \tag{A.110}$$

$$\theta = 29 + 3500\varepsilon_s \tag{A.111}$$

Where:

ε_s =   Longitudinal strain in the web (assumed positive for tension), in./in.

s_{xe} =   Crack spacing parameter, in.

$$\varepsilon_s = \frac{\dfrac{|M_u|}{d_v} + 0.5N_u + |V_u - V_p| - A_{ps}f_{po}}{E_s A_s + E_p A_{ps}} \tag{A.112}$$

AASHTO LRFD Specifications (2012) Article 5.8.3.4 suggests that the parameter f_{po} can be taken as:

$$f_{po} = 0.7f_{pu} = 189 \text{ ksi}$$

If the strain equation comes out to be negative, ε_s should be taken as zero or the value should be recalculated using Equation (A.113):

$$\varepsilon_s = \frac{\dfrac{|M_u|}{d_v} + 0.5N_u + |V_u - V_p| - A_{ps}f_{po}}{E_s A_s + E_p A_{ps} + E_c A_{ct}} \tag{A.113}$$

Where:

A_{ct} =   Area of concrete on the flexural tension side of the member, in.^{2}.

From Equation (A.112):

$$\varepsilon_s = \frac{\dfrac{345.7 \times 12}{19.35} + 0.5(0.0) + |196.8 - 0.0| - 56(0.153)(189)}{29000(0.0) + 28500(56)(0.153)} = -4.95 \times 10^{-3}$$

The net longitudinal strain (ε_s) value is negative. In this case, AASHTO LRFD Specifications (2012) states that ε_s may be taken as zero or recalculated using Equation (A.113). The value for ε_s is conservatively taken as zero for the transverse shear strength check.
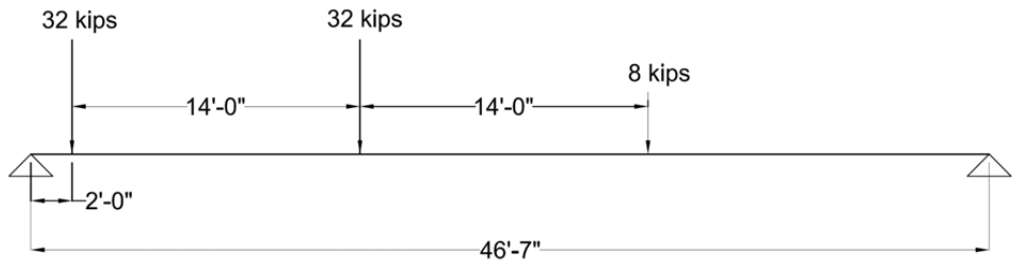
(a) HS20 Shear Critical Position
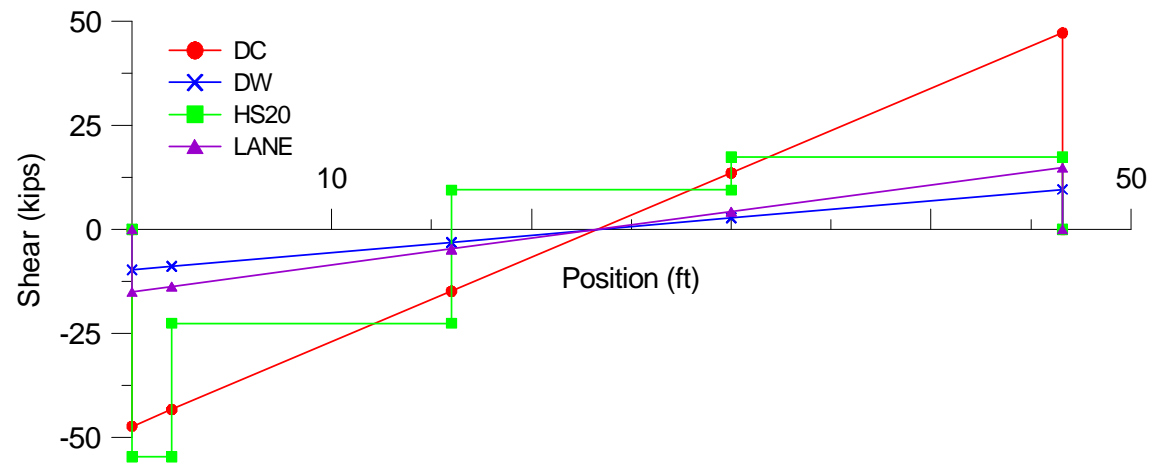
(b) Shear Forces
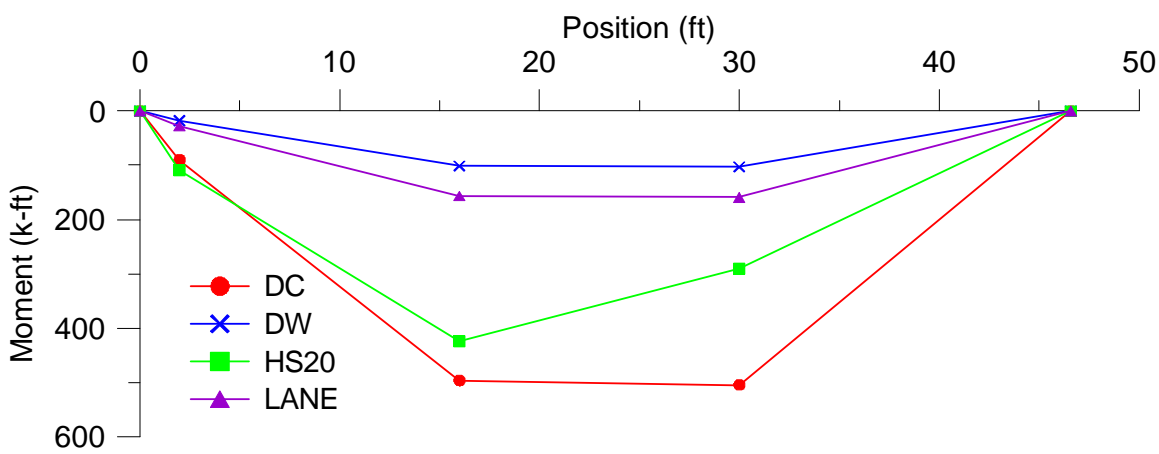
(c) Moment Reactions at Shear Critical Section

Figure A.8. Moment and Shear Reaction When Vehicle Is at Shear Critical Position.

The crack spacing parameter can be determined using the equation below.

$$s_{xe} = \frac{s_x 1.38}{a_g + 0.63} \tag{A.114}$$

Where:

s_x =   The lesser of d_v or the maximum distance between layers of longitudinal crack control reinforcement, in.

a_g =   Maximum aggregate size, in.

The value of s_x may be taken equal to d_v for the design of slab beams because no longitudinal crack control reinforcement is provided.

$$s_{xe} = \frac{(17.55)1.38}{3/8 + 0.63} = 24.1 \text{ in.}$$

Because the longitudinal strain value and crack spacing parameter are calculated, the β and θ parameters can be determined using Equations (A.110) and (A.111).

$$\beta = \frac{4.8}{1 + 750(0)} \frac{51}{(39 + 24.1)} = 3.88$$

$$\theta = 29 + 3500(0) = 29^\circ$$

Using the calculated β value, the concrete contribution to the shear strength can be determined.

$$V_c = 0.0316(3.88)\sqrt{7}(60)(17.55) = 341.6 \text{ kips}$$

$$0.5\phi V_c = 0.5(0.9)(341.6) = 153.7 \text{ kips} < V_u$$

Half of the reduced nominal shear strength contribution of the concrete ($0.5\phi V_c$) is lower than the ultimate factored shear V_u at the shear critical section. Therefore, transverse shear reinforcement is required. Transverse steel currently provided in the *TxDOT Bridge Division Standard Drawings* (TxDOT 2013b) standard slab beam details is 04 in²/ft. The contribution of shear reinforcement to transverse shear resistance can be calculated as follows.

$$V_s = 0.4(60)\frac{17.55}{12}\cot(29) = 63.3 \text{ kips}$$

The nominal shear resistance is the lesser of:

$$V_n = V_c + V_s + V_p = 405 \text{ kips} > V_u$$

$$V_n = 0.25 f_c' b_v d_v + V_p = 2031.8 \text{ kips}$$

Therefore, the transverse steel currently provided in the TxDOT standard slab beam details is adequate based on the design calculations.

A.7.2 Interface Shear Design

The factored interface shear resistance should be greater than the factored interface shear force due to total load at service.

$$V_{ri} = \phi V_{ni} \tag{A.115}$$

In addition, the design should satisfy:

$$V_{ri} \geq V_{ui} \tag{A.116}$$

Where:

V_{ni} = Nominal interface shear resistance, kips.

V_{ui} = Factored interface shear force due to total load, kips.
For a unit length segment, the factored shear force may be calculated as:

$$V_{ui} = \frac{12V_u}{d_v} \tag{A.117}$$

Where:

d_v = Distance between the centroid of the tension steel and the mid-thickness of the

slab, in.

$$d_v = 19.5 - 4 = 15.5 \text{ in.}$$

The haunch thickness is assumed to be 2 in.

$$V_{ui} = \frac{12(196.8)}{15.5} = 152.4 \text{ kip/ft}$$

Nominal shear resistance of the interface plane can be taken as:

$$V_{ni} = cA_{cv} + \mu \left(A_{vf} f_y + P_c \right) \tag{A.118}$$

The nominal shear resistance can be taken as the lesser of:

$$V_{ni} \leq K_1 f_c' A_{cv} \tag{A.119}$$

$$V_{ni} \leq K_2 A_{cv} \tag{A.120}$$

306

Where:

A_{cv} = $b_{vi}L_{vi}$ = Area of concrete that is engaged in interface shear transfer, in^2.

A_{vf} = Area of interface shear reinforcement, in^2.

b_{vi} = Interface width considered to be engaged in shear transfer, in.

L_{vi} = Interface length considered to be engaged in shear transfer, in.

P_c = Permanent net compressive force acting normal to the shear plane, kips.

c = Cohesion factor, ksi.

μ = Friction factor.

f_y = Yield stress of reinforcement, ksi.

K_1 = Fraction of concrete strength available to resist interface shear.

K_2 = Limiting interface shear resistance, ksi.

Parameters, c, μ, K_1, and K_2 are specified in AASHTO LRFD Specifications (2012) Article 5.8.4.3.

For a cast-in-place concrete slab on clean concrete girder surfaces, free of laitance but surface not intentionally roughened, $c = 0.075$ ksi, $\mu = 0.6$, $K_1 = 0.2$, $K_2 = 0.8$ ksi.

The bedding strip thickness should be taken into account when calculating the effective width of the interface shear surface. The thickness of the bedding strip is taken as 2 in.

$$b_v = b - 2w_b \tag{A.121}$$

$$b_v = 60 - 2(2) = 56 \text{ in.}$$

The effective concrete surface area for a unit length is:

$$A_{cv} = b_v(1.0) = 56 \text{ in}^2/\text{in.}$$

The interface shear force due to cohesion between deck concrete and slab beam concrete only is:

$$V_{ni} = 0.075(56)(12) + 0.8(60) = 98.4 \text{ kips/ ft}$$

$$\phi V_{ni} = 0.9(98.4) = 88.56 \text{ kips/ ft} < V_{ui}$$

The amount of interface shear reinforcement provided for the standard slab beam type cannot achieve the required interface shear strength. Interface shear reinforcement must be increased to 1.8 $in^2/$ft for the first quarter of the span. A detailed methodology for determining interface shear demand of segments using global force equilibrium is shown in Chapter 3.

APPENDIX B   RIVERSIDE BRIDGE CONSTRUCTION

B.1 CONSTRUCTION PROCESS

The Riverside Bridge was built as an on-grade bridge. The elevation of the finished deck is the same as the adjoining runway. In order to create a bridge span, the runway pavement in the immediate area was removed and the soil below was excavated to a certain depth. To set the depth of the excavated pit, several parameters were taken into account. First, the clearance underneath the slab beams allowed a workable space, and the depth was kept at an optimum level in order to limit substructure costs. It was decided that a 6.5 ft deep excavated pit, which allowed a minimum 4.5 ft clearance below the slab beams, would provide sufficient space to install instrumentation. Figure B.1 shows the bridge superstructure details and the clear distance below the bridge.

B.1.1 Soil Testing of the Bridge Site

In order to begin designing the substructure components, it was necessary to have the engineering parameters of the supporting soil. Two bore holes were drilled at the north and south ends of the bridge where the load-bearing elements would be constructed. At the time of boring, the foundation had been designed as a deep foundation with drilled shafts. Therefore, the holes were drilled to a 60 ft depth.

Figure B.2 shows a view of drilling operations. The subsurface arrangement of the strata and groundwater conditions was evaluated at these two bore holes. Groundwater was observed at a depth of approximately 25 ft. Soil strength was tested by means of the Texas cone penetration (TCP) test. This test was performed by counting the number of blows required for a 170 lb hammer free falling from a 24 in. height to drive a conical point for two consecutive sets of 6 in. The test results helped determine the skin friction and load-bearing capacity. In addition to strength tests, geotechnical laboratory tests were conducted on the recovered samples to determine the engineering properties of the strata.

The test results were used to determine the skin friction and load-bearing capacity. In addition to strength tests, geotechnical laboratory tests were conducted on the recovered specimens in order to determine engineering properties of the strata. Table B.1 lists the engineering properties of each soil stratum, including friction angle and plasticity index (PI). In general, the soil stratigraphy from the surface to 12 ft indicated gray, brown, and multicolored lean clay, followed by brown and light brown sand from 12 to 25 ft, and then brown, gray, and

multicolored fat clay (high plasticity) to the termination of the bore hole at approximately 60 ft below the existing grade.

(a) Side Elevation View

(b) Section 1-1: Cross-Section of Spread Slab Beam Deck

(c) Section 2-2: Cross-Section at Abutment
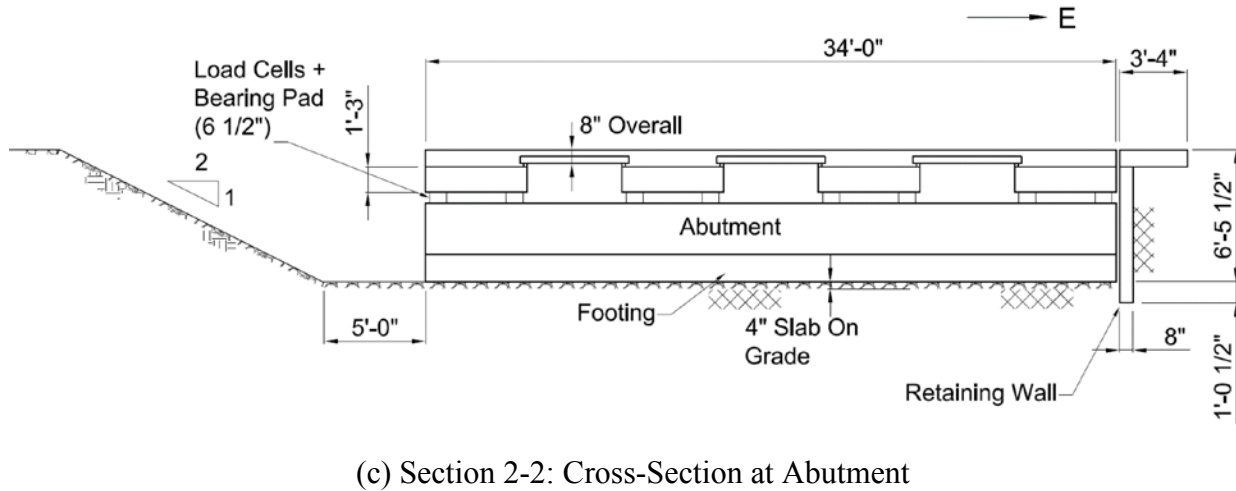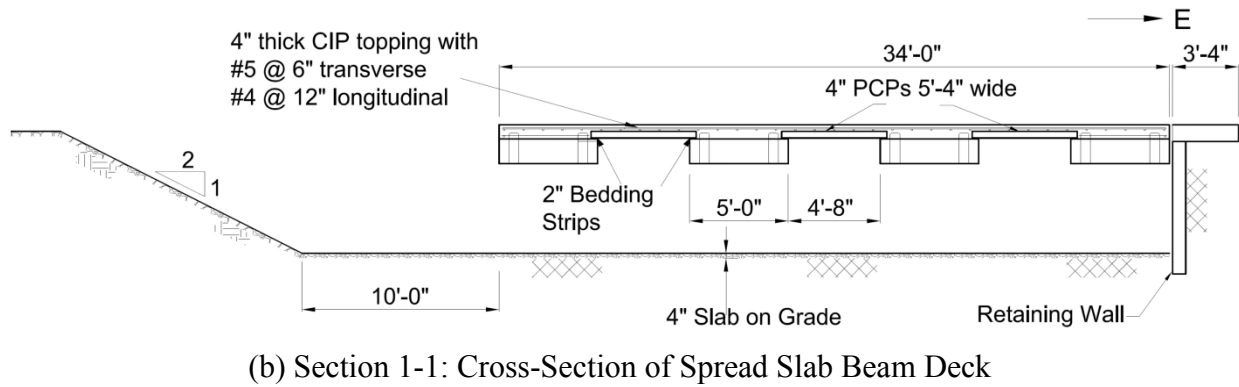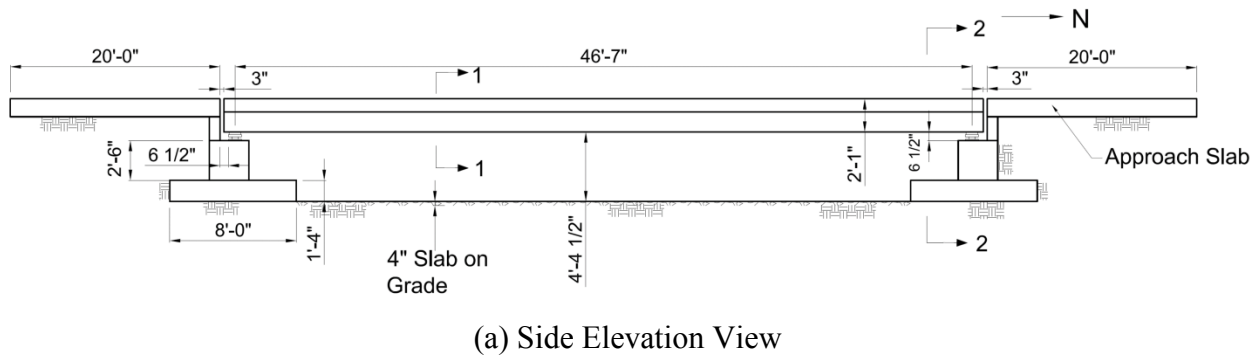
Figure B.1. The Riverside Bridge Superstructure.

As shown by the PI of the different soil strata, the soil at the construction site has a high shrink-swell potential. This type of clay is called fat clay and has high plasticity. The PI was taken into account when designing structural elements. For a deep foundation option (drilled piers supporting the bridge abutment), a depth versus skin friction capacity plot was provided for several different pier diameters. Figure B.3 shows the friction capacity of different diameter piers.

The deep foundation option was eliminated because of the high cost. A shallow foundation was designed for supporting the bridge abutment. The compressive strength of the soil for a shallow depth is provided in the log of the bore hole (Figure B.4).

Figure B.2. Soil Testing of the Bridge Site.

Table B.1. Engineering Properties of Each Soil Strata (Gessner 2012).

Depth (ft)	Strata	PI Range	Moisture Content Range (%)	Shear Strength (tsf); Friction Angle
0–12	Gray, Brown, and Multicolored Clay (CL)	6–33	4 to 8 Wet	0.4–1.5; N/A
12–24	Brown and Light Brown Sand (SP)	NP (Nonplastic)	2 to 6 Wet	N/A; 34.5º–41º
24–59	Brown, Gray, and Multicolored Clay (CH)	35–55	6 to 12 Wet	0.78–12.0; N/A
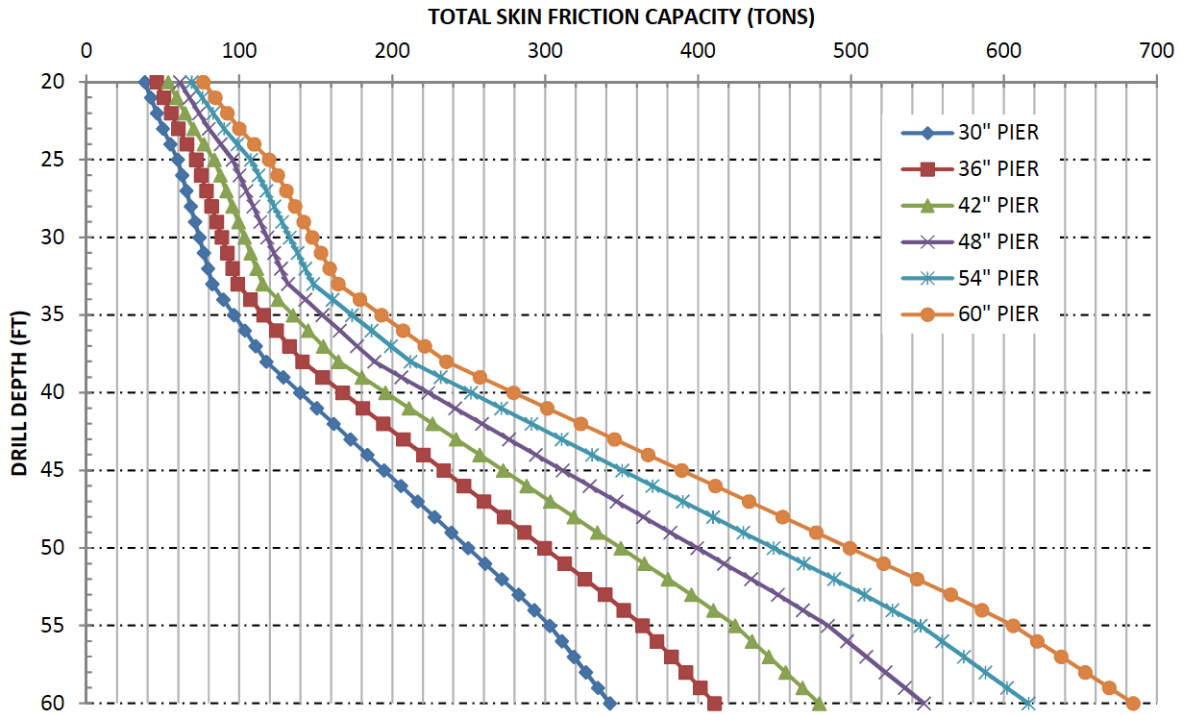
Figure B.3. Total Skin Friction Capacity of Pier (Gessner 2012).

313

LOG OF BORE HOLE

PROJECT:	Bridge Footings
	Runway 17L
	College Station, Texas
PROJECT NO:	12-0251
CLIENT:	Mr. James Frazier
DATE:	June 12, 2012
DRILLER:	Van and Sons

BORING NO. #1
LOCATION: Bridge Abutments

BORING TYPE: Core/Auger
GROUND ELEV: Cleared Pavement Area

SOIL TECHNICIAN: RT

Legend:
- Texas Cone Penetrometer Test
- Shelby Tube Sample
- Standard Penetration Test Sample
- Augering (Disturbed) Sample
- No Recovery
- ▽ Initial Water Level
- ▼ Water Level After

Depth (in feet)	Sample Type & Soil Symbol	Water Level	Penetrometer or Blow Count	Liquid Limit (%)	Plasticity Index	Moisture Content (%)	Dry Density Lbs./Cu. Ft.	Compressive Strength Tons/Sq. Ft.	% Passing #200 Sieve (%)	Bar Linear Shrinkage (%)	Description of Stratum
			1.0 2.0								Firm to Stiff Light Brown Clay (CL)
5			3.0 4.5+ 6,6	41	26	19.1	110.5	2.44	82	16.3	Hard Gray Clay (CL)
			4.5 1.5								Very Stiff to Firm Multicolored Clay (CL) -w/ Some Calcareous Nodules
10			2.5 2.0 2,4	46	33	21.0	105.4	1.6	90	--	Stiff Multicolored Clay (CL) -w/ Some Calcareous Nodules
											Stiff Multicolored Clayey Sand (SC) -w/ Some Calcareous Nodules
15			25,26	--	NP	5.95	--	--	23	--	Very Dense Brown Sand (SP)
20			5/7/10 16,24								Medium Dense Brown Sand (SP)
25		▽	6/8/12 22,28								Medium Dense Brown Sand (SP)
30			4/3/5 7,10	70	53	29.2	--	--	97	--	Stiff Multicolored Clay (CH)

Figure B.4. Log of Bore Hole (Gessner 2012).

B.1.2   Design and Construction of Substructure Components

B.1.2.1   *Reinforced Concrete Retaining Wall*

The bridge cross-section in relation to the existing runway is shown in Figure B.5. Because the bridge span was built over an excavated pit at the edge of the runway, it created unstable soil conditions along the east edge of the bridge. Researchers had two options to overcome this problem: excavate at a slope, which would create a gap between the existing runway and the bridge deck, or install a retaining structure. Based on Texas A&M Riverside Campus regulations, researchers decided to build a retaining structure and have the top of the bridge deck flush with the rest of the existing runway.

Several different retaining structure options were evaluated and designed based on the soil test results. A steel sheet pile installation was investigated, but the option was relatively expensive due to the small size of the project relative to typical construction. Building a cantilever reinforced concrete retaining wall would have been as expensive as the sheet pile application and would have taken more time. Instead, a trenched retaining wall was built and anchored to the existing runway slab at the top and buried into soil at the bottom.

Figure B.5 shows the geometric and reinforcement details of the retaining wall. The retaining wall was designed based on the soil pressure and a possible surcharge that may result due to a vehicle driving near the wall. Soil parameters were used as provided by the soil test results. Based on an ultimate strength design, the same reinforcement was provided for positive and negative moments. One layer of #4 rebar mesh was provided at the mid-thickness of the 8 ft high and 8 in. thick retaining wall.

Figure B.6 shows the rebar preparation and installation procedure. Reinforcing bars were tied on the existing runway and lowered into the excavated trench with a forklift. The rebar mesh was aligned at the center of the excavated trench. The necessary clear cover between the mesh and soil was provided with 3 in. spacer wheels.

The retaining wall concrete was specified as Texas Department of Transportation (TxDOT) Class C having 3600 psi compressive strength. The slump was specified as 5.0–5.5 in. to have a relatively higher workability in the narrow trench. Fresh properties of concrete were tested, and specimens were fabricated to determine the mechanical properties of the concrete.
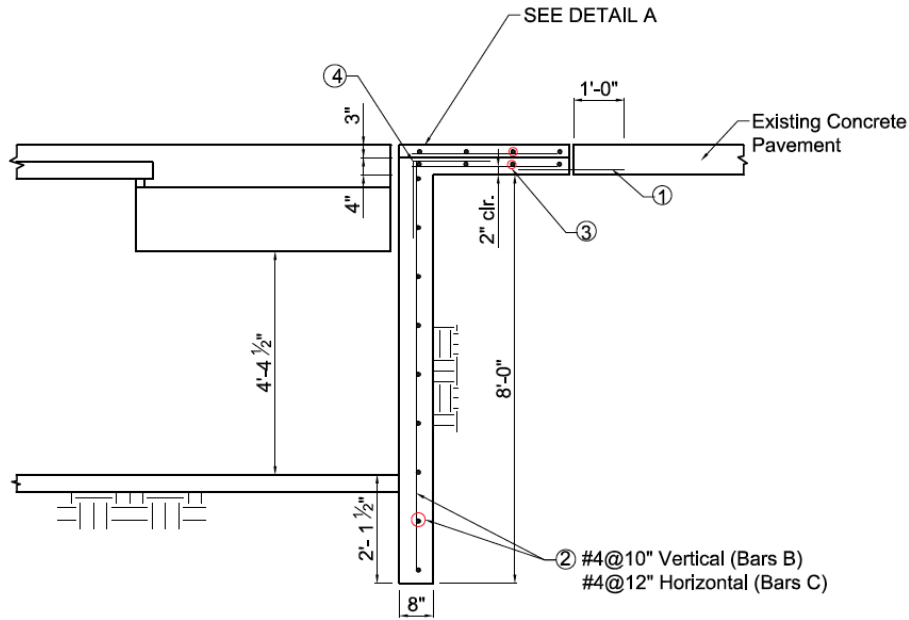
Figure B.5. Retaining Structure in Relation with the Existing Runway.

Figure B.7 shows the excavation operation. Concrete pavement sections at the bridge site had already been removed before casting the retaining wall. A 75 ft long section along the retaining wall was excavated to about a 6.5 ft depth. The Texas A&M Transportation Institute (TTI) Riverside Campus crew performed the excavation using a trackhoe and hauled off soil as it was excavated.

Figure B.8 presents the elevations of the slab on grade below the transverse centerline of the bridge. The exact elevation of the slab on grade was adjusted during the formwork construction. The slope of the slab was provided toward the center of the bridge in the north-south direction and toward the west (toward the future drainage pit).

Reinforcing bars were tied on the runway before the start of the excavation. The objective was to place the reinforcing bar mesh immediately after excavation and to cast the slab on grade as soon as possible. Rain would have the potential of filling up the excavated pit and creating a muddy working area, and pumping the water out would also be time consuming. In order to avoid all these complications, the slab-on-grade construction was planned ahead of time and finished in two weeks.

(a) Rebar Tying

(b) Rebar Mesh Installation

(c) Slump Test

(d) Cylinder Specimens

(e) Retaining Wall Concrete Pour

Figure B.6. Retaining Wall Construction.

(a) Main Excavation of the Bridge Foundation

(b) Excavation for Slab on Grade below Footings

Figure B.7. Excavation of the Bridge Site.
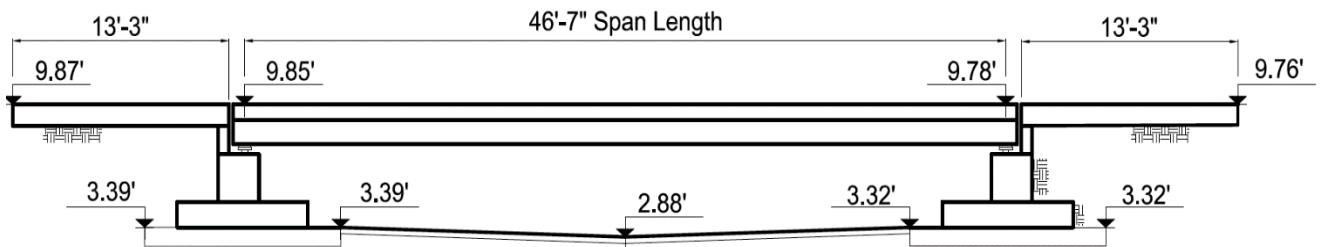
Figure B.8. Target Elevations of Structural Components.

Figure B.9 shows construction of the slab-on-grade under footings. These slabs were placed first to aid in the overall construction of the substructure elements. All the rebar meshes used for the slab on grade were #3 bars spaced at 12 in. centers. The on-grade slabs were poured in two steps. First, the 12 ft wide, 12 in. deep slabs below the north and south footings were poured. These slabs had two layers of #3 mesh. Based on the American Association of State Highway and Transportation Officials (AASHTO) Load and Resistance Factor Design (LRFD) Specifications (2012) requirements, reinforced concrete components that are in contact with soil should have 3 in. of clear cover. Therefore, 3 in. high chairs were used to provide necessary bottom clear cover. In addition, 6 in. high standees were used to keep the spacing between the two layers of steel constant. The formwork was supported by 2 in. by 4 in. (nominal dimensions) stakes nailed every 4 ft. The top of the formwork elevation was adjusted according to target elevations, which provided the required slope for each component.

The reinforcement layout and construction of the middle slab-on-grade are shown in Figure B.10. The slab on grade for the middle region was 4 in. thick and was cast in four sections separated by transverse construction joints. The continuity of the reinforcing bars was satisfied by feeding reinforcing bars through the drilled holes in the construction joint formwork. To provide a barrier between the slab and the expansive clay soil, a 10 mil plastic sheet was laid. The previously tied #3 reinforcement mesh was placed on 2 in. slab bolsters.

Figure B.9. Reinforcing Bar Mesh for the Slab-on-Grade.

(a) Formwork and Reinforcement

(b) Slab-on-Grade Pour

(c) View of Slab-on-Grade after Broom Finish

Figure B.10. Construction of Middle Section of Slab-on-Grade.

B.1.2.3   Footing and Abutment Construction

Several options were evaluated for the pier construction. First, drilled shafts were designed based on the *TxDOT Bridge Design Manual* (TxDOT 2013a) guidelines as load-carrying elements supporting the abutments. The deep foundation design was abandoned because of the high cost due to a relatively small number of piers as compared to standard projects. The spread footing solution was determined to be the most economical solution for this short-span bridge. The spread footing was designed by taking into account the highly plastic soil conditions of the site, which had high swell-shrink potential. Specifically, a conservative flexural design for the footing was used, including an increased footing depth for added stiffness.

The footing was designed according to the *TxDOT Geotechnical Manual* (TxDOT 2012) and the AASHTO LRFD Specifications (2012). A critical step for designing the footing was determining the strata and reasonable strength values to be assigned to each stratum so that the soil bearing capacity could be calculated at the base of the footing. The soil test data were reviewed, and the engineering parameters were taken from the geotechnical soil report.

For a structural load-bearing member to be safe in terms of geotechnical design considerations, it needs to satisfy certain safety requirements, including stability in terms of overturning moment, sliding, and bearing capacity. To investigate the most critical effect, the truck load was considered as a uniform distributed pressure for the calculation of active pressure forces, whereas for the resisting moment and shear force calculations, only the dead load of the structural components was considered. This approach led to a conservative design.

Because of the shallow depth of the abutment, overturning moment was not an issue. In addition, the large contact area of the 34 ft long footing provided adequate resistance against sliding. The geometry of the footing was controlled by the bearing pressure. Based on the bearing capacity of the soil (2246 psf), an 8 ft wide spread footing was found to be satisfactory according to allowable stress design.

Figure B.11 shows the reinforcement details and geometry of the footings and abutments. The reinforcement for the footing was designed based on the ultimate strength design and the AASHTO LRFD Specifications (2012). Although it was possible to achieve adequate strength with a 12 in. depth, the depth of the footing was increased to 14 in., and 20 percent more flexural reinforcement was provided for additional rigidity. The thickness of the slab on grade under each footing was also increased to 12 in. for additional bearing area and rigidity against the high plastic clay conditions of the bridge site. Reinforcing bars for footings and abutments were tied on the runway to save time during substructure construction work. A reinforcing bar cage for the footing and abutment is shown in Figure B.12.
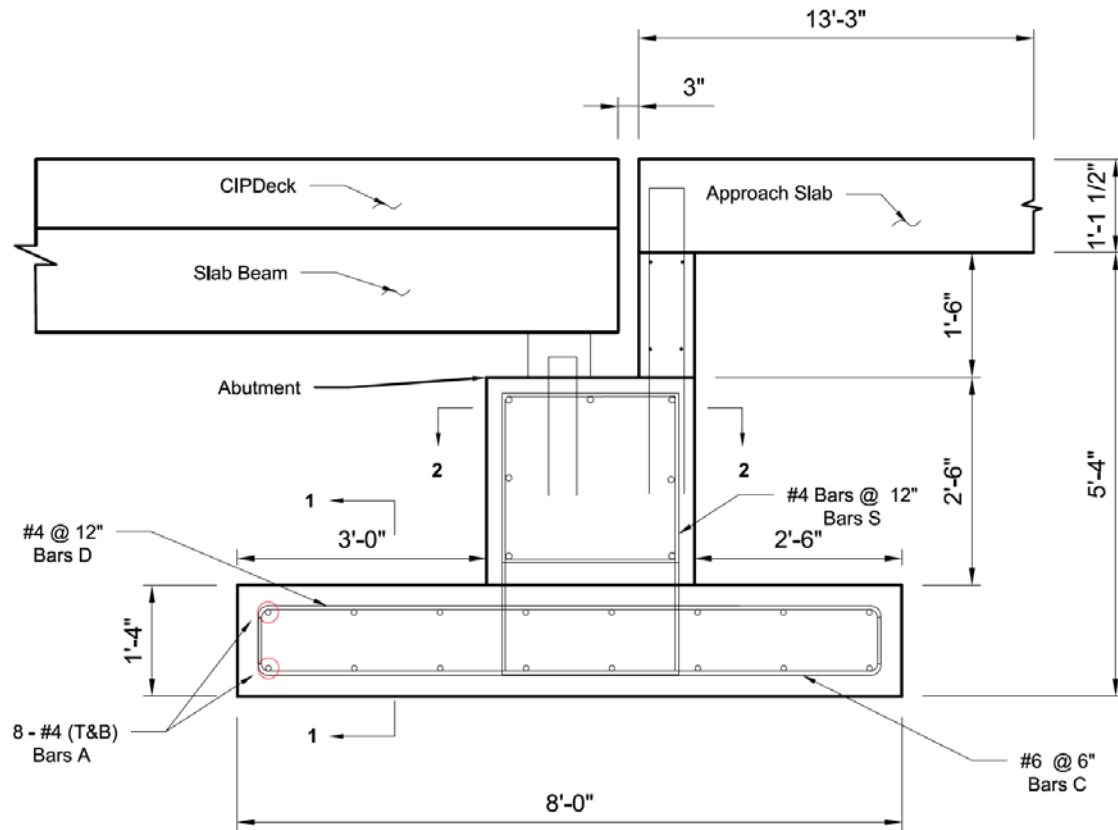
Figure B.11. Dimensions and Reinforcement of Footing and Abutment.

Figure B.12. Footing and Abutment Reinforcement Cage.

Because of the length of the longitudinal bars in the abutment, the rebar tying process was completed on the runway. The locations of both footings were measured precisely by using a

total station, and the back face of the formwork was placed to have a reference point before placing the rebar cages. A TTI trackhoe was used to pick up the rebar cages and place them within the marked location at the north and south ends of the bridge. Figure B.13(a) shows the rebar placement operation.

After placement of the rebar, previously prepared formwork pieces were assembled for the footing construction. Concrete for all substructure components was specified as TxDOT Class C having 3600 psi compressive strength. The footing and abutment were cast in two different pours due to the geometry of the members. The pour for both footings took place during slight rain.

A silt fence was placed around the perimeter to hold back soil that washed down during each rainfall. Also, a sump pit was dug at the center on the west edge for pumping the water after rainy days. Eventually, a drainage manhole was constructed and connected to the main drainage channel.

All the rebar for the abutment was already tied and in place. The previously built abutment formwork was placed and assembled. The back faces of the formwork were supported by diagonal supports, and the front face was held using tie rods. Reinforcing bars for the back wall were tied because they needed to be connected to the abutment for interface shear resistance. Wing-wall reinforcement was also placed during this step. Figure B.13(c) shows the abutment and wing-wall formwork construction.

(a) Reinforcing Cage Placement

(b) Footing Concrete Pour

Figure B.13. Footing and Abutment Construction.

(c) Abutment and Wing-Wall Formwork Construction

(d) Abutment Concrete Pour

Figure B.13. Footing and Abutment Construction (Continued).

The abutment and half of the wing-wall concrete were poured together due to geometry and ease of construction. In order to provide a connection between the abutment and elevated pedestals located at the bearing pad locations, #5 rebar hooks were embedded into the fresh concrete. Concrete was poured and floated. Then an evaporation retardant agent was applied at the surface because of the hot weather. After the concrete was sufficiently hardened, cotton curing mats were placed and watered. A plastic sheet covered the curing mats. The curing process took place during the first four days after each pour.

B.1.2.4 Back-Wall, Elevated Pedestal, and Wing-Wall Construction

The back walls and the top half of the wing walls were cast together. This pour was the last pour of the substructure components before the slab beam girders were placed. The wing-wall thickness had already been changed from 12 to 8 in. during the design phase due to the load cell configuration to create more room at the back of the load cells.

The rebar for the back walls and wing walls was tied before the abutment pour to provide interface shear resistance. Also, the back face of the formwork was built as part of the abutment formwork. The only pieces that were constructed were the front faces of the back walls and elevated pedestals. Elevated pedestals were not part of the structure design and did not support the girders. They were placed as a replacement for the load cells in case the load cells were removed later.

Figure B.14 shows the abutment construction and backfilling operations. The formwork for all the substructure components was removed before the start of the backfilling operation. The operation used 350 tons of Type A Grade 1 backfill material to backfill the abutments. A sheep-foot roller was used to compact the material. To achieve 100 percent compaction, the soil was watered until it was saturated and then was backfilled into the area in 4 to 6 in. thick layers. Every layer was compacted using the sheep-foot roller. The compaction rate was tested twice for each bridge end.

B.1.2.5 Construction of the Drainage Line

The slab below the bridge is 6.5 ft deeper than the existing runway, and the bridge location is the low spot of the second runway. All runoff water comes toward the bridge site and fills up the excavated pit. The best option was to drain the water naturally without the use of a pumping system requiring long-term maintenance. The depth of the drop inlet close to the bridge site was 4 ft deeper than the floor level, so a trench was dug connecting the sump pit location to the main inlet collecting runoff. The slope of the trench was measured and adjusted using an automatic level to be approximately 1 percent.

Figure B.15 shows the drainage channel construction. To collect the water draining toward the center of the bridge floor, a manhole was constructed using a concrete pipe oriented vertically. A 6 in. diameter hole was drilled at the side of the pipe. A 100 ft long schedule 40 pipe was used for the drainage line. After the drainage pipe was connected to the manhole, the

main inlet wall was drilled to provide access for a 6 in. diameter pipe. Figure B.15(c) shows the drainage trench and pipe before backfilling.

(a) Back-Wall, Pedestal, and Wing-Wall Pour

(b) View of the Substructure after Removal of the Forms

(c) Backfilling and Compaction Process

Figure B.14. Abutment Construction and Backfilling.

(a) Trench Excavation

(b) Manhole Placement
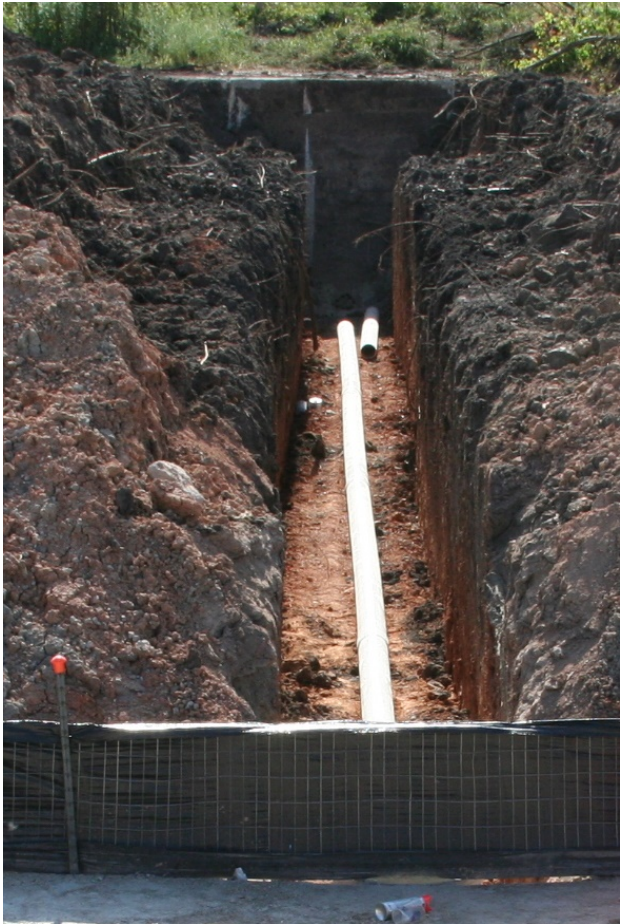
(c) Drainage Pipe Installation

Figure B.15. Construction of the Drainage System.

B.1.3 Construction of Bridge Superstructure

The bridge superstructure is composed of four slab beam girders spaced at 4 ft 8 in. apart, PCPs that span between girders as stay-in-place forms, and a CIP reinforced concrete deck that combines all the pieces and creates the monolithic bridge superstructure. Detailed dimensions and the geometry of these components are shown in Figure B.16.

The slab beam girders are standard TxDOT 5SB15 slab beams, and the PCPs are 4 in. thick, 8 ft long, and 5 ft 4 in. wide. The CIP deck thickness varies along the length due to the camber of the girders. The minimum deck thickness at the center of the bridge is 8 in. including the PCP thickness.

B.1.3.1 Precast Member Fabrication

The prestressed slab beam girders were designed based on the AASHTO LRFD Specifications (2012) and *TxDOT Bridge Design Manual* (TxDOT 2013a). The number of prestressing tendons and the amount of debonding required are shown in Figure B.16.

The mild steel reinforcing bars were placed based on the standard TxDOT drawing PSB-5SB15. The only detail that was changed was the length of the H-bars. The height of the H-bars was increased to 6 in. above the slab beam surface because the increased deck thickness allowed this dimension to be increased to provide proper development length into the CIP deck slab.

The prestressed slab beam and PCP construction was performed by Bexar Concrete Works in San Antonio, Texas. A detailed drawing for prestressing and mild reinforcement was provided to the precaster. Figure B.17 shows the slab beam construction process, with the reinforcing cage fabrication shown in Figure B.17(a). All 56 strands were stressed up to 31 kips per strand, and specified strands were debonded up to 6 ft from both ends of the girders. For debonding application, a plastic tube was placed around the strands, and then duct tape was used to cover the tube. The concrete was specified as self-consolidating concrete (SCC), having a compressive strength at release of 6 ksi and a compressive strength at service (28 days) of 8.5 ksi. To capture the different mechanical properties of the concrete, 96 cylinder samples and 12 modulus of rupture beam specimens were fabricated by the research team. Also, fresh concrete properties (slump flow, unit weight, and concrete temperature) were tested by the research team for each girder. Ambient temperature and humidity were also recorded during the

concrete pour. Detailed concrete properties and the mechanical property test results are provided in Chapter 2. Figure B.17(b) shows the cylinder molds that were prepared and oiled before the slab beam pour, along with a sample slump flow test.
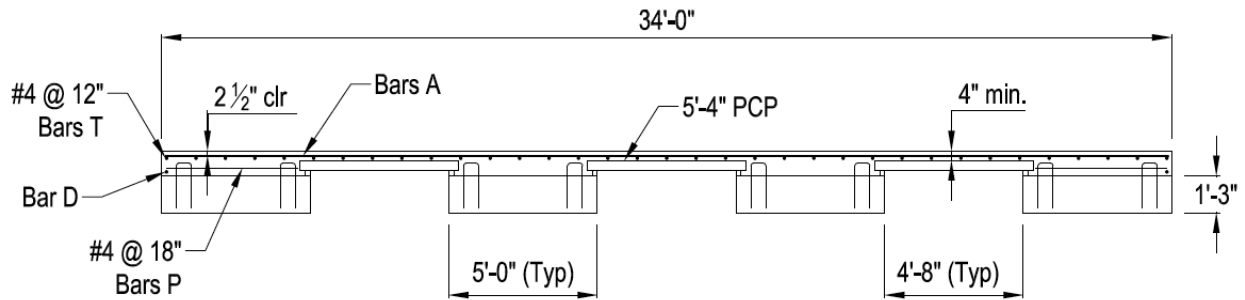
(a) Bridge Composite Cross-Section
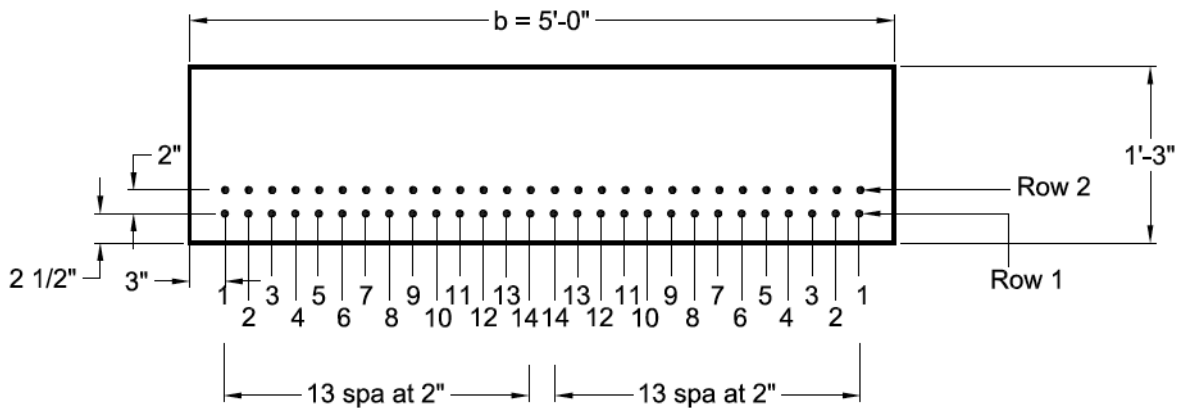
STRAND LOCATIONS
CROSS-SECTION

DEBONDING DATA		
Measurement from End	Strand No. (Row 1)	Number of Debonded Strands
0'-0" – 3'-0"	No.5,9,13	6
3'-0" – 6'-0"	No. 9,13	4

(b) Slab Beam Prestressing Detail

Figure B.16. Bridge Superstructure Cross-Section.

(a) Slab Beam Reinforcing Bar Placement
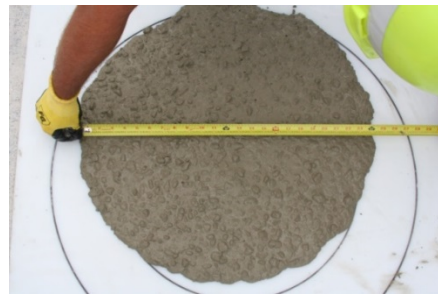
(b) Material Specimens and Slump Flow Tests

(c) Slab Beam Pour

Figure B.17. Slab Beam Construction.

Before closure of the formwork of the slab beams, the bottom of the formwork was cleaned and oiled. Steel forms were assembled along the sides of all four slab beams and supported from the top. The ends of the slab beams were separated by plywood caps. All four girders were poured together and then submerged in water.

Figure B.18 shows the reinforcement placement and concrete pour for the PCPs. Precast concrete panels were also cast at the same precast plant in San Antonio. Eighteen 8 ft long PCPs were cast to span the three openings between the 48 ft long slab beams. The width of the panels is 5 ft 4 in. As transverse reinforcement, 0.5 in. diameter prestressing strands, stressed at 16.1 kips, were placed at 6 in. spacing. As longitudinal reinforcement, deformed welded wire reinforcement was used as specified in the *TxDOT Bridge Division Standard Drawings* (TxDOT 2013b). The concrete for the PCPs was specified as TxDOT Class H with a release strength of 4 ksi and 28-day compressive strength of 5 ksi.

Figure B.18. Precast Concrete Panel Construction.

B.1.3.2 Erection of Precast Members

Before the erection of the slab beams, the load cell assembly was placed. Figure B.19 shows the load cell assembly. The load cell assembly consisted of a 1 in. thick bottom steel plate and a 1.5 in. thick top steel plate. There are two different load cell assemblies due to the two-bearing-pad and one-bearing-pad configurations. At the south end of the bridge, there are two bearing pads (9 in. x 9 in.) at the corners of the slab beam, and the steel plates are 10 in. x 10 in. At the north end of the bridge, the bearing pads (9 in. x 18 in.) are at the center of the bridge, and the steel plates are 10 in. x 20 in. The bottom plates were placed and attached to their exact locations using a high-strength fast-gain grout. Load cells were placed within circular indentations machined in the bottom steel plates. Then the top steel plates were placed on the buttons of the load cells. Small Styrofoam pieces were placed between the steel plates at the corners to provide enough stability during the erection of the slab beams.

The slab beams weighed around 45 kips each. Due to weight limitations on the highway, each slab beam was delivered by an 18-wheeler. A crane with a 100 ton capacity was rented and ready early in the morning. The bearing pads had already been placed on top of the steel plates, and the edges of the slab beams were marked on the abutment before the start of the crane operation. Four slab beams were successfully positioned at their locations. The spacing between the slab beams was 4 ft 8 in. per design. Figure B.20 shows the view of precast members during erection. After the erection of the slab beams, bedding strips were cut to the required depth. In order to have a flat deck surface, the depth of the bedding strip is critical. Before determining the bedding strip dimensions, the camber of the slab beams was measured to be 4.5 in., which was 1.5 in. higher than the expected value. The beams were expected to deform about 0.5 in. after the erection of PCPs and about 1 in. more after the CIP deck pour. The bedding strip depth was adjusted accordingly to compensate for the 3 in. camber difference. The bedding strip depth can be a minimum of 0.5 in. and a maximum of 4 in. according to the *TxDOT Bridge Design Manual* (TxDOT 2013a). Based on these dimensions, the bedding strip depth was taken to be 0.5 in. at the midspan and 3.5 in. at the end of the slab beams, changing linearly in between. The thickness of the bedding strips was 2 in., as specified by *TxDOT Bridge Design Manual* (TxDOT 2013a) standards. Dow® high-load 40 Styrofoam (extruded polystyrene foam), which conforms to the requirements in the *TxDOT Bridge Design Manual* (TxDOT 2013a), was used as bedding strip material. Bedding strip pieces were glued at the edges of the slab beams using the proper glue.

333

(a) South End Load Cell Assembly

(b) North End Load Cell Assembly

(c) Bridge Span Ready for Taking the Girders

Figure B.19. Load Cell Assembly.

(a) Slab Beam Erection Operation

(b) Bedding Strip Application
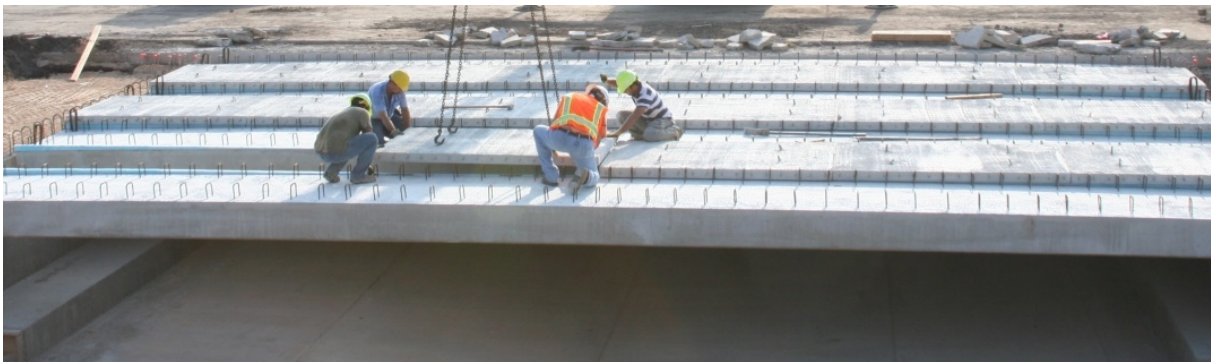
(c) Erection of Precast Concrete Panels

Figure B.20. Precast Member Placement.

335

Bedding strips were glued down two days before the erection of the precast panels. The glue was hardened at the time of PCP erection. Because of the relatively light weight of the PCPs, a smaller crane was used for the placement of the panels. Six PCPs were placed at each span between slab beams. According to the *TxDOT Bridge Design Manual* (TxDOT 2013a), the length of a PCP hanging over the bedding strip should be at least 1.5 in. For the Riverside Bridge, the length of PCP hanging over the bedding strip was designed as 2 in. During the erection of the panels, construction workers made sure that this distance was more than 1.5 in. at both ends for all panels.

B.1.3.3   Reinforced Concrete Deck Construction

The bridge deck reinforcing bars were placed based on *TxDOT Bridge Division Standard Design Drawings* (TxDOT 2013b), and #5 transverse reinforcing bars at 6 in. spacing and #4 longitudinal bars at 12 in. spacing were placed over the panels. One more layer of transverse reinforcement was provided at the top of the exterior girders only. Figure B.16(a) shows the reinforcing bar details and orientation. The deck design was checked based on ultimate strength design, and the strength of the PCPs was found to be adequate to carry the additional deck load and HS20 truckload.

The deck formwork plywood boards were assembled at the bridge site. The formwork was supported using wood wedges along the north, south, and east edges of the bridge. The formwork along the west edge was supported down to the ground level below the bridge. The deck formwork was not attached to the bridge girders because the bridge girders would deflect about 1 in. and the formwork should not move down with the edge girder. The finished deck formwork is shown in Figure B.21(a).

After building the formwork, reinforcing mesh was placed and tied together. According to *TxDOT Bridge Division Standard Drawings* (TxDOT 2013b), the clear cover at the top of the deck rebar should be 2 in. In order to keep the top covered, the rebar can be laid directly on top of the panels. Because of the high camber of the slab beams, the reinforcing mesh was laid on top of the panels at most places. Slab bolsters were provided only on the last panel at the ends of the slab beams. Reinforcing mesh construction is shown in Figure B.21(b).

(a) Deck Formwork Construction

(b) Deck Reinforcing Bar Construction

(c) Deck Concrete Pour

Figure B.21. Cast-in-Place Deck Construction.

For the deck pour, 40 cyds of TxDOT Class S concrete were ordered. The compressive strength of the concrete was specified as 4000 psi. The bridge deck slope was dictated by the elevation of the formwork, and the elevation of the northwest section of the bridge was similar to the rest of the runway. The deck concrete pour was subcontracted. The subcontractor adjusted the concrete slope by using string lines based on the formwork height.

The concrete surface was finished using a bull float. After it hardened to an appropriate degree, a medium-level broom finish was applied in the transverse direction. Figure B.22 shows the deck concrete surface finishing operation. The concrete was cured by covering it with wet blankets and a plastic sheet for four days. An evaporation retardant agent was not applied due to humid and cool weather conditions. A view of the curing practice is shown in Figure B.23.

Figure B.22. Deck Concrete Finishing.

Figure B.23. Curing of Deck Concrete.

B.1.3.4   Approach Slab Construction

Before the start of the approach slab construction, one more row of concrete pavement blocks was removed from the existing runway at both ends of the bridge due to damage during construction. With the removal of these pieces, the total length of the slab was 29 ft at each end of the bridge. The first 20 ft was designed as a 13 in. deep approach slab having two layers of reinforcing mesh, and the remaining 9 ft was designed as a 7 in. deep reinforced concrete slab having one layer of reinforcing mesh. Most of the approach slab region had already been backfilled and compacted. Recently excavated parts were also backfilled and compacted to create a stronger bearing surface under the slab.

The remaining top portion of the slab along the east edge of the deck was also poured with the approach slabs. The 3 ft 4 in. wide slab was 2 in. lower than the existing runway. This was done so that the top of the bridge deck could be smoothly transitioned to the existing runway.

A 1 in. thick bituminous expansion joint material was glued at both ends of the bridge as a separation between the bridge deck and approach slab. A 1 in. thick Styrofoam board was glued along the east edge of the bridge as an expansion joint. A 3 to 4 in. gap remained between the retaining wall and bridge deck along the east edge of the bridge. To close that gap, a 6 in. wide 0.25 in. thick steel sheet was attached to the top of the slab by wedge anchors. The rest of the small gaps, due to the roughness of the retaining wall surface, were sealed with expanding foam. Figure B.24 shows the expansion joint material and steel sheet formwork.

The west side of the approach slabs was closed using 2 in. x 12 in. nominal lumber. The reinforcing mesh was provided according to *TxDOT Bridge Division Standard Drawings* (TxDOT 2013b). The approach slab was 20 ft long. The bottom reinforcing mesh had #8

339

transverse bars at 6 in. spacing and #5 longitudinal bars at 12 in. spacing. The top mesh was #5 bars with 12 in. spaced mesh in both directions. The last 9 ft of the reinforced concrete slab had only #5 bars at 12 in. spacing. The top mesh of the approach slab was extended to the existing slab. Figure B.24(b) shows the reinforcing bar mesh construction for the approach slabs.

The concrete for the approach slab was specified as TxDOT Class S having 4000 psi compressive strength. This item was also subcontracted due to the large concrete finishing surface. The top of the deck elevation was about 1.5 in. higher than the existing runway. This difference caused a gradual slope away from the bridge at both ends of the bridge over a 29 ft length.

Figure B.24 shows the approach slab construction for both ends and the 3 ft 4 in. wide slab along the east edge that was poured at the same time. After the pour, the concrete was given a smooth surface concrete finish using a bull float. After the concrete hardened to a certain level, a medium-level broom finish was applied in the transverse direction, as was done for the bridge deck.

(a) Expansion Joint and Steel Sheet Form.

Figure B.24. Approach Slab Construction.

(b) Approach Slab Reinforcing Mesh

(c) Approach Slab Pour

(d) Approach Slab Broom Finish

Figure B.24. Approach Slab Construction (Continued).

B.2   MATERIAL PROPERTIES FOR RIVERSIDE BRIDGE

B.2.1   General

Several fundamental mechanical properties are essential to design structural members, including compressive strength, splitting tensile strength (STS), modulus of elasticity (MOE), and modulus of rupture (MOR). To obtain the concrete mechanical properties that could predict structural behavior, a large number of concrete samples including cylinders and beams for different structural components were fabricated and tested during the construction process of the Riverside Bridge. Slump tests were conducted before conventional concrete pours to verify workability, while slump flow was measured for SCC. In addition, for the purpose of controlling the quality of SCC for precast prestressed slab beams and PCPs, the ambient temperature, ambient humidity, concrete weight, and concrete temperature were measured.

B.2.2   Test Procedures

B.2.2.1   *Mechanical Properties*

B.2.2.1.1   **Compressive Strength**

Compressive strength is an important index for structural capacity design and is often used to predict other mechanical properties (MOE, MOR, and STS). Test samples were cast in accordance with American Society for Testing and Materials (ASTM) C31/31M, *Standard Practice for Making and Curing Concrete Test Specimens in the Field* (ASTM 2012a). Sample sizes were 4 in. x 8 in. cylinders. Cylinder molds for casting concrete test specimens conformed to the requirements of ASTM (2010c) C470/C470M, *Specification for Molds for Forming Concrete Test Cylinders Vertically*, and were placed on a level, rigid surface free of vibration and other disturbances. Concrete was placed in the mold in two layers of approximately equal volume, and 25 roddings and 10–15 light hand tappings were used for each layer. Specimens were not transported until at least eight hours after final set. For SCC, only 10–15 hand tappings for each layer were required in the process of making test cylinders.

In accordance with ASTM (2010a) C39/C39M, *Standard Test Method for Compressive Strength of Cylindrical Concrete Specimens*, the compressive strength of test specimens was determined at 24 hours, 3 days, 7 days, 28 days, and 90 days. The load was applied at a rate of movement corresponding to a stress rate on the specimen of 35 ± 7 psi/s. A 500-kips capacity

Materials Testing System (MTS) machine in the High Bay Structural and Materials Testing Laboratory at Texas A&M University was used to test all mechanical characteristics of the conventional concrete (CC) and SCC cylindrical specimens. The MTS testing machine is shown in Figure B.25.

Figure B.25. MTS Testing Machine.

B.2.2.1.2 Modulus of Elasticity

The MOE represents the stress-strain relationship in the elastic range and is used in the prediction of the deflection and camber of precast prestressed concrete members.

Test samples were cast in accordance with ASTM (2012a) C31/C31M, *Standard Practice for Making and Curing Concrete Test Specimens in the Field*. For the MOE test, the sample size was a 4 in. x 8 in. cylinder. The mold requirement, fabrication procedure, and curing regime were the same as those used in the compressive strength test.

In accordance with ASTM (2011) C469/C469M, *Standard Test Method for Static Modulus of Elasticity and Poisson's Ratio of Concrete in Compression*, two linear variable differential transducers (LVDTs) measured the strain of concrete in compression up to

40 percent of the compressive strength at the age of testing. The MOE test was conducted at 24 hours, 3 days, 7 days, 28 days, and 56 days. The compressometer with LVDTs used during testing is shown in Figure B.26.
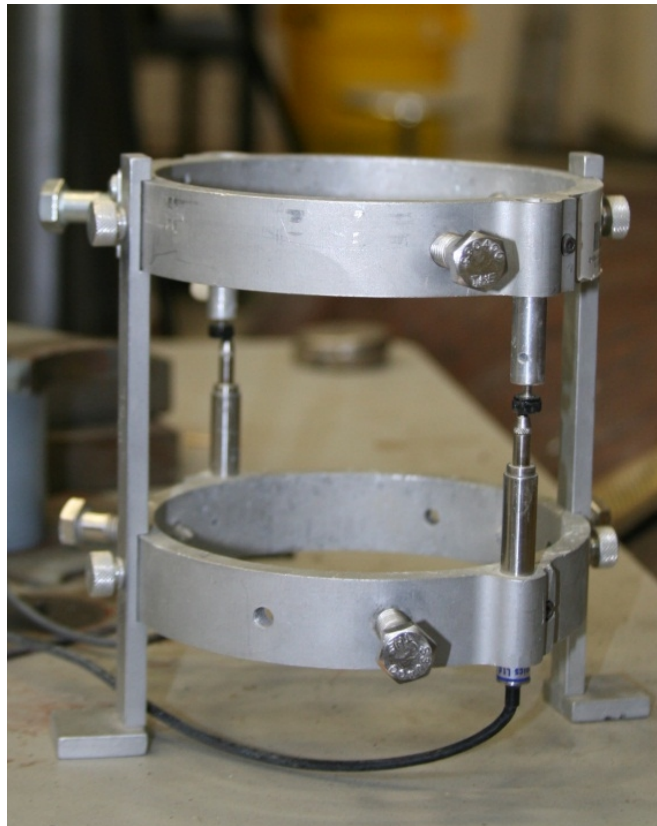
Figure B.26. Compressometer.

The modulus of elasticity to the nearest 200 MPa (50,000 psi) was calculated according to Equation (B.1):

$$E = (S_2 - S_1) / (\varepsilon_2 - 0.000050)$$
(A.122)

Where:

E = Chord modulus of elasticity, psi.

S_2 = Stress corresponding to 40 percent of ultimate load, psi.

S_1 = Stress corresponding to a longitudinal strain, ε_1, of millionths, psi.

ε_2 = Longitudinal strain produced by stress, S_2.

B.2.2.1.3   Modulus of Rupture

The MOR test is a measurement of flexural strength, and its value is also useful for the design and prediction of structural behavior (Trejo et al. 2008). Test samples were cast in accordance with ASTM (2012a) C31/31M, *Standard Practice for Making and Curing Concrete Test Specimens in the Field.* The standard beam was 6 in. x 6 in. in cross-section, and the beam length was 18 in. The concrete was placed in the mold in two layers of approximately equal volume, and each layer was consolidated as required. In placing the final layer, an amount of concrete was added to fill the mold after consolidation. The concrete was placed so that it was uniformly distributed within each layer. Specimens were not transported until at least eight hours after final set.

In accordance with ASTM (2010b) C78/C78M, *Standard Test Method for Flexural Strength of Concrete (Using Simple Beam with Third-Point Loading),* the load was applied continuously and without shock, at a constant rate within the range 100 to 200 psi/min tensile stress until failure of the specimen. The maximum applied load indicated by the testing machine at failure was recorded. The MOR test was conducted at 28 days. The apparatus for the MOR test is shown in Figure B.27.

Figure B.27. Schematic and Photo of Apparatus for MOR Test (ASTM 2012a).

If the fracture initiates in the tension surface within the middle third of the span length, the modulus of rupture is calculated according to Equation (B.2):

$$R = \frac{PL}{bd^2}$$ (A.123)

Where:

R = Modulus of rupture, psi.

P = Maximum applied load indicated by the testing machine, lbf.

L = Span length, in.

b = Average width of specimen at fracture, in.

d = Average depth of specimen at fracture, in.

If the fracture occurs in the tension surface outside of the middle third of the span length by not more than 5 percent of the span length, the modulus of rupture is calculated according to Equation (B.3):

$$R = \frac{3Pa}{bd^2}$$ (A.124)

Where a is the average distance between the line of fracture and the nearest support measured on the tension surface of the beam measured in inches.

If the fracture occurs in the tension surface outside of the middle third of the span length by more than 5 percent of the span length, the results of the test are discarded.

B.2.2.1.4   Splitting Tensile Strength

The STS test is an indirect measurement of the tensile strength of concrete and is used to predict and limit the allowable stresses in critical regions in precast prestressed concrete members. Test samples were cast in accordance with ASTM (2012a) C31/31M. For the STS test, the sample size was a 4 x 8 in. cylinder. The mold requirements, fabrication procedure, and curing regime were the same as those in the compressive strength test.

In accordance with ASTM (2011) C496/C496M, *Standard Test Method for Splitting Tensile Strength of Cylindrical Concrete Specimens,* the load was applied continuously and without shock, at a constant rate within the range of 100 to 200 psi/min splitting tensile stress until failure of the specimen. The maximum applied load indicated by the testing machine at failure was recorded.

The splitting tensile strength of the specimen is calculated as follows:

$$T = 2P / \pi l d \qquad\qquad (A.125)$$

Where:

- T = Splitting tensile strength, psi.
- P = Maximum applied load indicated by the testing machine, lbf.
- l = Length, in.
- d = Diameter, in.

B.2.2.2   Fresh Properties

B.2.2.2.1   Slump Test

The slump flow test should be conducted before placing the concrete to evaluate filling ability and stability. The slump test procedures for CC and SCC are different. In accordance with ASTM (2012b) C143, *Standard Test Method for Slump of Hydraulic Cement Concrete*, the slump test procedure of CC had the following steps:

1. Dampen the interior of the slump mold.
2. Place the mold on a flat, moist, nonabsorbent, and rigid surface.
3. Hold the mold firmly in place by standing on the two brackets on either side of the mold.
4. Using a scoop, fill the mold in three layers (of equal volume), moving the scoop around the perimeter of the mold opening to ensure an even distribution of the concrete.
5. Rod each layer 25 times throughout its depth.
6. Remove any concrete that has collected around the base of the mold during strike-off.
7. Immediately remove the mold by raising the mold in a steady, vertical direction. Lift the mold off the concrete a distance of 12 in. in 5 +/− 2 seconds.
8. Measure the slump immediately. This is the vertical distance between the top of the mold (upside down next to the specimen) and the displaced original center of the top surface of the specimen.

To evaluate the fresh properties of SCC, the slump was measured in accordance with ASTM (2009) C1611, *Test Method for Slump Flow of Self-Consolidating Concrete.* Slump flow is the measured maximum diameter of flow after lifting an inverted slump cone. The average

diameter of the slump flow is the average value of two perpendicular measurements. The slump test measurements for CC and SCC are shown in Figure B.28 and Figure B.29, respectively.

Figure B.28. Slump Measurement (CC).

Figure B.29. Slump Measurement (SCC).

B.2.2.2.2 Density (Unit Weight)

Unit weight is measured in accordance with ASTM (2013) C138, *Standard Test Method for Density (Unit Weight), Yield, and Air Content (Gravimetric) of Concrete*. The unit weight test had the following steps:

- Determine the mass (pounds or kilograms) of the empty measure (bucket) to be used.

- Using a scoop, place the concrete in the measure in three layers of approximately equal volume, moving the scoop around the perimeter of the measure opening to ensure an even distribution of the concrete.

- Rod each layer 25 times throughout its depth; distribute the rodding uniformly over the cross-section of the measure, starting near the perimeter, and progress spirally toward the center.

- Tap the outside of the measure 10 to 15 times with the mallet to close voids left by the tamping rod.

- Completely clean the exterior of the measure and determine the mass (pounds or kilograms) of the measure filled with concrete.

B.2.2.2.3 Additional Fresh Properties

Ambient temperature, ambient humidity, and concrete temperature were also measured to evaluate external factors for the concrete.

B.2.3 Test Results

During the different stages of bridge construction, a large number of samples including cylinders and beams were made and then tested at the specified day in the High Bay Structural and Materials Testing Laboratory at Texas A&M University. The test results are summarized according to the sequence of the construction.

B.2.3.1 Retaining Wall

A 75 ft long retaining wall was built before the excavation to resist the soil pressure below the adjacent runway. TxDOT Class C concrete with compressive strength of 3.60 ksi at 28 days was required. Cylinder samples for compressive strength at 7 days and 28 days, MOE at 28 days, and STS at 28 days were taken in the field. The mechanical property test results are shown in Table

B.2. The slump test was also conducted before pouring the concrete; the slump value was 6.6 in., which is less than the target (7 in.) and was considered acceptable. The average compressive strength at 28 days was 6.28 ksi, which satisfied the design requirement.

Table B.2. Mechanical Property Test Results for Retaining Wall.

Sample No.	Compressive Strength					STS		MOE	
	f_c'/7d (ksi)	Avg. f_c'/7d (ksi)	f_c'/28d (ksi)	Avg. f_c'/28d (ksi)	Design f_c' (ksi)	T/28d (ksi)	Avg. T/28d (ksi)	E/28d (ksi)	Avg. E/28d (ksi)
1	4.04		6.34			0.710		5928.63	
2	4.13	4.11	6.32	6.28	3.6	0.711	0.693	6049.90	5980.34
3	4.16		6.18			0.659		5962.49	

B.2.3.2   Slab on Grade

A 58 ft 10 in. long, 34 ft wide, and 4 in. thick concrete slab on grade was provided at the base of the excavated pit. For this slab, TxDOT Class C concrete with 3600 psi compressive strength at 28 days and a 7 in. slump was specified. Three trucks of concrete were used in the construction process of the mud slab. For each truck, three cylinder samples for compressive strength at 28 days were taken in the field. The compressive strength test results are shown in Table B.3. The concrete compressive strength for the slab-on-grade satisfies the design requirement, and the compressive strength values increased as concrete age increased.

Table B.3. Compressive Strength at 28 Days for Slab-on-Grade.

Truck No.	Sample No.	f_c' (ksi)	Avg. f_c' (ksi)
1	1	4.65	
	2	4.38	4.63
	3	4.87	
2	1	4.67	
	2	5.05	4.84
	3	4.81	
3	1	4.79	
	2	4.82	5.00
	3	5.40	

B.2.3.3   Footings

A 34 ft long, 8 ft wide, and 1 ft 4 in. high spread reinforced concrete footing was constructed at both ends of the bridge. For the spread footings, TxDOT Class C concrete with 3600 psi compressive strength at 28 days and 5 in. slump was required. Three trucks of concrete were used in the construction process for spread footings. For each truck, three cylinder samples for compressive strength at 28 days were taken. Three cylinder samples from Truck 1 for the MOE test at 28 days were also taken in the field. The compressive strength and MOE test results are shown in Table B.4. and Table B.5. , respectively.

Table B.4. Compressive Strength for Spread Footings.

Truck No.	Sample No.	f_c'/28d (ksi)	Avg. f_c'/28d (ksi)
1	1	6.02	5.96
	2	5.98	
	3	5.89	
2	1	6.26	6.39
	2	6.36	
	3	6.54	
3	1	5.88	5.81
	2	5.80	
	3	5.74	

Table B.5. MOE Values for Spread Footings.

Truck No.	Sample No.	E/28d (ksi)	Avg. E/28d (ksi)
1	1	6226	5842
	2	6017	
	3	5283	

Table B.4. shows that the concrete compressive strength for the spread footings satisfied the design requirement.

B.2.3.4   Abutments

Two 34 ft long abutments with 2.5 by 2.5 ft cross-sections were built at both sides. TxDOT Class C concrete with 3600 psi compressive strength at 28 days and 5 in. slump was required. Two trucks of concrete were used in the construction process for the spread footings. For each truck, three cylinder samples for compressive strength at 7 and 28 days were taken. The

compressive strength test results are shown in Table B.6. The concrete compressive strength for the abutments satisfied the design requirement.

Table B.6. Compressive Strength for Abutments.

Truck No.	Sample No.	f_c'/7d (ksi)	Avg. f_c'/7d (ksi)	f_c'/28d (ksi)	Avg. f_c'/28d (ksi)	Design f_c' (ksi)
1	1	4.46		5.94		
	2	4.40	4.43	5.84	5.92	
	3	4.43		5.97		3.6
2	1	4.31		5.70		
	2	4.36	4.36	5.49	5.61	
	3	4.41		5.65		

B.2.3.5 Slab Beams

After substructure construction work was finished, Bexar Concrete Works manufactured the slab beams by precaster in San Antonio, Texas. Four 48 ft long 5SB15 (15 by 5 ft) prestressed slab beams were needed for the bridge construction. High-strength TxDOT Class H concrete with f'_{ci} = 6 ksi at release and f'_c = 7 ksi at 28 days was required. In order to control the quality of the slab beam, a large number of specimens including cylinders and beams were taken in the field, and fresh properties tests were also conducted there. For different beams, cylinder samples were taken for compressive strength at 24 hours, 3 days, 7 days, 28 days, and 56 days; MOE at 7 and 28 days; and STS at 7 and 28 days. Beam samples for MOR tests were taken at 56 days. The cylinder casting procedures are shown in Figure B.30 and Figure B.31. The compressive strength values for each slab beam are shown in Table B.7.

Figure B.30. Test Specimen Casting.

Figure B.31. All Cylinder Samples.

Table B.7. Compressive Strength for Slab Beams.

Beam No.	Sample No.	f_c'/1d (ksi)	Avg. f_c'/1d (ksi)	f_c'/3d (ksi)	Avg. f_c'/3d (ksi)	f_c'/7d (ksi)	Avg. f_c'/7d (ksi)	f_c'/28d (ksi)	Avg. f_c'/28d (ksi)	f_c'/56d (ksi)	Avg. f_c'/56d (ksi)	Design f_c' (ksi)
1	1	6.49		8.27		9.10		10.63		11.25		
	2	6.62	6.50	8.34	8.35	9.38	9.25	10.58	10.64	11.41	11.26	
	3	6.39		8.43		9.27		10.72		11.12		
2	1	–		–		9.89		10.96		–		
	2	–	–	–	–	9.55	9.74	11.57	10.95	–	–	
	3	–		–		9.78		10.31		–		3.6
3	1	6.50		8.43		9.29		10.40		11.05		
	2	6.41	6.44	7.79	8.22	9.34	9.29	10.04	10.29	11.18	11.24	
	3	6.41		8.43		9.23		10.43		11.49		
4	1	–		–		9.05		11.04		–		
	2	–	–	–	–	9.58	9.21	10.95	10.86	–	–	
	3	–		–		8.99		10.60		–		

Fresh properties including slump, unit weight test, ambient temperature, ambient humidity, and concrete temperature were measured in the field. The fresh properties of the concrete are shown in Table B.8. The relationship between concrete strength and concrete age is shown in Figure B.32. The splitting tensile strength values for each slab beam are shown in Table B.9. The relationship between splitting tensile strength and concrete age is shown in Figure B.33. The modulus values of elasticity values for each slab beam are shown in Table B.10. The MOR strength values for each slab beam are shown in Table B.11. The values in the table and relevant figures show that the compressive strength for the slab beams satisfied the strength requirement for the release strength and final design strength. As concrete age increased, the values of compressive strength and STS strength for the concrete increased.

Table B.8. Fresh Properties of Concrete for Slab Beams.

Beam No.	Slump (in.)		Ambient Temperature (°F)	Ambient Humidity (%)	Unit Weight (kips/ft³)	Concrete Temperature (°F)
1	25	24	93.3	47.4	0.1462	88
2	24	23	94.6	45.0	0.1466	87
3	27	24	94.0	46.0	0.1468	87
4	28	25	92.3	48.6	0.1466	87
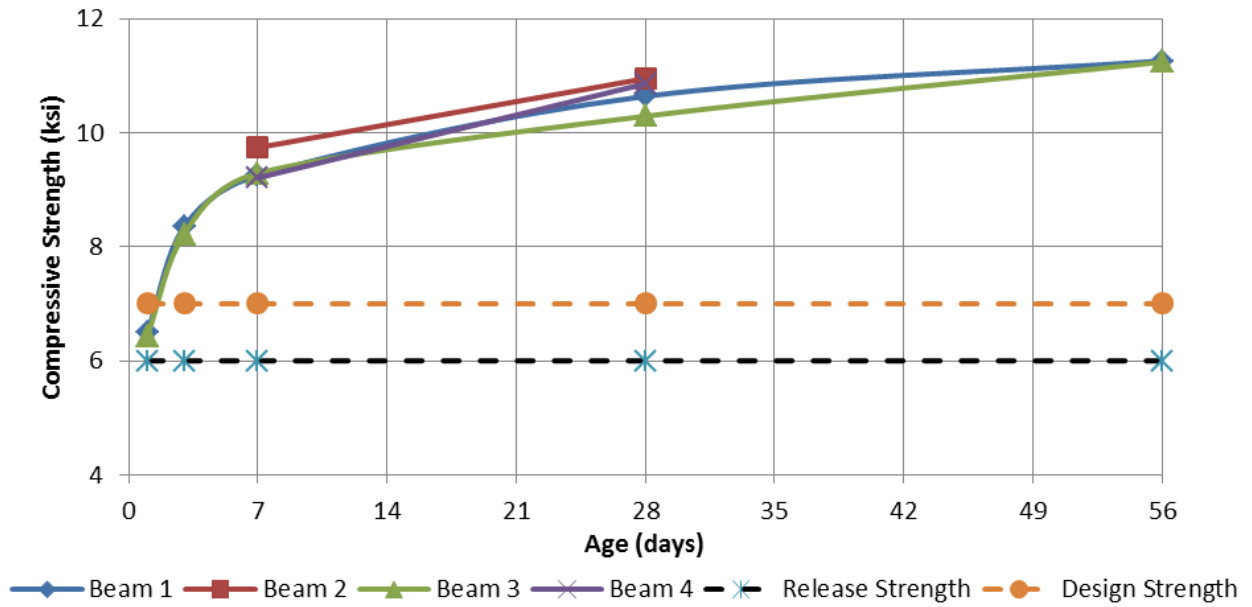
Figure B.32. Relationship between Compressive Strength and Concrete Age.
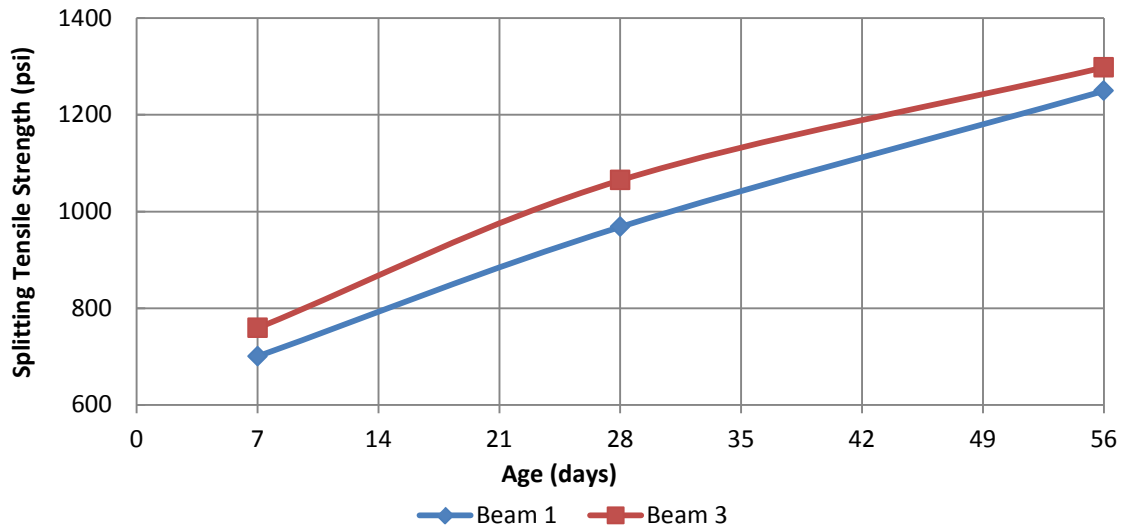
Figure B.33. Relationship between STS and Concrete Age.

355

Table B.9. Splitting Tensile Strength for Slab Beams.

Beam No.	Sample No.	T/28d (ksi)	Avg. T/7d (ksi)	T/28d (ksi)	Avg. T/28d (ksi)	T/28d (ksi)	Avg. T/56d (ksi)
1	1	0.812		1.316		1.209	
	2	0.873	0.700	0.951	0.968	1.342	1.249
	3	0.617		0.637		1.197	
3	1	0.729		1.152		1.239	
	2	0.776	0.759	0.787	1.065	1.294	1.298
	3	0.772		1.256		1.361	

Table B.10. Modulus of Elasticity for Slab Beams.

Beam No.	Sample No.	E/7d (ksi)	Avg. E/7d (ksi)	E/28d (ksi)	Avg. E /28d (ksi)	E/56d (ksi)	Avg. E /56d (ksi)
1	1	4656		4980.36		3349.32	
	2	4657	4735	4951.85	4908	5465.88	4653
	3	4891		4792.51		5143.19	
2	1	–		4318.34		–	
	2	–	–	4820.37	4658	–	–
	3	–		4833.90		–	
3	1	4607		5036.29		5393.22	
	2	4541	4630	5005.38	4978	5441.17	5393
	3	4740		4892.14		5343.97	
4	1	–		5214.23		–	
	2	–	–	4837.09	5064	–	–
	3	–		5140.89		–	

Table B.11. MOR Strength for Slab Beams.

Beam No.	Sample No.	R/56d (ksi)	Avg. R/56d (ksi)	Beam No.	Sample No.	R/56d (ksi)	Avg. R/56d (ksi)
1	1	0.666		3	1	0.708	
	2	–	0.648		2	0.690	0.660
	3	0.630			3	0.582	

B.2.3.6   PCPs

Bexar Concrete Works also manufactured the PCPs by precaster in San Antonio, Texas. Eighteen total PCPs (8 ft long with a 4 in. depth and 5 ft 4 in. width) were needed for the bridge construction. TxDOT Class H concrete with f'_{ci} = 4 ksi at release and f'_c = 5 ksi at 28 days was required. Given that the manufacturer made the panels in a rush, only eight cylinder samples were taken and tested for mechanical properties including compressive strength, modulus of

elasticity, and splitting tensile strength. The values of mechanical properties are shown in Table B.12. also shows that the compressive strength values for PCPs satisfied the design requirement.

Table B.12. Mechanical Property Test Results for PCPs.

Sample No.	Compressive Strength			STS		MOE	
	f_c'/7d (ksi)	Avg. f_c'/7d (ksi)	Design (ksi)	T/28d (ksi)	Avg. T/28d (ksi)	E/28d (ksi)	Avg. E/28d (ksi)
1	10.0			1.06		5086	
2	9.82	9.93	5	0.961	1.05	5891	5489
3	9.96			1.13		–	

B.2.3.7 Deck

The deck was cast in place after the slab beams and PCPs were positioned. TxDOT Class S concrete with 4000 psi compressive strength at 28 days was required. Fresh properties including slump, unit weight test, ambient temperature, ambient humidity, and concrete temperature were also measured in the field. The fresh properties of the concrete are shown in Table B.13. Cylinder samples for compressive strength at 28 days and MOE at 28 days, as well as beam samples for MOR at 28 days, were made in the field. The mechanical property test results are shown in Table B.14 and Table B.15. Table B.16. shows that the compressive strength for the deck satisfies the design strength requirement.

Table B.13. Fresh Properties of Concrete for Deck.

Truck No.	Slump (in.)	Ambient Temperature (°F)	Ambient Humidity (%)	Unit Weight (kips/ft³)	Concrete Temperature (°F)
1	5.6	77.4	88.8	0.1527	85
2	4.8	77.4	88.8	0.1545	90
3	5.5	77.4	88.8	0.1548	90
4	4.0	77.4	88.8	0.1531	91

Table B.14. Compressive Strength Values for Deck.

Truck No.	Sample No.	$f_c'/28d$ (ksi)	Avg. $f_c'/28d$ (ksi)
1	1	5.09	5.16
	2	5.35	
	3	5.03	
2	1	6.91	6.99
	2	7.09	
	3	6.98	
3	1	6.00	6.61
	2	6.97	
	3	6.87	
4	1	6.94	7.01
	2	7.05	
	3	7.05	

Table B.15. MOR Values for Deck.

Truck No.	Sample No.	$R/28d$ (ksi)	Avg. $R/28d$ (ksi)
2	1	0.865	0.851
	2	0.798	
	3	0.891	

Table B.16. MOE Values for Deck.

Truck No.	Sample No.	$E/28d$ (ksi)	Avg. $E/28d$ (ksi)
2	1	6312	6466
	2	6701	
	3	6385	
3	1	6736	6467
	2	6346	
	3	6320	

APPENDIX C   LDF TABLES FOR THE CONSIDERED BRIDGE
GEOMETRIES

C.1   INTRODUCTION

Live load distribution factor (LDF) formulas were derived by analyzing 31 different spread slab beam bridge geometries using the finite element method (FEM). Key parameters (span L, spacing S, and girder depth d) were varied, and FEM shear and moment values were obtained for each girder, for both one-lane-loaded and multiple-lane-loaded cases. These shear and moment values were used to determine shear and moment LDF values for interior and exterior girders. LDF values were also calculated using the American Association of Sate Highway and Transportation Officials (AASHTO) Load and Resistance Factor Design (LRFD) Specifications (2012) spread box beam formulas, least square fitted relations, and proposed spread slab beam equations for all eight LDF cases. Detailed derivation of the least square fitted relations and proposed equations are provided in Chapter 7. The maximum moment and shear forces obtained by FEM analysis for all 31 bridge models are provided in Table C.1. The LDF values obtained using the three methods, for all eight equations, and their ratios to the LDFs obtained through FEM analysis are listed in Table C.2 through Table C.9. The median values and lognormal standard deviations of these ratios are also provided to show the accuracy and variation of these equations.

Table C.1. Maximum Moment and Shear Forces from FEM Analysis.

No.	L (ft)	S (ft)	d (in.)	One-Lane-Loaded Interior Beam Max. Moment (kip-ft)	Max. Shear (kips)	Exterior Beam Max. Moment (kip-ft)	Max. Shear (kips)	Multiple-Lanes-Loaded Interior Beam Max. Moment (kip-ft)	Max. Shear (kips)	Exterior Beam Max. Moment (kip-ft)	Max. Shear (kips)
1	29.58	9.67	15.0	181	39	138	21	297	53	281	46
2	33.58	9.67	15.0	198	41	160	23	333	56	319	49
3	37.58	9.67	15.0	214	42	181	23	369	58	357	51
4	39.58	9.67	15.0	223	43	193	23	389	59	378	52
5	41.58	9.67	15.0	232	43	206	23	409	60	399	53
6	44.58	9.67	15.0	250	44	227	24	447	61	439	54
7	45.58	9.67	15.0	255	44	233	23	459	62	451	54
8	44.58	7.00	15.0	210	33	206	23	371	41	371	37
9	44.58	7.67	15.0	221	38	212	24	389	47	388	42
10	44.58	8.33	15.0	230	41	218	24	410	54	408	48
11	44.58	9.00	15.0	240	42	223	24	429	58	424	52
12	44.58	9.67	15.0	250	44	227	24	447	61	439	54
13	44.58	10.33	15.0	260	45	229	22	466	64	454	55
14	44.58	11.00	15.0	271	46	230	21	523	67	472	57
15	44.58	8.75	15.0	226	42	214	24	415	56	395	50
16	44.58	9.25	15.0	234	43	218	24	433	59	411	52
17	44.58	9.75	15.0	244	44	223	23	452	61	426	54
18	44.58	10.25	15.0	253	45	225	22	471	63	440	55
19	39.58	9.67	12.0	215	41	189	22	379	57	370	51
20	39.58	9.67	13.5	219	42	191	23	384	58	374	51
21	39.58	9.67	15.0	223	43	193	23	389	59	378	52
22	39.58	9.67	16.5	228	44	195	23	394	60	382	53
23	39.58	9.67	18.0	233	44	196	23	399	61	386	53
24	39.58	9.67	19.5	238	45	197	24	404	61	390	54
25	39.58	9.67	21.0	242	46	199	24	410	62	394	54
26	39.58	7.33	12.0	187	35	183	24	321	41	319	37
27	40.58	6.50	12.0	166	29	167	22	280	37	280	33
28	35.58	10.00	12.0	207	41	175	24	355	57	343	51
29	49.58	7.25	15.0	226	37	222	23	392	43	392	39
30	36.58	9.00	12.0	192	39	175	24	385	52	322	48
31	49.58	7.00	15.0	209	33	210	23	453	40	454	36

Table C.2. LDF Results for One-Lane-Loaded Moment in Interior Beams.

	Bridge Parameters			LDF Results and Ratios						
No.	L (ft)	S (ft)	d (in.)	FEM	AASHTO	AASHTO/ FEM	Fitted	Fitted/ FEM	Proposed	Proposed/ FEM
1	29.58	9.67	15.0	0.552	0.516	0.935	0.550	0.996	0.567	1.026
2	33.58	9.67	15.0	0.510	0.485	0.949	0.509	0.997	0.532	1.042
3	37.58	9.67	15.0	0.482	0.458	0.950	0.475	0.985	0.503	1.043
4	39.58	9.67	15.0	0.467	0.446	0.956	0.460	0.986	0.490	1.050
5	41.58	9.67	15.0	0.447	0.435	0.975	0.446	1.000	0.478	1.070
6	44.58	9.67	15.0	0.429	0.421	0.980	0.428	0.997	0.462	1.075
7	45.58	9.67	15.0	0.424	0.416	0.981	0.422	0.995	0.456	1.076
8	44.58	7.00	15.0	0.363	0.347	0.955	0.362	0.996	0.380	1.048
9	44.58	7.67	15.0	0.381	0.366	0.960	0.379	0.994	0.402	1.053
10	44.58	8.33	15.0	0.396	0.385	0.970	0.396	0.999	0.422	1.065
11	44.58	9.00	15.0	0.412	0.403	0.978	0.412	1.000	0.442	1.073
12	44.58	9.67	15.0	0.429	0.421	0.980	0.428	0.997	0.462	1.075
13	44.58	10.33	15.0	0.447	0.438	0.979	0.443	0.991	0.480	1.075
14	44.58	11.00	15.0	0.465	0.454	0.977	0.458	0.983	0.499	1.072
15	44.58	8.75	15.0	0.388	0.396	1.021	0.406	1.047	0.435	1.120
16	44.58	9.25	15.0	0.403	0.410	1.017	0.418	1.038	0.449	1.116
17	44.58	9.75	15.0	0.419	0.423	1.010	0.430	1.026	0.464	1.108
18	44.58	10.25	15.0	0.434	0.436	1.004	0.441	1.016	0.478	1.101
19	39.58	9.67	12.0	0.449	0.422	0.941	0.438	0.977	0.463	1.032
20	39.58	9.67	13.5	0.458	0.435	0.949	0.450	0.982	0.477	1.041
21	39.58	9.67	15.0	0.467	0.446	0.956	0.460	0.986	0.490	1.050
22	39.58	9.67	16.5	0.477	0.457	0.959	0.470	0.986	0.502	1.053
23	39.58	9.67	18.0	0.486	0.467	0.960	0.479	0.984	0.513	1.054
24	39.58	9.67	19.5	0.496	0.477	0.960	0.487	0.981	0.523	1.054
25	39.58	9.67	21.0	0.507	0.486	0.958	0.495	0.977	0.533	1.051
26	39.58	7.33	12.0	0.394	0.358	0.907	0.380	0.963	0.392	0.996
27	40.58	6.50	12.0	0.334	0.329	0.984	0.351	1.052	0.361	1.080
28	35.58	10.00	12.0	0.499	0.454	0.910	0.476	0.954	0.499	0.999
29	49.58	7.25	15.0	0.329	0.336	1.019	0.345	1.048	0.368	1.118
30	36.58	9.00	12.0	0.450	0.421	0.935	0.443	0.985	0.462	1.026
31	49.58	7.00	15.0	0.305	0.329	1.076	0.339	1.109	0.361	1.180
Median (50th Percentile)				–	0.9701	–	1.0004	–	1.0479	
Lognormal Standard Deviation, β_D				–	0.0342	–	0.0295	–	0.0309	

Table C.3. LDF Results for Multiple-Lane-Loaded Moment in Interior Beams.

	Bridge Parameters			LDF Results and Ratios						
No.	*L* (ft)	*S* (ft)	*d* (in.)	FEM	AASHTO	AASHTO/ FEM	Fitted	Fitted/ FEM	Proposed	Proposed/ FEM
1	29.58	9.67	15.0	0.756	0.757	1.001	0.757	1.000	0.757	1.001
2	33.58	9.67	15.0	0.720	0.733	1.019	0.719	0.999	0.733	1.018
3	37.58	9.67	15.0	0.694	0.713	1.028	0.688	0.991	0.713	1.028
4	39.58	9.67	15.0	0.680	0.704	1.035	0.673	0.991	0.704	1.035
5	41.58	9.67	15.0	0.658	0.695	1.056	0.660	1.003	0.695	1.056
6	44.58	9.67	15.0	0.642	0.683	1.064	0.642	1.000	0.683	1.064
7	45.58	9.67	15.0	0.637	0.679	1.066	0.636	0.999	0.679	1.066
8	44.58	7.00	15.0	0.534	0.541	1.012	0.520	0.973	0.541	1.012
9	44.58	7.67	15.0	0.559	0.578	1.034	0.552	0.988	0.578	1.033
10	44.58	8.33	15.0	0.589	0.613	1.042	0.583	0.990	0.613	1.042
11	44.58	9.00	15.0	0.616	0.649	1.054	0.613	0.995	0.649	1.053
12	44.58	9.67	15.0	0.642	0.683	1.064	0.642	1.000	0.683	1.064
13	44.58	10.33	15.0	0.671	0.717	1.069	0.671	1.000	0.717	1.069
14	44.58	11.00	15.0	0.740	0.750	1.014	0.699	0.944	0.750	1.014
15	44.58	8.75	15.0	0.591	0.636	1.075	0.602	1.018	0.635	1.075
16	44.58	9.25	15.0	0.615	0.662	1.076	0.624	1.014	0.662	1.076
17	44.58	9.75	15.0	0.640	0.687	1.075	0.646	1.009	0.687	1.074
18	44.58	10.25	15.0	0.665	0.713	1.072	0.667	1.003	0.713	1.072
19	39.58	9.67	12.0	0.663	0.684	1.033	0.653	0.985	0.684	1.033
20	39.58	9.67	13.5	0.671	0.695	1.034	0.664	0.988	0.695	1.034
21	39.58	9.67	15.0	0.680	0.704	1.035	0.673	0.991	0.704	1.035
22	39.58	9.67	16.5	0.689	0.712	1.034	0.682	0.991	0.712	1.034
23	39.58	9.67	18.0	0.698	0.720	1.032	0.691	0.990	0.720	1.032
24	39.58	9.67	19.5	0.707	0.727	1.028	0.698	0.987	0.727	1.028
25	39.58	9.67	21.0	0.716	0.734	1.025	0.706	0.985	0.734	1.025
26	39.58	7.33	12.0	0.562	0.560	0.996	0.545	0.969	0.560	0.996
27	40.58	6.50	12.0	0.467	0.510	1.092	0.499	1.067	0.510	1.091
28	35.58	10.00	12.0	0.717	0.720	1.004	0.697	0.971	0.720	1.004
29	49.58	7.25	15.0	0.477	0.540	1.133	0.510	1.070	0.540	1.133
30	36.58	9.00	12.0	0.616	0.663	1.076	0.643	1.043	0.663	1.076
31	49.58	7.00	15.0	0.467	0.526	1.127	0.498	1.067	0.526	1.127
Median (50th Percentile)				−	1.0481	−	1.0004	−	1.0479	
Lognormal Standard Deviation, β_D				−	0.0309	−	0.0271	−	0.0309	

363

Table C.4. LDF Results for One-Lane-Loaded Moment in Exterior Beams.

	Bridge Parameters			LDF Results and Ratios						
No.	L (ft)	S (ft)	d (in.)	FEM	AASHTO	AASHTO/ FEM	Fitted	Fitted/ FEM	Proposed	Proposed/ FEM
1	29.58	9.67	15.0	0.632	0.890	1.407	0.641	1.013	0.660	1.044
2	33.58	9.67	15.0	0.595	0.890	1.496	0.593	0.997	0.611	1.028
3	37.58	9.67	15.0	0.562	0.890	1.583	0.553	0.985	0.572	1.017
4	39.58	9.67	15.0	0.544	0.890	1.635	0.536	0.985	0.554	1.018
5	41.58	9.67	15.0	0.519	0.890	1.716	0.520	1.003	0.538	1.037
6	44.58	9.67	15.0	0.495	0.890	1.797	0.499	1.007	0.516	1.042
7	45.58	9.67	15.0	0.487	0.890	1.827	0.492	1.010	0.509	1.046
8	44.58	7.00	15.0	0.391	0.771	1.972	0.385	0.985	0.398	1.018
9	44.58	7.67	15.0	0.413	0.809	1.960	0.415	1.005	0.429	1.039
10	44.58	8.33	15.0	0.437	0.840	1.922	0.443	1.013	0.458	1.048
11	44.58	9.00	15.0	0.464	0.867	1.867	0.471	1.015	0.487	1.050
12	44.58	9.67	15.0	0.495	0.890	1.797	0.499	1.007	0.516	1.042
13	44.58	10.33	15.0	0.527	0.910	1.725	0.526	0.997	0.544	1.031
14	44.58	11.00	15.0	0.559	0.927	1.659	0.553	0.989	0.572	1.024
15	44.58	8.75	15.0	0.446	0.857	1.920	0.460	1.032	0.476	1.067
16	44.58	9.25	15.0	0.470	0.876	1.862	0.481	1.024	0.498	1.059
17	44.58	9.75	15.0	0.496	0.892	1.800	0.502	1.012	0.519	1.048
18	44.58	10.25	15.0	0.521	0.907	1.742	0.522	1.003	0.541	1.038
19	39.58	9.67	12.0	0.523	0.890	1.701	0.513	0.980	0.518	0.991
20	39.58	9.67	13.5	0.534	0.890	1.665	0.525	0.982	0.537	1.005
21	39.58	9.67	15.0	0.544	0.890	1.635	0.536	0.985	0.554	1.018
22	39.58	9.67	16.5	0.555	0.890	1.603	0.547	0.985	0.570	1.027
23	39.58	9.67	18.0	0.565	0.890	1.574	0.556	0.984	0.585	1.035
24	39.58	9.67	19.5	0.575	0.890	1.546	0.565	0.982	0.599	1.042
25	39.58	9.67	21.0	0.585	0.890	1.520	0.574	0.980	0.613	1.047
26	39.58	7.33	12.0	0.426	0.709	1.666	0.411	0.966	0.415	0.976
27	40.58	6.50	12.0	0.363	0.646	1.779	0.368	1.013	0.372	1.023
28	35.58	10.00	12.0	0.565	0.840	1.486	0.562	0.995	0.568	1.004
29	49.58	7.25	15.0	0.361	0.786	2.176	0.371	1.028	0.384	1.064
30	36.58	9.00	12.0	0.511	0.800	1.566	0.508	0.995	0.513	1.004
31	49.58	7.00	15.0	0.343	0.771	2.248	0.361	1.052	0.374	1.089
Median (50th Percentile)				–	1.7271	–	1.0002	–	1.0327	
Lognormal Standard Deviation, β_D				–	0.1071	–	0.0182	–	0.0222	

Table C.5. LDF Results for Multiple-Lane-Loaded Moment in Exterior Beams.

	Bridge Parameters			LDF Results and Ratios						
No.	L (ft)	S (ft)	d (in.)	FEM	AASHTO	AASHTO/ FEM	Fitted	Fitted/ FEM	Proposed	Proposed/ FEM
1	29.58	9.67	15.0	0.663	0.801	1.207	0.663	0.999	0.673	1.014
2	33.58	9.67	15.0	0.651	0.776	1.191	0.644	0.989	0.656	1.007
3	37.58	9.67	15.0	0.638	0.754	1.182	0.629	0.985	0.641	1.005
4	39.58	9.67	15.0	0.630	0.744	1.182	0.621	0.986	0.635	1.007
5	41.58	9.67	15.0	0.620	0.735	1.186	0.615	0.992	0.629	1.014
6	44.58	9.67	15.0	0.608	0.723	1.188	0.605	0.995	0.620	1.019
7	45.58	9.67	15.0	0.603	0.719	1.191	0.602	0.998	0.617	1.023
8	44.58	7.00	15.0	0.515	0.572	1.111	0.501	0.972	0.511	0.992
9	44.58	7.67	15.0	0.531	0.611	1.150	0.528	0.994	0.539	1.015
10	44.58	8.33	15.0	0.553	0.649	1.173	0.555	1.002	0.567	1.025
11	44.58	9.00	15.0	0.579	0.686	1.186	0.580	1.003	0.594	1.026
12	44.58	9.67	15.0	0.608	0.723	1.189	0.605	0.996	0.620	1.020
13	44.58	10.33	15.0	0.640	0.758	1.186	0.629	0.984	0.645	1.008
14	44.58	11.00	15.0	0.672	0.794	1.182	0.653	0.973	0.670	0.997
15	44.58	8.75	15.0	0.550	0.672	1.223	0.571	1.038	0.584	1.062
16	44.58	9.25	15.0	0.575	0.700	1.217	0.590	1.025	0.604	1.049
17	44.58	9.75	15.0	0.602	0.727	1.208	0.608	1.011	0.623	1.035
18	44.58	10.25	15.0	0.628	0.754	1.200	0.627	0.997	0.642	1.022
19	39.58	9.67	12.0	0.620	0.724	1.167	0.611	0.985	0.621	1.001
20	39.58	9.67	13.5	0.626	0.735	1.174	0.617	0.986	0.628	1.004
21	39.58	9.67	15.0	0.630	0.744	1.182	0.621	0.986	0.635	1.007
22	39.58	9.67	16.5	0.635	0.753	1.187	0.626	0.986	0.641	1.010
23	39.58	9.67	18.0	0.639	0.762	1.192	0.630	0.986	0.646	1.012
24	39.58	9.67	19.5	0.643	0.769	1.197	0.634	0.986	0.652	1.014
25	39.58	9.67	21.0	0.647	0.776	1.201	0.637	0.985	0.656	1.015
26	39.58	7.33	12.0	0.512	0.593	1.158	0.519	1.015	0.526	1.027
27	40.58	6.50	12.0	0.448	0.540	1.205	0.481	1.074	0.487	1.087
28	35.58	10.00	12.0	0.630	0.762	1.209	0.638	1.013	0.647	1.027
29	49.58	7.25	15.0	0.469	0.571	1.218	0.499	1.065	0.511	1.089
30	36.58	9.00	12.0	0.576	0.701	1.216	0.596	1.035	0.604	1.048
31	49.58	7.00	15.0	0.447	0.557	1.245	0.489	1.093	0.500	1.118
Median (50th Percentile)				–	1.1901	–	1.0040	–	1.0254	
Lognormal Standard Deviation, β_D				–	0.0205	–	0.0279	–	0.0269	

Table C.6. LDF Results for One-Lane-Loaded Shear in Interior Beams.

	Bridge Parameters			LDF Results and Ratios						
No.	L (ft)	S (ft)	d (in.)	FEM	AASHTO	AASHTO/ FEM	Fitted	Fitted/ FEM	Proposed	Proposed/ FEM
1	29.58	9.67	15.0	0.846	0.714	0.844	0.844	0.998	0.846	1.001
2	33.58	9.67	15.0	0.814	0.705	0.866	0.809	0.993	0.820	1.007
3	37.58	9.67	15.0	0.785	0.697	0.888	0.780	0.993	0.797	1.015
4	39.58	9.67	15.0	0.771	0.694	0.900	0.766	0.995	0.787	1.021
5	41.58	9.67	15.0	0.757	0.690	0.911	0.754	0.996	0.777	1.026
6	44.58	9.67	15.0	0.740	0.685	0.927	0.737	0.996	0.764	1.032
7	45.58	9.67	15.0	0.734	0.684	0.931	0.732	0.996	0.760	1.034
8	44.58	7.00	15.0	0.568	0.565	0.995	0.595	1.048	0.619	1.091
9	44.58	7.67	15.0	0.642	0.597	0.930	0.632	0.985	0.657	1.024
10	44.58	8.33	15.0	0.680	0.627	0.921	0.668	0.981	0.693	1.019
11	44.58	9.00	15.0	0.712	0.657	0.922	0.703	0.987	0.729	1.024
12	44.58	9.67	15.0	0.740	0.686	0.927	0.737	0.996	0.764	1.033
13	44.58	10.33	15.0	0.763	0.713	0.934	0.770	1.009	0.797	1.045
14	44.58	11.00	15.0	0.785	0.741	0.944	0.803	1.023	0.831	1.058
15	44.58	8.75	15.0	0.696	0.646	0.928	0.690	0.991	0.716	1.029
16	44.58	9.25	15.0	0.719	0.668	0.928	0.716	0.995	0.742	1.032
17	44.58	9.75	15.0	0.735	0.689	0.938	0.741	1.009	0.768	1.046
18	44.58	10.25	15.0	0.753	0.710	0.942	0.766	1.017	0.793	1.053
19	39.58	9.67	12.0	0.738	0.678	0.919	0.733	0.993	0.744	1.008
20	39.58	9.67	13.5	0.755	0.686	0.909	0.751	0.994	0.766	1.015
21	39.58	9.67	15.0	0.771	0.694	0.900	0.766	0.995	0.787	1.021
22	39.58	9.67	16.5	0.786	0.700	0.891	0.781	0.994	0.806	1.026
23	39.58	9.67	18.0	0.800	0.706	0.883	0.794	0.993	0.824	1.030
24	39.58	9.67	19.5	0.812	0.712	0.877	0.807	0.994	0.840	1.035
25	39.58	9.67	21.0	0.823	0.717	0.871	0.819	0.994	0.856	1.039
26	39.58	7.33	12.0	0.624	0.575	0.920	0.611	0.978	0.622	0.996
27	40.58	6.50	12.0	0.529	0.533	1.009	0.559	1.058	0.571	1.081
28	35.58	10.00	12.0	0.777	0.700	0.900	0.777	1.000	0.781	1.005
29	49.58	7.25	15.0	0.579	0.571	0.985	0.588	1.015	0.617	1.065
30	36.58	9.00	12.0	0.728	0.655	0.899	0.718	0.986	0.724	0.995
31	49.58	7.00	15.0	0.527	0.559	1.061	0.575	1.091	0.603	1.145
Median (50th Percentile)				–	0.9217	–	1.0028	–	1.0334	
Lognormal Standard Deviation, β_D				–	0.0455	–	0.0226	–	0.0283	

Table C.7. LDF Results for Multiple-Lane-Loaded Shear in Interior Beams.

	Bridge Parameters			LDF Results and Ratios						
No.	L (ft)	S (ft)	d (in.)	FEM	AASHTO	AASHTO/ FEM	Fitted	Fitted/ FEM	Proposed	Proposed/ FEM
1	29.58	9.67	15.0	0.961	0.902	0.939	0.949	0.988	0.979	1.018
2	33.58	9.67	15.0	0.935	0.891	0.953	0.922	0.986	0.954	1.021
3	37.58	9.67	15.0	0.910	0.881	0.968	0.898	0.986	0.933	1.025
4	39.58	9.67	15.0	0.899	0.877	0.975	0.887	0.986	0.923	1.027
5	41.58	9.67	15.0	0.888	0.872	0.982	0.877	0.987	0.914	1.029
6	44.58	9.67	15.0	0.873	0.866	0.992	0.863	0.988	0.902	1.032
7	45.58	9.67	15.0	0.870	0.864	0.994	0.858	0.987	0.898	1.032
8	44.58	7.00	15.0	0.639	0.669	1.047	0.638	0.999	0.674	1.055
9	44.58	7.67	15.0	0.667	0.720	1.079	0.695	1.041	0.732	1.097
10	44.58	8.33	15.0	0.768	0.769	1.002	0.751	0.978	0.789	1.027
11	44.58	9.00	15.0	0.827	0.818	0.989	0.807	0.975	0.845	1.022
12	44.58	9.67	15.0	0.873	0.866	0.992	0.863	0.988	0.902	1.033
13	44.58	10.33	15.0	0.916	0.913	0.998	0.918	1.002	0.957	1.045
14	44.58	11.00	15.0	0.957	0.961	1.003	0.973	1.017	1.013	1.058
15	44.58	8.75	15.0	0.798	0.800	1.002	0.786	0.985	0.824	1.033
16	44.58	9.25	15.0	0.839	0.836	0.997	0.828	0.987	0.867	1.033
17	44.58	9.75	15.0	0.869	0.872	1.003	0.870	1.000	0.909	1.045
18	44.58	10.25	15.0	0.902	0.908	1.007	0.911	1.010	0.950	1.054
19	39.58	9.67	12.0	0.868	0.857	0.988	0.856	0.986	0.883	1.017
20	39.58	9.67	13.5	0.884	0.867	0.981	0.872	0.986	0.904	1.023
21	39.58	9.67	15.0	0.899	0.877	0.975	0.887	0.986	0.923	1.027
22	39.58	9.67	16.5	0.913	0.885	0.969	0.901	0.986	0.941	1.030
23	39.58	9.67	18.0	0.926	0.893	0.964	0.913	0.986	0.958	1.034
24	39.58	9.67	19.5	0.939	0.900	0.959	0.925	0.986	0.973	1.037
25	39.58	9.67	21.0	0.950	0.907	0.954	0.937	0.986	0.988	1.040
26	39.58	7.33	12.0	0.676	0.687	1.017	0.661	0.978	0.689	1.019
27	40.58	6.50	12.0	0.545	0.622	1.142	0.587	1.077	0.615	1.128
28	35.58	10.00	12.0	0.920	0.890	0.968	0.905	0.984	0.930	1.011
29	49.58	7.25	15.0	0.593	0.681	1.148	0.643	1.085	0.681	1.149
30	36.58	9.00	12.0	0.830	0.816	0.983	0.815	0.982	0.841	1.013
31	49.58	7.00	15.0	0.547	0.662	1.211	0.623	1.139	0.660	1.207
Median (50th Percentile)				–	1.0041	–	1.0006	–	1.0450	
Lognormal Standard Deviation, β_D				–	0.0563	–	0.0342	–	0.0388	

Table C.8. LDF Results for One-Lane-Loaded Shear in Exterior Beams.

	Bridge Parameters			LDF Results and Ratios						
No.	L (ft)	S (ft)	d (in.)	FEM	AASHTO	AASHTO/ FEM	Fitted	Fitted/ FEM	Proposed	Proposed/ FEM
1	29.58	9.67	15.0	0.713	0.890	1.247	0.703	0.986	0.712	0.999
2	33.58	9.67	15.0	0.689	0.890	1.292	0.700	1.017	0.712	1.034
3	37.58	9.67	15.0	0.702	0.890	1.267	0.698	0.994	0.712	1.015
4	39.58	9.67	15.0	0.699	0.890	1.272	0.696	0.996	0.712	1.019
5	41.58	9.67	15.0	0.696	0.890	1.278	0.695	0.998	0.712	1.023
6	44.58	9.67	15.0	0.692	0.890	1.286	0.694	1.002	0.712	1.029
7	45.58	9.67	15.0	0.700	0.890	1.271	0.693	0.990	0.712	1.017
8	44.58	7.00	15.0	0.560	0.771	1.377	0.556	0.993	0.568	1.014
9	44.58	7.67	15.0	0.604	0.809	1.339	0.592	0.980	0.606	1.003
10	44.58	8.33	15.0	0.633	0.840	1.326	0.626	0.989	0.642	1.013
11	44.58	9.00	15.0	0.659	0.867	1.316	0.660	1.003	0.677	1.029
12	44.58	9.67	15.0	0.692	0.890	1.286	0.694	1.003	0.712	1.029
13	44.58	10.33	15.0	0.734	0.910	1.238	0.726	0.989	0.746	1.016
14	44.58	11.00	15.0	0.771	0.927	1.202	0.758	0.983	0.780	1.011
15	44.58	8.75	15.0	0.648	0.857	1.323	0.648	1.000	0.664	1.025
16	44.58	9.25	15.0	0.675	0.876	1.298	0.673	0.998	0.690	1.024
17	44.58	9.75	15.0	0.700	0.892	1.275	0.698	0.997	0.716	1.024
18	44.58	10.25	15.0	0.732	0.907	1.240	0.722	0.987	0.742	1.014
19	39.58	9.67	12.0	0.688	0.890	1.293	0.686	0.997	0.712	1.035
20	39.58	9.67	13.5	0.694	0.890	1.281	0.692	0.996	0.712	1.026
21	39.58	9.67	15.0	0.699	0.890	1.272	0.696	0.996	0.712	1.019
22	39.58	9.67	16.5	0.704	0.890	1.265	0.701	0.996	0.712	1.012
23	39.58	9.67	18.0	0.708	0.890	1.257	0.705	0.996	0.712	1.006
24	39.58	9.67	19.5	0.711	0.890	1.251	0.709	0.996	0.712	1.001
25	39.58	9.67	21.0	0.714	0.890	1.245	0.712	0.997	0.712	0.997
26	39.58	7.33	12.0	0.563	0.709	1.260	0.568	1.008	0.587	1.043
27	40.58	6.50	12.0	0.527	0.646	1.226	0.522	0.990	0.539	1.023
28	35.58	10.00	12.0	0.659	0.840	1.274	0.705	1.069	0.729	1.106
29	49.58	7.25	15.0	0.571	0.786	1.376	0.567	0.993	0.582	1.019
30	36.58	9.00	12.0	0.625	0.800	1.279	0.655	1.047	0.677	1.083
31	49.58	7.00	15.0	0.542	0.771	1.424	0.554	1.022	0.568	1.049
Median (50th Percentile)				–	1.2843	–	1.0001	–	1.0241	
Lognormal Standard Deviation, β_D				–	0.0351	–	0.0173	–	0.0211	

Table C.9. LDF Results for Multiple-Lane-Loaded Shear in Exterior Beams.

	Bridge Parameters			LDF Results and Ratios						
No.	L (ft)	S (ft)	d (in.)	FEM	AASHTO	AASHTO/ FEM	Fitted	Fitted/ FEM	Proposed	Proposed/ FEM
1	29.58	9.67	15.0	0.627	0.948	1.512	0.622	0.992	0.667	1.064
2	33.58	9.67	15.0	0.631	0.936	1.482	0.627	0.993	0.667	1.056
3	37.58	9.67	15.0	0.635	0.925	1.457	0.632	0.994	0.667	1.050
4	39.58	9.67	15.0	0.637	0.920	1.445	0.634	0.995	0.667	1.047
5	41.58	9.67	15.0	0.639	0.916	1.434	0.636	0.996	0.667	1.044
6	44.58	9.67	15.0	0.640	0.910	1.420	0.639	0.997	0.667	1.041
7	45.58	9.67	15.0	0.649	0.908	1.399	0.640	0.986	0.667	1.028
8	44.58	7.00	15.0	0.549	0.703	1.279	0.530	0.966	0.549	1.000
9	44.58	7.67	15.0	0.569	0.756	1.329	0.559	0.983	0.580	1.020
10	44.58	8.33	15.0	0.591	0.807	1.366	0.586	0.992	0.610	1.031
11	44.58	9.00	15.0	0.611	0.859	1.405	0.613	1.003	0.639	1.045
12	44.58	9.67	15.0	0.640	0.910	1.420	0.639	0.997	0.667	1.041
13	44.58	10.33	15.0	0.679	0.959	1.413	0.664	0.978	0.694	1.022
14	44.58	11.00	15.0	0.715	1.009	1.411	0.688	0.962	0.720	1.008
15	44.58	8.75	15.0	0.598	0.840	1.405	0.603	1.009	0.628	1.051
16	44.58	9.25	15.0	0.620	0.878	1.416	0.623	1.004	0.649	1.047
17	44.58	9.75	15.0	0.644	0.916	1.422	0.642	0.997	0.670	1.041
18	44.58	10.25	15.0	0.673	0.953	1.417	0.661	0.982	0.691	1.027
19	39.58	9.67	12.0	0.641	0.900	1.405	0.638	0.996	0.667	1.040
20	39.58	9.67	13.5	0.639	0.911	1.425	0.636	0.995	0.667	1.043
21	39.58	9.67	15.0	0.637	0.920	1.445	0.634	0.995	0.667	1.047
22	39.58	9.67	16.5	0.635	0.929	1.464	0.632	0.995	0.667	1.050
23	39.58	9.67	18.0	0.633	0.937	1.481	0.630	0.995	0.667	1.053
24	39.58	9.67	19.5	0.631	0.945	1.497	0.628	0.996	0.667	1.056
25	39.58	9.67	21.0	0.629	0.952	1.512	0.627	0.996	0.667	1.059
26	39.58	7.33	12.0	0.527	0.722	1.369	0.544	1.033	0.565	1.072
27	40.58	6.50	12.0	0.496	0.654	1.317	0.509	1.025	0.525	1.059
28	35.58	10.00	12.0	0.604	0.935	1.548	0.646	1.070	0.680	1.126
29	49.58	7.25	15.0	0.542	0.715	1.320	0.545	1.006	0.561	1.036
30	36.58	9.00	12.0	0.572	0.857	1.497	0.609	1.065	0.639	1.116
31	49.58	7.00	15.0	0.523	0.695	1.330	0.534	1.022	0.549	1.051
Median (50th Percentile)				–		1.4194	–	1.0002	–	1.0472
Lognormal Standard Deviation, β_D				–		0.0443	–	0.0222	–	0.0232

369

APPENDIX D   COMPARATIVE INSTRUMENTATION VERIFICATION

D.1 GENERAL

In order to verify the reliability of the test setup using strain gages and linear variable differential transformer (LVDT) transducers for inferring moment and shear load distribution factors (LDFs), various types of instrumentation were installed on the Riverside Bridge together with other sensors (loads cells, string potentiometers, and accelerometers) to measure the bridge structural response during a series of static and dynamic tests. By comparing the test results from different types of instrumentation, the research team was able to evaluate the reliability of strain gages and LVDTs to be deployed for field monitoring the US 69 Bridge. Also, static cyclic tests and dynamic tests on two types of bearing pads with different geometric dimensions were conducted to demonstrate that the rubber bearing pads at the supports exhibit linear elastic behavior for the vehicular loading range. Therefore, shear LDFs were determined at the US 69 Bridge by measuring and comparing relative deformations of the bearing pads at the north end bearing seats.

D.2 BEARING PAD TEST

With the purpose of evaluating the load-displacement behavior of bearing pads during vehicular loading, a series of static cyclic tests and dynamic tests on two sizes of bearing pads (18 in. by 9 in. and 9 in. by 9 in.) were conducted using a 500 kips capacity Materials Testing System (MTS) machine in the TAMU High Bay Structural and Materials Testing Laboratory. A steel plate was placed on top of the bearing pad to apply a uniform axial load from the MTS machine. Two external LVDTs were attached on opposite sides to measure the bearing pad deformation during the loading process. Both load-controlled and displacement-controlled cyclic tests were utilized. For the displacement-controlled case, the target displacement was monitored using the actuator LVDT. Given that dead load caused by the self-weight of the bridge structure is constantly applied to the bearing pad in an actual bridge structure, the cyclic load in the dynamic test starts from a specified value instead of zero. Figure D.1 shows the test setup for the two bearing pad sizes. Detailed information about the bearing pad test protocol including control type, load rate, and duration is listed in Table D.1.

Load-deformation curves for both bearing pads during selected static cyclic and dynamic load cases are shown in Figure D.2. The load-deformation curves in the figure show that deformation values obtained from the two LVDTs on either side were similar to each other

during the test process, indicating that the bearing pads withstood uniform pressure under the applied loading. The average value of the two instruments was used to analyze the data from the test. It is also clear that both types of bearing pads exhibited linear elastic behavior under the vehicular loading range. Therefore, it is reasonable to obtain the shear distribution factor by comparing the deformation of the bearing pad under each beam with LVDT measurements. The measured stiffness values for the 18 in. by 9 in. and 9 in. by 9 in. bearing pads are 6100 kips/in. and 1270 kips/in., respectively; and were used for the computational modeling analysis of the test bridge with bearing pads at both ends.

(a) 18 in. by 9 in. Bearing Pad   (b) 9 in. by 9 in. Bearing Pad

Figure D.1. Bearing Pad Test Setup.

Table D.1. Bearing Pad Test Protocol.

Description	Control Type	Target	No. of Cycles	Load Rate	Frequency (Hz)	Duration (s)
Static Cyclic 1	Load	70 kips/ 130 kips[1]	3	0.4 kips/s	–	325
Static Cyclic 2	Displacement	0.1 in.	3	0.0005 in./s	–	200
Dynamic 1[2]	Displacement	0.1 in.	60	–	0.25	240
Dynamic 2	Displacement	0.1 in.	60	–	0.5	120
Dynamic 3	Displacement	0.1 in.	60	–	1.0	60
Dynamic 4	Displacement	0.1 in.	60	–	2.0	30

[1] Target load: 70 kips and 130 kips for 9 in. by 9 in. and 18 in. by 9 in. bearing pads, respectively.
[2] Cyclic load range in dynamic test: 20–70 kips (9 in. by 9 in.) and 45–135 kips (18 in. by 9 in.).
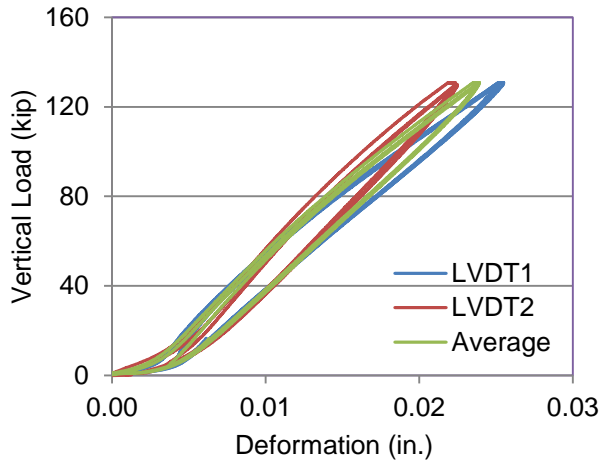
(a) Static Cyclic Test (18 in. by 9 in.)
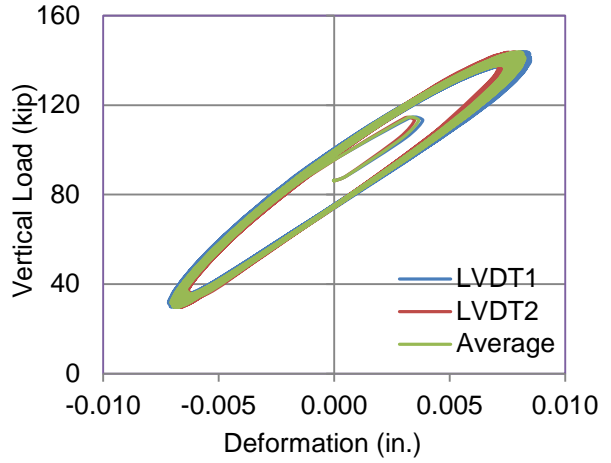
(b) Dynamic Test (18 in. by 9 in.)
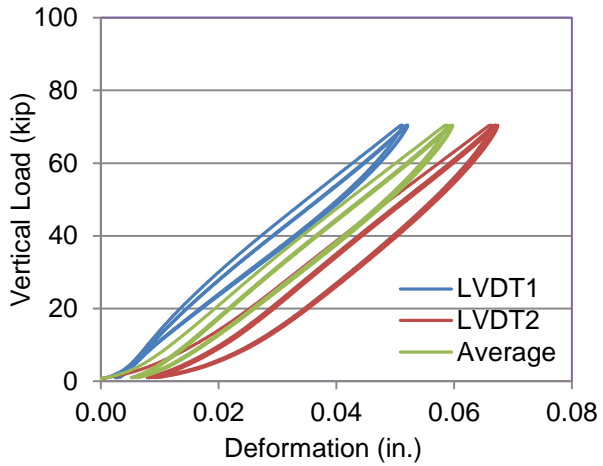
(c) Static Cyclic Test (9 in. by 9 in.)
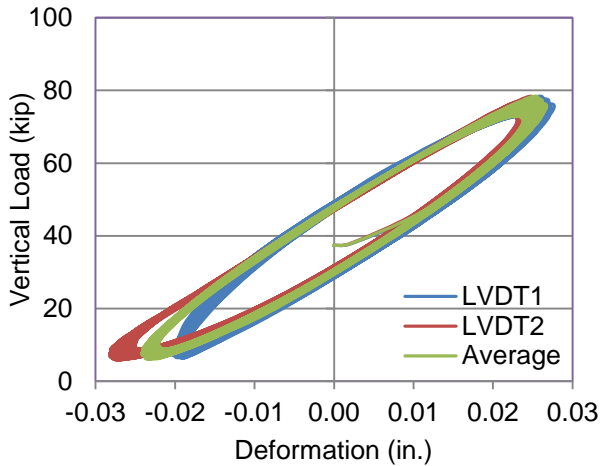
(d) Dynamic Test (9 in. by 9 in.)

Figure D.2. Bearing Pad Test Results.

D.3 INSTRUMENTATION VERIFICATION AT THE RIVERSIDE BRIDGE

D.3.1 Description of Instrumentation

In order to determine the feasibility and reliability of instrumentation to be applied at the US 69 Bridge, 12 strain gages and four LVDTs were also installed on the Riverside Bridge together with other sensors (load cells and string potentiometers) to measure the structural response during the field test. By comparing test results obtained from different types of sensors, it is possible to evaluate the accuracy of the instrumentation method.

Strain gages were attached at the midspan of each slab beam to capture the strain value during the critical load case for moments. For the purpose of determining the neutral axis of the beam section and obtaining the moment curvature, strain values on both the deck and soffit surfaces were measured. Also, for Beam 1 and Beam 2 (Figure D.4), strain gages were attached near both edges on the bottom surface of slab beams to investigate the strain difference between the two sides of the slab beam.

To measure the bearing pad deformations, four LVDTs were attached to the abutment close to the north end support of each beam. In addition, 16 load cells, eight at each end of the bridge, were installed during the bridge construction. Those load cells provided accurate reaction forces, and experimental shear load distribution factors were easily obtained from the reaction forces. The information obtained from load cells provided a reference point to evaluate the reliability of LVDTs for measuring shear LDFs. In addition, a large number of string potentiometers were installed at the Riverside Bridge to obtain the deflection field during the test. Detailed information about the data acquisition system, channel numbers, and instrumentation labels used at the Riverside Bridge are listed in Table D.2. The labeling of all sensors is explained in Figure D.3. A plan view of instrumentation on the deck and soffit surfaces for the Riverside Bridge is shown in Figure D.4 and Figure D.5. A section view of the LVDT and strain gage arrangement is shown in Figure D.6. Figure D.7 shows the pictures of sensors installed at the bridge site.

Table D.2. Detailed Information for Strain Gages and LVDTs on Riverside Bridge.

Data Acquisition	Channel No.	Label	Instrument Type
Strain Book	CH17	SG1-4TC	PL60-11-3LT
	CH18	SG2-4TC	
	CH19	SG3-4TW	
	CH20	SG3-4TE	
	CH21	SG4-4TW	
	CH22	SG4-4TE	
	CH23	SG1-4BC	
	CH24	SG2-4BC	
WBK16-1	CH25	SG3-4BW	PL60-11-3LT
	CH26	SG3-4BE	
	CH27	SG4-4BW	
	CH28	SG4-4BE	
	CH29	L1-1B	Omega
	CH30	L2-1B	
	CH31	L3-1B	
	CH32	L4-1B	

Sensor Type

Top/Bottom
East/West

X#-#X

Beam No.
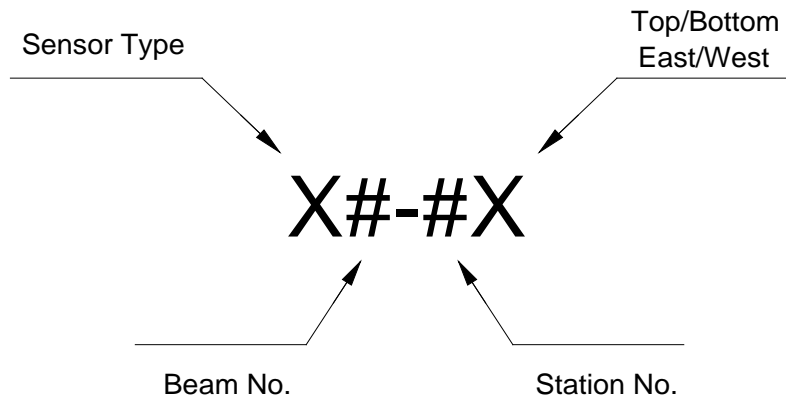
Station No.

Figure D.3. Instrumentation Labeling Notes.
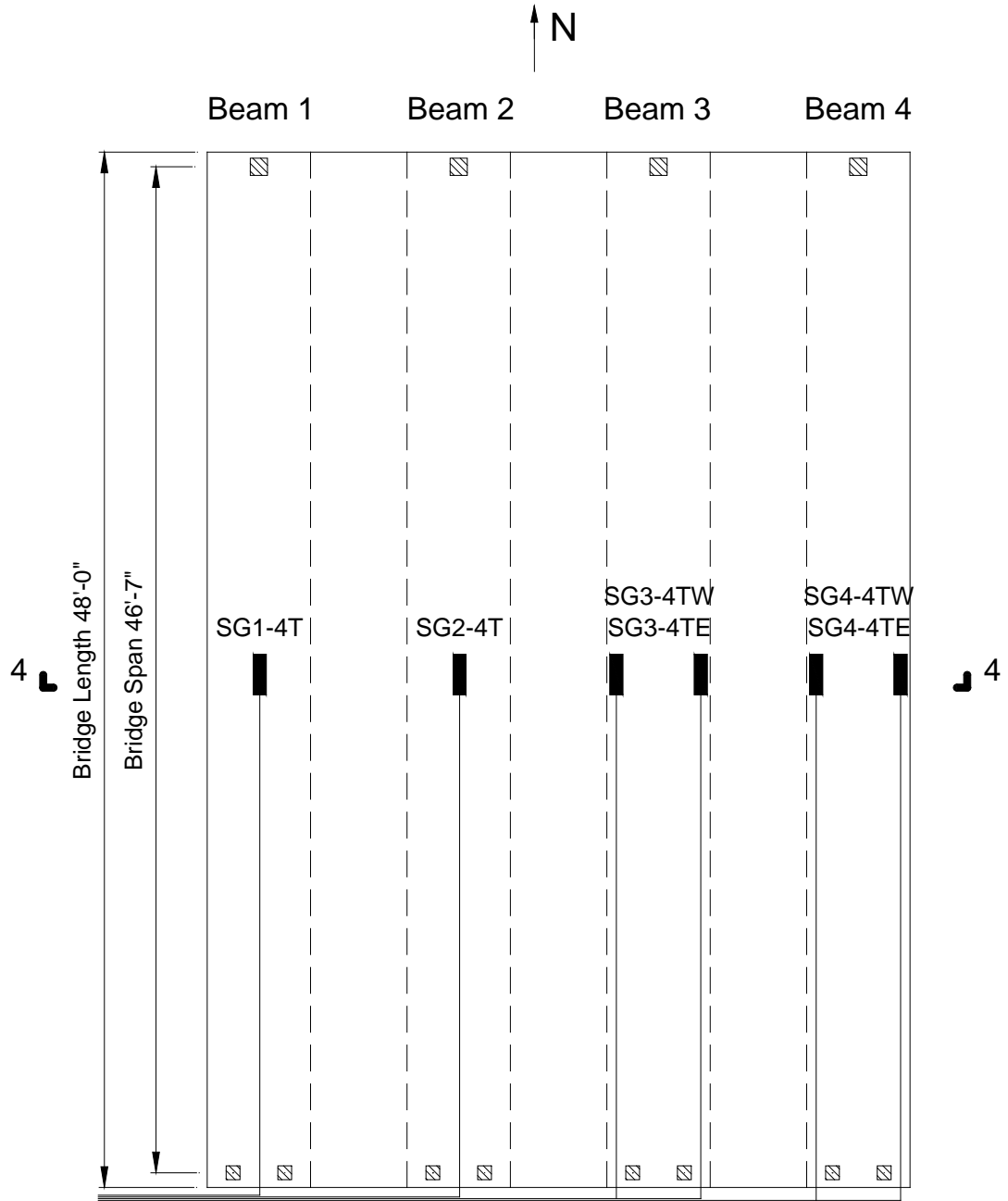
Figure D.4. Plan View of Instrumentation on Top Deck Surface of Riverside Bridge.
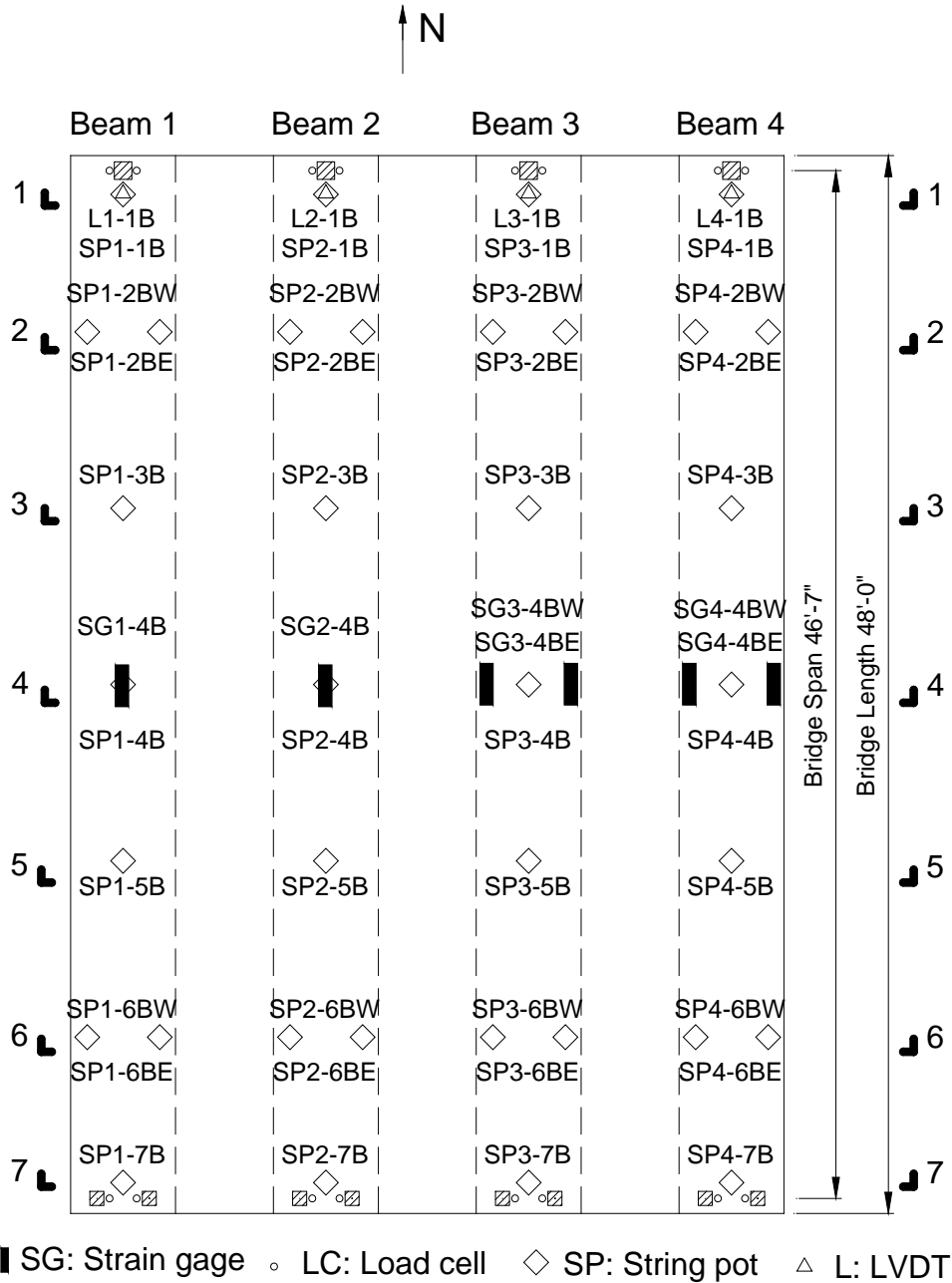
Figure D.5. View of Instrumentation on Bottom Surface of Riverside Bridge Beams.

(a) LVDT Locations, Section at Station 1-1

| Beam 1 | Beam 2 | Beam 3 | Beam 4 |
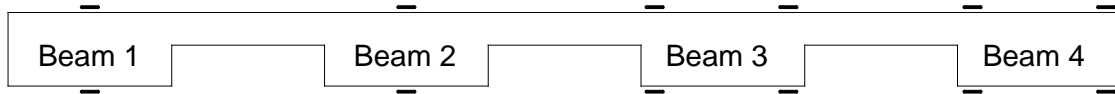
(b) Strain Gage Locations, Section at Station 4-4

Figure D.6. Transverse Section Views of LVDT and Strain Gage Arrangements.

(a) Load Cells and LVDT   (b) Strain Gage and String Potentiometer

Figure D.7. Installed Sensors on Riverside Bridge.

D.3.2 Verification Results

Two types of vehicles (dump truck and water tanker) were utilized during the Riverside Bridge test. Detailed information about the test protocol and vehicle alignments for Riverside Bridge testing is provided in Chapter 4. By analyzing the data from the strain gage readings, it was found that the strain values near the two bottom edges of the beam section are almost identical. Because the strain difference between the two sides is very small, the mean value was utilized for further analysis. Therefore, only one strain gage was attached at the center of the beam for the US 69 Bridge test.

By using strain values at the bottom surface and bearing pad deformations, moment and shear LDFs could be determined. The detailed calculation procedure is explained in Section 5.4.1. The comparison of moment LDFs calculated from strain gage data and deflection values in selected static load cases with two different vehicles are shown in Figure D.8. The figure shows that the experimental moment LDFs obtained from strain gages and string potentiometers are very close to each other, indicating that the strain gages are evidently suitably reliable for general use.
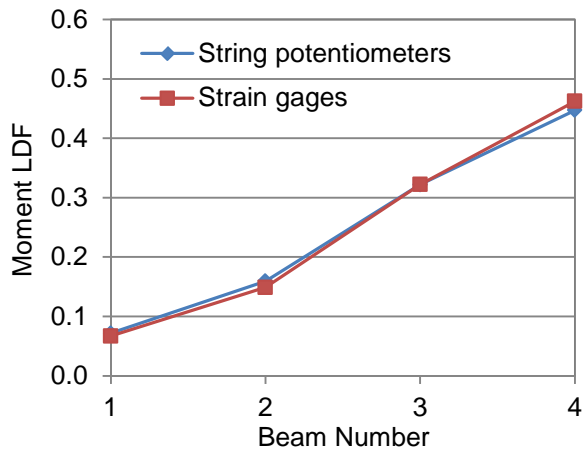
The comparison of experimental shear LDFs computed from LVDT values and load cell data in selected static load cases with two different vehicles are shown in Figure D.9. As the figure shows, there are some differences between the shear LDFs obtained from the LVDTs and load cells, but the LVDT data tends to give conservative results when there is a difference. In general, the LVDT measurements of the bearing pads provided an indication of the relative shear load sharing between the slab beams. This instrumentation was later included in the field monitoring of the US 69 Bridge.
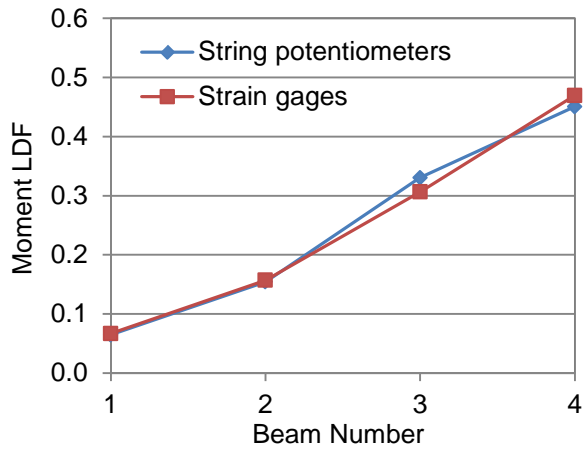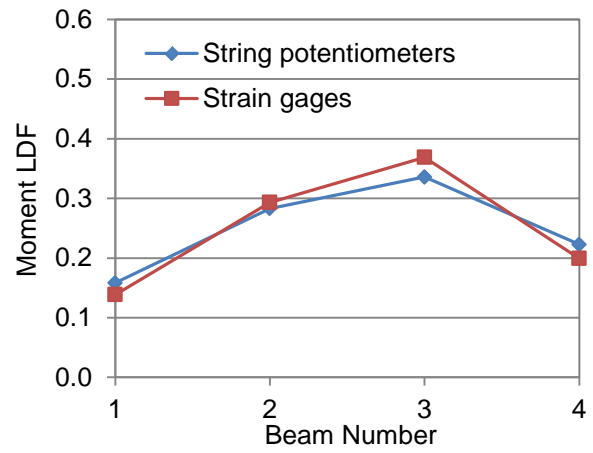
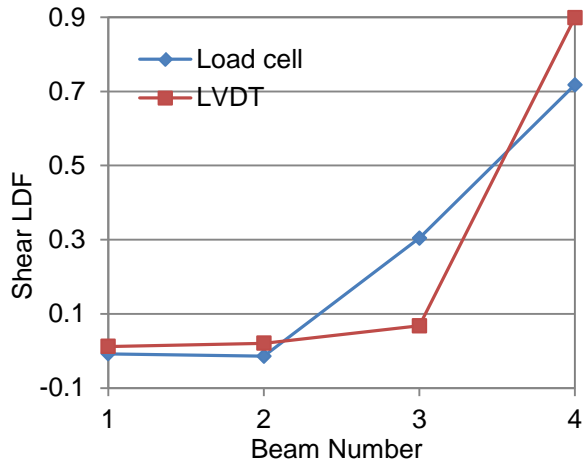(a) Dump Truck (Alignment 1)
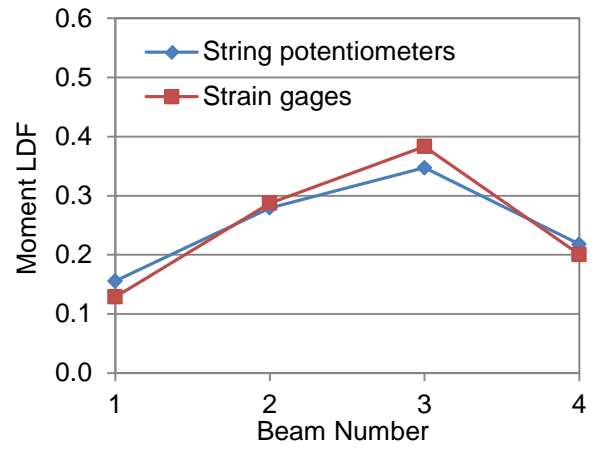
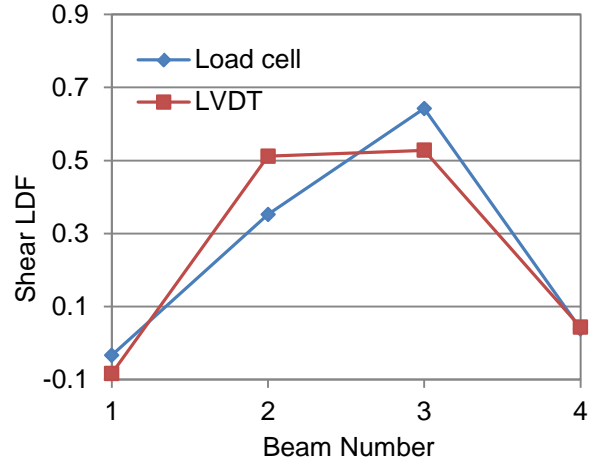(b) Dump Truck (Alignment 2)

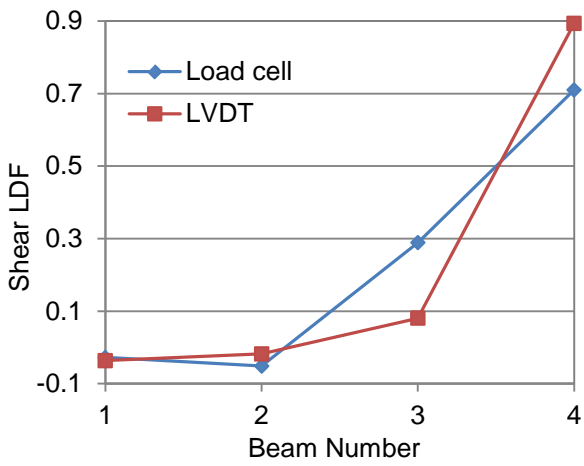(c) Water Tanker (Alignment 1)

(d) Water Tanker (Alignment 2)

Figure D.8. Comparison of Experimental Moment LDFs for Riverside Bridge.
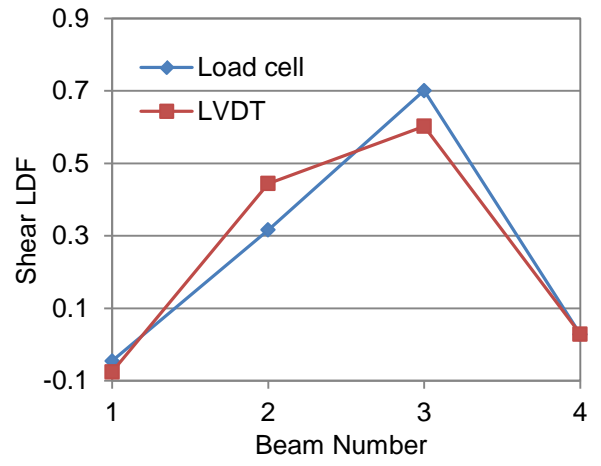
(a) Dump Truck (Alignment 1)

(b) Dump Truck (Alignment 2)

(c) Water Tanker (Alignment 1)

(d) Water Tanker (Alignment 2)

Figure D.9. Comparison of Experimental Shear LDFs for Riverside Bridge.

D.4 FINDINGS FROM THE INSTRUMENTATION EVALUATION

Various types of instrumentation (load cells, strain gages, LVDTs, and string potentiometers) were utilized in the Riverside Bridge test. The following lessons were learned from both laboratory and field testing. The instrumentation plan for the US 69 Bridge was then designed based on these findings and the actual site conditions.

1. The laboratory test showed that the bearing pads exhibit linear elastic behavior under the vehicular loading range.

2. Strain gages can reliably capture the moment LDFs and can be used for field monitoring of the US 69 Bridge.

3. LVDTs provide an indication of the shear distribution among slab beams but are not as accurate as the load cells.

4. String potentiometers are robust sensors to obtain the bridge deflection field and can be used to field test the US 69 Bridge.

APPENDIX E   SUPPLEMENT TO REPORT: DRAWING SET FOR

RIVERSIDE BRIDGE (CD)